Using Earth Deformation Caused by Surface Mass Loading to Constrain the Elastic Structure of the Crust and Mantle

Thesis by

Hilary Rose Martens

In Partial Fulfillment of the Requirements

for the Degree of

Doctor of Philosophy

California Institute of Technology

Pasadena, California

2016

Defended 8 March 2016

Hilary Rose Martens

ORCID: 0000-0003-2860-9013

TO MY SISTER, EMILY

Acknowledgments

This thesis would not have been possible without support, inspiration, and guidance from many colleagues, mentors, friends, and family. Since I have limited space with which to express my gratitude, suffice to say that the immeasurable contributions of countless individuals have not gone unnoticed and are deeply appreciated.

First of all, I thank my primary research adviser, Professor Mark Simons, for introducing me to interesting topics in geodesy and surface mass loading. Despite the inevitable challenges of research, Mark provided me with consistent motivation and encouragement throughout the five years of this project. He believed in the value of our work, even when I failed to see the value in it myself at times. I am grateful to have had the opportunity to learn from Mark's tremendous expertise and scientific creativity, particularly on the subject of geophysical inverse problems.

I am also deeply indebted to my honorary adviser, mentor, and friend, Professor Luis Rivera of the University of Strasbourg, for his extraordinary kindness and generosity. Through innumerable hours of patient instruction, Luis shared with me his expert knowledge of Earth deformation and numerical modeling, which shaped a significant portion of my thesis research and led to the development of our software suite, `LoadDef`. Luis has an extraordinary ability to distill difficult concepts into a fundamental form and to convey the information clearly and coherently. I am grateful for his support and continually inspired by his positivity, modesty, and passion for science.

In addition, I appreciate the ongoing support of my thesis advisory committee: Jennifer Jackson, Michael Gurnis, and Victor Tsai. Susan Owen of the Jet Propulsion Laboratory graciously mentored me on application-specific methods of GPS data processing. Duncan Agnew, Richard Ray, Takeo Ito, Jean-Paul Boy, and Shailen Desai, among others, contributed substantially to my understanding of ocean tidal loading and related phenomena.

Prior to Caltech, I benefited greatly from the mentorship of dedicated research advisers

who laid the foundation for my doctoral work: Bob White (Cambridge University), Geraint Jones (University College London), Andrew Coates (Mullard Space Science Laboratory), and Daniel Reisenfeld (University of Montana). Moreover, I thank the Marshall Aid Commemoration Commission for providing academic, personal, and financial support during my studies in the United Kingdom as well as the staff and donors of the Davidson Honors College for facilitating my academic and research pursuits as an undergraduate student at the University of Montana.

I am grateful to my friends and colleagues who helped me to find balance in life over the years, including through music, outdoor adventures, coffee chats, and traveling. I also thank the Caltech Residence Life staff, students of Ruddock House, and the residents of Marks and Braun for welcoming me into their communities. Serving as a Resident Associate has been a most meaningful experience for me during the past four years.

In its early stages, this research was supported by the National Science Foundation under grant number DGE-1144469. Subsequent support from the NASA Earth and Space Science Fellowship commenced in September 2014 under grant number NNX14AO04H and from the National Science Foundation Geophysics Program under grant number EAR-1417245.

Finally, I wholeheartedly thank my family for their unconditional love and support. I especially thank my grandparents for always believing in me, as well as my parents, Roger and Barbara Martens, my sister, Emily, and my partner, Juerg Schuler, for remaining by my side every step of the way.

Abstract

Surface mass loads come in many different varieties, including the oceans, atmosphere, rivers, lakes, glaciers, ice caps, and snow fields. The loads migrate over Earth's surface on time scales that range from less than a day to many thousand years. The weights of the shifting loads exert normal forces on Earth's surface. Since the Earth is not perfectly rigid, the applied pressure deforms the shape of the solid Earth in a manner controlled by the material properties of Earth's interior. One of the most prominent types of surface mass loading, ocean tidal loading (OTL), comes from the periodic rise and fall in sea-surface height due to the gravitational influence of celestial objects, such as the moon and sun. Depending on geographic location, the surface displacements induced by OTL typically range from millimeters to several centimeters in amplitude, which may be inferred from Global Navigation and Satellite System (GNSS) measurements with sub-millimeter precision. Spatiotemporal characteristics of observed OTL-induced surface displacements may therefore be exploited to probe Earth structure. In this thesis, I present descriptions of contemporary observational and modeling techniques used to explore Earth's deformation response to OTL and other varieties of surface mass loading. With the aim to extract information about Earth's density and elastic structure from observations of the response to OTL, I investigate the sensitivity of OTL-induced surface displacements to perturbations in the material structure. As a case study, I compute and compare the observed and predicted OTL-induced surface displacements for a network of GNSS receivers across South America. The residuals in three distinct and dominant tidal bands are sub-millimeter in amplitude, indicating that modern ocean-tide and elastic-Earth models well predict the observed displacement response in that region. Nevertheless, the sub-millimeter residuals exhibit regional spatial coherency that cannot be explained entirely by random observational uncertainties and that suggests deficiencies in the forward-model assumptions. In particular, the discrepancies may reveal sensitivities to deviations from spherically symmetric, non-rotating, elastic, and isotropic (SNREI) Earth structure due to the presence of the South American craton.

Published Content and Contributions

* Figure 1.1 reproduced and modified with permission from Agnew (2015).

* Figure 8.6 reproduced and modified with permission from Williams & Penna (2011).

* The work described in Chapter 6 has been accepted for publication by *Journal of Geophysical Research*. The current reference is: Martens, H.R., L. Rivera, M. Simons, and T. Ito, 2016. The sensitivity of surface mass loading displacement response to perturbations in the elastic structure of the crust and mantle, *J. Geophys. Res. Solid Earth*, 121, doi:10.1002/2015JB012456. | H.R.M. co-wrote and implemented the software used to compute the load Love numbers, load Green's functions, and predicted load-induced surface displacements; generated the figures; analyzed the results; and wrote the manuscript.

* The work described in Chapter 7 has been published in *Geophysical Journal International*. The reference is: Martens, H.R., M. Simons, S. Owen, and L. Rivera, 2016. Observations of ocean tidal load response in South America from sub-daily GPS positions, *Geophys. J. Int.*, 205(3), doi:10.1093/gji/ggw087, pp. 1637–1664, Oxford University Press. | H.R.M. co-wrote and implemented the software used to compute the load Love numbers, load Green's functions, and predicted load-induced surface displacements; processed the Global Positioning System (GPS) data; wrote and implemented the software to perform the tidal harmonic analysis of geodetic time series; generated the figures; analyzed the results; and wrote the manuscript.

Contents

List of Figures

List of Tables

1

Tidal Theory

1.1 Introduction and Motivation

Gravitational forcing by the moon and sun deforms the solid Earth both directly through the gravitational potential (*body tides*) and indirectly through loading by the periodic redistribution of Earth's oceans (*load tides*). Ocean tidal loading (OTL) refers to the process by which tidally redistributed seawater exerts a normal force on Earth's surface. The material properties of the crust and upper mantle govern the flexural response of the solid Earth to the weight of the additional water; thus, the OTL response signal, contained within all geodetic measurements, may be exploited to explore Earth's interior structure.

Whereas the spatial distribution of the body-tide response generally follows that of the equilibrium tide derived directly from the gravitational potential, ocean tides exhibit a complex spatial pattern due to interactions with continental boundaries and bathymetry (Jentzsch, 1997). Thus, whereas body tides are long wavelength phenomena that sample a very large-scale average of Earth structure (e.g., Farrell, 1972a; Latychev et al., 2009), ocean tidal loads are shorter wavelength features that probe Earth's material properties at finer spatial scales (e.g., Farrell, 1972a; Baker, 1984; Ito & Simons, 2011; Agnew, 2015; Bos et al., 2015). Constraints on Earth's interior properties derived from surface mass loading (SML) provide an independent means of testing scaling laws and assumptions commonly adopted in seismology, rejecting existing proposed Earth models that are inconsistent with the geodetic observations (e.g., Ito & Simons, 2011; Bos et al., 2015), and addressing outstanding questions in geophysics, such as the long-term stability of continental cratons against tectonic deformation (e.g., Jordan, 1978).

Although the concept of using tidal displacements to probe the Earth's interior emerged several decades ago (Takeuchi, 1950; Longman, 1962; Farrell, 1972a), early attempts to

implement the theory using gravity, strain and tilt measurements were limited in effectiveness due to insufficient spatial coverage and high sensitivities to local variations in material properties (Baker, 1984; Agnew, 2015). Modern Global Navigation Satellite System (GNSS) receivers do not suffer from the same sparsity or sensitivity constraints and record Earth's response to OTL with sub-millimeter precision (e.g., Penna et al., 2015). Given the precision of modern GNSS observations (Blewitt, 2015), the rapid expansion of global and regional GNSS networks, and the accuracy of contemporary ocean-tide models (Stammer et al., 2014), the possibility of using observed OTL-induced surface displacements to investigate Earth's interior structure has become increasingly tractable.

The current chapter provides a basic introduction to tidal theory, including a derivation of the equilibrium tide and a decomposition of the tidal potential into individual harmonic terms. Ch. 2 reviews one of the most successful and widely used methods for extracting the amplitudes and phases of major tidal constituents from a displacement time series: harmonic analysis. Ch. 3 discusses the details of processing Global Positioning System (GPS) data for use in OTL-response analysis. Ch. 4 considers techniques used to model Earth's deformation response to surface mass loading. I first discuss the computational procedure for deriving load Love numbers and load Green's functions for spherically symmetric, nonrotating, elastic, and isotropic (SNREI) Earth models. I then document a strategy for convolving the load Green's functions with a spatially distributed load. Ch. 5 briefly describes methods that may be used to develop an inverse problem relating measured load-induced surface displacements to structural model parameters. In Ch. 6, I analyze the sensitivity of load-induced surface displacements to SNREI Earth structure. Ch. 7 presents a case study that explores observed and predicted OTL-induced surface displacements in South America. In Ch. 8, I provide some remarks on extending the methodology for predicting surface displacements induced by ocean tidal loading to surface displacements induced by variations in surface pressure from additional sources, such as the atmosphere and hydrosphere. Ch. 9 includes a brief summary and a short discussion on possible future directions in the field. The appendices provide additional data tables and figures, information about the GPS station network, and supplementary information about GPS data processing.

1.2 Tide-Generating Forces

According to Newton's law of universal gravitation, the force of gravity, F_g, on a test mass, m, is given by:

$$\overline{F}_g = \frac{G\,M\,m}{R^2}, \tag{1.1}$$

where G is the universal gravitational constant, M is the mass of the reference body, and R is the distance between the center of mass of the reference body and the center of mass of the test body.

Taking the sun as a reference body and the Earth as a test body, followed by the moon as a reference body and the Earth again as a test body, demonstrates that the gravitational force of the sun on the Earth is about 178 times greater than the gravitational force of the moon on the Earth. Thus, although the moon orbits the Earth, the Earth-moon system orbits the sun.

The moon, on the other hand, generates tidal disturbances that are more than twice as large as those due to the sun. Since the tides are created by gravitational forcing, and the sun exerts a greater gravitational pull on the Earth, the relatively large lunar tides might seem counterintuitive.

The key to resolving the apparent discrepancy lies in the definition of the tides as the periodic rise and fall in sea level (or deformation of the solid Earth) that results from differential, or unbalanced, gravitational forces throughout the Earth (e.g., Doodson & Warburg, 1941, Sec. 2.2). The differential forces arise because the Earth has a finite diameter over which the gravitational forces are distributed. In other words, the unequal distances between various points on and in the Earth with respect to the external attracting body lead to an unbalanced response to the gravitational forcing.

The Earth and moon, for example, revolve around a common center of mass known as the barycenter, generating a centrifugal force (in a non-inertial, rotating reference frame) that is always directed away from the center of revolution. Since the Earth revolves about the barycenter as a coherent body, the centrifugal force is the same everywhere inside and on

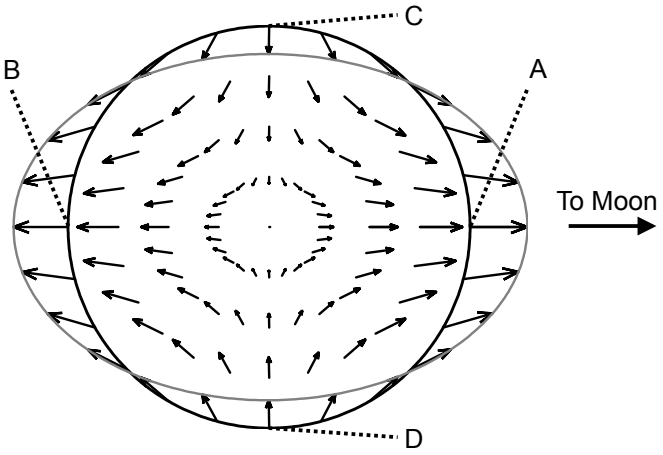

Figure 1.1: Schematic diagram depicting tidal forces, or accelerations, generated by a two-body system. For the Earth-Moon system, the largest arrows represent an acceleration of 1.14 μm s^{-2}. The elliptical outline illustrates a tide-generated equipotential surface (greatly exaggerated). The points A–D, indicated by the dashed lines, are referred to within the text. The diagram has been reproduced and modified with permission from Agnew (2015).

the surface of the Earth, and always directed away from the moon (e.g., Godin, 1972; Pugh, 1987; Pugh & Woodworth, 2014).

The centrifugal force due to revolution about the barycenter is perfectly balanced at the Earth's center of mass by the gravitational force due to the moon. At other locations in and on the Earth, however, the gravitational force varies, but the centrifugal force remains the same, thereby giving rise to differential forces. Fig. 1.1 illustrates the tidal forces generated by a two-body system.

Since the centrifugal force balances the lunar gravitational force at the center of mass of the Earth, the equation for the centrifugal force on a test mass, m, is given by (e.g., Pugh & Woodworth, 2014, Sec. 3.1):

$$\overline{F}_{\text{centrifugal}} = \frac{G\, M_L\, m}{R_{LE}^2}, \tag{1.2}$$

where M_L is the mass of the moon and R_{LE} is the distance between the center of mass of the moon and the center of mass of Earth. For a test mass located at the sub-lunar point (point A, Fig. 1.1), the centrifugal force would remain the same, but the gravitational force

would instead be given by (e.g., Pugh & Woodworth, 2014):

$$\overline{F}_{g_A} = \frac{G\,M_L\,m}{(R_{LE}-a)^2}, \tag{1.3}$$

where a is the radius of the Earth (assumed spherical). The difference between the gravitational and centrifugal forces yields the tide-generating force, $\overline{F}_{T_A}$, at point A:

$$\begin{aligned}
\overline{F}_{T_A} &= \overline{F}_{g_A} - \overline{F}_{\text{centrifugal}} \\
&= \frac{G\,M_L\,m}{(R_{LE}-a)^2} - \frac{G\,M_L\,m}{R_{LE}^2} \\
&= \frac{G\,M_L\,m}{R_{LE}^2}\left(\frac{1}{\left(1-\frac{a}{R_{LE}}\right)^2}-1\right) \\
&\approx \frac{G\,M_L\,m}{R_{LE}^2}\left(1+2\frac{a}{R_{LE}}\cdots-1\right) \\
&= \frac{2\,G\,M_L\,m\,a}{R_{LE}^3}.
\end{aligned} \tag{1.4}$$

Since $\frac{a}{R_{LE}}$ is only about $\frac{1}{60}$ (e.g., Pugh & Woodworth, 2014), I have only kept the first non-zero term in the expansion. Repeating the procedure for point B in Fig. 1.1 yields a vector of the same magnitude, but pointed in the opposite direction (i.e., away from the moon), which generates the familiar tidal bulges.

To examine what happens at the poles, I decompose the tidal forces, or tide-generating forces, into radial and tangential components relative to Earth's surface (e.g., Doodson & Warburg, 1941). Since R_{LE} is approximately equal to R_{LC}, where R_{LC} is the distance between point C and the center of mass of the moon, the tangential components of the force vectors effectively cancel. The unit vector situated at point C and directed along the path R_{LC}, however, also has a small surface-normal component, which is approximately equal to $-\frac{a}{R_{LE}}$ (e.g., Doodson & Warburg, 1941, Sec. 2.3). Thus, the tidal force at point C in Fig. 1.1 is given approximately by:

$$\overline{F}_{T_C} = -\frac{G\,M_L\,m\,a}{R_{LE}^3}. \tag{1.5}$$

Analogously, $\overline{F}_{T_D}$ is equivalent in magnitude but opposite in direction to $\overline{F}_{T_C}$.

It turns out that the components of the tidal forces directed tangential to the surface, otherwise known as the tidal **tractive** forces (e.g., Doodson & Warburg, 1941), are principally responsible for generating the tides (e.g., Doodson & Warburg, 1941; Boon, 2004). Computing the radial component of the force helps to elucidate this point. In particular, I examine the gravitational force due to the moon versus the gravitational force due to the Earth on a test mass at point A. The gravitational force due to the Earth is given by

$$\overline{F}_E = \frac{G\, M_E\, m}{a^2} \tag{1.6}$$

and the gravitational force due to the moon is given by

$$\overline{F}_L = \frac{G\, M_L\, m}{R_{LA}^2}, \tag{1.7}$$

where R_{LA} is the distance between point A and the center of mass of the moon. The force due to the moon relative to the force due to the Earth is therefore:

$$\overline{F}_L = \frac{M_L\, a^2}{M_E\, R_{LA}^2}\, \overline{F}_E \approx 3.4 \times 10^{-6}\, \overline{F}_E. \tag{1.8}$$

Thus, for a test mass on the surface of the Earth, the radial component of the gravitational force due to the moon is extremely small relative to Earth's gravity and does not play a significant role in the generation of the tides (e.g., Doodson & Warburg, 1941, Sec. 2.3). The tangential component of the tidal-force vector, however, does not face an opposing gravitational force, thereby allowing the water to move freely across Earth's surface. As illustrated by Fig. 1.2, the flow direction due to the tidal forcing is away from points C and D (Fig. 1.1) and towards points A and B. The solid Earth cannot move as freely as the liquid ocean water, but still responds to the forcing by material deformation.

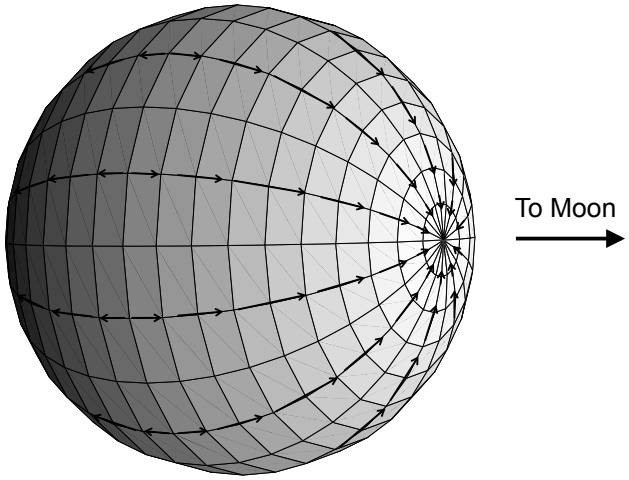

Figure 1.2: The surface-tangential components of the tidal force vectors resolved onto Earth's surface. The so-called tractive forces are unopposed by Earth's gravity and therefore principally responsible for generating the tidal response.

1.3 Tidal Potential

Computing the tide-generating forces is worthwhile for gaining some physical intuition about tides, but for more complete analyses of the tidal spectrum, deriving the tidal potential is preferable. The tidal potential is a scalar, rather than a vector, quantity and hence much easier to develop in computations. The gravitational potential at a point, P, on the Earth's surface due to the gravitational influence of an external body may be written as (e.g., Doodson, 1921; Melchior, 1983; Pugh & Woodworth, 2014, Sec. 3.2.1):

$$V = \frac{G\,M}{r}, \tag{1.9}$$

where G is the universal gravitational constant, M is the mass of the external body (e.g., the moon), and r is the distance between the observation point, P, and the center of mass of the external body. In geodesy, the convention is to define the gravitational potential as a positive quantity such that an increase in potential results in an increase in the height of the geoid (e.g., Pugh & Woodworth, 2014).

Using the geometry shown in Fig. 1.3, I apply the law of cosines to obtain a formula for r:

$$r^2 = a^2 + R^2 - 2aR\cos\theta \tag{1.10}$$

and use this to re-write the equation for the potential:

$$V = \frac{GM}{R}\left\{1 - 2\frac{a}{R}\cos\theta + \frac{a^2}{R^2}\right\}^{-\frac{1}{2}}. \tag{1.11}$$

The bracketed term is a generating function for Legendre polynomials (e.g., Boas, 1983, Sec. 12.5). Thus, the potential may be expanded as:

$$\begin{aligned} V &= \frac{GM}{R}\left\{P_0(\cos\theta) + \frac{a}{R}P_1(\cos\theta) + \frac{a^2}{R^2}P_2(\cos\theta) + \frac{a^3}{R^3}P_3(\cos\theta) + \cdots\right\} \\ &= \frac{GM}{R}\sum_{n=0}^{\infty}\left(\frac{a}{R}\right)^n P_n(\cos\theta), \end{aligned} \tag{1.12}$$

where $P_n(\cos\theta)$ are the Legendre polynomials. The first few Legendre polynomials are (e.g., Boas, 1983; Pugh & Woodworth, 2014):

$$\begin{aligned} P_0(\cos\theta) &= 1 \\ P_1(\cos\theta) &= \cos\theta \\ P_2(\cos\theta) &= \frac{1}{2}(3\cos^2\theta - 1) \\ P_3(\cos\theta) &= \frac{1}{2}(5\cos^3\theta - 3\cos\theta). \end{aligned}$$

The first term in Eq. 1.12 is constant-valued and does not generate a force. The second term represents a uniform force in the direction of $\overline{\mathrm{OC}}$, and therefore does not generate a tidal effect. The third term, in contrast, produces the largest tidal effect (e.g., Pugh & Woodworth, 2014). Higher-degree terms (beyond the third term) are sometimes neglected, since the potential is proportional to $\left(\frac{a}{R}\right)^n$, where n represents the spherical harmonic degree (Pugh & Woodworth, 2014). For the moon, $\frac{a}{R} \approx \frac{1}{60}$, and for the sun, $\frac{a}{R} \approx 4.3 \times 10^{-5}$. Contributions to the tidal potential therefore drop off rapidly with increasing n. Note that, even though the sun is much more massive than the moon, the sun is also much further away. Since the

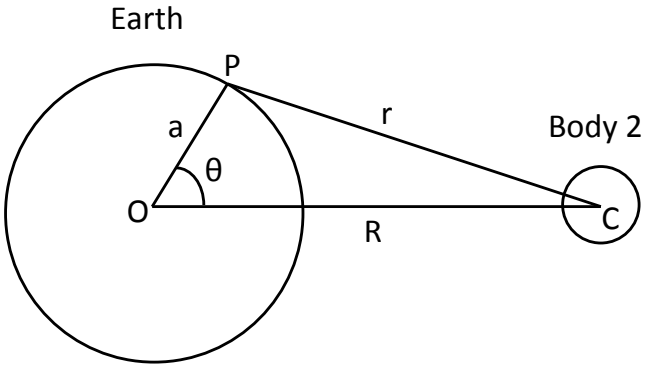

Figure 1.3: Schematic diagram depicting the geometry used to construct the gravitational potential observed at point P on the Earth due to the gravitational forcing imposed by a secondary body, "Body 2." Body 2 is typically the moon or sun, but may be any external body, such as another planet.

magnitude of the potential drops off as $\frac{M}{R^{n+1}}$, it is not necessary to expand the potential for the sun to as high of a degree as for the moon. In the case of the second-degree expansion, for example, $\frac{M_S}{R_S^3} = 0.46\frac{M_L}{R_L^3}$, where M_S is the mass of the sun, M_L is the mass of the moon, and R_S and R_L are the distances between the center of mass of the Earth and the sun and moon, respectively. Furthermore, it is generally not necessary for practical purposes to expand the potential for either body beyond the third- or fourth-degree (e.g., Cartwright & Taylor, 1971).

Focusing on the degree-2 expansion, the tide-generating potential, V_T, may be written as:

$$V_T = \frac{1}{2}GM\frac{a^2}{R^3}(3\cos^2\theta - 1). \tag{1.13}$$

This equation, however, is not very useful, since θ and R are complicated functions of the astronomical ephemeris and P is an arbitrary point on the Earth's surface. Fortunately, the angle between $\overline{\mathrm{OP}}$ and $\overline{\mathrm{OC}}$ (i.e., θ) may be related to the astronomical ephemeris using spherical trigonometry. For the Earth-moon system, θ depends on the declination angle of the moon north of the equator, d_L; the latitude of point P (positive north), ϕ_P; and the hour angle of the moon, C_L. The lunar hour angle is the difference in longitude between

the meridian of point P and the meridian of the sub-lunar point. The spherical trigonometric formula relating these quantities is (e.g., Doodson, 1921; Doodson & Warburg, 1941; Schureman, 1971; Pugh & Woodworth, 2014):

$$\cos\theta = \sin\phi_P \sin d_L + \cos\phi_P \cos d_L \cos C_L. \tag{1.14}$$

As such,

$$\begin{aligned} \cos^2\theta &= \sin^2\phi_P \sin^2 d_L + \cos^2\phi_P \cos^2 d_L \cos^2 C_L + \\ &\quad 2\sin\phi_P \sin d_L \cos\phi_P \cos d_L \cos C_L. \end{aligned} \tag{1.15}$$

Using the trigonometric identity

$$\sin 2u = 2\sin u \cos u, \tag{1.16}$$

Eq. 1.15 simplifies to:

$$\begin{aligned} \cos^2\theta &= \sin^2\phi_P \sin^2 d_L + \cos^2\phi_P \cos^2 d_L \cos^2 C_L + \\ &\quad \frac{1}{2}\sin 2\phi_P \sin 2d_L \cos C_L. \end{aligned} \tag{1.17}$$

To reduce the order of terms in $\cos C_L$, I use

$$\cos^2 C_L = \frac{1}{2}(\cos 2C_L + 1) \tag{1.18}$$

to re-arrange Eq. 1.17, which results in:

$$\begin{aligned} \cos^2\theta &= \sin^2\phi_P \sin^2 d_L + \cos^2\phi_P \cos^2 d_L \left(\frac{1}{2}(\cos 2C_L + 1)\right) + \\ &\quad \frac{1}{2}\sin 2\phi_P \sin 2d_L \cos C_L, \\ &= \sin^2\phi_P \sin^2 d_L + \frac{1}{2}\cos^2\phi_P \cos^2 d_L \cos 2C_L + \\ &\quad \frac{1}{2}\cos^2\phi_P \cos^2 d_L + \frac{1}{2}\sin 2\phi_P \sin 2d_L \cos C_L. \end{aligned} \tag{1.19}$$

Following (Pugh & Woodworth, 2014), the trigonometric identity

$$\cos^2 u = 1 - \sin^2 u \tag{1.20}$$

may be used to re-write Eq. 1.19 as:

$$\begin{aligned}
\cos^2\theta &= \sin^2\phi_P \sin^2 d_L + \frac{1}{2}\cos^2\phi_P \cos^2 d_L \cos 2C_L + \\
&\quad \frac{1}{2}(1-\sin^2\phi_P)(1-\sin^2 d_L) + \frac{1}{2}\sin 2\phi_P \sin 2d_L \cos C_L, \\
&= \sin^2\phi_P \sin^2 d_L + \frac{1}{2}\cos^2\phi_P \cos^2 d_L \cos 2C_L + \\
&\quad \frac{1}{2}(1-\sin^2\phi_P - \sin^2 d_L + \sin^2\phi_P \sin^2 d_L) + \\
&\quad \frac{1}{2}\sin 2\phi_P \sin 2d_L \cos C_L \\
&= \frac{1}{2}\cos^2\phi_P \cos^2 d_L \cos 2C_L + \\
&\quad \frac{1}{2}(1-\sin^2\phi_P - \sin^2 d_L + 3\sin^2\phi_P \sin^2 d_L) + \\
&\quad \frac{1}{2}\sin 2\phi_P \sin 2d_L \cos C_L \\
&= \frac{3}{2}\sin^2\phi_P \sin^2 d_L + \frac{1}{2}\cos^2\phi_P \cos^2 d_L \cos 2C_L + \\
&\quad \frac{1}{2}(1-\sin^2\phi_P - \sin^2 d_L) + \frac{1}{2}\sin 2\phi_P \sin 2d_L \cos C_L \\
&= \frac{1}{3} + \frac{3}{2}\left(\sin^2\phi_P - \frac{1}{3}\right)\left(\sin^2 d_L - \frac{1}{3}\right) + \\
&\quad \frac{1}{2}\cos^2\phi_P \cos^2 d_L \cos 2C_L + \frac{1}{2}\sin 2\phi_P \sin 2d_L \cos C_L.
\end{aligned} \tag{1.21}$$

Eq. 1.21 can then be substituted into Eq. 1.13 to obtain a formula for the lunar tide-generating potential, V_L, in terms of the astronomical ephemeris (e.g., Doodson, 1921; Pugh, 1987; Pugh & Woodworth, 2014):

$$\begin{aligned}
V_L &= \frac{3}{2} ga \frac{M_L}{M_E}\left(\frac{a}{R}\right)^3 \left\{ \frac{3}{2}\left(\sin^2 d_L - \frac{1}{3}\right)\left(\sin^2\phi_P - \frac{1}{3}\right) + \right. \\
&\quad \left. \frac{1}{2}\sin 2d_L \sin 2\phi_P \cos C_L + \frac{1}{2}\cos^2 d_L \cos^2\phi_P \cos 2C_L \right\},
\end{aligned} \tag{1.22}$$

where M_L is the mass of the moon and I have made use of the relationship

$$G = \frac{ga^2}{M_E}, \tag{1.23}$$

where M_E is the mass of the Earth and g is the gravitational acceleration at Earth's surface.

This formulation provides the foundation for a development of the equilibrium tide, which is equivalent to the tidal equipotential on a perfectly rigid Earth (e.g., Agnew, 2015). Note, however, that Eq. 1.22 is only of second-degree (i.e., spherical harmonic degree $n = 2$), though for practical purposes the potential is typically expanded to at least the third- or fourth-degree for the moon and at least second- or third-degree for the sun (e.g., Cartwright & Taylor, 1971; Cartwright & Edden, 1973; Hartmann & Wenzel, 1995).

Furthermore, Eq. 1.22 does not account for the flattening of the Earth due to rotation or other distortions of the geoid (e.g., Cartwright & Taylor, 1971). Accounting for the shape of the geoid introduces higher-order terms into the development of the tidal potential (e.g., Hartmann & Wenzel, 1995; Roosbeek, 1996, Sec. 4.5), but the effect is apparently small: $\sim$1.8 ngal for lunar tidal gravity (Roosbeek, 1996). The tidal potential catalogues developed by Doodson (1921), Cartwright & Taylor (1971), and Cartwright & Edden (1973), for example, were not adjusted to account for the secondary effects that arise due to the non-spherical shape of the geoid.

1.4 Equilibrium Tide Formulation

1.4.1 Direct Mathematical Approach

Much of the following development has been reproduced from Pugh (1987) and Pugh & Woodworth (2014), but may also be found in other sources dating back to the cardinal works on tidal harmonic analysis by Darwin (1898) and Doodson (1921) in the late 19th and early 20th centuries.

The **equilibrium tide**, or the height of an ideal ocean that is in perfect equilibrium with the tidal forcing (assuming negligible self-attraction effects) (e.g., Schureman, 1971, Par. 88), is given by:

$$\xi = \frac{V_T}{g}, \tag{1.24}$$

which has units of length. Eq. 1.24 may be roughly derived by relating the gravitational

and tide-generating forces to the slope of the equilibrium sea surface (Pugh & Woodworth, 2014).

Combining Eq. 1.24 with Eq. 1.22, an expression for the degree-2 equilibrium tide due to the moon may be derived (e.g., Doodson, 1921; Melchior, 1983; Pugh & Woodworth, 2014, Sec. 3.2.2):

$$\xi_L(t) = \frac{a\,M_L}{M_E}\left[C_0(t)\left(\frac{3}{2}\sin^2\phi_P - \frac{1}{2}\right) + C_1(t)\sin 2\phi_P + C_2(t)\cos^2\phi_P\right], \quad (1.25)$$

where

$$C_0(t) = \left(\frac{a}{R_L(t)}\right)^3\left(\frac{3}{2}\ \sin^2 d_L(t)\ - \frac{1}{2}\right) \quad (1.26)$$

$$C_1(t) = \left(\frac{a}{R_L(t)}\right)^3\left(\frac{3}{4}\ \sin 2d_L(t)\ \cos C_L(t)\right) \quad (1.27)$$

$$C_2(t) = \left(\frac{a}{R_L(t)}\right)^3\left(\frac{3}{4}\ \cos^2 d_L(t)\ \cos 2C_L(t)\right). \quad (1.28)$$

Eq. 1.25 expresses the equilibrium tide in terms of the north latitude of the observation point P (ϕ_P) and three time-dependent coefficients, which vary with lunar declination (d_L), the distance between the center of mass of the Earth and moon (R_L), and the lunar hour angle (C_L).

For clarity, a general geodetic factor, G^*, may be defined:

$$G^* = \frac{3}{4}\frac{a\,g\,M_L}{M_E}\frac{a^3}{c^3}, \quad (1.29)$$

where M_L is the mass of the moon, M_E is the mass of Earth, g is the mean acceleration due to gravity at Earth's surface, a is the radius of the Earth (assumed spherical), and $\frac{1}{c}$ is the mean value of $\frac{1}{R_L}$ (e.g., Doodson, 1921; Melchior, 1983). Dropping the time-dependent notation and multiplying by g to convert tidal height back to gravitational potential, Eq. 1.25 may be re-written as (Doodson, 1921):

$$\xi_L^{\text{Degree}-2}\,g = V_L^{\text{Degree}-2} = \left(\frac{c}{R_L}\right)^3(G_0^*H_0 + G_1^*H_1 + G_2^*H_2), \quad (1.30)$$

Doodson's Geodetic Coefficients	
Symbol	Formula
Second Degree ($n = 2$)	
G_0^*	$\frac{1}{2}G^*(1 - 3\ \sin^2\phi_P)$
G_1^*	$G^*\ \sin(2\phi_P)$
G_2^*	$G^*\ \cos^2\phi_P$
Third Degree ($n = 3$)	
$G_0^{*\prime}$	$1.11803\ G^*\ \sin\phi_P(3 - 5\sin^2\phi_P)$
$G_1^{*\prime}$	$0.72618\ G^*\ \cos\phi_P(1 - 5\sin^2\phi_P)$
$G_2^{*\prime}$	$2.59808\ G^*\ \sin\phi_P\cos^2\phi_P$
$G_3^{*\prime}$	$G^*\ \cos^3\phi_P$
Fourth Degree ($n = 4$)	
$G_0^{*\prime\prime}$	$0.12500\ G^*\ (3 - 30\sin^2\phi_P + 35\sin^4\phi_P)$
$G_1^{*\prime\prime}$	$0.47346\ G^*\ \sin(2\phi_P)\ (3 - 7\sin^2\phi_P)$
$G_2^{*\prime\prime}$	$0.77778\ G^*\ \cos^2\phi_P(1 - 7\sin^2\phi_P)$
$G_3^{*\prime\prime}$	$3.07920\ G^*\ \sin\phi_P\cos^3\phi_P$
$G_4^{*\prime\prime}$	$G^*\ \cos^4\phi_P$

Table 1.1: The general geodetic factor $G^* = \frac{3}{4}\frac{a\,g\,M_L}{M_E}\frac{a^3}{c^3}$, where M_L is the mass of the moon, M_E is the mass of Earth, g is the mean acceleration due to gravity at Earth's surface, a is the radius of Earth (assumed spherical), and $\frac{1}{c}$ is the mean value of $\frac{1}{R_L}$. The numerical coefficients that precede G^* in the third- and fourth-degree coefficients are derived from the quantity $\frac{a}{c}$, which is approximately equivalent to the sine of the mean equatorial horizontal parallax (Doodson, 1921).

where

$$H_0 = \frac{2}{3} - 2\sin^2 d_L \tag{1.31}$$

$$H_1 = \sin 2d_L\ \cos C_L \tag{1.32}$$

$$H_2 = \cos^2 d_L\ \cos 2C_L, \tag{1.33}$$

and G_0^*, G_1^*, and G_2^* are Doodson's **Geodetic Coefficients**, defined in Table 1.1.

Additional details regarding the expansion of the equilibrium tide may be found in, e.g., Cartwright & Taylor (1971); Doodson (1921); Doodson & Warburg (1941), Ch. 4; Godin (1972), pg. 16-27 and Appendix 1; Pugh (1987), Chs. 3 and 4; and Pugh & Woodworth (2014). Note that, for solar terms, $G_S^* = 0.46\ G^*$. A short discussion of equilibrium tide catalogues will be provided later in this chapter (Sec. 1.5).

From Eq. 1.25 for the equilibrium tide, along with its time-dependent coefficients, note

that each coefficient depends on the lunar hour angle as a cosine term with a different frequency: the $C_2(t)$ coefficient includes a $\cos(2C_L(t))$ term, the $C_1(t)$ coefficient includes a $\cos(C_L(t))$ term, and the $C_0(t)$ coefficient does not include a cosine term with dependence on the hour angle. The response of the equilibrium tide to astronomical forcing is separated into these three coefficients, which vary in spherical harmonic mode as a result of their dependence on the hour angle (e.g., Pugh & Woodworth, 2014).

Tides that do not depend on the hour angle (i.e., coefficient $C_0(t)$) are known as **long-period** tides and are characterized by a **zonal** spherical harmonic function (i.e., $n = 2$, $m = 0$, where m is the spherical harmonic order) (e.g., Melchior, 1983, Ch. 1). Tidal signals proportional to $\cos(C_L(t))$ (i.e., $C_1(t)$), characterized by a frequency of one cycle per day, are known as **diurnal** tides and are represented by a **tesseral** spherical harmonic function (i.e., $n = 2$, $m = 1$). Tidal signals proportional to $\cos(2C_L(t))$ (i.e., $C_2(t)$), characterized by a frequency of two cycles per day, are known as **semidiurnal** tides and are represented by a **sectorial** spherical harmonic function (i.e., $n = 2$, $m = 2$).

Note also the dependence of the coefficients on lunar declination. From the $\left(\frac{3}{2}\sin^2 d_L(t) - \frac{1}{2}\right)$ portion of the $C_0(t)$ term, it is clear that the long-period tides reach a maximum amplitude at the poles and zero amplitude at $\pm 35.27^\circ$ declination (e.g., Pugh & Woodworth, 2014, Sec. 3.2.2). The $C_1(t)$ term, which is proportional to $\sin 2d_L(t)$, also varies at twice the rate of variations in lunar declination, reaching a maximum amplitude at $\pm 45^\circ$ and a minimum amplitude at the equator and poles. The $C_2(t)$ term varies with $\cos^2 d_L(t)$; thus, semidiurnal tides reach a maximum amplitude at the equator and zero amplitude at the poles.

Similarly, the equilibrium tide depends on the latitude (positive north) of the observation point, ϕ_P. The long-period tides, proportional to $\sin^2 \phi_P$, reach maximum values at the poles. The diurnal tides, proportional to $\sin 2\phi_P$, are maximized at $\pm 45^\circ$ latitude. The semidiurnal tides, proportional to $\cos^2 \phi_P$, are maximized at the equator.

Plugging in average values for a, R_L, M_E, and M_L, the amplitude of the semidiurnal equilibrium tide is 0.27 m (54 cm peak-to-peak) at the equator (assuming $d_L = 0^\circ$).

To compute the equilibrium tide due to the sun, the variables d_L, M_L, and R_L in Eq. 1.25

Parameter Description	**Symbol**	**Temporal Evolution**
Lunar Hour Angle (radians)	C_L	$\lambda_P + (\omega_0 + \omega_3)t - \pi - A_L$
Solar Hour Angle (radians)	C_S	$\lambda_P + (\omega_0 + \omega_3)t - \pi - A_S$
Mean longitude of moon (°)	s	$277.02 + 481267.89T + 0.0011T^2$
Mean longitude of sun (°)	h	$280.19 + 36000.77T + 0.0003T^2$
Longitude of lunar perigee (°)	p	$334.39 + 4069.04T - 0.0103T^2$
Longitude of lunar ascending node (°)	N	$259.16 - 1934.14T + 0.0021T^2$
Longitude of perihelion (°)	p'	$281.22 + 1.72T + 0.0005T^2$
Spatiotemporal Variables		
Time in Julian centuries	T	$\frac{365(Y-1900)+(D-1)+i+HMS}{36525}$
Current year	Y	
Current day	D	
Current hour, minute, second	HMS	units of days
Leap year correction	i	integer part of (Y-1901)/4
East longitude of observation point P	λ_P	units of radians
Sidereal time at Greenwich Meridian	t	measured from First Point of Aries
Right Ascension of Moon/Sun	A_L/A_S	see text for equations

Table 1.2: Astronomical parameters used to describe the temporal variations of the moon and sun relative to the Earth (e.g., Pugh, 1987). Only six of the seven parameters listed are independent. The variables ω_0 and ω_3 represent angular speeds of the astronomical parameters, which are listed in Table 1.3. See also, e.g., Doodson (1921), Doodson & Warburg (1941), Schureman (1971), Melchior (1983), and Meeus (1998).

are replaced with d_S, M_S, and R_S, respectively, where d_S represents the solar declination, M_S is the mass of the sun, and R_S is the distance between the center of mass of the Earth and the center of mass of the sun. Furthermore, the hour angle, C_S, represents the angular separation between the sub-solar point and the observation point, P.

Earth-Sun System: The distance between the Earth and sun, R_S, is given by (e.g., Doodson & Warburg, 1941; Munk & Cartwright, 1966; Pugh, 1987; Pugh & Woodworth, 2014):

$$R_S = \frac{R_S^*}{1 + e_S \cos(h - p')}, \tag{1.34}$$

where e_S is the eccentricity of the Earth's orbit about the sun (≈0.0167504 from Munk & Cartwright (1966)), R_S^* is proportional to 1/(mean equatorial parallax) (Munk & Cartwright, 1966) or equal to the mean solar distance (Doodson & Warburg, 1941; Pugh, 1987; Pugh & Woodworth, 2014), and h and p' are defined in Table 1.2. Note that the mean equatorial

(solar) parallax, $8.79415''$ from Munk & Cartwright (1966), may be related to the mean earth-sun distance by:

$$\frac{6371\,\mathrm{km}}{\frac{1}{60}\frac{8.79415}{60}\frac{\pi}{180}} \approx 1.5 \times 10^8\,\mathrm{km}. \tag{1.35}$$

Additional tabulations of astronomical parameters can be found in Wenzel (1997) and Meeus (1998).

The right ascension for the sun, in equatorial coordinates, is (e.g., Pugh & Woodworth, 2014):

$$A_S = \lambda_S - \tan^2\left(\frac{\epsilon_S}{2}\right)\sin(2\lambda_S), \tag{1.36}$$

where

$$\lambda_S = h + 2e\sin(h - p') \tag{1.37}$$

and ϵ_S is the solar ecliptic latitude, or $\approx 23.452^\circ$ (Munk & Cartwright, 1966). The solar declination in terms of equatorial coordinates is then (e.g., Pugh & Woodworth, 2014):

$$d_S = \sin^{-1}(\sin(\lambda_S)\ \sin(\epsilon_S)). \tag{1.38}$$

Earth-Moon System: The distance between the Earth and moon, R_L, is given by (Pugh, 1987; Pugh & Woodworth, 2014):

$$R_L = \frac{R_L^*}{1 + e_L\cos(s - p) + \text{solar perturbations}}, \tag{1.39}$$

where e_L is the eccentricity of the moon's orbit about the Earth, which varies from 0.044 to 0.067, and R_L^* is the mean lunar distance. The right ascension for the moon is (e.g., Pugh & Woodworth, 2014):

$$A_L = \lambda_L - \tan^2\left(\frac{\epsilon_L}{2}\right)\sin(2\lambda_L), \tag{1.40}$$

where

$$\lambda_L = s + 2\ e\ \sin(s - p) + \text{solar perturbations}\ , \tag{1.41}$$

and

$$\epsilon_L = \sin^{-1}(\sin(\lambda_L - N)\ \sin(5^\circ 09')) \tag{1.42}$$

is the lunar ecliptic latitude. The lunar declination is given by:

$$d_L = \sin^{-1}(\sin(\lambda_L)\ \sin(\epsilon_L))\ . \tag{1.43}$$

Characteristics of the actual ocean tides turn out to be quite different from the ideal equilibrium tide due to complicated effects related to finite ocean depths, bathymetry, and continental boundaries.

1.4.2 Harmonic Decomposition Approach

Six independent parameters are necessary to describe the temporal variations of R, d, and C in the tidal potential for both the sun and moon. After careful consideration, Doodson (1921) selected six astronomical parameters that are well-suited to harmonic analysis and often used in practice (e.g., Foreman, 1977, Sec. 2.1.1):

$$\begin{aligned}
\tau &= \text{local mean lunar time,} \\
s &= \text{mean longitude of moon,} \\
h &= \text{mean longitude of sun,} \\
p &= \text{mean longitude of lunar perigee,} \\
N' &= -N\text{, where } N \text{ is the mean longitude of lunar ascending node,} \\
p' &= \text{mean longitude of perihelion.}
\end{aligned}$$

Local mean lunar time is typically measured relative to the Greenwich Meridian. The mean longitudes of the moon, sun, perigee, lunar ascending node, and perihelion are typically referenced to the mean vernal equinox of the date (Meeus, 1998; Pugh & Woodworth, 2014). Relationships describing how the astronomical parameters vary in time are provided in Table 1.2 as well as in the literature (e.g., Meeus, 1998). Time derivatives of the astronomical parameters yield angular speeds, which may be combined by integer sums and differences to compute the periods of individual tidal harmonics. The period of s, for example, is a sidereal month (27.32 days) and the period of h is a tropical year (365.24 days).

Note that τ is equivalent to C_L when referenced to the same observation point, which is typically set at the Greenwich Meridian. Furthermore, the two parameters have the same angular speed. Alternatively, the mean solar time, t, may be used in place of τ; the two parameters are related by other fundamental astronomical parameters: $\tau = t - s + h$ (e.g., Doodson, 1921).

The expression for the equilibrium tide may now be expanded into a series of harmonic terms. For example, I make use of Eq. 1.39 and Doodson's astronomical parameters to re-write Eq. 1.28 as (e.g., Pugh & Woodworth, 2014, Sec. 4.2.1):

$$\begin{aligned} C_2(t) &= \left[\left(\frac{a}{R_L^*}\right)^3 \frac{3}{4}\cos^2 d_L\right] [1 + e_L\ \cos(s-p)]^3\ \cos(2C_L) \\ &\approx \left[\left(\frac{a}{R_L^*}\right)^3 \frac{3}{4}\cos^2 d_L\right] \left[\cos(2\omega_0 t + 2h - 2s) + \frac{7}{2}e_L\ \cos(2\omega_0 t + 2h - 3s + p) + \right. \\ &\quad \left. \frac{1}{2}e_L\ \cos(2\omega_0 t + 2h - s - p + 180^\circ)\right], \end{aligned} \tag{1.44}$$

where e_L is the lunar eccentricity and I have kept only the lowest-degree terms. For the full expansion, one would need to substitute expressions for the declination in terms of the astronomical parameters as well. A more complete expansion of the equilibrium tide contains thousands of terms (infinite in a full expansion), but in practice, only a few dominant harmonics are essential. Equilibrium tide catalogues, expanded to include hundreds to thousands of tidal harmonics, may be found in the literature (e.g., Cartwright & Taylor, 1971; Cartwright & Edden, 1973; Hartmann & Wenzel, 1995).

The $C_2(t)$ term from the expansion of the equilibrium tide contains the semidiurnal tidal harmonics. The first harmonic term in Eq. 1.44, $\cos(2\omega_0 t + 2h - 2s)$, has an angular speed of $2(\omega_0 - \omega_2 + \omega_3)$, where ω_0 is the angular speed of C_S, ω_2 is the angular speed of s, and ω_3 is the angular speed of h. Table 1.3 lists the frequencies and periods of each astronomical parameter. Note that $2(\omega_0 - \omega_2 + \omega_3) = 0.5059$ rad/hour $= 28.9842^\circ$/hour, which is equivalent to $2\omega_1$, or twice the frequency of the mean lunar day. The tidal harmonic that arises from this combination of astronomical parameters is called the M_2 harmonic, by convention. The second harmonic term in Eq. 1.44, given the name N_2, has an angular

Angular Speeds of Astronomical Parameters					
	Period	Frequency	Angular Speed		
Parameter	(days)	(cycles/day)	Symbol	(rad/hour)	(°/hour)
Mean solar day	1.00	1.00	$\dot{C}_S = \dot{t}$	ω_0 = 0.26	σ_0=15.00
Mean lunar day	1.04	9.66E-1	$\dot{C}_L = \dot{\tau}$	ω_1 = 0.25	σ_1=14.49
Sidereal month	27.32	3.66E-2	$\dot{s}$	ω_2 = 9.58E-3	σ_2=0.55
Tropical year	365.24	2.74E-3	$\dot{h}$	ω_3 = 7.173E-4	σ_3=0.04
Lunar perigee	8.85 (years)	3.09E-4	$\dot{p}$	ω_4 = 8.03E-5	σ_4=4.6E-3
Lunar nodal regression	18.61 (years)	1.47E-4	$-\dot{N} = \dot{N}'$	ω_5 = 3.84E-5	σ_5=2.2E-3
Perihelion	20942 (years)	-	$\dot{p}'$	$\omega_6 \approx 0$	$\sigma_6 \approx 0$

Table 1.3: Angular speeds, or frequencies, of the astronomical parameters from Table 1.2. The angular speeds, ω, represent the mean rates of change, in radians per hour, of the astronomical parameters: C_S, C_L, s, h, p, N', p'. For units of degrees per hour, the angular speeds are denoted by σ. A dot above an astronomical parameter indicates differentiation with respect to time. Since the astronomical parameters vary in time with terms higher than first order, the angular speeds also change with time, albeit slowly (see text for details).

speed of $2\omega_0 + 2\omega_3 - 3\omega_2 + \omega_4 = 2\omega_1 - \omega_2 + \omega_4 = 0.4964$ rad/hour $= 28.4398°$/hour. Furthermore, the third harmonic term in Eq. 1.44, given the name L_2, has an angular speed of $2\omega_0 + 2\omega_3 - \omega_2 - \omega_4 = 2\omega_1 + \omega_2 - \omega_4 = 0.5154$ rad/hour $= 29.5286°$/hour. Note that the three harmonics differ in amplitude, which is modulated in this case by the lunar orbital eccentricity.

Recall that I have made many simplifying assumptions to arrive at the succinct form of Eq. 1.44. In reality, the tidal potential contains an infinite number of unique harmonics. A more rigorous expansion would account not only for changes in lunar perigee and hour angle, but also for variations in declination. Moreover, expressions for the astronomical parameters could be expanded to include higher order terms as well. Note also that this expansion can be done for both the moon and the sun (and planets, etc.) as well as for higher degrees of the gravitational potential (only second-degree has been developed here), which would eventually yield an extensive collection of tidal constituents.

Angular Speed: The general form for the angular speed, ω, of a given tidal harmonic, η, is (e.g., Pugh & Woodworth, 2014, Sec. 2.4.1):

$$\omega_\eta = \eta_a\,\omega_1 + \eta_b\,\omega_2 + \eta_c\,\omega_3 + \eta_d\,\omega_4 + \eta_e\,\omega_5 + \eta_f\,\omega_6, \tag{1.45}$$

where ω_1 to ω_6 are angular speeds, generally in rad/hour, derived from the lunar and solar ephemera. First-order approximations of the angular speeds are provided in Table 1.3. More precise values may be obtained by taking the first time derivatives of the astronomical parameters (Table 1.2). The coefficients η_a to η_f are small integer values that form the **Doodson number** for harmonic η. Distinct sets of integer coefficients (η_a through η_f) are used to determine unique sums and differences of the astronomical frequencies, which represent individual tidal harmonics in the expansion of the equilibrium tide (e.g., Doodson & Warburg, 1941; Pugh & Woodworth, 2014).

The M_2 harmonic, for example, has a Doodson number of [2 0 0 0 0 0]; thus, the M_2 tide has a frequency of $\omega_{M_2} = 2\omega_1 + 0\omega_2 + 0\omega_3 + ... = 0.5059$ rad/hour $= 28.9842^\circ$/hour. Note that it is not necessary to include ω_0, since ω_0 may be written in terms of other astronomical frequencies (i.e., $\omega_0 = \omega_1 + \omega_2 - \omega_3$). For a degree-2 expansion of the tidal potential, the coefficient η_a may only be 0, 1, or 2, representing the long-period, diurnal, and semidiurnal tidal **species**, respectively (e.g., Pugh & Woodworth, 2014, Sec. 4.2.1). The value of coefficient η_b defines the tidal **group** and the value of coefficient η_c defines the tidal **constituent**. Coefficients η_b through η_f generally range from -5 to +5. Values greater than two for coefficient η_a represent species at frequencies higher than semidiurnal, such as terdiurnal tides ($\eta_a = 3$), that arise from higher-order expansions of the tidal potential. The full set of six integer coefficients defines a tidal **harmonic**, also sometimes referred to as a tidal **argument**.

To make the connection back to the spherical harmonic expansion of the tidal potential, the tidal species coefficient, η_a, is equivalent to the spherical harmonic order, m. Some tidal harmonics arise from the second-degree ($n = 2$) expansion of the equilibrium tide, whereas others arise only from a higher-order expansion and are generally smaller in amplitude. As in spherical harmonics, the order m cannot exceed the degree n. Therefore, terdiurnal tides

Astronomical Frequencies to Higher Order			
Element	Frequency Formula (deg/hour)	Symbols	
Mean solar day	$1 * (360/24)$	ω_0	$\dot{C_S} = \dot{t}$
Mean lunar day	1 + ω_2 - ω_3	ω_1	$\dot{C_L} = \dot{\tau}$
Sidereal month	$[(481267.89 + 0.0022\,T)/36525]/24$	ω_2	$\dot{s}$
Tropical year	$[(36000.77 + 0.0006\,T)/36525]/24$	ω_3	$\dot{h}$
Lunar perigee	$[(4069.04 - 0.0206\,T)/36525]/24$	ω_4	$\dot{p}$
Lunar nodal regression	$-\{[(-1934.14 + 0.0042\,T)/36525]/24\}$	ω_5	$\dot{N'} = -\dot{N}$
Perihelion	$[(1.72 + 0.0010\,T)/36525]/24$	ω_6	$\dot{p'}$

Table 1.4: Astronomical frequencies in general form. The angular speeds, ω, represent the mean rates of change of the astronomical parameters: C_S, C_L, s, h, p, N', p'. Time derivates were taken of the astronomical parameters in Table 1.2 to derive the frequency formulae in column 2. T is in Julian centuries.

only manifest after an expansion to at least the third degree (e.g., Godin, 1972).

To avoid negative numbers in the six-digit set, Doodson added $+5$ to each of the integers η_b through η_f. With the arithmetic adjustment to the Doodson number, the angular speed must also be adjusted by subtracting $\omega_\eta = 5\ \omega_2 + 5\ \omega_3 + 5\ \omega_4 + 5\ \omega_5 + 5\ \omega_6$. Unadjusted Doodson numbers, which include negative values, are also common in the literature (e.g., Cartwright & Taylor, 1971; Godin, 1972). Here, I adopt the unadjusted Doodson-number convention, and therefore eliminate the need to correct for the offset in computing the angular speed (as well as other parameters, such as the astronomical argument, that are discussed later).

Constituent clusters in the development of the equilibrium tide contain many individual tidal harmonics with different amplitudes. A given harmonic may be separated from another harmonic, in the frequency domain, by only one cycle in 8.85 years ($\Delta f_4 = 3.094$E-4 cycles per day), 18.6 years ($\Delta f_5 = 1.471$E-4 cycles per day), or even 20942 years ($\Delta f_6 = 1.037$E-7 cycles per day). 8.85 years represents the period of precession of the lunar perigee, 18.6 years represents the period of regression of the lunar ascending node, and 20942 years represents the precession of perihelion (Table 1.3). Fig. 1.4 shows spectra of tidal amplitudes as a function of frequency.

Astronomical Argument: Analogous to the angular speed, the astronomical argument may be written as (e.g., Godin, 1972, Sec. 0.4.2):

$$V_\eta(t) = \eta_a\ \tau(t) + \eta_b\ s(t) + \eta_c\ h(t) + \eta_d\ p(t) + \eta_e\ N'(t) + \eta_f\ p'(t). \tag{1.46}$$

The astronomical argument, which may be evaluated using Table 1.2 (and $V_\eta(t)$ modulo 360° for large angles), provides the reference phase angle for tidal harmonic η at time t.

1.5 Tidal Potential Catalogues

Tidal potential catalogues, or equilibrium tide catalogues, distill the gravitational interactions between the Earth and neighboring astronomical bodies into individual harmonic terms, each with a unique Doodson number and a potential height. Sir G.H. Darwin developed the first tidal potential catalogue of harmonic terms in the late 19th century (Darwin, 1898). Subsequently, Doodson made great advancements in the theory of tidal harmonic analysis, expanding substantially upon the number of catalogued harmonics (Doodson, 1921). Doodson's catalogue was used for most of the 20th century until Cartwright & Taylor (1971) and Cartwright & Edden (1973) further expanded and improved the catalogue using modern computer power. Although the Cartwright, Taylor, and Edden catalogue (abbreviated as the CTE catalogue) is still often used today, additional and yet more extensive catalogues have since been developed. For example, Hartmann & Wenzel (1995) expanded the tidal potential to include nearly 13000 harmonics, with gravitational contributions from the moon and sun as well as from Mercury, Venus, Mars, Jupiter, and Saturn. More on the history of tidal analysis and the development of tidal potential catalogues may be found in Cartwright (1999).

The total tidal potential, V_T, is given by:

$$V_T = V_L + V_S + \text{contributions from other external bodies}, \tag{1.47}$$

where V_L is the contribution to the tidal potential by the moon and V_S is the contribution to the tidal potential by the sun.

Dominant Tidal Harmonics									
	Doodson Number						Speed		Equilibrium
Constituent	η_a	η_b	η_c	η_d	η_e	η_f	σ (°/hour)	f (cycles/day)	Amplitude
Z_0	0	0	0	0	0	0	0.0000	0.0000	$0.73869G_0^*$
S_{a}	0	0	1	0	0	-1	0.0411	0.0027	$0.01160G_0^*$
S_{sa}	0	0	2	0	0	0	0.0821	0.0055	$0.07299G_0^*$
M_{m}	0	1	0	-1	0	0	0.5444	0.0363	$0.08254G_0^*$
M_{f}	0	2	0	0	0	0	1.0980	0.0732	$0.15642G_0^*$
$2Q_1$	1	-3	0	2	0	0	12.8543	0.8570	$0.00955G_1^*$
σ_1	1	-3	2	0	0	0	12.9271	0.8618	$0.01153G_1^*$
Q_1	1	-2	0	1	0	0	13.3987	0.8932	$0.07216G_1^*$
ρ_1	1	-2	2	-1	0	0	13.4715	0.8981	$0.01371G_1^*$
O_1	1	-1	0	0	0	0	13.9430	0.9295	$0.37689G_1^*$
τ_1	1	-1	2	0	0	0	14.0252	0.9350	$0.00491G_1^*$
M_1	1	0	0	-1	0	0	14.4874	0.9658	$0.01065G_1^*$
NO_1	1	0	0	1	0	0	14.4967	0.9664	$0.02964G_1^*$
χ_1	1	0	2	-1	0	0	14.5695	0.9713	$0.00566G_1^*$
π_1	1	1	-3	0	0	1	14.9179	0.9945	$0.01029G_1^*$
P_1	1	1	-2	0	0	0	14.9589	0.9973	$0.17584G_1^*$
S_1	1	1	-1	0	0	1	15.0000	1.0000	$0.00423G_1^*$
K_1	1	1	0	0	0	0	15.0411	1.0027	$0.53050G_1^*$
ψ_1	1	1	1	0	0	-1	15.0821	1.0055	$0.00423G_1^*$
ϕ_1	1	1	2	0	0	0	15.1232	1.0082	$0.00756G_1^*$
θ_1	1	2	-2	1	0	0	15.5126	1.0342	$0.00566G_1^*$
J_1	1	2	0	-1	0	0	15.5854	1.0390	$0.02964G_1^*$
OO_1	1	3	0	0	0	0	16.1391	1.0759	$0.01623G_1^*$
ϵ_2	2	-3	2	1	0	0	27.4238	1.8283	$0.00671G_2^*$
$2N_2$	2	-2	0	2	0	0	27.8954	1.8597	$0.02301G_2^*$
μ_2	2	-2	2	0	0	0	27.9682	1.8645	$0.02777G_2^*$
N_2	2	-1	0	1	0	0	28.4397	1.8960	$0.17387G_2^*$
ν_2	2	-1	2	-1	0	0	28.5126	1.9008	$0.03303G_2^*$
M_2	2	0	0	0	0	0	28.9841	1.9322	$0.90812G_2^*$
λ_2	2	1	-2	1	0	0	29.4556	1.9637	$0.00670G_2^*$
L_2	2	1	0	-1	0	0	29.5285	1.9686	$0.02567G_2^*$
T_2	2	2	-3	0	0	1	29.9589	1.9973	$0.02479G_2^*$
S_2	2	2	-2	0	0	0	30.0000	2.0000	$0.42358G_2^*$
R_2	2	2	-1	0	0	-1	30.0411	2.0027	$0.00354G_2^*$
K_2	2	2	0	0	0	0	30.0821	2.0055	$0.11506G_2^*$
η_2	2	3	0	-1	0	0	30.6265	2.0418	$0.00643G_2^*$

Table 1.5: A selection of important tidal harmonics, including all named constituents from the Doodson expansion of the tidal potential (Doodson, 1921), also found in Appendix 1 of Godin (1972). The formulas for the geodetic coefficients are listed in Table 1.1 and are used to convert the normalized amplitudes to actual equilibrium tidal heights.

In terms of the astronomical parameters, the expansion of the tidal potential to spherical harmonic degree-3 may be written as (Godin, 1972):

$$V_{T_{0,2}} = \sum_{\eta_a=0,2} [G^*_{\eta_a} \sum_{\eta_b\,\eta_c\,\eta_d\,\eta_e\,\eta_f} A_{\eta_a\,\eta_b\,\eta_c\,\eta_d\,\eta_e\,\eta_f} \times \cos(\eta_a\tau + \eta_b s + \eta_c h + \eta_d p + \eta_e N' + \eta_f p') + G^{*\prime}_{\eta_a} \sum_{\eta_b\,\eta_c\,\eta_d\,\eta_e\,\eta_f} B_{\eta_a\,\eta_b\,\eta_c\,\eta_d\,\eta_e\,\eta_f} \times \sin(\eta_a\tau + \eta_b s + \eta_c h + \eta_d p + \eta_e N' + \eta_f p')], \quad (1.48)$$

for the long-period and semidiurnal tidal harmonics, and:

$$V_{T_{1,3}} = \sum_{\eta_a=1,3} [G^{*\prime}_{\eta_a} \sum_{\eta_b\,\eta_c\,\eta_d\,\eta_e\,\eta_f} A_{\eta_a\,\eta_b\,\eta_c\,\eta_d\,\eta_e\,\eta_f} \times \cos(\eta_a\tau + \eta_b s + \eta_c h + \eta_d p + \eta_e N' + \eta_f p') + G^*_{\eta_a} \sum_{\eta_b\,\eta_c\,\eta_d\,\eta_e\,\eta_f} B_{\eta_a\,\eta_b\,\eta_c\,\eta_d\,\eta_e\,\eta_f} \times \sin(\eta_a\tau + \eta_b s + \eta_c h + \eta_d p + \eta_e N' + \eta_f p')]. \quad (1.49)$$

for the diurnal and terdiurnal tidal harmonics. $G^*_{\eta_a}$ and $G^{*\prime}_{\eta_a}$ are Doodson's geodetic coefficients for degree-2 and degree-3 harmonic species (Table 1.1), respectively, $(\eta_a\tau + \eta_b s + \eta_c h + \eta_d p + \eta_e N' + \eta_f p')$ defines the astronomical argument for harmonic η, and $A_{\eta_a\,\eta_b\,\eta_c\,\eta_d\,\eta_e\,\eta_f}$ and $B_{\eta_a\,\eta_b\,\eta_c\,\eta_d\,\eta_e\,\eta_f}$ represent the (scaled) amplitude coefficients of the harmonic terms (Godin, 1972). All variables and coefficients are equivalent in Eqs. 1.48 and 1.49, but note the swap of the geodetic coefficients. Also note that, for an expansion up to degree-3 only, G^*_3 is undefined and all the sine terms will be zero (Godin, 1972; Cartwright & Taylor, 1971).

Either A or B will be nonzero for a particular tidal harmonic (i.e., for a unique sequence $[\eta_a\,\eta_b\,\eta_c\,\eta_d\,\eta_e\,\eta_f]$), but not both. Tidal potential catalogues list each unique sequence $[\eta_a\,\eta_b\,\eta_c\,\eta_d\,\eta_e\,\eta_f]$, which is also the Doodson number of each harmonic, along with its corresponding amplitude coefficient, typically scaled. In Eqs. 1.48 and 1.49, the amplitudes are scaled by Doodson's geodetic coefficients. In this case, it is simple to convert catalogue amplitudes (given as the A and B coefficient terms) back to actual tidal heights:

$$A_\eta = \frac{G^*_{\eta_a}}{g}\, A_{\eta_a\,\eta_b\,\eta_c\,\eta_d\,\eta_e\,\eta_f} \quad (1.50)$$

and

$$B_\eta = \frac{G^{*\prime}_{\eta_a}}{g}\, B_{\eta_a\, \eta_b\, \eta_c\, \eta_d\, \eta_e\, \eta_f}. \tag{1.51}$$

Section 0.4 of Godin (1972) provides more information on the Doodson catalogue scheme. Also note that $G^*_S = 0.46G^*$, and hence tidal heights derived from solar ephemeris must be adjusted by this constant factor, which is based on the mass ratio between the moon and the sun as well as the ratio of earth-moon distance to earth-sun distance.

Cartwright & Taylor (1971) adopted an alternative approach to Doodson's lengthy algebraic expansions: they generated the time-dependent, spherical harmonic coefficients directly using the most up-to-date lunar and solar ephemeris and the "response method" of tidal analysis (Munk & Cartwright, 1966). Amplitudes of individual tidal harmonics, shown in Fig. 1.4 using the Doodson scaling convention, were then extracted from the time series using filtering methods. Agnew (2015) reviews this approach. The CTE scaling convention differs from that of Doodson, though the definitions are directly related (Cartwright & Taylor (1971), Table 2).

Regardless of the tidal potential catalogue adopted for a tidal harmonic analysis, making note of the catalogue's sign convention is important. The most common variation in sign convention occurs with the fifth astronomical parameter pertaining to the regression of the lunar ascending node. Sometimes the fifth astronomical parameter is taken to be the precession of the lunar ascending node, N, but perhaps more commonly, the fifth astronomical parameter is taken to be the regression of the lunar ascending node, $N' = -N$. The adopted convention therefore affects the sign of the fifth Doodson coefficient, η_e, as well as the sign of ω_5 and the astronomical parameter itself. It is simply important to be consistent throughout an analysis, regardless of which convention is assumed.

1.6 Physical Interpretation of Tidal Harmonics

To gain intuition for the physical meaning of individual tidal harmonics, imagine that each tidal harmonic is the result of a unique "fictitious" body that has specific characteristics and orbital properties that generate a specific contribution to the total equilibrium tide (e.g.,

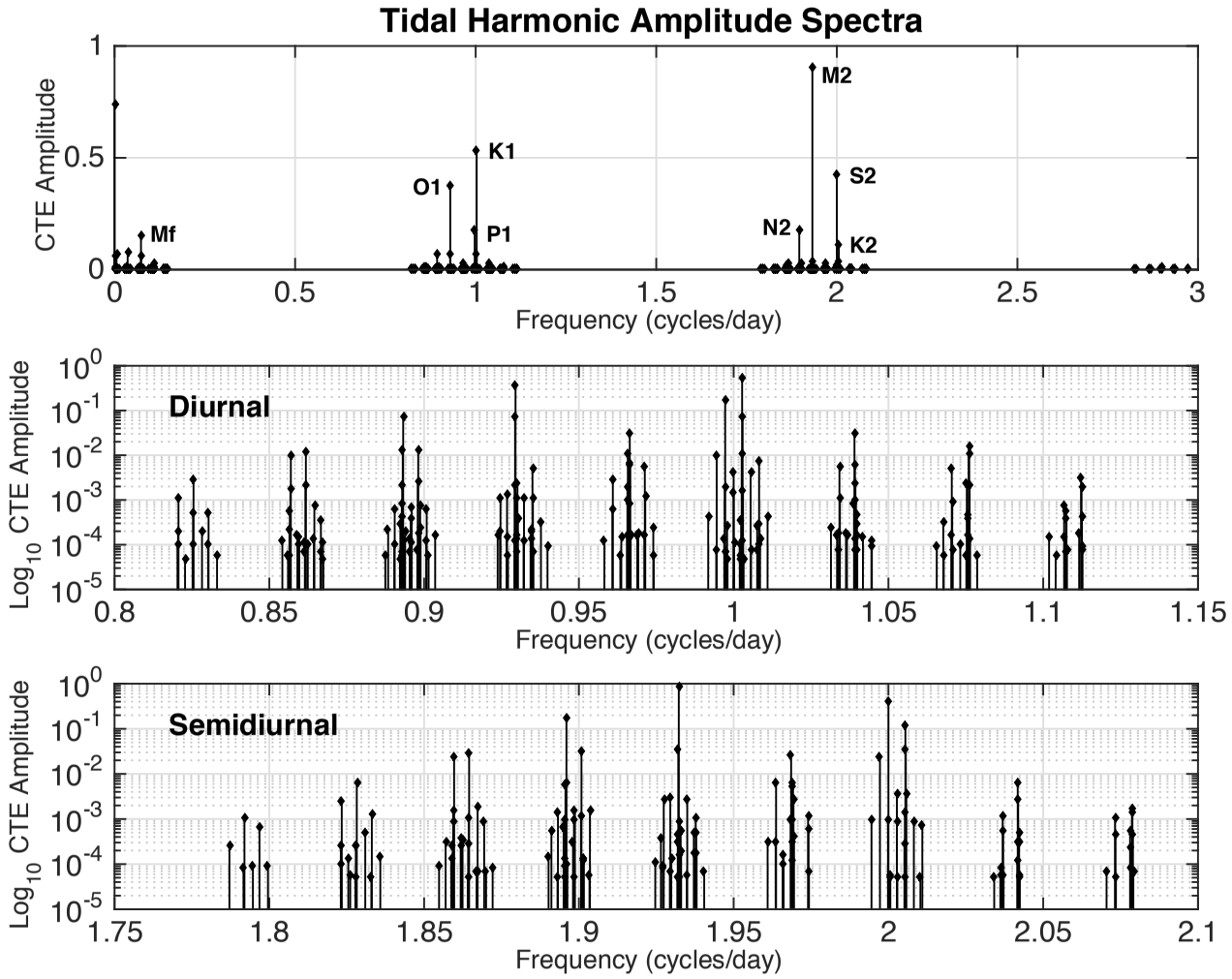

Figure 1.4: Amplitude spectra of tidal harmonics from the Cartwright-Taylor-Edden (CTE) catalogue (Cartwright & Taylor, 1971; Cartwright & Edden, 1973). The top panel shows the equilibrium tidal-harmonic amplitudes on a linear scale. The middle panel shows the semidiurnal tidal harmonic amplitudes on a logarithmic scale. The bottom panel shows the diurnal tidal harmonic amplitudes on a logarithmic scale. All amplitudes have been normalized according to the Doodson scaling convention (Doodson, 1921; Cartwright & Taylor, 1971).

Darwin, 1898; Pugh & Woodworth, 2014, Sec. 4.2.1). Here, I highlight a few examples that elucidate the origins of some of the most prominent astronomical constituents, beginning with the semidiurnal species.

From Eqs. 1.30 and 1.33, the lunar *semidiurnal* equilibrium tide varies as:

$$\left(\frac{c_L}{R_L}\right)^3 \cos^2 d_L \ \cos 2C_L. \tag{1.52}$$

First, imagine a fictitious body that moves only in the plane of Earth's equator (i.e., $d_L = 0$). Next, suppose that the fictitious body moves at the moon's mean speed and at the moon's mean distance from Earth (i.e., $\frac{c_L}{R_L} = 1$). The two stipulations yield a lunar semidiurnal tide that is proportional only to $\cos 2C_L$, which has a period of half a lunar day, a Doodson number of [2 0 0 0 0 0], and an angular speed of $2\omega_1$. The particular harmonic just described is the principal lunar semidiurnal tide and, due to its large amplitude and significant presence around the world, has been given a special name: the $\mathbf{M_2}$ tidal harmonic (e.g., Doodson & Warburg, 1941; Pugh & Woodworth, 2014).

Next, I consider a situation in which the moon remains in the plane of the equator, but the orbital distance of the moon is allowed to vary (i.e., $R_L \neq$ const). This gives rise to, in the first instance, two additional "fictitious" bodies that have angular speeds that differ from that of M_2 by the addition and subtraction of the speed of variation in moon-Earth separation distance, R_L. The variation in moon-Earth separation distance has a period 27.555 mean solar days, which is nearly but not precisely equivalent to the length of a sidereal month (or the period of revolution of the moon in longitude). In terms of the six fundamental astronomical parameters defined previously, the astronomical argument for this special type of lunar month could be expressed either as $(-s + p)$ or $(s - p)$. Each of these combinations of astronomical parameters yields a period equivalent to that of the period of variation in moon-Earth separation distance (e.g., drawing from Table 1.3, $\frac{1}{f_2 - f_4} = \frac{1}{0.0366009 - 0.00030937} = 27.555$ days). Therefore, the two tides generated from the modulation of M_2 by variations in lunar distance have astronomical arguments of $(2\tau - s + p)$ and $(2\tau + s - p)$. The tide that arises from a fictitious body that orbits Earth with an angular speed of $(2\omega_1 - \omega_2 + \omega_4)$ is called $\mathbf{N_2}$ and the tide that arises from

a fictitious body that orbits Earth with an angular speed of $(2\omega_1 + \omega_2 - \omega_4)$ is called $\mathbf{L_2}$ (e.g., Pugh & Woodworth, 2014, Sec. 4.2.1). N_2 is also referred to as the larger lunar elliptic semidiurnal tidal harmonic, whereas L_2 is also referred to as the smaller lunar elliptic semidiurnal harmonic (e.g., Doodson & Warburg, 1941, Ch. 6).

From Eqs. 1.30 and 1.32, the lunar *diurnal* equilibrium tide varies as:

$$\left(\frac{c_L}{R_L}\right)^3 \sin 2d_L \cos C_L. \tag{1.53}$$

Note that, according to the degree-2 expansion of the equilibrium tide (Eq. 1.30), all diurnal tides generated from fictitious bodies that orbit in the plane of the equator ($d_L = 0$) have zero amplitude. Due to the finite size of the Earth, however, a small diurnal tide, $\mathbf{M}_1$, arises even for $d_L = 0$ because the tide at the sub-lunar point will be slightly larger than the tide at the antipode. The first three Doodson numbers for the M_1 constituent cluster are [1 0 0]. Within that cluster, the harmonic with the largest amplitude has a Doodson number of [1 0 0 -1 0 0], which matches the frequency of a prominent shallow-water tide, to be discussed later. The harmonics [1 0 0 0 0 0] and [1 0 0 1 0 0] also make significant contributions to the constituent cluster. The harmonic [1 0 0 0 0 0] has a frequency of 14.4921° per mean solar hour and represents the difference in tidal heights on opposite sides of Earth for a mean moon, which orbits Earth in the equatorial plane at a mean distance and at mean speed. The harmonics [1 0 0 1 0 0] and [1 0 0 -1 0 0] differ from the harmonic [1 0 0 0 0 0] by the 8.85-year cycle of the longitude of lunar perigee.

The largest diurnal tides occur when the absolute value of $(\sin 2d_L)$ is maximized, or when $(\sin 2d_L)' = 2\cos 2d_L = 0$, which corresponds to lunar declinations of $\pm 45^\circ$. The period over which the moon completes one full declinational cycle, north and south of the equator, is equivalent to the lunar orbital period, which is referred to as a sidereal month. A sidereal month has a period of 27.3217 mean solar days, which is equivalent to the period of Doodson's second astronomical parameter, s (see Table 1.3). Modulating the principle lunar diurnal cycle by the period of the declinational cycle yields two of the largest diurnal tidal harmonics: $\mathbf{K}_1$ and $\mathbf{O}_1$ (e.g., Doodson & Warburg, 1941, Ch. 6). K_1 has an astronomical argument of $(\tau + s)$ and O_1 has an astronomical argument of $(\tau - s)$. Additional harmonics

arise by accounting for variations in the moon-Earth separation distance, as for the semidiurnal tides. Recalling that variations in lunar distance, or lunar parallax, are represented by astronomical arguments of $(s-p)$ or $(-s+p)$, four new harmonics may be readily derived: $[\tau + s + (s-p)]$, $[\tau + s + (-s+p)]$, $[\tau - s + (s-p)]$, and $[\tau - s + (-s+p)]$. The first has an angular speed of $14.4921 + 0.5490 + 0.5490 - 0.0046 = 15.5855^\circ$ per mean solar hour and has been given the special name of $\mathbf{J}_1$ (e.g., Pugh & Woodworth, 2014, Sec. 4.2.1). The second and third are simply [1 0 0 1 0 0] and [1 0 0 -1 0 0], which are harmonics within the M_1 constituent cluster as mentioned previously. The fourth, $\mathbf{Q}_1$, has an angular speed of $14.4921 - 0.5490 - 0.5490 + 0.0046 = 13.3987^\circ$ per mean solar hour.

The conceptual key to understanding diurnal tides is visualizing a tidal bulge that is inclined relative to the equator (Boon, 2004). Thus, as Earth rotates, an observer at a nonzero latitude will observe a slightly larger high-tide at one time of day and a slightly lower high-tide approximately half a day later. This difference in the tidal heights may roughly be considered the diurnal tide, though other processes (including contributions from long-period tides) will also play a role.

From Eqs. 1.30 and 1.31, the lunar equilibrium *long-period* tide varies as:

$$\left(\frac{c_L}{R_L}\right)^3 \left(\frac{1}{3} - \sin^2 d_L\right). \tag{1.54}$$

In this case, tidal height does not depend on lunar hour angle, and hence tidal periods of the so-called long-period harmonics are never shorter than one day in length. The first Doodson number, which defines the tidal species, is therefore zero for all long-period harmonic terms. Tides of this nature arise as a consequence of the longer period astronomical parameters, such as the sidereal month and the cycle of lunar perigee.

One of the most important long-period tides is the lunar fortnightly tide, $\mathbf{M}_\mathrm{f}$. Noting that $\sin^2 d_L$ may be re-written as $\frac{1-\cos 2d_L}{2}$ by the half-angle formula, the lunar equilibrium long-period tide varies as:

$$\left(\frac{c_L}{R_L}\right)^3 \left(\frac{1}{2}\cos 2d_L - \frac{1}{6}\right). \tag{1.55}$$

Thus, the period of the declination-dependent term is one-half of the full declinational cycle, or one-half of a sidereal month, which corresponds to an angular speed of $2\sigma_2 = 1.0980^\circ$ per mean solar hour and a Doodson number of [0 2 0 0 0 0]. The variation in lunar parallax (or moon-Earth distance), which has an angular speed of $\sigma_2 - \sigma_4 = 0.5444^\circ$ per mean solar hour, yields the lunar monthly harmonic constituent, $\mathbf{M}_\mathrm{m}$, with a period of 27.555 days.

Solar constituents are, of course, derived in much the same way, except that solar parameters are substituted for the lunar parameters (e.g., R_S is substituted for R_L, d_S is substituted for d_L, and C_S is substituted for C_L). More information may be found in, e.g., Boon (2004), Ch. 6 of Doodson & Warburg (1941), and Ch. 4 of Pugh & Woodworth (2014).

1.7 Tidal Dynamics

Here, I briefly summarize a few important points related to tidal dynamics. For more elaborate introductions, the reader may consult, e.g., Doodson & Warburg (1941) or Pugh & Woodworth (2014). The concept of the equilibrium tide does not apply directly to the dynamic ocean tides observed on Earth. The true ocean tides contend with sharp continental boundaries, bathymetry, Earth rotation, elastic deformation of the sea floor, and frictional interfaces.

Neglecting non-linear effects, the dispersion relation for gravity waves is given by (e.g., Wright et al., 1999):

$$c = \sqrt{\frac{g}{k}\tanh(kH)}, \tag{1.56}$$

where c is the wave speed, g is the gravitational acceleration at Earth's surface, H is the water depth, and k is the wavenumber. If the water depth is much less than the wavelength, λ, then $\tanh(kH) \approx kH$. Thus, the wave speed reduces to (e.g., Doodson & Warburg, 1941; Pugh & Woodworth, 2014):

$$c = \sqrt{g\,H} \tag{1.57}$$

in the so-called "shallow-water approximation," which well describes tides in the pelagic ocean (e.g., Pugh & Woodworth, 2014). In practice, Eq. 1.57 is assumed to apply when H/λ is less than about $1/20$ (e.g., Wright et al., 1999). In addition to a small ratio of

water depth to tidal wavelength, the amplitude of the tidal wave must also be much smaller than the water depth in order to mitigate non-linear effects (e.g., Parker, 2007; Pugh & Woodworth, 2014). Note that $\lambda = c\,T$, where T is the tidal period, and that $\omega = c\,k$, where ω is the angular frequency of the tidal wave.

The continental boundaries form ocean basins as well as constricted bays and seas, leading to local resonance effects. In general, the world's oceans exhibit resonant frequencies near to the semidiurnal tidal frequency, reinforcing the strength and amplitude of the tidal waves (e.g., Pugh & Woodworth, 2014). In some parts of the world, such as the Bay of Fundy, resonant effects generate tidal amplitudes in excess of 10 m (e.g., Pugh & Woodworth, 2014, Sec. 1.3).

Although it may be natural to assume that the ocean tides respond directly in-phase with the lunar and solar gravitational forcing, it turns out that the actual response of Earth's oceans is very complicated. The discrete continental boundaries, for example, have a large effect on tidal phase. Even in the absence of continental boundaries, however, a global ocean would generally respond out-of-phase, or *inverted*, with respect to the forcing body (Souchay et al., 2012; Pugh & Woodworth, 2014). To estimate the phase of the response, the period of the forcing may be compared with the natural period of the responding body. As an analogy, Souchay et al. (2012) considers the response of a simple pendulum to external forcing at different frequencies. For a forcing frequency that is very low with respect to the natural frequency, the response is approximately in-phase with the source. For a forcing frequency that is very high with respect to the natural frequency, the response is approximately out-of-phase with the source. The phase-response (as well as the amplitude-response) of the simple pendulum is therefore a function of the frequency, with perfectly in-phase and perfectly out-of-phase end members. Considering a mass on a spring, forced oscillations at very high frequency will not allow the mass time to respond; therefore, the mass remains effectively static and its motion (from the perspective of the source) will be minus the applied motion to the spring. In this case, the mass is seen to be completely out-of-phase ($\pm\pi$) with the source. On the other end of the spectrum, forced oscillations at very low frequency provide the mass with ample time to respond to the forcing. In this case, the relative motion between

the source and the mass (amplitude response) is approximately zero, and the relative phase between the source and the mass (phase response) is also approximately zero.

For Earth's oceans, the natural period may be estimated as the time required for a wave to propagate a quarter of the Earth's circumference and back again (Souchay et al., 2012). Assuming that the speed of the wave is given by Eq. 1.57 with no impeding continents, the natural period of Earth's oceans is approximately equivalent to 30 hours for a water depth of 4 km, which is significantly longer than the semidiurnal tidal period of $\sim$12 hours. In this idealized case, the oceans are generally out-of-phase with respect to the moon and sun at semidiurnal and diurnal periods. To be in-phase with the gravitational forcing, the oceans would need to be significantly deeper ($>\sim$20 km). The solid Earth, in contrast, exhibits a natural period of $\sim$1 hour (derived from Earth's free oscillations), which is much shorter than the forcing period and therefore more or less in-phase with the gravitational forcing. Recall, however, that the oceans are much more complicated than this simple thought experiment might suggest, largely due to continental boundaries and Earth rotation.

1.8 Suggestions for Further Reading

Cartwright (1999), Boon (2004), and Pugh (2004) provide introductions to tidal theory and analysis with an emphasis on qualitative and conceptual understanding over mathematical development. For one interested in a more quantitative, yet still accessible and comprehensive, overview of tidal analysis, I recommend Agnew (2015), Pugh & Woodworth (2014), Pugh (1987), Melchior (1983), Godin (1972), Schureman (1971), Doodson & Warburg (1941), Doodson's classic papers on harmonic analysis (Doodson, 1921, 1924a, 1928), and Darwin (1898). A comprehensive and quantitative, albeit now somewhat out-dated, account of geophysical methods as applied to geodesy, including a development of the gravitational potential as well as details about tides and Earth rotation, is given by Lambeck (1988).

2

Harmonic Analysis

2.1 Introduction

The forcing function that generates the tides (i.e., the astronomical ephemeris) may be broken down into individual harmonic periods (e.g., Darwin, 1898; Doodson, 1921; Doodson & Warburg, 1941). The total forcing from the combined harmonics excites responses within and on the Earth that are also periodic. Harmonic analysis aims to extract the amplitude and phase of individual tidal harmonics, each with a unique frequency, from a time series of arbitrary length. In other words, the tidal signal at a particular location may be represented by the summation of a series of cosine terms. It is worth noting that non-harmonic techniques have also been developed to describe the tidal response, such as the response method (e.g., Munk & Cartwright, 1966; Pugh & Woodworth, 2014).

Formally, a tidal harmonic, η, may be characterized by a harmonic expression of the form (e.g., Pugh & Woodworth, 2014, Sec. 4.2):

$$A_\eta \cos(\sigma_\eta t - \phi_\eta), \tag{2.1}$$

where A is the amplitude, σ is the angular speed in degrees per mean solar hour ($\sigma = \left(\frac{180}{\pi}\right)\omega$), t is the time in mean solar hours, and ϕ is the phase lag in degrees measured relative to the start of the time series.

Rather than reference the phase of a harmonic, ϕ_η, to the start of the time series, it is more useful for comparison to reference the phase to a common standard. Typically, phases are referenced to the peak in the equilibrium tide height for the harmonic η at a certain longitude, such as the Greenwich Meridian (e.g., Doodson & Warburg, 1941; Godin, 1972; Foreman, 1977). For long-period tides, which do not depend on the lunar hour angle, the

phases are generally referenced to the peak in the equilibrium tide at the equator (e.g., Bos et al., 2000). Thus, an additional term must be included: the astronomical argument, $V_\eta(t_0)$. With the astronomical argument included, the harmonic expression becomes:

$$A_\eta \cos(V_\eta(t_0) + \sigma_\eta t - \phi_\eta). \tag{2.2}$$

Since the angular speed contains higher-order secular terms, the expression may be written more precisely. Rather than evaluating the astronomical argument at the beginning of the time series and assuming a linear relationship in its temporal progression, the astronomical argument may be computed explicitly at every epoch (e.g., Foreman et al., 2009). Formally,

$$A_\eta \cos(V_\eta(t) - \phi_\eta), \tag{2.3}$$

where

$$V_\eta(t) \sim V_\eta(t_0) + \sigma_\eta t. \tag{2.4}$$

Time series of tidal data contain many individual harmonics, some of which may be very close in the frequency domain. If two harmonics are not separable in frequency over the length of the time series, then the smaller amplitude harmonic will modulate the amplitude and phase of the larger amplitude harmonic over time. Given a time series less than 18.6 years in length, for example, two tidal harmonics separated by one cycle in the regression of the lunar ascending node will not be resolvable. Attempts to extract the amplitude and phase of one of the harmonics, however, will be contaminated by the other harmonic. Thus, correction factors are introduced to account for the modulations introduced by the subsidiary harmonics in the frequency domain (e.g., Doodson, 1924a; Doodson & Warburg, 1941; Godin, 1972; Pugh & Woodworth, 2014):

$$A_\eta \ f_\eta(t) \ \cos(V_\eta(t) + u_\eta(t) - \phi_\eta), \tag{2.5}$$

where $f_\eta(t)$ is the harmonic-modulation correction factor for the amplitude and $u_\eta(t)$ is the harmonic-modulation correction factor for the phase. In the special case that harmonics

are separated from a primary harmonic by integer cycles in the lunar ascending node, the harmonic-modulation correction factors are referred to as **nodal modulations** (e.g., Pugh & Woodworth, 2014). Since modulations also occur due to harmonic separations in other astronomical cycles, such as lunar perigee, the modulations have also been more generally referred to as **satellite modulations** (Foreman et al., 2009). The nomenclature of *satellite* modulations, however, may cause confusion with modern space-based geodesy platforms; thus, I refer to the modulations in a generic sense as **harmonic modulations**.

Traditionally, to save on computational resources, tidal analyses have applied harmonic-modulation correction factors after an initial least squares fit to the time series (e.g., Godin, 1972; Pawlowicz et al., 2002). Accounting for the harmonic modulations a posteriori often involves the application of constant correction factors that may be assumed constant only over short time windows, such as one year of data or less (e.g., Schureman, 1971, Par. 346). Correcting for the harmonic modulations at the post-processing stage and thereby limiting an analysis to a short time span of data are unnecessary sacrifices with modern computational resources (Foreman et al., 2009). Updating the harmonic-modulation corrections, as well as the astronomical argument, at every epoch in the time series allows for seamless processing of multiple years of data in a single estimation step.

2.2 Harmonic Modulations and Corrections

Recall that a tidal constituent represents a cluster of tidal harmonics that share the same first three coefficients in a Doodson number (i.e., η_a, η_b, and η_c). The harmonic with the largest amplitude from the tidal potential catalogue is typically taken to be the primary, or dominant, harmonic. Additional harmonics within the same constituent cluster are referred to as **satellite** (e.g., Godin, 1972; Foreman, 1977; Foreman et al., 2009) or **subsidiary** (e.g., Doodson, 1924a) harmonics. For very long time series, many of the subsidiary harmonics may be resolvable from the primary harmonic outright. For harmonics separated in frequency by cycles of the lunar perigee, a time series of at least 8.9 years in length is required for separation. For harmonics separated in frequency by cycles of the lunar ascending node, a time series of at least 18.6 years in length is required for separation. Any additional harmonics

Harmonic Modulations		
Constituent	f	u
$M_{\rm m}$	$1.000 - 0.130\cos N$	0.0°
$M_{\rm f}$	$1.043 + 0.414\cos N$	$-23.7^\circ\sin N + 2.7^\circ\sin(2N)$ - $0.4^\circ\sin(3N)$
Q_1,O_1	$1.009 + 0.187\cos N$ - $0.015\cos(2N)$	$10.8^\circ\sin N - 1.3^\circ\sin(2N)+$ $0.2^\circ\sin(3N)$
K_1	$1.006 + 0.115\cos N$ - $0.009\cos(2N)$	$-8.9^\circ\sin N + 0.7^\circ\sin(2N)$
J_1	$1.013 + 0.168\cos N$ - $0.017\cos(2N)$	$-12.9^\circ\sin N + 1.3^\circ\sin(2N)$ - $0.2^\circ\sin(3N)$
$2N_2$,μ_2,ν_2, N_2,M_2	$1.000 - 0.037\cos N$	$-2.1^\circ\sin N$
K_2	$1.024 + 0.286\cos N$ + $0.008\cos(2N)$	$-17.7^\circ\sin N + 0.7^\circ\sin(2N)$
L_2	$f\cos u = 1.00 - 0.25\cos(2p) - 0.11\cos(2p - N) - 0.02\cos(2p - 2N) - 0.04\cos N$ $f\sin u = -0.25\sin(2p) - 0.11\sin(2p - N) - 0.02\sin(2p - 2N) - 0.04\sin N$	
M_1	$f\cos u = 2\cos p + 0.4\cos(p - N)$ $f\sin u = \sin p + 0.2\sin(p - N)$	

Table 2.1: Harmonic-modulation corrections for primary tidal harmonics from several dominant constituents (e.g., Doodson & Warburg, 1941; Pugh & Woodworth, 2014).

that are too close in frequency to separate outright will contaminate the complex-valued amplitude of the primary harmonic during an inversion. Correction factors are therefore invoked to treat the effects of the harmonic modulation (e.g., Doodson & Warburg, 1941; Godin, 1972; Pawlowicz et al., 2002; Foreman et al., 2009; Pugh & Woodworth, 2014). Alternatively, the response method of Munk & Cartwright (1966) includes the correction factors implicitly.

Table 2.1 provides a list of harmonic-modulation corrections for dominant tidal harmonics in various constituent clusters. Note that the harmonic modulations have a much greater effect on the diurnal and long-period harmonics than on most of the semidiurnal harmonics. L_2 and M_1 require corrections that address both the 8.85- and 18.6-year modulations. To distinguish the different origins of modulations, the lunar-perigee modulations are sometimes denoted by j and v instead of the conventional f and u. Here, I use f and u to represent harmonic-modulation corrections from both origins.

To develop a general formulation for deriving harmonic-modulation corrections, I return to the expansion of the tidal potential. In particular, the signal for a particular tidal constituent (primary harmonic + subsidiary harmonics) may be written as (e.g., Doodson, 1924a; Foreman, 1977):

$$a_\eta \ \cos(V_\eta - \phi_\eta) + \sum_k A_{\eta k} \ a_{\eta k} \ \cos(V_{\eta k} - \phi_{\eta k}) + \sum_l A_{\eta l} \ a_{\eta l} \ \sin(V_{\eta l} - \phi_{\eta l}), \quad (2.6)$$

for long-period and semidiurnal constituents, and

$$a_\eta \ \sin(V_\eta - \phi_\eta) + \sum_k A_{\eta k} \ a_{\eta k} \ \sin(V_{\eta k} - \phi_{\eta k}) + \sum_l A_{\eta l} \ a_{\eta l} \ \cos(V_{\eta l} - \phi_{\eta l}), \quad (2.7)$$

for diurnal constituents, where a is the equilibrium-tide amplitude (obtained from a tidal potential catalogue), ϕ is the phase of harmonic η referenced to Greenwich, and V is the astronomical argument. A single η subscript refers to the primary harmonic in the tidal constituent cluster, whereas the ηk and ηl subscripts refer to subsidiary harmonics of second- and third-degree, respectively, in the development of the tidal potential. A is an interaction matrix that accounts for the interference between the primary harmonic and its subsidiary harmonics (Godin, 1972; Foreman, 1977), computed as:

$$A_{\eta k} = \frac{\sin[N\Delta t(\sigma_{\eta k} - \sigma_\eta)/2]}{N \sin[\Delta t(\sigma_{\eta k} - \sigma_\eta)/2]}, \quad (2.8)$$

where N is the number of consecutive observations, Δt is time difference between observations, $\sigma_{\eta k}$ is the frequency of subsidiary harmonic k, and σ_η is the frequency of the primary harmonic η. In practice, A is very close to one.

Since terdiurnal terms arise only in the third-degree expansion of the tidal potential ($n = 3$, $m = 3$), they are treated slightly differently. Both the primary and the subsidiary harmonics are due to third-order terms and, since m is odd, the third-order contribution will be in the form of a cosine term (e.g., Foreman, 1977, Sec. 2.3.2). This is analogous to the diurnal terms, where the third-degree subsidiary harmonics are cosines, except that in this case, the primary harmonic is also of third-degree, and hence also a cosine term. Alternatively, terdi-

urnal terms can be considered analogous to second-degree semidiurnal harmonics, without any third-degree subsidiary harmonics. Here, I do not consider the terdiurnal terms to have any subsidiary harmonics beyond degree-3.

Tidal analyses typically assume that all harmonics are represented by a cosine term with positive amplitude (i.e., in the form of $a_\eta \cos(V_\eta - \phi_\eta)$ for $a_\eta > 0$). Thus, phase corrections of 180° (i.e., $\frac{1}{2}$ cycle) must be applied to primary harmonics with a negative amplitude (e.g., Foreman, 1977, Sec. 2.3.2). Furthermore, a phase correction of $-\frac{1}{4}$ is necessary to convert degree-2 diurnal harmonics from sine to cosine terms.

Therefore, the signal due to a tidal constituent cluster may be represented by (e.g., Foreman, 1977):

$$|a_\eta| \cos(V'_\eta - \phi_\eta) + \sum_k A_{\eta k} \, |a_{\eta k}| \, \cos(V'_{\eta k} + \alpha_{\eta k} - \phi_{\eta k}) + \sum_l A_{\eta l} \, |a_{\eta l}| \, \cos(V'_{\eta l} + \alpha_{\eta l} - \phi_{\eta l}), \tag{2.9}$$

where

$$V'(\text{i.e.}, V'_\eta, V'_{\eta k}, V'_{\eta l}) = \begin{cases} V + \frac{1}{2} & \text{if } a_\eta < 0, \\ V & \text{otherwise;} \end{cases}$$

$$\alpha_{\eta k} = \begin{cases} 0 & \text{if } a_{\eta k} \text{ and } a_\eta \text{ have the same sign,} \\ \frac{1}{2} & \text{otherwise;} \end{cases}$$

$$\alpha_{\eta l} = \begin{cases} -\frac{1}{4} & \text{if } a_{\eta l} \text{ and } a_\eta \text{ have the same sign,} \\ \frac{1}{4} & \text{otherwise} \end{cases}$$

for the long-period and semidiurnal constituents,

$$V' = \begin{cases} V + \frac{1}{4} & \text{if } a_\eta < 0, \\ V - \frac{1}{4} & \text{otherwise;} \end{cases}$$

$$\alpha_{\eta k} = \begin{cases} 0 & \text{if } a_{\eta k} \text{ and } a_\eta \text{ have the same sign,} \\ \frac{1}{2} & \text{otherwise;} \end{cases}$$

$$\alpha_{\eta l} = \begin{cases} \frac{1}{4} & \text{if } a_{\eta l} \text{ and } a_{\eta} \text{ have the same sign,} \\ \frac{3}{4} & \text{otherwise} \end{cases}$$

for the diurnal constituents, and

$$V' = \begin{cases} V + \frac{1}{2} & \text{if } a_{\eta} < 0, \\ V & \text{otherwise;} \end{cases}$$

$$\alpha_{\eta k} = \begin{cases} 0 & \text{if } a_{\eta k} \text{ and } a_{\eta} \text{ have the same sign,} \\ \frac{1}{2} & \text{otherwise} \end{cases}$$

for the terdiurnal constituents. Note that V applies to all V_{η}, $V_{\eta k}$, $V_{\eta l}$.

If, on the other hand, $V'_{\eta k}$ and $V'_{\eta l}$ are left as-is (i.e., equal to $V_{\eta k}$ and $V_{\eta l}$, respectively), then the argument corrections become:

$$V'_{\eta} = \begin{cases} V_{\eta} + \frac{1}{2} & \text{if } a_{\eta} < 0, \\ V_{\eta} & \text{otherwise;} \end{cases}$$

$$\alpha_{\eta k} = \begin{cases} 0 & \text{if } a_{\eta k} > 0, \\ \frac{1}{2} & \text{otherwise;} \end{cases}$$

$$\alpha_{\eta l} = \begin{cases} -\frac{1}{4} & \text{if } a_{\eta l} > 0, \\ \frac{1}{4} & \text{otherwise; and} \end{cases}$$

$$\begin{aligned} V'_{\eta k} &= V_{\eta k} \\ V'_{\eta l} &= V_{\eta l} \end{aligned}$$

for the long-period and semidiurnal constituents,

$$V'_\eta = \begin{cases} V_\eta + \frac{1}{4} & \text{if } a_\eta < 0, \\ V_\eta - \frac{1}{4} & \text{otherwise;} \end{cases}$$

$$\alpha_{\eta k} = \begin{cases} -\frac{1}{4} & \text{if } a_{\eta k} > 0, \\ \frac{1}{4} & \text{otherwise;} \end{cases}$$

$$\alpha_{\eta l} = \begin{cases} 0 & \text{if } a_{\eta l} > 0, \\ \frac{1}{2} & \text{otherwise; and} \end{cases}$$

$$\begin{aligned} V'_{\eta k} &= V_{\eta k} \\ V'_{\eta l} &= V_{\eta l} \end{aligned}$$

for the diurnal constituents, and

$$V'_\eta = \begin{cases} V_\eta + \frac{1}{2} & \text{if } a_\eta < 0, \\ V_\eta & \text{otherwise;} \end{cases}$$

$$\alpha_{\eta k} = \begin{cases} 0 & \text{if } a_{\eta k} > 0, \\ \frac{1}{2} & \text{otherwise; and} \end{cases}$$

$$V'_{\eta k} = V_{\eta k}$$

for the terdiurnal constituents. The reason that it is nice to keep the argument corrections in the first form (i.e., with all of the Vs modified by the same amount), is that when one takes the difference between them for the harmonic-modulation corrections (shown later), the phase offset cancels out, and hence all one needs to worry about are the original, uncorrected astronomical arguments, because all of the corrections for positive-sign and cosine coefficients will be taken care of with the α terms.

Note that amplitudes from the tide-generating potential are coefficients of cosine terms for the case $(m + n)$ even and coefficients of sine terms for the case $(m + n)$ odd (e.g., Cartwright & Taylor, 1971). Thus, cosines are appropriate for degree-2 long-period and semidiurnal harmonics, as well as for degree-3 diurnal and terdiurnal harmonics. Likewise, sines are appropriate for degree-2 diurnal harmonics as well as for degree-3 long-period and semidiurnal harmonics.

Since the admittance across the frequency window of a tidal constituent cluster is nearly constant, I assume that the Greenwich phase is equivalent between the primary and subsidiary harmonics (i.e., $\phi_\eta = \phi_{\eta k} = \phi_{\eta l}$) (Foreman, 1977). It is also assumed that the amplitude ratios between the subsidiary harmonics and the primary harmonic are equal to the ratio of the tidal equilibrium amplitudes from the tidal potential catalogue (i.e., $r_{\eta k} \equiv \frac{|a_{\eta k}|}{|a_\eta|}$ and $r_{\eta l} \equiv \frac{|a_{\eta l}|}{|a_\eta|}$, where $|a_\eta|$, $|a_{\eta k}|$, and $|a_{\eta l}|$ are obtained from a tidal potential catalogue). Ratios of third-degree terms relative to second-degree terms also involve a latitudinal correction factor based on the ratio of Doodson's geodetic coefficients (Sec. 1.4, Table 1.1).

I seek to write Eq. 2.9 in terms of a single tidal harmonic, where the contributions to the signal from subsidiary harmonics are accounted for by two time-varying factors, f and u. As discussed previously, f and u represent harmonic-modulation corrections to the amplitude and phase of the primary harmonic. Therefore, I seek an equation of the form (e.g., Doodson, 1928; Schureman, 1971; Foreman et al., 2009):

$$f_\eta \, |a_\eta| \, \cos(V_\eta + u_\eta - \phi_\eta). \tag{2.10}$$

It is more useful, however, to write Eq. 2.10 in terms of $f_\eta \cos u_\eta$ and $f_\eta \sin u_\eta$ (e.g., Doodson, 1928), such that:

$$\begin{aligned} f_\eta &= \sqrt{(f_\eta \cos u_\eta)^2 + (f_\eta \sin u_\eta)^2} \\ u_\eta &= \tan^{-1}\left[\frac{f_\eta \sin u_\eta}{f_\eta \cos u_\eta}\right]. \end{aligned} \tag{2.11}$$

L_2 Tidal Constituent								
	Doodson Number						Harmonic	Equilibrium
Classification	η_a	η_b	η_c	η_d	η_e	η_f	Degree	Amplitude
Satellite	2	1	0	-1	-1	0	Second	0.00095
Main	**2**	**1**	**0**	**-1**	**0**	**0**	**Second**	**-0.02567**
Satellite	2	1	0	0	-1	0	Third	-0.00031
Satellite	2	1	0	0	0	0	Third	0.00525
Satellite	2	1	0	0	1	0	Third	0.00099
Satellite	2	1	0	1	-1	0	Second	-0.00012
Satellite	2	1	0	1	0	0	Second	0.00643
Satellite	2	1	0	1	1	0	Second	0.00283
Satellite	2	1	0	1	2	0	Second	0.00040

Table 2.2: Primary and subsidiary harmonics from the L_2 tidal harmonic. The primary harmonic is that which has the largest equilibrium amplitude. Note that the primary and subsidiary harmonics are separated only by cycles of lunar nodal regression and lunar perigee.

Using a trigonometric identity, I can re-write Eq. 2.10 as

$$f_\eta \, |a_\eta| \, [\, \cos(V_\eta - \phi_\eta) \cos u_\eta - \sin(V_\eta - \phi_\eta) \sin u_\eta \,], \tag{2.12}$$

and rearrange to arrive at:

$$(f_\eta \cos u_\eta) \, |a_\eta| \, \cos(V_\eta - \phi_\eta) - (f_\eta \sin u_\eta) \, |a_\eta| \, \sin(V_\eta - \phi_\eta). \tag{2.13}$$

Thus, $f_\eta \cos u_\eta$ is equivalent to the summation of the coefficients in front of the $[\, |a_\eta| \, \cos(V_\eta - \phi_\eta) \,]$ terms in the expansion of all harmonic terms (primary and subsidiaries) associated with a particular tidal harmonic. Likewise, $f_\eta \sin u_\eta$ is equivalent to the summation of the coefficients in front of the $[\, |a_\eta| \, \sin(V_\eta - \phi_\eta) \,]$ terms (e.g., Doodson, 1928).

The harmonic-modulation corrections may thus be written in a generalized form for any tidal constituent, η, as follows (e.g., Foreman, 1977; Yuan et al., 2013):

$$f_\eta \cos u_\eta = 1 + \sum_k A_{\eta k} \, r_{\eta k} \, \cos(\Delta_{\eta k} + \alpha_{\eta k}) \tag{2.14}$$

$$f_\eta \sin u_\eta = \sum_k A_{\eta k} \, r_{\eta k} \, \sin(\Delta_{\eta k} + \alpha_{\eta k}), \tag{2.15}$$

where

$$\Delta_{\eta k} = V_{\eta k} - V_{\eta}, \tag{2.16}$$

and $A_{\eta k}$, $r_{\eta k}$, and $\alpha_{\eta k}$ are defined previously (cf., Eqs. 2.11).

2.2.1 Example: L_2 Harmonic

Practical methods for computing the harmonic modulations may be found in the literature (e.g., Godin, 1972, Secs. 2.8.1–2.8.2). As an example, consider the harmonic-modulation corrections for tidal harmonic L_2 (cf., Doodson, 1928, Sec. 9.6). The Doodson number for L_2 is [2 1 0 -1 0 0] and the scaled equilibrium amplitude from the Doodson catalogue is -0.02567 (e.g., Godin, 1972). The subsidiary harmonics for the L_2 constituent share the same first three Doodson coefficients with the primary L_2 harmonic. Here, I consider five second-order harmonic terms and three third-order harmonic terms that neighbor the primary L_2 harmonic in the constituent cluster. Table 2.2 lists the selected (significant) second- and third-order primary and subsidiary harmonics associated with the L_2 tidal constituent.

Since the L_2 constituent is a semidiurnal tidal species, it may be represented by a harmonic expansion in the form of Eq. 2.6:

$$\begin{aligned}
&G_2^* \times -0.02567 \cos(V_{L_2} - \phi_{L_2}) + \ldots \\
&A_{L_{21}} \times G_2^* \times 0.00095 \cos(V_{L_2} - \phi_{L_2} - N') + \ldots \\
&A_{L_{22}} \times G_2^{*\prime} \times -0.00031 \sin(V_{L_2} - \phi_{L_2} + p - N') + \ldots \\
&A_{L_{23}} \times G_2^{*\prime} \times 0.00525 \sin(V_{L_2} - \phi_{L_2} + p) + \ldots \\
&A_{L_{24}} \times G_2^{*\prime} \times 0.00099 \sin(V_{L_2} - \phi_{L_2} + N') + \ldots \\
&A_{L_{25}} \times G_2^* \times -0.00012 \cos(V_{L_2} - \phi_{L_2} + 2p - N') + \ldots \\
&A_{L_{26}} \times G_2^* \times 0.00643 \cos(V_{L_2} - \phi_{L_2} + 2p) + \ldots \\
&A_{L_{27}} \times G_2^* \times 0.00283 \cos(V_{L_2} - \phi_{L_2} + 2p + N') + \ldots \\
&A_{L_{28}} \times G_2^* \times 0.00040 \cos(V_{L_2} - \phi_{L_2} + 2p + 2N').
\end{aligned}$$

Here, I have assumed that the phase of each subsidiary harmonic is equivalent to the phase

of the primary harmonic; smooth admittance across the tidal constituent band is assumed (e.g., Foreman, 1977). V_{L_2} is the astronomical argument for the primary L_2 harmonic (i.e., $V_{L_2} = 2\tau + s - p$). Recall that A_{L_2k} is an interaction matrix given by Eq. 2.8, which is approximately equal to one. As discussed previously, constituents are conventionally expressed by a cosine term with a positive amplitude. This can be accomplished by making slight adjustments to the phases of the harmonics as follows:

$$
\begin{aligned}
& G_2^* \times 0.02567 \cos(V_{L_2} - \phi_{L_2} + 180^\circ) + \ldots \\
& A_{L_{21}} \times G_2^* \times 0.00095 \cos(V_{L_2} - \phi_{L_2} + 180^\circ + 180^\circ - N') + \ldots \\
& A_{L_{22}} \times G_2^{*\prime} \times 0.00031 \cos(V_{L_2} - \phi_{L_2} + 180^\circ - 90^\circ + 0^\circ + p - N') + \ldots \\
& A_{L_{23}} \times G_2^{*\prime} \times 0.00525 \cos(V_{L_2} - \phi_{L_2} + 180^\circ - 90^\circ + 180^\circ + p) + \ldots \\
& A_{L_{24}} \times G_2^{*\prime} \times 0.00099 \cos(V_{L_2} - \phi_{L_2} + 180^\circ - 90^\circ + 180^\circ + N') + \ldots \\
& A_{L_{25}} \times G_2^* \times 0.00012 \cos(V_{L_2} - \phi_{L_2} + 180^\circ + 0^\circ + 2p - N') + \ldots \\
& A_{L_{26}} \times G_2^* \times 0.00643 \cos(V_{L_2} - \phi_{L_2} + 180^\circ + 180^\circ + 2p) + \ldots \\
& A_{L_{27}} \times G_2^* \times 0.00283 \cos(V_{L_2} - \phi_{L_2} + 180^\circ + 180^\circ + 2p + N') + \ldots \\
& A_{L_{28}} \times G_2^* \times 0.00040 \cos(V_{L_2} - \phi_{L_2} + 180^\circ + 180^\circ + 2p + 2N').
\end{aligned}
$$

Note that 180° was added to the phase of each harmonic since the primary harmonic had a negative amplitude. Furthermore, sine terms were shifted in phase by -90°. Finally, any subsidiary harmonics that had amplitudes opposite in sign to the primary harmonic were shifted in amplitude by an additional 180°. Now, pulling the quantity $(A_{L_2}\, G_2^*)$ out front and adding the phase adjustments together, the expression becomes:

$$
\begin{aligned}
0.02567\, G_2^* \times \quad & [\, \cos(V_{L_2} - \phi_{L_2} + 180^\circ) + \\
& A_{L_{21}} \frac{0.00095}{0.02567} \cos(V_{L_2} - \phi_{L_2} - N') + \\
& A_{L_{22}} \frac{0.00031}{0.02567} \frac{G_2^{*\prime}}{G_2^*} \cos(V_{L_2} - \phi_{L_2} + 90^\circ + p - N') + \\
& A_{L_{23}} \frac{0.00525}{0.02567} \frac{G_2^{*\prime}}{G_2^*} \cos(V_{L_2} - \phi_{L_2} - 90^\circ + p) +
\end{aligned}
$$

$$A_{L_{24}}\frac{0.00099}{0.02567}\frac{G_2^{*\prime}}{G_2^*}\cos(V_{L_2}-\phi_{L_2}-90^\circ+N')+$$
$$A_{L_{25}}\frac{0.00012}{0.02567}\cos(V_{L_2}-\phi_{L_2}+180^\circ+2p-N')+$$
$$A_{L_{26}}\frac{0.00643}{0.02567}\cos(V_{L_2}-\phi_{L_2}+2p)+$$
$$A_{L_{27}}\frac{0.00283}{0.02567}\cos(V_{L_2}-\phi_{L_2}+2p+N')+$$
$$A_{L_{28}}\frac{0.00040}{0.02567}\cos(V_{L_2}-\phi_{L_2}+2p+2N')\ ].$$

Now, the cosine terms may be rewritten using a common trigonometric identity: $\cos(V+u)=\cos V\cos u-\sin V\sin u$. After simplifying the fractions, the result is:

$$\begin{aligned}
0.02567\,G_2^*\times\ & \{\ \cos V_m+\\
& A_{L_{21}}0.037\ [\cos V_m\cos(-N'-180^\circ)-\sin V_m\sin(-N'-180^\circ)]+\\
& A_{L_{22}}0.012(2.59808\sin\phi_P)\ [\cos V_m\cos(p-N'-90^\circ)-\\
& \sin V_m\sin(p-N'-90^\circ)]+\\
& A_{L_{23}}0.205(2.59808\sin\phi_P)\ [\cos V_m\cos(p+90^\circ)-\\
& \sin V_m\sin(p+90^\circ)]+\\
& A_{L_{24}}0.039(2.59808\sin\phi_P)\ [\cos V_m\cos(N'+90^\circ)-\\
& \sin V_m\sin(N'+90^\circ)]+\\
& A_{L_{25}}0.005\ [\cos V_m\cos(2p-N')-\sin V_m\sin(2p-N')]+\\
& A_{L_{26}}0.250\ [\cos V_m\cos(2p-180^\circ)-\sin V_m\sin(2p-180^\circ)]+\\
& A_{L_{27}}0.110\ [\cos V_m\cos(2p+N'-180^\circ)-\\
& \sin V_m\sin(2p+N'-180^\circ)]+\\
& A_{L_{28}}0.016\ [\cos V_m\cos(2p+2N'-180^\circ)-\\
& \sin V_m\sin(2p+2N'-180^\circ)]\ \},
\end{aligned}\tag{2.17}$$

where V_m is the argument of the primary harmonic (i.e., $V_m=V_{L_2}-\phi_{L_2}+180^\circ$).

Since I seek an expression of the form

$$a_m \; f_{L_2} \; \cos(V_m + u_{L_2}) = a_m \; [f_{L_2} \cos u_{L_2}] \cos V_m - a_m \; [f_{L_2} \sin u_{L_2}] \sin V_m, \quad (2.18)$$

where $a_m = 0.02567 \; G_2^*$, I now extract the expressions for $[f_{L_2} \cos u_{L_2}]$ and $[f_{L_2} \sin u_{L_2}]$ immediately from Eq. 2.17, purely by inspection. The results are:

$$\begin{aligned} f_{L_2} \cos u_{L_2} \;\; = \;\; & 1 + A_{L_{21}} \; 0.037 \cos(-N' - 180^\circ) + \\ & A_{L_{22}} \; 0.012 (2.59808 \sin \phi_P) \cos(p - N' - 90^\circ) + \\ & A_{L_{23}} \; 0.205 (2.59808 \sin \phi_P) \cos(p + 90^\circ) + \\ & A_{L_{24}} \; 0.039 (2.59808 \sin \phi_P) \cos(N' + 90^\circ) + \\ & A_{L_{25}} \; 0.005 \cos(2p - N') + A_{L_{26}} \; 0.250 \cos(2p - 180^\circ) + \\ & A_{L_{27}} \; 0.110 \cos(2p + N' - 180^\circ) + \\ & A_{L_{28}} \; 0.016 \cos(2p + 2N' - 180^\circ), \end{aligned} \quad (2.19)$$

and

$$\begin{aligned} f_{L_2} \sin u_{L_2} \;\; = \;\; & A_{L_{21}} \; 0.037 \sin(-N' - 180^\circ) + \\ & A_{L_{22}} \; 0.012 (2.59808 \sin \phi_P) \sin(p - N' - 90^\circ) + \\ & A_{L_{23}} \; 0.205 (2.59808 \sin \phi_P) \sin(p + 90^\circ) + \\ & A_{L_{24}} \; 0.039 (2.59808 \sin \phi_P) \sin(N' + 90^\circ) + \\ & A_{L_{25}} \; 0.005 \sin(2p - N') + A_{L_{26}} \; 0.250 \sin(2p - 180^\circ) + \\ & A_{L_{27}} \; 0.110 \sin(2p + N' - 180^\circ) + \\ & A_{L_{28}} \; 0.016 \sin(2p + 2N' - 180^\circ). \end{aligned} \quad (2.20)$$

Note that the results here could have been derived directly from Eq. 2.14.

2.3 Shallow-Water Harmonics

In the pelagic ocean, where the tide amplitudes are much smaller than the water depth and the tide wavelengths are much longer than the water depth, the tides are well described by the astronomical harmonics. In shallow seas and estuaries, however, non-linear effects become important and produce higher-order harmonics, including overtides and compound tides (e.g., Doodson & Warburg, 1941; Doodson, 1957; Schureman, 1971; Godin, 1972; Foreman, 1977; Parker, 2007; Pugh & Woodworth, 2014). The non-linear distortions of the astronomical tides occur due to several mechanisms, including bottom friction, an increase in the ratio of tide amplitude to water depth, and coastal bathymetry (e.g., Parker, 2007; Pugh & Woodworth, 2014).

Following the development in Doodson & Warburg (1941), suppose that the heights of two tidal harmonics, such as M_2 and S_2, are given by $\eta_1 = A\cos a$ and $\eta_2 = B\cos b$. The total tide height, y, resulting from a linear interaction between the two tides is then:

$$y = \eta_1 + \eta_2 = A\cos a + B\cos b. \tag{2.21}$$

In shallow water, non-linear effects distort the shape of the tide as a function of the square and higher powers of the original tidal amplitude, thereby generating higher-order harmonic terms (e.g., Doodson & Warburg, 1941; Doodson, 1957; Godin, 1972; Pugh & Woodworth, 2014, Sec. 4.2.3). For example, the square of the total tide height obtained from the interactions of two harmonics, η_1 and η_2, is given by (e.g., Doodson & Warburg, 1941; Pugh & Woodworth, 2014):

$$y^2 = A^2\cos^2 a + B^2\cos^2 b + 2AB\cos a\cos b, \tag{2.22}$$

which, using simple trigonometric identities, can be expanded further to:

$$y^2 = \frac{1}{2}A^2\cos 2a + \frac{1}{2}B^2\cos 2b + AB\cos(a+b) + AB\cos(a-b) + \text{constants}. \tag{2.23}$$

Note that four harmonic terms in y^2 are generated by the non-linear interaction of two

Shallow-Water Tidal Harmonics								
	Astronomical Contribution							
Name	iM_2	iS_2	iN_2	iK_2	iO_1	iQ_1	iP_1	iK_1
MS_f	-1	1	0	0	0	0	0	0
NO_1	0	0	1	0	-1	0	0	0
SO_1	0	1	0	0	-1	0	0	0
$2MS_2$	2	-1	0	0	0	0	0	0
OP_2	0	0	0	0	1	0	1	0
$2MN_2$	2	0	-1	0	0	0	0	0
$2PO_1$	0	0	0	0	-1	0	2	0
MKS_2	1	-1	0	1	0	0	0	0
OQ_2	0	0	0	0	1	1	0	0
MKS_2	1	-1	0	1	0	0	0	0
MSN_2	1	1	-1	0	0	0	0	0
$2SM_2$	-1	2	0	0	0	0	0	0
MO_3	1	0	0	0	1	0	0	0
SO_3	0	1	0	0	1	0	0	0
MK_3	1	0	0	0	0	0	0	1
SK_3	0	1	0	0	0	0	0	1
MN_4	1	0	1	0	0	0	0	0
M_4	2	0	0	0	0	0	0	0
SN_4	0	1	1	0	0	0	0	0
MS_4	1	1	0	0	0	0	0	0
MK_4	1	0	0	1	0	0	0	0
S_4	0	2	0	0	0	0	0	0
SK_4	0	1	0	1	0	0	0	0
$2MN_6$	2	0	1	0	0	0	0	0
M_6	3	0	0	0	0	0	0	0
MSN_6	1	1	1	0	0	0	0	0
$2MS_6$	2	1	0	0	0	0	0	0
$2MK_6$	2	0	0	1	0	0	0	0
$2SM_6$	1	2	0	0	0	0	0	0
MSK_6	1	1	0	1	0	0	0	0
$3MN_8$	3	0	1	0	0	0	0	0
M_8	4	0	0	0	0	0	0	0
$2MSN_8$	2	1	1	0	0	0	0	0
$3MS_8$	3	1	0	0	0	0	0	0
$2(MS)_8$	2	2	0	0	0	0	0	0
$2MSK_8$	2	1	0	1	0	0	0	0

Table 2.3: Shallow-water tidal harmonics. Additional shallow-water harmonics may be found in the literature (e.g., in the appendices of Foreman (1977)).

harmonic terms in y. In this case, the arguments of the four shallow-water tides are $2a$, $2b$, $a+b$, and $a-b$. If the two interacting harmonics are M_2 and S_2, then $a = 2\sigma_1 t$ and $b = 2\sigma_0 t$, yielding four shallow-water tides that have frequencies of $4\sigma_1$, $4\sigma_0$, $2(\sigma_1+\sigma_0)$, and $2(\sigma_0-\sigma_1)$.[1] The four frequencies correspond to the M_4, S_4, MS_4, and MS_f shallow-water tidal harmonics, respectively. The amplitudes, which should be compared only to other harmonics of the same tidal species and interpreted only in a relative sense (e.g., Doodson & Warburg, 1941, Sec. 8.3), are $\frac{1}{2}A^2$, $\frac{1}{2}B^2$, and AB. Thus, in a relative sense, the MS_4 and MS_f tidal harmonics have equivalent amplitudes. This theory provides the basis for the derivation of shallow-water harmonics. Additional terms arise through interactions between other astronomical constituents and expansions of the tidal interaction equations to higher order. For example, expanding the interaction between the two astronomical tides in Eq. 2.21 to third order (i.e., $y^3 = y^2\ y$) yields six independent shallow-water harmonics.

Table 2.3 lists some of the most important shallow-water tidal harmonics, including the astronomical harmonics from which they are derived. Doodson numbers for the shallow-water harmonics are obtained by forming the sum of the products between the Doodson coefficients and contribution factors for each astronomical harmonic. In pseudo-mathematical notation, the Doodson numbers for l shallow-water harmonics could be derived as follows (e.g., Doodson & Warburg, 1941; Foreman, 1977):

$$[\text{Astronomical Contribution}] \times [\text{Astronomical Doodson}] = [\text{Shallow-Water Doodson}]\,,$$

or, in terms of matrix dimensions,

$$[\ l \times m\ ] \times [\ m \times 6\ ] = [\ l \times 6\ ]\,, \tag{2.24}$$

where m is the number of interacting astronomical tidal harmonics. For the particular shallow-water harmonics listed in Table 2.3, $m = 8$ because the non-linear interactions required to produce them involve some combination of eight specific astronomical tidal harmonics: M_2, S_2, N_2, K_2, O_1, Q_1, P_1, and K_1. For the first five shallow-water harmonics

[1] Note that $\cos(a-b) = \cos(-(a-b)) = \cos(b-a)$.

listed in Table 2.3 (MS_f, NO_1, SO_1, $2MS_2$, and OP_2) as well as an additional and generic shallow-water tide (sw), the matrix multiplication required to derive the Doodson numbers for the shallow-water tides becomes:

$$\begin{array}{r} MS_f \\ NO_1 \\ SO_1 \\ 2MS_2 \\ OP_2 \\ sw \end{array} \begin{bmatrix} -1 & 1 & 0 & 0 & 0 & 0 & 0 & 0 \\ 0 & 0 & 1 & 0 & -1 & 0 & 0 & 0 \\ 0 & 1 & 0 & 0 & -1 & 0 & 0 & 0 \\ 2 & -1 & 0 & 0 & 0 & 0 & 0 & 0 \\ 0 & 0 & 0 & 0 & 1 & 0 & 1 & 0 \\ iM_{2_s} & iS_{2_s} & iN_{2_s} & iK_{2_s} & iO_{1_s} & iQ_{1_s} & iP_{1_s} & iK_{1_s} \end{bmatrix} \times$$

$$\begin{array}{r} M_2 \\ S_2 \\ N_2 \\ K_2 \\ O_1 \\ Q_1 \\ P_1 \\ K_1 \end{array} \begin{bmatrix} 2 & 0 & 0 & 0 & 0 & 0 \\ 2 & 2 & -2 & 0 & 0 & 0 \\ 2 & -1 & 0 & 1 & 0 & 0 \\ 2 & 2 & 0 & 0 & 0 & 0 \\ 1 & -1 & 0 & 0 & 0 & 0 \\ 1 & -2 & 0 & 1 & 0 & 0 \\ 1 & 1 & -2 & 0 & 0 & 0 \\ 1 & 1 & 0 & 0 & 0 & 0 \end{bmatrix} = \begin{array}{r} MS_f \\ NO_1 \\ SO_1 \\ 2MS_2 \\ OP_2 \\ sw \end{array} \begin{bmatrix} 0 & 2 & -2 & 0 & 0 & 0 \\ 1 & 0 & 0 & 1 & 0 & 0 \\ 1 & 3 & -2 & 0 & 0 & 0 \\ 2 & -2 & 2 & 0 & 0 & 0 \\ 2 & 0 & -2 & 0 & 0 & 0 \\ \eta_{a_s} & \eta_{b_s} & \eta_{c_s} & \eta_{d_s} & \eta_{e_s} & \eta_{f_s} \end{bmatrix}.$$

The Doodson numbers for the shallow-water harmonics may then be used to derive the frequencies, σ, of the shallow-water harmonics in the same way as for the astronomical harmonics. Some of the shallow-water harmonics have Doodson numbers that coincide with astronomical tides, and hence shallow-water tides may mask or be masked by astronomical tides on occasion. Care must be exercised when deriving the argument and harmonic-modulation corrections for the shallow-water tides.

Arguments for shallow-water harmonics are computed as follows (e.g., Doodson & War-

burg, 1941; Foreman, 1977; Pugh & Woodworth, 2014):

$$\begin{aligned} V_{SW} &= iM_2\,(\arg \text{of } M_2) + iS_2\,(\arg \text{of } S_2) + iN_2\,(\arg \text{of } N_2) + iK_2\,(\arg \text{of } K_2) + \\ & \quad iO_1\,(\arg \text{of } O_1) + iQ_1\,(\arg \text{of } Q_1) + iP_1\,(\arg \text{of } P_1) + iK_1\,(\arg \text{of } K_1) \\ & \quad + \ldots, \end{aligned} \tag{2.25}$$

where $(\arg \text{of } M_2)$, for instance, refers to the argument of the astronomical M_2 harmonic. Additional astronomical harmonics may be added as needed. The argument for the shallow-water tide M_6, for example, is $[3 \times (\arg \text{of } M_2)]$ and the argument for the shallow-water tide $2MS_2$ is $[2 \times (\arg \text{of } M_2) - (\arg \text{of } S_2)]$.

Harmonic-modulation corrections for the shallow-water tides are computed as follows (e.g., Doodson & Warburg, 1941; Foreman, 1977; Pugh & Woodworth, 2014):

$$\begin{aligned} u_{SW} &= iM_2\,(u \text{ of } M_2) + iS_2\,(u \text{ of } S_2) + iN_2\,(u \text{ of } N_2) + iK_2\,(u \text{ of } K_2) + \\ & \quad iO_1\,(u \text{ of } O_1) + iQ_1\,(u \text{ of } Q_1) + iP_1\,(u \text{ of } P_1) + iK_1\,(u \text{ of } K_1) + \ldots \end{aligned} \tag{2.26}$$

$$\begin{aligned} f_{SW} &= (f \text{ of } M_2)^{iM_2} + (f \text{ of } S_2)^{iS_2} + (f \text{ of } N_2)^{iN_2} + (f \text{ of } K_2)^{iK_2} + \\ & \quad (f \text{ of } O_1)^{iO_1} + (f \text{ of } Q_1)^{iQ_1} + (f \text{ of } P_1)^{iP_1} + (f \text{ of } K_1)^{iK_1} + \ldots. \end{aligned} \tag{2.27}$$

As an example, the astronomical contribution for $2MSN_8$ is $iM_2 = 2$, $iS_2 = 1$, and $iN_2 = 1$. Therefore, the Doodson number for the shallow-water harmonic is $2\times$[2 0 0 0 0 0] $+1\times$[2 2 -2 0 0 0] $+1\times$[2 -1 0 1 0 0] = [8 1 -2 1 0 0]. The argument is then $2 \times (\arg \text{of } M_2) + 1 \times (\arg \text{of } S_2) + 1 \times (\arg \text{of } N_2)$. Furthermore, the harmonic-modulation corrections are $u_{2MSN_8} = 2(u \text{ of } M_2) + (u \text{ of } S_2) + (u \text{ of } N_2)$ and $f_{2MSN_8} = (f \text{ of } M_2)^2 + (f \text{ of } S_2) + (f \text{ of } N_2)$. Note that the harmonic-modulation corrections differ significantly between the astronomical and shallow-water harmonics, even between those that share the same Doodson number and frequency. Thus, monitoring harmonic modulations has become a valuable tool used for differentiating between the shallow-water and astronomical contributions to observations of tidal height (e.g., Godin, 1972; Foreman, 1977).

It is worth noting, however, that shallow-water harmonics are produced through several dif-

ferent physical mechanisms that generate different non-linear effects. The M_6 harmonic, for example, can arise due to both asymmetrical and symmetrical frictional effects (Parker, 2007). The second-order asymmetrical effect occurs when the crest of the primary tide propagates faster than the trough due to bottom friction and shallow water depths. The first-order symmetrical effect occurs because the frictional energy loss is proportional to the square of the current speed (i.e., a quadratic frictional non-linear mechanism). In some locations, the quadratic frictional mechanism may dominate, in which case the amplitude-modulation correction factor for M_6 should be the square of the amplitude-modulation correction factor for M_2, rather than the cube (Parker, 2007).

2.4 Constituent Selection

A small subset of carefully selected tidal constituents can often account for nearly all of the tidal signal (e.g., Godin, 1972, Sec. 2.8.2). Since time series of tidal observations are finite in length, the selection of appropriate constituents must involve a consideration of the frequency resolution of the time series (e.g., Godin, 1972, Sec. 1.5.1). In particular, the order of the constituent selection is important, since some harmonics are more dominant than others in terms of amplitude. Selecting a subsidiary harmonic to the M_2 harmonic, for example, would generally not be a good choice, since its selection could preclude the inclusion of M_2 in the analysis, even though M_2 generally has a large amplitude.

No single method exists to select the ideal set of tidal constituents to include in an analysis (e.g., Foreman et al., 2009). One option is the Rayleigh comparison, which tests for the ability to separate two harmonics in the frequency domain over a given length of observations (e.g., Foreman, 1977, Sec. 2.1.2). A Rayleigh comparison is performed as follows:

$$|\sigma_0 - \sigma_1| \times T \geq R, \tag{2.28}$$

where σ_0 and σ_1 are the frequencies of the two tidal harmonics being compared (in deg/hour), T is the length of the time series (in hours), and R is the Rayleigh parameter. The Rayleigh parameter must be at least 1 cycle, or 360°, but may be increased for time series with gaps.

Furthermore, to prevent aliasing, harmonics must only be selected if they have frequencies at least less than half the sampling rate.

For astronomical tidal harmonics, priority for inclusion in an analysis is commonly based on equilibrium-tide amplitudes from tidal potential catalogues (e.g., Godin, 1972; Foreman, 1977, Sec. 2.1.2). The largest amplitude harmonics within each tidal species are typically selected first. For a time series of intermediate length ($\gtrapprox$ 1 month but $<$ 8.85 years), additional harmonics within each tidal species will be considered for inclusion, commencing with the largest amplitude harmonics. Each harmonic considered for inclusion will be compared against larger-amplitude harmonics that were already selected using the Rayleigh criterion. If the test harmonic may be separated from all other harmonics over the length of the time series, then the test harmonic will also be selected for inclusion in the analysis. The process continues in descending order of equilibrium-tide amplitude until no more harmonics are available to test. Generally, only the largest amplitude harmonic from each constituent cluster will be considered for inclusion in an analysis, and contributions from the remaining harmonics in the constituent (above an arbitrary amplitude threshold) will be accounted for with harmonic-modulation corrections. A reasonable Doodson-scaled amplitude threshold is 0.0025 (e.g., Cartwright & Taylor, 1971). Foreman (1977) makes a few minor exceptions to the strict amplitude hierarchies in order to maximize the number of large-amplitude harmonics in an analysis, given the available frequency resolution.

For time series that are less than 1 month in length, it may be necessary to consider terms separated in period by the sidereal month (η_c) as subsidiary harmonics, in addition to the usual modulations in lunar perigee, nodal regression, and perihelion. Similarly, for time series longer than about 20 years, it would no longer be necessary to apply harmonic-modulation corrections for harmonics separated by cycles in p or N', since the harmonics are separable outright.

Selection of shallow-water harmonics presents a more complicated problem (e.g., Doodson, 1957, Sec. 6), since shallow-water harmonics do not have equilibrium-tide amplitudes (e.g., Godin, 1972, Sec. 2.7). One technique typically used, however, is to refrain from including a shallow-water harmonic until all of its astronomical components have also been included

(e.g., Foreman, 1977, Sec. 2.1.2). Furthermore, shallow-water harmonics may be compared against previously selected shallow-water and astronomical harmonics using the Rayleigh criterion. The order of selection for shallow-water harmonics, however, is not straightforward. Godin (1972) and Foreman (1977) make some suggestions about the hierarchy for shallow-water harmonics based on Godin's extensive experience with tidal analysis. Other options involve comparing the relative amplitudes of astronomical harmonics that give rise to the shallow-water harmonics (e.g., Doodson & Warburg, 1941, Sec. 8.3) or practical experience and analysis at specific locations (e.g., Doodson, 1957; Doodson & Warburg, 1941, Sec. 15.3).

2.5 Inversion

In this section, I discuss a method for inverting time-series data to recover tidal-harmonic components. Recall that the general expression for a single tidal harmonic, η, was given by Eq. 2.5. For a signal that includes contributions from many different tidal harmonics, the equation becomes:

$$Z(t) = m_0 + m_1 t + \sum_{\eta=1}^{N} A_\eta \; f_\eta(t) \; \cos(\sigma_\eta t - \phi_\eta + V_\eta(t_0) + u_\eta(t)), \tag{2.29}$$

where $Z(t)$ represents the amplitude of the total signal at epoch t, m_0 accounts for a constant offset in the data, m_1 accounts for a linear trend in the data, η represents a tidal harmonic, and N represents the total number of tidal harmonics considered. The trigonometric argument may be simplified and made more precise by recalling that (e.g., Foreman et al., 2009):

$$V_\eta(t_0) + \sigma_\eta t \sim V_\eta(t). \tag{2.30}$$

Indeed, $V_\eta(t_0) + \sigma_\eta t$ is actually a linear approximation to $V_\eta(t)$, which represents the astronomical argument at time t. Thus, Eq. 2.29 becomes:

$$Z(t) = m_0 + m_1 t + \sum_{n=1}^{N} A_\eta \; f_\eta(t) \; \cos(V_\eta(t) + u_\eta(t) - \phi_\eta). \tag{2.31}$$

Since f, u, and V are known quantities derived from the astronomical ephemeris (Tables 1.2 and 2.1), I seek the set of model terms [m_0, m_1, A_η, ϕ_η]. Least-squares optimization is a common method used to solve for the model terms. To apply the least-squares technique, I first linearize the problem by separating the harmonic portion of Eq. 2.31 into in-phase and quadrature components. In particular, each harmonic may be decomposed using a trigonometric identity: $\cos(u - v) = \cos u \cos v + \sin u \sin v$. Formally,

$$\begin{aligned}
& A_\eta\ f_\eta(t)\ \cos(V_\eta(t) + u_\eta(t) - \phi_\eta) \\
= \quad & A_\eta\ f_\eta(t)\ \cos(V_\eta(t) + u_\eta(t))\ \cos(\phi_\eta) + \\
& A_\eta\ f_\eta(t)\ \sin(V_\eta(t) + u_\eta(t))\ \sin(\phi_\eta) \\
= \quad & A_\eta\ f_\eta(t)\ \cos(\phi_\eta)\ \cos(V_\eta(t) + u_\eta(t)) + \\
& A_\eta\ f_\eta(t)\ \sin(\phi_\eta)\ \sin(V_\eta(t) + u_\eta(t)) \\
= \quad & A_\eta\ \cos(\phi_\eta)\ f_\eta(t)\ \cos(V_\eta(t) + u_\eta(t)) + \\
& A_\eta\ \sin(\phi_\eta)\ f_\eta(t)\ \sin(V_\eta(t) + u_\eta(t)) \\
= \quad & c_\eta\ f_\eta(t)\ \cos(V_\eta(t) + u_\eta(t)) + s_\eta\ f_\eta(t)\ \sin(V_\eta(t) + u_\eta(t)), \qquad (2.32)
\end{aligned}$$

where

$$c_\eta \equiv A_\eta\ \cos(\phi_\eta) \qquad (2.33)$$

and

$$s_\eta \equiv A_\eta\ \sin(\phi_\eta). \qquad (2.34)$$

Substituting Eq. 7.8 into Eq. 2.31:

$$\begin{aligned}
Z(t) \quad = \quad & m_0 + m_1 t + \sum_{n=1}^{N} [c_\eta\ f_\eta(t)\ \cos(V_\eta(t) + u_\eta(t)) + \\
& s_\eta\ f_\eta(t)\ \sin(V_\eta(t) + u_\eta(t))]. \qquad (2.35)
\end{aligned}$$

Eq. 7.10 may be used to invert time series of tidal data for the unknown model parameters [m_0, m_1, c_η, s_η]. The construct is specific to linear, overdetermined problems. Note that if Z_0 (mean sea level) is included as a tidal harmonic, then m_0 must be removed from the set

of model parameters to avoid ill-conditioning in the matrix inversion.

For least-squares harmonic analysis, the system of linear equations to be solved takes the form:

$$G\,m = d, \tag{2.36}$$

where d is the observed tidal data, m is a vector of model parameters, and G is a matrix of known quantities that interact with the model parameters. The objective is to minimize the misfit between the model, $G\,m$, and the observed data, d, specifically by minimizing the norm of the squared residuals. In other words, I seek to minimize:

$$\sqrt{\sum_{i=1}^{m} r_i^2} = \sqrt{\sum_{i=1}^{m} (d_i - (G\,m)_i)^2} = ||d - G\,m||_2, \tag{2.37}$$

where r corresponds to the residuals between the observed data and the predicted model (i.e., $r = d - G\,m$) (Aster et al., 2013).

The normal equations for the inversion are given by:

$$m = (G^T\,G)^{-1}\,G^T\,d, \tag{2.38}$$

where

$$m = [\; m_0 \;\; m_1 \;\; c_1 \;\; s_1 \;\; c_2 \;\; s_2 \;\; c_3 \;\; s_3 \;\; c_4 \;\; s_4 \;\; \cdots \;]^T \tag{2.39}$$

and

$$d = [\; d(t_0) \;\; d(t_1) \;\; d(t_2) \;\; d(t_3) \;\; d(t_4) \;\; d(t_5) \;\; d(t_6) \;\; d(t_7) \;\; \cdots \;]^T. \tag{2.40}$$

The subscripts for c and s represent individual tidal harmonics (e.g., M_2).

The G^T matrix (transpose of G) is given by:

$$G^T = \begin{bmatrix} 1 & 1 & 1 & \cdots \\ t_0 & t_1 & t_2 & \cdots \\ f_1(t_0)\cos[V_1(t_0)+u_1(t_0)] & f_1(t_1)\cos[V_1(t_1)+u_1(t_1)] & \cdots & \cdots \\ f_1(t_0)\sin[V_1(t_0)+u_1(t_0)] & f_1(t_1)\sin[V_1(t_1)+u_1(t_1)] & \cdots & \cdots \\ f_2(t_0)\cos[V_2(t_0)+u_2(t_0)] & f_2(t_1)\cos[V_2(t_1)+u_2(t_1)] & \cdots & \cdots \\ f_2(t_0)\sin[V_2(t_0)+u_2(t_0)] & f_2(t_1)\sin[V_2(t_1)+u_2(t_1)] & \cdots & \cdots \\ f_3(t_0)\cos[V_3(t_0)+u_3(t_0)] & f_3(t_1)\cos[V_3(t_1)+u_3(t_1)] & \cdots & \cdots \\ f_3(t_0)\sin[V_3(t_0)+u_3(t_0)] & f_3(t_1)\sin[V_3(t_1)+u_3(t_1)] & \cdots & \cdots \\ f_4(t_0)\cos[V_4(t_0)+u_4(t_0)] & f_4(t_1)\cos[V_4(t_1)+u_4(t_1)] & \cdots & \cdots \\ f_4(t_0)\sin[V_4(t_0)+u_4(t_0)] & f_4(t_1)\sin[V_4(t_1)+u_4(t_1)] & \cdots & \cdots \\ \vdots & \vdots & \vdots & \vdots \end{bmatrix}.$$

Some of the harmonic-modulation formulae in Table 2.1 are given in the form $[f\cos u]$ and $[f\sin u]$. The current construct for G does not have the harmonic-modulation terms in this form; however, the corrections may be easily recast using additional trigonometric manipulations:

$$\cos(u+v) = \cos u\cos v - \sin u\sin v \tag{2.41}$$

and

$$\sin(u+v) = \sin u\cos v + \cos u\sin v. \tag{2.42}$$

Thus,

$$\begin{aligned} f\ \cos[V+u] &= f\ \cos V\ \cos u - f\ \sin V\ \sin u \\ &= [f\cos u]\ \cos V - [f\sin u]\ \sin V \end{aligned} \tag{2.43}$$

and

$$f\ \sin[V+u] = f\ \sin V\ \cos u + f\ \cos V\ \sin u$$

$$= \quad [f \cos u] \ \sin V + [f \sin u] \ \cos V, \tag{2.44}$$

which may be substituted into G.

To perform the inversion, I aim to minimize the misfit between the observations and model, $d - Gm$, by adopting an iteratively reweighted least-squares (IRLS) algorithm, which evaluates a series of weighted least-squares problems that converge to an L1-norm solution (Aster et al., 2013). The L1-norm minimizes the absolute value of the residuals and is therefore highly effective at down-weighting outliers. A preliminary L2-norm solution forms the initial model vector. A weighting matrix is then constructed based on the residuals between the observations and the forward model. Since the weighting matrix is a non-linear function of the model vector, the normal equations must be solved iteratively. Thus, an updated model vector is derived from the L1-norm solution to the normal equations and tested against a tolerance value. The iterations continue until the tolerance is satisfied, at which point the inversion yields a model vector (Eq. 2.39) that provides a constant offset value, linear trend coefficient, and the harmonic coefficients.

The in-phase and quadrature components of the harmonic coefficients may be re-combined to compute amplitude and phase values for each tidal harmonic. For a given tidal harmonic, η:

$$A_\eta = \sqrt{c_\eta^2 + s_\eta^2} \tag{2.45}$$

and

$$\phi_\eta = \text{atan2}(s_\eta, c_\eta), \tag{2.46}$$

where A_η is the amplitude and ϕ_η is the phase.

2.6 Error Analysis

One method for determining uncertainties in the estimated harmonic coefficients involves computing power spectra of the residuals, as described in (Pawlowicz et al., 2002). In particular, the variance in the c and s parameters may be estimated by multiplying the average spectral density, $\bar{P}$, by the frequency interval of the time series, $\Delta f = (N \Delta t)^{-1}$,

where N represents the total number of epochs in the time series and Δt represents the temporal spacing of the time series. Periodograms for real time series often do not exhibit spectral flatness; thus, frequency windows centered on each tidal harmonic may be applied to the periodograms prior to computing $\bar{P}$.

Since $\bar{P}\Delta f$ provides a variance estimate for the harmonic coefficients (c_η and s_η in Eq. 7.10), the error estimates must be mapped into amplitude and phase. The mapping may be accomplished using a parametric bootstrap algorithm. In particular, random noise estimates may be sampled from Gaussian distributions of the residual variance and added to the original harmonic coefficients derived from inversion of the time series. The addition of randomly sampled noise to the harmonic coefficients generates many additional instances of the harmonic coefficients, which may be converted into distributions of amplitude and phase for each tidal harmonic. Standard statistical analyses may then be performed on the bootstrapped distributions of amplitude and phase.

2.7 Particle Motion Ellipses

For an individual tidal harmonic, the OTL-induced surface displacements at a particular station may be represented by a closed particle motion ellipse (PME) in three-dimensional space, which is traced out completely during each tidal period (e.g., Godin, 1972, Sec. 2.6.1). To illustrate three-dimensional harmonic displacements on a two-dimensional map, however, the horizontal motion can be depicted by the size and orientation of the PME (generated from the east-west and north-south displacement) and the vertical motion can be depicted by the color of the PME.

The horizontal-ellipse parameters may be derived analytically from the harmonic time functions for the north- and east-displacement components:

$$\begin{aligned} x(t) &= A\cos(\omega_0\, t - \alpha) \\ y(t) &= B\cos(\omega_0\, t - \beta), \end{aligned}$$

where $x(t)$ represents the time function for the east component and $y(t)$ represents the

time function for the north component. Since the frequency, ω_0, is the same for each time function, the time functions may be combined (e.g., Thornton & Marion, 2004):

$$\begin{aligned} y(t) &= \frac{B}{A}\,x(t)\,\cos\delta - B\sqrt{1-\left(\frac{x(t)}{A}\right)^2}\,\sin\delta \\ A^2\,B^2\,\sin^2\delta &= B^2\,x(t)^2 - 2\,A\,B\,x(t)\,y(t)\,\cos\delta + A^2\,y(t)^2 \\ \sin^2\delta &= \frac{x(t)^2}{A^2} - \frac{2\,x(t)\,y(t)\,\cos\delta}{A\,B} + \frac{y(t)^2}{B^2}, \end{aligned} \tag{2.47}$$

where $\delta = \alpha - \beta$.

The east- and north-displacement components may then be rotated into a new frame of reference such that the semi-major and semi-minor axes of the ellipse are aligned with the horizontal and vertical axes of the new coordinate system. The new coordinates, x' and y', are related to the old coordinates (x and y) by a rotation angle, θ (e.g., Boas, 1983, Sec. 3.6):

$$\begin{aligned} x(t) &= x'(t)\,\cos\theta - y'(t)\,\sin\theta \\ y(t) &= x'(t)\,\sin\theta + y'(t)\,\cos\theta. \end{aligned}$$

Substituting the rotated coordinates into Eq. 2.47 yields:

$$\begin{aligned} &\frac{(x'(t)\,\cos\theta - y'(t)\,\sin\theta)^2}{A^2} + \frac{(x'(t)\,\sin\theta + y'(t)\,\cos\theta)^2}{B^2} \quad - \\ &\frac{2\,(x'(t)\,\cos\theta - y'(t)\,\sin\theta)\,(x'(t)\,\sin\theta + y'(t)\,\cos\theta)\,\cos\delta}{A\,B} \quad = \quad \sin^2\delta. \end{aligned} \tag{2.48}$$

Expanding and rearranging leads to:

$$\begin{aligned} \sin^2\delta &= \frac{x'(t)^2\,\cos^2\theta}{A^2} - \frac{2\,x'(t)\,y'(t)\,\sin\theta\cos\theta}{A^2} + \frac{y'(t)^2\,\sin^2\theta}{A^2} + \\ &\quad \frac{x'(t)^2\,\sin^2\theta}{B^2} - \frac{2\,x'(t)\,y'(t)\,\sin\theta\cos\theta}{B^2} + \frac{y'(t)^2\,\cos^2\theta}{B^2} - \\ &\quad \frac{2\,\cos\delta}{A\,B}\,[x'(t)^2\,\cos\theta\,\sin\theta - y'(t)\,x'(t)\,\sin^2\theta + \\ &\quad y'(t)\,x'(t)\,\cos^2\theta - y'(t)^2\,\sin\theta\,\cos\theta] \\ &= x'(t)^2\left[\frac{\cos^2\theta}{A^2} - \frac{2\,\cos\theta\,\sin\theta\,\cos\delta}{A\,B} + \frac{\sin^2\theta}{B^2}\right] + \end{aligned}$$

$$y'(t)^2 \left[\frac{\sin^2\theta}{A^2} + \frac{2\,\cos\theta\,\sin\theta\,\cos\delta}{A\,B} + \frac{\cos^2\theta}{B^2}\right] + x'(t)\,y'(t)\left[-\frac{2\,\sin\theta\,\cos\theta}{A^2} + \frac{2\,\cos\delta\,(\sin^2\theta - \cos^2\theta)}{A\,B} + \frac{2\,\cos\theta\,\sin\theta}{B^2}\right]. \tag{2.49}$$

Setting the $x'(t)\,y'(t)$ term in Eq. 2.49 equal to zero yields:

$$\left[-\frac{\sin(2\,\theta)}{A^2} - \frac{2\,\cos\delta\,\cos(2\,\theta)}{A\,B} + \frac{\sin(2\,\theta)}{B^2}\right] = 0, \tag{2.50}$$

where the trigonometric identities

$$\begin{aligned}\sin(2\,u) &= 2\,\sin u\cos u\\ \cos(2\,u) &= \cos^2 u - \sin^2 u\end{aligned}$$

have been applied. I then solve Eq. 2.50 for θ:

$$\begin{aligned}0 &= -B^2\sin(2\theta) - 2\,A\,B\,\cos\delta\,\cos(2\theta) + A^2\sin(2\theta)\\ &= \sin(2\theta)[A^2 - B^2] - \cos(2\theta)[2\,A\,B\,\cos\delta]\\ \frac{\sin(2\theta)}{\cos(2\theta)} &= \left[\frac{2\,A\,B\,\cos\delta}{A^2 - B^2}\right]\\ \tan(2\theta) &= \left[\frac{2\,A\,B\,\cos\delta}{A^2 - B^2}\right]\\ 2\,\theta &= \arctan\left[\frac{2\,A\,B\,\cos\delta}{A^2 - B^2}\right]\\ \theta &= \frac{1}{2}\arctan\left[\frac{2\,A\,B\,\cos\delta}{A^2 - B^2}\right].\end{aligned} \tag{2.51}$$

Returning to Eq. 2.49:

$$\begin{aligned}\sin^2\delta &= x'(t)^2\left[\frac{\cos^2\theta}{A^2} - \frac{2\,\cos\theta\,\sin\theta\,\cos\delta}{A\,B} + \frac{\sin^2\theta}{B^2}\right] +\\ &\quad y'(t)^2\left[\frac{\sin^2\theta}{A^2} + \frac{2\,\cos\theta\,\sin\theta\,\cos\delta}{A\,B} + \frac{\cos^2\theta}{B^2}\right] +\\ &\quad x'(t)\,y'(t)\,[0],\end{aligned} \tag{2.52}$$

which equates to

$$\frac{x'(t)^2}{a^2} + \frac{y'(t)^2}{b^2} = 1, \tag{2.53}$$

where

$$\begin{aligned} \frac{1}{a^2} &= \frac{1}{\sin^2\delta}\left[\frac{\cos^2\theta}{A^2} - \frac{2\,\cos\theta\,\sin\theta\,\cos\delta}{A\,B} + \frac{\sin^2\theta}{B^2}\right] \\ \frac{1}{b^2} &= \frac{1}{\sin^2\delta}\left[\frac{\sin^2\theta}{A^2} + \frac{2\,\cos\theta\,\sin\theta\,\cos\delta}{A\,B} + \frac{\cos^2\theta}{B^2}\right]. \end{aligned} \tag{2.54}$$

The PME representing the horizontal motion is now aligned along the x' and y' axes, where a and b are the semi-major and semi-minor axes and θ is given by Eq. 2.51.

2.8 Suggestions for Further Reading

A selection of useful resources for tidal harmonic analysis includes: Doodson (1921, 1924a, 1928, 1957), Doodson & Warburg (1941), Schureman (1971), Godin (1972), Foreman (1977), Melchior (1983), Pugh (1987), Pawlowicz et al. (2002), Foreman et al. (2009), and Pugh & Woodworth (2014).

3

GNSS-Inferred Measurements of Ocean Tidal Loading Response

3.1 Introduction

Earth's displacement response to periodic loading by the ocean tides may be inferred using Global Navigation Satellite System (GNSS) networks of ground-based receivers and space-based satellites (e.g., Ito & Simons, 2011; Yuan et al., 2013; Bos et al., 2015). The Global Positioning System (GPS), operated by the United States government, makes up one sector of the broader GNSS system. Currently, the space-based GPS constellation consists of approximately 30 satellites (Blewitt, 2015). Typically, at least five GPS satellites are visible to an Earth-based observer at any time and at any location worldwide. The satellites record surface displacements, indirectly by means of pseudorange and phase observables, with an accuracy of about a few millimeters and a precision down to about 1 mm (Blewitt, 2015).

Traditionally, gravity, tilt, and strain measurements have been used to investigate Earth's response to ocean tidal loading (OTL) (e.g., Baker, 1980a,b; Melchior, 1983; Baker, 1984; Agnew, 2015). The load Green's functions for tilt and strain, however, decrease as r^{-2} from the load point, where r is distance; thus, OTL response estimates obtained using strain- and tilt-meters primarily reflect the local Earth structure (Baker, 1984; Jentzsch, 1997). Local inhomogeneities, such as cavities, limit the effectiveness of using strain and tilt observations to investigate OTL response. Gravity and displacement load Green's functions, on the other hand, decrease as r^{-1} from the load point and therefore exhibit sensitivity to a wider expanse of ocean loads as well as to regional solid Earth structure (Baker, 1984). Since GPS stations are also extensively deployed around the globe, GPS has emerged as a preferred method for investigations into OTL response (e.g., Penna et al., 2015).

For many geodetic studies, OTL response is an inconvenient source of noise. Thus, the signal is often removed at the GPS processing stage using forward-modeled coefficients for the main tidal constituents. Smaller tidal harmonics are often modeled and removed as well by interpolation of the admittance, which is assumed smooth across each tidal constituent band (e.g., Agnew, 2012). One can also remove the OTL signal at the post-processing stage by simply fitting a harmonic series of sine and cosine terms, each with a specific tidal frequency, and removing the modeled values from the time series. Since precise estimates of the phases relative to a common reference point are not required for simply removing the tidal components, the astronomical ephemeris need not be considered (except for determining the frequencies of the tidal harmonics, which are widely known).

When OTL response is the signal of interest, however, the astronomical argument and harmonic-modulation corrections must be considered as well. Isolating the OTL-response signal in a geodetic time series requires the modeling and removal of additional signals that might contaminate the time series, including the solid-Earth body tides, transient effects (such as earthquakes, diking, rifting, creep, or volcanism), tectonic plate motions, glacial rebound, multipath effects, atmospheric loading, antenna imperfections, and tropospheric refraction. Here, I discuss strategies for processing raw GPS data and isolating the OTL-response signal.

3.2 Basic GPS Theory

The GPS satellites, deployed and maintained primarily by the US Department of Defense, emit electromagnetic (EM) signals at two separate microwave frequencies: 1575.42 MHz (19.0 cm wavelength) for the L1 band and 1227.60 MHz (24.4 cm wavelength) for the L2 band (e.g., Blewitt, 1997, 2015). Each satellite transmitter encodes the two carrier wave signals via phase modulation into binary bits that contain the time of transmission, satellite clock bias estimates, and satellite position information, supplied by three distinct codes: the Course Acquisition (C/A) Code, the Precise (P) Code, and the Navigation Message.

Ground-based GPS receivers detect the dual-frequency carrier waves and cross-correlate the waves internally with replica signals generated by the receiver clocks. Two pseudo-

ranges, one for each frequency band, as well as two carrier phase observables are then computed by the receiver. The pseudoranges are derived based on the travel time of the carrier waves. The phase observables are derived based on the difference in phase between the transmitted signal and the replica signal generated internally by the receiver. Note that an ambiguity of an integer number of wavelengths will be introduced when the phase observables are converted to a distance measurement. Modern, research-grade software includes the functionality to estimate the integer ambiguities through a process known as *ambiguity resolution* (Blewitt, 1997; Bertiger et al., 2010; Blewitt, 2015).

For high-precision estimates of GPS receiver positions, the receiver must compute the two pseudoranges and two carrier phase observables simultaneously for *at least* five satellites in current view. The measurements are combined using trilateration (Blewitt, 2015). Thus, three satellites are required to obtain an estimate of receiver position. The fourth and fifth satellites facilitate estimation of receiver-clock bias and delays in signal transmission through the troposphere. Transmission delays through the ionosphere may also be removed through an appropriate combination of the dual-frequency signals, known as an *ionosphere-free* combination (Zumberge et al., 1997; Blewitt, 2015).

Although satellite navigation information is provided by the transmitting satellite itself, higher-precision satellite ephemeris information may be obtained through the International GNSS Service (IGS) or the Jet Propulsion Laboratory (JPL). Geodetic-quality positioning requires advanced signal processing software with the capacity to implement sophisticated algorithms, including multi-parameter estimation, ambiguity resolution, cycle-slip detection, and body-tide removal (Blewitt, 2015).

The design of the GPS satellite constellation maximizes the number of satellites visible to receivers across the globe at any time (Blewitt, 2015). The satellites occupy six evenly-spaced orbital planes at $\sim$26 600 km altitude, each inclined at 55° relative to the equatorial plane. Although $\sim$30 GPS satellites are currently deployed, only about 24 are considered currently active, with the remainder serving as spares. Each satellite completes one orbit about the earth in 11 hours and 58 minutes, and hence two orbits are completed in 23 hours and 56 minutes, a time period equivalent to the length of one **sidereal day**, or Earth's

rotational period. Since the ground tracks and geometry of the satellite constellation repeat every sidereal day, error sources specific to each satellite-receiver pair, such as *multipath*, repeat at the same period (Larson et al., 2010; Blewitt, 2015).

The satellite orbital inclinations have important implications for sensor deployment, including site selection and receiver orientation, as well as the precision of the estimated receiver positions (Blewitt, 1997, 2015). Due to the 55° inclination of the orbital tracks, the satellites never cross the polar regions and never rise more than 55° above the horizon from the perspective of a polar observer. For this reason, positioning precision worsens towards the poles. Moreover, in equatorial regions, GPS satellites appear to orbit primarily in the north-south direction; thus, estimation of the north displacement-component tends to be better constrained than the east displacement-component.

3.3 Data Acquisition and Formatting

The International GNSS Service (IGS) maintains an extensive network of more than 350 GNSS stations worldwide, with data freely available on-line for research purposes. Many additional local and regional networks have also been deployed, both on a permanent basis as well as campaign-style, by numerous governments and research organizations. The standard format for GNSS data is known as Receiver Independent Exchange (RINEX).

3.4 GPS Data Processing Strategies

Several software packages are available for the high-level processing of RINEX data (Blewitt, 1997, 2015). Here, I focus on software developed and maintained by JPL: the *GNSS-Inferred Positioning System and Orbit Analysis and Simulation Software II*, or GIPSY-OASIS II (GOA-II) (e.g., Gregorius, 1996; Zumberge et al., 1997). GOA-II includes the functionality to estimate **static** (daily) as well as **kinematic** (sub-daily/high-rate) receiver positions; either technique may be used to investigate OTL response (e.g., Allinson et al., 2004; King, 2006; Ito & Simons, 2011; Yuan & Chao, 2012; Yuan et al., 2013; Agnew, 2015; Penna et al., 2015). I adopt the kinematic approach, whereby the OTL response

remains un-modeled at the GPS processing stage and subsequently estimated through harmonic analysis (Ch. 2).

3.4.1 Kinematic Precise Point Positioning

GOA-II processes GNSS data using **Precise Point Positioning** (PPP) (Zumberge et al., 1997). Motivated by reducing the computation time for large GNSS networks, PPP provides an efficient and precise method for estimating receiver positions without inter-station double-differencing. The modules executed by GOA-II (*gd2p* script) include a data editor module (*ninja*), a measurement model module (*qregres*), a parameter estimation module (*wash cycle*), and a solution module (e.g., *tdpfile* and *stacov*). In addition to a RINEX file, GOA-II requires the data rate, solution rate, and solution type (i.e., static or kinematic). The data rate, rather than the solution rate, predominantly controls the processing time. Additional parameters may optionally be specified, such as the stochastic process noise settings for the coordinate estimates and tropospheric zenith delay.

PPP requires pre-computed satellite orbit and clock products, determined from a global network of GNSS satellites and permanent receivers. The precise ephemeris information effectively eliminates the need for local base stations, which would be required for traditional differential GNSS analysis (e.g., Zumberge et al., 1997; King & Aoki, 2003). Furthermore, GOA-II performs single-receiver ambiguity resolution by pre-computing wide-lane and phase bias estimates relative to an extensive global network of ground-based receivers (Bertiger et al., 2010).

Particularly for sub-daily solutions, treatment of the tropospheric zenith delay plays a critical role in the ability to resolve receiver positions accurately due to the direct trade-off in the two sets of parameters (Bar-Sever et al., 1998). A range of process noise values for the tropospheric zenith delay appear in the literature for mass-loading applications, including 3 mm $\text{hr}^{-\frac{1}{2}}$ (5.0E-8 km $\text{s}^{-\frac{1}{2}}$) (e.g., Williams & Penna, 2011; Yuan & Chao, 2012; Yuan et al., 2013), 4.8 mm $\text{hr}^{-\frac{1}{2}}$ (e.g., King & Aoki, 2003), 6 mm $\text{hr}^{-\frac{1}{2}}$ (e.g., Larson et al., 2010; Allinson et al., 2004), and 10.2 mm $\text{hr}^{-\frac{1}{2}}$ (e.g., King et al., 2005). Typically, a tropospheric zenith delay is estimated, from which delays at any elevation angle may be extrapolated us-

ing a mapping function (e.g., Blewitt, 2015). One of the simplest examples of an effective mapping function is the inverse sine of the elevation angle multiplied by the zenith delay, which assumes a horizontally stratified atmosphere (a reasonable assumption for elevation angles greater than about 20°). More accurate mapping functions treat the *wet* and *dry* components of the tropospheric delay separately and account for the curvature of Earth's surface (e.g., Blewitt, 2015).

3.4.2 Recovery of the OTL-Response Signal

Synthetic testing may be used to assess the optimal settings for GOA-II parameters (e.g., King & Aoki, 2003; Penna et al., 2015). Penna et al. (2015) introduced a small synthetic signal into a frequency band unoccupied by large-amplitude harmonics, but between M_2 and O_1. By tuning the coordinate and tropospheric process noise settings for the kinematic PPP analysis, Penna et al. (2015) demonstrated that the synthetic harmonics could be recovered with a precision of about 0.2 mm for stations in western Europe. As an alternative option, the synthetic signals could simulate real OTL-response signals, such as the modeled OTL response at a given location. For a kinematic PPP analysis, fine tuning the coordinate and tropospheric process noise settings are priorities (Penna et al., 2015).

To introduce a modeled OTL-response signal into GPS data, the complex-valued amplitudes of the synthetic harmonic(s) must be converted into pseudorange and phase observables for each transmitter-receiver pair. The conversion may be accomplished within GIPSY by computing two static PPP solutions. For the first solution, the raw data should be processed as normal, with receiver-specific OTL-response estimates included. For the second solution, the raw data should be processed using the same procedure, but with the synthetic OTL-response estimates substituted for the receiver-specific estimates. All other parameters should remain the same between the two runs. For the method to work well, the synthetic OTL-response signal should be much larger in amplitude than the receiver-specific OTL-response signal. The difference in pre-fit residuals from the two static solutions may be used to modify directly the GOA-II quick-measurement file, which includes the pseudorange and

phase observables for each satellite relative to the receiver[2].

The pre-fit residuals represent the differences between the GNSS observations and contributions from input-model parameters prior to the determination of station positions. Since all parameters remain unchanged between the two static runs except for the OTL-response model, the difference in pre-fit residuals simply yields the difference between the OTL-response models. Formally,

$$\begin{aligned} \mathrm{R_{pred}} - \mathrm{R_{syn}} &= (\mathrm{O} - \mathrm{M_{pred}}) - (\mathrm{O} - \mathrm{M_{syn}}) \\ &= \mathrm{M_{syn}} - \mathrm{M_{pred}}, \end{aligned} \tag{3.1}$$

where $\mathrm{R_{pred}}$ represents the pre-fit residuals computed based on the predicted tidal response at the receiver, $\mathrm{R_{syn}}$ represents the pre-fit residuals computed based on the synthetic tidal response, O represents the observations tabulated in the RINEX file, and M represents contributions to the data from input models. All model contributions cancel out in the differencing of the pre-fit residuals except for the OTL-response models; $\mathrm{M_{syn}} - \mathrm{M_{pred}}$ simply yields the difference between the synthetic OTL-response signal and predicted OTL-response signal at the receiver. Importantly, the differences between the OTL-response models are now given in the form of pseudorange and phase observables for individual satellites. When the model differences are added to the true pseudorange and phase observables in the *qmfile*, which includes the actual (recorded) OTL-response signal at the receiver, the resulting OTL-response signal should reflect only the synthetic harmonics. Since minor differences between the predicted and observed OTL response at the receiver will undoubtedly be present, receivers selected for synthetic testing should exhibit small OTL-response amplitudes relative to the synthetic. Ideally, the predicted and observed OTL-response sig-

[2]In order to export the pre-fit residuals, the *qregres.nml* file must be adjusted to include the line "Prefit = .True." in the *run_type* block. The adjustment must be made after the initial static PPP runs and followed by a re-execution of *qregres*. To re-execute *qregres*, run the command located at the top of the *qregres1.log* file at the command line, after adding "-res syn_test" to the end of the command list. Now, the pre-fit residuals may be found in a file called "syn_test;" the seventh column contains the residuals. After computing the difference in pre-fit residuals, the result must be inserted appropriately into the *qmfile*. Since the *qmfile* is binary, it must be converted to ascii format to make the changes. To do this, I use the *dump_qm* command: "dump_qm -d qmfile $>$ qmascii," where *-d* indicates double precision. I then edit the *qmascii* file by adding the pre-fit residual differences to the observation column (column 9), taking great care to keep track of satellite number, epoch, and type of observable. After the edits have been made, the ascii file can be dumped back to binary: "dump2qm ascii_file bin_file." Now, *gd2p* can be run with the *qmfile* as input instead of a RINEX file using the "-ae" flag.

nals would be zero (or perfectly modeled) such that the OTL-response contributions to the modified *qmfile* would come entirely from the synthetic signal. Any discrepancies, however, between the predicted and observed OTL response at the receiver remain consistent between various recovery tests. Thus, whereas uncertainty estimates garnered from the synthetic tests might be biased by inaccurate modeling of the OTL-response at the receiver, the process of finding optimal parameters should not be significantly impacted.

3.4.3 Removal of the Solid Earth Body Tides

GOA-II currently adopts a model for the solid-Earth body tides (SEBTs) from the 2010 International Earth Rotation and Reference Systems Service (IERS) standards (Petit & Luzum, 2010, Sec. 7.1.1). The SEBTs are computed from complex-valued Love numbers, where imaginary components arise due to mantle anelasticity and core resonances. Furthermore, the Love numbers are latitude dependent due to Earth's non-sphericity and frequency dependent due to Earth's rotation, mantle anelasticity, and the Nearly Diurnal Free Wobble (NDFW) resonance. The Love numbers are computed based on an oceanless version of the Preliminary Reference Earth Model (PREM) (Dziewonski & Anderson, 1981), with the model for mantle Q obtained from Widmer et al. (1991). For more information, see (Petit & Luzum, 2010, Secs. 6.2.1 & 7.1.1).

3.5 Post-Processing Techniques

3.5.1 Cleaning the Time Series

Even though *gd2p* performs some editing of data outliers, it is often necessary to detect and remove outliers at the post-processing stage as well. One method for removing outliers is to employ a running median absolute deviation. Furthermore, appropriately placed heaviside functions may be necessary to remove large offsets in the time series, perhaps due to tectonic events or local site disturbances. When extracting tidal harmonics from a GPS-inferred time series, an iterative re-weighted least squares (IRLS) approach, which converges to an L1-norm solution, can help to suppress the influence of large outliers (e.g.

Aster et al., 2013).

In addition to large outliers, local reflections of the carrier wave signals, known as multipath, can contribute significantly to the noise level of the time series (e.g., Larson et al., 2010). Since the reflections are specific to each satellite-receiver pair, and since the positions of the satellites relative to a receiver repeat every sidereal day, the multipath effects may be mitigated through **sidereal filtering**. A rough estimate for the sidereal filter may be obtained at the post-processing stage: a sidereal average may be computed for every epoch in the residual time series. In other words, a running average will be applied to the residual time series, whereby a mean multipath value for a given epoch will be derived from a series of neighboring epochs separated by multiples of a sidereal day. Since the multipath signals can change over time (e.g., a nearby tree may be cut down), temporal windows should not be too long. I have found that a window of ± 10 days (20 total days) works well.

3.5.2 Spectral Analysis

Common methods for computing the power spectrum of a time series include the Fourier Transform (e.g., Press et al., 2007, Sec. 13.4) and autoregressive, or "all-poles," models (e.g., Press et al., 2007, Sec. 13. 7). The methods, however, cannot be applied directly to unevenly sampled data, and simply filling in the missing values using interpolation techniques can generate false signals at low frequencies (e.g., Press et al., 2007, Sec. 13.8). In practice, tidal data is rarely evenly spaced, typically due to measurement gaps. Thus, alternative algorithms are required to compute the power spectra of time series with gaps. A couple options include mulit-tapering methods (e.g., Fodor & Stark, 2000) as well as the Lomb (also known as the Lomb-Scargle) periodogram (e.g., Press et al., 2007, Sec. 13.8).

3.5.3 Removal of Non-OTL Mass Loading Signals

The GNSS time series may be further improved by predicting and removing signals due to other effects, such as atmospheric pressure loading (e.g., van Dam et al., 1994; van den Dool et al., 1997; Ponte & Ray, 2002; Ray & Ponte, 2003; Petrov & Boy, 2004; Guo et al., 2004; Tregoning & van Dam, 2005; Tregoning & Watson, 2009; van Dam et al., 2010; Tregoning

& Watson, 2011), hydrological loading (e.g., van Dam et al., 2001; Bevis et al., 2005; Fu et al., 2015), and non-tidal ocean loading (e.g., van Dam et al., 1997; Williams & Penna, 2011; Nordman et al., 2015). More information on non-OTL variations in surface pressure and associated deformation is provided in Ch. 8.

4

Modeling Earth Deformation Induced by Surface Mass Loading

4.1 Introduction

Predicting the displacement-response of a radially symmetric Earth to surface mass loading (SML) involves a convolution of displacement load Green's functions (LGFs) with a load model (e.g., Farrell, 1973; Jentzsch, 1997):

$$\overline{U}(r, S, Z, \rho) = \int_{\Omega} \rho(r')\, G(|\overline{r}' - \overline{r}|, S)\, Z(r')\, d\Omega, \tag{4.1}$$

where $\overline{U}$ is the response of Earth at the observation point r, ρ is the mass density of the load at point r', G is the Green's function per kg load, and Z is the height of the load at point r'. The integral is taken over the surface area of the Earth, Ω. The LGFs depend on the distance between the load point and the observation point, $|\overline{r}' - \overline{r}|$, where $\overline{r}$ represents the position vector of the observation point and $\overline{r}'$ represents the position vector of the load point (e.g., Jentzsch, 1997, Sec. 2.3). The LGFs additionally depend on Earth structure, S, where S represents radially symmetric structure (e.g., PREM). The LGFs are derived from combinations of load Love numbers (LLNs) (e.g., Farrell, 1972a). Self-gravitating, spherically symmetric, non-rotating, elastic, and isotropic (SNREI) Earth models are typically assumed (e.g., Longman, 1962; Smylie, 2013), though more sophisticated models may also be adopted, such as to include mantle anelasticity (e.g., Pagiatakis, 1990; Bos et al., 2015). Here, I develop the procedure for computing load Love numbers, displacement load Green's functions, and SML-induced surface displacements for realistic mass loads.

4.2 Love Number Computation

4.2.1 Introduction

Love numbers are dimensionless parameters that characterize the yielding of the elastic Earth to body forces and surface tractions (Love, 1911; Munk & MacDonald, 1960). For the response of an elastic Earth to an external gravitational potential, V (Eq. 1.9), three Love numbers are defined: $h_n(r)$, $k_n(r)$, and $l_n(r)$. The subscript n denotes a dependence on spherical harmonic degree and (r) indicates a radial dependence. Augustus Edward Hough (A.E.H.) Love introduced $h_n(r)$ and $k_n(r)$ in 1909 (Love, 1909); Toshi Shida subsequently introduced $l_n(r)$ in 1912. All three parameters are commonly referred to as *Love* numbers, or alternatively referred to as the *Love and Shida* numbers. Although the parameters exhibit a radial dependence, here I consider deformation observed only at Earth's surface, and thus drop the (r) notation.

The parameter h_n characterizes Earth's vertical displacement in response to an external potential. The radial displacement, u_n, of Earth's surface in response to an external gravitational potential of spherical harmonic degree, n, is given by (e.g., Munk & MacDonald, 1960; Farrell, 1972a; Melchior, 1983; Baker, 1984; Agnew, 2015):

$$u_n = h_n \frac{V_n}{g}, \tag{4.2}$$

where g is the gravitational acceleration at Earth's surface, $\frac{V_n}{g}$ represents the equilibrium tidal height, and h_n scales the equilibrium height to a realistic vertical displacement based on the density and elastic properties of Earth's interior. Gravitational self-attraction, generated by the redistributed mass, is accounted for in the response parameter h_n (Munk & MacDonald, 1960).

The parameter k_n characterizes the change in the gravitational potential resulting from the redistribution of mass that occurs in response to the external potential field. Due to the self-attraction effect, the magnitude of the gravitational potential increases by a factor $k_n V_n$ from the location of the displaced surface. Thus, the total potential, accounting for self-

attraction, becomes (e.g., Munk & MacDonald, 1960; Agnew, 2015):

$$V_n^{\text{total}} = (1 + k_n)V_n. \tag{4.3}$$

Dividing Eq. 4.3 by the gravitational acceleration at the surface gives the height of the tidal equipotential:

$$u_n^{\text{equipotential}} = (1 + k_n)\frac{V_n}{g}, \tag{4.4}$$

and, thus, the radial displacement of a perfectly fluid Earth relative to its initial, undisturbed height. Now, the vertical displacement of a fluid layer covering the solid Earth, and with respect to the solid Earth, is given by (e.g., Agnew, 2015):

$$u_n^{\text{fluid layer}} = (1 + k_n - h_n)\frac{V_n}{g}. \tag{4.5}$$

In other words, Eq. 4.5 represents the height of the equipotential surface minus the vertical deformation of the solid Earth due to the load.

The Shida number l_n is defined as the horizontal displacement of Earth relative to the gradient of the equilibrium tide. The two components of the horizontal displacement are:

$$\begin{aligned} v_n^{\text{north}} &= -\frac{l_n}{g}\frac{\partial V_n}{\partial \delta} \\ v_n^{\text{east}} &= \frac{l_n}{g}\frac{1}{\sin\delta}\frac{\partial V_n}{\partial \lambda}, \end{aligned} \tag{4.6}$$

where δ is colatitude and λ is east longitude (e.g., Munk & MacDonald, 1960; Harrison, 1985).

For a rigid Earth, $h_n = k_n = l_n = 0$. For a perfectly fluid Earth, $h_n = l_n = 1$ and k_n depends on the density profile of the redistributed fluid (e.g., Stacey & Davis, 2009). For a homogeneous, perfectly fluid Earth, $k_n = \frac{3}{2}$.

The Love and Shida numbers described so far characterize Earth's response to an external gravitational potential; thus, I refer to them as **potential Love numbers**. A second class of Love numbers, referred to as **load Love numbers**, may also be introduced to describe the

deformation of Earth under normal tractions, typically applied at Earth's surface (Munk & MacDonald, 1960; Lambeck, 2005). Surface mass loads come from a variety of sources, including glaciers, lakes, the atmosphere, and oceans. The load Love numbers are distinguished from the potential Love numbers by a superscript prime: h'_n, k'_n, and l'_n. A third class of Love numbers exists to characterize Earth's response to surface-tangential tractions (Lambeck, 2005), distinguished from the other classes by superscript double primes (h''_n, k''_n, l''_n) and known as **shear Love numbers**. Only six of the nine Love numbers from the three sets (potential, load, and shear) are independent, and hence expressions exist to relate the Love numbers to one another (Molodenskiy, 1977; Lambeck, 1988).

4.2.2 Equilibrium Equations for Material Deformation

Here, I review the equilibrium equations describing spheroidal deformations of an elastic, self-gravitating, and hydrostatically pre-stressed body (e.g., Takeuchi, 1950; Alterman et al., 1959; Longman, 1962; Takeuchi, 1966; Farrell, 1972a; Takeuchi & Saito, 1972; Cathles, 1975; Lanzano, 1982; Dahlen & Tromp, 1998; Bos & Scherneck, 2013; Smylie, 2013).

In continuum mechanics, conservation of linear momentum states:

$$\rho\,\overline{a} = \overline{\nabla}\cdot\overline{\overline{\sigma}} + \rho\,\overline{F}, \tag{4.7}$$

where $\overline{\overline{\sigma}}$ is the stress tensor, ρ is the density, $\overline{a}$ is the acceleration vector ($\overline{a}_i = \left(\frac{\partial^2 \overline{u}}{\partial t^2}\right)_i = (\overline{u}_{,tt})_i = u_{i,tt}$, where $\overline{u}$ is a three-component displacement vector) and $\overline{F}$ is the body-force vector per unit mass. In indicial notation, $(\overline{\nabla}\cdot\overline{\overline{\sigma}})_i = \sigma_{ij,j}$, where Einstein's summation convention for repeated indices applies. The system of equations 4.7 are also known as the *equations of motion* or the *momentum equations*. In static equilibrium, the inertial term vanishes and the divergence of the total stress field balances the sum of all body forces:

$$\overline{0} = \overline{\nabla}\cdot\overline{\overline{\sigma}} + \rho\,\overline{F}. \tag{4.8}$$

Since surface mass loading can be dynamic, however, I retain the acceleration term.

Assuming that the body is initially in hydrostatic equilibrium, I express the pre-existing stress field, T_{ij}, as (e.g., Smylie, 2013):

$$T_{ij} = -p_0\,\delta_{ij}, \tag{4.9}$$

where p_0 is the equilibrium pressure and δ_{ij} is the Kronecker delta function. In vector notation,

$$\overline{\overline{\mathbf{T}}} = -p_0\,\overline{\overline{\mathbf{I}}}, \tag{4.10}$$

where $\overline{\overline{\mathbf{I}}}$ is the identity matrix. The minus sign indicates that the hydrostatic pressure is compressive, based on the convention that positive stresses are directed outward normal to the surface (e.g., Sabadini & Vermeersen, 2004).

For a body subject to an elastic displacement $\overline{u}$, the initial stress field in the undeformed medium is given by (e.g., Lapwood & Usami, 1981; Lanzano, 1982; Sabadini & Vermeersen, 2004; Smylie, 2013):

$$\overline{\overline{\sigma}}_0 = \overline{\overline{\mathbf{T}}} - \overline{u}\cdot\overline{\nabla}\,\overline{\overline{\mathbf{T}}}. \tag{4.11}$$

Now, the total stress tensor $\overline{\overline{\sigma}}$ at coordinates in the undeformed medium becomes the sum of the hydrostatic prestress, $\overline{\overline{\sigma}}_0$, and an additional perturbation to the stress field due to deformation, $\overline{\overline{\sigma}}_1$:

$$\begin{aligned} \overline{\overline{\sigma}} &= \overline{\overline{\sigma}}_1 + \overline{\overline{\sigma}}_0 \\ \overline{\overline{\sigma}} &= \overline{\overline{\sigma}}_1 - p_0\,\overline{\overline{\mathbf{I}}} + \overline{u}\cdot\overline{\nabla}\,p_0. \end{aligned} \tag{4.12}$$

Hence, the equilibrium equation becomes (e.g., Sabadini & Vermeersen, 2004):

$$\rho\overline{a} = \overline{\nabla}\cdot\overline{\overline{\sigma}}_1 - \overline{\nabla}\,p_0 + \overline{\nabla}(\overline{u}\cdot\,\overline{\nabla}\,p_0) + \rho\,\overline{F}. \tag{4.13}$$

In hydrostatic equilibrium, the gradient of the pressure, p_0, is related to density and gravity

by the relation:

$$\frac{\partial p_0}{\partial x_i} = \rho_0 \, g_{0i}, \tag{4.14}$$

where ρ_0 and g_0 are the equilibrium density and gravity of the unperturbed medium, respectively. In spherical coordinates, I assume that the gravitational acceleration is everywhere directed perpendicular to the surface, and hence Eq. 4.14 becomes:

$$\frac{\partial p_0}{\partial r} = \rho_0 \, g_0 \, \hat{r}, \tag{4.15}$$

where $\hat{r}$ is a unit vector, directed outward normal to the surface. The equilibrium gravity, g_0, at radius r may be derived from a radially heterogeneous density distribution via (e.g., Longman, 1962):

$$g_0(r) = \frac{4\pi G}{r^2} \int_0^r \rho_0(s) s^2 ds, \tag{4.16}$$

where G is the universal gravitational constant.

The deformation also induces small perturbations in density and gravity. The resulting density, ρ, is equivalent to the sum of the initial undeformed density, ρ_0, and the perturbation to the density caused by the deformation, ρ_1 (e.g., Smylie, 2013). Hence:

$$\rho = \rho_0 + \rho_1, \tag{4.17}$$

where

$$\rho_1 = -\overline{\nabla} \cdot (\rho_0 \, \overline{u}) \tag{4.18}$$

is the continuity equation for mass advection and u_i represents the ith component of the displacement vector (e.g., Lanzano, 1982; Smylie, 2013).

The perturbation in density leads to a perturbation in the gravitational potential, ψ_1, which must satisfy Poisson's equation (e.g., Alterman et al., 1959; Longman, 1962; Lanzano, 1982):

$$\begin{aligned} \nabla^2 \psi_1 &= -4 \, \pi \, G \, \rho_1 \\ &= -4 \, \pi \, G \, (-\overline{\nabla} \cdot (\rho_0 \, \overline{u})) \end{aligned}$$

$$
\begin{aligned}
&= 4\,\pi\,G\left(\rho_0\,\overline{\nabla}\cdot\overline{u}+\overline{u}\cdot\hat{r}\,\frac{\partial\rho_0}{\partial r}\right)\\
&= 4\,\pi\,G\left(\rho_0\,\Delta+u_r\,\frac{\partial\rho_0}{\partial r}\right),
\end{aligned}
\tag{4.19}
$$

where Δ is the dilatation (i.e., the trace of the strain tensor, $\overline{\overline{\epsilon}}$). The total gravitational potential field, ψ, is equivalent to the sum of the initial field in its unperturbed state, ψ_0, and the additional small perturbation, ψ_1 (e.g., Sabadini & Vermeersen, 2004; Smylie, 2013).

The perturbation in gravity, $\overline{g}_1$, due to the perturbation in the gravitational potential is thus:

$$
\overline{g}_1=\overline{\nabla}\psi_1. \tag{4.20}
$$

Taking the body force per unit mass, $\overline{F}$, to be the acceleration of gravity, I arrive at:

$$
\rho\,\overline{F}=\rho\,(\overline{\nabla}\psi)=\rho\,(\overline{\nabla}\psi_0+\overline{\nabla}\psi_1)=\rho\,\overline{\nabla}\psi_0+\rho\,\overline{\nabla}\psi_1=\rho\,\overline{g}_0+\rho\,\overline{g}_1. \tag{4.21}
$$

Now, I also expand density into its unperturbed and perturbed components:

$$
\begin{aligned}
\rho\,\overline{F} &= \overline{g}_0(\rho_0+\rho_1)+\overline{g}_1(\rho_0+\rho_1)\\
&= \rho_0\,\overline{g}_0+\rho_1\,\overline{g}_0+\rho_0\,\overline{g}_1+\rho_1\,\overline{g}_1\\
&= \rho_0\,\overline{\nabla}\psi_0+\rho_1\,\overline{\nabla}\psi_0+\rho_0\,\overline{\nabla}\psi_1+\rho_1\,\overline{\nabla}\psi_1.
\end{aligned}
\tag{4.22}
$$

Putting this back into the momentum equations:

$$
\rho\overline{a}=\overline{\nabla}\cdot\overline{\overline{\sigma}}_1-\overline{\nabla}\,p_0+\overline{\nabla}(\overline{u}\cdot\,\overline{\nabla}\,p_0)+\rho_0\,\overline{\nabla}\psi_0+\rho_1\,\overline{\nabla}\psi_0+\rho_0\,\overline{\nabla}\psi_1+\rho_1\,\overline{\nabla}\psi_1. \tag{4.23}
$$

Note that $-\overline{\nabla}\,p_0=-\rho_0\,g_0\hat{r}=-\rho_0\,\overline{\nabla}\psi_0$; thus, two terms may be canceled, resulting in:

$$
\rho\overline{a}=\overline{\nabla}\cdot\overline{\overline{\sigma}}_1+\overline{\nabla}(\overline{u}\cdot\,\overline{\nabla}\,p_0)+\rho_1\,\overline{\nabla}\psi_0+\rho_0\,\overline{\nabla}\psi_1+\rho_1\,\overline{\nabla}\psi_1. \tag{4.24}
$$

Furthermore, since $\rho_1\,\overline{\nabla}\psi_1$ represents second-order displacements, it may be neglected here

(e.g., Lanzano, 1982). Therefore:

$$\begin{aligned}
\rho\overline{a} = \rho_0\,\overline{u}_{,tt} &= \overline{\nabla}\cdot\overline{\overline{\sigma}}_1 + \overline{\nabla}(\overline{u}\cdot\,\overline{\nabla}\,p_0) + \rho_0\,\overline{\nabla}\psi_1 + \rho_1\,\overline{\nabla}\psi_0 \\
&= \overline{\nabla}\cdot\overline{\overline{\sigma}}_1 + \overline{\nabla}(\rho_0\,\overline{u}\cdot\overline{g}_0) + \rho_0\,\overline{g}_1 + \rho_1\,\overline{g}_0 \\
&= \overline{\nabla}\cdot\overline{\overline{\sigma}}_1 + \overline{\nabla}(\rho_0\,\overline{u}\cdot\overline{g}_0) + \rho_0\,\overline{g}_1 - (\overline{\nabla}\cdot(\rho_0\overline{u}))\,\overline{g}_0 \\
&= \overline{\nabla}\cdot\overline{\overline{\sigma}}_1 + \overline{\nabla}(\rho_0\,\overline{u}\cdot\overline{g}_0) + \rho_0\,\overline{g}_1 - (\rho_0\overline{\nabla}\cdot\overline{u} + \overline{u}\cdot\overline{\nabla}\rho_0)\,\overline{g}_0 \\
&= \overline{\nabla}\cdot\overline{\overline{\sigma}}_1 + \overline{\nabla}(\rho_0\,\overline{u}\cdot\overline{g}_0) + \rho_0\,\overline{g}_1 - (\rho_0\,\Delta + \overline{u}\cdot\overline{\nabla}\rho_0)\,\overline{g}_0 \\
&= \overline{\nabla}\cdot\overline{\overline{\sigma}}_1 + \rho_0\,\overline{\nabla}(\overline{u}\cdot\overline{g}_0) + (\overline{u}\cdot\overline{g}_0)\,\overline{\nabla}\rho_0 + \rho_0\,\overline{g}_1 - \\
&\quad (\rho_0\,\Delta + \overline{u}\cdot\overline{\nabla}\rho_0)\,\overline{g}_0, \qquad (4.25)
\end{aligned}$$

which is a linearized version of the Navier-Stokes equation, and $\rho_1\,\overline{u}_{,tt}$ has been neglected since it is of second order in the displacements (e.g., Lanzano, 1982).

4.2.3 Conversion to Spherical Coordinates

A cartesian coordinate system (x_1, x_2, x_3) may be mapped to a spherical coordinate system (r, θ, ϕ) by the relations (e.g., Lapwood & Usami, 1981; Boas, 1983):

$$\begin{aligned}
x_1 &= r\,\sin\theta\,\cos\phi \\
x_2 &= r\,\sin\theta\,\sin\phi \\
x_3 &= r\,\cos\theta, \qquad (4.26)
\end{aligned}$$

where r is radial distance from Earth's center, θ is colatitude, and ϕ is longitude. Furthermore, I define the displacement vector $\overline{u}$ as (e.g., Alterman et al., 1959):

$$\begin{aligned}
u_r &= u \\
u_\theta &= v \\
u_\phi &= w. \qquad (4.27)
\end{aligned}$$

The covariant base vectors, a_i, in the spherical coordinate system are thus (e.g., Takeuchi, 1966; Lapwood & Usami, 1981):

$$\begin{aligned} \overline{a}_r &= \frac{\partial \overline{x}}{\partial r} = (\sin\theta\cos\phi, \sin\theta\sin\phi, \cos\theta) \\ \overline{a}_\theta &= \frac{\partial \overline{x}}{\partial \theta} = (r\cos\phi\cos\theta, r\sin\phi\cos\theta, -r\sin\theta) \\ \overline{a}_\phi &= \frac{\partial \overline{x}}{\partial \phi} = (-r\sin\theta\sin\phi, r\sin\theta\cos\phi, 0). \end{aligned} \tag{4.28}$$

Furthermore, the metric tensor, g_{ij}, is computed by:

$$g_{ij} = a_i \cdot a_j, \tag{4.29}$$

yielding

$$g_{ij} = \begin{bmatrix} 1 & 0 & 0 \\ 0 & r^2 & 0 \\ 0 & 0 & r^2\sin^2\theta \end{bmatrix}.$$

Scale factors, h_i, may now be derived from the metric tensor via:

$$h_i = \sqrt{g_{(ii)}}, \tag{4.30}$$

resulting in:

$$\begin{aligned} h_r &= 1 \\ h_\theta &= r \\ h_\phi &= r\sin\theta. \end{aligned} \tag{4.31}$$

From here, the components of the nabla operator are directly derived:

$$\nabla_i = \frac{1}{h_{(i)}}\frac{\partial}{\partial\theta_i} = \left(\frac{\partial}{\partial r}, \frac{1}{r}\frac{\partial}{\partial\theta}, \frac{1}{r\sin\theta}\frac{\partial}{\partial\phi}\right). \tag{4.32}$$

Furthermore, the corresponding normalized base vectors, $\overline{g}_i$, are:

$$\begin{aligned}
\overline{g}_r &= \frac{\overline{a}_{(r)}}{h_r} = (\sin\theta\cos\phi,\ \sin\theta\sin\phi,\ \cos\theta) \\
\overline{g}_\theta &= \frac{\overline{a}_{(\theta)}}{h_\theta} = (\cos\phi\cos\theta,\ \sin\phi\cos\theta,\ -\sin\theta) \\
\overline{g}_\phi &= \frac{\overline{a}_{(\phi)}}{h_\phi} = (-\sin\phi,\ \cos\phi,\ 0).
\end{aligned} \tag{4.33}$$

The divergence of the vector displacement field, $\overline{u}$, also referred to as the dilatation, becomes:

$$\begin{aligned}
\overline{\nabla}\cdot\overline{u} = \Delta &= \nabla_i(\overline{u})\cdot\overline{g}_i \\
&= \nabla_i(u_j\,\overline{g}_j)\cdot\overline{g}_i \\
&= (\nabla_i\,u_j)\overline{g}_j\cdot\overline{g}_i + u_j\,(\nabla_i\,\overline{g}_j)\cdot\overline{g}_i \\
&= \nabla_i\,u_i + u_j\,(\nabla_i\,\overline{g}_j)\cdot\overline{g}_i \\
&= \frac{\partial u}{\partial r} + \frac{1}{r}\frac{\partial v}{\partial\theta} + \frac{1}{r\sin\theta}\frac{\partial w}{\partial\phi} + u_j\,(\nabla_i\,\overline{g}_j)\cdot\overline{g}_i \\
&= \frac{\partial u}{\partial r} + \frac{1}{r}\frac{\partial v}{\partial\theta} + \frac{1}{r\sin\theta}\frac{\partial w}{\partial\phi} + \frac{u}{r} + \frac{u}{r} + \frac{\cot\theta}{r}v \\
&= \frac{\partial u}{\partial r} + \frac{1}{r}\frac{\partial v}{\partial\theta} + \frac{1}{r\sin\theta}\frac{\partial w}{\partial\phi} + \frac{2u}{r} + \frac{\cot\theta}{r}v \\
&= \frac{1}{r^2\sin\theta}\left[\frac{\partial}{\partial r}(r^2\,u\,\sin\theta) + \frac{\partial}{\partial\theta}(r\,v\,\sin\theta) + \frac{\partial}{\partial\phi}(r\,w)\right].
\end{aligned} \tag{4.34}$$

Putting the vertical load at the pole and assuming symmetric deformation about the line $\theta = 0$; the ϕ component of the equations of motion will be zero (e.g., Longman, 1962). Now, the dilatation may be rewritten as:

$$\Delta = \frac{\partial u}{\partial r} + \frac{2u}{r} + \frac{1}{r\sin\theta}\frac{\partial}{\partial\theta}(v\,\sin\theta). \tag{4.35}$$

Following the development of Lapwood & Usami (1981), I denote the rule for differentiation of a second-order tensor, T_{ij}, as follows:

$$T_{ij,\gamma} = \frac{\partial}{\partial\gamma}\,T_{ij} + \Gamma^i_{\sigma\gamma}\,T_{\sigma j} + \Gamma^j_{\sigma\gamma}\,T_{i\sigma}, \tag{4.36}$$

where Γ^i_{jk} represent Christoffel symbols. In spherical coordinates, the components of the Christoffel symbols are:

$$\begin{aligned}
\Gamma^1_{22} &= -r \\
\Gamma^1_{33} &= -r\sin^2\theta \\
\Gamma^2_{33} &= -\sin\theta\cos\theta \\
\Gamma^2_{12} &= \Gamma^2_{21} = \frac{1}{r} \\
\Gamma^3_{13} &= \Gamma^3_{31} = \frac{1}{r} \\
\Gamma^3_{23} &= \Gamma^3_{32} = \cot\theta, \qquad (4.37)
\end{aligned}$$

where 1, 2, and 3 correspond to r, θ, and ϕ. All other components are zero. Inserting the components of Eq. 4.37 into Eq. 4.36 yields:

$$\begin{aligned}
T_{11,1} &= \frac{\partial}{\partial r}T_{11} \\
T_{12,2} &= \frac{\partial}{\partial \theta}T_{12} - r\,T_{22} + \frac{1}{r}\,T_{11} \\
T_{13,3} &= \frac{\partial}{\partial \phi}T_{13} - r\sin^2\theta\,T_{33} + \frac{1}{r}\,T_{11} + \cot\theta\,T_{12} \\
T_{21,1} &= \frac{\partial}{\partial r}T_{21} + \frac{1}{r}\,T_{21} \\
T_{22,2} &= \frac{\partial}{\partial \theta}T_{22} + \frac{2}{r}\,T_{12} \\
T_{23,3} &= \frac{\partial}{\partial \phi}T_{23} - \sin\theta\cos\theta\,T_{33} + \frac{1}{r}\,T_{21} + \cot\theta\,T_{22} \\
T_{31,1} &= \frac{\partial}{\partial r}T_{31} + \frac{1}{r}\,T_{31} \\
T_{32,2} &= \frac{\partial}{\partial \theta}T_{32} + \cot\theta\,T_{32} + \frac{1}{r}\,T_{31} \\
T_{33,3} &= \frac{\partial}{\partial \phi}T_{33} + 2\cot\theta\,T_{23}. \qquad (4.38)
\end{aligned}$$

Normalizing back to the physical components of the stress tensor, I use the relation (e.g., Lapwood & Usami, 1981, Appendix A.2):

$$\sigma_{ij} = \sqrt{g_{(ii)}\,g_{(jj)}}\,T_{ij}, \qquad (4.39)$$

where $g_{(11)} = 1$, $g_{(22)} = r^2$ and $g_{(33)} = r^2 \sin^2\theta$ (Eq. 4.29). Thus, the components of the stress tensor are:

$$\begin{aligned}
\sigma_{rr} &= T_{11} \\
\sigma_{\theta\theta} &= r^2\, T_{22} \\
\sigma_{\phi\phi} &= r^2 \sin^2\theta\, T_{33} \\
\sigma_{r\theta} &= r\, T_{12} \\
\sigma_{r\phi} &= r\, \sin\theta\, T_{13} \\
\sigma_{\theta\phi} &= r^2 \sin\theta\, T_{23}. \qquad (4.40)
\end{aligned}$$

Recall that the divergence of the stress tensor is given by:

$$\overline{\nabla} \cdot \overline{\overline{\sigma}} = \sigma_{ij,j} = \partial_j\, \sigma_{ij}. \qquad (4.41)$$

Thus, for the r component:

$$\begin{aligned}
\sigma_{rj,j} &= \left(\frac{\partial}{\partial r} T_{11} + \frac{\partial}{\partial \theta} T_{12} - r\, T_{22} + \frac{1}{r}\, T_{11} + \frac{\partial}{\partial \phi} T_{13} - r \sin^2\theta\, T_{33} + \frac{1}{r}\, T_{11} + \cot\theta\, T_{12} \right) \hat{r} \\
&= \left(\frac{\partial}{\partial r}\sigma_{rr} + \frac{1}{r}\frac{\partial}{\partial \theta}\sigma_{r\theta} - \frac{1}{r}\,\sigma_{\theta\theta} + \frac{2}{r}\,\sigma_{rr} + \frac{1}{r\sin\theta}\frac{\partial}{\partial\phi}\sigma_{r\phi} - \frac{1}{r}\,\sigma_{\phi\phi} + \frac{\cot\theta}{r}\,\sigma_{r\theta} \right) \hat{r} \\
&= \left(\frac{\partial}{\partial r}\sigma_{rr} + \frac{1}{r}\frac{\partial}{\partial \theta}\sigma_{r\theta} + \frac{1}{r}\left[2\sigma_{rr} - \sigma_{\theta\theta} - \sigma_{\phi\phi} + \frac{1}{\sin\theta}\frac{\partial}{\partial\phi}\sigma_{r\phi} + \cot\theta\,\sigma_{r\theta} \right] \right) \hat{r} \\
&= \left(\frac{\partial}{\partial r}\sigma_{rr} + \frac{1}{r}\frac{\partial}{\partial \theta}\sigma_{r\theta} + \frac{1}{r}\left[2\sigma_{rr} - \sigma_{\theta\theta} - \sigma_{\phi\phi} + \cot\theta\,\sigma_{r\theta} \right] \right) \hat{r}, \qquad (4.42)
\end{aligned}$$

where I have canceled the ∂_ϕ term in the final line due to the assumed azimuthal symmetry (i.e., deformation is assumed to be symmetric about the line $\theta = 0$).

Performing the same expansion for the θ component yields:

$$\begin{aligned}
\sigma_{\theta j,j} &= \left(\frac{\partial}{\partial r} T_{21} + \frac{4}{r}\, T_{12} + \frac{\partial}{\partial \theta} T_{22} + \frac{\partial}{\partial \phi} T_{23} - \sin\theta\cos\theta\, T_{33} + \cot\theta\, T_{22} \right) r\,\hat{\theta} \\
&= \left(\frac{\partial}{\partial r}\frac{\sigma_{r\theta}}{r} + \frac{4\sigma_{r\theta}}{r^2} + \frac{1}{r^2}\frac{\partial}{\partial\theta}\sigma_{\theta\theta} + \frac{1}{r^2\sin\theta}\frac{\partial}{\partial\phi}\sigma_{\theta\phi} - \frac{\cos\theta}{r^2\sin\theta}\,\sigma_{\phi\phi} + \frac{\cot\theta}{r^2}\,\sigma_{\theta\theta} \right) r\,\hat{\theta} \\
&= \left(\frac{1}{r}\frac{\partial}{\partial r}\sigma_{r\theta} - \frac{\sigma_{r\theta}}{r^2} + \frac{4\sigma_{r\theta}}{r^2} + \frac{1}{r^2}\frac{\partial}{\partial\theta}\sigma_{\theta\theta} + \frac{1}{r^2\sin\theta}\frac{\partial}{\partial\phi}\sigma_{\theta\phi} - \frac{\cot\theta}{r^2}\,\sigma_{\phi\phi} + \frac{\cot\theta}{r^2}\,\sigma_{\theta\theta} \right) r\,\hat{\theta}
\end{aligned}$$

$$
\begin{aligned}
&= \left(\frac{1}{r}\frac{\partial}{\partial r}\sigma_{r\theta} + \frac{1}{r^2}\frac{\partial}{\partial \theta}\sigma_{\theta\theta} + \frac{1}{r^2}\left[(\sigma_{\theta\theta} - \sigma_{\phi\phi})\cot\theta + 3\sigma_{r\theta}\right] + \frac{1}{r^2\sin\theta}\frac{\partial}{\partial\phi}\sigma_{\theta\phi}\right) r\,\hat{\theta} \\
&= \left(\frac{1}{r}\frac{\partial}{\partial r}\sigma_{r\theta} + \frac{1}{r^2}\frac{\partial}{\partial \theta}\sigma_{\theta\theta} + \frac{1}{r^2}\left[(\sigma_{\theta\theta} - \sigma_{\phi\phi})\cot\theta + 3\sigma_{r\theta}\right]\right) r\,\hat{\theta} \\
&= \left(\frac{\partial}{\partial r}\sigma_{r\theta} + \frac{1}{r}\frac{\partial}{\partial \theta}\sigma_{\theta\theta} + \frac{1}{r}\left[(\sigma_{\theta\theta} - \sigma_{\phi\phi})\cot\theta + 3\sigma_{r\theta}\right]\right)\hat{\theta}, \qquad (4.43)
\end{aligned}
$$

where, again, I have canceled the ∂_ϕ term in the final line due to the assumed azimuthal symmetry. Expanding the ϕ component is unnecessary due to the azimuthal symmetry as well (e.g., Sabadini & Vermeersen, 2004).

Now, I recast Eq. 4.25 in terms of the r and θ components of the stress tensor from Eqs. 4.42 and 4.43 (e.g., Alterman et al., 1959; Longman, 1962; Lapwood & Usami, 1981; Lanzano, 1982):

$$
\begin{aligned}
\rho_0\,\frac{\partial^2 u}{\partial t^2} &= \frac{\partial}{\partial r}\sigma_{rr} + \frac{1}{r}\frac{\partial}{\partial\theta}\sigma_{r\theta} + \frac{1}{r}\left[2\sigma_{rr} - \sigma_{\theta\theta} - \sigma_{\phi\phi} + \cot\theta\,\sigma_{r\theta}\right] + \\
&\quad \rho_0\,\overline{\nabla}(\overline{u}\cdot\overline{g}_0) + (\overline{u}\cdot\overline{g}_0)\,\overline{\nabla}\rho_0 + \rho_0\,\overline{g}_1 - (\rho_0\,\Delta + \overline{u}\cdot\overline{\nabla}\rho_0)\,\overline{g}_0 \\
&= \frac{\partial}{\partial r}\sigma_{rr} + \frac{1}{r}\frac{\partial}{\partial\theta}\sigma_{r\theta} + \frac{1}{r}\left[2\sigma_{rr} - \sigma_{\theta\theta} - \sigma_{\phi\phi} + \cot\theta\,\sigma_{r\theta}\right] - \\
&\quad \rho_0\frac{\partial(g_0\,u)}{\partial r} + \rho_0\,\overline{g}_1 + \rho_0\,g_0\,\Delta + (\overline{u}\cdot\overline{g}_0)\,\overline{\nabla}\rho_0 - (\overline{u}\cdot\overline{g}_0)\,\overline{\nabla}\rho_0 + \\
&\quad \overline{u}\times(\overline{\nabla}\,\rho_0\times\overline{g}_0) \\
&= \frac{\partial}{\partial r}\sigma_{rr} + \frac{1}{r}\frac{\partial}{\partial\theta}\sigma_{r\theta} + \frac{1}{r}\left[2\sigma_{rr} - \sigma_{\theta\theta} - \sigma_{\phi\phi} + \cot\theta\,\sigma_{r\theta}\right] - \\
&\quad \rho_0\frac{\partial(g_0\,u)}{\partial r} + \rho_0\frac{\partial\psi_1}{\partial r} + \rho_0\,g_0\,\Delta \\
\rho_0\,\frac{\partial^2 v}{\partial t^2} &= \frac{\partial}{\partial r}\sigma_{r\theta} + \frac{1}{r}\frac{\partial}{\partial\theta}\sigma_{\theta\theta} + \frac{1}{r}\left[(\sigma_{\theta\theta} - \sigma_{\phi\phi})\cot\theta + 3\sigma_{r\theta}\right] + \\
&\quad \rho_0\,\overline{\nabla}(\overline{u}\cdot\overline{g}_0) + (\overline{u}\cdot\overline{g}_0)\,\overline{\nabla}\rho_0 + \rho_0\,\overline{g}_1 - (\rho_0\,\Delta + \overline{u}\cdot\overline{\nabla}\rho_0)\,\overline{g}_0 \\
&= \frac{\partial}{\partial r}\sigma_{r\theta} + \frac{1}{r}\frac{\partial}{\partial\theta}\sigma_{\theta\theta} + \frac{1}{r}\left[(\sigma_{\theta\theta} - \sigma_{\phi\phi})\cot\theta + 3\sigma_{r\theta}\right] + \\
&\quad \frac{\rho_0}{r}\frac{\partial\psi_1}{\partial\theta} - \rho_0\,g_0\,\frac{1}{r}\frac{\partial u}{\partial\theta}, \qquad (4.44)
\end{aligned}
$$

where I have made use of the vector triple product, the relationship $\overline{g}_1 = \overline{\nabla}\psi_1$, and the relationship $\overline{g}_0\cdot\hat{r} = -g_0$, with positive $\hat{r}$ directed outward normal to the surface. Furthermore, $\overline{u}\times(\overline{\nabla}\,\rho_0\times\overline{g}_0)$ is taken to be zero since I assume that ρ_0 is only a function of r (i.e., no lateral variations) and that $\overline{g}_0$ acts only in the radial direction. Recall that u represents

the displacement in the direction of $\hat{r}$ ($u_r = u$) and that v represents displacement in the direction of $\hat{\theta}$ ($u_\theta = v$), as defined in Eqs. 4.27.

Note that I have not yet made any assumptions about a constitutive law. I have, however, assumed radial forcing, which implies only spheroidal deformation. The Eqs. 4.44 are general to spheroidal deformation and may be used for multiple applications, including Earth's free oscillations, Earth's response to external gravitational potentials, and Earth's response to surface mass loading. The distinction between the different applications enters only through the boundary conditions applied at the surface.

4.2.4 Linear Elastic Constitutive Relation

In the small-strain approximation, the strain tensor may be related to displacements by:

$$\overline{\epsilon} = \frac{1}{2}\left((\nabla\,\overline{u})^T + (\nabla\,\overline{u})\right), \tag{4.45}$$

or in indicial notation by:

$$\epsilon_{ij} = \frac{1}{2}\left(u_{i,j} + u_{j,i}\right). \tag{4.46}$$

For linear elasticity, the constitutive relation is given by:

$$\sigma_{ij} = \mathbb{C}_{ijkl}\,\epsilon_{kl}, \tag{4.47}$$

where $\mathbb{C}_{ijkl}$ represents the elasticity modulus (or *stiffness tensor*), which is a tensor of fourth-order. Eq. 4.47 is also known as Hooke's Law. For isotropic materials, the elasticity modulus reduces to:

$$\mathbb{C}_{ijkl} = \lambda\,\delta_{ij}\,\delta_{kl} + \mu(\delta_{ik}\,\delta_{jl} + \delta_{il}\,\delta_{jk}), \tag{4.48}$$

where λ and μ are Lamé's constants, which are related to compressional (P) and shear (S) sound-wave velocities by:

$$V_P^2 \;=\; \frac{\lambda + 2\,\mu}{\rho} \tag{4.49}$$

$$V_S^2 = \frac{\mu}{\rho}. \tag{4.50}$$

Thus, for linear elastic and isotropic materials, the constitutive relation is given by (Eqs. 4.47 and 4.48):

$$\sigma_{ij} = \lambda\, \epsilon_{kk}\, \delta_{ij} + 2\, \mu\, \epsilon_{ij}. \tag{4.51}$$

Note that Einstein's summation convention is implied; thus, ϵ_{kk} represents the trace, as well as the first invariant, of the strain tensor.

In spherical coordinates, the components of the stress tensor, $\overline{\overline{\sigma}}_1$, arising from the material deformation (without the hydrostatic pre-stress terms) are given by (e.g., Takeuchi, 1966; Lapwood & Usami, 1981):

$$\sigma_{rr} = \lambda\, \Delta + 2\, \mu\, \epsilon_{rr} \tag{4.52}$$

$$\sigma_{\theta\theta} = \lambda\, \Delta + 2\, \mu\, \epsilon_{\theta\theta} \tag{4.53}$$

$$\sigma_{\phi\phi} = \lambda\, \Delta + 2\, \mu\, \epsilon_{\phi\phi} \tag{4.54}$$

$$\sigma_{r\theta} = 2\mu\, \epsilon_{r\theta} \tag{4.55}$$

$$\sigma_{r\phi} = 2\mu\, \epsilon_{r\phi} \tag{4.56}$$

$$\sigma_{\theta\phi} = 2\mu\, \epsilon_{\theta\phi}, \tag{4.57}$$

where

$$\epsilon_{rr} = \frac{\partial u}{\partial r} \tag{4.58}$$

$$\epsilon_{\theta\theta} = \left(\frac{1}{r} \frac{\partial v}{\partial \theta} + \frac{u}{r} \right) \tag{4.59}$$

$$\epsilon_{\phi\phi} = \left(\frac{1}{r \sin\theta} \frac{\partial w}{\partial \phi} + \frac{v}{r} \cot\theta + \frac{u}{r} \right) \tag{4.60}$$

$$\epsilon_{r\theta} = \left(\frac{1}{2} \frac{\partial v}{\partial r} - \frac{v}{2r} + \frac{1}{2r} \frac{\partial u}{\partial \theta} \right) \tag{4.61}$$

$$\epsilon_{r\phi} = \left(\frac{1}{2} \frac{1}{r \sin\theta} \frac{\partial u}{\partial \phi} + \frac{1}{2} \frac{\partial w}{\partial r} - \frac{w}{2r} \right) \tag{4.62}$$

$$\epsilon_{\theta\phi} = \left[\frac{1}{2r} \left(\frac{\partial w}{\partial \theta} - w \cot\theta \right) + \frac{1}{2r \sin\theta} \frac{\partial v}{\partial \phi} \right]. \tag{4.63}$$

Thus, both elastic and gravitational restoring forces contribute to the deformation response. Note that definitions of the shear strain can differ by a factor of two in the literature, which must then be reflected consistently in the equations of motion (e.g., Alterman et al., 1959; Longman, 1962).

Inserting the constitutive relations back into Eqs. 4.44:

$$\begin{aligned}
\rho_0 \frac{\partial^2 u}{\partial t^2} &= \frac{\partial}{\partial r}(\lambda\,\Delta + 2\,\mu\,\epsilon_{rr}) + \frac{1}{r}\frac{\partial}{\partial \theta}(2\mu\,\epsilon_{r\theta}) + \\
&\quad \frac{1}{r}\left[2(\lambda\,\Delta + 2\,\mu\,\epsilon_{rr}) - (\lambda\,\Delta + 2\,\mu\,\epsilon_{\theta\theta}) - (\lambda\,\Delta + 2\,\mu\,\epsilon_{\phi\phi}) + \cot\theta\,(2\mu\,\epsilon_{r\theta})\right] - \\
&\quad \rho_0 \frac{\partial(g_0\,u)}{\partial r} + \rho_0 \frac{\partial \psi_1}{\partial r} + \rho_0\,g_0\,\Delta \\
&= \frac{\partial}{\partial r}(\lambda\,\Delta + 2\,\mu\,\epsilon_{rr}) + \frac{2\mu}{r}\frac{\partial \epsilon_{r\theta}}{\partial \theta} + \frac{2\mu}{r}\left[2\,\epsilon_{rr} - \epsilon_{\theta\theta} - \epsilon_{\phi\phi} + \cot\theta\,\epsilon_{r\theta}\right] - \\
&\quad \rho_0 \frac{\partial(g_0\,u)}{\partial r} + \rho_0 \frac{\partial \psi_1}{\partial r} + \rho_0\,g_0\,\Delta \\
\rho_0 \frac{\partial^2 v}{\partial t^2} &= \frac{\partial}{\partial r}(2\mu\,\epsilon_{r\theta}) + \frac{1}{r}\frac{\partial}{\partial \theta}(\lambda\,\Delta + 2\,\mu\,\epsilon_{\theta\theta}) + \\
&\quad \frac{1}{r}\left[((\lambda\,\Delta + 2\,\mu\,\epsilon_{\theta\theta}) - (\lambda\,\Delta + 2\,\mu\,\epsilon_{\phi\phi}))\cot\theta + 3(2\mu\,\epsilon_{r\theta})\right] + \\
&\quad \frac{\rho_0}{r}\frac{\partial \psi_1}{\partial \theta} - \rho_0\,g_0\,\frac{1}{r}\frac{\partial u}{\partial \theta} \\
&= 2\frac{\partial}{\partial r}(\mu\,\epsilon_{r\theta}) + \frac{1}{r}\frac{\partial}{\partial \theta}(\lambda\,\Delta + 2\,\mu\,\epsilon_{\theta\theta}) + \frac{2\mu}{r}\left[(\epsilon_{\theta\theta} - \epsilon_{\phi\phi})\cot\theta + 3\,\epsilon_{r\theta}\right] + \\
&\quad \frac{\rho_0}{r}\frac{\partial \psi_1}{\partial \theta} - \rho_0\,g_0\,\frac{1}{r}\frac{\partial u}{\partial \theta}.
\end{aligned} \tag{4.64}$$

Moreover, inserting the expressions relating strain to displacement into Eqs. 4.64:

$$\begin{aligned}
\rho_0 \frac{\partial^2 u}{\partial t^2} &= \frac{\partial}{\partial r}\left(\lambda\,\Delta + 2\,\mu\,\frac{\partial u}{\partial r}\right) + \frac{2\mu}{r}\frac{\partial\left(\frac{1}{2}\frac{\partial v}{\partial r} - \frac{v}{2r} + \frac{1}{2r}\frac{\partial u}{\partial \theta}\right)}{\partial \theta} + \\
&\quad \frac{2\mu}{r}\left[2\frac{\partial u}{\partial r} - \left(\frac{1}{r}\frac{\partial v}{\partial \theta} + \frac{u}{r}\right) - \left(\frac{v}{r}\cot\theta + \frac{u}{r}\right) + \cot\theta\left(\frac{1}{2}\frac{\partial v}{\partial r} - \frac{v}{2r} + \frac{1}{2r}\frac{\partial u}{\partial \theta}\right)\right] - \\
&\quad \rho_0 \frac{\partial(g_0\,u)}{\partial r} + \rho_0 \frac{\partial \psi_1}{\partial r} + \rho_0\,g_0\,\Delta \\
&= \frac{\partial}{\partial r}\left(\lambda\,\Delta + 2\,\mu\,\frac{\partial u}{\partial r}\right) + \frac{2\mu}{r}\frac{\partial\left(\frac{1}{2}\frac{\partial v}{\partial r} - \frac{v}{2r} + \frac{1}{2r}\frac{\partial u}{\partial \theta}\right)}{\partial \theta} + \\
&\quad \frac{2\mu}{r}\left[2\frac{\partial u}{\partial r} - \frac{1}{r}\frac{\partial v}{\partial \theta} - \frac{2u}{r} + \cot\theta\left(\frac{1}{2}\frac{\partial v}{\partial r} - \frac{3v}{2r} + \frac{1}{2r}\frac{\partial u}{\partial \theta}\right)\right] - \\
&\quad \rho_0 \frac{\partial(g_0\,u)}{\partial r} + \rho_0 \frac{\partial \psi_1}{\partial r} + \rho_0\,g_0\,\Delta \\
\rho_0 \frac{\partial^2 v}{\partial t^2} &= 2\frac{\partial}{\partial r}\left(\mu\left(\frac{1}{2}\frac{\partial v}{\partial r} - \frac{v}{2r} + \frac{1}{2r}\frac{\partial u}{\partial \theta}\right)\right) + \frac{1}{r}\frac{\partial}{\partial \theta}\left(\lambda\,\Delta + 2\,\mu\,\left(\frac{1}{r}\frac{\partial v}{\partial \theta} + \frac{u}{r}\right)\right) +
\end{aligned}$$

$$
\begin{aligned}
& \frac{2\mu}{r}\left[\left(\left(\frac{1}{r}\frac{\partial v}{\partial\theta}+\frac{u}{r}\right)-\left(\frac{v}{r}\cot\theta+\frac{u}{r}\right)\right)\cot\theta+3\left(\frac{1}{2}\frac{\partial v}{\partial r}-\frac{v}{2r}+\frac{1}{2r}\frac{\partial u}{\partial\theta}\right)\right]+ \\
& \frac{\rho_0}{r}\frac{\partial\psi_1}{\partial\theta}-\rho_0\, g_0\,\frac{1}{r}\frac{\partial u}{\partial\theta} \\
= \; & 2\frac{\partial}{\partial r}\left(\mu\left(\frac{1}{2}\frac{\partial v}{\partial r}-\frac{v}{2r}+\frac{1}{2r}\frac{\partial u}{\partial\theta}\right)\right)+\frac{1}{r}\frac{\partial}{\partial\theta}\left(\lambda\,\Delta+2\,\mu\left(\frac{1}{r}\frac{\partial v}{\partial\theta}+\frac{u}{r}\right)\right)+ \\
& \frac{2\mu}{r}\left[\left(\frac{1}{r}\frac{\partial v}{\partial\theta}-\frac{v}{r}\cot\theta\right)\cot\theta+3\left(\frac{1}{2}\frac{\partial v}{\partial r}-\frac{v}{2r}+\frac{1}{2r}\frac{\partial u}{\partial\theta}\right)\right]+ \\
& \frac{\rho_0}{r}\frac{\partial\psi_1}{\partial\theta}-\rho_0\, g_0\,\frac{1}{r}\frac{\partial u}{\partial\theta},
\end{aligned}
\tag{4.65}
$$

where I have allowed for radial heterogeneity in the density and elastic moduli.

4.2.5 Solutions to the Equations of Motion

The spheroidal-deformation Eqs. 4.65 for a self-gravitating, radially heterogeneous Earth may be satisfied by solutions of the form (e.g., Alterman et al., 1959; Longman, 1962):

$$
\begin{aligned}
u_n &= U_n(r)\, P_n(\cos\theta)\, e^{i\omega t} \\
v_n &= V_n(r)\,\frac{\partial P_n(\cos\theta)}{\partial\theta}\, e^{i\omega t} \\
\psi_n &= P_n(r)\, P_n(\cos\theta)\, e^{i\omega t},
\end{aligned}
\tag{4.66}
$$

where $U(r)$, $V(r)$, and $P(r)$ are radial coefficients of the spherical harmonic expansions and $P_n(\cos\theta)$ is a Legendre polynomial of order n. For periodic forcing, such as loading by the ocean tides, ω represents the frequency of the forcing. Since the tides exhibit periods much longer than the free oscillations of the Earth ($\sim$1 hour), a quasi-static formulation of the equations of motion is sometimes adopted anyway (e.g., Longman, 1962; Takeuchi, 1966; Farrell, 1972a; Guo et al., 2004). For static or quasi-static formulations, $\omega = 0$, and temporal variations in the loading are removed from the problem. Since the divergence of the stress tensor must then balance the sum of all forces, the static equations may be referred to as the equilibrium equations (e.g., Longman, 1962). Nevertheless, to maintain generality, I retain the time-varying factors in the development of the displacement solution presented here (e.g., Na & Baek, 2011; Wang et al., 2012). The time-varying factors are also retained in normal-mode seismology (e.g., Alterman et al., 1959; Lapwood & Usami, 1981).

The dilatation, Δ, may be written as:

$$
\begin{aligned}
\Delta &= \epsilon_{rr} + \epsilon_{\theta\theta} + \epsilon_{\phi\phi} \\
&= \frac{\partial u}{\partial r} + \frac{1}{r}\frac{\partial v}{\partial \theta} + \frac{u}{r} + \frac{v}{r}\cot\theta + \frac{u}{r} \\
&= \frac{\partial u}{\partial r} + \frac{2u}{r} + \frac{1}{r}\frac{\partial v}{\partial \theta} + \frac{v}{r}\cot\theta \\
&= e^{i\omega t}\,[\,\frac{\partial U}{\partial r}P_n(\cos\theta) + \frac{2U}{r}P_n(\cos\theta) + \frac{1}{r}\frac{\partial}{\partial\theta}\left[V\frac{\partial P_n(\cos\theta)}{\partial\cos\theta}\frac{\partial\cos\theta}{\partial\theta}\right] + \\
&\quad \frac{\cot\theta}{r}V\frac{\partial P_n(\cos\theta)}{\partial\cos\theta}\frac{\partial\cos\theta}{\partial\theta}\,] \\
&= e^{i\omega t}\,[\,\frac{\partial U}{\partial r}P_n(\cos\theta) + \frac{2U}{r}P_n(\cos\theta) + \frac{1}{r}\frac{\partial}{\partial\theta}\left[V\frac{\partial P_n(\cos\theta)}{\partial\cos\theta}(-\sin\theta)\right] + \\
&\quad \frac{V\cot\theta}{r}\frac{\partial P_n(\cos\theta)}{\partial\cos\theta}(-\sin\theta)\,] \\
&= e^{i\omega t}\,[\,\frac{\partial U}{\partial r}P_n(\cos\theta) + \frac{2U}{r}P_n(\cos\theta) + \frac{V}{r}\frac{\partial}{\partial\theta}\left[-\sin\theta\frac{\partial P_n(\cos\theta)}{\partial\cos\theta}\right] + \\
&\quad +\frac{1}{r}\left[-\sin\theta\frac{\partial P_n(\cos\theta)}{\partial\cos\theta}\right]\frac{\partial V}{\partial\theta} - \frac{V\cos\theta}{r}\frac{\partial P_n(\cos\theta)}{\partial\cos\theta}\,] \\
&= e^{i\omega t}\,[\,\frac{\partial U}{\partial r}P_n(\cos\theta) + \frac{2U}{r}P_n(\cos\theta) - \frac{V\sin\theta}{r}\frac{\partial}{\partial\theta}\left[\frac{\partial P_n(\cos\theta)}{\partial\cos\theta}\right] - \\
&\quad \frac{V}{r}\frac{\partial P_n(\cos\theta)}{\partial\cos\theta}\frac{\partial\sin\theta}{\partial\theta} - \frac{V\cos\theta}{r}\frac{\partial P_n(\cos\theta)}{\partial\cos\theta}\,] \\
&= e^{i\omega t}\,[\,\frac{\partial U}{\partial r}P_n(\cos\theta) + \frac{2U}{r}P_n(\cos\theta) - \frac{V\sin\theta}{r}\left[\frac{\partial^2 P_n(\cos\theta)}{\partial\cos^2\theta}(-\sin\theta)\right] - \\
&\quad \frac{V\cos\theta}{r}\frac{\partial P_n(\cos\theta)}{\partial\cos\theta} - \frac{V\cos\theta}{r}\frac{\partial P_n(\cos\theta)}{\partial\cos\theta}\,] \\
&= e^{i\omega t}\,[\,\frac{\partial U}{\partial r}P_n(\cos\theta) + \frac{2U}{r}P_n(\cos\theta) + \frac{V\sin^2\theta}{r}\left[\frac{\partial^2 P_n(\cos\theta)}{\partial\cos^2\theta}\right] - \\
&\quad \frac{2V\cos\theta}{r}\frac{\partial P_n(\cos\theta)}{\partial\cos\theta}\,] \\
&= e^{i\omega t}\,[\,\frac{\partial U}{\partial r}P_n(\cos\theta) + \frac{2U}{r}P_n(\cos\theta) + \frac{V}{r}[\,\sin^2\theta\frac{\partial^2 P_n(\cos\theta)}{\partial\cos^2\theta} - \\
&\quad 2\cos\theta\frac{\partial P_n(\cos\theta)}{\partial\cos\theta}\,]\,] \\
&= e^{i\omega t}\,[\,\frac{\partial U}{\partial r}P_n(\cos\theta) + \frac{2U}{r}P_n(\cos\theta) - \frac{n(n+1)}{r}V\,P_n(\cos\theta)\,] \\
&= e^{i\omega t}\,P_n(\cos\theta)\,[\,\frac{\partial U}{\partial r} + \frac{2U}{r} - \frac{n(n+1)}{r}V\,] \\
&= X(r)\,P_n(\cos\theta)\,e^{i\omega t}, \qquad (4.67)
\end{aligned}
$$

where

$$X(r) = \dot{U} + \frac{2U}{r} - \frac{n(n+1)}{r}V, \qquad (4.68)$$

and I have made use of the Legendre differential equation (e.g., Boas, 1983). A dot implies differentiation with respect to r. Note that the term containing $\frac{\partial V}{\partial \theta}$ was canceled since V is only a function of r.

From the set of Eqs. 4.66:

$$\begin{aligned}
\frac{\partial u}{\partial \theta} &= -U \sin\theta P_n' \\
\frac{\partial v}{\partial \theta} &= V \sin^2\theta P_n'' - V \cos\theta P_n' \\
\frac{\partial u}{\partial r} &= \dot{U} P_n(\cos\theta) \\
\frac{\partial v}{\partial r} &= -\dot{V} \sin\theta P_n' \\
\frac{\partial^2 u}{\partial \theta^2} &= U \sin^2\theta P_n'' - U \cos\theta P_n' \\
\frac{\partial^2 v}{\partial \theta^2} &= \frac{\partial}{\partial \theta}[V \sin^2\theta P_n'' - V \cos\theta P_n'] \\
&= V[\sin^2\theta P_n'''(-\sin\theta) + 3P_n'' \sin\theta\cos\theta + \sin\theta P_n'], \qquad (4.69)
\end{aligned}$$

where

$$P_n' = \frac{\partial P_n(\cos\theta)}{\partial \cos\theta}, P_n'' = \frac{\partial^2 P_n(\cos\theta)}{\partial \cos^2\theta}, P_n''' = \frac{\partial^3 P_n(\cos\theta)}{\partial \cos^3\theta}, \qquad (4.70)$$

and, according to the Legendre differential equation (Boas, 1983),

$$\sin^2\theta P_n'' - 2\cos\theta P_n' = -n(n+1)P_n. \qquad (4.71)$$

Only P_n and P_n' are required to derive additional derivatives of the Legendre polynomials recursively. For example, the third derivative of the Legendre polynomial, P_n''', is given by:

$$\begin{aligned}
0 &= \frac{\partial}{\partial \cos\theta}[(1-\cos^2\theta)P_n'' - 2\cos\theta P_n' + n(n+1)P_n] \\
&= P_n''' - 2\cos\theta P_n'' - \cos^2\theta P_n''' - 2P_n' - 2\cos\theta P_n'' + n(n+1)P_n' \\
&= (1-\cos^2\theta)P_n''' - 4\cos\theta P_n'' + (-2 + n(n+1))P_n' \\
&= \sin^2\theta P_n''' - 4\cos\theta P_n'' - (2 - n(n+1))P_n' \\
\sin^2\theta P_n''' &= 4\cos\theta P_n'' + 2P_n' - n(n+1)P_n'. \qquad (4.72)
\end{aligned}$$

Now, I can rewrite the radial component of Eq. 4.65 as:

$$
\begin{aligned}
\rho_0 \frac{\partial^2 u}{\partial t^2} &= \frac{\partial}{\partial r}\left(\lambda\,\Delta + 2\,\mu\,\frac{\partial u}{\partial r}\right) + \frac{\mu}{r}\frac{\partial\left(\frac{\partial v}{\partial r} - \frac{v}{r} + \frac{1}{r}\frac{\partial u}{\partial \theta}\right)}{\partial \theta} + \\
&\quad \frac{2\mu}{r}\left[2\frac{\partial u}{\partial r} - \frac{1}{r}\frac{\partial v}{\partial \theta} - \frac{2u}{r} + \cot\theta\left(\frac{1}{2}\frac{\partial v}{\partial r} - \frac{3v}{2r} + \frac{1}{2r}\frac{\partial u}{\partial \theta}\right)\right] - \\
&\quad \rho_0 \frac{\partial(g_0\,u)}{\partial r} + \rho_0 \frac{\partial \psi_1}{\partial r} + \rho_0\,g_0\,\Delta \\
&= \frac{\partial}{\partial r}\left(\lambda\,X + 2\,\mu\,\dot{U}\right) + \frac{\mu}{r}\frac{\partial^2 v}{\partial r \partial \theta} + \frac{\mu}{r^2}\frac{\partial^2 u}{\partial \theta^2} + \\
&\quad \frac{\mu}{r^2}\left[4\,r\dot{U} - 3\frac{\partial v}{\partial \theta} - 4U + r\,\cot\theta\left(\frac{\partial v}{\partial r} - \frac{3v}{r} + \frac{1}{r}\frac{\partial u}{\partial \theta}\right)\right] - \\
&\quad \rho_0 \frac{\partial(g_0\,U)}{\partial r} + \rho_0 \dot{P} + \rho_0\,g_0\,X \\
&= \frac{\partial}{\partial r}\left(\lambda\,X + 2\,\mu\,\dot{U}\right) + \frac{\mu}{r}(\dot{V}\sin^2\theta P_n'' - \dot{V}\cos\theta P_n') + \frac{\mu}{r^2}(U\sin^2\theta P_n'' - U\cos\theta P_n') + \\
&\quad \frac{\mu}{r^2}[4\,r\dot{U} - 3(V\sin^2\theta P_n'' - V\cos\theta P_n') - 4U + \\
&\quad r\,\cot\theta(-\dot{V}\sin\theta P_n' + \frac{3V}{r}\sin\theta P_n' + \frac{-U}{r}\sin\theta P_n')] - \\
&\quad \rho_0 \frac{\partial(g_0\,U)}{\partial r} + \rho_0 \dot{P} + \rho_0\,g_0\,X \\
&= \frac{\partial}{\partial r}\left(\lambda\,X + 2\,\mu\,\dot{U}\right) + \dot{V}\,\frac{\mu}{r}(\sin^2\theta P_n'' - 2\cos\theta P_n') + U\,\frac{\mu}{r^2}(\sin^2\theta P_n'' - 2\cos\theta P_n') + \\
&\quad \frac{\mu}{r^2}[4\,r\dot{U} - 3V(\sin^2\theta P_n'' - 2\cos\theta P_n') - 4U] - \rho_0\frac{\partial(g_0\,U)}{\partial r} + \rho_0\dot{P} + \rho_0\,g_0\,X \\
&= \frac{\partial}{\partial r}\left(\lambda\,X + 2\,\mu\,\dot{U}\right) + \dot{V}\,\frac{\mu}{r}(-n(n+1)) + U\,\frac{\mu}{r^2}(-n(n+1)) + \\
&\quad \frac{\mu}{r^2}[4\,r\dot{U} - 3V(-n(n+1)) - 4U] - \rho_0\frac{\partial(g_0\,U)}{\partial r} + \rho_0\dot{P} + \rho_0\,g_0\,X \\
-\omega^2\rho_0 U &= \frac{\partial}{\partial r}\left(\lambda\,X + 2\,\mu\,\dot{U}\right) + \frac{\mu}{r^2}[4\,r\dot{U} - 4U + n(n+1)(3V - U - r\dot{V})] - \\
&\quad \rho_0 \frac{\partial(g_0\,U)}{\partial r} + \rho_0 \dot{P} + \rho_0\,g_0\,X, \qquad (4.73)
\end{aligned}
$$

where common terms in $e^{i\omega t}$ and P_n have been canceled (Alterman et al., 1959).

Similarly, the surface-tangential component of Eq. 4.65 may be written as:

$$
\begin{aligned}
\rho_0 \frac{\partial^2 v}{\partial t^2} &= 2\frac{\partial}{\partial r}\left(\mu\left(\frac{1}{2}\frac{\partial v}{\partial r} - \frac{v}{2r} + \frac{1}{2r}\frac{\partial u}{\partial \theta}\right)\right) + \frac{1}{r}\frac{\partial}{\partial \theta}\left(\lambda\,\Delta + 2\,\mu\,\left(\frac{1}{r}\frac{\partial v}{\partial \theta} + \frac{u}{r}\right)\right) + \\
&\quad \frac{2\mu}{r}\left[\left(\frac{1}{r}\frac{\partial v}{\partial \theta} - \frac{v}{r}\cot\theta\right)\cot\theta + 3\,\left(\frac{1}{2}\frac{\partial v}{\partial r} - \frac{v}{2r} + \frac{1}{2r}\frac{\partial u}{\partial \theta}\right)\right] + \\
&\quad \frac{\rho_0}{r}\frac{\partial \psi_1}{\partial \theta} - \rho_0\,g_0\,\frac{1}{r}\frac{\partial u}{\partial \theta}
\end{aligned}
$$

$$
\begin{aligned}
= \quad & \frac{\partial}{\partial r}\left(\mu\left(-\dot{V}\sin\theta P_n' + \sin\theta P_n'\frac{V}{r} - \frac{U}{r}\sin\theta P_n'\right)\right) + \\
& \frac{1}{r}\frac{\partial}{\partial\theta}\left(\lambda X P_n + 2\mu\left(\frac{1}{r}\frac{\partial v}{\partial\theta} + \frac{u}{r}\right)\right) + \\
& \frac{2\mu}{r^2}\left[\left(\frac{\partial v}{\partial\theta} - v\cot\theta\right)\cot\theta + \frac{3}{2}\left(r\frac{\partial v}{\partial r} - v + \frac{\partial u}{\partial\theta}\right)\right] + \frac{\rho_0}{r}\frac{\partial\psi_1}{\partial\theta} - \frac{\rho_0 g_0}{r}\frac{\partial u}{\partial\theta} \\
= \quad & \frac{\partial}{\partial r}\left(\mu\left(-\dot{V}\sin\theta P_n' + \sin\theta P_n'\frac{V}{r} - \frac{U}{r}\sin\theta P_n'\right)\right) + \\
& \frac{1}{r}\lambda X P_n'(-\sin\theta) + \frac{2\mu}{r^2}\left(\frac{\partial^2 v}{\partial\theta^2} + \frac{\partial u}{\partial\theta}\right) + \\
& \frac{2\mu}{r^2}\left[\left(\frac{\partial v}{\partial\theta} - v\cot\theta\right)\cot\theta + \frac{3}{2}\left(r\frac{\partial v}{\partial r} - v + \frac{\partial u}{\partial\theta}\right)\right] + \frac{\rho_0}{r}\frac{\partial\psi_1}{\partial\theta} - \frac{\rho_0 g_0}{r}\frac{\partial u}{\partial\theta} \\
= \quad & -\sin\theta P_n'\left(\frac{\partial}{\partial r}\left(\mu\dot{V} - \mu\frac{V}{r} + \mu\frac{U}{r}\right) + \frac{\lambda}{r}X\right) + \frac{\rho_0}{r}\frac{\partial\psi_1}{\partial\theta} - \frac{\rho_0 g_0}{r}\frac{\partial u}{\partial\theta} + \\
& \frac{2\mu}{r^2}\left[\frac{\partial^2 v}{\partial\theta^2} + \frac{\partial u}{\partial\theta} + \left(\frac{\partial v}{\partial\theta} - v\cot\theta\right)\cot\theta + \frac{3}{2}\left(r\frac{\partial v}{\partial r} - v + \frac{\partial u}{\partial\theta}\right)\right] \\
= \quad & -\sin\theta P_n'\left(\frac{\partial}{\partial r}\left(\mu\dot{V} - \mu\frac{V}{r} + \mu\frac{U}{r}\right) + \frac{\lambda}{r}X\right) + \frac{\rho_0}{r}\frac{\partial\psi_1}{\partial\theta} - \frac{\rho_0 g_0}{r}\frac{\partial u}{\partial\theta} + \\
& \frac{2\mu}{r^2}\left[\frac{\partial^2 v}{\partial\theta^2} + \frac{\partial u}{\partial\theta} + \cot\theta\frac{\partial v}{\partial\theta} - v\cot^2\theta + \frac{3}{2}\left(r\frac{\partial v}{\partial r} - v + \frac{\partial u}{\partial\theta}\right)\right] \\
= \quad & -\sin\theta P_n'\left(\frac{\partial}{\partial r}\left(\mu\dot{V} - \mu\frac{V}{r} + \mu\frac{U}{r}\right) + \frac{\lambda}{r}X\right) + \frac{\rho_0}{r}\frac{\partial\psi_1}{\partial\theta} - \frac{\rho_0 g_0}{r}\frac{\partial u}{\partial\theta} + \\
& \frac{2\mu}{r^2}\left[\frac{\partial^2 v}{\partial\theta^2} + \frac{5}{2}\frac{\partial u}{\partial\theta} - v\left(\cot^2\theta + \frac{3}{2}\right) + \cot\theta\frac{\partial v}{\partial\theta} + \frac{3r}{2}\frac{\partial v}{\partial r}\right] \\
= \quad & -\sin\theta P_n'\left(\frac{\partial}{\partial r}\left(\mu\dot{V} - \mu\frac{V}{r} + \mu\frac{U}{r}\right) + \frac{\lambda}{r}X\right) + \frac{\rho_0}{r}\frac{\partial\psi_1}{\partial\theta} - \frac{\rho_0 g_0}{r}\frac{\partial u}{\partial\theta} + \\
& \frac{\mu}{r^2}\left[2\frac{\partial^2 v}{\partial\theta^2} + 5\frac{\partial u}{\partial\theta} - v\left(2\cot^2\theta + 3\right) + 2\cot\theta\frac{\partial v}{\partial\theta} + 3r\frac{\partial v}{\partial r}\right] \\
= \quad & -\sin\theta P_n'\left(\frac{\partial}{\partial r}\left(\mu\dot{V} - \mu\frac{V}{r} + \mu\frac{U}{r}\right) + \frac{\lambda}{r}X\right) + \frac{\rho_0}{r}\frac{\partial\psi_1}{\partial\theta} - \frac{\rho_0 g_0}{r}\frac{\partial u}{\partial\theta} + \\
& \frac{\mu}{r^2}\left[2V(\sin^2\theta P_n'''(-\sin\theta) + 3\sin\theta\cos\theta P_n'' + \sin\theta P_n') + 5\frac{\partial u}{\partial\theta} - \right. \\
& \left. v(2\cot^2\theta + 3) + 2\cot\theta(V\sin^2\theta P_n'' - V\cos\theta P_n') - 3r\dot{V}\sin\theta P_n'\right] \\
= \quad & -\sin\theta P_n'\left(\frac{\partial}{\partial r}\left(\mu\dot{V} - \mu\frac{V}{r} + \mu\frac{U}{r}\right) + \frac{\lambda}{r}X\right) + \frac{\rho_0}{r}\frac{\partial\psi_1}{\partial\theta} - \frac{\rho_0 g_0}{r}\frac{\partial u}{\partial\theta} + \\
& \frac{\mu}{r^2}\left[2V((4\cos\theta P_n'' + 2P_n' - n(n+1)P_n')(-\sin\theta) + 3\sin\theta\cos\theta P_n'' + \sin\theta P_n') + \right. \\
& 5U P_n'(-\sin\theta) - V P_n'(-\sin\theta)(2\cot^2\theta + 3) + \\
& \left. 2\cot\theta(V\sin^2\theta P_n'' - V\cos\theta P_n') - 3r\dot{V}\sin\theta P_n'\right] \\
= \quad & -\sin\theta P_n'\left(\frac{\partial}{\partial r}\left(\mu\dot{V} - \mu\frac{V}{r} + \mu\frac{U}{r}\right) + \frac{\lambda}{r}X\right) + \frac{\rho_0}{r}\frac{\partial\psi_1}{\partial\theta} - \frac{\rho_0 g_0}{r}\frac{\partial u}{\partial\theta} +
\end{aligned}
$$

$$
\begin{aligned}
& \frac{\mu}{r^2}\left[2V(-\sin\theta\cos\theta P_n'' - \sin\theta P_n' + n(n+1)\sin\theta P_n') + \right. \\
& 5UP_n'(-\sin\theta) - 2V\cot^2\theta P_n'(-\sin\theta) - 3VP_n'(-\sin\theta) + \\
& \left. 2V\cot\theta\sin^2\theta P_n'' - 2V\cot\theta\cos\theta P_n' - 3r\dot{V}\sin\theta P_n'\right] \\
= \; & -\sin\theta P_n'\left(\frac{\partial}{\partial r}\left(\mu\dot{V} - \mu\frac{V}{r} + \mu\frac{U}{r}\right) + \frac{\lambda}{r}X\right) + \frac{\rho_0}{r}\frac{\partial\psi_1}{\partial\theta} - \frac{\rho_0 g_0}{r}\frac{\partial u}{\partial\theta} + \\
& \frac{\mu}{r^2}\left[2V(-\sin\theta\cos\theta P_n'' - \sin\theta P_n' + n(n+1)\sin\theta P_n') + \right. \\
& 5UP_n'(-\sin\theta) + 2V\cot\theta\cos\theta P_n' - 3VP_n'(-\sin\theta) + \\
& \left. 2V\cos\theta\sin\theta P_n'' - 2V\cot\theta\cos\theta P_n' - 3r\dot{V}\sin\theta P_n'\right] \\
= \; & -\sin\theta P_n'\left(\frac{\partial}{\partial r}\left(\mu\dot{V} - \mu\frac{V}{r} + \mu\frac{U}{r}\right) + \frac{\lambda}{r}X\right) + \frac{\rho_0}{r}\frac{\partial\psi_1}{\partial\theta} - \frac{\rho_0 g_0}{r}\frac{\partial u}{\partial\theta} + \\
& \frac{\mu}{r^2}\left[2V(-\sin\theta P_n' + n(n+1)\sin\theta P_n') + \right. \\
& \left. 5UP_n'(-\sin\theta) - 3VP_n'(-\sin\theta) - 3r\dot{V}\sin\theta P_n'\right] \\
= \; & -\sin\theta P_n'\left(\frac{\partial}{\partial r}\left(\mu\dot{V} - \mu\frac{V}{r} + \mu\frac{U}{r}\right) + \frac{\lambda}{r}X\right) + \\
& \frac{\rho_0}{r}PP_n'(-\sin\theta) - \frac{\rho_0 g_0}{r}UP_n'(-\sin\theta) + \\
& \frac{\mu}{r^2}\left[2V(-\sin\theta P_n' + n(n+1)\sin\theta P_n') + \right. \\
& \left. 5UP_n'(-\sin\theta) - 3VP_n'(-\sin\theta) - 3r\dot{V}\sin\theta P_n'\right] \\
-\omega^2\rho_0 V \; = \; & \frac{\partial}{\partial r}\left(\mu\dot{V} - \mu\frac{V}{r} + \mu\frac{U}{r}\right) + \frac{\lambda}{r}X + \frac{\rho_0}{r}P - \frac{\rho_0 g_0}{r}U + \\
& \frac{\mu}{r^2}\left[5U - V - 2n(n+1)V + 3r\dot{V}\right] \\
-\omega^2\rho_0 V r \; = \; & r\frac{\partial}{\partial r}\left(\mu\dot{V} - \mu\frac{V}{r} + \mu\frac{U}{r}\right) + \lambda X + \rho_0 P - \rho_0 g_0 U + \\
& \frac{\mu}{r}\left[5U - V - 2n(n+1)V + 3r\dot{V}\right], \qquad (4.74)
\end{aligned}
$$

where common terms in $e^{i\omega t}$ and $[-\sin\theta P_n']$ have been canceled (Alterman et al., 1959).

Finally, Poisson's equation (Eq. 4.19) may be written as:

$$
\begin{aligned}
\nabla^2\psi_1 &= 4\,\pi\,G\,\left(\rho_0\,\Delta + u\,\frac{\partial\rho_0}{\partial r}\right) \\
&= 4\,\pi\,G\,\left(\rho_0\,X + U\,\dot{\rho}_0\right). \qquad (4.75)
\end{aligned}
$$

I can also write the Laplacian in spherical coordinates (neglecting the azimuthal component)

as:

$$\begin{aligned}
\nabla^2\psi_1 &= \frac{1}{r^2}\frac{\partial}{\partial r}\left(r^2\frac{\partial\psi_1}{\partial r}\right) + \frac{1}{r^2\sin\theta}\frac{\partial}{\partial\theta}\left(\sin\theta\frac{\partial\psi_1}{\partial\theta}\right) \\
&= \frac{1}{r^2}[2r\dot{P} + r^2\ddot{P}] + \frac{1}{r^2\sin\theta}\left[\cos\theta\frac{\partial\psi_1}{\partial\theta} + \sin\theta\frac{\partial^2\psi_1}{\partial\theta^2}\right] \\
&= \frac{2}{r}\dot{P} + \ddot{P} - \frac{\cos\theta}{r^2}PP'_n + \frac{P\sin\theta\sin^2\theta P''_n}{r^2\sin\theta} - \frac{P\sin\theta\cos\theta P'_n}{r^2\sin\theta} \\
&= \frac{2}{r}\dot{P} + \ddot{P} + \frac{P}{r^2}[-\cos\theta P'_n + \sin^2\theta P''_n - \cos\theta P'_n] \\
&= \frac{2}{r}\dot{P} + \ddot{P} + \frac{P}{r^2}[\sin^2\theta P''_n - 2\cos\theta P'_n] \\
&= \frac{2}{r}\dot{P} + \ddot{P} - \frac{n(n+1)}{r^2}P, \qquad (4.76)
\end{aligned}$$

where

$$\begin{aligned}
\frac{\partial\psi_1}{\partial\theta} &= PP'_n(-\sin\theta) \\
\frac{\partial^2\psi_1}{\partial\theta^2} &= P[\sin^2\theta P''_n - \cos\theta P'_n].
\end{aligned}$$

Combining Eq. 4.75 with Eq. 4.76 yields (Alterman et al., 1959):

$$\ddot{P} + \frac{2}{r}\dot{P} - \frac{n(n+1)}{r^2}P = 4\,\pi\,G\,\left(\rho_0\,X + U\,\dot{\rho}_0\right), \qquad (4.77)$$

where I have again canceled common factors of $e^{i\omega t}$ and P_n.

The equations of motion for spheroidal deformation are now given by three second-order differential equations (Eqs. 4.73, 4.74, and 4.77) that may be solved for the coefficients U, V, and P.

4.2.6 Reduction of the Equations of Motion to First Order

For convenience, a set of handy substitutions may be made to simplify Eqs. 4.73, 4.74, and 4.77 prior to numerical integration (e.g., Alterman et al., 1959; Longman, 1962; Melchior,

1983, Ch. 5):

$$\begin{aligned} y_1 &= U \\ y_2 &= \lambda X + 2\mu \dot{U} \\ y_3 &= V \\ y_4 &= \mu \left(\dot{V} - \frac{V}{r} + \frac{U}{r} \right) \\ y_5 &= P \\ y_6 &= \dot{P} - 4\pi G \rho_0 U. \end{aligned} \tag{4.78}$$

With the substitutions, Eqs. 4.73, 4.74, and 4.77 become a system of six first-order differential equations (e.g. Alterman et al., 1959):

$$\begin{aligned} \dot{y}_1 &= \frac{-2\lambda}{\lambda + 2\mu} \frac{y_1}{r} + \frac{y_2}{\lambda + 2\mu} + \frac{\lambda\, n(n+1)}{\lambda + 2\mu} \frac{y_3}{r}, \\ \dot{y}_2 &= \left[-\omega^2 \rho_0 r^2 - 4\rho_0 g_0 r + \frac{4\mu(3\lambda + 2\mu)}{\lambda + 2\mu} \right] \frac{y_1}{r^2} - \frac{4\mu}{\lambda + 2\mu} \frac{y_2}{r} \\ &+ \left[n(n+1)\rho_0 g_0 r - \frac{2\mu(3\lambda + 2\mu)\, n(n+1)}{\lambda + 2\mu} \right] \frac{y_3}{r^2} \\ &+ n(n+1) \frac{y_4}{r} - \rho_0 y_6, \\ \dot{y}_3 &= -\frac{y_1}{r} + \frac{y_3}{r} + \frac{y_4}{\mu}, \\ \dot{y}_4 &= \left[g_0 \rho_0 r - \frac{2\mu(3\lambda + 2\mu)}{\lambda + 2\mu} \right] \frac{y_1}{r^2} - \frac{\lambda}{\lambda + 2\mu} \frac{y_2}{r} \\ &+ \left[-\omega^2 \rho_0 r^2 + \frac{2\mu}{\lambda + 2\mu} [\lambda(2n^2 + 2n - 1) + 2\mu(n^2 + n - 1)] \right] \frac{y_3}{r^2} \\ &- \frac{3y_4}{r} - \rho_0 \frac{y_5}{r}, \\ \dot{y}_5 &= 4\pi G \rho_0 y_1 + y_6, \\ \dot{y}_6 &= -4\pi G \rho_0\, n(n+1) \frac{y_3}{r} + n(n+1) \frac{y_5}{r^2} - \frac{2y_6}{r}, \end{aligned} \tag{4.79}$$

where dots represent differentiation with respect to r. Importantly, by reducing the equations of motion to first order, the derivatives of the elastic parameters no longer appear. The variables y_1 and y_3 characterize the radial and tangential displacements, respectively; y_2 and y_4 characterize the radial and tangential stress, respectively; y_5 characterizes the grav-

itational potential; and the equation for $\dot{y}_5$ defines y_6. Additional details may be found in the literature (e.g., Takeuchi & Saito, 1972; Lapwood & Usami, 1981; Guo et al., 2004; Smylie, 2013).

Note also that the six equations may now be written in the form $\dot{y} = A\ y$:

$$\begin{bmatrix} \frac{dy_1}{dr} \\ \frac{dy_2}{dr} \\ \frac{dy_3}{dr} \\ \frac{dy_4}{dr} \\ \frac{dy_5}{dr} \\ \frac{dy_6}{dr} \end{bmatrix} = \begin{bmatrix} -\frac{2\lambda\xi}{r} & \xi & \frac{k^2\lambda\xi}{r} & 0 & 0 & 0 \\ \left(-\omega^2\rho_0 - \frac{4g_0\rho_0}{r} + \frac{2\delta}{r^2}\right) & -\frac{4\mu\xi}{r} & \left(\frac{k^2 g_0\rho_0}{r} - \frac{k^2\delta}{r^2}\right) & \frac{k^2}{r} & 0 & -\rho_0 \\ -\frac{1}{r} & 0 & \frac{1}{r} & \frac{1}{\mu} & 0 & 0 \\ \left(\frac{g_0\rho_0}{r} - \frac{\delta}{r^2}\right) & -\frac{\lambda\xi}{r} & \left(-\omega^2\rho_0 + \frac{\epsilon}{r^2}\right) & -\frac{3}{r} & -\frac{\rho_0}{r} & 0 \\ 4\pi G\rho_0 & 0 & 0 & 0 & 0 & 1 \\ 0 & 0 & -4\pi G\rho_0\frac{k^2}{r} & 0 & \frac{k^2}{r^2} & -\frac{2}{r} \end{bmatrix} \begin{bmatrix} y_1 \\ y_2 \\ y_3 \\ y_4 \\ y_5 \\ y_6 \end{bmatrix}, \tag{4.80}$$

where

$$k^2 = n(n+1) \tag{4.81}$$

$$\xi = \frac{1}{\lambda + 2\mu} \tag{4.82}$$

$$\delta = 2\mu(3\lambda + 2\mu)\xi \tag{4.83}$$

$$\epsilon = 4k^2\mu(\lambda + \mu)\xi - 2\mu. \tag{4.84}$$

The matrix equation, $\dot{y} = A\ y$, may be solved using numerical methods, such as the commonly adopted Runge-Kutta algorithm and the propagator matrix technique (Sec. 4.2.11) (Gilbert & Backus, 1966) .

For the special case of $n = 0$, the equations for y_3 and y_4 are undefined and the system reduces to (e.g., Smylie, 2013):

$$\begin{bmatrix} \frac{dy_1}{dr} \\ \frac{dy_2}{dr} \\ \frac{dy_5}{dr} \\ \frac{dy_6}{dr} \end{bmatrix} = \begin{bmatrix} -\frac{2\lambda\xi}{r} & \xi & 0 & 0 \\ \left(-\omega^2\rho_0 - \frac{4g_0\rho_0}{r} + \frac{2\delta}{r^2}\right) & -\frac{4\mu\xi}{r} & 0 & -\rho_0 \\ 4\pi G\rho_0 & 0 & 0 & 1 \\ 0 & 0 & 0 & -\frac{2}{r} \end{bmatrix} \begin{bmatrix} y_1 \\ y_2 \\ y_5 \\ y_6 \end{bmatrix}. \tag{4.85}$$

4.2.7 Non-dimensionalization

Suitable scaling parameters must be introduced to maintain numerical stability during the integration of the equations of motion (e.g., Longman, 1962; Crossley, 1975). I adopt a characteristic length scale, a, equal to Earth's mean radius (6371 km) and a characteristic mass scale close to Earth's mass, $4\pi a^3\bar{\rho}/3$, where $\bar{\rho}$ is an approximate value for Earth's average density (5500 kg/m^3). A handy way of scaling the time is to define the characteristic time scale as $1/\sqrt{\pi G\bar{\rho}}$ where G is the universal gravitational constant. Since G has units of $[M^{-1}L^3T^{-2}]$, it becomes

$$G' = G/(\bar{\rho}^{-1}a^{-3}a^3\pi G\bar{\rho}) = 1/\pi \tag{4.86}$$

in the scaled system. M, L, and T represent units of mass, length, and time, respectively. In summary I have

Length :

$$l' = l/a \tag{4.87}$$

Mass :

$$m' = m/(4\pi\bar{\rho}a^3/3) \tag{4.88}$$

Time :

$$t' = t\sqrt{\pi G\bar{\rho}} \tag{4.89}$$

Another way of stating the above mass scaling is simply to say that I adopt a characteristic density scale equal to $\bar{\rho}$, where

$$\rho' = \rho/\bar{\rho}. \tag{4.90}$$

4.2.8 Starting Solutions: Power Series Expansion

The six first-order ordinary differential equations (Eq. 4.79) require six starting solutions to initialize the Runge-Kutta integration. Three of the functions, U, V, and P, diverge at $r = 0$; thus, the starting solutions for U, V, and P are necessarily set to zero to ensure

regularity at Earth's center (e.g., Crossley, 1975; Wu & Peltier, 1982). The remaining three linearly independent solutions at Earth's center may be computed by a power series expansion near the geocenter (Crossley, 1975; Smylie, 2013). Following the development of Crossley (1975) and Smylie (2013), the power series expansion of the y variables takes the form:

$$y_i(r) = r^{\alpha} \sum_{\nu=0}^{\infty} A_{i,\nu}\, r^{\nu}, \qquad i = 1, 2, \ldots, 6, \tag{4.91}$$

where α and ν are integers and the coefficients $A_{i,\nu}$ are to be determined. The variable α must be non-negative and the coefficients $A_{i,\nu} = 0$ for $\nu < 0$. The derivate of Eq. 4.91 is given by (Crossley, 1975):

$$\frac{dy_i(r)}{dr} = r^{\alpha-1} \sum_{\nu=0}^{\infty} (\alpha + \nu)\, A_{i,\nu}\, r^{\nu}. \tag{4.92}$$

Additionally, gravity can be expanded as:

$$g_0(r) = \gamma r, \tag{4.93}$$

where terms beyond first-order have been dropped since the expansion will be implemented close to the geocenter, and

$$\gamma = \frac{4}{3}\pi G \rho_0. \tag{4.94}$$

Within an arbitrarily small radius, such as $r = 1$ km, the density and elastic moduli are assumed to be constant and equivalent to their values at the geocenter.

Eqs. 4.91, 4.92, and 4.93 are inserted back into the system of equations (Eq. 4.79). Matching powers of the radius are equated to obtain a set of characteristic, or *indicial*, equations. Eigenvalues of the characteristic equations yield the acceptable values for variable α, and the corresponding eigenvectors may then be used to compute the values of the coefficients $A_{i,\nu}$ in terms of three free constants: $A_{1,1}$, $A_{6,1}$, and $A_{4,0}$ (Smylie, 2013). Choice of the free constants is arbitrary, since multiplying each of the y variables in a fundamental-solution set by the same constant factor does not affect the result; only ratios between the y variables are important. A convenient option is to set each of the three constants equal to one.

To facilitate numerical integration, I transform the variables (e.g., Smylie, 2013; Crossley, 1975):

$$\begin{aligned} z_1(r) &= \frac{y_1(r)}{r^{\alpha+1}} \\ z_2(r) &= \frac{y_2(r)}{r^{\alpha}} \\ z_3(r) &= \frac{y_3(r)}{r^{\alpha+1}} \\ z_4(r) &= \frac{y_4(r)}{r^{\alpha}} \\ z_5(r) &= \frac{y_5(r)}{r^{\alpha+2}} \\ z_6(r) &= \frac{y_6(r)}{r^{\alpha+1}}, \end{aligned} \tag{4.95}$$

where $\alpha = n - 2$ for the starting solutions associated with the free constants $A_{1,1}$ and $A_{6,1}$ and $\alpha = n$ for the starting solution associated with the free constant $A_{4,0}$.

Following Smylie (2013), the first starting solution, associated with free constant $A_{1,1}$, is given by:

$$\begin{aligned} z_1(r) &= A_{1,1} + A_{1,3}r^2 + A_{1,5}r^4 + \cdots \\ z_2(r) &= 2(n-1)\mu A_{1,1} + A_{2,2}r^2 + A_{2,4}r^4 + \cdots \\ z_3(r) &= \frac{1}{n}A_{1,1} + A_{3,3}r^2 + A_{3,5}r^4 + \cdots \\ z_4(r) &= 2\mu\frac{n-1}{n}A_{1,1} + A_{4,2}r^2 + A_{4,4}r^2 + \cdots \\ z_5(r) &= \frac{4\pi G\rho_0}{n}A_{1,1} + A_{5,4}r^2 + A_{5,6}r^4 + \cdots \\ z_6(r) &= A_{6,3}r^2 + A_{6,5}r^4 + \cdots, \end{aligned} \tag{4.96}$$

where the value of $A_{1,1}$ is arbitrary. The r^2 coefficients are given by:

$$\begin{aligned} A_{1,3} &= \frac{-\rho_0 n}{p_1(n)}[(3-n)\gamma + \omega^2]A_{1,1} \\ A_{2,2} &= \frac{-\rho_0\, q_1(n)}{p_1(n)}[(3-n)\gamma + \omega^2]A_{1,1} \\ A_{3,3} &= \frac{\rho_0}{p_1(n)}[(3-n)\gamma + \omega^2]A_{1,1} \\ A_{4,2} &= 0 \end{aligned}$$

$$
\begin{aligned}
A_{5,4} &= \frac{4\pi G\rho_0}{2(2n+3)}[(n+3)A_{1,3} - k^2 A_{3,3}] \\
A_{6,3} &= (n+2)A_{5,4} - 4\pi G\rho_0 A_{1,3}, \qquad (4.97)
\end{aligned}
$$

where

$$
\begin{aligned}
p_1(n) &= 2n[n(n+2)\lambda + (n(n+2)-1)\mu] \qquad (4.98) \\
q_1(n) &= [n(n+1) + n(n+3)]\lambda + 2n(n+1)\mu. \qquad (4.99)
\end{aligned}
$$

The r^4 coefficients are obtained from:

$$
\begin{bmatrix}
0 \\
\rho_0[-(4\gamma+\omega^2)A_{1,3} + (k^2\gamma)A_{3,3} - A_{6,3}] \\
0 \\
\rho_0[\gamma A_{1,3} - \omega^2 A_{3,3} - A_{5,4}] \\
0 \\
0
\end{bmatrix} =
$$

$$
\begin{bmatrix}
2\lambda\xi + n + 3 & -\xi & -k^2\lambda\xi & 0 & 0 & 0 \\
-2\delta & 4\mu\xi + n + 2 & k^2\delta & -k^2 & 0 & 0 \\
1 & 0 & n+2 & -\frac{1}{\mu} & 0 & 0 \\
\delta & \lambda\xi & -\epsilon & n+5 & 0 & 0 \\
-3\gamma & 0 & 0 & 0 & n+4 & -1 \\
0 & 0 & 3\gamma k^2 & 0 & -k^2 & n+5
\end{bmatrix}
\begin{bmatrix}
A_{1,5} \\ A_{2,4} \\ A_{3,5} \\ A_{4,4} \\ A_{5,6} \\ A_{6,5}
\end{bmatrix}, \qquad (4.100)
$$

where parameters are defined as in Eqs. 4.81–4.84 and 4.94.

The second starting solution, associated with free constant $A_{6,1}$, is given by:

$$
\begin{aligned}
z_1(r) &= -n\frac{\rho_0}{p_1(n)}A_{6,1}r^2 + A_{1,5}r^4 + \cdots \\
z_2(r) &= -\frac{q_1(n)}{p_1(n)}\rho_0 A_{6,1}r^2 + A_{2,4}r^4 + \cdots
\end{aligned}
$$

$$
\begin{aligned}
z_3(r) &= \frac{\rho_0}{p_1(n)} A_{6,1} r^2 + A_{3,5} r^4 + \cdots \\
z_4(r) &= A_{4,4} r^4 + \cdots \\
z_5(r) &= \frac{1}{n} A_{6,1} + A_{5,4} r^2 + A_{5,6} r^4 + \cdots \\
z_6(r) &= A_{6,1} + A_{6,3} r^2 + A_{6,5} r^4 + \cdots ,
\end{aligned} \tag{4.101}
$$

where the value of $A_{6,1}$ is arbitrary. The r^2 coefficients are:

$$
\begin{aligned}
A_{1,3} &= -n \frac{\rho_0}{p_1(n)} A_{6,1} \\
A_{2,2} &= -q_1(n) \frac{\rho_0}{p_1(n)} A_{6,1} \\
A_{3,3} &= \frac{\rho_0}{p_1(n)} A_{6,1} \\
A_{4,2} &= 0 \\
A_{5,4} &= \frac{4\pi G \rho_0}{2(2n+3)} [(n+3) A_{1,3} - k^2 A_{3,3}] \\
A_{6,3} &= (n+2) A_{5,4} - 4\pi G \rho_0 A_{1,3},
\end{aligned} \tag{4.102}
$$

where $p_1(n)$ and $q_1(n)$ are given by Eqs. 4.98 and 4.99, respectively. The r^4 coefficients are obtained from Eq. 4.100.

The third starting solution, associated with free constant $A_{4,0}$, is given by:

$$
\begin{aligned}
z_1(r) &= \left(\frac{1}{\mu} - n \frac{p_2(n)}{p_1(n)} \right) A_{4,0} + A_{1,3} r^2 + A_{1,5} r^4 + \cdots \\
z_2(r) &= \left(q_2(n) - q_1(n) \frac{p_2(n)}{p_1(n)} \right) A_{4,0} + A_{2,2} r^2 + A_{2,4} r^4 + \cdots \\
z_3(r) &= \frac{p_2(n)}{p_1(n)} A_{4,0} + A_{3,3} r^2 + A_{3,5} r^4 + \cdots \\
z_4(r) &= A_{4,0} + A_{4,2} r^2 + A_{4,4} r^4 + \cdots \\
z_5(r) &= A_{5,2} + A_{5,4} r^2 + A_{5,6} r^4 + \cdots \\
z_6(r) &= A_{6,1} + A_{6,3} r^2 + A_{6,5} r^4 + \cdots ,
\end{aligned} \tag{4.103}
$$

where the value of $A_{4,0}$ is arbitrary. The r^0 coefficients are given by:

$$
A_{1,1} = \left(\frac{1}{\mu} - n \frac{p_2(n)}{p_1(n)} \right) A_{4,0}
$$

$$
\begin{aligned}
A_{2,0} &= \left(q_2(n) - q_1(n)\frac{p_2(n)}{p_1(n)}\right) A_{4,0} \\
A_{3,1} &= \frac{p_2(n)}{p_1(n)} A_{4,0} \\
A_{4,0} &= A_{4,0} \\
A_{5,2} &= \frac{4\pi G\rho_0}{2(2n+3)}[(n+3)A_{1,1} - k^2 A_{3,1}] \\
A_{6,1} &= (n+2)A_{5,2} - 4\pi G\rho_0 A_{1,1}, \qquad (4.104)
\end{aligned}
$$

where

$$
p_2(n) = n(n+5) + \frac{\lambda\, n\,(n+3)}{\mu} \qquad (4.105)
$$

$$
q_2(n) = 2(n+1) + \frac{\lambda\,(n+3)}{\mu}. \qquad (4.106)
$$

The r^2 coefficients are obtained from:

$$
\begin{bmatrix}
0 \\
\rho_0[-(4\gamma+\omega^2)A_{1,1} + (k^2\gamma)A_{3,1} - A_{6,1}] \\
0 \\
\rho_0[\gamma A_{1,1} - \omega^2 A_{3,1} - A_{5,2}] \\
0 \\
0
\end{bmatrix} =
$$

$$
\begin{bmatrix}
2\lambda\xi + n + 3 & -\xi & -k^2\lambda\xi & 0 & 0 & 0 \\
-2\delta & 4\mu\xi + n + 2 & k^2\delta & -k^2 & 0 & 0 \\
1 & 0 & n+2 & -\frac{1}{\mu} & 0 & 0 \\
\delta & \lambda\xi & -\epsilon & n+5 & 0 & 0 \\
-3\gamma & 0 & 0 & 0 & n+4 & -1 \\
0 & 0 & 3\gamma k^2 & 0 & -k^2 & n+5
\end{bmatrix}
\begin{bmatrix}
A_{1,3} \\ A_{2,2} \\ A_{3,3} \\ A_{4,2} \\ A_{5,4} \\ A_{6,3}
\end{bmatrix}. \qquad (4.107)
$$

The r^4 coefficients are obtained from:

$$\begin{bmatrix} 0 \\ \rho_0[-(4\gamma+\omega^2)A_{1,3}+(k^2\gamma)A_{3,3}-A_{6,3}] \\ 0 \\ \rho_0[\gamma A_{1,3}-\omega^2 A_{3,3}-A_{5,4}] \\ 0 \\ 0 \end{bmatrix} =$$

$$\begin{bmatrix} 2\lambda\xi+n+5 & -\xi & -k^2\lambda\xi & 0 & 0 & 0 \\ -2\delta & 4\mu\xi+n+4 & k^2\delta & -k^2 & 0 & 0 \\ 1 & 0 & n+4 & -\frac{1}{\mu} & 0 & 0 \\ \delta & \lambda\xi & -\epsilon & n+7 & 0 & 0 \\ -3\gamma & 0 & 0 & 0 & n+6 & -1 \\ 0 & 0 & 3\gamma k^2 & 0 & -k^2 & n+7 \end{bmatrix} \begin{bmatrix} A_{1,5} \\ A_{2,4} \\ A_{3,5} \\ A_{4,4} \\ A_{5,6} \\ A_{6,5} \end{bmatrix}, \quad (4.108)$$

which differs from the 6×6 matrix in Eq. 4.100 by the addition of $2\overline{\overline{I}}$, where $\overline{\overline{I}}$ is the identity matrix.

Modifications must be made for the special cases of $n = 1$ and $n = 0$ (Smylie, 2013). For $n = 0$, only one starting solution is regular at the geocenter.

4.2.9 Starting Solutions: Homogeneous Sphere

An alternative approach to the power series expansions is to compute the analytical solution for a homogeneous sphere (e.g., Farrell, 1972a; Takeuchi & Saito, 1972; Lambeck, 1988; Dahlen & Tromp, 1998). Takeuchi & Saito (1972) provide a very complete description of the homogeneous sphere solutions, albeit with a focus on frequencies in the free-oscillation band for application to normal-mode seismology. Here, I review the analytical solutions of the equations of motion for a homogeneous sphere.

Two of the independent solutions (note the $\mp$ in the equation for b^2 below) for spherical

harmonic degree, n, and forcing frequency, ω, are given by (e.g., Takeuchi & Saito, 1972):

$$\begin{aligned}
y_1 &= -\frac{r^{n+1}}{2n+3}\left[\frac{1}{2}nh\psi_n(x) + f\phi_{n+1}(x)\right] \\
y_2 &= -(\lambda+2\mu)r^n f\phi_n(x) + \frac{\mu r^n}{2n+3}[-n(n+1)h\psi_n(x) + 2(2f+k^2)\phi_{n+1}(x)] \\
y_3 &= -\frac{r^{n+1}}{2n+3}\left[\frac{1}{2}h\psi_n(x) - \phi_{n+1}(x)\right] \\
y_4 &= \mu r^n\left[\phi_n(x) - \frac{1}{2n+3}[(n-1)h\psi_n(x) + 2(f+1)\phi_{n+1}(x)]\right] \\
y_5 &= r^{n+2}\left[\frac{V_P^2 f - (n+1)V_S^2}{r^2} - \frac{3\gamma f}{2(2n+3)}\psi_n(x)\right] \\
y_6 &= \frac{1}{r}\left[(2n+1)y_5 + \frac{3n\gamma h r^{n+2}}{2(2n+3)}\psi_n(x)\right], \qquad (4.109)
\end{aligned}$$

where V_P is the compressional wave velocity, V_S is the shear wave velocity, r is the radius, λ and μ are Lamé parameters, and

$$\begin{aligned}
\gamma &= \frac{4}{3}\pi\rho G \\
x &= b\,r \\
b^2 &= \frac{1}{2}\left[\frac{\omega^2+4\gamma}{V_P^2} + \frac{\omega^2}{V_S^2} \mp \left(\left(\frac{\omega^2}{V_S^2} - \frac{\omega^2+4\gamma}{V_P^2}\right)^2 + \frac{4k^2\gamma^2}{V_P^2 V_S^2}\right)^{\frac{1}{2}}\right] \\
f &= \frac{V_S^2}{\gamma}\left(b^2 - \frac{\omega^2}{V_S^2}\right) \\
h &= f - (n+1). \qquad (4.110)
\end{aligned}$$

Furthermore,

$$\begin{aligned}
\phi_n(x) &= \frac{(2n+1)!!}{x^n} j_n(x) \\
&= 1 - \frac{x^2}{2(2n+3)} + \frac{x^4}{2^2(2n+3)(2n+5)2} - \ldots \qquad (4.111) \\
\psi_n(x) &= \frac{2(2n+3)}{x^2}[1 - \phi_n(x)] \\
&= 1 - \frac{x^2}{2(2n+5)2} + \frac{x^4}{2^2(2n+5)(2n+7)3} - \ldots \qquad (4.112)
\end{aligned}$$

where $j_n(x)$ represents the spherical Bessel function of the first kind (e.g., Abramowitz & Stegun, 1964; Takeuchi & Saito, 1972). Since the Bessel functions tend toward zero at high

n, I approximate them using the power-series expansions given by Eqs. 4.111 and 4.112, carried out to several terms.

The third independent solution is given by (e.g., Takeuchi & Saito, 1972):

$$\begin{aligned} y_1 &= nr^{n-1} \\ y_2 &= 2\mu n(n-1)r^{n-2} \\ y_3 &= r^{n-1} \\ y_4 &= 2\mu(n-1)r^{n-2} \\ y_5 &= (n\gamma - \omega^2)r^n \\ y_6 &= \frac{1}{r}(2n+1)y_5(r) - 3n\gamma r^{n-1}. \end{aligned} \tag{4.113}$$

4.2.10 Starting Solutions: Approximation

Since the initial starting values for y_2, y_4, and y_6 are of order n larger than the starting values for y_1, y_3, and y_5, it is possible to approximate the starting solutions as vectors of ones and zeros. In other words, the first independent solution would be $[0\ \ 1\ \ 0\ \ 0\ \ 0\ \ 0]$, the second independent solution would be $[0\ \ 0\ \ 0\ \ 1\ \ 0\ \ 0]$, and the third independent solution would be $[0\ \ 0\ \ 0\ \ 0\ \ 0\ \ 1]$. These starting solutions are clearly much simpler than those derived from the homogeneous sphere or power series expansion. Furthermore, they are also more stable, since they are fully linearly independent. However, caution must be exercised when substituting these vectors for the initial conditions since they represent a relatively crude approximation for the actual starting solutions and are most suitable only at large n.

4.2.11 Runge-Kutta Integration

For $n \leq 15$, I integrate from Earth's center through the cores, mantle, and crust to the surface. In the inner core, I compute starting solutions using power series expansions of the governing equations of motion (Smylie, 2013) with transformed z variables (Sec. 4.2.8). Boundary conditions are applied at all solid-solid and solid-fluid interfaces, as well as at the surface. For $n > 15$, and for reasons of numerical stability, I begin the integration within the

mantle from a starting radius specified by the r for which $\left(\frac{r}{a}\right)^n$ exceeds a sufficiently small threshold, such as 10^{-4}. The starting solutions within the mantle are computed analytically using a homogeneous sphere formulation (Sec. 4.2.9).

From the starting solutions y_i (or z_i within the inner core) at initial radius r_i, the solutions y_{i+1} at the new radius $r_i + h$ are given by:

$$y_{i+1} = y_i + \frac{h}{6}(k_1 + 2k_2 + 2k_3 + k_4), \tag{4.114}$$

where h is a suitably small step in radius,

$$k_1 = A(r_i)\ y(r_i) \tag{4.115}$$

$$k_2 = A\left(r_i + \frac{h}{2}\right)\ \left[y(r_i) + \frac{k_1}{2}\right] \tag{4.116}$$

$$k_3 = A\left(r_i + \frac{h}{2}\right)\ \left[y(r_i) + \frac{k_2}{2}\right] \tag{4.117}$$

$$k_4 = A(r_i + h)\ [y(r_i) + k_3], \tag{4.118}$$

and A is given by Eq. 4.80. The fourth-order Runge-Kutta formulation in Eq. 4.114 is derived from a Taylor series expansion of $\dot{y}$. The system of equations, $\dot{y}$, may be computed at each radial step using the propagator matrix technique (i.e., $\dot{y} = A\ y$, as in Eqs. 4.115–4.118) (Gilbert & Backus, 1966).

As an alternative to the finite difference method for solving the system of differential equations, fully numerical methods, such as spectral element techniques, may also be employed (e.g., Guo et al., 2004; Ito & Simons, 2011).

4.2.12 Fluid Layers

In fluid regions, the shear modulus vanishes ($\mu = 0$). Hence $y_4 = 0$, $y_2 = \lambda X$, and $\dot{y}_3$ is undefined (Alterman et al., 1959). Therefore, the system of equations for spheroidal

deformation reduces to (e.g., Smylie, 2013):

$$\begin{bmatrix} \frac{dy_1}{dr} \\ \frac{dy_2}{dr} \\ 0 \\ \frac{dy_5}{dr} \\ \frac{dy_6}{dr} \end{bmatrix} = \begin{bmatrix} -\frac{2}{r} & \frac{1}{\lambda} & \frac{k^2}{r} & 0 & 0 \\ \left(-\omega^2\rho_0 - \frac{4g_0\rho_0}{r}\right) & 0 & \frac{k^2 g_0\rho_0}{r} & 0 & -\rho_0 \\ \frac{g_0\rho_0}{r} & -\frac{1}{r} & -\omega^2\rho_0 & -\frac{\rho_0}{r} & 0 \\ 4\pi G\rho_0 & 0 & 0 & 0 & 1 \\ 0 & 0 & -4\pi G\rho_0\frac{k^2}{r} & \frac{k^2}{r^2} & -\frac{2}{r} \end{bmatrix} \begin{bmatrix} y_1 \\ y_2 \\ y_3 \\ y_5 \\ y_6 \end{bmatrix}.$$

The third equation in the system can be solved for y_3 as follows (Alterman et al., 1959):

$$\begin{aligned} 0 &= \frac{\rho_0 g_0}{r} y_1 - \frac{1}{r} y_2 - \omega^2\rho_0 y_3 - \frac{\rho_0}{r} y_5 \\ \omega^2\rho_0 y_3 &= \frac{\rho_0 g_0}{r} y_1 - \frac{1}{r} y_2 - \frac{\rho_0}{r} y_5 \\ y_3 &= \frac{1}{\omega^2\rho_0}\left(\frac{\rho_0 g_0}{r} y_1 - \frac{1}{r} y_2 - \frac{\rho_0}{r} y_5\right) \\ y_3 &= \frac{1}{\omega^2 r}\left(g_0 y_1 - \frac{1}{\rho_0} y_2 - y_5\right). \end{aligned} \tag{4.119}$$

Since y_3 is now written in terms of y_1, y_2, and y_5, it may be substituted back into the matrix system, which then reduces to:

$$\begin{bmatrix} \frac{dy_1}{dr} \\ \frac{dy_2}{dr} \\ \frac{dy_5}{dr} \\ \frac{dy_6}{dr} \end{bmatrix} = \begin{bmatrix} -\frac{2}{r} + \frac{k^2}{r} y_3^1 & \frac{1}{\lambda} + \frac{k^2}{r} y_3^2 & \frac{k^2}{r} y_3^5 & 0 \\ \left(-\omega^2\rho_0 - \frac{4g_0\rho_0}{r} + \frac{k^2 g_0\rho_0}{r} y_3^1\right) & \frac{k^2 g_0\rho_0}{r} y_3^2 & \frac{k^2 g_0\rho_0}{r} y_3^5 & -\rho_0 \\ 4\pi G\rho_0 & 0 & 0 & 1 \\ -4\pi G\rho_0\frac{k^2}{r} y_3^1 & -4\pi G\rho_0\frac{k^2}{r} y_3^2 & \left(\frac{k^2}{r^2} - 4\pi G\rho_0\frac{k^2}{r} y_3^5\right) & -\frac{2}{r} \end{bmatrix} \begin{bmatrix} y_1 \\ y_2 \\ y_5 \\ y_6 \end{bmatrix},$$

where

$$\begin{aligned} y_3^1 &= \frac{g_0}{\omega^2 r} \\ y_3^2 &= -\frac{1}{\rho_0\omega^2 r} \\ y_3^5 &= -\frac{1}{\omega^2 r}. \end{aligned} \tag{4.120}$$

4.2.13 Boundary Conditions at Solid-Fluid Interfaces

All independent variables $y_1, y_2, \ldots y_6$ are continuous at solid-solid internal boundaries (e.g., Alterman et al., 1959; Takeuchi & Saito, 1972; Guo et al., 2004). At solid-fluid boundaries, however, the shear stress vanishes; thus, all y variables are continuous with the exception of y_3, which is undefined across the interface. The system of six first-order ODEs within the solid layer reduces to a system of four first-order ODEs within the fluid layer. Thus, whereas three independent solutions are required for solid layers, only two independent solutions are required for fluid layers.

Following the method of Takeuchi & Saito (1972), I form a linear combination of the three independent solutions on the solid side of a solid-fluid interface:

$$y_i = Q_1^s\, y_{i1}^s + Q_2^s\, y_{i2}^s + Q_3^s\, y_{i3}^s, \tag{4.121}$$

where $i = 1, 2, \ldots, 6$ and Q_1^s, Q_2^s, and Q_3^s are constants of integration for each of the three solutions. Similarly, on the fluid side of the interface, the linear combination of the two independent solution sets for the fluid layer is:

$$y_i = Q_1^f\, y_{i1}^f + Q_2^f\, y_{i2}^f, \tag{4.122}$$

where $i = 1, 2, 5, 6$. Since $y_4 = 0$ at the solid-fluid boundary, one of the integration constants in Eq. 4.121 may be determined directly:

$$Q_3^s = -\frac{y_{41}^s}{y_{43}^s}\, Q_1^s - \frac{y_{42}^s}{y_{43}^s}\, Q_2^s. \tag{4.123}$$

Now, combining Eqs. 4.121 and 4.122, and inserting the expression for Q_3^s, yields:

$$\begin{aligned} Q_1^f\, y_{i1}^f + Q_2^f\, y_{i2}^f &= Q_1^s\, y_{i1}^s + Q_2^s\, y_{i2}^s + \left(-\frac{y_{41}^s}{y_{43}^s}\, Q_1^s - \frac{y_{42}^s}{y_{43}^s}\, Q_2^s \right) y_{i3}^s \\ &= Q_1^s \left(y_{i1}^s - \frac{y_{41}^s}{y_{43}^s} y_{i3}^s \right) + Q_2^s \left(y_{i2}^s - \frac{y_{42}^s}{y_{43}^s} y_{i3}^s \right). \end{aligned} \tag{4.124}$$

At this point, the two sets of solutions may again be equated independently. Furthermore,

$Q_1^s = Q_1^f$ and $Q_2^s = Q_2^f$ at the interface (Takeuchi & Saito, 1972). Thus, the mapping of solutions across a solid-fluid boundary becomes:

$$y_{i1}^f = y_{i1}^s - \frac{y_{41}^s}{y_{43}^s}\, y_{i3}^s \tag{4.125}$$

$$y_{i2}^f = y_{i2}^s - \frac{y_{42}^s}{y_{43}^s}\, y_{i3}^s, \tag{4.126}$$

for $i = 1, 2, 5, 6$.

For a fluid-solid interface, two independent sets of solutions from the fluid layer transition into three sets of solutions for propagation through the solid layer. On the solid side of the interface (e.g., Takeuchi & Saito, 1972),

$$\begin{aligned}
y_{j1}^s &= y_{j1}^f \\
y_{j2}^s &= y_{j2}^f \\
y_{31}^s &= y_{41}^s = y_{32}^s = y_{42}^s = 0 \\
y_{33}^s &= 1 \\
y_{i3}^s &= 0 \\
Q_1^f &= Q_1^s \\
Q_2^f &= Q_2^s,
\end{aligned} \tag{4.127}$$

where $j = 1, 2, 5, 6$ and $i = 1, 2, 4, 5, 6$.

4.2.14 Surface Boundary Conditions

The surface boundary conditions differ depending on the type of response being investigated, such as Earth's free oscillations, Earth's response to an external gravitational potential, or Earth's response to surface mass loading. For free oscillations of the Earth, the absence of an applied load requires that the radial and tangential stresses vanish at the surface (e.g., Alterman et al., 1959; Wiggins, 1968; Takeuchi & Saito, 1972). Thus, $y_2 = y_4 = 0$.

Additionally, the total gravitational potential and gradients of the potential must remain continuous everywhere. Therefore, the continuity of y_5 and

$$y_6 = \dot{y}_5 - 4\pi G\rho_0 y_1 \tag{4.128}$$

must be ensured at all internal boundaries as well as at the surface (Takeuchi & Saito, 1972). In the absence of an external gravitational potential, ψ_E, as in the case of Earth's free oscillations, Poisson's equation reduces to Laplace's equation:

$$\nabla^2 \psi_E = 0. \tag{4.129}$$

Outside of the Earth, the solution to Laplace's equation, based on the definition for the potential in Eq. 4.66, is given by:

$$\psi_E = C \left(\frac{a}{r}\right)^{(n+1)} P_n(\cos\theta)\, e^{i\omega t}, \tag{4.130}$$

where C is a constant (e.g., Longman, 1962; Takeuchi & Saito, 1972; Melchior, 1983). Since the potential must remain continuous across the free surface, $C = y_5(a)$. To ensure continuity of the derivative of the potential, y_6 must also be continuous. Hence,

$$\dot{\psi}_1 - 4\pi G\rho_0 u = \dot{\psi}_E, \tag{4.131}$$

where

$$\begin{aligned} \dot{\psi}_E = \frac{d\psi_E}{dr} &= -\frac{n+1}{r}\left(\frac{a}{r}\right)^{(n+1)} y_5(r) P_n(\cos\theta)\, e^{i\omega t} \\ &\Rightarrow -\frac{n+1}{a}\, y_5(a) P_n(\cos\theta)\, e^{i\omega t} \\ &= -\frac{n+1}{a}\, \psi_E, \end{aligned} \tag{4.132}$$

and I have substituted $r = a$ for the condition at the surface. Therefore,

$$\dot{y}_5 - 4\pi G\rho_0 y_1 = -\frac{n+1}{r} y_5, \tag{4.133}$$

and at the surface,

$$\dot{y}_5 - 4\pi G\rho_0 y_1 + \frac{n+1}{a}y_5 = y_6 + \frac{n+1}{a}y_5 = 0. \tag{4.134}$$

An alternative definition for y_6 in Eq. 4.78 is therefore

$$y_6 = \dot{y}_5 - 4\pi G\rho_0 y_1 + \frac{n+1}{r}y_5, \tag{4.135}$$

which simplifies the surface boundary condition to $y_6 = 0$ (e.g., Takeuchi & Saito, 1972; Na & Moon, 2010). With internal consistency, however, the end result remains the same.

Now suppose that a mass, m, outside Earth sets up an external gravitational potential. The external gravitational potential, ψ_E, must now be added to the perturbed field, ψ_1, in the equations of motion (e.g., Farrell, 1972a). Since mass m exists entirely outside Earth, however, the external potential field satisfies Laplace's equation everywhere inside the Earth and thus is only implicit in the equations of motion. The surface boundary conditions, however, contain ψ_E explicitly. At the surface, both ψ_1 and ψ_E must be continuous. Furthermore, $\dot{\psi}_1 - 4\pi G\rho_0 u$ must be continuous, as stated previously, and additionally $\dot{\psi}_E + 4\pi G\gamma$ must also be continuous, where γ represents a unit of external mass distributed uniformly over a disk of radius α (e.g., Longman, 1962; Farrell, 1972a). Following the method of Longman (1962), γ is expanded as a harmonic Legendre series of the form:

$$\gamma = \sum_{n=0}^{\infty} K_n P_n(\cos\theta)\, e^{i\omega t}. \tag{4.136}$$

The coefficients K_n are then given by (e.g., Longman, 1962; Farrell, 1972a; Lanzano, 1982):

$$\begin{aligned} K_0 &= \frac{1}{4\pi a^2} \\ K_n &= \frac{P_{n-1}(\cos\alpha) - P_{n+1}(\cos\alpha)}{4\pi a^2(1-\cos\alpha)}, \qquad n > 0 \end{aligned} \tag{4.137}$$

where a is Earth's radius. In the limit $\alpha \to 0$,

$$K_n = \frac{2n+1}{4\pi a^2} \ . \tag{4.138}$$

From a Legendre recursion relation,

$$P_{n-1}(x) - P_{n+1}(x) = \frac{2n+1}{n(n+1)}(1-x^2)P_n'(x) \ ; \tag{4.139}$$

therefore (Farrell, 1972a),

$$K_n = \frac{2n+1}{4\pi a^2}\left[-\frac{(1+\cos\alpha)}{n(n+1)\sin\alpha}\frac{\partial P_n(\cos\alpha)}{\partial\alpha}\right] \ . \tag{4.140}$$

The quantity in brackets is known as the **disk factor** and represents a mass distribution of finite size. The quantity in front of the bracketed terms represents the Legendre expansion of the delta function in spherical coordinates (e.g., Farrell, 1972a; Sun & Okubo, 1993).

Equating the two continuous functions that represent gradients of the perturbed internal and applied external gravitational potential fields at Earth's surface yields (e.g., Longman, 1962; Farrell, 1972a):

$$\dot{\psi}_1 - 4\pi G\rho_0 u = \dot{\psi}_E + 4\pi G K_n P_n(\cos\theta), \tag{4.141}$$

where ψ_1 and u are given by Eq. 4.66. Moreover, at the surface,

$$\psi_1 = \psi_E \tag{4.142}$$

and

$$\dot{\psi}_E = -\frac{n+1}{a}\,\psi_E \tag{4.143}$$

as shown previously in Eq. 4.132. The boundary condition is thus:

$$\dot{\psi}_1 + \frac{n+1}{a}\,\psi_1 = 4\pi G\rho_0 u + 4\pi G K_n P_n(\cos\theta) \tag{4.144}$$

or, in terms of the y-variables:

$$y_6 + \frac{n+1}{a}\, y_5 = 4\pi G K_n \; . \tag{4.145}$$

Now, instead of a unit mass external to Earth, consider m equal to the mass of Earth, m_E (e.g., Longman, 1962). Thus,

$$m = m_E = \frac{a^2 g_S}{G}, \tag{4.146}$$

where g_S is the acceleration due to gravity at Earth's surface. Setting $m = m_E$ requires final solutions to be multiplied by $\frac{m'}{m_E}$, where m' is the actual external mass, but also simplifies the boundary condition (Longman, 1962). The coefficients of the external mass distribution become:

$$K_n = m_E \, \frac{2n+1}{4\pi a^2} \; , \tag{4.147}$$

which leads to the surface boundary condition (e.g., Farrell, 1972a; Lanzano, 1982; Guo et al., 2004):

$$\begin{aligned} y_6 + \frac{n+1}{a}\, y_5 &= 4\pi G K_n \\ &= 4\pi G \, m_E \frac{2n+1}{4\pi a^2} \\ &= 4\pi G \, \frac{2n+1}{4\pi} \frac{g_S}{G} \\ &= (2n+1)\, g_S \, . \end{aligned} \tag{4.148}$$

The surface boundary condition for the potential, given by Eq. 4.148, applies to masses that are either loading the surface or completely external to Earth. For Earth's response to a gravitational potential field generated by an external mass not loading Earth, the radial and tangential tractions vanish at the free surface (e.g., Melchior, 1983). Thus, $y_2 = y_4 = 0$, as for the free oscillations (e.g., Alterman et al., 1959; Takeuchi & Saito, 1972). For the case of surface mass loading, however, the radial traction will be non-zero (e.g., Longman, 1962; Farrell, 1972a; Lanzano, 1982; Guo et al., 2004). The radial traction is given by the acceleration of gravity multiplied by the surface mass distribution (e.g., Lanzano, 1982,

Surface Boundary Conditions					
	Free Oscillations	External Potential	Surface Mass Loading	Surface Shear Forcing	Surface Stress (n=1)
y_2	0	0	$-g_S^2 \frac{2n+1}{4\pi G}$	0	$-\frac{3\,g_S^2}{4\pi G}$
y_4	0	0	0	$\frac{(2n+1)\,g_S^2}{4\pi G\,n\,(n+1)}$	$\frac{3\,g_S^2}{8\pi G}$
$y_6 + \frac{n+1}{a}\,y_5$	0	$(2n+1)\,g_S$	$(2n+1)\,g_S$	0	0

Table 4.1: Summary of surface boundary conditions for the cases of (a) free oscillations, (b) the presence of an external potential, (c) surface mass loading, (d) surface shear forcing, and (e) surface stress (e.g., Alterman et al., 1959; Longman, 1963; Wiggins, 1968; Lanzano, 1982; Melchior, 1983; Okubo & Saito, 1983; Okubo & Endo, 1986; Guo et al., 2004). The surface stress solution satisfies the consistency relation and provides a linearly independent secondary solution for static degree-1 modes (Okubo & Endo, 1986). Note that the boundary conditions stated in Longman (1963) are presented in terms of normalized y-variables, whereas here I state the boundary conditions directly in terms of the y-variables. Also note that the Love number definitions of Okubo & Saito (1983) differ from the definitions stated here by a factor of $(a\,g_S)$, where a is Earth's radius and g_S is the acceleration due to gravity. Different scalings for the Love numbers must be reflected in the boundary conditions.

Sec. 3.06). Thus,

$$\begin{aligned} y_2 &= -g_S\,K_n \\ &= -g_S\,m_E\frac{2n+1}{4\pi a^2} \\ &= -g_S\,\frac{2n+1}{4\pi}\frac{g_S}{G} \\ &= -g_S^2\,\frac{2n+1}{4\pi G}. \end{aligned} \tag{4.149}$$

The surface boundary conditions for free oscillations, external potential fields, and surface mass loading (SML) are summarized in Table 4.1. Solving the spheroidal-deformation equations using external-potential boundary conditions yields potential Love numbers. Solving the equations using SML boundary conditions yields load Love numbers. Another set of boundary conditions may be developed to represent surface shear forcing (also listed in Table 4.1). Solutions generated from applying shear-forcing boundary conditions to the equations of motion yield shear Love numbers. Only six of the nine Love numbers (potential, load, and shear) are independent and expressions exist to relate them (e.g., Molodenskiy, 1977; Saito, 1978).

For the special case of $n = 0$, the equations for y_3 and y_4 (the tangential components) are undefined and the system reduces to four equations (Eq. 4.85) (e.g., Longman, 1963; Smylie, 2013). Furthermore, only two solutions and two boundary conditions exist for $n = 0$. The boundary conditions are identical to those listed in Table 4.1, with the exception that the conditions for y_4 must be excluded.

For the special case of $n = 1$, the gravitational potential load Love number, k_n, must be zero in a reference frame centered at the center of mass of the solid Earth, CE (Blewitt, 2003, Sec. 4.1). Thus, the boundary conditions are modified accordingly to force $k_1 = 0$ (e.g., Guo et al., 2004; Wang et al., 2012). Namely, the third surface boundary condition, for the cases of the external potential and surface mass loading, becomes:

$$y_5 = a\, g_S. \tag{4.150}$$

Sec. 4.3.5 provides a description of reference frames applicable to the loading problem.

4.2.15 Load Love Numbers

Load Love numbers are computed by equating linear combinations of the three independent solutions with boundary conditions at the surface. In matrix form,

$$\begin{bmatrix} -g_S^2\,\frac{2n+1}{4\pi G} \\ 0 \\ (2n+1)\,g_S \end{bmatrix} = \begin{bmatrix} y_2^{\mathrm{I}} & y_2^{\mathrm{II}} & y_2^{\mathrm{III}} \\ y_4^{\mathrm{I}} & y_4^{\mathrm{II}} & y_4^{\mathrm{III}} \\ (y_6^{\mathrm{I}} + \frac{n+1}{a} y_5^{\mathrm{I}}) & (y_6^{\mathrm{II}} + \frac{n+1}{a} y_5^{\mathrm{II}}) & (y_6^{\mathrm{III}} + \frac{n+1}{a} y_5^{\mathrm{III}}) \end{bmatrix} \begin{bmatrix} m_1 \\ m_2 \\ m_3 \end{bmatrix}, \tag{4.151}$$

where the superscript Roman numerals represent each of the three independent solutions that were propagated to the surface. Note that if the y-variables are non-dimensional, then the other variables must be scaled appropriately (Sec. 4.2.7). The system of equations may now be solved for the model parameters m_1, m_2, and m_3. When the system is solved using a direct matrix inversion or the normal equations, large instabilities in the Love numbers can arise, particularly at high spherical harmonic degrees (see Sec. 4.2.19). Therefore, to promote stability, I solve the system using the Moore-Penrose pseudoinverse, also known

as the generalized inverse, which is evaluated using singular value decomposition (e.g., Aki & Richards, 1980).

With the model parameters in hand, Y_1, Y_3, and Y_5 at the surface may now be derived:

$$Y_1(a) = m_1\, y_1^{\mathrm{I}} + m_2\, y_1^{\mathrm{II}} + m_3\, y_1^{\mathrm{III}} \tag{4.152}$$

$$Y_3(a) = m_1\, y_3^{\mathrm{I}} + m_2\, y_3^{\mathrm{II}} + m_3\, y_3^{\mathrm{III}} \tag{4.153}$$

$$Y_5(a) = m_1\, y_5^{\mathrm{I}} + m_2\, y_5^{\mathrm{II}} + m_3\, y_5^{\mathrm{III}}\,. \tag{4.154}$$

The load Love numbers are given by (e.g., Longman, 1962; Farrell, 1972a; Guo et al., 2004):

$$h'_n = \frac{Y_1(a)}{a} \tag{4.155}$$

$$l'_n = \frac{Y_3(a)}{a} \tag{4.156}$$

$$k'_n = \frac{Y_5(a)}{a\, g_S} - 1. \tag{4.157}$$

Here, I have considered a spherically symmetric, non-rotating, elastic and isotropic (SNREI) Earth; thus, the load Love numbers are real-valued and latitude independent. Rotation and ellipticity introduce a latitudinal dependency (e.g., Lambeck, 1988) and anelastic effects produce complex-valued load Love numbers (e.g., Pagiatakis, 1990).

4.2.16 Potential Love Numbers

The potential, or "tidal" (e.g., Saito, 1978), Love numbers are computed analogously to the load Love numbers, with the exception of different boundary conditions. For potential Love numbers, boundary conditions for an external gravitational potential are applied to the momentum-equation solutions at the surface (e.g., Farrell, 1972a; Melchior, 1983):

$$\begin{bmatrix} 0 \\ 0 \\ (2n+1)\, g_S \end{bmatrix} = \begin{bmatrix} y_2^{\mathrm{I}} & y_2^{\mathrm{II}} & y_2^{\mathrm{III}} \\ y_4^{\mathrm{I}} & y_4^{\mathrm{II}} & y_4^{\mathrm{III}} \\ (y_6^{\mathrm{I}} + \frac{n+1}{a} y_5^{\mathrm{I}}) & (y_6^{\mathrm{II}} + \frac{n+1}{a} y_5^{\mathrm{II}}) & (y_6^{\mathrm{III}} + \frac{n+1}{a} y_5^{\mathrm{III}}) \end{bmatrix} \begin{bmatrix} m_1 \\ m_2 \\ m_3 \end{bmatrix}. \tag{4.158}$$

The potential Love numbers are derived from

$$Y_1(a) = m_1\, y_1^{\mathrm{I}} + m_2\, y_1^{\mathrm{II}} + m_3\, y_1^{\mathrm{III}} \tag{4.159}$$

$$Y_3(a) = m_1\, y_3^{\mathrm{I}} + m_2\, y_3^{\mathrm{II}} + m_3\, y_3^{\mathrm{III}} \tag{4.160}$$

$$Y_5(a) = m_1\, y_5^{\mathrm{I}} + m_2\, y_5^{\mathrm{II}} + m_3\, y_5^{\mathrm{III}} \tag{4.161}$$

using the following formulae:

$$h_n = \frac{Y_1(a)}{a} \tag{4.162}$$

$$l_n = \frac{Y_3(a)}{a} \tag{4.163}$$

$$k_n = \frac{Y_5(a)}{a\, g_S} - 1. \tag{4.164}$$

4.2.17 Shear Love Numbers

The shear Love numbers are computed analogously to the load and potential Love numbers, except for different boundary conditions. Shear-traction boundary conditions are applied to derive the shear Love numbers (Table 4.1). Furthermore,

$$k_n = \frac{Y_5(a)}{a\, g_S}, \tag{4.165}$$

since the external force is free of a gravitational potential (e.g., Saito, 1978; Okubo & Saito, 1983).

4.2.18 Stress Love Numbers and Degree-1 Modes

Since potential and shear Love numbers are undefined for the degree-1 static case, stress Love numbers may be introduced to satisfy the consistency relation (e.g., Farrell, 1972a; Okubo & Endo, 1986). The consistency relation, given by

$$y_2(r) + 2\, y_4(r) + \frac{g(r)}{4\pi G}\, y_6(r) = 0, \tag{4.166}$$

ensures that, in the static case for $n = 1$, the solid Earth experiences no net force (e.g., Saito, 1974; Okubo & Endo, 1986). As with the shear Love numbers, the stress Love numbers characterize Earth's response to potential-free external forcing (Table 4.1).

One additional special consideration must be made for the degree-1 mode: accounting for a rigid-body translation (e.g., Merriam, 1985; Okubo & Endo, 1986; Okubo, 1993; Blewitt, 2003). For a reference frame centered at the center of mass of the solid Earth (CE), the degree-1 potential field must vanish outside the Earth. To satisfy the restriction, a rigid-body translation may be added to the solution vector derived from the equations of motion for spheroidal deformation (e.g., Merriam, 1985; Okubo & Endo, 1986):

$$\begin{aligned} y_1(r) &= \alpha \\ y_2(r) &= 0 \\ y_3(r) &= \alpha \\ y_4(r) &= 0 \\ y_5(r) &= g(r)\,\alpha \\ y_6(r) &= \frac{-2\,g(r)}{r}\,\alpha, \end{aligned} \tag{4.167}$$

where

$$y_5(a)^{Load} = 1 \tag{4.168}$$

$$y_5(a)^{Stress} = 0 \tag{4.169}$$

and a corresponds to an evaluation at Earth's surface. Thus,

$$\alpha^{Load} = -\frac{y_5(a)}{g(a)} \tag{4.170}$$

$$\alpha^{Stress} = -\frac{y_5(a)}{g(a)} + \frac{1}{g(a)}. \tag{4.171}$$

A careful reader might recognize that the set of equations 4.167 correspond precisely to equations 4.113 for the case of $n = 1$, $\omega = 0$, and $y_5(a)$ = 1 for the load solution or $y_5(a)$ =

0 for the stress solution (Takeuchi & Saito, 1972). Note that definitions of the "y" equations (Eqs. 4.79) may differ in the literature. For example, to convert between the convention used here (Table 4.1) (e.g., Alterman et al., 1959) and the convention of Okubo & Saito (1983) and Okubo & Endo (1986), one must divide the y-variables by a factor $[a\, g(a)]$. Furthermore, y_6 is also defined differently; thus, the convention adopted here requires an extra factor of $[\frac{-(n+1)}{r}\, g(r)\, \alpha = \frac{-2\, g(r)}{r}\, \alpha]$ for the rigid-body translation.

4.2.19 Numerical Considerations

Numerical instabilities can easily arise in load Love number computations up to spherical harmonic degree $n = 10000$ or greater, particularly since the three linearly independent starting solutions become less linearly independent with integration to the surface. In addition to non-dimensionalization, I found it important to compute the surface model parameters (Eq. 4.158) using a generalized inverse (e.g., Moore-Penrose pseudoinverse), rather than by direct inversion. Furthermore, the integration solver can also influence stability. I have elected to use a Runge-Kutta scheme with adaptive step-sizing within `python`. In particular, I find good stability with the `scipy` differential-equation solvers *dopri5* and *dopri853*, which perform explicit fourth- and eighth-order Runge-Kutta integration, respectively. Reducing the absolute and relative tolerance values for the integration can improve precision, ableit at the expense of computation time (e.g., Press et al., 2007). Another method for improving stability involves variable transformations (e.g., Wang et al., 2012; Smylie, 2013). Also, although I have not found it necessary here, the matrix minor method of Woodhouse (1988) might further improve stability. Finally, the starting solutions and choice of starting radius also have significant effects on precision and stability, as discussed in the following section.

4.2.20 Starting Radius within the Mantle

Vertical and horizontal displacements induced by either an external gravitational potential or by surface mass loading at spherical harmonic degree, n, are proportional to the external potential field, which is proportional to $\left(\frac{r}{a}\right)^n$ (e.g., Farrell, 1972a; Baker, 1984; Jentzsch,

1997). Therefore, since the influence of the potential drops off rapidly inside Earth with increasing n, integration through the inner and outer cores becomes less important (and may generate instabilities in the solution vectors) for spherical harmonic degrees higher than about $n = 15$ (e.g., Na & Baek, 2011). In practice, I have found that commencing the integrations from a radius at which $\left(\frac{r}{a}\right)^n$ just exceeds a tolerance level of 10^{-4} works well for spherical harmonic degrees beyond $n = 15$. For spherical harmonic degrees lower than $n = 15$, I commence integration from Earth's center.

4.2.21 Asymptotic Solutions

As a function of spherical harmonic degree, the load Love numbers approach asymptotic values after about $n = 1000$ (e.g., Farrell, 1972a; Guo et al., 2004). The asymptotic expressions may be obtained by solving the flat-Earth Boussinesq problem (e.g., Farrell, 1972a) or by deriving asymptotic solutions to the system of governing ordinary differential equations (e.g., Guo et al., 2004). Using the latter method, the asymptotic expressions are given by:

$$\begin{aligned} h'_n &= h^*_\infty + \frac{1}{n}\, h^{**}_\infty \\ n l'_n &= l^*_\infty + \frac{1}{n}\, l^{**}_\infty \\ n k'_n &= k^*_\infty + \frac{1}{n}\, k^{**}_\infty, \end{aligned} \tag{4.172}$$

where

$$\begin{aligned} h^*_\infty &= -\frac{g_S^2\, \sigma_S}{4\pi\, G\, \mu_S\, \eta_S} \\ l^*_\infty &= \frac{g_S^2}{4\pi\, G\, \eta_S} \\ k^*_\infty &= -\frac{a\, \rho_S\, g_S}{2\, \mu_S} \\ h^{**}_\infty &= \frac{g_S^2}{4\pi\, G\, \eta_S} \left[-\frac{\mu_S}{\eta_S} + \frac{a\, \rho_S\, g_S\, (\lambda_S^2 + \lambda_S\, \mu_S - \mu_S^2)}{2\, \mu_S^2\, \eta_S} + \frac{2\pi\, G\, a\, \rho_S\, \eta_S}{g_S\, \mu_S} \right] \\ l^{**}_\infty &= \frac{g_S^2}{4\pi\, G\, \eta_S} \left[-\frac{3\lambda_S^2 + 8\lambda_S\, \mu_S + 3\mu_S^2}{2\mu_S\, \eta_S} + \frac{a\, \rho_S\, g_S\, \sigma_S}{2\mu_S\, \eta_S} \right] \\ k^{**}_\infty &= \frac{a\, g_S\, \rho_S}{\mu_S} \left[\frac{\lambda_S}{4\eta_S} + \frac{a\, \rho_S\, g_S\, (2\lambda_S + \mu_S)}{8\mu_S\, \eta_S} + \frac{\pi\, G\, a\, \rho_S}{g_S} \right] \end{aligned} \tag{4.173}$$

and

$$\begin{aligned} \sigma_S &= \lambda_S + 2\,\mu_S \\ \eta_S &= \lambda_S + \mu_S\,. \end{aligned} \tag{4.174}$$

A subscript S refers to the value of the parameter at Earth's surface.

4.3 Displacement Load Green's Functions

4.3.1 Introduction

Infinite sums of Love numbers may be formed to determine the impulse-response function, or **Green's Function**, of a body to a certain stimulus. Here, I focus on surface mass loading boundary conditions, though a similar procedure may be applied to other types of boundary conditions, such as an external gravitational potential. The variables Y_1, Y_3, and Y_5 obtained in Sec. 4.2.15 represent the radial coefficients of the spherical harmonic expansions (Eqs. 4.66). Namely, for mass loading at Earth's surface,

$$\begin{aligned} U_n(r) &= Y_1 = a\,h'_n \\ V_n(r) &= Y_3 = a\,l'_n \\ P_n(r) &= Y_5 = a\,g\,(k'_n + 1), \end{aligned} \tag{4.175}$$

where a is Earth's radius. Referring back to Eqs. 4.66, the radial displacement for spherical harmonic degree n is given by:

$$\begin{aligned} u_n &= U_n(r)\,P_n(\cos\theta)\,e^{i\omega t} \\ &= a\,h'_n\,P_n(\cos\theta)\,e^{i\omega t}, \end{aligned} \tag{4.176}$$

where $e^{i\omega t}$ represents the temporal evolution of the applied load, such as a periodic ocean tide.

Since the boundary conditions in Sec. 4.2.14 were formulated based on the mass of the

Earth, Eq. 4.176 may be rewritten to represent an arbitrary mass load m' (e.g., Longman, 1963):

$$\begin{aligned} u_n &= a\,\frac{m'}{m_E}\,h'_n\,P_n(\cos\theta)\,e^{i\omega t} \\ &= \frac{a}{m_E}\,h'_n\,P_n(\cos\theta)\,e^{i\omega t}, \end{aligned} \tag{4.177}$$

where, in the second line, I have taken m' to be a load of unit mass.

The vertical-displacement load Green's function (LGF) for a 1-kg load applied at Earth's surface is given by a summation of Eq. 4.177 over all n:

$$u = \frac{a}{m_E}\sum_{n=0}^{\infty} h'_n\,P_n(\cos\theta)\,e^{i\omega t}. \tag{4.178}$$

Similarly, the horizontal-displacement LGF for a 1-kg load at Earth's surface is given by:

$$v = \frac{a}{m_E}\sum_{n=1}^{\infty} l'_n\,\frac{\partial P_n(\cos\theta)}{\partial\theta}\,e^{i\omega t}. \tag{4.179}$$

Note that the sum for v begins at $n = 1$, since horizontal displacements do not apply to the degree-0 mode.

The radial coefficients of the spherical harmonic expansions may also be expressed in terms of the transformed surface potential for a point load of unit mass, $\Phi_{2,n}$ (e.g., Munk & MacDonald, 1960; Farrell, 1972a; Melchior, 1983; Jentzsch, 1997):

$$\begin{aligned} U_n(r) &= h'_n(r)\,\frac{\Phi_{2,n}}{g} \\ V_n(r) &= l'_n(r)\,\frac{\Phi_{2,n}}{g}\,, \end{aligned} \tag{4.180}$$

where

$$\begin{aligned} \Phi_{2,n} &= \frac{4\pi G a}{2n+1}\,K_n \\ &= \frac{4\pi G a}{2n+1}\,\frac{2n+1}{4\pi a^2} \\ &= \frac{G m_E}{a^2}\,\frac{a}{m_E} \end{aligned}$$

$$= \frac{a\,g}{m_E}. \tag{4.181}$$

The displacement LGFs in Eqs. 4.178 and 4.179 may also be derived from Eqs. 4.180 and 4.181. In other words, the load Love numbers scale the equipotential height, $\frac{\Phi_{2,n}}{g}$, to the true displacements expected for Earth's material structure. To derive the predicted SML-induced displacements within Earth's interior, an extra factor of $\left(\frac{r}{a}\right)^n$ must be included in Eq. 4.181 (e.g., Munk & MacDonald, 1960; Melchior, 1983).

In summary, the amplitudes of the displacement LGFs (i.e., written without the dynamic component of the forcing term) are:

$$u = \frac{a}{m_E} \sum_{n=0}^{\infty} h'_n \, P_n(\cos\theta) \tag{4.182}$$

and

$$v = \frac{a}{m_E} \sum_{n=1}^{\infty} l'_n \, \frac{\partial P_n(\cos\theta)}{\partial\theta}. \tag{4.183}$$

For surface displacements induced by an external gravitational potential, the potential Love numbers scale the equipotential height generated by the external gravitational potential, V_n (Eq. 4.2). For a mass a distance R away from Earth's center, the gravitational potential at Earth's surface, a, is given by (Eq. 1.12):

$$V_n^{\text{potential}} = \frac{GM}{R} \left(\frac{a}{R}\right)^n P_n(\cos\theta) e^{i\omega t}, \tag{4.184}$$

where the time-dependent harmonic term ($e^{i\omega t}$) has been included to account for periodic dynamic forcing. Hence, the vertical and horizontal displacements due to an external gravitational potential may be derived by inserting the expression for V_n (Eq. 4.184) into Eqs. 4.2 and 4.6, respectively, and summing over all n.

Since GNSS receivers infer ground displacements, I have only reviewed the development of displacement LGFs here. Developemnts for additional types of Green's functions, such as gravity, tilt, and strain, may be found in the literature (e.g., Farrell, 1972a; Francis & Dehant, 1987; Jentzsch, 1997; Guo et al., 2004; Na & Baek, 2011).

4.3.2 Kummer's Transformation

The series in Eqs. 4.182 and 4.183 can be slow to converge. Kummer's series transformation may be implemented to speed convergence (e.g., Farrell, 1972a; Francis & Dehant, 1987; Guo et al., 2004; Na & Baek, 2011). The general form of Kummer's transformation is given by (e.g., Abramowitz & Stegun, 1964; Na & Baek, 2011):

$$\sum_n f(n)Q_n = f_\infty \sum_n Q_n + \sum_n (f(n) - f_\infty)\, Q_n, \tag{4.185}$$

where $f_\infty = \lim_{n\to\infty} f(n)$.

Thus, Eqs. 4.182 and 4.183 may be expressed in terms of the asymptotic expressions of the load Love numbers as:

$$u = \frac{a}{m_E}\, h^*_\infty \sum_{n=0}^{\infty} P_n(\cos\theta) + \frac{a}{m_E} \sum_{n=0}^{\infty} (h'_n - h^*_\infty)\, P_n(\cos\theta) \tag{4.186}$$

and

$$v = \frac{a}{m_E}\, l^*_\infty \sum_{n=1}^{\infty} \frac{1}{n} \frac{\partial P_n(\cos\theta)}{\partial\theta} + \frac{a}{m_E} \sum_{n=1}^{\infty} (nl'_n - l^*_\infty)\, \frac{1}{n} \frac{\partial P_n(\cos\theta)}{\partial\theta}. \tag{4.187}$$

The factor $\frac{1}{n}$ in Eq. 4.187 enters because l^*_∞ represents the asymptotic value of nl'_n (Eq. 4.172) (cf., Farrell, 1972a).

Eqs. 4.186 and 4.187 include only the first term in the asymptotic expressions of the load Love numbers (Eq. 4.172). Guo et al. (2004) introduced an additional term to the asymptotic expressions, improving accuracy by a factor $\frac{1}{n}$. With the extra term included, Eqs. 4.182 and 4.183 become:

$$\begin{aligned} u \;=\; & \frac{a}{m_E}\, h^*_\infty \sum_{n=1}^{\infty} P_n(\cos\theta) + \frac{a}{m_E}\, h^{**}_\infty \sum_{n=1}^{\infty} \frac{1}{n}\, P_n(\cos\theta) + \\ & \frac{a}{m_E}\, h'_0 + \frac{a}{m_E} \sum_{n=1}^{\infty} (h'_n - (h^*_\infty + \frac{1}{n}\, h^{**}_\infty))\, P_n(\cos\theta) \end{aligned} \tag{4.188}$$

and

$$v = \frac{a}{m_E} l^*_\infty \sum_{n=1}^{\infty} \frac{1}{n} \frac{\partial P_n(\cos\theta)}{\partial\theta} + \frac{a}{m_E} l^{**}_\infty \sum_{n=1}^{\infty} \frac{1}{n^2} \frac{\partial P_n(\cos\theta)}{\partial\theta} + \frac{a}{m_E} \sum_{n=1}^{\infty} (n l'_n - (l^*_\infty + \frac{1}{n} l^{**}_\infty)) \frac{1}{n} \frac{\partial P_n(\cos\theta)}{\partial\theta}. \quad (4.189)$$

Note that the second-order terms for the asymptotes are undefined for $n = 0$. Some of the Legendre sums in Eqs. 4.188 and 4.189 are known analytically (e.g., Farrell, 1972a; Guo et al., 2004):

$$\sum_{n=0}^{\infty} P_n(\cos\theta) = \frac{1}{x} \quad (4.190)$$

$$\sum_{n=1}^{\infty} \frac{1}{n} P_n(\cos\theta) = \ln \frac{2}{x + 1 - \cos\theta} \quad (4.191)$$

$$\sum_{n=1}^{\infty} \frac{1}{n} \frac{\partial P_n(\cos\theta)}{\partial\theta} = -\frac{\sin\theta(\frac{1}{x} + 1)}{x + 1 - \cos\theta} \quad (4.192)$$

$$\sum_{n=1}^{\infty} \frac{1}{n^2} \frac{\partial P_n(\cos\theta)}{\partial\theta} = \frac{1}{\sin\theta} \ln \frac{(2-x)^2(1-\cos\theta)}{2(x-1+\cos\theta)(1+\cos\theta)} - \frac{\cos\theta}{\sin\theta} \ln \frac{\sin^2\theta}{2(x-1+\cos\theta)}, \quad (4.193)$$

where $x = \sqrt{2 - 2\cos\theta}$.

In practice, the load Love number computations are often carried out to spherical harmonic degree $n = 10000$, beyond which the load Love numbers are assumed to be equivalent to the asymptotic values (Eq. 4.172) (e.g., Farrell, 1972a; Guo et al., 2004). Thus, the arguments in Eqs. 4.188 and 4.189 that contain load Love numbers become zero beyond spherical harmonic degree, N. Furthermore, the Legendre polynomials and their derivatives may be computed recursively using the so-called *recursion relations*, which will be discussed in Sec. 4.3.3.

In summary, the displacement load Green's functions are computed using the formulae:

$$u(\theta) = \frac{a}{m_E} h^*_\infty \sum_{n=1}^{\infty} P_n(\cos\theta) + \frac{a}{m_E} h^{**}_\infty \sum_{n=1}^{\infty} \frac{1}{n} P_n(\cos\theta) +$$

$$\frac{a}{m_E}\,h'_0 + \frac{a}{m_E}\sum_{n=1}^{N=10000}\left(h'_n - \left(h^*_\infty + \frac{1}{n}\,h^{**}_\infty\right)\right)P_n(\cos\theta) \qquad (4.194)$$

for the vertical-displacement response, and

$$\begin{aligned} v(\theta) &= \frac{a}{m_E}\,l^*_\infty\sum_{n=1}^{\infty}\frac{1}{n}\,\frac{\partial P_n(\cos\theta)}{\partial\theta} + \frac{a}{m_E}\,l^{**}_\infty\sum_{n=1}^{\infty}\frac{1}{n^2}\,\frac{\partial P_n(\cos\theta)}{\partial\theta} + \\ &\quad \frac{a}{m_E}\sum_{n=1}^{N=10000}\left(nl'_n - \left(l^*_\infty + \frac{1}{n}\,l^{**}_\infty\right)\right)\frac{1}{n}\,\frac{\partial P_n(\cos\theta)}{\partial\theta} \end{aligned} \qquad (4.195)$$

for the horizontal-displacement response. The Legendre sums without Love-number coefficients may be determined analytically (Eqs. 4.190–4.193). The Legendre contributions to the final terms in Eqs. 4.194 and 4.195 are computed recursively (Sec. 4.3.3). Since Eq. 4.193 is undefined for $\theta = 180°$, I compute the LGFs at that angular distance by linear interpolation of the values for $\theta = 179.998°$ and $\theta = 179.999°$ and subsequent extrapolation to $\theta = 180°$ (Guo et al., 2004).

4.3.3 Legendre Polynomial Recursion Relations

To evaluate the final terms in Eqs. 4.194 and 4.195, the Legendre functions and their derivatives must be determined for every n. Recursion relations, derived from the Legendre generating function, are commonly used (e.g., Farrell, 1972a; Guo et al., 2004; Na & Baek, 2011).

Two useful recursion, or recurrence, relations are (e.g., Boas, 1983):

$$nP_n(x) = (2n-1)xP_{n-1}(x) - (n-1)P_{n-2}(x) \qquad (4.196)$$

$$(1-x^2)\frac{\partial P_n(x)}{\partial x} = nP_{n-1}(x) - nxP_n(x). \qquad (4.197)$$

For $x = \cos\theta$, the recursion relations become:

$$\begin{aligned} nP_n(\cos\theta) &= (2n-1)\cos\theta P_{n-1}(\cos\theta) - \\ &\quad (n-1)P_{n-2}(\cos\theta) \end{aligned} \qquad (4.198)$$

$$(1-\cos^2\theta)\frac{\partial P_n(\cos\theta)}{\partial\cos\theta} = nP_{n-1}(\cos\theta) - n\cos\theta P_n(\cos\theta). \quad (4.199)$$

Since Eq. 4.195 requires the derivative of the Legendre function with respect to θ (as opposed to $\cos\theta$), each side of Eq. 4.199 can be multiplied by $\frac{\partial\cos\theta}{\partial\theta}$, leading to:

$$\begin{aligned}(1-\cos^2\theta)\frac{\partial P_n(\cos\theta)}{\partial\cos\theta}\frac{\partial\cos\theta}{\partial\theta} &= [nP_{n-1}(\cos\theta) - n\cos\theta P_n(\cos\theta)]\frac{\partial\cos\theta}{\partial\theta} \\ (\sin^2\theta)\frac{\partial P_n(\cos\theta)}{\partial\theta} &= [nP_{n-1}(\cos\theta) - n\cos\theta P_n(\cos\theta)](-\sin\theta) \\ \frac{\partial P_n(\cos\theta)}{\partial\theta} &= -\frac{n}{\sin\theta}[P_{n-1}(\cos\theta) - \cos\theta P_n(\cos\theta)]. \quad (4.200)\end{aligned}$$

4.3.4 Disk Factor

To speed the convergence of the series in Eqs. 4.194 and 4.195, distant loads (e.g., several tens of degrees away from the observer) may be approximated by finite circular caps rather than delta functions (e.g., Farrell, 1972a). In practice, the disk factor from Eq. 4.140 may be inserted back into Eqs. 4.194 and 4.195. For displacement LGFs, which converge relatively rapidly, disk factors are generally not necessary; however, disk factors can be very useful for other types of LGFs, such as tilt and strain (e.g., Na & Baek, 2011).

The disk factor,

$$\left[-\frac{(1+\cos\alpha)}{n(n+1)\sin\alpha}\frac{\partial P_n(\cos\alpha)}{\partial\alpha}\right], \quad (4.201)$$

is only valid in the limit $\alpha \to 0$, where α specifies the finiteness of the circular cap (e.g., Farrell, 1972a); thus, the disk factor should only be invoked with small α (e.g., $\sim 0.004^\circ$).

4.3.5 Reference Frames

The vector displacement field generated by surface mass loading depends both on the physical characteristics of the deformation as well as the chosen reference frame (e.g., Blewitt, 2003; Petit & Luzum, 2010). The load Love numbers and corresponding load Green's functions described thus far have been computed in a reference frame fixed to the center of mass of the solid Earth, abbreviated CE. The CE reference frame is convenient for computing Love numbers and Green's functions, but not directly observable in practice

(e.g., Farrell, 1972a; Blewitt, 2003; Agnew, 2012). A more appropriate reference frame for GNSS-inferred surface displacements is one fixed to the center of mass of the entire Earth system, abbreviated CM, which includes the solid Earth as well as its fluid exterior (e.g., oceans and atmosphere) (e.g., Blewitt, 2003; Fu et al., 2012).

Blewitt (2003) demonstrated that conversions between the various reference frames involve only simple transformations of the degree-one load Love numbers. The conversions for CE to CM, for example, are given by:

$$\begin{aligned} [h'_1]_{CM} &= [h'_1]_{CE} - 1 \\ [l'_1]_{CM} &= [l'_1]_{CE} - 1 \\ [1 + k'_1]_{CM} &= [1 + k'_1]_{CE} - 1. \end{aligned} \tag{4.202}$$

Similarly, the conversions for CE to CF (center of figure) are given by:

$$\begin{aligned} [h'_1]_{CF} &= \frac{2}{3}\,[h'_1 - l'_1]_{CE} \\ [l'_1]_{CF} &= -\frac{1}{3}\,[h'_1 - l'_1]_{CE} \\ [1 + k'_1]_{CF} &= \left[1 - \frac{1}{3}h'_1 - \frac{2}{3}l'_1\right]_{CE}. \end{aligned} \tag{4.203}$$

From the equations for the displacement LGFs (Eqs. 4.182 and 4.183), the degree-1 components are:

$$u_1 = \frac{a}{m_E}\, h'_1\, \cos\theta \tag{4.204}$$

and

$$v_1 = \frac{a}{m_E}\, l'_1\, \frac{\partial}{\partial\theta} \cos\theta = -\frac{a}{m_E}\, l'_1\, \sin\theta \tag{4.205}$$

for the vertical- and horizontal-displacement components, respectively.

The difference between LGFs computed in the CM and CE frames involves only a degree-one transformation. Thus, (e.g., Agnew, 2012):

$$u^{\mathrm{CM}} - u^{\mathrm{CE}} = u_1^{\mathrm{CM}} - u_1^{\mathrm{CE}} = \frac{a}{m_E}\, \cos\theta\, ([h'_1]_{\mathrm{CM}} - [h'_1]_{\mathrm{CE}}) = -\frac{a}{m_E}\, \cos\theta \tag{4.206}$$

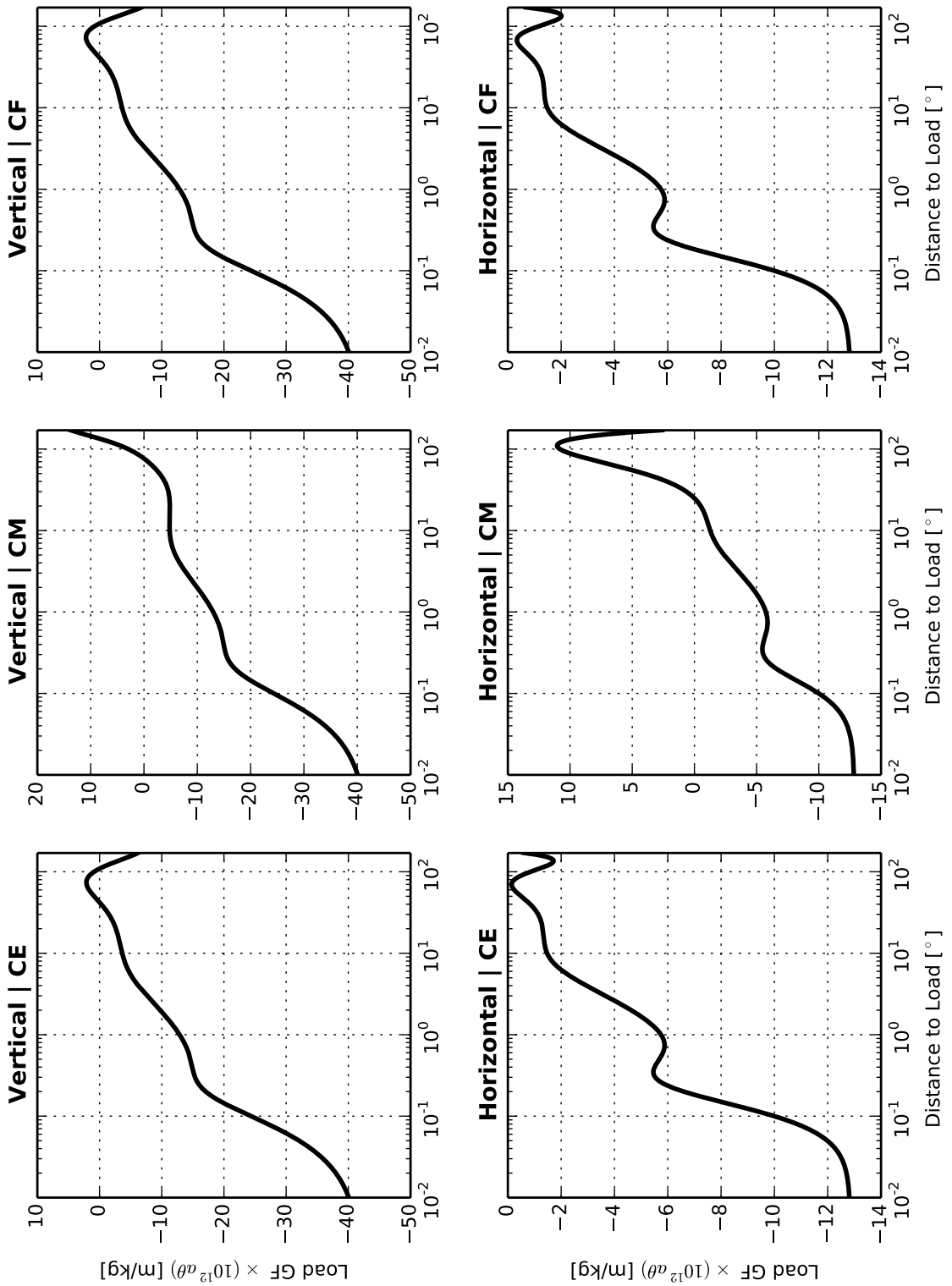

Figure 4.1: Vertical (top) and horizontal (bottom) displacement load Green's functions (LGFs) for a 1 kg surface mass load, computed using an isotropic and oceanless version of PREM. The left panels show the LGFs in the CE reference frame, the central panels show the LGFs in the CM reference frame, and the right panels show the LGFs in the CF reference frame (Blewitt, 2003). The load Green's functions have been normalized according to the Farrell convention (Farrell, 1972a): displacement $\times\, (a\,\theta)\, 10^{12}$, where a is the radius of the Earth in meters and θ is the angular distance from the load in radians.

for the vertical-displacement component, and

$$v^{\mathrm{CM}} - v^{\mathrm{CE}} = v_1^{\mathrm{CM}} - v_1^{\mathrm{CE}} = -\frac{a}{m_E}\sin\theta\left([l_1']_{\mathrm{CM}} - [l_1']_{\mathrm{CE}}\right) = \frac{a}{m_E}\sin\theta \tag{4.207}$$

for the horizontal-displacement component.

The straightforward conversions between the CE and CM LGFs simplify to (Agnew, 2012):

$$u^{\mathrm{CM}} = u^{\mathrm{CE}} - \frac{a}{m_E}\cos\theta \tag{4.208}$$

for the vertical-displacement component, and

$$v^{\mathrm{CM}} = v^{\mathrm{CE}} + \frac{a}{m_E}\sin\theta \tag{4.209}$$

for the horizontal-displacement component.

The vertical- and horizontal-displacement LGFs computed in the CE, CM, and CF reference frames for the Preliminary Reference Earth Model (PREM) (Dziewonski & Anderson, 1981) are shown in Fig. 4.1. The different reference frames clearly have a significant effect on the displacement LGFs (e.g., Farrell, 1972a).

4.3.6 Loading and Gravitational Self-Attraction

The parameters h_n' and l_n' account for the combined effect of pressure due to the loading and attraction of the additional applied mass; thus, loading and gravitational attraction (both *direct* due to the applied external mass and *indirect* due to the redistributed internal mass) are accounted for in the displacement LGFs (e.g., Munk & MacDonald, 1960).

On a perfectly rigid Earth, for example, SML would induce gravity and tilt responses but not displacements, since h_n' and l_n' would be zero (e.g., Farrell, 1972a; Agnew, 2015). The gravity and tilt LGFs may therefore be partitioned into two components: **Newtonian**, resulting from direct attraction of the load, and **elastic**, due to Earth's elastic yielding (e.g., Farrell, 1972a,b, 1973; Agnew, 1997; Bos & Baker, 2005; Agnew, 2012, 2015). The direct attraction component is also referred to as *self* attraction of the load (e.g., Ray, 1998).

Accounting for the effects of loading and self-attraction (LSA) is also essential for the development of accurate ocean tide models (e.g., Hendershott, 1972) and for the analysis of satellite altimetry data (e.g., Ray, 1998).

4.3.7 Mass Conservation

To ensure conservation of mass in ocean tidal loading problems, which can be particularly important for gravity and tilt LGFs (e.g., Melchior, 1983), the total integrated tide height over all the oceans should be zero (e.g., Farrell, 1972b; Agnew, 1983). As an extreme case, I consider a tidal harmonic that has the same phase everywhere in the oceans. In other words, the entire ocean will experience maximum tide at the same time and, half a tidal cycle later, experience minimum tide at the same time. Based on this scenario, a mass imbalance occurs over the course of the tidal cycle: water is "created" during high tide and "destroyed" during low tide, requiring a migration of water across the oceanic boundaries. The ocean-continent boundaries, however, should not permit a significant flux of water across the interface. Moreover, a perfectly modeled ocean tide would satisfy the mass-conservation constraint of the bounded system.

Mass conservation may be approximated by discarding the degree-0 term in the LGFs (e.g., Farrell, 1973; Guo et al., 2004); Agnew (1983) pointed out, however, that removing the degree-0 term is not strictly correct for Newtonian components of LGFs. Furthermore, retaining the degree-0 term in the vertical-displacement LGFs, which allows for Earth compressibility (Hendershott, 1972), remains the prevailing convention (e.g., Farrell, 1972a; Guo et al., 2004). Horizontal displacements do not include a degree-0 term by definition. Another option for enforcing mass conservation is to subtract a mass layer of constant amplitude and phase from the ocean model just prior to convolution with the LGFs (e.g., Farrell, 1972b, 1973; Agnew, 1983; Bos & Baker, 2005).

Alternatively, the ocean model itself can be designed to prevent the flow of water across boundaries (e.g., Farrell, 1973). The advent of satellite altimetry and advancements in data-assimilation and hydrodynamic-modeling methods have dramatically improved the ability to constrain tidal circulation systems and therefore to conserve mass in global ocean tide

models (e.g., Stammer et al., 2014). Older, now-obsolete ocean tide models struggled to conserve mass primarily due to insufficient treatment of bottom friction, coastline morphology, bathymetry, and loading and self-attraction (LSA) effects (e.g., Hendershott, 1972; Schwiderski, 1980); modern ocean models, however, are far more accurate (Ray, 2013; Stammer et al., 2014). The precision of contemporary ocean models renders the mass-imbalance issue of little concern in the modern era (e.g., Bos & Baker, 2005).

4.4 Convolution Methods

SML-induced surface displacements may now be computed for loads of finite size through a convolution of LGFs with a load model. Eqs. 4.182 and 4.183 represent the load-induced displacements per 1-kg load. For an applied load of arbitrary mass, dm, the induced displacements, du and dv, are given by (e.g., Scherneck & Bos, 2002):

$$du = \frac{a}{m_E} \sum_{n=0}^{\infty} h'_n \, P_n(\cos\theta) \; dm = G_u(\theta) \; dm \tag{4.210}$$

and

$$dv = \frac{a}{m_E} \sum_{n=1}^{\infty} l'_n \, \frac{\partial P_n(\cos\theta)}{\partial \theta} \; dm = G_v(\theta) \; dm, \tag{4.211}$$

where $G_u(\theta)$ and $G_v(\theta)$ represent the vertical- and horizontal-displacement LGFs, respectively.

For a spatially variable, non-point-source load, the LGFs are convolved with a load model:

$$\overline{U}_j(r, S, \rho_{sea}, Z_j) = \int_{\Omega} G(|\overline{r} - \overline{r}'|, S) \, \rho_{sea}(r') \, Z_j(r') \, d\Omega. \tag{4.212}$$

In the context of ocean tidal loading (OTL), $\overline{U}_j$ represents the surface displacement at observation point r due to loading by tidal harmonic j, ρ_{sea} is the density of seawater at the load point r', G represents the displacement LGF, and Z_j is the complex-valued tidal height at the load point r' (e.g., Farrell, 1973; Melchior, 1983; Baker, 1984; Harrison, 1985; Francis & Mazzega, 1990; Scherneck, 1991; Agnew, 1997; Jentzsch, 1997; Bos & Baker, 2005; Agnew, 2012; Bos & Scherneck, 2013). The LGF depends on distance to the load as well

as Earth structure, S, which is assumed radially symmetric (e.g., PREM). The mass of the load, dm, at each load point, r', is equivalent to the product of the amplitude, area element for a spherical surface, and density of the load (Eqs. 4.210 and 4.211).

Since OTL is confined to Earth's surface, Eq. 4.212 may be re-expressed as:

$$\overline{U}_j(\Theta, \lambda, \rho_{sea}, Z_j, S) = \int_0^{2\pi} \int_0^{\pi} \rho_{sea}(\Theta', \lambda')\ Z_j(\Theta', \lambda')\ G(\theta, S)\ T(\alpha)\ a^2 \sin\Theta'\ d\Theta' d\lambda', \tag{4.213}$$

where Θ and λ are the co-latitude and longitude of the observation point, respectively; Θ' and λ' are the co-latitude and longitude of the load point; G is the displacement LGF; $T(\alpha)$ is a trigonometric factor that decomposes the horizontal-displacement response into two-component vectors (for the vertical response, $T(\alpha) = 1$); α is the azimuth (measured clockwise from north); Z_j is the complex-valued tide height at the load point; and a is Earth's radius. Note that $a^2 \sin\Theta'\ d\Theta'\ d\lambda'$ represents an area element for a spherical surface.

As an alternative to the spatial-convolution approach, the load model and the predicted response may be developed in the frequency domain in terms of spherical harmonics (e.g., Farrell, 1972a; Agnew, 2015, Sec. 3.06.4.1). The spherical-harmonic approach can be highly efficient, particularly when seeking the deformation response globally (Farrell, 1972a; Agnew, 2015, Sec. 3.06.4.1). The spherical harmonics, however, must be expanded to high degree and order to mitigate the Gibbs phenomenon at coastal boundaries and to characterize fine-scale features of the ocean-tide model. The spatial-convolution method also allows for enhanced accuracy very near to the receiver without requiring a global refinement in the integration mesh (e.g., Farrell, 1972a; Bos & Baker, 2005; Agnew, 2015, Sec. 3.06.4.2). Furthermore, the spatial convolution allows for easy combination of multiple loading models from different grids (e.g., Agnew, 1997, 2015, Sec. 3.06.4.2). I have adopted the spatial-convolution approach in the development presented here; however, with modern computing power and recent advancements in ocean-tide modeling, the spherical-harmonic method might now be a viable (and preferred) option.

4.4.1 Integration Mesh

For practical implementation, the integral in Eq. 4.213 is replaced by a sum over discrete cells. The discrete cells are collectively known as the integration mesh. The integration mesh may be defined in two primary ways (e.g., Hofmann-Wellenhof & Moritz, 2005): templates or gridlines. Templates are formed by subdividing concentric circles about the observation point. Gridlines are formed by subdividing a geographic coordinate system into discrete blocks. Since ocean tide models are commonly distributed in gridline format, and the gridline method is not specific to an observation point, defining the integration mesh in terms of gridlines may seem the natural and obvious choice (e.g., Scherneck, 1991; Scherneck & Bos, 2002; Bos & Baker, 2005; Yeh et al., 2008). Defining the integration mesh in terms of templates, however, has distinct advantages for OTL analysis (e.g., Goad, 1980; Harrison, 1985; Agnew, 1997, 2012). First, since the LGFs depend only on the angular distance between the load and receiver, the station-centric coordinate system requires relatively few LGFs to be computed. Second, the integration mesh does not change with the load model and, thus, easily facilitates the combination of multiple load models, even on irregular grids. Third, the singularity in the LGFs at small θ is easily mitigated through appropriate scaling factors and integration over the area of the cells.

A drawback to the template method is that it requires interpolation of the load model onto the integration mesh and, therefore, does not represent the load model exactly. The ocean model itself, however, is also an approximation of the true load. Moreover, the gridline method also might require some interpolation of the load model (e.g., if a finer integration mesh is adopted near the station). In practice, Bos & Baker (2005) determined through rigorous testing that the choice of template or gridline method had little effect on predicted OTL-induced surface displacements.

As a result of the straightforward implementation and algorithmic flexibility, I have adopted the template method. Since the template grid is centered on the station, Eq. 4.213 becomes

(e.g., Harrison, 1985; Agnew, 1997):

$$\overline{U}_j(\Theta, \lambda, \rho_{sea}, Z_j, S) = \int_0^{2\pi} \int_0^{\pi} \rho_{sea}(\theta, \alpha)\ Z_j(\theta, \alpha)\ G(\theta, S)\ T(\alpha)\ a^2 \sin\theta\ d\theta\ d\alpha, \tag{4.214}$$

where the load model, Z, and load density, ρ_{sea}, have been interpolated onto the integration mesh. Due to the rapid changes in the LGFs as $\theta \to 0$, the integration mesh should be refined near the station and neighboring coastlines in order to obtain accurate response predictions (e.g., Scherneck & Bos, 2002; Bos & Baker, 2005; Penna et al., 2008; Agnew, 2012).

4.4.2 Interpolation and Integration of Load Green's Function

One method to alleviate the singularity in the displacement LGFs at $\theta = 0$ is to scale the LGFs by a factor proportional to θ. Following (Agnew, 2012),

$$G'(\theta) = a^2\ G(\theta)\ 2\ \sin(\theta/2), \tag{4.215}$$

where $G'(\theta)$ is the normalized LGF, $G(\theta)$ is the original LGF, and a is Earth's radius. With the singularity reduced, the normalized LGFs are easily interpolated to intermediary values of θ using, e.g., cubic-spline interpolation. Since tabulated LGFs necessarily contain a greater number of entries at small θ, where the LGFs vary rapidly, interpolation on $\log\theta$ provides a more even spacing (e.g., Bos & Baker, 2005). When working with a template grid, another option is to integrate the LGFs directly at the LLN-summation stage (e.g., Goad, 1980), which has the added benefit of improving the convergence of the series.

Using the normalized LGFs, Eq. 6.9 becomes:

$$\overline{U}_j(\Theta, \lambda, \rho_{sea}, Z_j, S) = \int_0^{2\pi} \int_0^{\pi} \rho_{sea}\ Z(\theta, \alpha)\ G'(\theta)\ T(\alpha)\ \frac{\sin\theta}{2\ \sin(\theta/2)}\ d\theta\ d\alpha. \tag{4.216}$$

The tide height, seawater density, and normalized LGFs are given by the value at the mid-

point of each cell. Thus, I rewrite Eq. 4.216 as:

$$\overline{U}_j(\Theta, \lambda, \rho_{sea}, Z_j, S) = \rho_{sea}\ Z(\theta, \alpha)\ G'(\theta) \int_0^{\pi} \frac{\sin\theta}{2\ \sin(\theta/2)}\ d\theta \int_0^{2\pi} T(\alpha)\ d\alpha. \quad (4.217)$$

In this form, the integration may be performed over individual cells and then summed together (Agnew, 2012):

$$\overline{U}_j(\Theta, \lambda, \rho_{sea}, Z_j, S) = \sum_{i=1}^{N} \rho_i\ Z_i\ G'(\theta_i) \int_{\theta_i - \frac{\delta}{2}}^{\theta_i + \frac{\delta}{2}} \frac{\sin\theta}{2\ \sin(\theta/2)}\ d\theta \int_{\alpha_i - \frac{\beta}{2}}^{\alpha_i + \frac{\beta}{2}} T(\alpha)\ d\alpha, \quad (4.218)$$

where N is the total number of cells in the integration mesh, Z_i is the tide height at the center of cell i, ρ_i is the seawater density at the center of cell i, $G'(\theta_i)$ is the normalized LGF computed for the center of cell i, θ_i is the angular separation between the station and the center of the load patch, δ_i is the inclination width of the load patch, α_i is the azimuth between the station and center of the load patch (as measured at the station in degrees clockwise from north), and β_i is the azimuthal width of the load patch.

For vertical-displacement response, $T(\alpha) = 1$. For the north component of the horizontal response, $T(\alpha) = -\cos(\alpha)$. For the east component of the horizontal response, $T(\alpha) = -\sin(\alpha)$. The minus signs are required because the horizontal response is directed radially outwards from the load point; thus, the azimuth of the response at the receiver is $\alpha + 180°$, where α is the vector geodesic pointing from the receiver to the load point (e.g., Scherneck, 1991).

The integral over θ reduces to (Agnew, 2012):

$$\int_{\theta_i - \frac{\delta_i}{2}}^{\theta_i + \frac{\delta_i}{2}} \frac{\sin\theta}{2\ \sin(\theta/2)}\ d\theta = 4\ \cos\left(\frac{\theta_i}{2}\right)\ \sin\left(\frac{\delta_i}{4}\right). \quad (4.219)$$

Since θ_i and δ_i are determined solely from the integration mesh, the integrated LGFs may be computed and stored prior to convolution with a load model. The integral over α for the

vertical-displacement response reduces to:

$$\int_{\alpha_i-\frac{\beta_i}{2}}^{\alpha_i+\frac{\beta_i}{2}} T(\alpha)\, d\alpha = \int_{\alpha_i-\frac{\beta_i}{2}}^{\alpha_i+\frac{\beta_i}{2}} d\alpha = \beta_i. \tag{4.220}$$

The integral over α for the horizontal-displacement response (north component) reduces to:

$$\begin{aligned}
\int_{\alpha_i-\frac{\beta_i}{2}}^{\alpha_i+\frac{\beta_i}{2}} T(\alpha)\, d\alpha &= -\int_{\alpha_i-\frac{\beta_i}{2}}^{\alpha_i+\frac{\beta_i}{2}} \cos(\alpha)\, d\alpha \\
&= -\left\{\sin\left(\alpha_i+\frac{\beta_i}{2}\right)-\sin\left(\alpha_i-\frac{\beta_i}{2}\right)\right\} \\
&= -\left[\sin(\alpha_i)\ \cos\left(\frac{\beta_i}{2}\right)+\cos(\alpha_i)\ \sin\left(\frac{\beta_i}{2}\right)\right]+ \\
&\quad \left[\sin(\alpha_i)\ \cos\left(\frac{\beta_i}{2}\right)-\cos(\alpha_i)\ \sin\left(\frac{\beta_i}{2}\right)\right] \\
&= -2\ \sin\left(\frac{\beta_i}{2}\right)\ \cos(\alpha_i).
\end{aligned} \tag{4.221}$$

The integral over α for the horizontal-displacement response (east component) reduces to:

$$\begin{aligned}
\int_{\alpha_i-\frac{\beta_i}{2}}^{\alpha_i+\frac{\beta_i}{2}} T(\alpha)\, d\alpha &= -\int_{\alpha_i-\frac{\beta_i}{2}}^{\alpha_i+\frac{\beta_i}{2}} \sin(\alpha)\, d\alpha \\
&= -\left\{\cos\left(\alpha_i-\frac{\beta_i}{2}\right)-\cos\left(\alpha_i+\frac{\beta_i}{2}\right)\right\} \\
&= -\left[\cos(\alpha_i)\ \cos\left(\frac{\beta_i}{2}\right)+\sin(\alpha_i)\ \sin\left(\frac{\beta_i}{2}\right)\right]+ \\
&\quad \left[\cos(\alpha_i)\ \cos\left(\frac{\beta_i}{2}\right)-\sin(\alpha_i)\ \sin\left(\frac{\beta_i}{2}\right)\right] \\
&= -2\ \sin\left(\frac{\beta_i}{2}\right)\ \sin(\alpha_i).
\end{aligned} \tag{4.222}$$

4.4.3 Convolution Procedure

After the integration mesh has been defined and the LGFs have been normalized and integrated, the next step is to determine the geographic coordinates for the midpoint of each cell. From spherical trigonometry, I compute the latitude and longitude of the cell midpoints

(Φ_i, λ_i) using the so-called direct geodesic problem (e.g., Karney, 2013):

$$\Phi_i = \arcsin(\sin\Phi_R \cos\theta_i + \cos\Phi_R \sin\theta_i \cos\alpha_i) \quad (4.223)$$

$$\lambda_i = \lambda_R + \arctan\left(\frac{\sin\alpha_i \sin\theta_i \cos\Phi_R}{\cos\theta_i - \sin\Phi_R \sin\Phi_i}\right), \quad (4.224)$$

where $\Phi_i = 90 - \Theta_i$ is the latitude at the midpoint of mesh cell i, λ_i is the longitude at the midpoint of mesh cell i, Φ_R is the latitude of the station, λ_R is the longitude of the station, θ_i is the inclination angle between the station and the midpoint of mesh cell i, and α_i is the azimuth from the station to the midpoint of mesh cell i (measured at the station in degrees clockwise from north). Note that to account for Earth flattening effects, the geographic coordinates may be converted to geocentric coordinates when computing azimuth and inclination.

The load model, provided on a geographic coordinate grid, may now be interpolated to the specific geographic coordinates at the center of each integration-mesh cell. One option is to use bilinear interpolation of the four neighboring load points (e.g., Penna et al., 2008; Agnew, 2012). Another option, as long as the grid is rectangular, is to use two-dimensional bivariate spline interpolation, which is provided as a built-in function within `python`.

The discrete convolution now may be written as (e.g., Harrison, 1985; Agnew, 1997):

$$\overline{U}_{\text{vert}}(\Theta,\lambda) = 4\sum_{i=1}^{N} Z_i\,\rho_i\,G'(\theta_i)\cos\left(\frac{\theta_i}{2}\right)\sin\left(\frac{\delta_i}{4}\right)\beta_i \quad (4.225)$$

$$\overline{U}_{\text{north}}(\Theta,\lambda) = 8\sum_{i=1}^{N} Z_i\,\rho_i\,G'(\theta_i)\cos\left(\frac{\theta_i}{2}\right)\sin\left(\frac{\delta_i}{4}\right)\sin\left(\frac{\beta_i}{2}\right) \cos(\alpha_i + 180^\circ) \quad (4.226)$$

$$\overline{U}_{\text{east}}(\Theta,\lambda) = 8\sum_{i=1}^{N} Z_i\,\rho_i\,G'(\theta_i)\cos\left(\frac{\theta_i}{2}\right)\sin\left(\frac{\delta_i}{4}\right)\sin\left(\frac{\beta_i}{2}\right) \sin(\alpha_i + 180^\circ). \quad (4.227)$$

For complex-valued loads, including the ocean tides, the amplitudes and phases are parti-

tioned into real and imaginary components (e.g., Bos & Baker, 2005):

$$Z_i = A_i \ \cos\phi_i + i \ A_i \ \sin\phi_i = c + i\, s, \tag{4.228}$$

where A_i is the amplitude of the load at the center of mesh cell i and ϕ_i is the phase at the center of mesh cell i. The real and imaginary components are convolved separately over all cells in the integration mesh using Eqs. 4.225–4.227. The convolution results for each harmonic coefficient, U_c and U_s, are then recombined into the amplitude and phase for each spatial component:

$$A = \sqrt{U_c^2 + U_s^2} \tag{4.229}$$

$$\phi = \mathrm{atan2}(U_s, U_c). \tag{4.230}$$

In addition to a spatially variable load model, a spatially variable model for seawater densities may also be included (e.g., Bos & Baker, 2005; Agnew, 2012; Ray, 2013). As with the load model, the densities would be interpolated onto the integration mesh, designed such that the average density within each cell is approximately equal to the value at the midpoint of each cell. Alternatively, the seawater density may be approximated as constant everywhere and applied after the convolution. The approximation of constant seawater density is good to about 1% (e.g., Bos & Baker, 2005).

4.4.4 Additional Considerations

To improve the convolution further, the load model should be refined around coastal boundaries, perhaps using bilinear interpolation (e.g., Agnew, 2012). Locally redistributing the water mass within the area of coastal refinement has been shown to be less effective than interpolation (Penna et al., 2008). Particularly for older ocean tide models, grid cells were too coarse to accurately reflect the coastline, leading to substantial inaccuracies for loads close to the observer or in shallow seas (e.g., Bos & Baker, 2005; Penna et al., 2008). Recent ocean tide models, such as TPXO8-Atlas and FES2012, do a much better job of fitting the coastline (e.g., Penna et al., 2008); thus, refining the ocean tide models around the coastline

has become less critical, but still influencial.

Further improvements may be made by supplementing global ocean tide models with local models. Care must be taken so as not to double-count loads, but the template method is well designed for combining multiple models, whereby unique cells in the mesh can be assigned to unique ocean tide models (e.g., Agnew, 1997, 2012).

It is also worth noting that the development presented here applies to an elastic Earth. For a viscoelastic Earth, the elastic moduli are frequency dependent and the load Love numbers become complex-valued (e.g., Lambeck, 1988; Pagiatakis, 1990; Bos et al., 2015). Francis & Mazzega (1990) reported differences between OTL-induced surface displacements of up to 1.5% in amplitude and 0.3° in phase when comparing elastic and anelastic models. More recently, Bos et al. (2015) found that discrepancies between observed and predicted OTL-induced surface displacements in western Europe could be reduced by about 0.2 mm on average by accounting for mantle anelasticity.

4.5 Suggestions for Further Reading

For computing the Love numbers, the texts I have found most helpful include: Alterman et al. (1959), Longman (1962, 1963), Takeuchi & Saito (1972), Saito (1978), Lapwood & Usami (1981), Lanzano (1982), Okubo & Saito (1983), Bos & Scherneck (2013), and Smylie (2013). For more information on deriving the displacement load Green's functions, I recommend Farrell (1972a), Okubo (1988a,b), and Guo et al. (2004). To learn more about the convolution procedure, I suggest Farrell (1973), Agnew (2012, 2015), and Harrison (1985). Overviews of the entire procedure are provided in Melchior (1983), Baker (1984), Jentzsch (1997), Bos & Scherneck (2013), and Agnew (2015).

5

Some Remarks on the Inverse Problem for Surface Mass Loading

5.1 Theory and Implementation

To investigate the elastic structure of the solid Earth from observations of OTL-induced surface displacements, the forward model developed in Ch. 4 may be adapted to an inversion framework. Although many inversion algorithms exist, here I review the straightforward technique of solving the weakly non-linear problem in a least-squares sense. Thus, I linearize the forward model, $\mathbf{G}(\mathbf{m})$, around an initial model for the elastic structure, $\mathbf{m}_{\text{prior}}$, using a first-order Taylor series expansion (e.g., Tarantola, 2005; Aster et al., 2013):

$$\mathbf{G}(\mathbf{m}) \approx \mathbf{G}(\mathbf{m}_{\text{prior}}) + \mathbf{J}(\mathbf{m}_{\text{prior}})\, \Delta\mathbf{m}, \tag{5.1}$$

where

$$\Delta\mathbf{m} = (\mathbf{m} - \mathbf{m}_{\text{prior}}) \tag{5.2}$$

and

$$\mathrm{J}^i_\alpha(\mathbf{m}_{\text{prior}}) = \left(\frac{\partial[\mathrm{G}(\mathbf{m})]_i}{\partial \mathrm{m}_\alpha} \right)_{\mathbf{m}_{\text{prior}}} \tag{5.3}$$

is the Jacobian. Furthermore, α corresponds to a specific model parameter and i corresponds to the real or imaginary component of the predicted OTL-induced surface displacements for a particular geographic location and spatial component. For Earth's elastic response to surface mass loading, the model parameters may be defined as logarithms of the two elastic moduli, μ and κ, and density, ρ, at various discrete depths, or *knots*, positioned through the crust and mantle. The differential model vector in Eq. 5.1, $\Delta\mathbf{m}$, represents small perturbations to the model parameters at each knot.

Written more explicitly, Eq. 5.1 becomes:

$$\begin{bmatrix} (\mathrm{G}(\mathbf{m}))_1 \\ (\mathrm{G}(\mathbf{m}))_2 \\ (\mathrm{G}(\mathbf{m}))_3 \\ (\mathrm{G}(\mathbf{m}))_4 \\ \vdots \end{bmatrix} \approx \begin{bmatrix} (\mathrm{G}(\mathbf{m}_{\mathrm{prior}}))_1 \\ (\mathrm{G}(\mathbf{m}_{\mathrm{prior}}))_2 \\ (\mathrm{G}(\mathbf{m}_{\mathrm{prior}}))_3 \\ (\mathrm{G}(\mathbf{m}_{\mathrm{prior}}))_4 \\ \vdots \end{bmatrix} + \begin{bmatrix} \frac{\partial[\mathrm{G}(\mathbf{m})]_1}{\partial \mathrm{m}_1} & \frac{\partial[\mathrm{G}(\mathbf{m})]_1}{\partial \mathrm{m}_2} & \frac{\partial[\mathrm{G}(\mathbf{m})]_1}{\partial \mathrm{m}_3} & \frac{\partial[\mathrm{G}(\mathbf{m})]_1}{\partial \mathrm{m}_4} & \cdots \\ \frac{\partial[\mathrm{G}(\mathbf{m})]_2}{\partial \mathrm{m}_1} & \frac{\partial[\mathrm{G}(\mathbf{m})]_2}{\partial \mathrm{m}_2} & \frac{\partial[\mathrm{G}(\mathbf{m})]_2}{\partial \mathrm{m}_3} & \frac{\partial[\mathrm{G}(\mathbf{m})]_2}{\partial \mathrm{m}_4} & \cdots \\ \frac{\partial[\mathrm{G}(\mathbf{m})]_3}{\partial \mathrm{m}_1} & \frac{\partial[\mathrm{G}(\mathbf{m})]_3}{\partial \mathrm{m}_2} & \frac{\partial[\mathrm{G}(\mathbf{m})]_3}{\partial \mathrm{m}_3} & \frac{\partial[\mathrm{G}(\mathbf{m})]_3}{\partial \mathrm{m}_4} & \cdots \\ \frac{\partial[\mathrm{G}(\mathbf{m})]_4}{\partial \mathrm{m}_1} & \frac{\partial[\mathrm{G}(\mathbf{m})]_4}{\partial \mathrm{m}_2} & \frac{\partial[\mathrm{G}(\mathbf{m})]_4}{\partial \mathrm{m}_3} & \frac{\partial[\mathrm{G}(\mathbf{m})]_4}{\partial \mathrm{m}_4} & \cdots \\ \vdots & \vdots & \vdots & \vdots & \vdots \end{bmatrix} \begin{bmatrix} \Delta \mathrm{m}_1 \\ \Delta \mathrm{m}_2 \\ \Delta \mathrm{m}_3 \\ \Delta \mathrm{m}_4 \\ \vdots \end{bmatrix}. \tag{5.4}$$

$\mathbf{G}(\mathbf{m})$ represents the forward model, which may be compared against observations of OTL-induced surface displacements inferred from the GPS data. In other words, I aim to derive a model vector, $\mathbf{m}$, that best describes the data. In the ideal case, the observed data vector, $\mathbf{d}$, would perfectly match the set of forward-modeled predictions:

$$\mathbf{d} = \mathbf{G}(\mathbf{m}). \tag{5.5}$$

To find the optimal solution, I combine Eq. 5.5 with Eq. 5.1 to obtain:

$$\mathbf{G}(\mathbf{m}) = \mathbf{d} \approx \mathbf{G}(\mathbf{m}_{\mathrm{prior}}) + \mathbf{J}(\mathbf{m}_{\mathrm{prior}})\, \Delta\mathbf{m}, \tag{5.6}$$

which, upon rearranging, becomes:

$$\mathbf{J}(\mathbf{m}_{\mathrm{prior}})\, \Delta\mathbf{m} \approx \mathbf{d} - \mathbf{G}(\mathbf{m}_{\mathrm{prior}}). \tag{5.7}$$

This problem may be solved iteratively for the model perturbations, $\Delta\mathbf{m}$. Model parameters are updated at each iteration until a suitable convergence is achieved.

To generate the Jacobian matrix, each model parameter is perturbed individually to generate a series of updated models for Earth structure. Multiple evaluations of the forward model are then performed to determine the change in predicted OTL-induced displacements at the surface due to perturbations in the model parameters. The process repeats until the effects of perturbations to all model parameters have been considered. In other words, the predicted OTL-induced surface displacements from each perturbed forward model are compared against the predicted OTL-induced surface displacements from the unperturbed

model ($\partial[\mathrm{G}(\mathbf{m})]_i$) and divided by the perturbation to the model parameter ($\partial \mathrm{m}_\alpha$), where i corresponds to a particular station/component/data-type and α corresponds to a particular model parameter. The model-parameter perturbations must be small enough to ensure stability in the inversion, although perturbations too small can increase computational time unnecessarily. The Jacobian will need to be recomputed when the perturbations to the original model parameters exceed a certain threshold, such as 2% (Ito & Simons, 2011).

For the nonlinear least-squares problem, the *a posteriori* probability density is approximately Gaussian and centered on (Tarantola, 2005):

$$\begin{aligned} \widetilde{\mathbf{m}} &\approx \mathbf{m}_{\mathrm{prior}} + (\mathbf{J}^t\,\mathbf{C}_{\mathrm{D}}^{-1}\,\mathbf{J} + \mathbf{C}_{\mathrm{M}}^{-1})^{-1}\,\mathbf{J}^t\,\mathbf{C}_{\mathrm{D}}^{-1}\,[\mathbf{d}_{\mathrm{obs}} - \mathbf{G}(\mathbf{m}_{\mathrm{prior}})] \\ &= \mathbf{m}_{\mathrm{prior}} + \mathbf{C}_{\mathrm{M}}\,\mathbf{J}^t\,(\mathbf{J}\,\mathbf{C}_{\mathrm{M}}\,\mathbf{J}^t + \mathbf{C}_{\mathrm{D}})^{-1}\,[\mathbf{d}_{\mathrm{obs}} - \mathbf{G}(\mathbf{m}_{\mathrm{prior}})], \end{aligned} \tag{5.8}$$

where $\mathbf{C}_{\mathrm{M}}$ is the model covariance matrix, $\mathbf{C}_{\mathrm{D}}$ is the data covariance matrix, and a superscript t indicates a matrix transpose. A variety of optimization algorithms exist to facilitate convergence upon the maximum likelihood model, $\mathbf{m}_{\mathrm{ML}}$, including Newton's method, the steepest descent method, the conjugate gradient method, and Monte Carlo methods (e.g., Tarantola, 2005; Aster et al., 2013).

For Newton's method, the updated model parameters at each iteration are given by:

$$\mathbf{m}_{n+1} = \mathbf{m}_n - \mu_n\,(\mathbf{J}_n^t\,\mathbf{C}_{\mathrm{D}}^{-1}\,\mathbf{J}_n + \mathbf{C}_{\mathrm{M}}^{-1})^{-1}\,\{\mathbf{J}_n^t\,\mathbf{C}_{\mathrm{D}}^{-1}\,[\mathbf{G}(\mathbf{m}_n) - \mathbf{d}_{\mathrm{obs}}] + \mathbf{C}_{\mathrm{M}}^{-1}\,[\mathbf{m}_n - \mathbf{m}_{\mathrm{prior}}]\}, \tag{5.9}$$

where

$$(\mathrm{J}_n)_\alpha^i = \left(\frac{\partial[\mathrm{G}(\mathbf{m})]_i}{\partial \mathrm{m}_\alpha}\right)_{\mathbf{m}_n} \tag{5.10}$$

and μ_n parameterizes the step size at each iteration (e.g., Tarantola, 2005). Typically, $\mu_n = 1$ for Newton's method (Tarantola, 2005). If multiple minima exist, then Newton's method will converge upon a *local* optimum. Thus, for the case of multiple minima, the *prior* model must initiate the inversion near to the global minimum when using Newton's method.

For the steepest descent method, the updated model parameters are given by (e.g., Tarantola,

2005):

$$\mathbf{m}_{n+1} = \mathbf{m}_n - \mu_n \left\{ \mathbf{C}_{\mathrm{M}} \, \mathbf{J}_n^t \, \mathbf{C}_{\mathrm{D}}^{-1} \left[\mathbf{G}(\mathbf{m}_n) - \mathbf{d}_{\mathrm{obs}} \right] + \left[\mathbf{m}_n - \mathbf{m}_{\mathrm{prior}} \right] \right\}. \tag{5.11}$$

Conjugate gradient least squares (CGLS) algorithms (e.g., Aster et al., 2013) are similar to steepest descent methods, but have more flexibility in exploring the model space. In cases where a nonlinear model cannot be linearized or a large number of local minima are present, Monte Carlo methods are generally preferred (e.g., Tarantola, 2005).

Since the elastic moduli and density are Jeffrey's parameters (Tarantola, 2005) (i.e., the quantities must remain positive), I parameterize the model vector in terms of ratios of the elastic moduli and density. For each knot in the model, the model parameters could be defined as:

$$\mathbf{m}_{knot} = \left\{ \log\left(\frac{\kappa_t}{\kappa_b}\right), \log\left(\frac{\mu_t}{\mu_b}\right), \log\left(\frac{\rho_t}{\rho_b}\right) \right\}, \tag{5.12}$$

where t corresponds to the model parameter in the upper layer and b corresponds to the model parameter in the lower layer. For a starting layer at the base of the model space, the model parameters at the first knot would be:

$$\mathbf{m}_0 = \left\{ \log\left(\frac{\kappa_0}{\kappa^*}\right), \log\left(\frac{\mu_0}{\mu^*}\right), \log\left(\frac{\rho_0}{\rho^*}\right) \right\}, \tag{5.13}$$

where κ^*, μ^*, and ρ^* represent scaling factors. For a given set of model parameters, one can determine the starting parameters (ρ_0, μ_0, κ_0) and subsequently "unwind" the remaining parameters. Parameterizing the model vector in terms of ratios of the elastic parameters also facilitates the inclusion of two knots at the same depth level, which allows for the possibility of a discrete jump in material properties at a boundary layer (e.g., compositional, chemical, thermal, etc.).

The initial model vector is constructed based on an *a priori* Earth model, such as PREM. After each iteration, k, of the non-linear least-squares inversion, the model vector will be updated:

$$\mathbf{m}^{k+1} = \mathbf{m}^k + \Delta\mathbf{m}. \tag{5.14}$$

5.2 Sensitivity Analysis

Here, I review quasi-analytical and numerical methods for computing load Love number and displacement LGF sensitivity kernels. Several previous studies have examined the sensitivity of OTL-induced deformation to input Earth model (e.g., Baker, 1980b, 1984; Baker & Bos, 2003; Penna et al., 2008; Bos, 2010; Na & Baek, 2011; Wang et al., 2012; Yuan et al., 2013), but none have yet performed a systematic investigation into the relative impacts of various model factors. Ito & Simons (2011) provided the most detailed sensitivity analysis to date, but also inadvertently contaminated the density kernel with extraneous perturbations to the elastic moduli. Exploring the sensitivity of OTL-induced deformation to perturbations in density and elastic structure provides some insight into the feasibility of inverting the observed OTL-induced deformation for the material properties (e.g., Ito & Simons, 2011; Baker, 1980b, and references therein).

Former studies have demonstrated that the LGFs associated with various SNREI Earth models, which typically differ most substantially in the crust and upper mantle, exhibit discrepancies primarily within 1° (or $\sim$100 km) of the loading point (e.g., Farrell, 1972a; Baker, 1984; Francis & Mazzega, 1990; Na & Baek, 2011; Wang et al., 2012; Yuan et al., 2013). For hydrological and atmospheric loading, with stations and loads nearly collocated, the influence of the crustal properties on the displacement LGFs can be upwards of 10-20% or more (Wang et al., 2012; Dill et al., 2015). Therefore, for the case of OTL-induced deformation, GPS stations located near the coastline are generally the most sensitive to structural perturbations of the solid Earth (Francis & Mazzega, 1990). Coastal stations, however, are also highly sensitive to errors in the input OTL model as well as the method of coastline refinement adopted by the convolution algorithm (Bos & Baker, 2005; Penna et al., 2008). Furthermore, stations located very near to the load are mostly sensitive to near-surface structure.

For a variety of seismologically derived Earth models, predicted OTL-induced deformation generally matches the observed OTL-induced deformation to within the current levels of instrumental and model precision (e.g., Baker, 1980b; Baker & Bos, 2003; Penna et al.,

2008; Bos, 2010; Pugh et al., 2011), implying that sensitivities to perturbations in spherically symmetric, elastic and isotropic Earth structure are relatively minor compared with sources of uncertainty (e.g., Bos & Baker, 2005; Penna et al., 2008; Bos, 2010; Bos et al., 2015). Claims to the contrary have been controversial (Richter et al., 2009; Bos, 2010; Richter et al., 2010).

5.2.1 Love Number Partial Derivatives

Sensitivity kernels for load Love numbers may be computed both numerically (Ito & Simons, 2011) and quasi-analytically (Okubo & Saito, 1983; Okubo et al., 1984; Okubo & Endo, 1986; Okubo, 1988a). A discussion of both methods is provided in the following chapter (Ch. 6). In this section, I review additional details of the quasi-analytical approach. In general, I follow the procedure of Okubo & Saito (1983) to derive the partial derivatives of the Love numbers, supplemented by the theory of Okubo & Endo (1986) for the special case of $n = 1$. In the following development, I consider only perturbations to the solid mantle and crust, where deformation induced by ocean tidal loading is concentrated (e.g., Ito & Simons, 2011; Bos et al., 2015).

The variational equations for the Love numbers are developed analogously to the variational equations for seismic surface waves (e.g., Takeuchi & Saito, 1972, Sec. III). In particular, a function, f, may be developed that satisfies Euler's equation (e.g., Thornton & Marion, 2004, Sec. 6.3). For spheroidal deformation of Earth's solid regions (e.g., crust and mantle), the function is given by:

$$
\begin{aligned}
f_S \;=\; & [\kappa + \frac{4}{3}\mu]\, r^2\, \dot{x_1}\, \dot{y_1} \;+\; [\kappa - \frac{2}{3}\mu]\, r\, (\dot{x_1}\, Y + \dot{y_1}\, X) \;+\; [\kappa + \frac{1}{3}\mu]\, X\, Y \;+ \\
& n\,(n+1)\,\mu\,[(r\dot{y_3} + y_1 - y_3)\,(r\dot{x_3} + x_1 - x_3) + (n-1)(n+2)\,x_3\,y_3] \;+ \\
& (n+1)\,\rho\, r\,[y_5(x_1 - n x_3) + x_5(y_1 - n y_3)] - \rho\, g\, r\, (x_1\, Y + y_1\, X) \;+ \\
& \frac{1}{4\pi G}\,[r\dot{y_5} - 4\pi G\rho r y_1 + (n+1)y_5]\,[r\dot{x_5} - 4\pi G\rho r x_1 + (n+1)x_5], \qquad (5.15)
\end{aligned}
$$

where

$$\begin{aligned} X &= 2x_1 - n(n+1)x_3 \\ Y &= 2y_1 - n(n+1)y_3. \end{aligned} \tag{5.16}$$

Importantly, f_S satisfies the Euler equations:

$$\begin{aligned} \frac{d}{dr}\frac{\partial f_S}{\partial \dot{y_j}} &= \frac{\partial f_S}{\partial y_j} \\ \frac{d}{dr}\frac{\partial f_S}{\partial \dot{x_j}} &= \frac{\partial f_S}{\partial x_j} \end{aligned} \tag{5.17}$$

for $j = 1, 3, 5$. The variables x_j and y_j, which are functions of radius r, represent solutions to the equations of motion (Sec. 4.2.6, Eq. 4.79) that accommodate various boundary conditions (Table 4.1). Dots above the variables indicate a partial derivative with respect to r. When $x_j = y_j$, f_S is equivalent to a Lagrangian function (Okubo & Saito, 1983).

Now consider a perturbation to a structural parameter, p_i, by an amount δp_i, where i corresponds to one of the elastic moduli or density. The perturbations generate new solutions to the equations of motion: $x_j + \delta x_j$ and $y_j + \delta y_j$. Using calculus of variations, the new solutions may be used to determine the predicted change in a Love number due to the perturbation in structure. From (Okubo & Saito, 1983), the partial derivative of the vertical-displacement load Love number, h', with respect to parameter p_i is given by:

$$\frac{\partial h'_n}{\partial p_i} = \frac{\partial}{\partial p_i}[I_{PL} - I_{LL} + \gamma(2h'_n - h_n)\rho r^2], \tag{5.18}$$

where $\gamma = (4\pi G)/(a^2\, g(a))$ and

$$I = -\frac{4\pi G}{(2n+1)a}\left[f_S(p_i) + \rho r^2\left(\int_r^a 4\pi G \frac{1}{s^2}\frac{\partial f_S}{\partial g}(s)ds\right)\right]. \tag{5.19}$$

As a reminder, core regions have been neglected here. The subscripts P and L correspond to potential and load solutions to the equations of motion, respectively. The order of assignment to x_j and y_j is unimportant (i.e., $I_{PL} = I_{LP}$). Note that the third term on the

right-hand side of Eq. 5.18 arises as a result of the density perturbation, which necessarily also changes the surface gravity. According to the boundary-condition convention of Okubo & Saito (1983), δy_1 expands as:

$$\begin{aligned} \delta y_1 &= \delta(h_n/g(a)) \\ \delta(h_n/g(a)) &= \frac{\delta h_n}{g(a)} - h_n \frac{\delta g(a)}{g(a)^2}. \end{aligned} \tag{5.20}$$

My definition for the surface boundary conditions (and, thus, for the Love numbers) differs from Okubo & Saito (1983) by a factor of $a\,g(a)$, where a is Earth's radius and $g(a)$ is the gravitational acceleration at Earth's surface. Solutions to the equations of motion computed using either definition are equivalent, however, since both conventions are internally consistent.

Similarly, the partial derivative of the tangential-displacement load Love number, l', with respect to parameter p_i is given by:

$$\frac{\partial l'_n}{\partial p_i} = \frac{\partial}{\partial p_i}[I_{LS} + \gamma(l'_n - h''_n)\rho r^2], \tag{5.21}$$

where S indicates the shear-traction solution to the equations of motion and h''_n represents the vertical-displacement shear Love number.

For additional details on the quasi-analytical procedure, including equations for the remaining Love number partial derivatives, the reader is referred to Okubo & Saito (1983). With the partial derivatives computed, the predicted change in a Love number due to perturbations in elastic structure may be derived. Specifically, each partial derivative, which is a function of the radius r, is multiplied by a radial profile of perturbations to the elastic parameters. The profiles for each of the two elastic moduli and density are then summed together and integrated over the entire perturbed region. Formally, the perturbation to a Love number induced by elastic structural perturbations is given by:

$$\delta H_n = \int_{\mathrm{CMB}}^{a} \left\{ \left[\frac{\partial H_n}{\partial \rho}(r)\right]_{\kappa\mu} \delta\rho(r) + \left[\frac{\partial H_n}{\partial \kappa}(r)\right]_{\mu\rho} \delta\kappa(r) + \left[\frac{\partial H_n}{\partial \mu}(r)\right]_{\rho\kappa} \delta\mu(r) \right\} dr, \tag{5.22}$$

where H_n represents a particular Love number (e.g., h_n, l'_n, or k''_n), CMB represents the core-mantle boundary, a is Earth's radius, and the partial derivatives are defined per unit thickness of the perturbed layer.

For the special case of $n = 0$, the tangential-displacement load Love number, l'_0, is zero; thus, the partial derivatives of l'_0 with respect to the elastic parameters are also zero. For the vertical-displacement load Love number, h'_0, the quasi-analytical partial derivative may be reduced to:

$$\frac{\partial h'_0}{\partial p_i} = \frac{\partial}{\partial p_i}[-I_{LL} + \gamma(2h'_0)\rho r^2], \tag{5.23}$$

since the potential Love numbers are zero for $n = 0$ and $\frac{\partial}{\partial p_i} I_{PL} = 0$. For the special case of $n = 1$, I follow the methods outlined in Okubo & Endo (1986) and compute the partial derivatives of the load and stress Love numbers only.

Recall that only six of the nine Love numbers are independent. The Love numbers may therefore be related by the following expressions (e.g., Okubo & Saito, 1983; Okubo & Endo, 1986):

$$k_n - h_n = k'_n \tag{5.24}$$

$$l_n = k''_n \tag{5.25}$$

$$k''_n = h''_n + l'_n \tag{5.26}$$

$$h'''_n = h'_n - l'_n, \tag{5.27}$$

where h'''_n denotes the vertical displacement stress Love number. Figs. D.1–D.14 in Appendix D show the partial derivatives of Love numbers, derived from PREM (as well as 1066A for comparison with the former studies), for a range of spherical harmonic degrees.

In the quasi-analytical development presented here, the Taylor-series expansions of the Love number partial derivatives were truncated at first-order. The formulas for the partial derivatives are therefore most accurate for small perturbations to structure that generate localized changes in the Love numbers. As an alternative to the quasi-analytical approach, finite differences of the Love numbers may be computed explicitly for structural pertur-

bations of any magnitude. From comparisons of the quasi-analytical and numerical techniques, I find that small perturbations to the elastic moduli and density ($<1\%$) generate differences in the partial derivatives of order 1%. As perturbations increase, however, the truncated quasi-analytical approach fails to accurately describe the partial derivatives at higher order. Table 5.1 compares changes in degree-2 load Love numbers for perturbations to a homogeneous sphere, computed using both quasi-analytical and numerical techniques.

5.2.2 Load Green's Function Partial Derivatives

As a natural extension from the load Love number partial derivatives, the partial derivatives of LGFs to perturbations in elastic structure may also be computed both numerically using finite-differences and quasi-analytically using calculus of variations. Numerically derived partial derivatives of LGFs are discussed in the following chapter (Ch. 6). For details on the quasi-analytical approach, the reader is referred to Okubo (1988a) and Okubo (1988b).

	0.1%	**0.2%**	**0.5%**	**1.0%**	**2.0%**	**5.0%**	**10.0%**	**20.0%**
	μ Perturbed							
$\Delta h_2'$ (Analytical)	2.861E-04	5.723E-04	1.431E-03	2.861E-03	5.723E-03	1.431E-02	2.861E-02	5.723E-02
$\Delta h_2'$ (Numerical)	2.859E-04	5.714E-04	1.425E-03	2.839E-03	5.633E-03	1.376E-02	2.651E-02	4.942E-02
$\Delta l_2'$ (Analytical)	6.273E-05	1.255E-04	3.136E-04	6.273E-04	1.255E-03	3.136E-03	6.273E-03	1.255E-02
$\Delta l_2'$ (Numerical)	6.268E-05	1.253E-04	3.124E-04	6.224E-04	1.235E-03	3.017E-03	5.812E-03	1.082E-02
$\Delta k_2'$ (Analytical)	1.639E-04	3.277E-04	8.194E-04	1.639E-03	3.277E-03	8.194E-03	1.639E-02	3.277E-02
$\Delta k_2'$ (Numerical)	1.637E-04	3.272E-04	8.160E-04	1.626E-03	3.225E-03	7.874E-03	1.516E-02	2.820E-02
	κ Perturbed							
$\Delta h_2'$ (Analytical)	3.121E-04	6.241E-04	1.560E-03	3.121E-03	6.241E-03	1.560E-02	3.121E-02	6.241E-02
$\Delta h_2'$ (Numerical)	3.117E-04	6.227E-04	1.552E-03	3.086E-03	6.104E-03	1.477E-02	2.805E-02	5.095E-02
$\Delta l_2'$ (Analytical)	-1.102E-04	-2.205E-04	-5.512E-04	-1.102E-03	-2.205E-03	-5.512E-03	-1.102E-02	-2.205E-02
$\Delta l_2'$ (Numerical)	-1.101E-04	-2.200E-04	-5.482E-04	-1.090E-03	-2.156E-03	-5.219E-03	-9.909E-03	-1.800E-02
$\Delta k_2'$ (Analytical)	2.514E-05	5.027E-05	1.257E-04	2.514E-04	5.027E-04	1.257E-03	2.514E-03	5.027E-03
$\Delta k_2'$ (Numerical)	2.511E-05	5.016E-05	1.250E-04	2.486E-04	4.916E-04	1.190E-03	2.258E-03	4.099E-03
	ρ Perturbed							
$\Delta h_2'$ (Analytical)	-1.193E-03	-2.386E-03	-5.965E-03	-1.193E-02	-2.386E-02	-5.965E-02	-1.193E-01	-2.386E-01
$\Delta h_2'$ (Numerical)	-1.195E-03	-2.392E-03	-5.991E-03	-1.202E-02	-2.417E-02	-6.148E-02	-1.266E-01	-2.692E-01
$\Delta l_2'$ (Analytical)	9.542E-05	1.908E-04	4.771E-04	9.542E-04	1.908E-03	4.771E-03	9.542E-03	1.908E-02
$\Delta l_2'$ (Numerical)	9.548E-05	1.914E-04	4.823E-04	9.772E-04	2.005E-03	5.408E-03	1.224E-02	3.114E-02
$\Delta k_2'$ (Analytical)	-3.763E-04	-7.526E-04	-1.881E-03	-3.763E-03	-7.526E-03	-1.881E-02	-3.763E-02	-7.526E-02
$\Delta k_2'$ (Numerical)	-3.773E-04	-7.548E-04	-1.889E-03	-3.783E-03	-7.588E-03	-1.914E-02	-3.885E-02	-7.999E-02

Table 5.1: A comparison of the direct differences between degree-2 load Love numbers, derived from perturbed and unperturbed homogeneous sphere models, computed quasi-analytically using the techniques of Okubo & Saito (1983) and numerically using finite differences. The Love numbers are, by definition, non-dimensional; thus, directly comparing the Love numbers alleviates the need to specify a normalization convention (which would be necessary for comparisons of partial derivatives). The initial (unperturbed) homogeneous sphere was assumed to have the elastic properties of V_P = 10 km/s, V_S = 5 km/s, and ρ = 5 g/cc.

6

The Sensitivity of Surface Mass Loading Displacement Response to Perturbations in the Elastic Structure of the Crust and Mantle

The work discussed in this chapter has been accepted for publication as:

Martens, H.R., L. Rivera, M. Simons, and T. Ito, 2016. The Sensitivity of Surface Mass Loading Displacement Response to Perturbations in the Elastic Structure of the Crust and Mantle, *J. Geophys. Res. Solid Earth*, 121, doi:10.1002/2015JB012456.

6.1 Abstract

Surface mass loads generate a rich spectrum of deformation responses in the solid Earth that might be exploited to probe the material properties of the crust and mantle. Here we present a detailed examination of load-induced surface displacements and their sensitivities to systematic perturbations in elastic Earth structure. We compute Love numbers and displacement load Green's functions (LGFs) by integrating the equations of motion for spheroidal deformation of a radially heterogeneous and self-gravitating Earth. Sensitivity kernels are derived for individual Love numbers numerically using finite differences and quasi-analytically using calculus of variations. We then generate sensitivity kernels for displacement LGFs by systematically perturbing the Preliminary Reference Earth Model. We find that displacement LGFs are most sensitive to elastic structural perturbations within 500 km depth from the surface and for short source-receiver distances. For separate perturbations to the shear modulus, bulk modulus, and density within the crust and mantle, the

sensitivity kernels exhibit unique patterns, consistent with the possibility to constrain the parameters independently given a spatially distributed set of sufficiently accurate loading response observations. The sensitivity to density structure, however, is generally weak in comparison to elastic structure. We also examine the sensitivity of surface displacements caused by M_2 ocean tidal loading (OTL) to systematic perturbations in the elastic moduli and density. Since OTL-induced surface displacements are load- and site-dependent, we focus on high-resolution profiles across Iceland as a case study. The sensitivity kernels constitute a key element in the formulation of the inverse problem with application to geodetic tomography.

6.2 Introduction

Surface mass loading (SML) deforms the solid Earth in a manner controlled by the material properties of the interior. Examples of surface mass loads include oceans, lakes, rivers, reservoirs, the atmosphere, and seasonal precipitation. Since surface mass loads excite both elastic and gravitational responses in the solid Earth, we are motivated by the prospect of using observed SML-induced surface displacements, perhaps in combination with seismic observations, to probe the composition of the crust and mantle (e.g., Baker, 1980b; Ito & Simons, 2011). In addition to refining models of Earth's rheological structure, the geodetically inferred constraints on material properties could potentially shed light on mantle mechanics, such as the long-term stability of continental cratons (e.g., Jordan, 1978).

The concept of using SML-induced deformation to probe Earth's interior structure emerged several decades ago (e.g., Takeuchi, 1950; Longman, 1962, 1963; Farrell, 1972a), yet early attempts to implement the theory using gravity, strain, and tilt measurements were limited in effectiveness due to insufficient spatial coverage of available observations, calibration uncertainties, and high sensitivities to local variations in material properties (e.g., Baker, 1980b, 1984; Baker & Bos, 2003). Space-based geodetic techniques, such as the Global Positioning System (GPS), do not suffer from the same sparsity or sensitivity constraints and may be used to discern centimeter-level SML-induced surface displacements with submillimeter precision (e.g., Agnew, 2015; Penna et al., 2015; Martens et al., 2016).

One type of prominent surface mass loading comes from the periodic redistribution of ocean water by tidal forcing, known as ocean tidal loading (OTL). Although the theories that we discuss in this manuscript apply generally to the elastic displacement of the solid Earth in response to any surface mass load, we often refer to OTL-induced surface displacements as pertinent and illustrative examples.

Ito & Simons (2011) used residual OTL-induced surface displacements to invert for small deviations in the elastic moduli and density relative to the Preliminary Reference Earth Model (PREM) (Dziewonski & Anderson, 1981) beneath the western United States. The study, however, inadvertently neglected the geocenter motion induced by the redistribution of surface mass when computing the forward model (e.g., Fu et al., 2012; Wu et al., 2012). As a result, the displacement load Green's functions (LGFs) yielded OTL response predictions in a reference frame inconsistent with the corresponding GPS observations. Thus, the residual surface displacements, which the authors attributed to unmodeled Earth structure, primarily reflected the long-wavelength differences between the two reference frames. Furthermore, the study used just a single year of GPS data, assumed an errorless model for the solid Earth body tides (SEBTs), and disregarded contributions to the time series from minor tidal harmonics, which compounded the uncertainties in their derived Earth model (Yuan & Chao, 2012).

More recently, Yuan & Chao (2012) and Yuan et al. (2013) reported spatially coherent residuals between GPS-inferred and forward-modeled OTL-induced surface displacements across a global distribution of sites located more than 150 km inland of the coast, where the influence of errors in the ocean-tide models is significantly diminished. The regional-scale spatial coherency was interpreted to indicate possible deficiencies in the adopted SEBT model. Moreover, Penna et al. (2015) and Bos et al. (2015) found spatially coherent discrepancies between observed and predicted OTL-induced surface displacements across western Europe. Adjusting the value for the shear modulus in the asthenosphere by invoking frequency-dependent dissipation effects within the mantle improved the model fit to their observations. In addition, Martens et al. (2016) observed spatial coherency among residual M_2 OTL-induced surface displacements across South America.

Given the inferred spatial coherencies in residual OTL-induced surface displacements, as well as the accuracy of modern Global Navigation Satellite System (GNSS) measurements (e.g., Penna et al., 2015) and of modern tide models (e.g., Stammer et al., 2014), the possibility to constrain Earth structure from observations of SML-induced deformation appears increasingly tractable. Prior to inversions for material properties, however, the sensitivity of the deformation response to perturbations in Earth structure must be investigated. Here, we focus on the sensitivities of SML-induced displacements to systematic perturbations in the elasticity and density of the crust and mantle.

Previous studies that explored the level of structural sensitivity contained within load-generated response signals have focused primarily on comparisons between published LGFs for a few seismologically derived Earth models (e.g., Francis & Mazzega, 1990; Penna et al., 2008; Wang et al., 2012; Yuan et al., 2013), which cannot resolve the sensitivities to individual model parameters independently. In other words, comparisons of LGFs from different reference Earth models provide a general sense for the average magnitude and pattern of structural sensitivity, but do not provide distinct information about the effects of layer thickness, perturbation depth, or elastic parameter. Vector differences between pairs of predicted OTL-induced surface displacements derived from various combinations of one-dimensional Earth models and modern ocean-tide models are at the sub-millimeter level or less for most land-based locations (e.g., Penna et al., 2008; Wang et al., 2012; Yuan et al., 2013; Martens et al., 2016).

Isolating the influence of various factors, such as the particular elastic parameter and depth of the perturbation, can further elucidate details of Earth's elastic response to SML. In particular, Baker (1980b) computed variations in tilt LGFs derived from individual perturbations to the two elastic moduli and density, albeit for only two separate layers in the crust and upper mantle. Other studies have also explored changes in the LGFs due to controlled differences in the material properties, but focused solely on near-surface structure (e.g., Bos, 2010; Wang et al., 2012; Dill et al., 2015). As expected, perturbations to crustal structure predominantly affect the high-degree load Love numbers and therefore the LGFs in the near field ($< 1^{\circ}$) (e.g., Baker, 1980b; Francis & Mazzega, 1990).

For regional or global analyses of SML-generated deformation, however, mantle structure also has a significant influence on the deformation response (e.g., Ito & Simons, 2011). Furthermore, in the case of OTL, coastal stations near to the load, which are very sensitive to local crustal structure, are also highly susceptible to errors in the input tide model as well as to the method of coastline refinement adopted by the requisite convolution process, and therefore may be of limited use in OTL-based geodetic tomography (Bos & Baker, 2005; Penna et al., 2008; Yuan et al., 2013).

Ito & Simons (2011) computed displacement LGF sensitivities numerically for perturbations to the two elastic moduli and density as a function of depth and distance to the load. They concluded that displacements excited by SML are most sensitive to elastic structural perturbations within a few hundred kilometers of the surface and also found a lack of trade-off between the kernels for density and the elastic moduli. The study did not, however, control the effects of layer thickness on response amplitude and also inadvertently contaminated the density kernel with extraneous perturbations to the elastic moduli. The contamination stemmed from parameterizing the input Earth model in terms of seismic velocities rather than the elastic moduli. In other words, density was perturbed with the p-wave (V_P) and s-wave (V_S) velocities held constant instead of the shear (μ) and bulk (κ) moduli held constant, resulting in unintended perturbations to the elastic moduli with each density perturbation.

Adopting a more analytical approach, Okubo & Saito (1983) used calculus of variations to explore the sensitivities of potential, load, and shear Love numbers to independent perturbations of the two elastic moduli and density as a function of depth. Okubo & Endo (1986) expanded upon the theory of Okubo & Saito (1983) to address the special case of the degree-1 spherical harmonic. Further, Okubo (1988a) and Okubo (1988b) outlined a method to derive partial derivatives of the vertical- and horizontal-displacement LGFs from summations of the load Love number partial derivatives.

Here, we quantify the sensitivities of Love numbers, displacement LGFs, and OTL-induced surface displacements to systematic perturbations in elastic and density structure through the crust and mantle at a variety of spatial scales. We begin by reviewing the numerical and

quasi-analytical methods for computing partial derivatives of the Love numbers. Our results include a specific discussion of the partial derivatives for high-degree load Love numbers, which had not been included in previous studies. We then compute LGF sensitivity kernels numerically, revising and expanding upon the work of Ito & Simons (2011) by recomputing the density kernel as well as varying the layer thicknesses in a controlled manner. Finally, we perform a case study to quantify the sensitivity of OTL-induced surface displacements to systematic perturbations in elastic and density structure along two high-resolution ($\approx$1 km spacing) profiles across Iceland.

In summary, we compute sensitivity kernels for the Love numbers, displacement LGFs, and OTL-induced surface displacements as a function of (1) elastic model parameter, (2) displacement spatial-component, (3) distance between the applied load and the measurement site, (4) depth of the perturbation, and (5) thickness of the perturbed layer. Our objective is to characterize the sensitivity of OTL-induced surface displacements to variations in elastic Earth structure. The techniques we develop here are directly applicable to future tomographic inversions using observations of SML-induced surface deformation. In particular, sensitivity kernels representing the effects of perturbed elastic material properties on the SML-induced surface displacements may be used to relate a model for Earth structure to the surface-displacement observations in the linearized inverse problem.

6.3 Methodology

Love numbers are dimensionless parameters that characterize the elastic deformation of Earth to applied body forces and surface tractions (Love, 1911; Munk & MacDonald, 1960). For example, we commonly represent the response of an elastic Earth to an external gravitational potential, V, by a set of three real-valued and dimensionless Love numbers: $h_n(r)$, $k_n(r)$, and $l_n(r)$. The $l_n(r)$ parameter is alternatively referred to as the Shida number. Although the parameters exhibit a radial dependence, here we consider deformation observed only at Earth's surface, and thus drop the (r) notation.

The radial displacement, u_n, of Earth's surface in response to the application of an external

gravitational potential of spherical harmonic degree, n, is given by (e.g., Agnew, 2015):

$$u_n = h_n \frac{V_n}{g}, \tag{6.1}$$

where g is the gravitational acceleration at Earth's surface, $\frac{V_n}{g}$ represents the equilibrium potential height, and h_n scales the equilibrium height to a vertical-displacement response commensurate with the density and elastic properties of Earth's interior. Gravitational self-attraction, generated by the redistributed mass, is accounted for in the response parameter h_n (e.g., Munk & MacDonald, 1960). Analogously, the Shida number l_n is defined as the horizontal displacement of a realistic Earth relative to the gradient of the equilibrium potential height. The parameter k_n characterizes the change in the gravitational potential resulting from the redistribution of mass that occurs in response to the external potential field.

The Love and Shida numbers presented thus far describe the response of the elastic Earth to an external gravitational potential; thus, we refer to them as *potential* Love numbers. A second class of Love numbers, referred to as *load* Love numbers (LLNs), describes the elastic deformation of Earth in response to normal tractions, typically applied at Earth's surface (e.g., Munk & MacDonald, 1960; Longman, 1962; Saito, 1978). External surface mass loads come from a variety of sources, including glaciers, lakes, the atmosphere, and oceans. The load Love numbers are distinguished from the potential Love numbers by a superscript prime: h'_n, l'_n, and k'_n. A third class of Love numbers characterizes Earth's response to tangential tractions (e.g., Saito, 1978), distinguished from the other classes by superscript double primes (h''_n, l''_n, k''_n) and known as *shear* Love numbers. Only six of the nine Love numbers from the three sets (potential, load, and shear) are independent and expressions exist to relate the Love numbers to one another (e.g., Molodenskiy, 1977; Saito, 1978; Lambeck, 1988).

To derive the various sets of Love numbers, we solve the equations of motion for spheroidal deformation of a self-gravitating, radially heterogeneous, spherically symmetric, non-rotating, elastic and isotropic (SNREI) Earth (e.g., Alterman et al., 1959; Longman, 1962; Takeuchi

& Saito, 1972). The equations of motion are given by:

$$
\begin{aligned}
\dot{y}_1 &= \frac{-2\lambda}{A}\frac{y_1}{r} + \frac{y_2}{A} + \frac{\lambda C}{A}\frac{y_3}{r}, \\
\dot{y}_2 &= \left[-\omega^2\rho r^2 - 4\rho g r + \frac{4\mu B}{A}\right]\frac{y_1}{r^2} - \frac{4\mu}{A}\frac{y_2}{r} \\
&+ \left[C\rho g r - \frac{2\mu B C}{A}\right]\frac{y_3}{r^2} + C\frac{y_4}{r} - \rho y_6, \\
\dot{y}_3 &= -\frac{y_1}{r} + \frac{y_3}{r} + \frac{y_4}{\mu}, \\
\dot{y}_4 &= \left[g\rho r - \frac{2\mu B}{A}\right]\frac{y_1}{r^2} - \frac{\lambda}{A}\frac{y_2}{r} \\
&+ \left[-\omega^2\rho r^2 + \frac{2\mu}{A}[\lambda(2n^2+2n-1) + 2\mu(n^2+n-1)]\right]\frac{y_3}{r^2} - \frac{3y_4}{r} - \rho\frac{y_5}{r}, \\
\dot{y}_5 &= 4\pi G\rho y_1 + y_6, \\
\dot{y}_6 &= -4\pi G\rho C\frac{y_3}{r} + C\frac{y_5}{r^2} - \frac{2y_6}{r},
\end{aligned}
\tag{6.2}
$$

where $A = \lambda + 2\mu$, $B = 3\lambda + 2\mu$, $C = n(n+1)$, λ and μ are Lamé parameters, ρ is density, g is gravity, G is the universal gravitational constant, and ω is the forcing frequency. The variables y_1 and y_3 characterize the radial and tangential displacements, respectively; y_2 and y_4 characterize the radial and tangential stress, respectively; y_5 characterizes the gravitational potential; and the equation for $\dot{y}_5$ defines y_6. Dots represent differentiation with respect to r. As an aside, we note that Takeuchi & Saito (1972) adopt a different convention for the definition of y_6, which requires a slight adjustment to the surface boundary conditions.

Only three of the six linearly independent solutions to the equations of motion (Eq. 6.3) are bounded at the origin. We compute the three sets of starting solutions using analytical formulae for a homogeneous sphere (Takeuchi & Saito, 1972). We then propagate the three solution sets through a radially heterogeneous Earth model to the surface for each spherical harmonic degree. Appropriate boundary conditions are applied across each internal interface, including solid-fluid boundaries (Takeuchi & Saito, 1972), as well as at the surface. Our internally developed software package (`LoadDef`) integrates the equations of motion using a Runge-Kutta algorithm and adaptive step sizing. Beyond spherical harmonic degree 20, we begin integration within the mantle for reasons of numerical stability. We retain the

inertial factors in the equations of motion and set the forcing frequency equivalent to the M_2 tidal harmonic.

Although here we focus primarily on LLNs derived for mass-loading boundary conditions at the surface (e.g., Longman, 1962, 1963; Melchior, 1983; Guo et al., 2004), additional Love numbers, including potential and shear, are easily computed by adopting alternative surface boundary conditions, several of which are listed in Table 6.1.

To compute the displacement LGFs, which represent the response to a delta-function unit normal force at Earth's surface, we combine the LLNs in spherical harmonic expansions (Farrell, 1972a). The amplitudes of the vertical- and horizontal-displacement LGFs, per unit of load mass, are given by:

$$u(\theta) = \frac{a}{m_E} \sum_{n=0}^{\infty} h'_n \, P_n(\cos\theta) \tag{6.3}$$

and

$$v(\theta) = \frac{a}{m_E} \sum_{n=1}^{\infty} l'_n \, \frac{\partial P_n(\cos\theta)}{\partial \theta}, \tag{6.4}$$

where a is the Earth radius, m_E is the Earth mass, n represents the spherical harmonic degree, P_n represents the Legendre polynomial of spherical harmonic degree n, θ represents the angular distance between a measurement site and the load point, h'_n is the vertical-displacement load Love number, and l'_n is the horizontal-displacement load Love number.

To facilitate convergence of the LGFs, we compute asymptotic expressions of the LLNs (Guo et al., 2004) and apply Kummer's series transformation to Eqs. 6.3 and 6.4 (e.g., Abramowitz & Stegun, 1964; Farrell, 1972a; Na & Baek, 2011). In practice, the LLN computations are carried out to spherical harmonic degree 10000, beyond which the LLNs are assumed to be equivalent to the asymptotic values (Farrell, 1972a; Guo et al., 2004). The asymptotic expressions are generally accurate to at least 0.01% and often accurate to within 0.0001% of the true values at n =10000.

In summary, the displacement LGFs are computed using the formulae:

$$\begin{aligned} u(\theta) &\approx \frac{a}{m_E}\, h_\infty^* \sum_{n=1}^{\infty} P_n(\cos\theta) + \frac{a}{m_E}\, h_\infty^{**} \sum_{n=1}^{\infty} \frac{1}{n}\, P_n(\cos\theta) \\ &+ \frac{a}{m_E}\, h_0' + \frac{a}{m_E} \sum_{n=1}^{N=10000} (h_n' - (h_\infty^* + \frac{1}{n}\, h_\infty^{**}))\, P_n(\cos\theta) \end{aligned} \tag{6.5}$$

for the vertical-displacement response, and

$$\begin{aligned} v(\theta) &\approx \frac{a}{m_E}\, l_\infty^* \sum_{n=1}^{\infty} \frac{1}{n}\, \frac{\partial P_n(\cos\theta)}{\partial\theta} + \frac{a}{m_E}\, l_\infty^{**} \sum_{n=1}^{\infty} \frac{1}{n^2}\, \frac{\partial P_n(\cos\theta)}{\partial\theta} \\ &+ \frac{a}{m_E} \sum_{n=1}^{N=10000} (n l_n' - (l_\infty^* + \frac{1}{n}\, l_\infty^{**}))\, \frac{1}{n}\, \frac{\partial P_n(\cos\theta)}{\partial\theta} \end{aligned} \tag{6.6}$$

for the horizontal-displacement response, where h_∞^* and h_∞^{**} represent the first- and second-order coefficients of the asymptotic expansions, respectively, for the vertical-displacement LLN (i.e., $\lim_{n\to\infty} h_n' \approx h_\infty^* + \frac{1}{n} h_\infty^{**}$), and l_∞^* and l_∞^{**} represent the first- and second-order coefficients of the asymptotic expansions, respectively, for the horizontal-displacement LLN (i.e., $\lim_{n\to\infty} n l_n' \approx l_\infty^* + \frac{1}{n} l_\infty^{**}$) (Guo et al., 2004). Because the analytical expression for the second-order Legendre sum (second term in Eq. 6.6) becomes undefined for $\theta = 180^\circ$, the displacement LGFs at that angular distance are computed by extrapolation of neighboring values with a resolution of 1 in 1000 (Guo et al., 2004).

Since estimates of site positions derived from analysis of GPS observations are usually referred to the center of mass of the entire Earth system (CM) (e.g., Wu et al., 2012; Agnew, 2015), we convert the LGFs, computed initially in a solid-Earth centered (CE) reference frame, to the CM reference frame by making the appropriate modifications to the degree-one LLNs (Blewitt, 2003):

$$\begin{aligned} [h_1']_{CM} &= [h_1']_{CE} - 1 \\ [l_1']_{CM} &= [l_1']_{CE} - 1 \\ [1 + k_1']_{CM} &= [1 + k_1']_{CE} - 1. \end{aligned} \tag{6.7}$$

To predict SML-induced surface displacements for a load of finite size, we convolve the

displacement LGFs with a model for the surface mass load (e.g., Farrell, 1973; Baker, 1984; Agnew, 2015). The equation for the predicted displacement response is given by:

$$U(r, S, \rho_z, Z) = \int_{\Omega'} G(|r - r'|, S)\ \rho_z(r')\ Z(r')\ d\Omega', \tag{6.8}$$

where U is the SML-induced surface displacement at observation point r, ρ_z is the mass density of the load at the load point r', G is the LGF representing the displacement response of a radially symmetric Earth to a 1-kg point-load, and Z represents the height of the load at point r'. The integral is taken over the entire surface of the Earth, Ω'. Note that the LGF depends on distance to the load as well as Earth structure, S, which varies with radius inside the SNREI Earth (e.g., PREM). Thus, the predicted response, U, depends on the position of the measurement site relative to the applied load as well as on Earth structure and the particular load model.

For the special case of OTL, ρ_z is the density of seawater, Z is complex-valued to represent both the amplitude and phase of the tide height, and the integral is evaluated only over the surface area of the oceans. Since ocean tidal loads are complex-valued, U also becomes complex-valued, returning both amplitude and phase components for the predicted OTL-induced surface displacements. The frequency of the response is equivalent to the frequency of the tidal harmonic.

To complete the work flow, we compute the entire forward model, from integration of the equations of motion to the convolution of the LGFs with a load model, within our `LoadDef` software. Our evaluation of Eq. 6.8, however, is closely modeled after the `SPOTL` package (Agnew, 1997, 2012). In particular, `LoadDef` adopts a station-centric template grid, which simplifies the ability to refine the integration grid around a station, include multiple loading models, and compute specific LGFs at the grid nodes (Goad, 1980; Agnew, 1997, 2012).

Since the mass loads that we consider are confined to Earth's surface, Eq. 6.8 may be expanded as (e.g., Harrison, 1985; Agnew, 1997):

$$U(r, S, \rho_z, Z) = \int_0^{2\pi} \int_0^{\pi} G(\theta, S)\ \rho_z(\theta, \alpha)\ Z(\theta, \alpha)\ T(\alpha)\ a^2 \sin\theta\ d\theta\ d\alpha, \tag{6.9}$$

where θ is the angular distance between the observer at r and a particular load point; $T(\alpha)$ is a trigonometric factor used to decompose the predicted horizontal displacements into separate vector components (for the vertical displacements, $T(\alpha) = 1$); α is the azimuth of a particular load point relative to the observer, measured clockwise from north; and a is Earth's radius. Note that for a station-centered template grid, the station is considered to be located at the pole of a spherical coordinate system, where θ is the polar angle and α is the azimuthal angle.

We evaluate Eq. 6.9 using numerical integration methods. Specifically, we discretize the surface integral into finite-sized cells and evaluate the integrand at the midpoint of each cell. Since the LGFs vary most rapidly in the near field, we increase the spatial resolution of the grid substantially in the immediate vicinity of the station (measurement site) by reducing the increment in the polar angle, $\Delta\theta$. The increment in the polar angle may be greater in the far field since changes in the LGF as a function of θ, as well as the absolute value of the LGF, diminish dramatically at large θ. We therefore generate an integration grid with tapered resolution as a function of distance to the station: $\Delta\theta = 0.001^\circ$, or about 100 m, within $\theta = 1^\circ$; $\Delta\theta = 0.01^\circ$ from $\theta = 1$–10°; $\Delta\theta = 0.1^\circ$ from $\theta = 10$–90°; and $\Delta\theta = 1.0^\circ$ beyond $\theta = 90^\circ$. For each θ in the integration grid, we set the increment in the azimuthal angle, $\Delta\alpha$, to 0.1°. The integration over finite grid cells alleviates the problem of the singularity in the LGFs at $\theta = 0$, which we also mitigate prior to integration using suitable normalization factors (Agnew, 1997, 2012).

Since the integration mesh is irregular, standard methods for estimating the quadrature accuracy cannot be directly applied (e.g., Press et al., 2007, Chpt. 4). Given the numerical-integration technique described above, an analytical estimation of the quadrature error would require an evaluation of the variation in the second derivative of the integrand from Eq. 6.9 over each cell. Instead, we compare predicted displacements derived from grids of different resolution to place bounds on the uncertainty in the discrete convolution. Using this strategy, we estimate that the bounds on the absolute error in the predicted displacements, U, are on the order of 0.01–0.1 mm for M_2 OTL. Furthermore, we are primarily concerned with the vector differences, $|U_1 - U_2|$, between pairs of predicted OTL-induced

surface displacements derived from different Earth models. Since the derivatives of the integrand in Eq. 6.9 do not vary much for small perturbations to Earth structure, the bounds on the quadrature error may be reduced to about 0.1 micron when considering the vector differences between pairs of predicted displacements.

In addition to quadrature errors, the discrete tide models can be imprecise near coastal boundaries. Thus, we refine the ocean-tide models around the coastlines by first extrapolating the complex-valued tide heights inland by one grid cell, then interpolating the tide model onto the integration grid, and finally applying a land-sea mask based on ETOPO1 (Amante & Eakins, 2009) in the far field and GSHHS (Wessel & Smith, 1996) within 1.5° of the measurement site. ETOPO1 provides global topographic and bathymetric relief information at 1 arc-minute resolution. The Global Self-consistent, Hierarchical, High-resolution Shoreline database (GSHHS) provides global shoreline information, which we adopt at full resolution. Around the Antarctic, we allow the ocean-model grid to define the coastline since ETOPO1 registers floating ice shelves as landmasses, but the tides remain active in those regions.

Although the tide models, method of coastline refinement, and adopted values for seawater density have been shown to generate erroneous OTL-induced displacement predictions at the level of ≈1–5% (e.g., Bos & Baker, 2005; Penna et al., 2008), here we only consider the differential displacement response. Thus, our results are not sensitive to the usual, and often dominant, sources of prediction error. In other words, we focus on perturbing the structural properties of the solid Earth, while keeping the load model, load density, and convolution procedure consistent throughout each comparison.

6.4 Results

6.4.1 Love Number Sensitivities

We first explore the sensitivity of Love numbers to perturbations in the elastic moduli, μ and κ, and density, ρ. The sensitivity kernels, K, are computed as:

$$K^j_{p,H} = \frac{H(\mathbf{m} + \Delta\mathbf{m}^j_p) - H(\mathbf{m})}{\Delta\mathbf{m}^j_p} = \frac{\Delta H}{\Delta\mathbf{m}^j_p}, \tag{6.10}$$

where j corresponds to a particular perturbed layer, p corresponds to the model parameter being perturbed (μ, κ, or ρ), and H corresponds to a particular Love number, which depends on Earth structure, $\mathbf{m}$. The perturbation to structure, $\Delta\mathbf{m}^j_p$, involves a perturbation to the p model parameter in layer j; all other model parameters remain unperturbed.

The sensitivity kernels may be computed both numerically (Ito & Simons, 2011) and quasi-analytically (Okubo & Saito, 1983; Okubo & Endo, 1986; Okubo, 1988a). For the numerical computation, we derive the Love numbers using two Earth models, the reference model and the perturbed model, and compute the finite differences explicitly. For the quasi-analytical computation, we follow the procedure of Okubo & Saito (1983) to derive the partial derivatives of the Love numbers, supplemented by the theory of Okubo & Endo (1986) for the special case of spherical harmonic degree $n = 1$. We consider only perturbations to the solid mantle and disregard the core regions. Unlike the SEBTs, the deformational influence of OTL is concentrated primarily within the upper mantle and crust, thereby justifying our neglect of perturbations to core structure (e.g., Ito & Simons, 2011; Bos et al., 2015).

The quasi-analytical technique, which is rooted in variational calculus, employs the same approach used to derive partial derivatives of surface-wave phase velocities in seismology (e.g., Jeffreys, 1961; Takeuchi & Saito, 1972). In particular, the method takes advantage of Rayleigh's principle to estimate variations in the LLNs due to small perturbations in the elastic and density structure, without relying on numerical differentiation (Okubo & Saito, 1983).

Integrated combinations of the partial derivatives yield the predicted variations in the Love

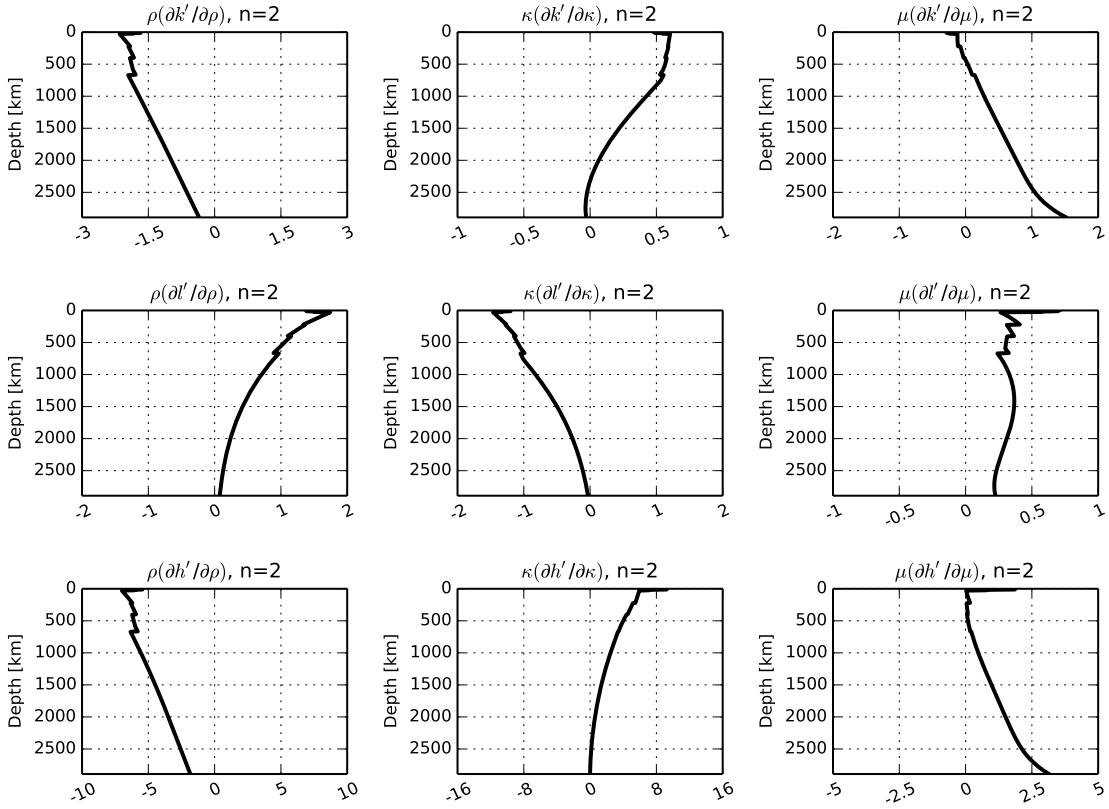

Figure 6.1: Partial derivatives of degree-2 load Love numbers with respect to the shear modulus, μ, the bulk modulus, κ, and density, ρ, for Earth model PREM (Dziewonski & Anderson, 1981). The partials have been multiplied by the depth profile of each elastic parameter, making them dimensionless. The horizontal axes are in units of 10^{-4} km^{-1}. The figure may be compared with fig. 1b in Okubo & Saito (1983), which was computed for Earth model 1066A.

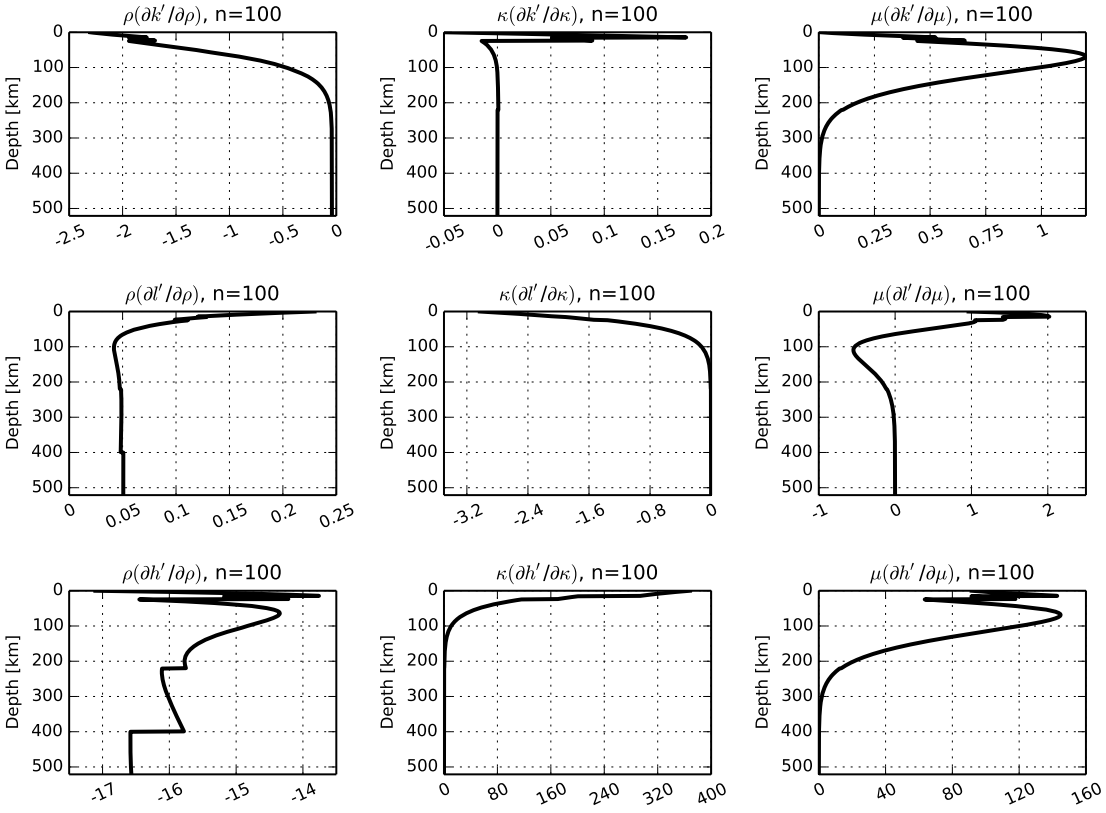

Figure 6.2: Same as Fig. 6.1, but for spherical harmonic degree n=100. Note that the sensitivity drops off rapidly beneath about 300 km depth from the surface. Perturbations to the density structure at deeper depths continue to affect the load Love numbers due to the associated change in mass.

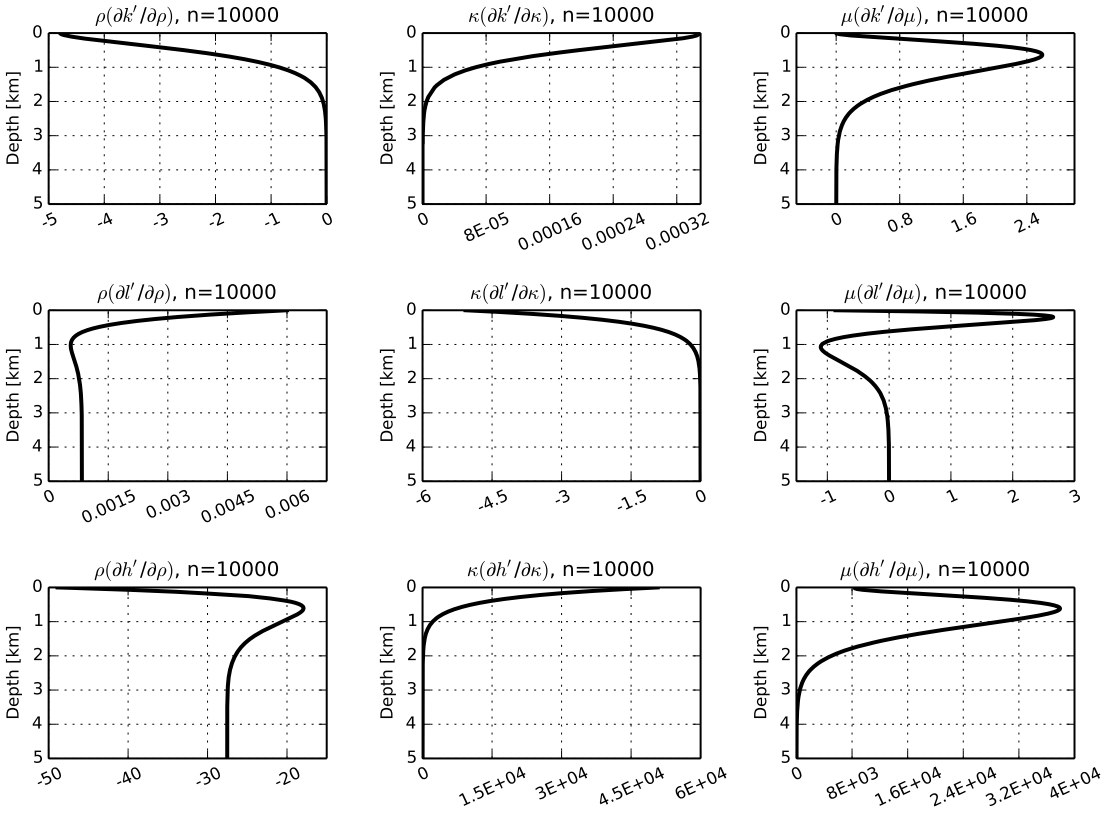

Figure 6.3: Same as Fig. 6.1, but for spherical harmonic degree n=10000. Note that the sensitivity drops off rapidly beneath about 3 km depth from the surface. Perturbations to the density structure at deeper depths continue to affect the LLNs due to the associated change in mass. Furthermore, we note that the magnitude range of the partial derivatives for the vertical-displacement load Love number, h', at n=10000 is significantly larger than for the lower spherical harmonic degrees (cf., Figs. 6.1 and 6.2), indicating that the sensitivities are heightened for the higher degrees, but also limited to the very near surface.

Table 6.1: Summary of surface boundary conditions and Love number definitions for the cases of (A) the presence of an external gravitational potential, (B) surface mass loading, (C) surface shear forcing, and (D) surface stress conditions (Longman, 1962, 1963; Wiggins, 1968; Farrell, 1972a; Lanzano, 1982; Melchior, 1983; Okubo & Saito, 1983; Okubo & Endo, 1986; Guo et al., 2004). The surface stress solution satisfies the consistency relation and thus provides an important linearly independent solution for the evaluation of degree-1 modes (Okubo & Endo, 1986). Note that our definitions for the Love numbers and surface boundary conditions differ from Okubo & Saito (1983) by a factor of $a\,g_S$, where a is Earth's radius and g_S is the gravitational acceleration at Earth's surface.

Surface Boundary Conditions				
	(A) External Potential	(B) Surface Mass Loading	(C) Surface Shear Forcing	(D) Surface Stress ($n=1$)
y_2	0	$-g_S^2\,\frac{2n+1}{4\pi G}$	0	$-\frac{3\,g_S^2}{4\pi G}$
y_4	0	0	$\frac{(2n+1)\,g_S^2}{4\pi G\,n\,(n+1)}$	$\frac{3\,g_S^2}{8\pi G}$
$y_6+\frac{n+1}{a}\,y_5$	$(2n+1)\,g_S$	$(2n+1)\,g_S$	0	0
Love Numbers				
y_1/a	h_n	h'_n	h''_n	h'''_1
y_3/a	l_n	l'_n	l''_n	l'''_1
$y_5/(a\,g_S)$	(k_n+1)	(k'_n+1)	k''_n	k'''_1

numbers (Takeuchi & Saito, 1972; Okubo & Saito, 1983). Formally, the change in a Love number due to elastic structural perturbations is given by

$$\delta H_n = \int_{\mathrm{CMB}}^{a} \left\{ \left[\frac{\partial H_n}{\partial \rho}(r)\right]_{\kappa\mu} \delta\rho(r) + \left[\frac{\partial H_n}{\partial \kappa}(r)\right]_{\mu\rho} \delta\kappa(r) + \left[\frac{\partial H_n}{\partial \mu}(r)\right]_{\kappa\rho} \delta\mu(r) \right\} dr \tag{6.11}$$

when we use (ρ, κ, μ) as independent parameters. In Eq. 6.11, H_n represents a particular Love number (e.g., h'_n, l'_n, k'_n, h_n, or h''_n), CMB represents the core-mantle boundary, a is the Earth radius, and the partial derivatives are defined per unit thickness of the perturbed layer.

Fig. 6.1 shows partial derivatives of degree-2 LLNs based on the crust and mantle structure of PREM. The partial derivatives are computed with respect to the bulk modulus, κ, shear modulus, μ, and density, ρ. Partial derivatives of the potential, load, and shear Love numbers derived from PREM for additional spherical harmonic degrees as well as from reference Earth model 1066A (Gilbert & Dziewonski, 1975) for spherical harmonic degree 2 (cf., fig. 1 of Okubo & Saito (1983)) are provided in Appendix D. As noted by Okubo &

Saito (1983), the partial derivatives of h_2' with respect to κ and of l_2'' with respect to μ are largest in the crust due to the strong influence of compressibility and rigidity on normal and tangential tractions, respectively, applied at the surface.

The quasi-analytical computation, although more complicated to implement than the numerical approach, reduces overall processing time since the Love numbers need only be computed once for a given Earth model. The development of the quasi-analytical approach outlined by Okubo & Saito (1983), however, involves a Taylor series expansion truncated to first-order. To investigate the consequences of a first-order truncation to the series on the computed sensitivities, we compare the quasi-analytically and numerically derived partial derivatives of degree-2 LLNs for a homogeneous sphere model in Table 6.2. Specifically, we compare ratios of the quasi-analytical partial derivatives to the numerical partial derivatives for a variety of model-parameter perturbations.

Note that we compute the quasi-analytical partial derivatives independent of any specified perturbation to a model parameter, since the quasi-analytical approach avoids explicit numerical differentiation (Jeffreys, 1961). For linear perturbations to the model parameters of 1% or less, the quasi-analytically and numerically derived LLN partial derivatives of degree-2 differ by less than about 1%. On the contrary, for 10% perturbations to the model parameters, the two methods of computation generate LLN partial derivatives that differ on the order of 10%.

Partial derivatives of the LLNs at higher degrees are shown in Figs. 6.2 and 6.3 as well as in Appendix D. As the spherical harmonic degree increases, the "skin depth" of the sensitivity decreases. For n=100 (Fig. 6.2), the sensitivity of the LLNs to perturbations in the elastic moduli effectively drops to zero ($<10^{-4}$ of the peak sensitivity) below about 300–400 km depth; for n=10000 (Fig. 6.3), the sensitivity effectively drops to zero below about 3–4 km depth. The observations are not surprising, since the load-induced displacements are proportional to $(r/a)^n$, where r is a particular radius within the Earth, a is Earth's radius, and n is the spherical harmonic degree (e.g., Farrell, 1972a). Note as well the significant increase in peak sensitivity at higher degrees. The most striking variations in peak sensitivity occur for the partial derivatives of the vertical-displacement LLN, h', with respect to

Table 6.2: Comparison of degree-2 load Love number partial derivatives for a homogeneous sphere, computed quasi-analytically using calculus of variations (Okubo & Saito, 1983) and numerically using finite differences. The model parameters considered here are the shear modulus, μ, bulk modulus, κ, and density, ρ. The original (unperturbed) homogeneous sphere has properties of V_P = 10000 m s^{-1}, V_S = 5000 m s^{-1}, and ρ = 5000 kg m^{-3}. The perturbations are computed as a linear percentage of the original model and applied to the entire sphere. All parameters were normalized: μ and κ by a factor $[\bar{\rho} \times a^2 \times \bar{t}^{-2}]$ and ρ by a factor $\bar{\rho}$, where a is Earth's radius (6371000 m), $\bar{\rho}$ is Earth's approximate mean density (5500 kg/m^3), and $\bar{t} = \frac{1}{\sqrt{\bar{\rho}\pi G}}$. The Love numbers are, by definition, non-dimensional. Note that the quasi-analytical partial derivatives are derived independent of a specified perturbation to the elastic parameters (i.e., they do not require explicit numerical differentiation).

		Magnitude of Linear Perturbation					
		+0.1%	**+0.5%**	**+1.0%**	**+5.0%**	**+10.0%**	**+20.0%**
	Quasi-Analytical Solution	**Ratio of Quasi-Analytical to Numerical Partial Derivatives**					
$\partial h'_2/\partial \mu_{\rm norm}$	0.5891	1.0008	1.0040	1.0079	1.0396	1.0792	1.1580
$\partial l'_2/\partial \mu_{\rm norm}$	0.1292	1.0008	1.0040	1.0079	1.0396	1.0793	1.1593
$\partial k'_2/\partial \mu_{\rm norm}$	0.3374	1.0008	1.0041	1.0081	1.0405	1.0810	1.1620
$\partial h'_2/\partial \kappa_{\rm norm}$	0.2409	1.0011	1.0056	1.0113	1.0563	1.1126	1.2251
$\partial l'_2/\partial \kappa_{\rm norm}$	-0.0851	1.0011	1.0056	1.0113	1.0563	1.1126	1.2252
$\partial k'_2/\partial \kappa_{\rm norm}$	0.0194	1.0011	1.0057	1.0113	1.0566	1.1132	1.2263
$\partial h'_2/\partial \rho_{\rm norm}$	-1.3124	0.9980	0.9957	0.9929	0.9703	0.9423	0.8865
$\partial l'_2/\partial \rho_{\rm norm}$	0.1050	0.9994	0.9891	0.9765	0.8821	0.7793	0.6129
$\partial k'_2/\partial \rho_{\rm norm}$	-0.4139	0.9974	0.9962	0.9947	0.9829	0.9687	0.9408

perturbations in the two elastic moduli (cf., Figs. 6.1, 6.2, and 6.3). The characteristic profiles of the LLN partial derivatives allow us to both visualize and quantify the sensitivity of the Love numbers to perturbations applied to individual structural parameters at each depth and for each spherical harmonic degree.

The work done to compute the LLN partial derivatives may be extended without much additional effort to compute partial derivatives of the potential and shear Love numbers as well (Okubo & Saito, 1983). We show partial derivatives of the potential and shear Love numbers, derived from PREM and 1066A for spherical harmonic degree 2, in Appendix D. Table 6.3 lists vertical- and horizontal-displacement potential Love numbers, h and l, for several seismologically derived Earth models.

Table 6.3: Degree-2 potential Love numbers for several seismologically derived SNREI Earth models.

Model	h_2	l_2
PREM	0.6067	0.0841
STW105	0.6078	0.0839
AK135f	0.6074	0.0847
SNA	0.6069	0.0844
CR	0.6054	0.0837
1066A	0.6130	0.0851

6.4.2 Load Green's Function Sensitivities

We now consider the influence of small (1%) perturbations in the elastic and density structure on the displacement LGFs (Eqs. 6.5 and 6.6). To illustrate our methodology, we first perturb the bulk modulus, shear modulus, and density separately for a single layer of PREM within the upper mantle (6291–6346.6 km). We adopt an isotropic and oceanless version of PREM as our reference model (see Appendix A for details). Since the two elastic moduli and density are Jeffrey's parameters (Tarantola, 2005), we parameterize the variables in common-log space.

We apply perturbations in the amount of $\Delta \mathbf{m}_p^j = \log_{10}(1.01)$ to the two elastic moduli and density of the reference model independently while holding the other two parameters fixed, thus generating three new Earth models that are perturbed with respect to PREM. The perturbation of $\Delta \mathbf{m}_p^j = \log_{10}(1.01)$, where j represents the perturbed region from 6291–6346.6 km and p represents the model parameter (κ, μ, or ρ), corresponds to a +1% linear perturbation to the original material properties. The four Earth models (original PREM and three perturbed) are shown in Fig. 6.4.

The four Earth models may now be used to compute four sets of displacement LGFs. The direct differences between the three perturbed and the unperturbed displacement LGFs are shown in Fig. 6.5. We scale the displacement LGFs by a conventional factor of $10^{12} a\theta$ (solid lines in Fig. 6.5), where a is Earth's radius and θ is the angular distance between the load point and the measurement site, to mitigate the singularity at the load point and to accentuate mid- and far-field features of the LGFs that are otherwise difficult to discern.

We note, however, that multiplying the LGFs by θ can also obscure LGF differences in the near field. The near-field LGFs are particularly significant for loads approximately collocated with a measurement site, such as in the cases of local hydrological or atmospheric loading. For globally distributed loads, on the other hand, the near-field loads generally account for only a small fraction of the total load. In our development of the LGF sensitivity kernels, we typically illustrate the LGF differences using the θ-scaling convention for clarity, recognizing that sensitivities in the very near field can be more substantial than the results might suggest. For comparison, we show LGF differences that are both scaled (solid lines) and unscaled (dashed lines) with respect to θ in Fig. 6.5.

In general, a perturbation of 1% to the density structure in the upper mantle yields relatively small changes in the displacement LGFs in comparison to a perturbation of 1% to either the bulk or shear modulus (Fig. 6.5). Within a few kilometers of the load point, however, the sensitivity of the LGFs to perturbations in density structure increases significantly. A perturbation to the shear modulus in the upper mantle generates both positive and negative changes in the LGFs as a function of distance to the load point, with the transition between the regimes occurring at approximately the same distance to the load point as the depth of the perturbation. Moreover, positive perturbations to the bulk modulus in the upper mantle generate predominantly positive differences between the perturbed and unperturbed LGFs. For SML-induced vertical depressions (i.e., negative-valued LGFs), a positive change in the LGFs indicates less deformation, or a smaller vertical displacement.

We now expand upon the direct differences between displacement LGFs to generate sensitivity kernels from finite differences. The sensitivities of displacement LGFs to small perturbations in the elasticity and density parameters are computed according to the equation:

$$K^j_{p,G}(\theta) = \frac{G(\theta, \mathbf{m} + \Delta\mathbf{m}^j_p) - G(\theta, \mathbf{m})}{\Delta\mathbf{m}^j_p} = \frac{\Delta G}{\Delta\mathbf{m}^j_p} \tag{6.12}$$

where j corresponds to a particular perturbed layer, p corresponds to the model parameter being perturbed (μ, κ, or ρ), and G represents the displacement LGF (vertical or horizontal), which depends on Earth structure, $\mathbf{m}$, and the angular distance between the load and the observer, θ. The perturbation to structure, $\Delta\mathbf{m}^j_p$, involves a perturbation to the model

parameter p in layer j; all other model parameters remain unperturbed.

In comparison, Ito & Simons (2011) defined their sensitivity kernels as a percentage difference between the perturbed and unperturbed LGFs, computed in response to 1% perturbations to the elastic structure. It is also worth noting that the sensitivity kernels, $K^j_{p,G}$, depend on the thickness of the perturbed layer, j, and that Eq. 6.12 does not explicitly normalize by layer thickness. Thus, we document specifically the layer thicknesses used throughout our analysis. Recall also that, since we have assumed a SNREI Earth structure, all perturbations are made to spherically symmetric shells.

Fig. 6.6 shows displacement LGFs and their corresponding sensitivity kernels, scaled by $10^{12}a\theta$, for perturbations to the bulk modulus (panels C and D), shear modulus (panels E and F), and density (panels G and H) for each of the major PREM regions above the core. We have adopted the CM reference frame for the LGF computations in order to remain consistent with conventional GPS analysis. We note, however, that the sensitivity kernels are reference-frame independent with the exception of the density kernel, which exhibits minor sensitivity differences between reference frames due to the change in total Earth mass associated with the perturbation.

We find that the magnitudes of the LGF sensitivities to perturbations in the elastic moduli are greatest when the perturbations are applied to near-surface structure and diminish with perturbations to deeper layers, even for perturbations to layers of far greater thickness than the shallowest layers. Perturbing a region as expansive as the central lower mantle (3630-5600 km), for example, yields peak sensitivities approximately an order-of-magnitude smaller than the estimated peak sensitivities for perturbations to much thinner, near-surface layers.

Furthermore, the peak sensitivity to perturbations in the elastic moduli occurs further from the load point as the perturbation depth increases. Perturbations to near-surface structure predominantly affect the LGFs in the near field, whereas perturbations to deeper structure have increasing influence over the LGFs at angular distances further from the load point. The characteristic "move-out" of the sensitivity kernels for the bulk and shear moduli could be predicted from the Love number analysis: the high-degree LLNs, which largely define

the displacement LGFs in the near field, are predominantly sensitive to near-surface structure (e.g., Fig. 6.3). The sensitivity kernels for the bulk and shear moduli exhibit strong resemblance, except the shear-modulus sensitivity transitions between positive and negative regimes whereas the bulk-modulus sensitivity remains mostly positive.

The density kernels, in contrast, exhibit peak sensitivities at short angular distances between the load point and the measurement site, regardless of perturbation depth. Moreover, perturbations to the thick central lower mantle generate the largest load-induced displacement differences. The observations are consistent with an increase to the total Earth mass that enhances the gravitational force on the applied mass load. The magnitude of density sensitivity, $K^j_{\rho,G}$, as a function of angular distance between load and observer, θ, generally follows the pattern of the original displacement LGF. In essence, the larger the magnitude of a displacement LGF at a particular angular distance, the larger the LGF sensitivity will be for a given density perturbation.

Since the layer thicknesses differ significantly among the regions of the PREM model, we also computed the LGF sensitivities for perturbations to layers of constant thicknesses. Again using the isotropic and oceanless version of PREM as our reference model, we subdivided the crust and mantle into 20-km-thick layers, or spherical shells, down to a depth of 800 km. Fig. 6.7 depicts LGF sensitivities derived from perturbations to the 20-km-thick shells. We perturbed the model parameters by an amount of $\Delta \mathbf{m}^j_p = \log_{10}(1.01)$. With the thickness of the layers held fixed, we find that the magnitude of peak sensitivity decreases with perturbation depth for the two elastic moduli and that most of the sensitivity stems from perturbations applied to the Earth's outermost 500 km. The density sensitivity, on the other hand, remains relatively constant as a function of perturbation depth. Furthermore, the sensitivity to 1% perturbations in density structure is significantly lower than the sensitivity to 1% perturbations in elastic structure.

To examine variations in the LGF sensitivities as a function of perturbation depth, Fig. 6.8 depicts slices through the sensitivity diagrams from Fig. 6.7 at an angular distance of 2.5° from the applied load. The range of the density sensitivity is far smaller than the sensitivity ranges for the two elastic moduli and, again, illustrates that the kernel remains approxi-

mately constant in magnitude regardless of the depth at which density is perturbed. The profiles also show that the density kernel remains mostly negative, the bulk-modulus kernel remains mostly positive, and the shear-modulus kernel exhibits both positive and negative sensitivity, depending on the perturbation depth. Note as well that the sensitivities are strongest within about 250 km depth from the surface, which is approximately equivalent to the distance of 2.5° between the profile line and the load point (cf., Okubo, 1988b).

For completeness, we acknowledge that alternative approaches exist for defining the model parameters. For example, rather than defining the model parameters in terms of common logarithms of the elastic moduli and density directly, one could instead use ratios of the elastic properties: $\mathbf{m}_{\mu}^{j} = \log_{10} \frac{\mu_{j+1}}{\mu_j}$, $\mathbf{m}_{\kappa}^{j} = \log_{10} \frac{\kappa_{j+1}}{\kappa_j}$ and $\mathbf{m}_{\rho}^{j} = \log_{10} \frac{\rho_{j+1}}{\rho_j}$. Reference values ($\mu_0$, κ_0 and ρ_0) must necessarily be defined for the elastic properties of the starting layer, which may be either at the top or the base of the model space in depth. According to this definition, LGF sensitivities would be computed based on perturbations to interface contrasts, rather than based on perturbations to distinct layers.

Furthermore, building upon the Love number partial derivatives, LGF sensitivities may also be computed quasi-analytically (Okubo, 1988a,b). The methodology combines the Love number partial derivatives already developed with Legendre polynomials in large algebraic expansions analogous to Eqs. 6.5 and 6.6. We defer a more complete analysis and description of the quasi-analytical LGF sensitivities to the future.

Finally, we consider the sensitivity of displacement LGFs to a variety of standard Earth models in order to obtain a general sense for the range of acceptable structural perturbations and LGF differences expected for a SNREI Earth. The models that we consider here include: PREM, STW105 (Kustowski et al., 2008), AK135f (Kennett et al., 1995), SNA (Grand & Helmberger, 1984), CR (Chu et al., 2012), and 1066A. AK135f represents the radially symmetric AK135 seismic velocity model of Kennett et al. (1995), supplemented by the density model of Montagner & Kennett (1996). PREM, STW105, AK135f, and 1066A represent globally averaged structure, whereas CR and SNA represent regional cratonic and stable North American structures, respectively. Below approximately 1000 km depth, both CR and SNA assume the structural properties of AK135f. For PREM, STW105, and

AK135f, we replaced the water layer at the surface with typical values for the upper crust: V_P=5800 m s^{-1}, V_S=3200 m s^{-1}, and ρ=2600 kg m^{-3}.

Fig. 6.9 shows profiles of the elastic moduli and density for the six reference Earth models as well as the deviation of each model from PREM. Discrepancies between the SNREI models are largest in the crust and upper mantle, primarily due to variations in crustal properties and different definitions of the Moho depth. In general, however, the differences are less than 0.05, or $\approx \log_{10}(1.1)$, which corresponds to variations in κ, μ, and ρ (in linear space) of about 10% or less at a given depth.

Fig. 6.10 shows displacement LGFs derived from each of the SNREI Earth models depicted in Fig. 6.9. The LGFs in panels C–H were multiplied by the factor $10^{12}\, a\, \theta$, whereas the LGFs in panels A and B remain unscaled with respect to θ. When the LGFs remain unscaled with respect to θ, the diminishing amplitudes of the load-induced displacements as a function of angular distance away from the load point are more apparent. Tables of the displacement LGFs and LLNs are provided in Appendix C.

Based on the direct differences between the displacement LGFs shown in Figs. 6.10G and 6.10H, we infer that the vertical-displacement sensitivities are generally larger in magnitude than the horizontal-displacement sensitivities. Sensitivities computed as a percentage difference of the reference LGF rather than a direct difference, however, are generally larger for the horizontal-displacement component (Ito & Simons, 2011). The LGFs associated with Earth model 1066A exhibit the largest differences with respect to PREM, particularly in the near-field (within 0.1° of the load point), mostly due to significant differences in the material properties of the upper crust.

In general, the LGF sensitivities for the reference Earth models tend to be largest at measurement sites within $\sim$1° of the load, and taper off substantially beyond 10°, even with perturbations to deep structure. Since we defined the globally averaged models PREM, STW105, and AK135f to have the same upper-crustal structure, the LGF differences between the models are very small in the near field and decrease toward zero as the angular distance between load and observer, θ, approaches zero. Even small perturbations to upper-crustal layers, however, can yield large variations in the LGFs at short observer-to-load

angular distances (cf., Wang et al., 2012; Dill et al., 2015; Bos et al., 2015), as exemplified by the high-degree LLNs shown in Fig. 6.3, the LGF differences between 1066A and PREM, and the LGF differences between the region-specific (CR and SNA) and globally averaged Earth models (PREM, STW105, and AK135f).

6.4.3 Predicted OTL-Induced Surface Displacements

So far, we have explored the patterns of load-induced surface displacements caused by point loads of unit mass. In reality, surface mass loads are not point sources, but rather distributed across regional and global scales. Furthermore, the mass density of a load can be highly spatially variable. Whereas the sensitivity kernels for the displacement LGFs are characterized in terms of perturbation depth and the angular distance between the point-load and the measurement site, sensitivity kernels for the surface displacements induced by a load of finite size are specific to the location of a measurement site in relation to the entire, distributed load.

Predicting the surface displacements generated by a spatially variable mass load of finite size requires a convolution of displacement LGFs with the load model (Eqs. 6.8 and 6.9). The predicted displacements depend on the spatial and temporal characteristics of the load, the LGFs derived for a particular Earth structure, and the location of the measurement site relative to the load. For the special case of OTL, measurement sites located directly adjacent to large-amplitude tides offshore tend to exhibit relatively large OTL-induced surface displacements (Fig. 6.10 and Eq. 6.8).

As an example, we consider OTL-induced surface displacements generated by the principal lunar semidiurnal (M_2) tidal harmonic. Fig. 6.11 shows a map of Iceland surrounded by the M_2 ocean tide from the TPXO8-Atlas model, which was constrained in part by empirical data from multiple satellite altimetry missions and validated against local tide gauge measurements (Egbert & Erofeeva, 2002; Egbert et al., 2010). Predicted surface displacements, produced by a convolution of the TPXO8-Atlas tide model with displacement LGFs based on PREM, are overlain on the map and depicted as particle motion ellipses (PMEs). Each of the PMEs, which are centered on the geographic locations of the prediction sites

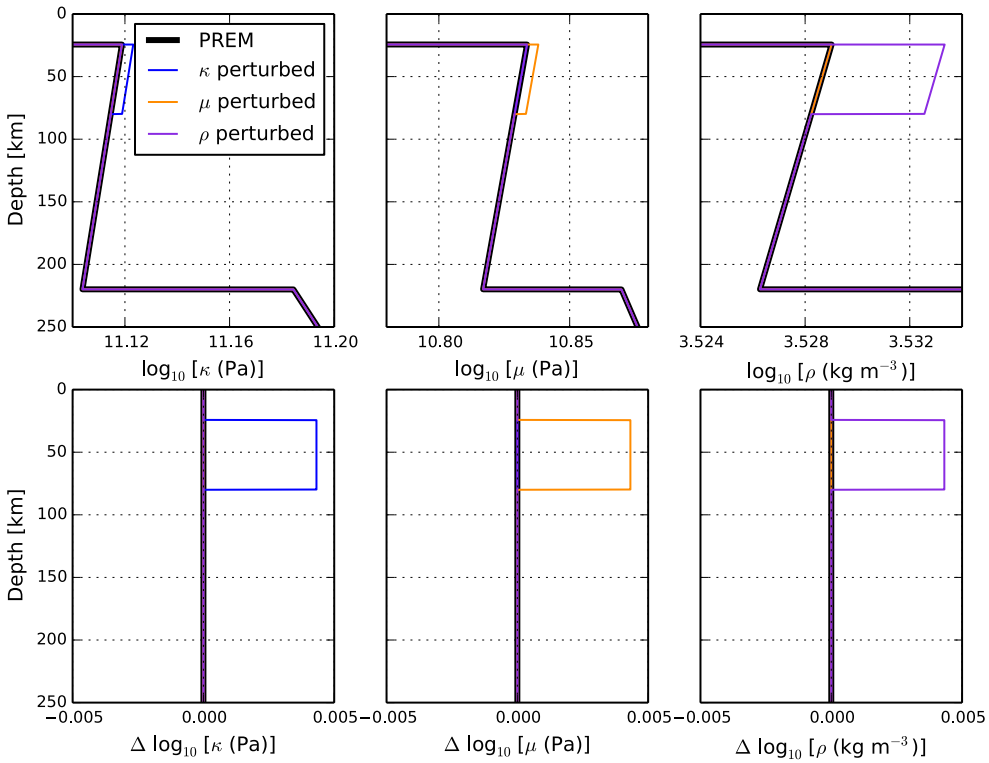

Figure 6.4: Three Earth models derived from perturbations applied to PREM in the upper mantle from 80–24.4 km depth. The top panels show profiles of the bulk modulus (left), shear modulus (center), and density (right) for each Earth model as a function of depth. The bottom panels show the differences in the bulk modulus (left), shear modulus (center), and density (right) profiles between each Earth model and the unperturbed PREM. All profiles are depicted in common-log space. To generate the three models, we perturbed the bulk modulus, shear modulus, and density separately by a factor of 1% in linear space, or $\log_{10}(1.01) = 0.0043$ in common-log space. The perturbed Earth models may be used to explore the sensitivities of load Green's functions (Fig. 6.5) and OTL-induced surface displacements (Fig. 6.18) to small perturbations in Earth structure.

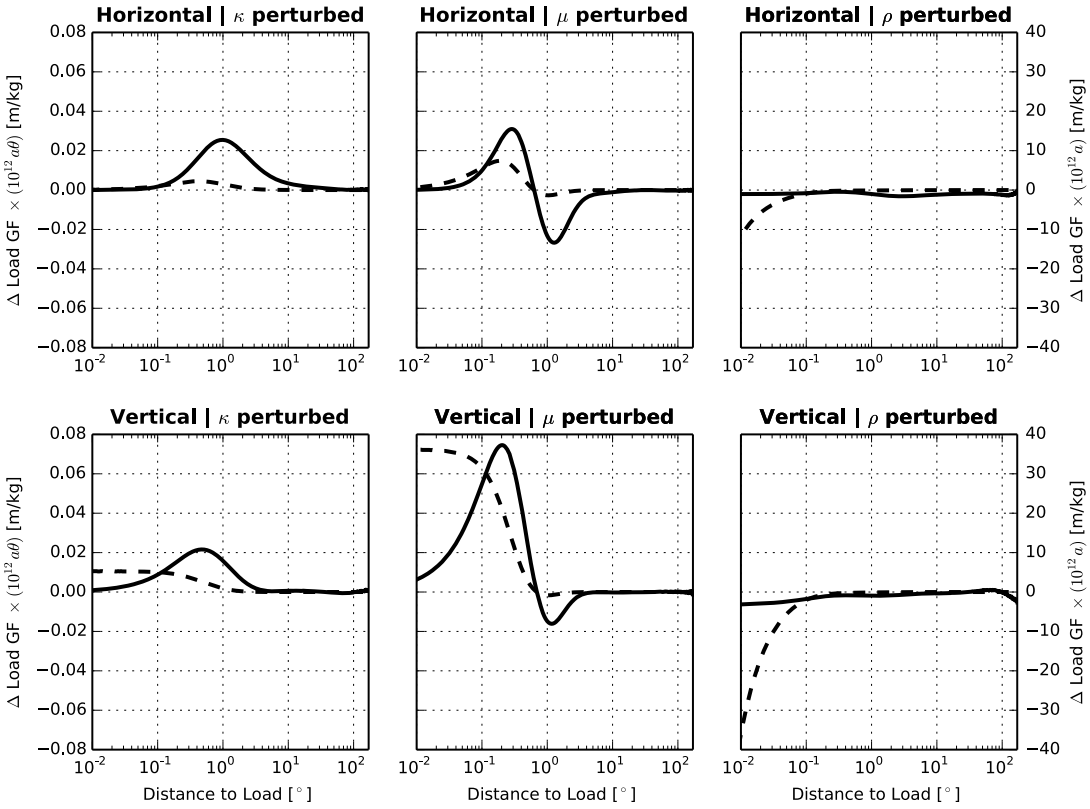

Figure 6.5: Direct differences between displacement load Green's functions derived from the three perturbed Earth models shown in Fig. 6.4 and the unperturbed PREM. The top panels show the horizontal component of the displacement LGF differences; the bottom panels show the vertical component of the displacement LGF differences. The perturbed models were generated by augmenting the bulk modulus (left), shear modulus (center), and density (right) profiles by a factor of 1% in linear space between 80 and 24.4 km depth (upper mantle). All panels are depicted on the same scale for comparison. The solid black lines show the direct LGF differences normalized by a factor of $10^{12}a\theta$, where a is Earth's radius and θ is the angular distance between the load point and the measurement site. The scales on the left pertain to the solid black lines. The dashed black lines show the direct LGF differences normalized by a factor of $10^{12}a$ (i.e., without multiplication by the angular distance, θ). The scales on the right pertain to the dashed black lines. Note that we depict the angular-distance dependence of the LGF differences on logarithmic scales.

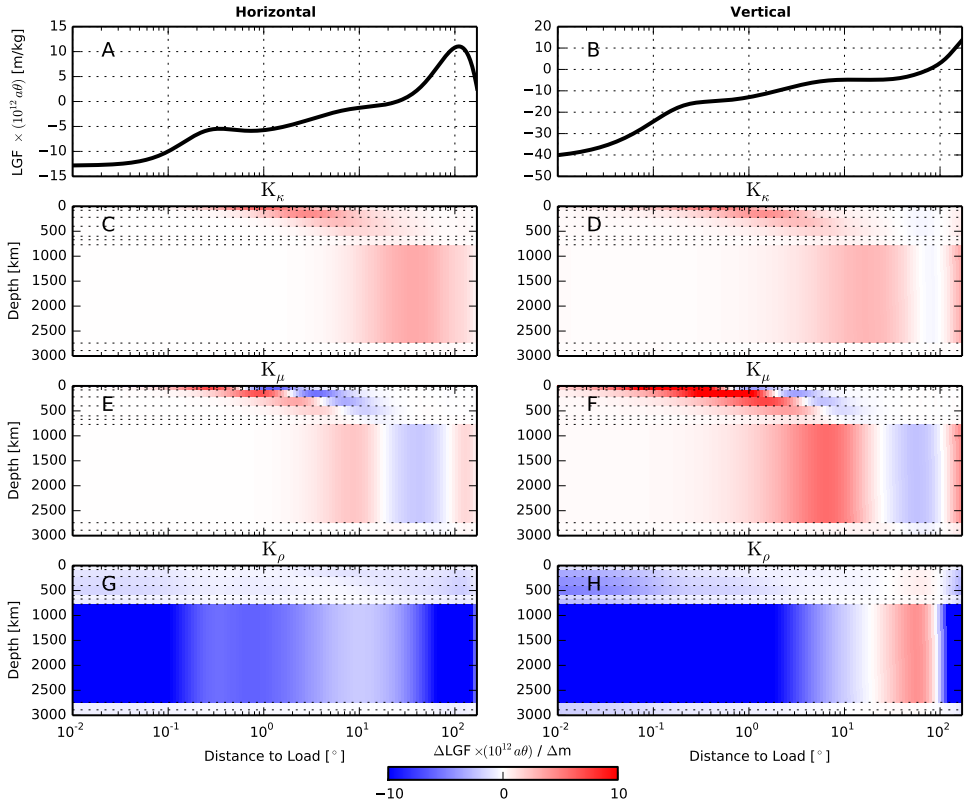

Figure 6.6: The sensitivity of displacement LGFs to perturbations in elastic structure for a radially heterogeneous Earth model. We adopt an isotropic and oceanless version of PREM as the reference model. We examine the sensitivity of the displacement LGFs to linear perturbations of 1% to the bulk modulus (panels C and D), shear modulus (panels E and F), and density (panels G and H) as a function of depth using Eq. 6.12. We independently perturb each of the major regions of PREM beyond the core as distinct blocks, separated by dashed lines in the figure. The regions include the lower mantle from 2891–2741 km depth, the lower mantle from 2741–771 km depth, the lower mantle from 771–670 km depth, the transition zone from 670–600 km depth, the transition zone from 600–400 km depth, the transition zone from 400–220 km depth, the low-velocity zone (LVZ) from 220–80 km depth, the region above the LVZ (LID) from 80–24.4 km depth, the lower crust from 24.4–15 km depth, the upper crust from 15–3 km depth, and the top layer from 3–0 km depth. Model parameters are defined in common-log space as $\mathbf{m}_\mu = \log_{10}\mu$, $\mathbf{m}_\kappa = \log_{10}\kappa$ and $\mathbf{m}_\rho = \log_{10}\rho$. The model parameter perturbation is $\Delta\mathbf{m}_p^j = \log_{10}(1.01)$. The horizontal components of the displacement LGFs and sensitivity kernels are shown in the left panels; the vertical components are shown in the right panels. The top panels (A & B) depict the the displacement LGFs in the CM reference frame derived from the reference model. The displacement LGFs, as well as the sensitivity kernels, were multiplied by the factor $10^{12}a\theta$ to remove the singularity at the load point and to scale the magnitude of the response, where a is Earth's radius in meters and θ is the angular distance from the load point in radians. Units of the unscaled LGFs are meters per kilogram.

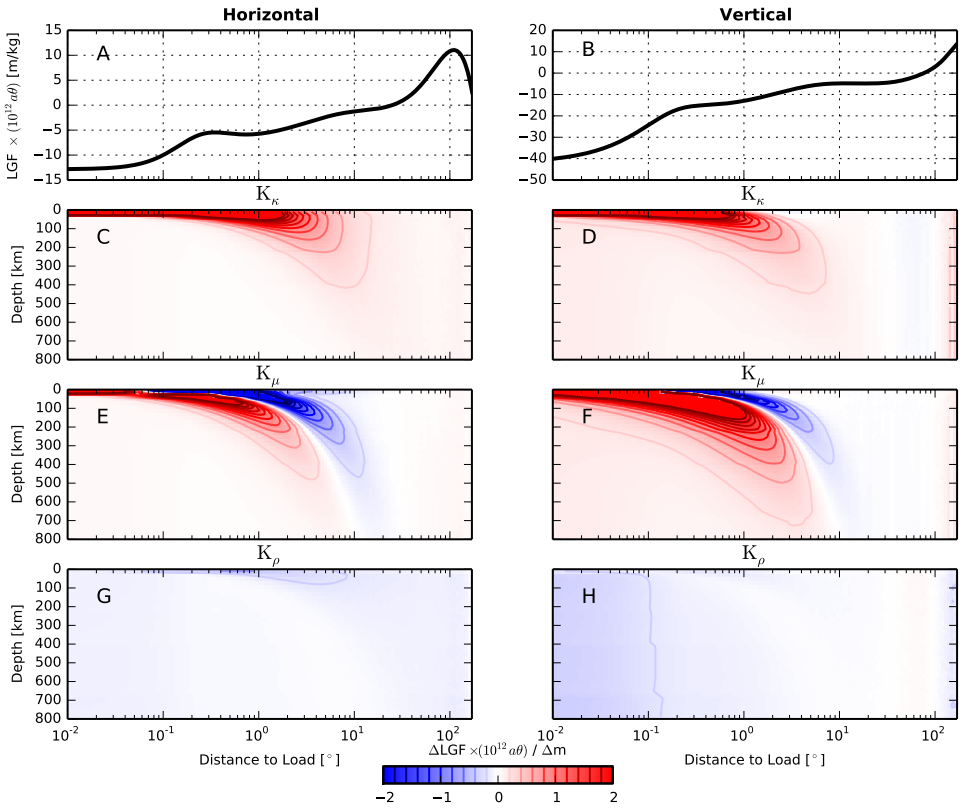

Figure 6.7: Same as Fig. 6.6, except that we have perturbed layers of constant thickness instead of the major regions of PREM. Specifically, we have partitioned the crust and mantle into a set of 20-km-thick spherical shells, which we perturb systematically down to 800 km depth. Again we adopted a model parameter perturbation of $\Delta \mathbf{m}_p^j = \log_{10}(1.01)$. Contour lines are included for clarity, with specific values denoted in the colorbar.

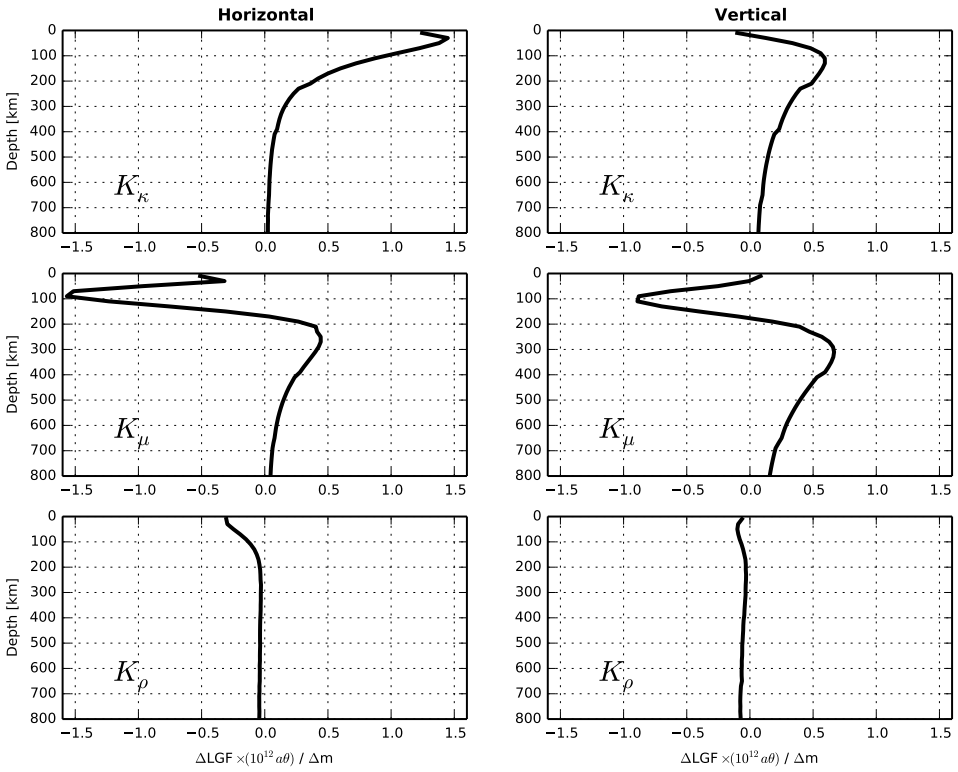

Figure 6.8: Sensitivity kernels for the displacement LGFs at an angular distance of 2.5° from the load point. The kernels depict slices through the sensitivity diagrams in Fig. 6.7 at $\theta = 2.5°$.

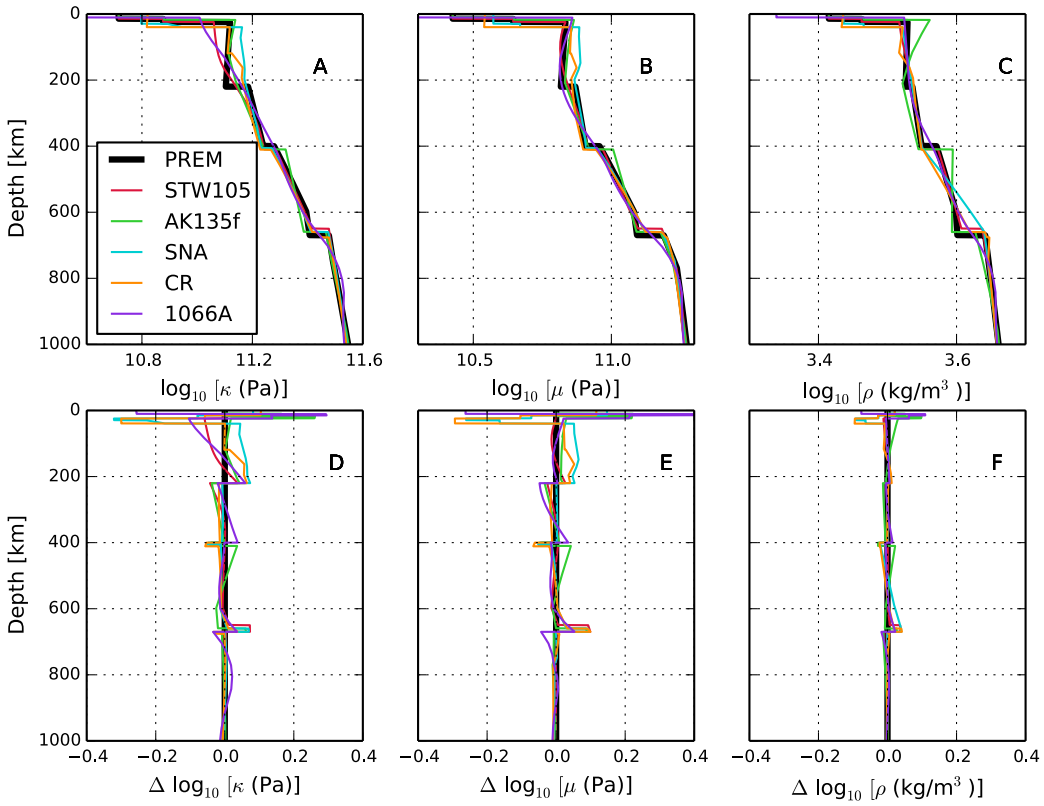

Figure 6.9: A comparison between seismologically derived Earth models: PREM (black), STW105 (red), AK135f (green), SNA (blue), CR (orange), and 1066A (purple). All models are assumed spherically symmetric, non-rotating, elastic, and isotropic (SNREI). The SNA and CR models, derived for stable North America and cratonic structures, assume a structure equivalent to AK135f below ∼1000 km depth. The top panels (A, B, & C) show profiles of the bulk modulus (κ), shear modulus (μ), and density (ρ) in log-space. The bottom panels (D, E & F) show the maximum differences between the models (in log-space) as a function of depth.

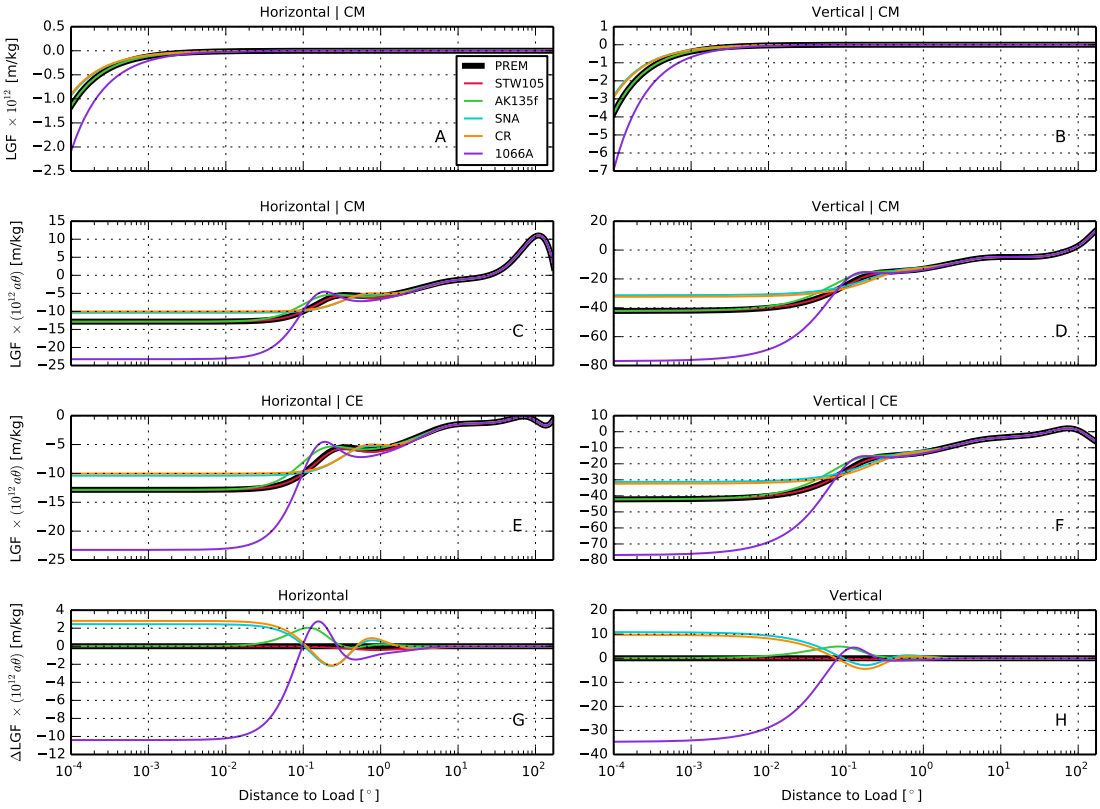

Figure 6.10: Displacement LGFs for various seismologically derived Earth models (Fig. 6.9). The top panels (A & B) show the horizontal and vertical components of the displacement LGFs, respectively, in the CM reference frame. Panels C and D reproduce panels A and B, respectively, but multiplied by an additional factor of $a\,\theta$, where a is Earth's radius and θ is the angular separation between the load point and the observer. Panels E and F show the horizontal and vertical components of the displacement LGFs, respectively, in the CE reference frame. The bottom panels, G and H, show the differences between the horizontal and vertical displacement LGFs, respectively, relative to the displacement LGFs derived from PREM. Since the total Earth mass varies only slightly between the different Earth models, the dependence of the LGF differences on reference frame is negligible.

($0.2^\circ \times 0.2^\circ$ resolution), depicts the displacement of Earth's surface due to the M_2 ocean tide. Each ellipse is traced out completely during a single tidal period of 12.42 hours.

We selected Iceland as a case study for several reasons: (1) Iceland is sufficiently small to facilitate the computation of many sets of predicted OTL-induced surface displacements along very high-resolution profiles that span from coast to coast; (2) the island is sufficiently large to examine differences in the predicted surface displacements even a couple hundred kilometers inland of the coast; (3) the amplitude of the M_2 tide is relatively large off the southwest shore of the island; (4) the amplitude of the M_2 tide is asymmetrical about the island, which allows for an examination of the effect of tide amplitude on response sensitivity, notwithstanding distance to the coast; and (5) Iceland is a place of great geophysical interest that could benefit from future tomographic inversions of observed deformation from OTL.

Fig. 6.12 shows the vector differences between pairs of M_2 OTL-induced surface displacements throughout Iceland derived from PREM and STW105. On the western coast, where the tide heights are largest, the vector differences between predicted displacements reach about 0.5 mm. Note that, since we use the same ocean-tide model and convolution procedure to generate each set of predictions, errors in the ocean-tide model and convolution scheme effectively cancel out when the predicted displacements are differenced. As mentioned previously, we estimate that the maximum quadrature error associated with computing the vector differences between pairs of predicted surface displacements, $|U_1 - U_2|$, is on the order of a fraction of a micron (Fig. 6.19).

For a $2^\circ \times 2^\circ$ global grid of land-based locations (coarsened relative to the Iceland grid for reasons of computational efficiency), 90% of the predicted M_2 OTL-induced surface displacements fall below about 3.1, 3.5, and 10.9 mm in the east, north, and vertical components, respectively. Fig. 6.13 shows the vector differences between pairs of predicted M_2 OTL-induced surface displacements derived from PREM and STW105 across the global grid as a function of distance to the nearest coastline. Histograms showing the magnitudes of the vector differences for additional SNREI-model pairs (Fig. 6.9) are shown in Fig. 6.14. Even for prediction sites located within 25 km of a coastline, the mean vec-

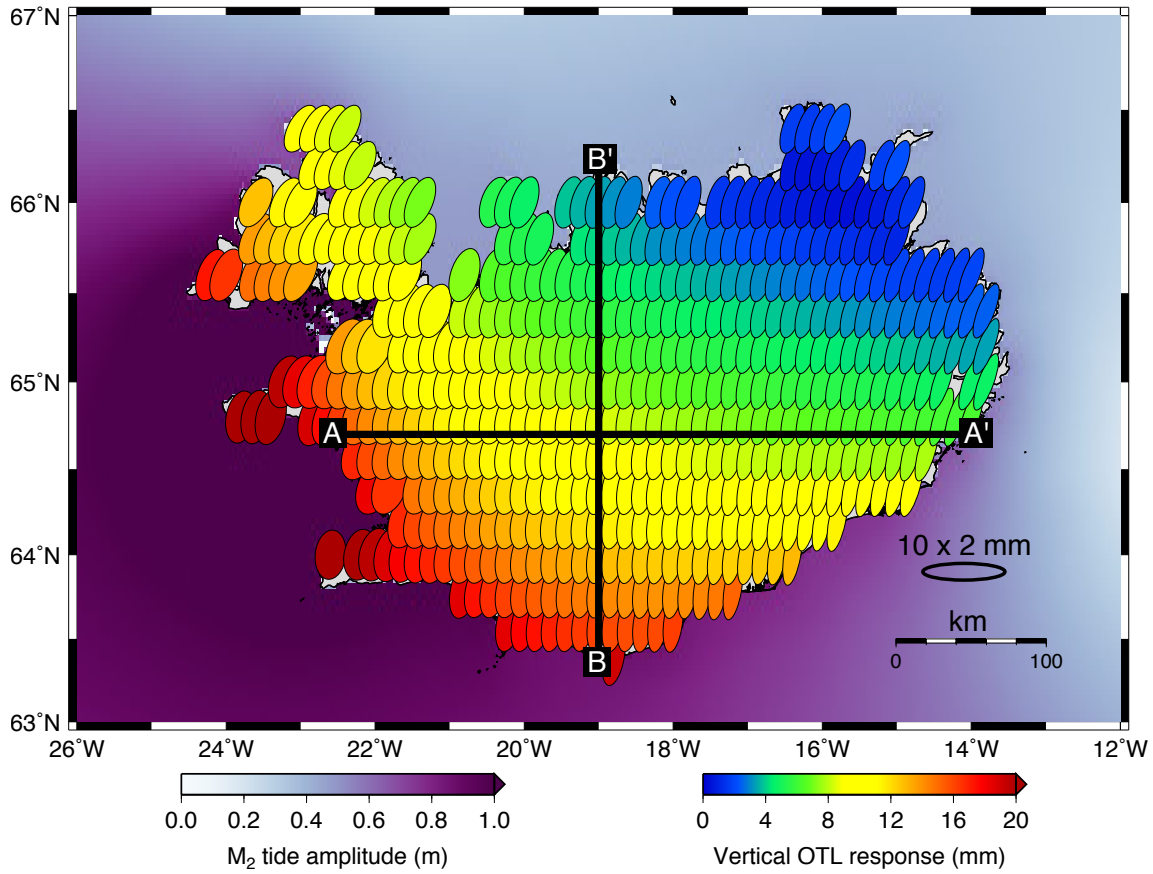

Figure 6.11: Predicted OTL-induced surface displacements for the M_2 tidal harmonic, derived from the TPXO8-Atlas ocean tide model (Egbert & Erofeeva, 2002; Egbert et al., 2010) and PREM, shown as particle motion ellipses (PMEs) on a $0.2^\circ \times 0.2^\circ$ grid across Iceland. The size and orientation of each ellipse represent the horizontal-displacement response; the color of each ellipse represents the vertical displacement response (right color bar). A reference ellipse for the horizontal motion is provided in the lower right corner of the figure. The left color bar depicts the M_2 tide amplitude in the oceans. Two profile lines (A–A′ and B–B′) are superimposed. In subsequent figures, we explore changes in predicted OTL-induced surface displacements due to small perturbations in the elastic structure of the crust and mantle at high spatial-resolution along the profile lines (Figs. 6.20–6.23).

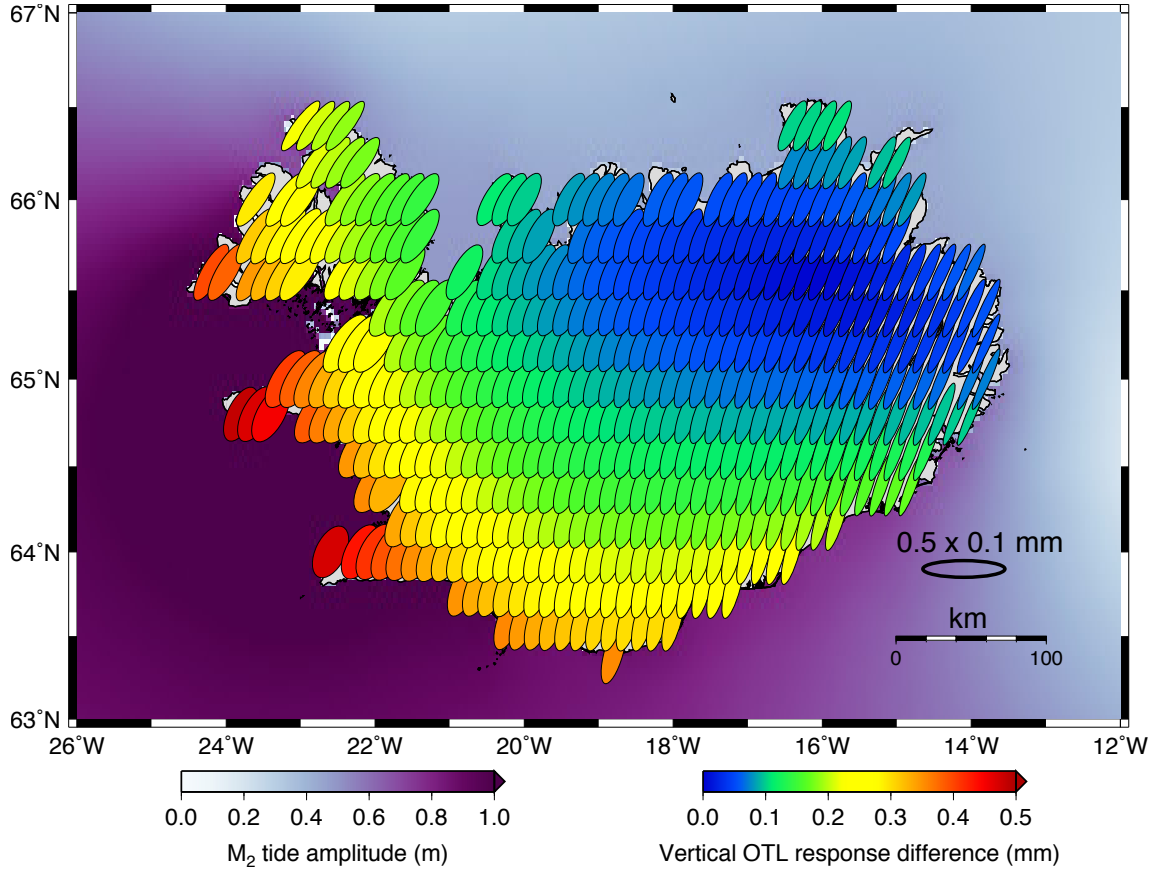

Figure 6.12: Vector differences between pairs of predicted M_2 OTL-induced surface displacements derived from PREM and STW105, shown as PMEs on a $0.2^\circ \times 0.2^\circ$ grid across Iceland. The size and orientation of each ellipse represent the differential horizontal-displacement response; the color of each ellipse represents the differential vertical displacement response (right color bar). A reference PME for the horizontal motion is provided in the lower right corner of the figure. Note the change in scale of the PMEs relative to Fig. 6.11. The left color bar depicts the M_2 tide amplitude in the oceans.

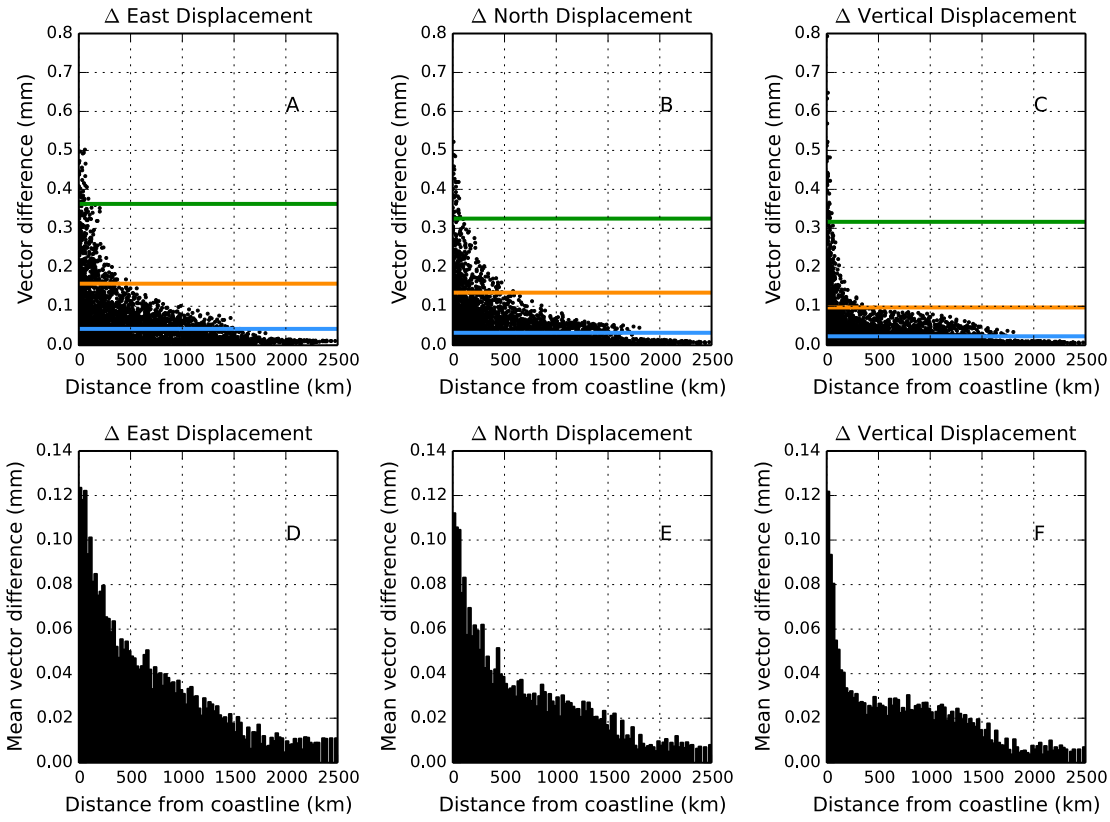

Figure 6.13: Vector differences between pairs of predicted M_2 OTL-induced surface displacements for PREM and STW105 as a function of distance to the nearest coastline. The two sets of predicted OTL-induced surface displacements (one set for PREM and one set for STW105) were computed on a $2^\circ \times 2^\circ$ global grid of land-based locations. Only the SNREI Earth model changes between the forward model computations; all other parameters, including the ocean tide model and convolution procedure, remain the same. Panels A, B, and C depict the east, north, and vertical components, respectively, of the vector differences between the pairs of predictions. The black dots indicate the vector differences for individual grid nodes. The horizontal lines in each panel represent the 50th- (blue), 90th- (orange), and 99th-percentiles (green) of the vector differences. Panels D, E, and F depict the mean vector differences as a function of distance to the coastline, computed in 25-km bins.

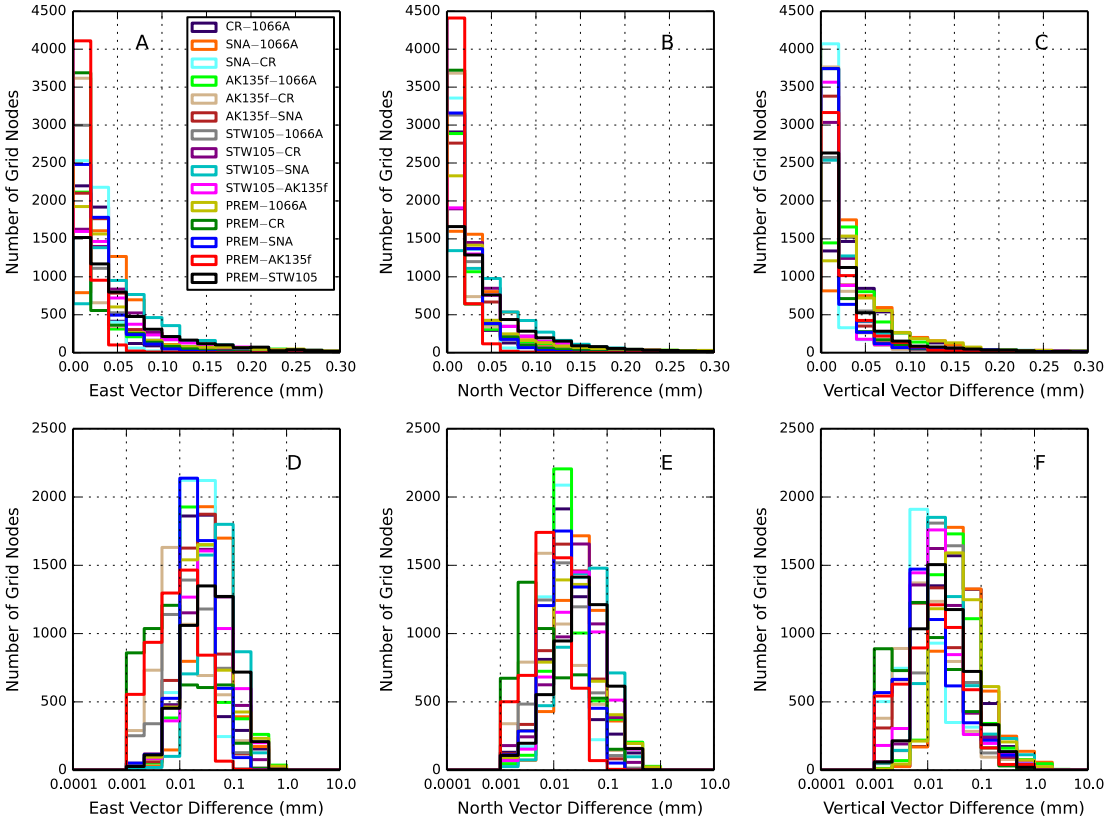

Figure 6.14: Histograms showing the magnitudes of the vector differences between predicted OTL-induced surface displacements for pairs of reference Earth models. Only the elastic Earth model changes between the forward model computations; all other parameters, including the ocean tide model and convolution procedure, remain the same. We consider only the M_2 tidal harmonic and predict the response on a $2^\circ \times 2^\circ$ global grid of land-based locations. The left, center, and right panels depict the east, north, and vertical components of the vector differences, respectively. The top row of panels shows the vector differences on a linear scale; the bottom row of panels shows the vector differences on a log scale.

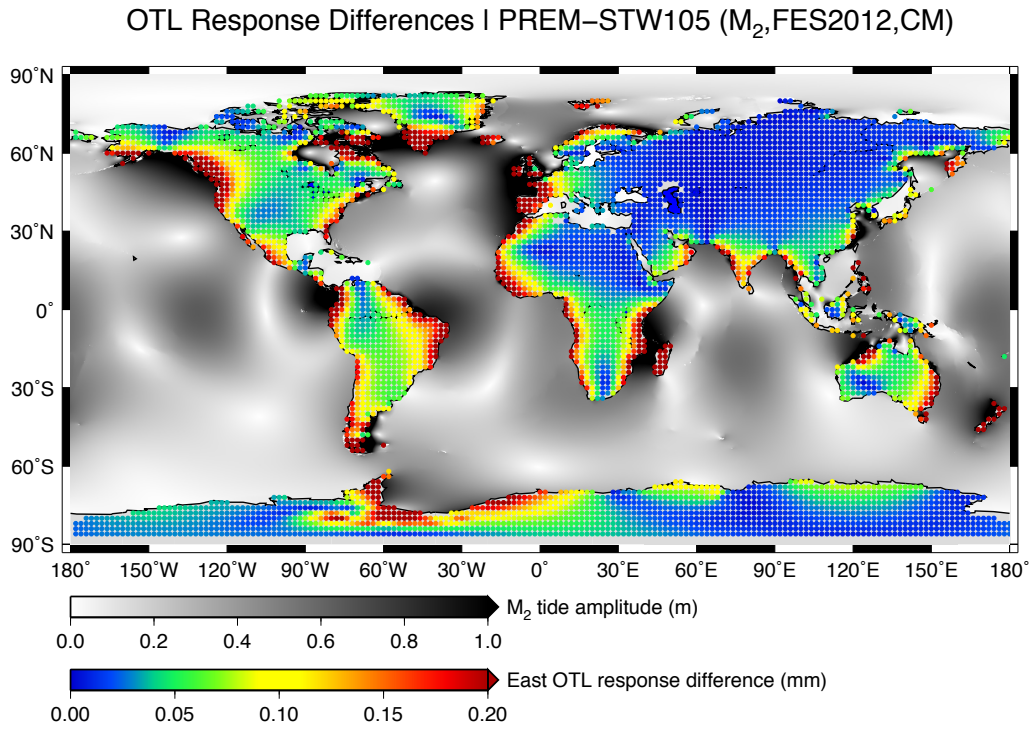

Figure 6.15: Magnitudes of the vector differences between predicted OTL-induced surface displacements in the east component across a $2^\circ \times 2^\circ$ global grid for two forward models: one computed using LGFs derived from PREM and the other computed using LGFs derived from STW105. All other parameters, including the ocean tide model (FES2012) and convolution procedure, remain consistent in each forward model computation. Histograms showing the magnitudes of the vector differences between predicted displacements for additional pairs of standard Earth models are shown in Fig. 6.14. The vector differences provide information about the sensitivity of OTL-induced surface displacements to different SNREI Earth models.

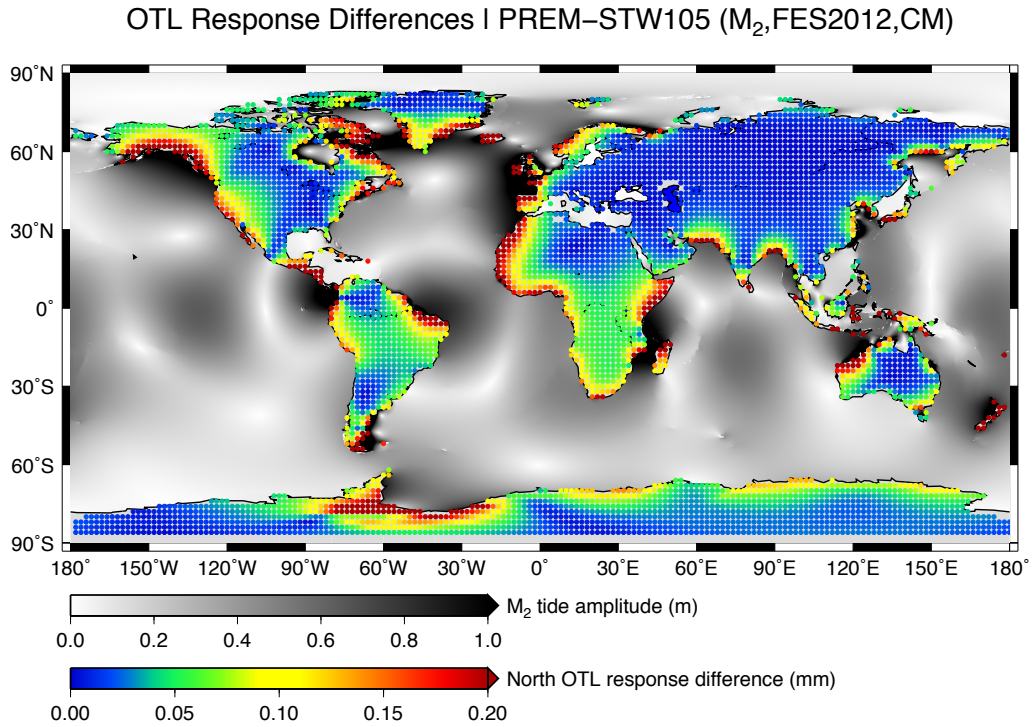

Figure 6.16: Same as Fig. 6.15, but for the north component of the predicted displacements.

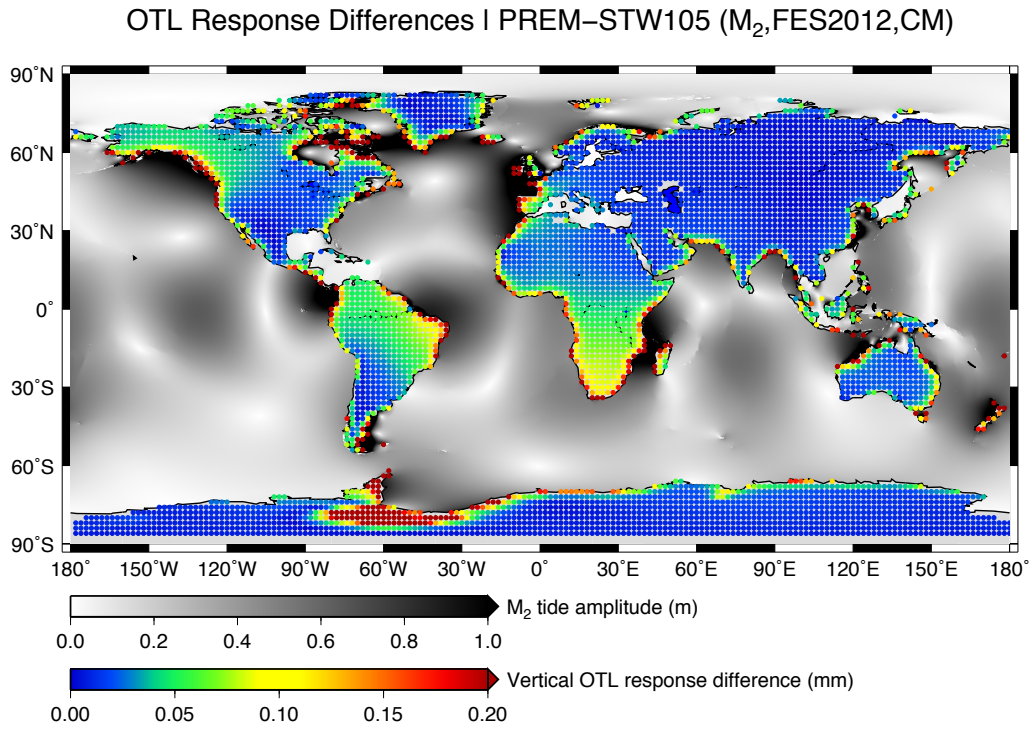

Figure 6.17: Same as Fig. 6.15, but for the vertical component of the predicted displacements.

tor difference between the PREM predictions and the STW105 predictions is only about 0.1 mm. For prediction sites located very near to the coastline and in close proximity to large-amplitude tides, however, vector differences between the OTL-induced surface displacements can reach several tenths of a mm or more (Fig. 6.12). Figs. 6.15, 6.16, and 6.17 provide a sense for the spatial variations in the predicted vector differences across the global grid ($2^\circ \times 2^\circ$), derived from PREM and STW105.

Since the various reference Earth models vary irregularly as a function of depth and model parameter, we also explore changes in OTL-induced surface displacements generated by *systematic* perturbations to elastic and density structure. Specifically, we investigate the effects of independent perturbations to the two elastic moduli and density on M_2 OTL-induced surface displacements along two high-resolution (0.01°, or $\approx$1 km) profiles through Iceland (Fig. 6.11). One of the profiles spans from west to east across the island along 64.7°N latitude (A–A′); the second profile spans from south to north across the island along 341°E longitude (B–B′).

As with the displacement LGFs (Fig. 6.5), we first consider the direct differences between OTL-induced surface displacements derived from the three perturbed models in Fig. 6.4 and unperturbed PREM. We define our model parameters in common-log space: $\mathbf{m}_\mu = \log_{10}\mu$, $\mathbf{m}_\kappa = \log_{10}\kappa$ and $\mathbf{m}_\rho = \log_{10}\rho$. Furthermore, we compute the response differences based on perturbations to the model parameters of $\Delta\mathbf{m}_p^j = \log_{10}(1.01)$, which correspond to +1% linear perturbations to the original elastic parameters.

For each prediction site along the high-resolution profiles (Fig. 6.11), the magnitudes of the vector differences between the predicted OTL-induced surface displacements derived from the perturbed Earth models and the unperturbed PREM are shown in Fig. 6.18. The procedure is analogous to the methods used to develop Fig. 6.5, although we now consider the finite-sized M_2 OTL rather than a point-source load of unit mass. For perturbations of 1% to the elastic moduli and density, the magnitudes of the vector differences are less than 0.02 mm (20 micron). Despite the extraordinarily small differences, Fig. 6.19 shows that the estimated bounds on the quadrature errors for the vector differences are sufficiently low (of order 10 nanometers) to allow for interpretation of the differences. For the vertical-

displacement component, a perturbation to the bulk modulus generates a larger change in the induced surface displacements on the western coast than on the eastern coast presumably due to the larger tidal amplitudes along the western coast. Consistent with the displacement LGFs, the 1% perturbation to density structure yields the smallest changes to the load-induced surface displacements overall. Specific details of the displacement differences along the profile, however, can be difficult to interpret, since the displacements depend on many factors, including the spatial distribution of the load relative to the prediction site and the characteristics of the LGFs as a function of distance to each load point.

We now extend our analysis of the direct vector-differences between OTL-induced surface displacements to explicit finite differences. The sensitivity kernels are given by:

$$K^{j}_{p,G}(r, \rho_z, Z) = \frac{U(r, \rho_z, Z, \mathbf{m} + \Delta\mathbf{m}^{j}_{p}) - U(r, \rho_z, Z, \mathbf{m})}{\Delta\mathbf{m}^{j}_{p}} = \frac{\Delta U}{\Delta\mathbf{m}^{j}_{p}}, \tag{6.13}$$

where j corresponds to a particular perturbed layer, p corresponds to the model parameter being perturbed (μ, κ, or ρ), and U represents a predicted OTL-induced surface displacement (Eq. 6.8), which depends on Earth structure, $\mathbf{m}$, the load model, $Z\rho_z$, and the location of the prediction site, r, relative to the load. The perturbation to structure, $\Delta\mathbf{m}^{j}_{p}$, involves a perturbation to the model parameter p in layer j; all other model parameters remain unperturbed.

Fig. 6.20 shows the sensitivity kernels for the west-to-east profile (A–A′). The results for the south-to-north profile (B–B′) are shown in Fig. 6.21. All of the sensitivity kernels, derived from Eq. 6.13, are depicted at full resolution (i.e., 0.01° spacing between prediction sites). Here, we have perturbed the major regions of PREM down to 400 km depth. Without accounting for the thickness of each perturbed layer, we find that perturbations to relatively thick layers in the upper mantle can influence the OTL-induced surface displacements more than perturbations to relatively thin layers in the crust. In particular, the sensitivity of the surface displacements to perturbations in elastic and density structure in the upper three km of the crust is weaker overall than the sensitivity to perturbations in any other layer.

In Fig. 6.22, we show the same sensitivity kernels depicted in Fig. 6.20, but normalized

by the thicknesses of the perturbed layers. Normalization by layer thickness allows us to better explore the effects of perturbation depth on the OTL-induced surface displacements. Particularly for the sensitivity of the displacements to perturbations in the shear modulus, it is apparent from Fig. 6.22 that the location of the peak sensitivity as a function of distance to the coast shifts further inland for perturbations to deeper structure. In general, perturbations to shallow crustal structure primarily affect the predicted surface displacements at coastal sites and at short wavelengths. In contrast, perturbations to mantle structure mostly affect the predicted surface displacements at longer wavelengths and beyond about 50 km inland of the coast.

Sensitivities in the vertical component tend to be higher at prediction sites on the southern and western edges of the profiles, where the tidal amplitudes are larger. Moreover, small deviations from a smooth coastline can generate jumps in the sensitivity profiles, such as when an ocean inlet is encountered on the eastern side of the profile line (e.g., Fig. 6.22). Analogous to the displacement LGFs, the sensitivity to 1% perturbations in density structure is generally weaker than the sensitivity to 1% perturbations in the elastic structure, and probably mostly reflects changes in the total Earth mass generated by the perturbation. When scaled by the layer thickness, sensitivities are typically strongest for perturbations to shallow structure, particularly near the coastlines.

It is important to note that the sensitivity kernels we present here are specific to the prediction sites that we have selected in Iceland as well as to the M_2 ocean-tide model. Thus, the sensitivity kernels for the predicted OTL-induced surface displacements across the profiles in Iceland should be considered examples, albeit illustrative and representative of the sensitivities expected for M_2 OTL in many locations around the globe.

The sensitivity kernels for the OTL-induced surface displacements (e.g., Fig. 6.20) constitute a key element in formulating the inverse problem. In particular, the kernels could be used to relate structural models to displacement observations in a linear inverse problem and to investigate the resolution of the model parameters (e.g., the two elastic moduli and density for the distinct layers of the PREM model) with application to geodetic tomography. Synthetic testing could reveal better the extent to which perturbations in the elastic

moduli and density could be resolved independently for the particular geographic locations considered and the M_2 ocean-tide model.

6.5 Discussion

We have explored the theoretical sensitivities of potential, load, and shear Love numbers as well as displacement LGFs to systematic perturbations in elastic Earth structure using both quasi-analytical and numerical techniques. Following the methodology of Okubo & Saito (1983), we developed profiles of LLN partial derivatives for a variety of spherical harmonic degrees (Figs. 6.1, 6.2, 6.3, and Appendix D). Perturbations to the elastic structure very near to the surface strongly affect the high-degree LLNs, as expected due to the short wavelengths of Legendre polynomials at large n. The high-degree LLNs are most sensitive to structural perturbations within a "skin depth" of approximately (a/n) of the surface (Okubo, 1988a), where a is Earth's radius and n is the spherical harmonic degree. The sensitivity of the high-degree LLNs to perturbations in elastic and density structure rapidly approaches zero beyond a few skin depths (Figs. 6.2 and 6.3). The density kernel constitutes an exception, since a perturbation to density at any depth generates a change in the total Earth mass.

We also computed numerically the sensitivities of displacement LGFs to systematic perturbations in elastic material properties (Figs. 6.6–6.8). The patterns of sensitivity vary as a function of perturbation depth as well as the angular distance between the measurement site and the load point for each of the three model parameters considered. The distinct patterns exhibited by each of the model parameters leave open the possibility that the two elastic moduli and density may be independently constrained through inversion of observed SML-induced surface displacements.

As a general rule of thumb, illustrated by Figs. 6.6 and 6.7, the elastic structure at a depth of D km strongly influences the displacement LGFs at a horizontal distance of D km from the load point (cf., Okubo, 1988b; Ito & Simons, 2011). We can also see from Figs. 6.6 and 6.7 that the sensitivities of SML-induced surface displacements to perturbations in density structure appear to be much weaker than for equivalent perturbations to the two elastic

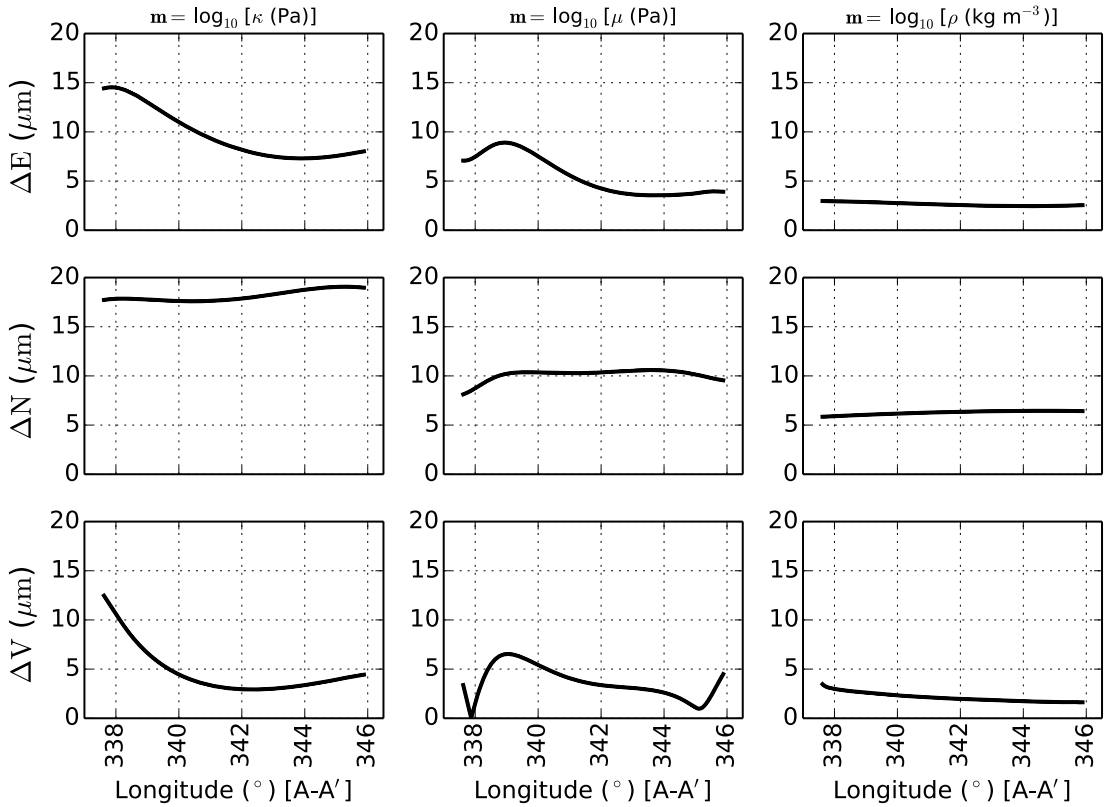

Figure 6.18: Differences between M_2 OTL-induced surface displacements derived from the three perturbed Earth models shown in Fig. 6.4 and the unperturbed PREM along the profile A–A$'$ in Fig. 6.11 at 0.01° (≈1 km) resolution. The left column of panels depicts the magnitudes of the vector differences between load-induced displacements computed from the κ-perturbed model and the unperturbed PREM. The center column of panels depicts the magnitudes of the vector differences between load-induced displacements computed from the μ-perturbed model and the unperturbed PREM. The right column of panels depicts the magnitudes of the vector differences between load-induced displacements computed from the ρ-perturbed model and the unperturbed PREM. The rows of panels show the east (top), north (center), and vertical (bottom) components of the differential displacements. The perturbed models were generated by augmenting the bulk modulus (left), shear modulus (center), and density (right) profiles by a factor of 1% in linear space between 80 and 24.4 km depth (upper mantle). All panels are depicted on the same scale for comparison; note that the units are in microns.

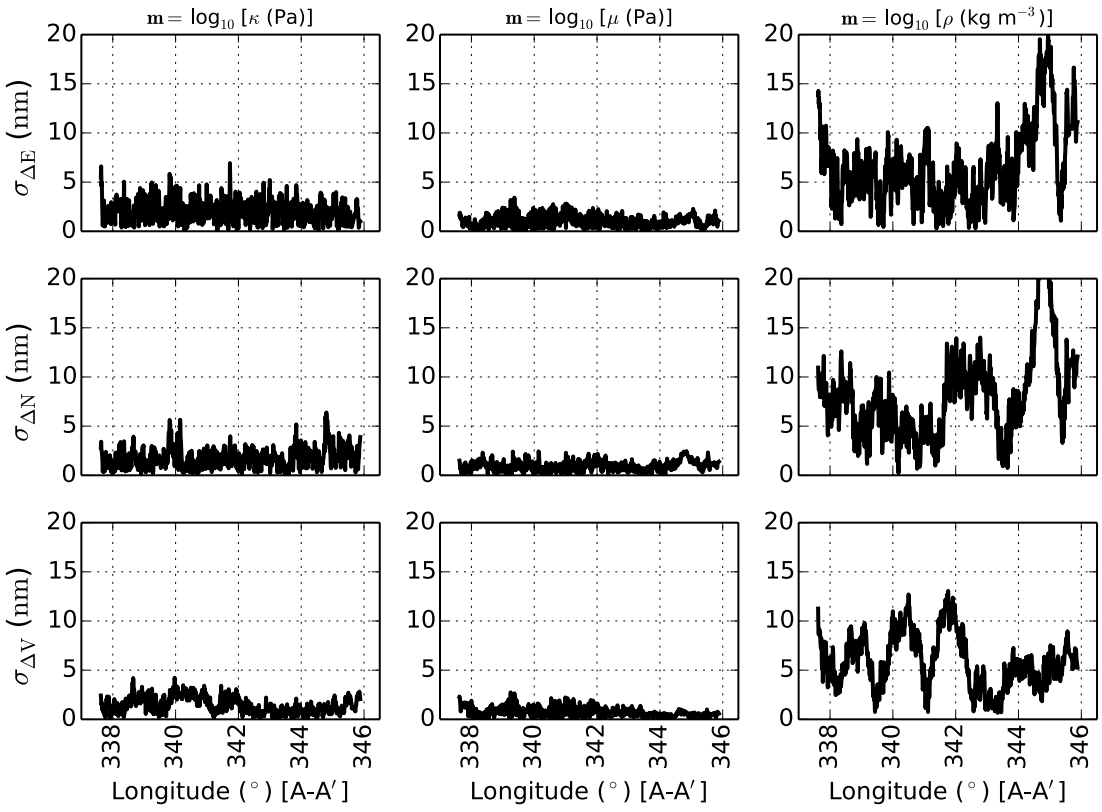

Figure 6.19: Estimated bounds on quadrature errors associated with the vector differences, $|U_1 - U_2|$, shown in Fig. 6.18. The error estimates, which correspond to the numerical uncertainties in the differences between predicted M_2 OTL-induced surface displacements, were computed along the profile A–A′ (Fig. 6.11) at 0.01° (≈1 km) resolution. All panels are depicted on the same scale for comparison; note that the units are in nanometers. We estimated the quadrature errors, σ_U, associated with deriving the predicted OTL-induced surface displacements, U, by varying the resolution of the integration grid. We then computed the vector difference between two sets of estimated errors: $\sigma_{\Delta U} = |\sigma_{U_1} - \sigma_{U_2}|$. For very small perturbations to structure, such as the 1% perturbations explored here, the higher-order derivatives of the integrand in Eq. 6.8 do not vary much. Thus, the quadrature errors also do not change much during comparisons of the different Earth models. Here, the errors do not exceed approximately 20 nm, and are therefore sufficiently small to resolve the 1–20 micron discrepancies between models shown in Fig. 6.18.

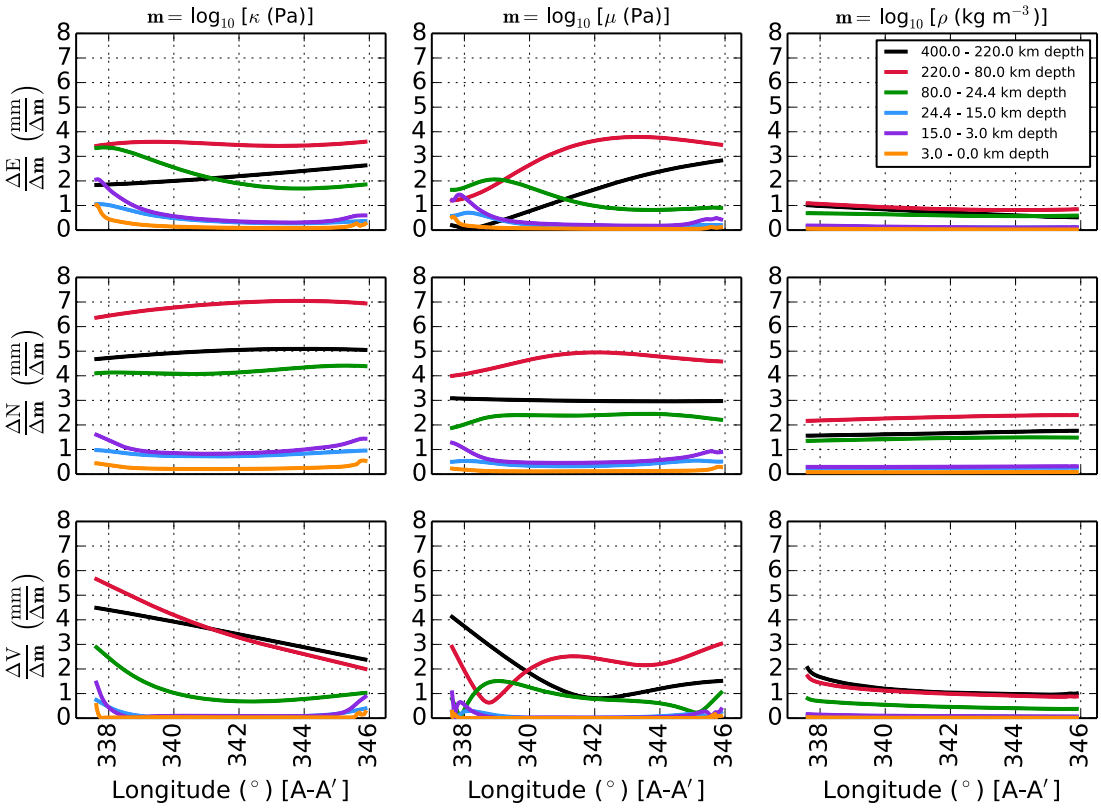

Figure 6.20: The sensitivity of predicted OTL-induced surface displacements to perturbations in elastic and density structure, computed along the profile A–A′ in Fig. 6.11. The profile maintains constant latitude at 64.7°N and a node spacing of 0.01° (≈1 km). The left column of panels shows the sensitivity of predicted surface displacements to perturbations in the bulk-modulus model parameter, $\Delta \log_{10} \kappa$. The center column of panels shows the sensitivity to perturbations in the shear-modulus model parameter, $\Delta \log_{10} \mu$. The right column of panels shows the sensitivity to perturbations in the density model parameter, $\Delta \log_{10} \rho$. In each case, we perturb the parameters by 1% in linear space, or by $\Delta \mathbf{m} = \log_{10}(1.01)$ in log space, where $\mathbf{m} = \log_{10} \kappa$, $\log_{10} \mu$, or $\log_{10} \rho$. The top, middle, and bottom rows of panels show sensitivity kernels for M_2 OTL-induced surface displacements in the east, north, and vertical components, respectively. The colored lines denote perturbations to distinct layers of PREM down to a depth of 400 km and correspond to the same layer in every panel (see legend). The sensitivity kernels are computed, separately for each layer, as the magnitudes of the vector differences between the predicted OTL-induced surface displacements (in millimeters) for the perturbed and reference (unperturbed PREM) models divided by the model-parameter perturbation, $\log_{10}(1.01)$.

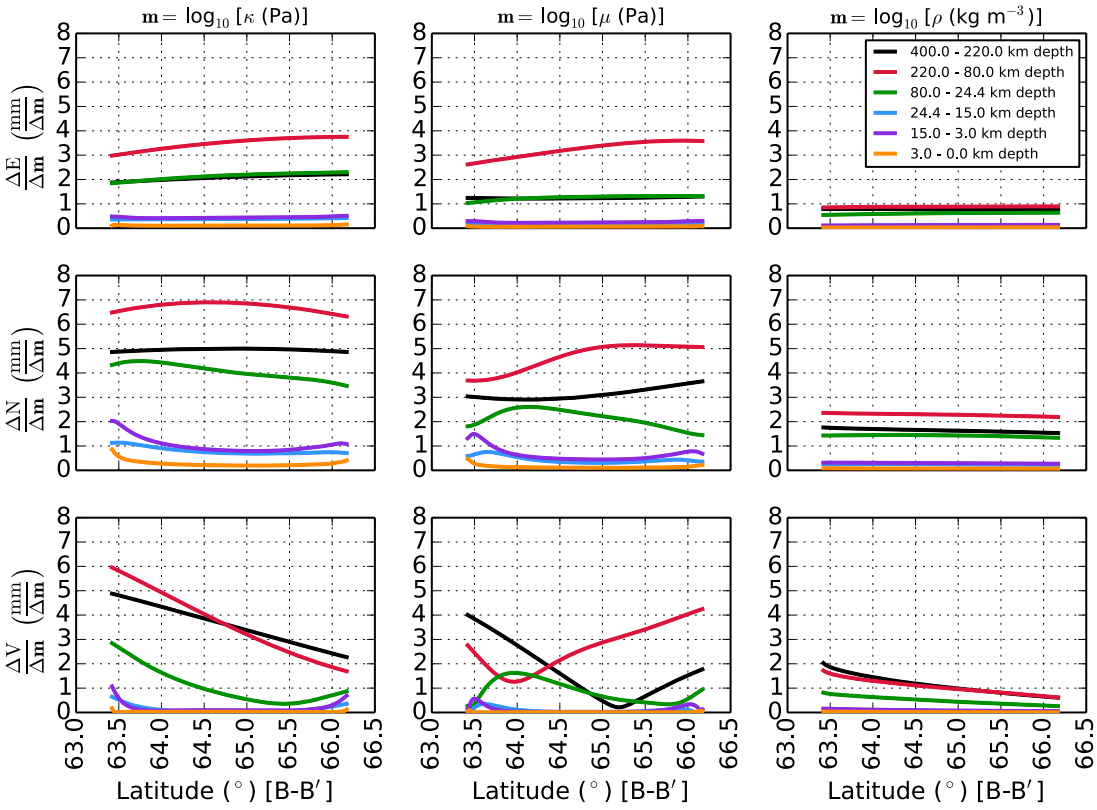

Figure 6.21: Sensitivities of OTL-induced surface displacements to perturbations in elastic and density structure along a great-circle path through Iceland (profile B–B′ from Fig. 6.11). The profile maintains constant longitude along the 341°E meridian and a node spacing of 0.01° (≈1 km). The left column of panels shows the sensitivity of predicted surface displacements to perturbations in the bulk-modulus model parameter, $\Delta \log_{10} \kappa$. The center column of panels shows the sensitivity to perturbations in the shear-modulus model parameter, $\Delta \log_{10} \mu$. The right column of panels shows the sensitivity to perturbations in the density model parameter, $\Delta \log_{10} \rho$. In each case, we perturb the parameters by 1% in linear space, or by $\Delta \mathbf{m} = \log_{10}(1.01)$ in log space, where $\mathbf{m} = \log_{10} \kappa$, $\log_{10} \mu$, or $\log_{10} \rho$. The top, middle, and bottom rows of panels show sensitivity kernels for M_2 OTL-induced surface displacements in the east, north, and vertical components, respectively. The colored lines denote perturbations to distinct layers of PREM down to a depth of 400 km and correspond to the same layer in every panel (see legend). The sensitivity kernels are computed, separately for each layer, as the magnitudes of vector differences between the predicted OTL-induced surface displacements (in millimeters) for the perturbed and reference (unperturbed PREM) models divided by the model-parameter perturbation, $\log_{10}(1.01)$.

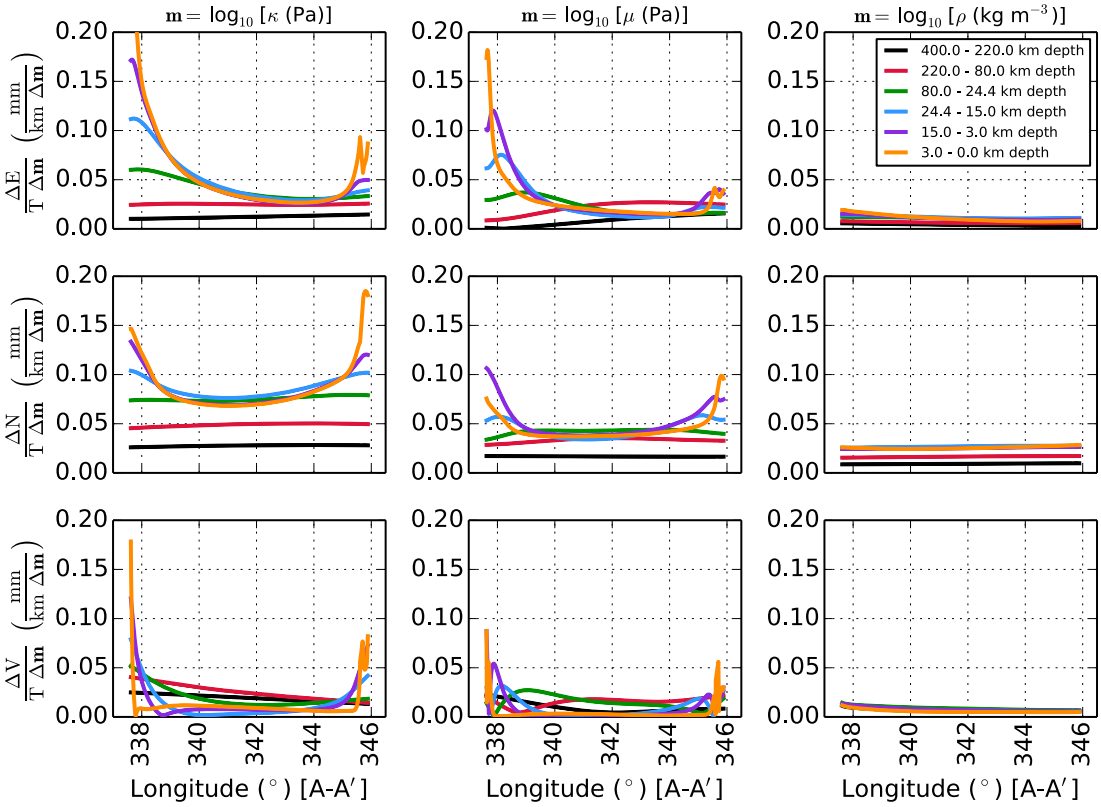

Figure 6.22: Same as Fig. 6.20, but normalized by the layer thickness, T, in kilometers. The discontinuous jump in the sensitivity just west of 346°, derived from perturbed upper crustal structure (orange line), is caused by the presence of an ocean inlet encountered along the profile.

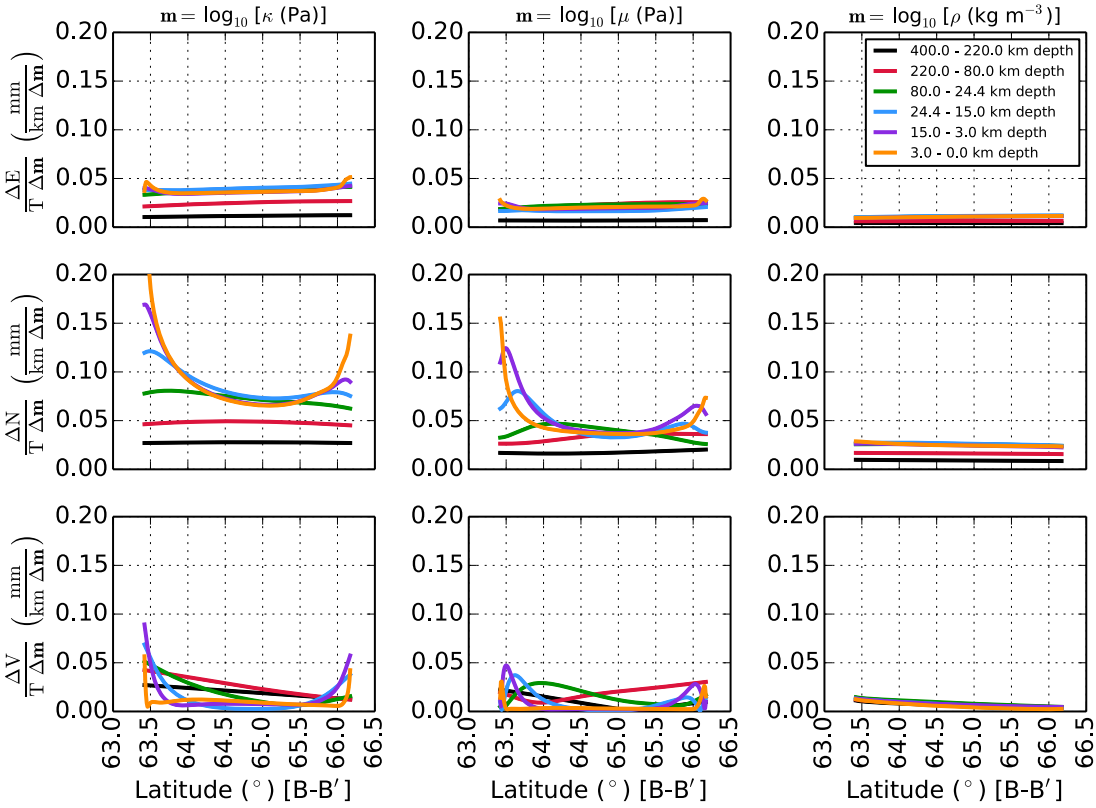

Figure 6.23: Same as Fig. 6.21, but normalized by the layer thickness, T (in kilometers).

moduli (cf., Baker, 1980b).

Furthermore, since the equations of motion account for the gravitational force exerted on the surface mass, increasing the density in any layer will increase the magnitude of the gravitational force exerted at the surface. An increased gravitational force attracting the mass load is consistent with the predominantly negative sensitivity of the displacement LGFs to positive perturbations in density, the approximately constant sensitivity as a function of perturbation depth, and the relatively weak sensitivity observed for perturbations to thin crustal layers (Fig. 6.7) (cf., Baker, 1980b). By this interpretation, we suggest that changes in the gravitational force, arising from changes to the total Earth mass due to perturbations in density structure, account for the most significant contribution to K_ρ. Unsurprisingly, the magnitude of LGF sensitivity to density perturbations increases with thickness of the perturbed layer. In contrast, the depth of a perturbation to the elastic moduli plays a significant role in enhancing (shallower) or diminishing (deeper) the LGF sensitivity.

Since combinations of positive and negative perturbations to an array of spherical shells and elastic parameters can theoretically produce equivalent surface displacements at a variety of observer-to-load angular distances, the inverse problem exhibits non-uniqueness, particularly when only a small number of measurement sites are considered (cf., Baker, 1980b). In other words, different Earth models could potentially explain the same observations of SML-induced surface displacements. Moreover, Figs. 6.20 and 6.21 show that perturbations to thick layers in the mantle can produce larger changes in the OTL-induced surface displacements than perturbations to thin layers in the crust. Perturbations applied to near-surface structure, however, predominantly affect the OTL-induced surface displacements at locations near to the load, corresponding to stations along the coast; perturbations to deeper structure generate changes at longer wavelengths and often exhibit peak sensitivities further inland. The non-uniqueness of the inverse problem may therefore be mitigated with a large and spatially distributed set of SML-response observations, which should be explored further through case-specific investigations of model resolution. The sensitivity of load-induced surface displacements to perturbations in structure also depends strongly on the distribution of the global load. Thus, the structural sensitivities of SML-induced surface

displacements are load- and site-specific.

In addition to adequate model resolution, the ability to use observations of SML-induced surface displacements to constrain solid Earth structure also requires the structural sensitivity of the deformation response to exceed observational and modeling errors. In the special case of OTL, peak sensitivities to structure are typically associated with the locations of the largest OTL-induced surface displacements, which generally coincide with coastal sites immediately adjacent to large-amplitude tides offshore. For most geodetic networks, however, only a spatially limited number of stations are deployed near the coast. Furthermore, even with a very dense network along the coast, the primary sensitivity would be to near-surface structure. Thus, to improve the ability to detect deeper mantle structure, OTL-induced surface displacements detected further inland must also be explored. The inland sites, however, tend to exhibit smaller displacement-responses as well as weaker structural sensitivities and therefore require more accurate empirical measurements of the OTL-induced deformation as well as minimal errors in the forward model.

Errors affecting the precision and accuracy of the forward model might arise from the numerical derivation of the LGFs, the development and resolution of the ocean-tide model, deficiencies in the SNREI Earth model, and the numerical convolution scheme. Errors in the ocean-tide model, in particular, tend to be largest near the coast and therefore disproportionately impact measurement sites near the coastline. Uncertainties affecting the observational precision may include contributions from the data acquisition and processing as well as the modeling techniques used to extract the individual tidal harmonics. SEBT displacement-response estimates, for example, are often removed at the GPS processing stage and can be erroneous at the $\sim$1 mm level (e.g., Yuan et al., 2013). The SEBTs, however, operate primarily at long wavelengths, or global spatial scales, and therefore sample more or less an average of Earth structure (e.g., Latychev et al., 2009). Thus, for a regional GPS network, any inaccuracies in the SEBT model would likely manifest predominantly as a residual displacement common to the entire network.

Recently, Bos et al. (2015) reported that observations and predictions of OTL-induced surface displacements across western Europe were of sufficient precision to explore structural

deficiencies, including both elastic and anelastic deficiencies. In addition, Martens et al. (2016) demonstrated that, after the removal of a uniform-displacement factor, vector differences between predicted M_2 OTL-induced surface displacements generated from a selection of modern ocean-tide models coincided with the approximate level of structural sensitivity for reasonable variations in SNREI Earth structure (Fig. 6.12). It should also be recalled that the sensitivity analyses presented here involve *differential* OTL-induced surface displacements and, therefore, errors related to the particular tide model and convolution scheme, which do not change between forward-model computations, cancel out to within about a fraction of a micron.

We also reiterate that the sensitivity kernels were derived for SNREI Earth models. At this stage, we have not considered the effects of anelasticity, anisotropy, or lateral heterogeneities on the sensitivities of LLNs, LGFs, and OTL-induced surface displacements to perturbations in structure. Bos et al. (2015) found that dissipation effects within the asthenosphere could account for up to about 0.3 mm of residual OTL-induced surface displacements in western Europe and that allowing for anisotropy could reduce the mean residual by approximately 0.1 mm. Incorporating an anelastic constitutive relation into the equations of motion produces complex-valued LLNs; thus, the differences between observed and predicted OTL-induced surface displacements would also include a small phase delay.

Regarding lateral heterogeneities, the computations of the LLNs and LGFs require radially symmetric structure by design. To explore the effects of lateral heterogeneities on the predicted SML-induced surface displacements, one might compute discrete grids of local LGFs (e.g., Dill et al., 2015). The Earth's displacement response to SML, however, depends on global Earth structure and particularly on the material properties spanning the region between the load and the observer. Thus, grids of local LGFs would not be particularly useful for regional or global studies, where stations might be located at a variety of distances from spatially complicated loads, as in the case of OTL. A better technique would be to use fully numerical approaches, such as finite element or spectral element methods. Using numerical techniques, albeit applied to the SEBTs rather than SML, Latychev et al. (2009) showed

that realistic three-dimensional variations in structure can perturb radial displacements by an amount on the order of 1 mm in the semi-diurnal tidal band.

It is also worth recalling that the forward model generates predicted SML-induced surface displacements based on a model for Earth structure as well as a load model. Here, we have focused on the sensitivity of OTL-induced surface displacements to perturbations in elastic structure, and taken the load model as given. In some cases, however, the Earth model could be considered given and the observations of SML-induced surface displacements used to constrain the spatial extent and volume of a load.

6.6 Summary and Conclusions

We have computed the sensitivities of Love numbers (potential, load, and shear), displacement load Green's functions, and M_2 OTL-induced surface displacements to perturbations in elastic and density structure through the crust and mantle. In each case, the sensitivities depend on the depth of the structural perturbation, the thickness of the perturbed layer, and the particular parameter that was perturbed (e.g., κ, μ, ρ). The sensitivities of the Love numbers additionally depend on the spherical harmonic degree of the deformation, since different degrees sample structure across different depth ranges. The sensitivities of the LGFs further depend on the angular separation between the measurement site and the location of the applied (point source) mass load. Furthermore, the sensitivities of the OTL-induced surface displacements are influenced by the specific tide model as well as the location of the measurement site.

Although the LLNs, LGFs, and OTL-induced surface displacements are sensitive to perturbations in both elastic and density structure, the sensitivity of the deformation response to perturbations in density structure appears to be relatively weak unless applied to a very thick layer (Figs. 6.6 and 6.7). We attribute the patterns of density sensitivity primarily to increases in the total Earth mass that occur with perturbations to the density and that generate deviations in the surface gravity. We find that most of the sensitivity to perturbations in the elastic moduli is concentrated within 500 km depth of the surface and within 10° of the load point (i.e., within an angular distance of 10° between the load and the observer).

Different combinations of positive and negative perturbations to the elastic and density structure of the crust and upper mantle can theoretically generate equivalent OTL-induced surface displacements at prediction sites on the surface, implying a non-uniqueness of the inverse problem. The apparent non-uniqueness might be mitigated through appropriately dense and strategically distributed geodetic networks, since structural perturbations applied at different depths influence the surface deformation more strongly at different distances from the load point (Figs. 6.7, 6.20 and 6.22). Moreover, the spatially and temporally complicated patterns of ocean tidal loads can further facilitate the sampling of structure at a variety of wavelengths.

In conclusion, the possibility of performing geodetic tomography using observations of Earth deformation induced by surface mass loading depends on many factors, including the specific geodetic network, the quality of the geodetic data, the computational methods, the quality and spatial distribution of the load model, and the sensitivity to structure. The sensitivity kernels presented here, however, lay the foundation for future tomographic studies since, along with models for the observational and prediction error, the kernels could be used to formulate the inverse problem.

6.7 Acknowledgments

We thank Duncan Agnew and Richard Ray for fruitful discussions on ocean tidal loading as well as thoughtful suggestions regarding the development of our loading-response convolution code. We also thank Shuhei Okubo for valuable guidance in understanding the development of the Love number variational equations. We gratefully acknowledge two anonymous reviewers for their insightful and comprehensive comments, which substantially strengthened the manuscript. We also acknowledge support from the National Science Foundation Geophysics Program funding under Grant No. EAR-1417245. This manuscript is based upon work supported by the NASA Earth and Space Science Fellowship to HRM under Grant No. NNX14AO04H. Some figures were generated using Generic Mapping Tools (Wessel et al., 2013).

7

Observations of Ocean Tidal Load Response in South America from Sub-daily GPS Positions

The work discussed in this chapter has been published as:
Martens, H.R., M. Simons, S. Owen, and L. Rivera, 2016. Observations of Ocean Tidal Load Response in South America from Sub-daily GPS Positions, *Geophys. J. Int.*, 205(3), doi:10.1093/gji/ggw087, pp. 1637–1664.

7.1 Abstract

We explore Earth's elastic deformation response to ocean tidal loading (OTL) using kinematic Global Positioning System (GPS) observations and forward-modeled predictions across South America. Harmonic coefficients are extracted from up to fourteen years of GPS-inferred receiver locations, which we estimate at five-minute intervals using precise point positioning. We compare the observed OTL-induced surface displacements against predictions derived from spherically symmetric, non-rotating, elastic, and isotropic (SNREI) Earth models. We also compare sets of modeled predictions directly for various ocean-tide and Earth-model combinations. The vector differences between predicted displacements computed using separate ocean tide models reveal uniform-displacement components common to all stations in the South America network. Removal of the network-mean OTL-induced displacements from each site substantially reduces the vector differences between observed and predicted displacements. We focus on the dominant astronomical tidal harmonics from three distinct frequency bands: semidiurnal (M_2), diurnal (O_1), and fortnightly (M_f). In each band, the observed OTL-induced surface displacements strongly resemble the

modeled displacement-response patterns, and the residuals agree to about 0.3 mm or better. Even with the sub-mm correspondence between observations and predictions, we detect regional-scale spatial coherency in the final set of residuals, most notably for the M_2 harmonic. The spatial coherency appears to be relatively insensitive to the specific choice of ocean-tide or SNREI-Earth model. Varying the load model or one-dimensional elastic structure yields predicted OTL-induced displacement differences of order 0.1 mm or less for the network. Furthermore, estimates of the observational uncertainty place the noise level below the magnitude of the residual displacements for most stations, supporting our interpretation that random errors cannot account for the entire misfit. Therefore, the spatially coherent residuals may reveal deficiencies in the a priori SNREI Earth models. In particular, the residuals may indicate sensitivity to regional deviations from standard globally averaged Earth structure due to the presence of the South American craton.

7.2 Introduction

Tidal forces, generated primarily by gravitational interactions with the moon and sun, deform the Earth both directly through the gravitational potential (body tides) and indirectly through the periodic redistribution of fluid mass loading Earth's surface (e.g., oceanic and atmospheric load tides). The density and elastic structure of Earth's interior controls the spatiotemporal characteristics of the deformation response; thus, observations of surface displacements caused by the tidal potential and tidal loading may potentially be exploited to study the material properties of the solid Earth (e.g., Love, 1909; Melchior, 1983; Baker, 1984; Bos et al., 2015).

Whereas body tides are long-wavelength phenomena that sample a large-scale average of Earth structure (e.g., Latychev et al., 2009), ocean tidal loads are shorter-wavelength features that probe Earth's material properties at finer spatial scales (e.g., Baker, 1984; Jentzsch, 1997; Agnew, 2015). Moreover, whereas the spatial distribution of amplitude and phase for body tides generally follows that of the equilibrium tide derived directly from the gravitational potential, ocean tides exhibit a complitcated spatial pattern due to interactions with continental boundaries and bathymetry (e.g., Zahel, 1997; Pugh & Woodworth, 2014),

thereby generating a rich spectrum of deformation responses.

Seismology remains a primary means for investigating Earth's interior structure, but is also limited in its ability to distinguish between variations in the two elastic moduli and density inside the Earth. Separating the three unknown parameters contained within measurements of body wave velocities necessarily involves scaling laws and assumptions about Earth's interior state (e.g., Dziewonski & Anderson, 1981), or additional information, such as normal mode or surface wave data (Ishii & Tromp, 1999; Lin et al., 2012), which are limited in spatial resolution and/or depth extent. Alternatively, ocean tidal loading (OTL) excites both elastic and gravitational deformation responses in the Earth at a variety of wavelengths that sample the crust and the upper mantle. Thus, combinations of OTL-induced deformation measurements and seismic body-wave observations should allow the two elastic moduli and the density to be independently constrained as a function of depth.

Although Earth's deformation response to OTL may be monitored using a variety of techniques, including very long baseline interferometry (VLBI), gravity, tilt, strain, and Global Positioning System (GPS)-inferred displacements (e.g., Baker, 1980b, 1984; Baker et al., 1991, 1996; Petrov & Ma, 2003; Pugh et al., 2011; Yuan et al., 2013; Penna et al., 2015), the load Green's functions (LGFs) for tilt and strain decrease as r^{-2} from the load point, where r is distance, and gravity and displacement LGFs decrease as r^{-1} from the load point. Thus, the gravitational and displacement responses are sensitive to a wider expanse of ocean loads and regional solid Earth structure than tilt and strain (Baker, 1984). In addition, local inhomogeneities in mechanical properties limit the effectiveness of using strain and tilt observations to investigate OTL response (Jentzsch, 1997; Baker, 1984). VLBI installations measure tidal response with high accuracy (Petrov & Ma, 2003; Thomas et al., 2007), but only a small number exist worldwide (King, 2006). GPS stations, in contrast, are now deployed extensively around the globe and also measure tidal deformation very accurately. Therefore, GPS has emerged as a preferred method for OTL-response investigations (e.g., Schenewerk et al., 2001; King, 2006; Thomas et al., 2007; Ito & Simons, 2011; Yuan & Chao, 2012; Bos et al., 2015).

Recent studies have explored various GPS processing techniques used to isolate tidal har-

monic signals (e.g., King, 2006; King et al., 2008; Penna et al., 2015). In particular, two main strategies have been proposed for extracting tidal harmonic information from GPS data: static and kinematic. In the static approach, also referred to as the harmonic parameter estimation approach (Penna et al., 2015), tidal harmonic coefficients are estimated along with daily station positions as part of a static GPS solution, generally using precise point positioning (PPP) or network estimation techniques (e.g., Schenewerk et al., 2001; Allinson et al., 2004; King, 2006; Thomas et al., 2007; Yuan & Chao, 2012; Yuan et al., 2013). A series of static solutions, along with their full variance-covariance matrices, are subsequently combined to form the final estimates for the harmonic coefficients, typically using a Kalman filter. For the kinematic approach, station positions are estimated from the GPS data at sub-daily intervals, without simultaneously estimating the OTL-induced displacements (e.g., Khan & Tscherning, 2001; King & Aoki, 2003; King, 2006; Penna et al., 2015). A post-processing analysis is then performed to extract harmonic coefficients from the kinematic time series. We adopt the kinematic approach in this study.

Since deformation responses induced by OTL depend on the material properties of Earth's interior, precise observations may potentially be exploited to constrain solid-Earth structure. Motivated by recent advancements in ocean tide models and deployments of dense GPS networks, Ito & Simons (2011) were the first to attempt to invert GPS-inferred observations of OTL-generated surface displacements for one-dimensional profiles of the elastic moduli and density through the crust and upper mantle beneath the western United States. Their forward modeling procedure, however, neglected to account for the motion of the geocenter induced by variations in the surface mass loads, which resulted in an inconsistent mapping between observations and predictions (Blewitt, 2003; Fu et al., 2012; Wu et al., 2012; Desai & Ray, 2014). The use of inconsistent reference frames introduced long-wavelength artifacts into the displacement-response residuals, which critically biased the analysis and results.

Furthermore, ocean tide models have long been considered a dominant source of error in predicting Earth's response to OTL, particularly near the coast (e.g., Francis & Mazzega, 1990; Agnew, 1997; Khan & Scherneck, 2003; Bos & Baker, 2005; Penna et al., 2008;

Yuan & Chao, 2012; Yuan et al., 2013). Citing the large coastal errors, Yuan & Chao (2012) and Yuan et al. (2013) opted to examine OTL and body-tide response residuals only at GPS stations located more than 150–200 km inland of the coast. Operating under the assumption that, at the accuracy of their GPS observations, the OTL prediction error could be neglected beyond 150–200 km of the coast, they attributed continental-scale spatial coherency with non-diminishing amplitudes exhibited by the inland residuals to possible elastic and anelsatic deficiencies in the a priori body tide model. They made no attempt to invert the residuals for perturbations to their pre-assumed Earth model, however, claiming that sensitivity to structure appears to be small compared with sources of error and requires further investigation.

Penna et al. (2015) and Bos et al. (2015) recently completed a study examining OTL-induced surface displacements in western Europe using kinematic GPS processing methods. For the M_2 harmonic, they found statistically significant residual displacements that exceeded the observational uncertainties of 0.2–0.4 mm, and suggested that the discrepancy could be explained in large part by accounting for mantle anelasticity and anisotropy.

Improving the ability to extract tidal harmonics from GPS data and to forward-model Earth's response to OTL not only enhances the possibility of constraining material properties from observations of Earth's OTL-induced deformation, but also of better accounting for the effects of loading response when examining other geodetic signals of interest, such as aseismic transients. Here, we investigate the precision and spatiotemporal characteristics of observed and predicted OTL-induced surface displacements across a regional network of GPS stations in Brazil, Argentina, and Uruguay. Since the tidal harmonics within a given tidal species exhibit similar patterns (e.g., Pugh, 1987), we focus our analysis on the dominant tides from three distinct frequency bands: the principal lunar semidiurnal tide (M_2), which has a period of 12.42 hours; the principal lunar diurnal tide (O_1), which has a period of 25.82 hours; and the principal lunar fortnightly tide (M_f), which has a period of 13.66 days. The global distributions of the tide amplitudes for the three harmonics are shown in Fig. 7.1.

We begin by introducing our procedure for modeling OTL-induced surface displacements

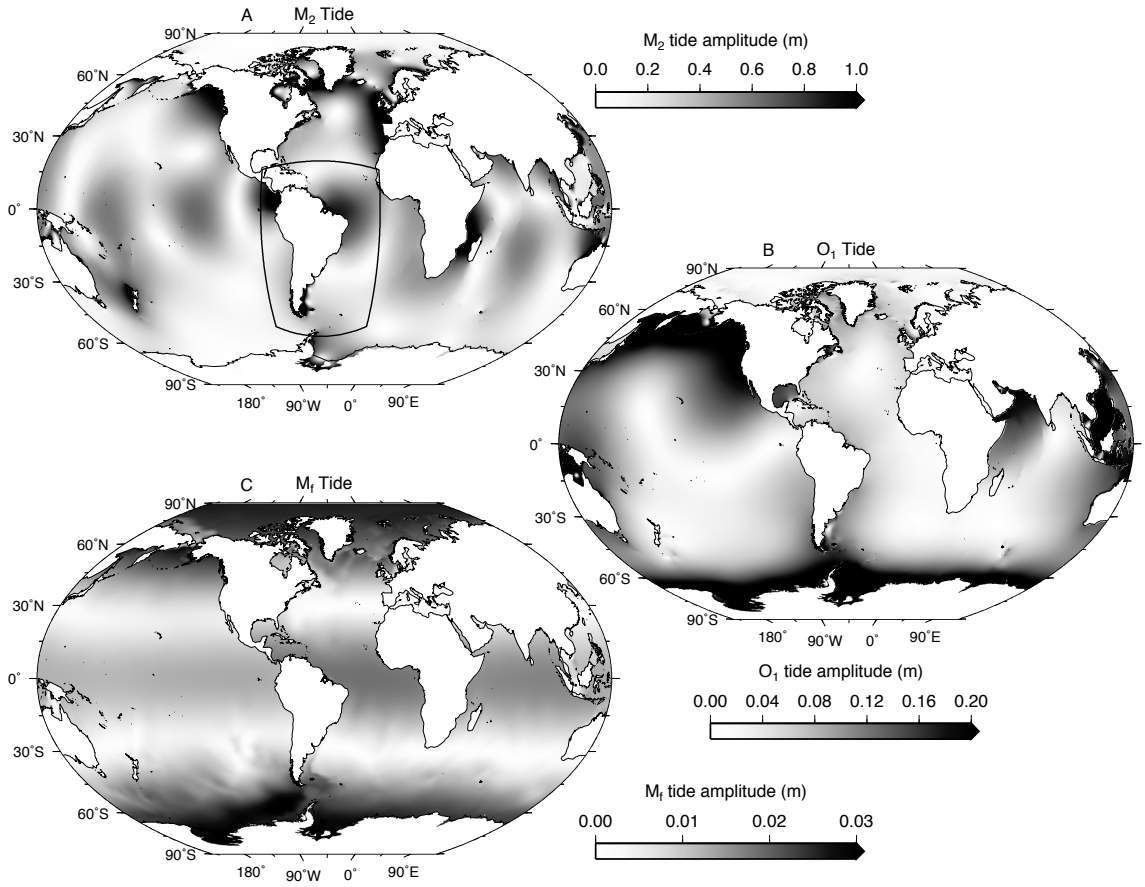

Figure 7.1: Spatial distribution of tide amplitudes based on the FES2012 ocean tide model (Carrère et al., 2012; Lyard et al., 2006) for the (A) principal lunar semidiurnal harmonic, M_2; (B) principal lunar diurnal harmonic, O_1; and (C) principal lunar fortnightly harmonic, M_f. The black box in panel A outlines our study area. Note also that the tides remain active beneath the floating ice shelves in Antarctica.

and exploring the sensitivity of the predicted deformation to a selection of ocean tide and elastic Earth models. We then transition into a discussion of the observational methods and results. Finally, we compare the observed and predicted OTL-induced surface displacements and consider the implications of the residual displacements. Additional details of our GPS processing and harmonic analysis techniques are provided in the Appendices.

7.3 Predictions

To predict Earth's elastic displacement response to surface mass loading, we convolve an ocean tide model with displacement LGFs that represent the response of a spherically symmetric, non-rotating, elastic, and isotropic (SNREI) Earth to a point load of unit mass. The predicted surface displacements induced by OTL are given by:

$$U(r, S, Z, \rho_{sea}) = \int_{\Omega} \rho_{sea}(r')\, G(|\overline{r} - \overline{r}'|, S)\, Z(r')\, d\Omega, \tag{7.1}$$

where U is the complex-valued response of Earth at observation point r, ρ_{sea} is the density of sea water at the load point r', G is the Green's function per kg load, and Z is the complex-valued height of the ocean tide at the load point. The integral is taken over the surface area of the oceans, Ω. The LGFs depend on the angular distance to the load as well as Earth structure, S, where the structure is assumed SNREI (e.g., PREM). The LGFs are formed by spherical harmonic combinations of load Love numbers, which are derived from integrating the equations of motion through the layered Earth structure with normal-traction boundary conditions applied at the surface (Farrell, 1973). We evaluate Eq. 7.1 using software developed in-house, `LoadDef`, which is parallelized and written in `Python`.

Initially, we compute the load Love numbers with respect to the center of mass of the solid Earth, known as the CE reference frame (Blewitt, 2003). The GPS orbit and clock products from our observational analysis, however, are provided in the CM reference frame, which is referenced to the center of mass of the entire Earth system (including the solid Earth, oceans, and atmosphere) (Desai & Ray, 2014). For investigations into Earth's OTL response, predictions and observations must be computed in the same reference frame;

otherwise, positioning errors of order 1 mm or more may arise (Wu et al., 2012; Fu et al., 2012; Desai & Ray, 2014). Thus, we transform the degree-1 load Love numbers into the CM reference frame prior to computation of the LGFs (Blewitt, 2003; Wang et al., 2012; Agnew, 2012).

For the convolution (Eq. 7.1), we adopt a station-centered template grid, which simplifies the integration of the LGFs across individual cells, easily facilitates the inclusion of multiple loading models, and naturally allows us to refine the resolution of the integration mesh near the station (Goad, 1980; Agnew, 1997, 2012). To develop the template grid, we place a station at the pole of a spherical coordinate system, where θ represents the polar angle and α represents the azimuthal angle, and vary the resolution in polar angle as a function of distance to the station: $\Delta\theta = 0.001^\circ$, or about 100 m, within $\theta = 1^\circ$; $\Delta\theta = 0.01^\circ$ from $\theta = 1$–10°; $\Delta\theta = 0.1^\circ$ from $\theta = 10$–90°; and $\Delta\theta = 1.0^\circ$ beyond $\theta = 90^\circ$. For each θ in the mesh, $\Delta\alpha = 0.1^\circ$.

To also refine the integration mesh around the coastline, we first extrapolate the ocean model inland by one grid cell and then apply a land-sea mask. In the far-field, we define the land-sea mask with ETOPO1, which provides global topographic and bathymetric relief information at 1 arc-minute resolution (Amante & Eakins, 2009). In the near-field (within 1.5° of a station), we use the Global Self-consistent, Hierarchical, High-resolution Shoreline (GSHHS) database at full resolution (Wessel & Smith, 1996). Since ETOPO1 registers floating ice shelves as landmasses, but the tides remain active in those regions (Fig. 7.6), we use the Scientific Committee on Antarctic Research (SCAR) Antarctic Digital Database version 6.0 to define the Antarctic coastline. The value for seawater density in Eq. 7.1 should represent the density of ocean water at the seafloor (Ray, 2013); here, we adopt a uniform value of 1035 kg m^{-3}.

`LoadDef` differs from most other OTL-response modeling software in that it derives LGFs on-the-fly from an input Earth model, rather than uses pre-computed LGFs from published tables. The convolution portion of `LoadDef`, however, is modeled after, and therefore not significantly different algorithmically from, the widely used `SPOTL` package (Agnew, 2012) and both codes yield very similar results (to within about 1–2% for SPOTL version

3.3.0.2). Minor differences arise from details of the coastline refinement, resolution of the integration mesh, and values adopted for seawater density.

In addition to an SNREI Earth model, the forward model (Eq. 7.1) also requires the input of an ocean tide model. One class of modern ocean tide models assimilates satellite altimetry and tide gauge data into global hydrodynamic simulations. A second class of ocean tide models involves purely empirical developments, relying primarily on satellite altimetry constraints. The models are often made available on regularly spaced latitude-longitude grids, with amplitude and phase values supplied for up to 30 tidal harmonics or more. The ocean-basin and Earth-rotational effects produce tidal circulation systems, centered on points of zero tidal amplitude called amphidromes. Complicated ocean-land interactions present challenges for global hydrodynamic modeling. Furthermore, altimetry satellites, which provide some of the primary data for ocean tide models, have difficulty sampling at high latitudes and near coastlines. Thus, the ocean tides are notoriously difficult to model, particularly in the polar regions and shallow seas, as depicted in Fig. 7.2. The resolution and accuracy of the ocean tide models, however, have improved considerably over the last decade (e.g., Stammer et al., 2014; Ray, 2013).

To investigate the sensitivity of the predicted OTL-induced surface displacements to various ocean tide and SNREI Earth models, we compare the vector differences between forward models. The magnitude of the vector difference, δ, between two sets of predicted OTL-induced surface displacements, $P1$ and $P2$, for each spatial component and at each prediction site is given by:

$$\delta = \sqrt{(A_{P1}\cos\phi_{P1} - A_{P2}\cos\phi_{P2})^2 + (A_{P1}\sin\phi_{P1} - A_{P2}\sin\phi_{P2})^2}, \qquad (7.2)$$

where A is the amplitude and ϕ is the phase. For an individual tidal harmonic, the OTL-induced displacements at a particular geographic location may be represented by a closed ellipse in three-dimensional space and traced out completely during each tidal period. To illustrate the harmonic displacements graphically, we depict the combined east and north displacement by a horizontal particle motion ellipse (PME) and denote the vertical motion by the color of the ellipse.

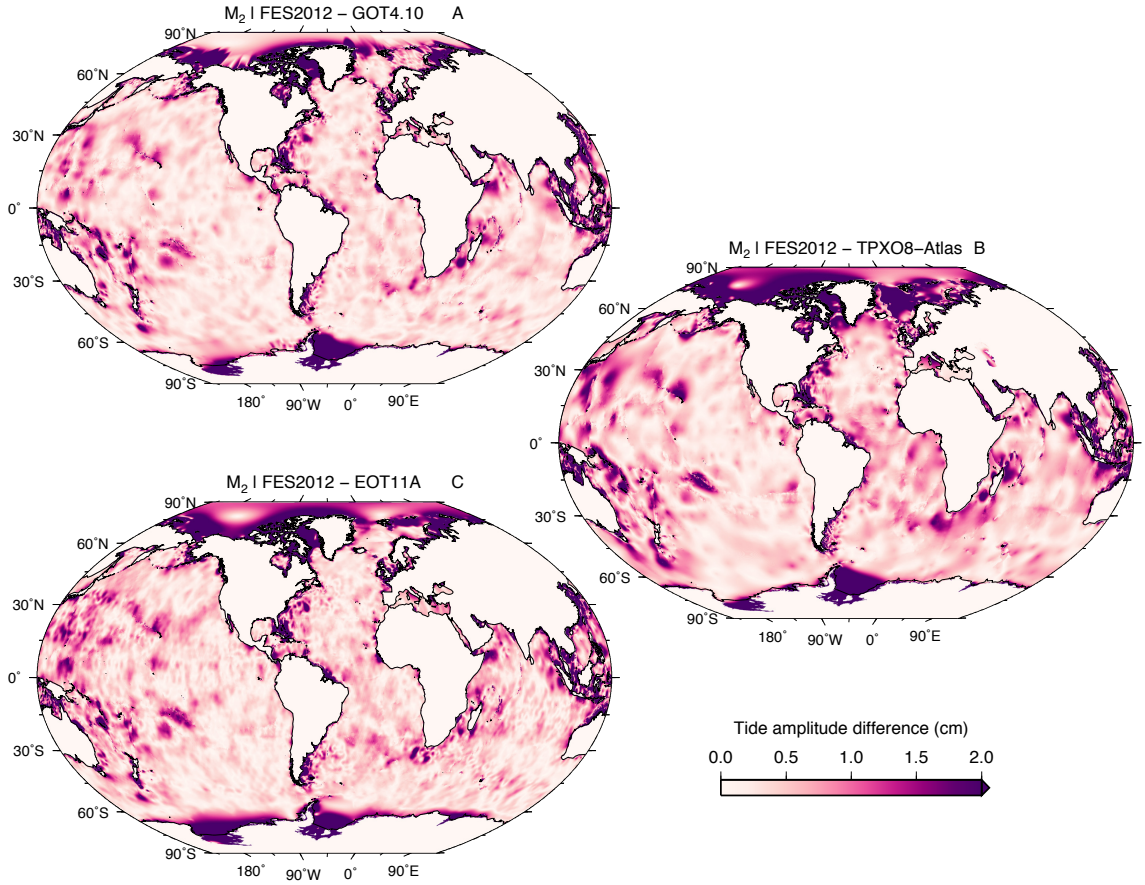

Figure 7.2: Differences in tide amplitude between the (A) FES2012 and GOT4.10, (B) FES2012 and TPX08-Atlas, and (C) FES2012 and EOT11A ocean tide models for the M_2 harmonic. The differences, denoted by the colorbar, represent the magnitude of vector differences between the complex-valued tide amplitudes at each grid cell.

7.3.1 Ocean Tide Model Comparisons

Acknowledging the availability of a large number of ocean tide models, we opt for a representative sampling in the interest of clarity. We consider FES2012 (Carrère et al., 2012; Lyard et al., 2006), TPXO8-Atlas (Egbert & Erofeeva, 2002; Egbert et al., 2010), EOT11A (Savcenko & Bosch, 2012) and GOT4.10 (Ray, 1999, 2013). FES2012 and TPXO8-Atlas were generated from global hydrodynamic simulations that assimilated tide gauge and satellite altimetry data, whereas EOT11A and GOT4.10 rely primarily on empirical altimetry observations. Moreover, the models FES2012, TPXO8-Atlas and EOT11A include estimates for the fortnightly astronomical tide, M_f. TPXO8-Atlas also has local tide models incorporated into its final solution.

As discussed in Desai & Ray (2014), a majority of altimetry-based ocean tide models do not yet account for the effects of tide-induced geocenter variations on altimetric determinations of ocean-tide heights. To the best of our knowledge, the four models considered here are no exception. Recently, however, the altimetry observations used to constrain GOT4.10 were adjusted for tidal geocenter variations, culminating in an updated model: GOT4.10c. To remain internally consistent in our comparisons of ocean tide models, we focus here on the four models that are presumably uncorrected for geocenter variations (i.e., FES2012, TPXO8-Atlas, EOT11A, and GOT4.10), but include a basic assessment of GOT4.10c with the Discussion.

Fig. 7.3 shows the vector differences between predicted OTL-induced surface displacements as PMEs for the M_2 tidal harmonic. Note the spatial coherency in size and orientation of many of the ellipses, suggesting the presence of a uniform OTL-induced displacement, or "common-mode," component that is constant across the entire network. In the context of this manuscript, a common-mode component refers to a constant OTL-response amplitude and a constant OTL-response phase-lag that are common to all stations in the network for a particular tidal harmonic (not to be confused with a network-averaged displacement removed from a geodetic time series). For example, a comparison of FES2012 with TPXO8-Atlas (Fig. 7.3, panel A) reveals ellipses oriented primarily in the north-south

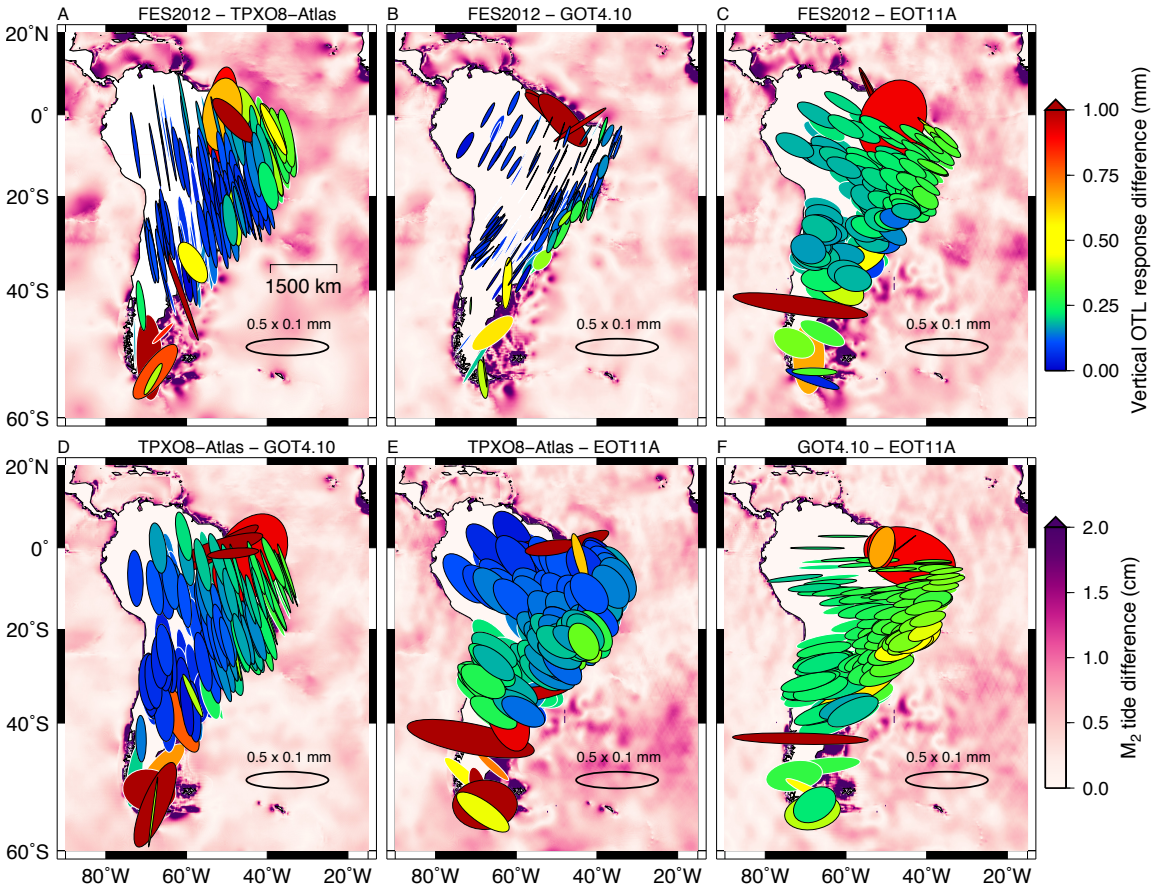

Figure 7.3: Particle motion ellipses (PMEs) depicting the vector differences between pairs of predicted OTL-induced surface displacements for the M_2 tidal harmonic made using selected ocean tide models: (A) FES2012 and TPXO8-Atlas, (B) FES2012 and GOT4.10, (C) FES2012 and EOT11A, (D) TPXO8-Atlas and GOT4.10, (E) TPXO8-Atlas and EOT11A, and (F) GOT4.10 and EOT11A. In each case, we adopted PREM as the input SNREI Earth model. The size and orientation of each ellipse represent the displacement differences for the horizontal components, with a reference ellipse shown in the lower right corner of each panel; the color of each ellipse represents the displacement difference for the vertical component (upper color bar). The lower color bar depicts the M_2 tide amplitude difference between each model pair (Fig. 7.2). Ellipses outlined in white (e.g., in Uruguay) indicate stations that recorded fewer than 1000 days of data during our study period, which we refer to later in the context of the observations.

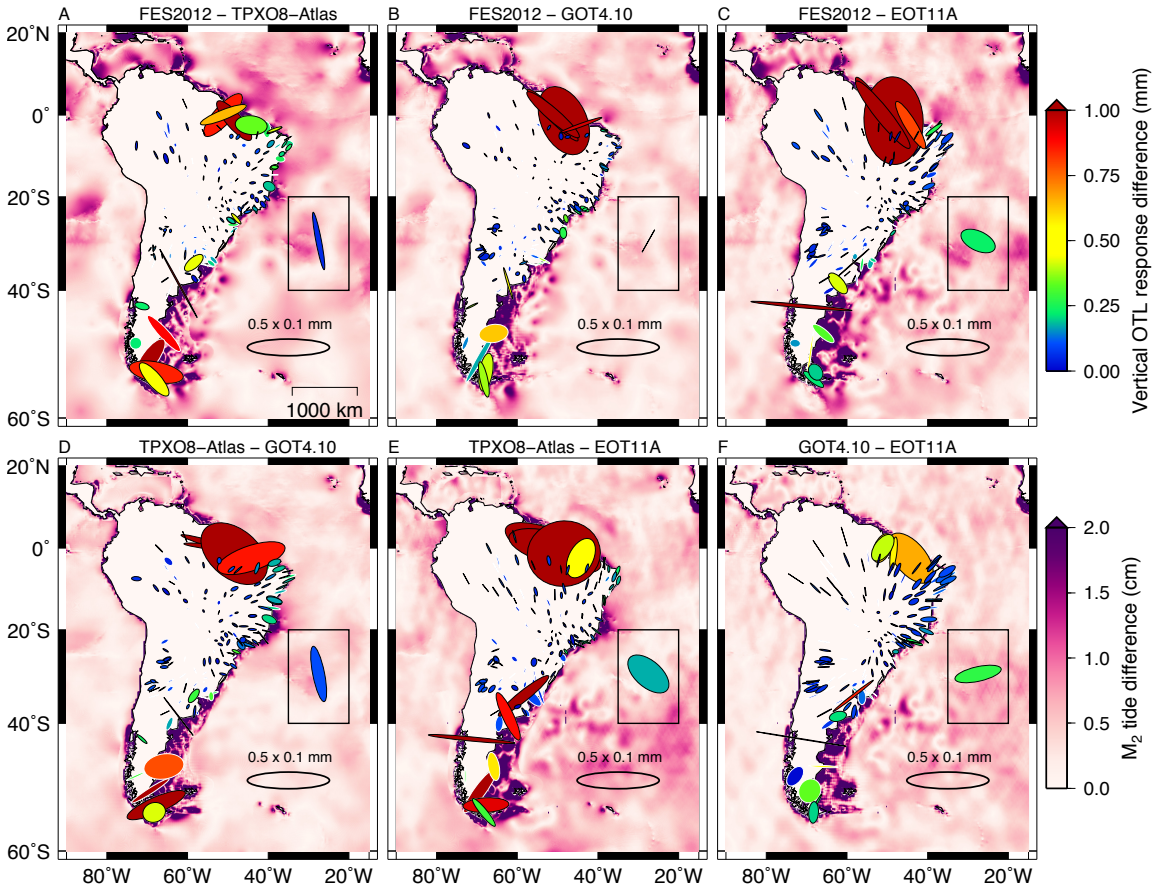

Figure 7.4: Same as Fig. 7.3, but with the common-mode component (network-mean OTL-induced displacement) removed across the network. The common-mode ellipse that was subtracted from all stations is shown in the black-box inset of each panel. Note the large residuals remaining near the Amazon river delta and Patagonian shelf, which are notoriously difficult regions to constrain in the development of the ocean tide models. Due to the large uncertainties, we remove stations immediately adjacent to Patagonia and the mouth of the Amazon from our analysis.

direction, with non-diminishing amplitudes inland of the coast. Removing the network-mean OTL-induced displacement from each station significantly reduces the magnitude of the differences, as depicted in Fig. 7.4.

With the common-mode component removed, regions of enhanced ocean tide model uncertainties appear prominently. Unsurprisingly, the coastal areas around the Amazon river delta and Patagonian shelf, which are difficult to constrain with satellite altimetry and difficult to model hydrodynamically, exhibit substantial inter-model discrepancies (Fig. 7.4). We therefore exclude nineteen of the most severely affected stations, located immediately adjacent to Patagonia and the mouth of the Amazon, from all of our subsequent analysis.

In Fig. 7.5, we show the root-mean-square (RMS) differences between pairs of displacement-response predictions for the M_2, O_1 and M_f tidal harmonics. The hatching on the bars denotes the RMS differences after the common-mode component has been removed (see also Table 7.1). Note that a substantial portion of the differences between models may be explained by the common mode. For the horizontal components of the M_2 harmonic, in particular, removing the network-mean OTL-induced displacement reduces the sensitivity to choice of ocean tide model by up to severalfold and, in some cases, even reduces it to below the sensitivity to some choices of SNREI Earth model (cf., Fig. 7.9, Tables 7.1 and 7.2).

The RMS values represent the network-averaged discrepancies between predicted OTL-induced surface displacements derived using different ocean tide models. A total of 97 stations were used in the computation of the RMS statistics, after the exclusion of the Patagonian and Amazon stations as well as stations that recorded less than 1000 days of data. Although the forward models are unaffected by data length and quality, we elect to remove the short-record stations from all RMS computations in order to allow direct comparisons with observational residuals (shown later). Unless specified otherwise, we continue to show the PMEs for stations that recorded less than 1000 days of data, but we distinguish them by white outlines (e.g., Figs. 7.3 and 7.4).

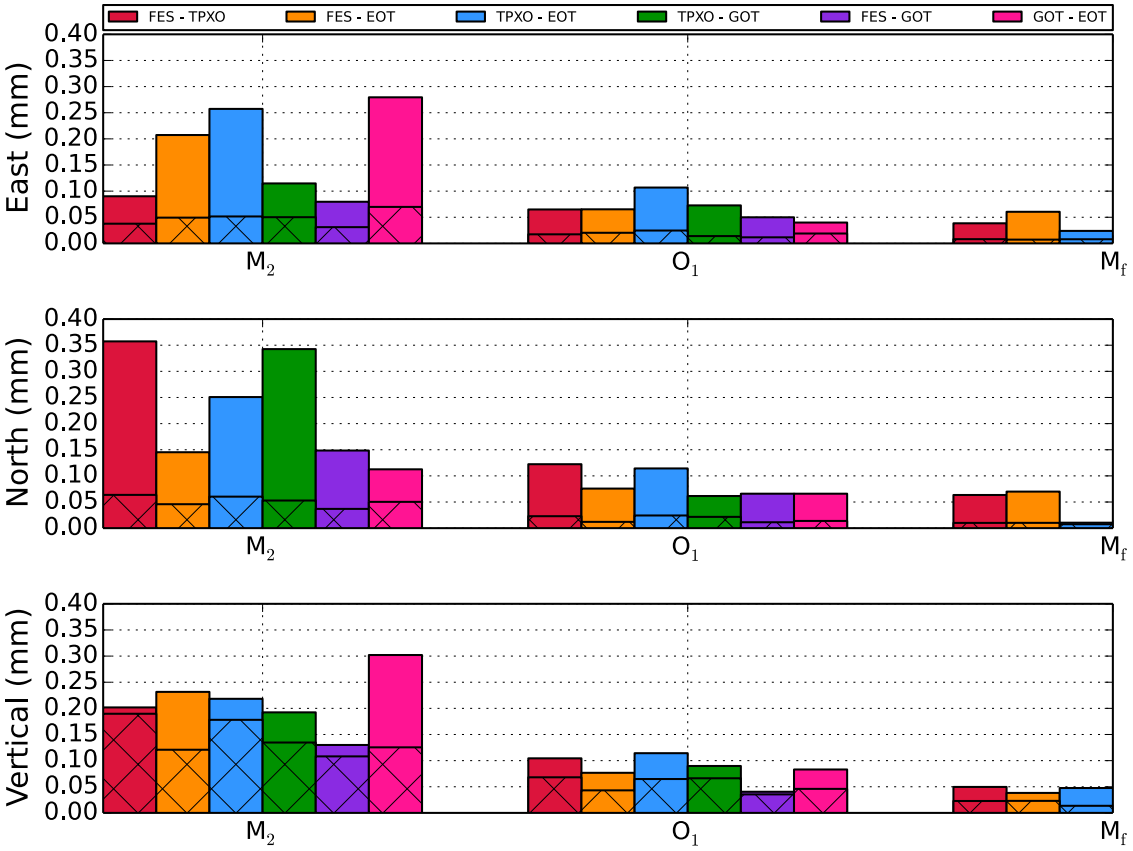

Figure 7.5: Root-mean-square (RMS) differences between pairs of predicted OTL-induced surface displacements for the South America network made using different ocean tide models. The hatching on the bars illustrates the RMS misfits after a common-mode component (network-mean OTL-induced displacement) was removed from all stations. The models considered include FES2012 (FES), TPXO8-Atlas (TPXO), EOT11A (EOT), and GOT4.10 (GOT). The ordering of the legend corresponds directly to the ordering of the bars in the figure. Note that the GOT4.10 model does not include the M_f harmonic. In each comparison, we adopted PREM as the input SNREI Earth model. As with all RMS statistics presented in this manuscript, we exclude stations immediately adjacent to Patagonia and the mouth of the Amazon as well as stations that recorded fewer than 1000 days of data.

Table 7.1: RMS differences between pairs of predicted OTL-induced surface displacements for various ocean tide models after removal of the common-mode component. The values listed in the table correspond to the hatched bars in Fig. 7.5. In each comparison, we adopted PREM as the input SNREI Earth model. Note that the GOT4.10 model does not include the M_f harmonic.

	Ocean Tide Model Comparisons								
	East (mm)			North (mm)			Vertical (mm)		
	M_2	O_1	M_f	M_2	O_1	M_f	M_2	O_1	M_f
FES2012 – TPXO8-Atlas	0.038	0.017	0.008	0.064	0.023	0.010	0.190	0.068	0.023
FES2012 – GOT4.10	0.031	0.012	–	0.037	0.011	–	0.108	0.036	–
FES2012 – EOT11A	0.049	0.020	0.007	0.046	0.012	0.010	0.121	0.043	0.023
TPXO8-Atlas – GOT4.10	0.050	0.014	–	0.053	0.022	–	0.135	0.066	–
TPXO8-Atlas – EOT11A	0.052	0.025	0.008	0.060	0.024	0.007	0.178	0.065	0.014
GOT4.10 – EOT11A	0.070	0.019	–	0.050	0.014	–	0.125	0.046	–

Table 7.2: RMS differences between pairs of predicted OTL-induced surface displacements for selected SNREI Earth models. For each comparison, we adopted the FES2012 ocean tide model. The values listed in the table correspond to the bars in Fig. 7.9.

	SNREI Earth Model Comparisons								
	East (mm)			North (mm)			Vertical (mm)		
	M_2	O_1	M_f	M_2	O_1	M_f	M_2	O_1	M_f
PREM – STW105	0.138	0.026	0.004	0.074	0.033	0.004	0.112	0.018	0.003
PREM – AK135f	0.023	0.003	0.001	0.020	0.006	0.001	0.060	0.011	0.001
PREM – SNA	0.032	0.010	0.001	0.040	0.013	0.002	0.045	0.009	0.001
STW105 – AK135f	0.125	0.026	0.004	0.069	0.029	0.003	0.118	0.018	0.003
STW105 – SNA	0.139	0.033	0.004	0.094	0.043	0.006	0.145	0.025	0.004
AK135f – SNA	0.046	0.010	0.001	0.053	0.018	0.003	0.061	0.011	0.002

7.3.2 SNREI Earth Model Comparisons

We now explore discrepancies between predicted OTL-induced surface displacements computed using four reference Earth models: PREM (Dziewonski & Anderson, 1981), STW105 (Kustowski et al., 2008), AK135f (Kennett et al., 1995; Montagner & Kennett, 1996), and SNA (Grand & Helmberger, 1984). PREM, STW105, and AK135f represent globally averaged structure, whereas SNA represents stable continental shield structure. Below approximately 1000 km depth, SNA assumes the structural properties of AK135f. For PREM, STW105, and AK135f, we replaced the water layer at the surface with typical values for the upper crust: V_P=5800 m s^{-1}, V_S=3200 m s^{-1}, and ρ=2600 kg m^{-3}. Profiles of the elastic moduli and density for the reference Earth models are shown in Fig. 7.6. The displacement LGFs derived from each model are depicted in Fig. 7.7.

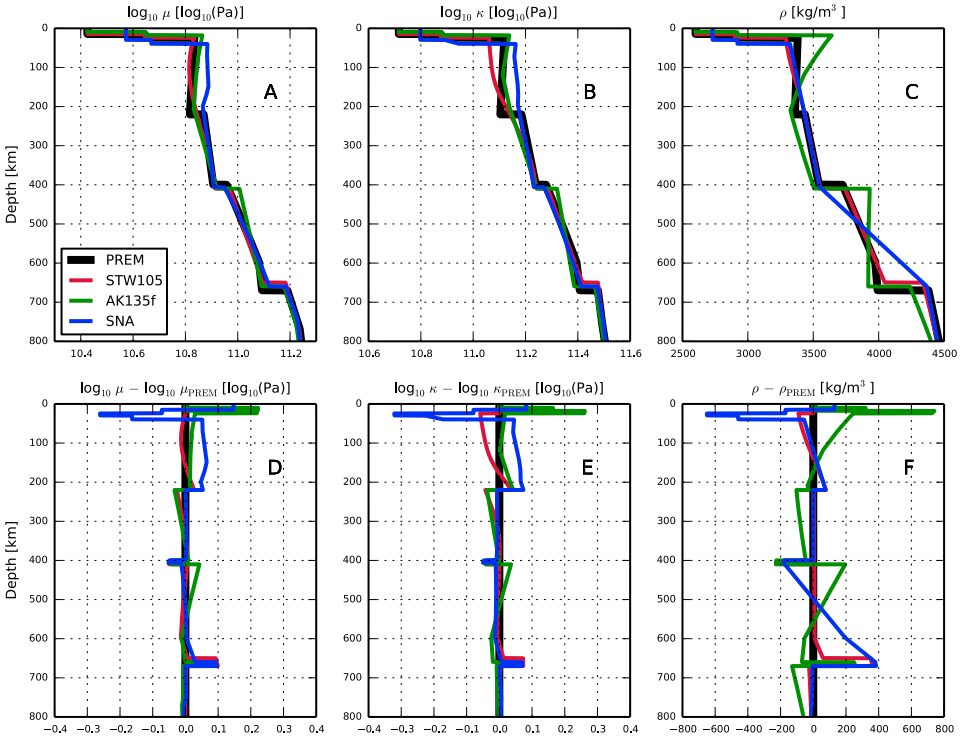

Figure 7.6: Profiles of PREM (black), STW105 (red), AK135f (green), and SNA (blue) through the crust and upper mantle. Panels A, B, and C show the shear modulus, bulk modulus, and density profiles, respectively. Panels D, E, and F show the differences in shear modulus, bulk modulus, and density, respectively, relative to PREM. Note that the elastic moduli are shown on common-log scales.

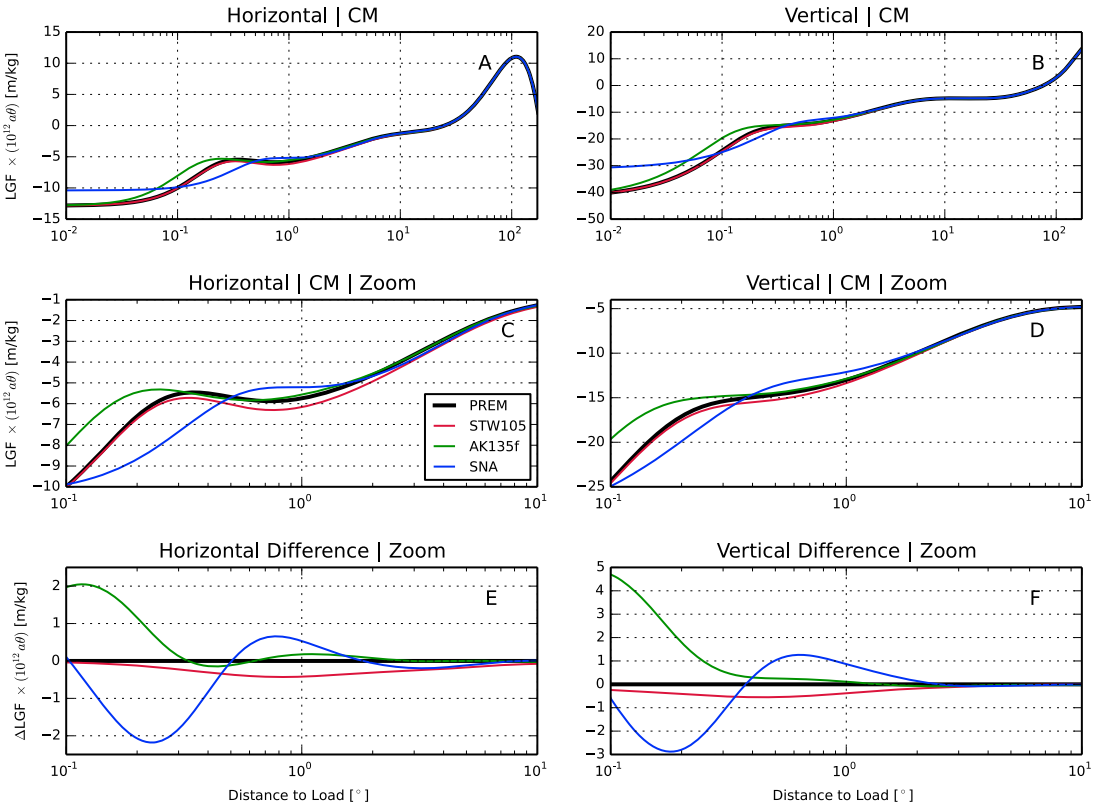

Figure 7.7: Displacement load Green's functions (LGFs) in the CM reference frame for the PREM (black), STW105 (red), AK135f (green), and SNA (blue) Earth models. The left panels show the horizontal-displacement component of the LGFs and the right panels show the vertical-displacement component. Panels A and B depict the LGFs over the angular distance range of 0.01–170°. The remaining panels show a zoomed-in section from 0.1–10°. Although the LGFs for STW105 track well the LGFs for PREM, they remain consistently negative in relation to PREM. In contrast, AK135f and SNA oscillate about PREM. Furthermore, note that the angular distances are plotted on a common-log scale. The displacement LGFs are scaled by a factor $10^{12}a\theta$, where a is Earth's radius (meters) and θ is the angular distance between the load point and the receiver (radians).

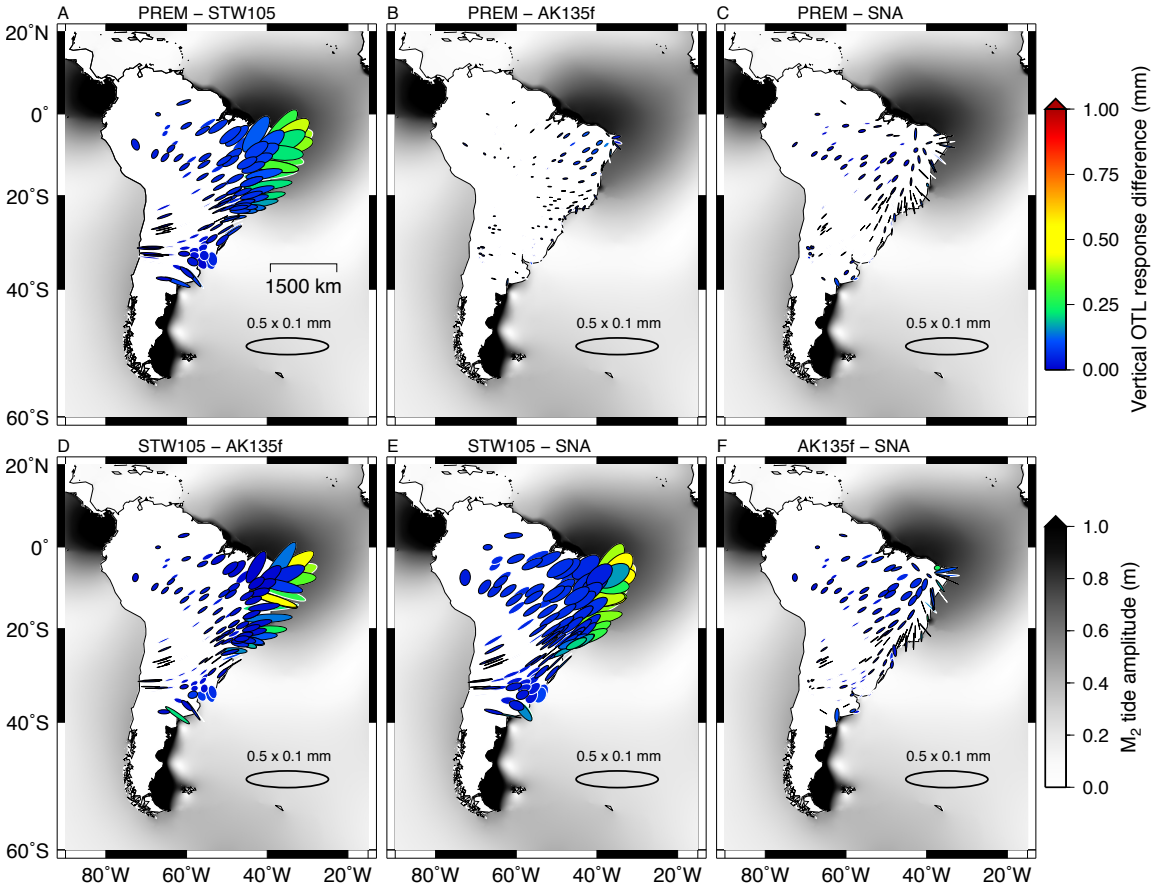

Figure 7.8: PMEs depicting the differences between pairs of predicted OTL-induced surface displacements for the M_2 tidal harmonic made using selected SNREI Earth models: (A) PREM and STW105, (B) PREM and AK135f, (C) PREM and SNA, (D) STW105 and AK135f, (E) STW105 and SNA, and (F) AK135f and SNA. In each case, we adopted FES2012 as the input ocean tide model. The size and orientation of each ellipse represent the differential horizontal-displacement response, with a reference ellipse shown in the lower right corner of each panel; the color of each ellipse represents the differential vertical-displacement response (upper color bar). The lower color bar depicts M_2 tide amplitude in the oceans.

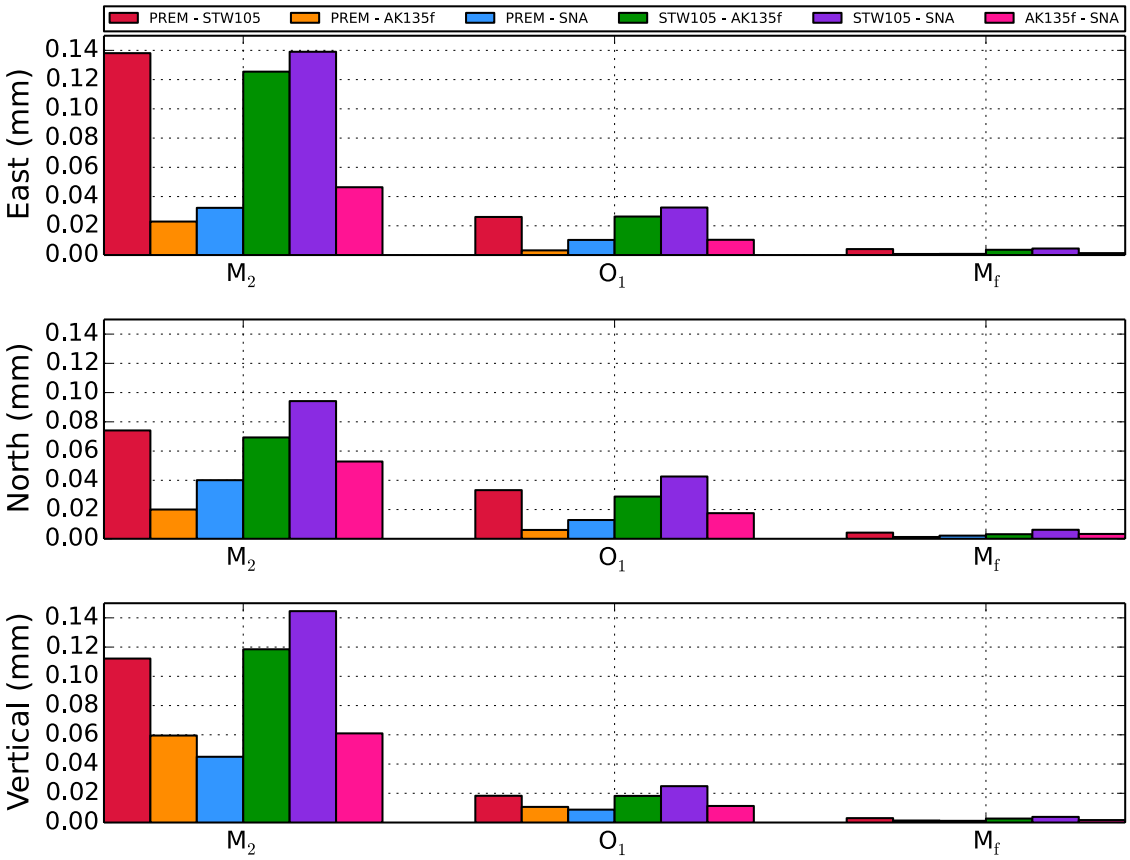

Figure 7.9: RMS differences between pairs of predicted OTL-induced surface displacements for the South America network made using selected reference Earth models (Fig. 7.6). The input ocean tide model, FES2012, remains consistent for each comparison. The ordering of the legend corresponds directly to the ordering of the bars in the figure.

Differences between predicted OTL-induced surface displacements for the M_2 harmonic, derived from the SNREI Earth models depicted in Fig. 7.6, are shown in Fig. 7.8 as PMEs. Consistent with previous studies, the largest sensitivities are observed near the coast, or at small observer-to-load angular distances (e.g., Ito & Simons, 2011; Bos et al., 2015). Rather surprisingly, STW105 exhibits the largest discrepancies in OTL-induced displacement relative to the other models. Although the displacement LGFs appear to suggest strong similarities between STW105 and PREM (Fig. 7.7), closer inspection reveals that the STW105 LGFs are most discrepant relative to the mean of the four models. In particular, integration of the LGFs shows that STW105 differs from the mean integrated-response of the four models by a factor of 0.3% in the horizontal and vertical displacement components. For PREM, AK135f and SNA, the discrepancies are generally less than 0.1% from the mean. Note that the LGFs in Fig. 7.7 have been plotted on a log-scale and that the AK135f and SNA LGFs oscillate about PREM, whereas STW105 remains consistently negative relative to PREM.

The specific structural reasons for the discrepancies between LGFs are not obvious, but the bulk modulus profile for STW105 remains relatively low within the upper 300 km, which might provide part of the explanation. Ultimately, despite the differences in elastic moduli and density, the corresponding perturbations to the LGFs, and by extension the OTL-response predictions, are very small. Fig. 7.9 shows the RMS differences between the selected models. The RMS differences for the M_2 tidal harmonic are largest, a reflection of its relatively large load amplitude. Despite the large contrast exhibited by STW105, however, the RMS differences never exceed 0.15 mm and are significantly smaller than that for both the O_1 and M_f tides, suggesting only a subtle sensitivity to SNREI-based structural variations. Table 7.2 lists the RMS differences explicitly.

7.4 Observations

7.4.1 Kinematic GPS Processing

For many geodetic studies, the OTL-response signal is an inconvenient source of noise; thus, the signal is often removed at the GPS processing stage using forward-modeled coefficients for the dominant tidal harmonics. Smaller tidal harmonics are typically modeled and removed as well by interpolation of the admittance for the dominant harmonics, where the admittance is assumed smooth across each tidal constituent band (e.g., Foreman, 1977; Agnew, 2012). We, however, aim to retain and isolate the OTL displacement-response signal by initially generating sub-daily time series of site displacements and then performing harmonic analyses to extract individual tidal harmonics.

We use `GIPSY` version 6.2 (Zumberge et al., 1997) in precise point positioning (PPP) mode to process the GPS data at individual receiver sites without requiring inter-station double-differencing. PPP implementation relies on precise satellite orbit and clock products determined from a global network of GPS satellites and permanent receivers (Zumberge et al., 1997). Our data set consists of up to 14 years of time series from 160 stations in South America. Tables of geographic coordinates and data availability for each station are provided in Appendix E. The median time-series length is 1760 days, or nearly 5 years.

`GIPSY` performs single-receiver ambiguity resolution by estimating wide-lane and phase biases for each station individually using double-differences relative to an extensive global network of other ground-based stations in view of the same satellites (Bertiger et al., 2010). The wide-lane and phase bias estimates are pre-computed and distributed by the Jet Propulsion Laboratory (JPL) along with the precise satellite orbit and clock products. Our standard, kinematic PPP methodology involves processing 30-second data to obtain position estimates every 5 minutes using a random-walk stochastic parameterization of the position estimate. We process the data in 30-hour batches (i.e., a full day plus 3 hours on either side of the day) and extract only the central 24 hours of positions in order to mitigate end effects (King & Aoki, 2003; King, 2006; Penna et al., 2015). The OTL displacement-response signals remain unmodeled at the GPS processing stage. Tidal harmonics are extracted from

the position time series using harmonic analysis (discussed later).

We use JPL's precise satellite orbit and clock products in final and fiducial form ("flinnR" format; version "repro2.0"). The reference frame adopted for the orbit and clock products at the time of processing was IGS08 (Altamimi et al., 2011; Rebischung et al., 2012), which has its coordinate origin at the center of mass of the total Earth system (CM) (Blewitt, 2003; Wu et al., 2011). To ensure consistency with the observations, we compute predictions of OTL-induced surface displacements in the CM frame as well (Fu et al., 2012). The ocean tide model used to develop the "repro2.0" version of the orbit and clock products was FES2004 (Lyard et al., 2006), which did not account for the effects of tidal geocenter variations on the altimetric observations used to constrain the ocean tide model (Desai & Ray, 2014).

Tropospheric zenith delay terms are estimated stochastically relative to nominal values provided by the European Centre for Medium-Range Weather Forecasts (ECMWF) and mapped to lower elevation angles using the Vienna Mapping Functions (VMF1) (Boehm et al., 2006). We apply an elevation-angle cutoff of 7° and assume elevation-dependent weighting according to the square root of the sine of the elevation. Guided by synthetic test results discussed in Sec. 7.8, we adopt a process noise setting for the tropospheric zenith delay of 5.0×10^{-8} km s$^{-\frac{1}{2}}$, or 3 mm hr$^{-\frac{1}{2}}$ (cf., Yuan & Chao, 2012; Yuan et al., 2013). Horizontal tropospheric gradient parameters are also estimated using a process noise value of 5.0×10^{-9} km s$^{-\frac{1}{2}}$, or 0.3 mm hr$^{-\frac{1}{2}}$ (Bar-Sever et al., 1998; Larson et al., 2010).

We apply phase-center corrections to the receiver antennas, extrapolating the models down to 7°-elevation as needed. The effects of solid Earth and pole tides are modeled and removed according to IERS conventions (Petit & Luzum, 2010). The JPL orbit and clock products did not include a second-order ionospheric correction at the time of our analysis. Since using different correction factors for a PPP analysis compared with those adopted by the orbit and clock products can lead to artifacts in the position estimates, we opted instead for first-order ionospheric corrections in our PPP computations to mitigate any potential bias.

The choice of stochastic parameters for the station-position estimates can critically control the ability to resolve an OTL-response signal. For a random-walk formulation, overly strict

stochastic parameters can dampen the true signal due to excessive smoothing. In contrast, overly loose stochastic parameters, such as in the extreme case of a white-noise parameterization, might unnecessarily keep noise levels high and therefore reduce the ability to extract the signal of interest (e.g., Larson et al., 2001; King & Aoki, 2003). To explore the tradeoff, we performed a second series of synthetic tests to determine an appropriate coordinate process noise setting, which we ultimately set to 5.0×10^{-7} km s$^{-\frac{1}{2}}$. Details of the synthetic tests are provided in Sec. 7.8.

7.4.2 Harmonic Analysis

The forcing function that generates the tides (i.e., the astronomical ephemeris) may be broken down into discrete periods that can be combined algebraically to excite responses within and on the Earth that are also periodic. A tidal harmonic, η, may be characterized by a harmonic expression of the form (e.g., Foreman et al., 2009):

$$A_\eta f_\eta(t) \cos(V_\eta(t) + u_\eta(t) - \phi_\eta), \tag{7.3}$$

where A_η is the amplitude of tidal harmonic η, V_η represents the astronomical argument relative to the Greenwich Meridian at time t, and ϕ_η is the phase lag in degrees measured relative to the equilibrium tide observed at Greenwich. We adopt the convention of phase lags positive. The time-dependent factors f_η and u_η correct for amplitude and phase modulations that arise due to the presence of subsidiary peaks in the frequency domain, which alter the complex-valued amplitude of a primary harmonic over time (e.g., Foreman, 1977; Foreman et al., 2009). The subsidiary harmonics are most commonly separated from a main harmonic by cycles of the lunar perigee (8.85 years) and lunar ascending node (18.6 years). Some harmonics are also separated by the cycles of perihelion, but since the period of perihelion is so long (>20 000 years), they are often neglected. Following Foreman et al. (2009), we update the astronomical argument as well as the amplitude- and phase-modulation factors at every epoch in the time series.

For the selection of primary harmonics, we consider the Rayleigh criterion (with a cutoff

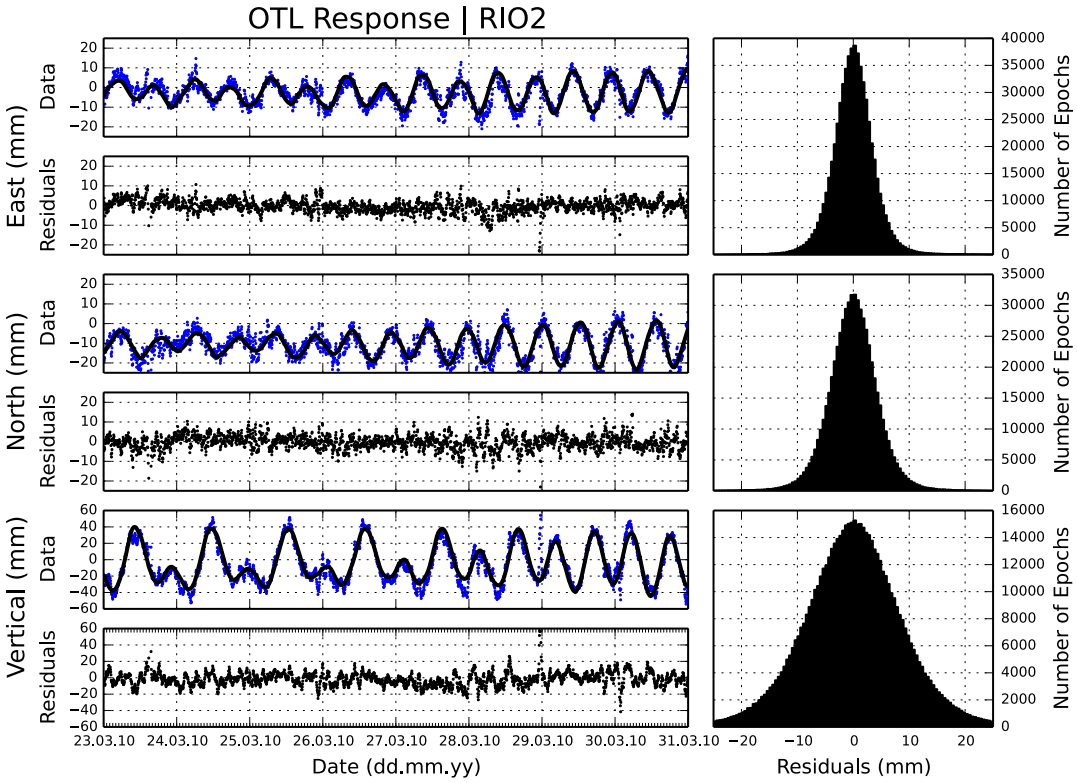

Figure 7.10: The left panels show time series of GPS-inferred receiver positions (top panel in each pair) and residuals (bottom panel in each pair) for station RIO2 during one week in 2010. Each pair of panels depicts the data (blue dots), model fit (solid black line), and residuals (black dots) for each spatial component of the displacement. The fits to the data for each component, which were made to the full seven-year time series, include tidal harmonics and a linear trend term; the mean has been subtracted from the position estimates. The right panels show histograms of residuals from the full seven-year time series for the east- (top), north- (center) and vertical-displacement (bottom) components.

factor of 1.1 cycles) to determine the ability to separate two constituents in frequency space over a given time span of observations. To prevent aliasing, we only consider harmonics that have frequencies less than half the sampling rate. We perform the Rayleigh comparison in hierarchical fashion, beginning with the largest-amplitude harmonics, based on the Cartwright-Taylor-Edden (CTE) equilibrium tide catalogue (Cartwright & Taylor, 1971; Cartwright & Edden, 1973).

In the pelagic ocean, where the tide amplitudes are much smaller than the water depth and the tide wavelengths are much longer than the water depth, the tides are well described

by the astronomical harmonics. In shallow seas and estuaries, however, non-linear effects become important and produce higher-order harmonics, including overtides and compound tides (e.g., Doodson & Warburg, 1941; Doodson, 1957; Parker, 2007; Pugh & Woodworth, 2014). We account for contributions to the time series by a selection of non-linear, or shallow-water, harmonics that arise from distortions and interactions of the semi-diurnal and diurnal astronomical harmonics. We follow the suggestions of Godin (1972) and Foreman (1977) to guide our selection and ordering of shallow-water harmonics to test using the Rayleigh criterion. We also refrain from including a particular shallow-water harmonic until all of its contributing astronomical tides have also been included.

Fig. 7.10 shows an example of our model fit to a kinematic GPS time series. In this particular case, the fit was made to seven years of data recorded at coastal station RIO2, from which we extracted a random snapshot of one week. To clean the data prior to the harmonic analysis, we removed isolated segments that spanned less than 30 days and that were separated from other data in the time series by more than 60 days. We also removed large outliers prior to the harmonic analysis based on a running median absolute deviation, with a cutoff criterion of three standard deviations. Further details of our estimation procedure are discussed in Sec. 7.9. After deriving an initial solution for the complex-valued amplitudes of the tidal harmonics, we applied a sidereal filter (20-day window) to the residuals to estimate the contribution of repeating multipath signals to the original time series. An estimate of the multipath was made for every epoch in the time series by averaging nearby position estimates (using a 10-day window on either side of each epoch) that were separated in time by integer multiples of the sidereal day. We then removed the receiver-specific multipath signals from the original time series and re-estimated the harmonic coefficients.

7.4.3 Residuals

The comparisons of predicted OTL-induced site displacements from Secs. 7.3.1 and 7.3.2 provide a general appreciation for the sensitivity of Earth's elastic response to different load and structural model inputs. To ascertain the applicability of the models to the South American continent, however, we must compare the predictions against GPS-inferred ob-

servations of OTL-induced surface displacements. In particular, we are motivated to explore the suitability of different elastic Earth models with application to the South American continent, which has been shown by seismic tomography to support a deep cratonic keel (Fig. 7.11).

The observational results for the M_2, O_1 and M_f tidal harmonics are shown in Fig. 7.12 as PMEs at each of the GPS stations considered in our analysis. The figure also shows a corresponding set of predictions derived from PREM and FES2012 using our convolution software `LoadDef`. In general, the observations and predictions show great resemblance for each harmonic, including the small-amplitude M_f harmonic. One notable discrepancy between observations and predictions, however, is the apparent northward offset of the vertical-displacement response for the M_f harmonic seen in the mid-continent (Fig. 7.12, panels E and F, 30°S–10°S). In particular, the smallest response amplitudes for the vertical component occur further to the north in the observational results (panel E) relative to the predicted results (panel F). Since the observations exhibit spatial coherency, the offset is unlikely to result solely from random observational error. Uncertainties in the ocean tide models, which are difficult to constrain for the small-amplitude long-period tides, might account for some of the spatial discrepancy.

Fig. 7.14 shows the residuals between observed and predicted OTL-induced surface displacements for the M_2 tidal harmonic based on multiple forward models. The common-mode components (network-mean OTL-induced displacements) have been removed (boxed PMEs). From Fig. 7.14, we note two important results. First, the residuals remain consistent across the various forward models. The consistency in the residuals, regardless of the SNREI Earth model or ocean tide model used to generate the predictions, implies a general insensitivity to variations in the particular forward models considered here. Second, each unique set of residuals (e.g., panel A of Fig. 7.14) exhibits a regional spatial coherency. Random observational errors are unlikely to produce such systematic results. We therefore suggest that the spatially non-random patterns of the PMEs across South America might result from deficiencies in our forward-model assumptions, such as spherical symmetry and pure frequency-independent elasticity.

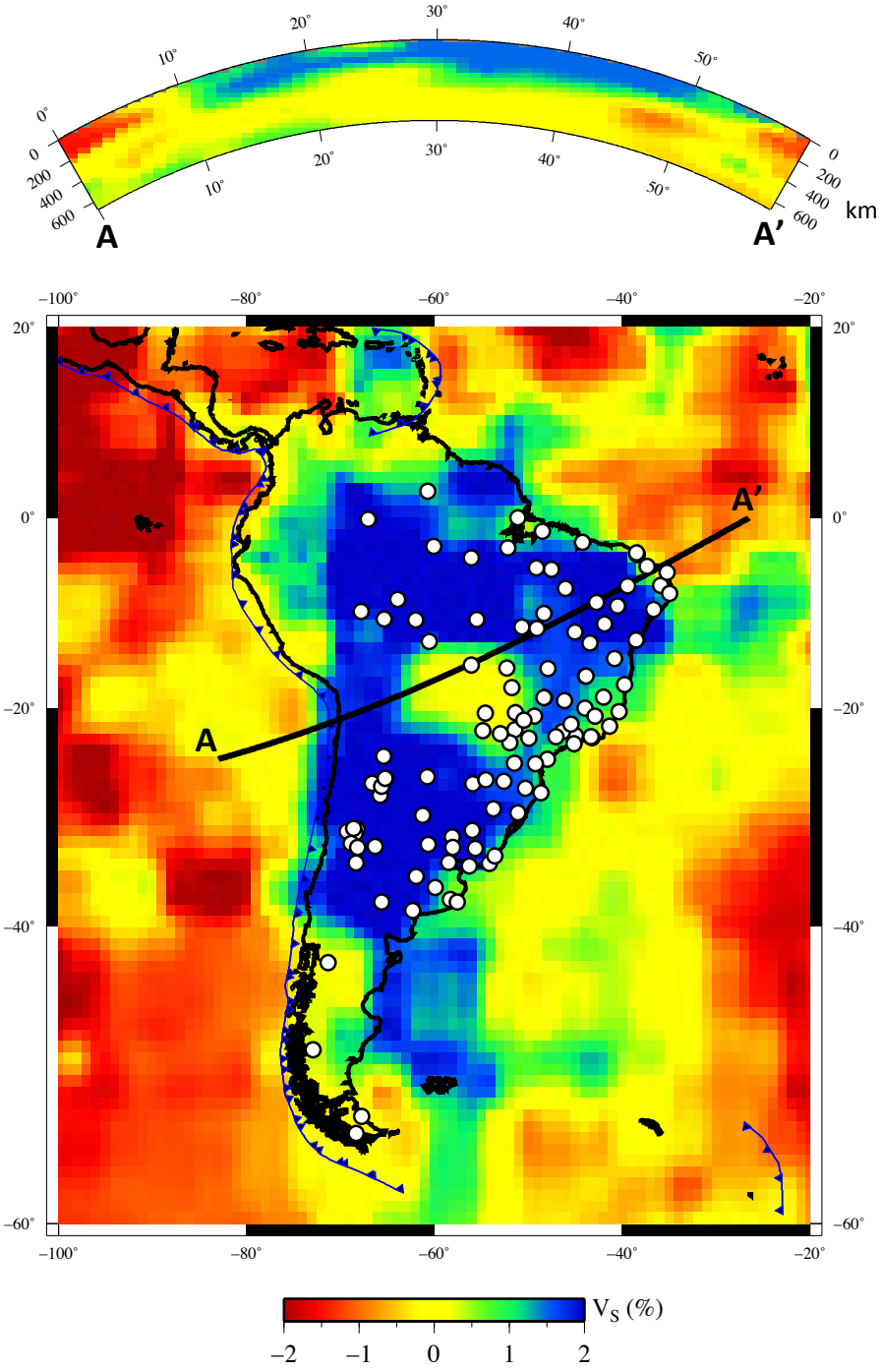

Figure 7.11: Top (annulus): Vertical profile through the global V_S seismic tomography model, TXBW, from Grand (2002), extending along the line A–A′ shown in the bottom panel and crossing the Amazonian Craton in South America. The reference model for TXBW is an average of the models TNA and SNA (Grand & Helmberger, 1984) for the upper mantle and PREM (Dziewonski & Anderson, 1981) for the lower mantle. Bottom: Horizontal map view slice at 213 km depth. White points depict GPS stations used in our analysis.

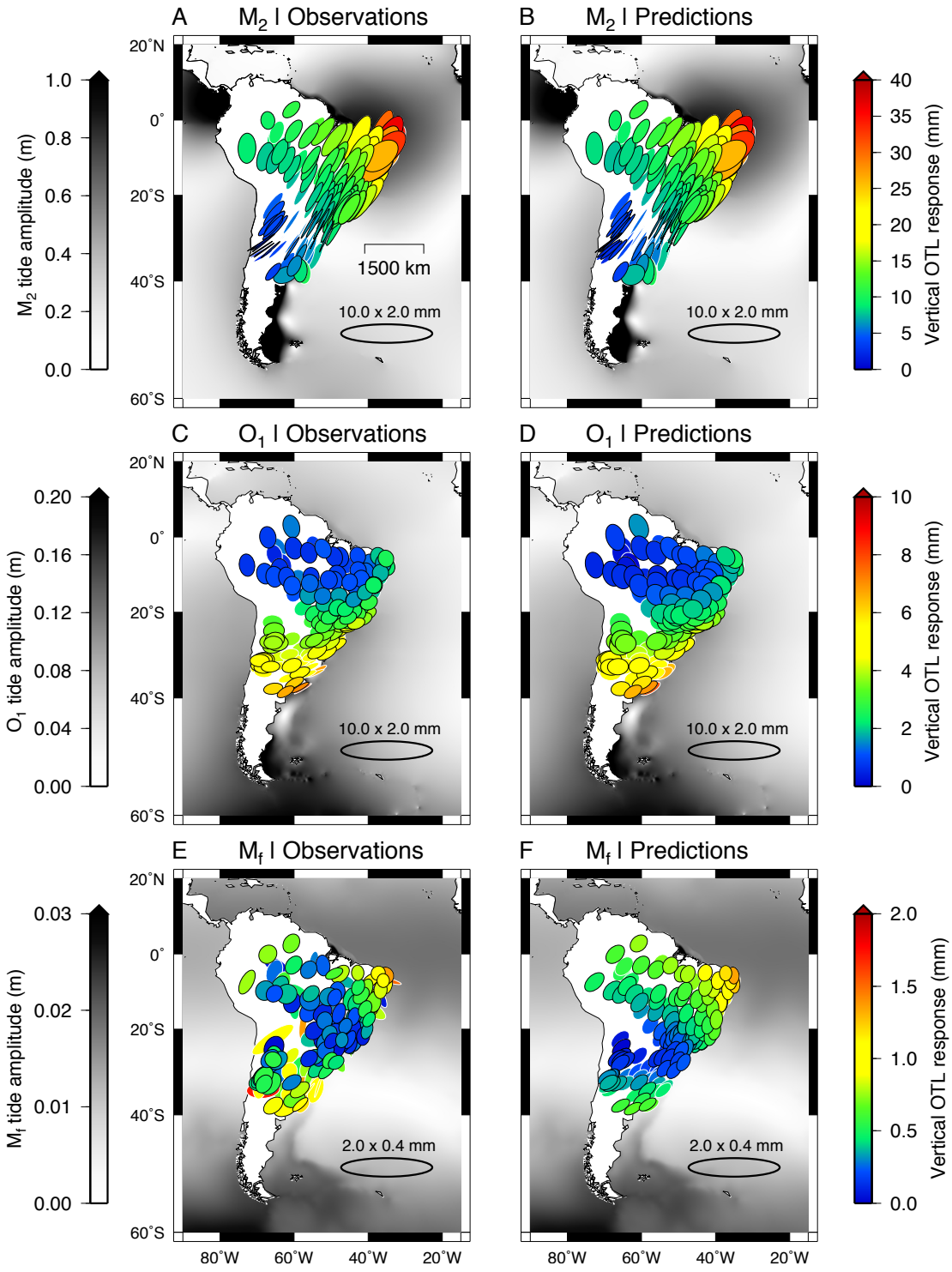

Figure 7.12: Observed and predicted OTL-induced surface displacements for the M_2 (top), O_1 (center) and M_f (bottom) tidal harmonics. The color bars on the left denote tidal amplitudes. The color bars on the right denote OTL-induced vertical displacements. The size and orientation of each ellipse indicate the horizontal-displacement response, with a reference ellipse shown in the lower-right corner of each panel. The predictions were computed using PREM and the FES2012 ocean tide model. Note that the PMEs do not show phase information explicitly.

Table 7.3: RMS misfits between observed and predicted OTL-induced surface displacements (from Figs. 7.20 and 7.21). Solid Earth body tides were removed according to IERS conventions at the GPS processing stage. A common-mode component (network-mean OTL-induced displacement) was also removed prior to the RMS computation. The SNREI Earth and ocean tide models used in each comparison are noted in the first column of the table.

	Observational Residuals								
	East (mm)			North (mm)			Vertical (mm)		
	M_2	O_1	M_f	M_2	O_1	M_f	M_2	O_1	M_f
STW105 & FES2012	0.237	0.125	0.082	0.255	0.130	0.073	0.342	0.206	0.251
AK135f & FES2012	0.180	0.124	0.081	0.234	0.128	0.073	0.340	0.207	0.251
SNA & FES2012	0.188	0.124	0.081	0.239	0.129	0.072	0.330	0.205	0.251
PREM & FES2012	0.177	0.124	0.081	0.234	0.127	0.072	0.319	0.205	0.251
PREM & TPXO8-Atlas	0.167	0.129	0.078	0.253	0.130	0.074	0.298	0.214	0.248
PREM & EOT11A	0.163	0.118	0.079	0.248	0.127	0.072	0.340	0.208	0.249
PREM & GOT4.10	0.195	0.127	–	0.237	0.129	–	0.321	0.210	–

Figs. 7.15 and 7.16 show the residuals for the O_1 and M_f tidal harmonics, respectively, also with the common-mode component removed. The residuals for O_1 and M_f are smaller than for M_2, albeit not substantially. As with M_2, the residuals remain consistent regardless of the adopted forward model, corroborating the general insensitivity to choice of SNREI Earth model and modern ocean tide model at the precision of the observations. In contrast to the residuals for M_2, the residuals for O_1 and M_f lack pronounced regional spatial coherency. However, many of the O_1 residual ellipses appear to be oriented in the direction of maximum loading, potentially indicating forward-model deficiencies (cf., Fig. 7.8). Moreover, some of the smaller M_f residual ellipses appear to be systematically oriented in the east-west direction. Figs. 7.20 and 7.21 show the RMS misfits between the observed and predicted OTL-induced surface displacements derived from combinations of SNREI-Earth and ocean-tide models, respectively. Table 7.3 lists the RMS misfits explicitly. Since PMEs do not show phase information explicitly, Figs. 7.17 and 7.18 show the residuals as vectors.

7.4.4 Uncertainty Estimates

To estimate the statistical significance of the residuals relative to observational noise levels, we compute errors for the derived amplitude and phase parameters using the techniques

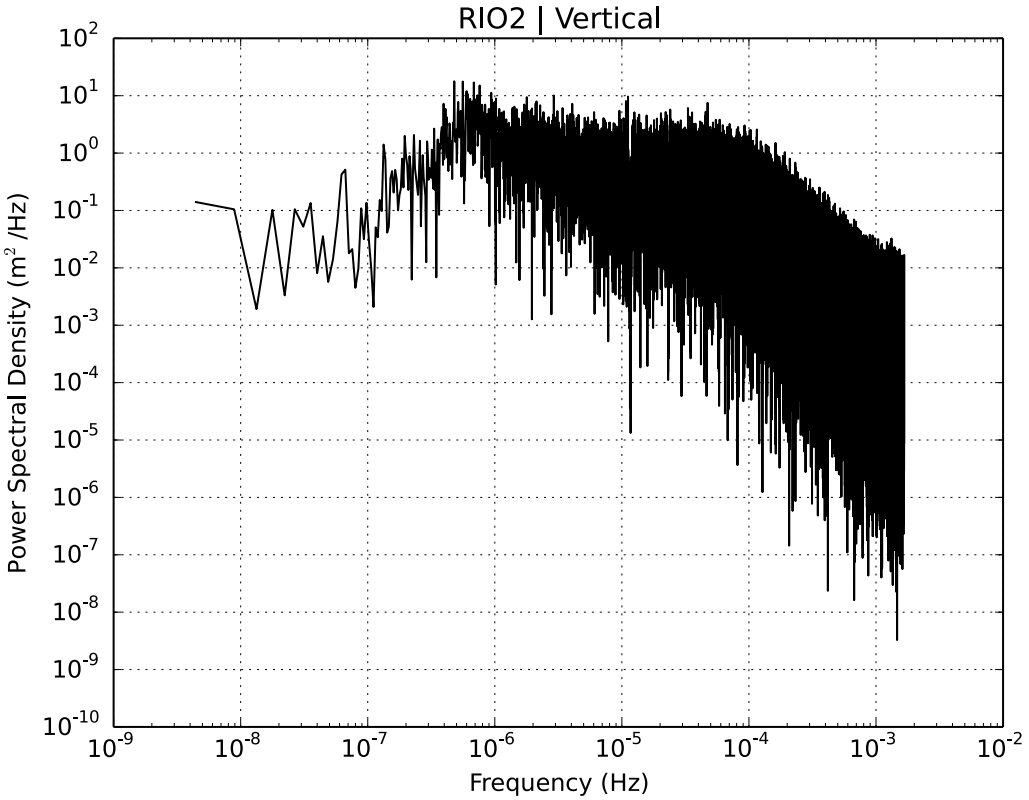

Figure 7.13: A periodogram of time series residuals for the vertical-displacement component of station RIO2 (cf., Fig. 7.10). The residuals represent the difference between the original GPS-inferred displacement time series and the harmonic fit to the displacement time series. In other words, the tidal contributions to the original time series were modeled and removed to generate the residual time series. I also applied a sidereal filter to the residuals prior to generation of the periodogram to mitigate multipath effects.

outlined in Pawlowicz et al. (2002). In particular, we determined the average power spectral density of the post-fit residuals within a frequency window of width 0.4 cycles per day centered around each tidal harmonic. The width of the frequency window is chosen such that the power spectrum may be assumed approximately flat within the window. A representative power spectrum is shown in Fig. 7.13.

Since the average power spectral density provides a variance estimate for the harmonic coefficients (c and s in Eq. 7.13), we must also map the error estimates into amplitude and phase values. We use a parametric bootstrap algorithm to derive distributions of several thousand amplitude and phase values for each harmonic. To derive each instance, we add noise to the original amplitude and phase values based on randomly selected samples from

a normal distribution, with the variance of the normal distribution determined from the power spectra. Standard statistical analyses may then be performed on the bootstrapped distributions. The results are shown as PMEs in Fig. 7.19.

To verify the appropriateness of the error estimates, we made a second assessment of the observational uncertainties using an alternative technique. For the second method, we performed independent harmonic analyses on yearly chunks of time series data. For thirteen stations that recorded at least ten years of data, we computed statistics on the distributions of harmonic coefficients derived from the yearly analyses. The two-sigma standard deviations for the amplitudes and phases are listed in Table 7.4. Although the estimates may seem relatively high, in this case we have only performed the harmonic analyses on up to one year of data at a time, rather than on multiple years of data. Performing the power-spectrum analysis (Method 1) on a single year of data also shows similarly larger errors (Table 7.4, center columns) and provides an additional level of confidence in the error estimates. Moreover, the estimates of observational uncertainty are generally consistent with the 0.2 mm-level uncertainties derived by Penna et al. (2015) through rigorous synthetic testing.

The accuracy of the harmonic estimates generally improves with longer time spans of data. Since good convergence for the lunar-derived harmonics may be achieved with at least $\sim$1000 days of data (Yuan et al., 2013) and the median time series length for our station network is nearly five years, we elect to exclude all stations that recorded less than 1000 days of data from the RMS computations. As stated previously, we also removed nineteen stations with demonstrable sensitivity to large ocean tide model errors around Patagonia and the Amazon delta. Unless stated otherwise, we retain the short-record stations in the figures showing PMEs, which we distinguish from the long-record stations by white-outlined PMEs (e.g., Fig. 7.12).

Table 7.4: Error estimates for the observational results from thirteen stations that operated for periods of at least ten years: BELE, BOMJ, BRAZ, CUIB, IGM1, IMPZ, POAL, RECF, RIOD, SMAR, TUCU, UNSA, and VICO. All errors are quoted as two-sigma standard deviations from the mean. We directly compare two methods for computing the errors based on the same set of stations. For Method 1, we computed the errors based on an analysis of the power spectrum around each tidal harmonic, following the techniques discussed in Pawlowicz et al. (2002). We performed Method 1 with the full datasets ($>$ 10 years) at each station as well as just for one year of data during 2013. For Method 2, we processed the data at each station in yearly chunks and then performed a statistical analysis of the resulting sets of amplitude and phase parameters.

	Observational Error Analysis								
	Method 1 (Full Dataset)			Method 1 (One Year)			Method 2 (Yearly Chunks)		
	M_2	O_1	M_f	M_2	O_1	M_f	M_2	O_1	M_f
East Amplitude (mm)	0.036	0.046	0.070	0.123	0.154	0.283	0.193	0.210	0.212
East Phase (°)	0.913	1.316	11.666	3.090	4.656	66.316	4.625	4.928	39.738
North Amplitude (mm)	0.036	0.041	0.069	0.125	0.140	0.273	0.209	0.267	0.301
North Phase (°)	0.613	1.353	9.573	2.220	5.575	27.520	2.936	5.600	39.814
Vertical Amplitude (mm)	0.147	0.161	0.206	0.469	0.515	0.674	0.600	0.588	0.720
Vertical Phase (°)	0.931	4.396	46.217	3.055	16.031	58.333	4.500	18.170	123.031

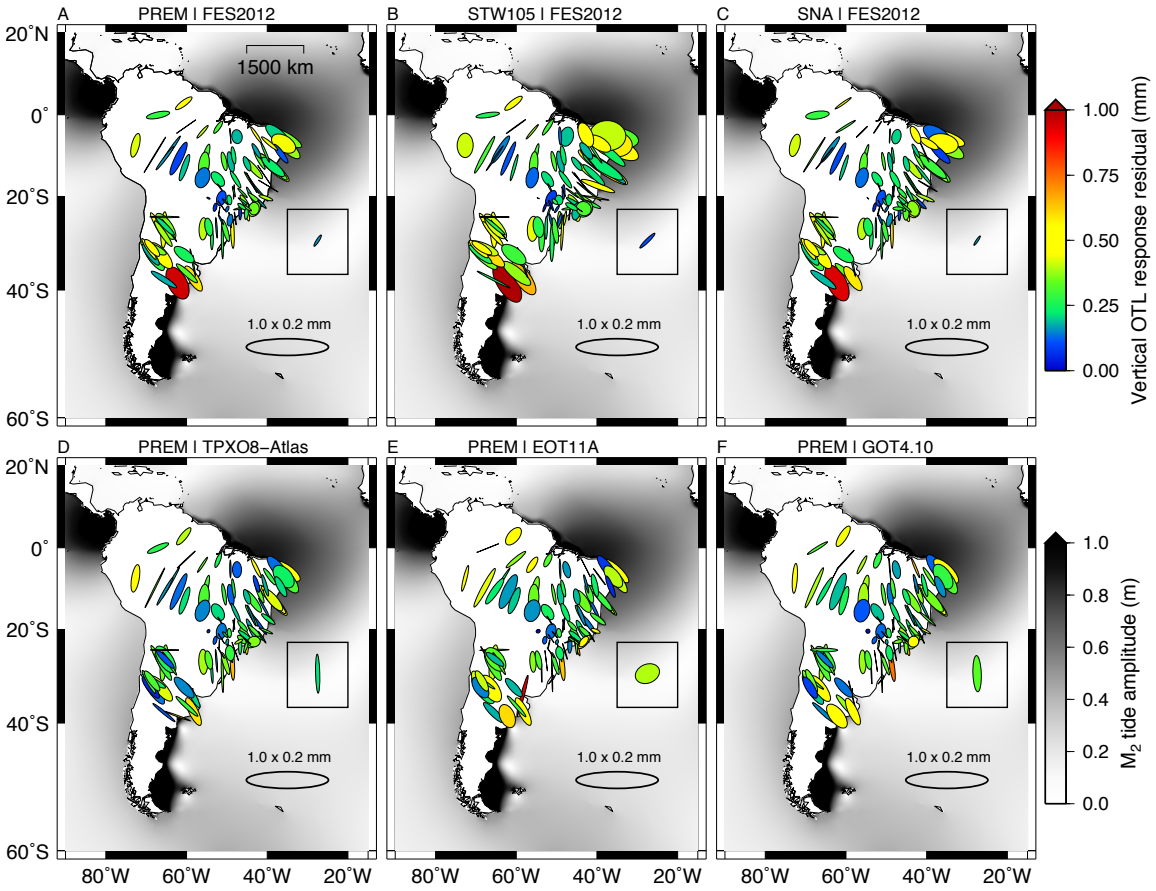

Figure 7.14: Residuals between observed and predicted OTL-induced surface displacements for the M_2 harmonic, shown as PMEs. The size and orientation of each ellipse represent the residual horizontal-displacement response; the color of each ellipse represents the residual vertical-displacement response (upper color bar). A mean particle motion ellipse (common-mode component) has been removed from the residual displacements in each panel (shown in the black box inset). The lower color bar depicts the M_2 tide amplitude. The predicted OTL-induced displacements were computed using the following ocean and Earth model combinations: (A) PREM and FES2012; (B) STW105 and FES2012; (C) SNA and FES2012; (D) PREM and TPXO8-Atlas; (E) PREM and EOT11A; and (F) PREM and GOT4.10. Here, we have excluded stations that recorded fewer than 1000 days of data in addition to the stations already removed near the Amazon basin and Patagonian shelf; a total of 97 stations remain.

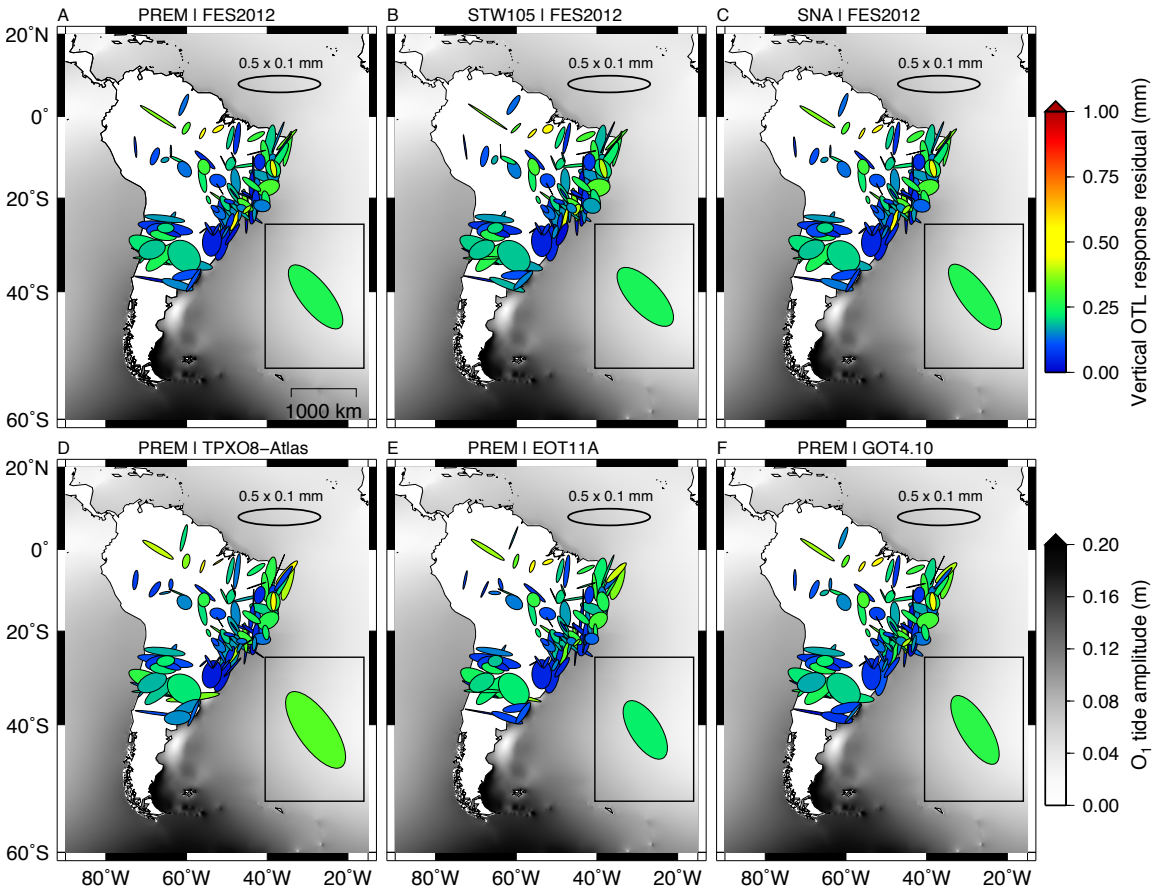

Figure 7.15: Same as Fig. 7.14, but for the O_1 tidal harmonic. Note, however, that the scales for the ellipses and ocean-tide amplitude differ from Fig. 7.14.

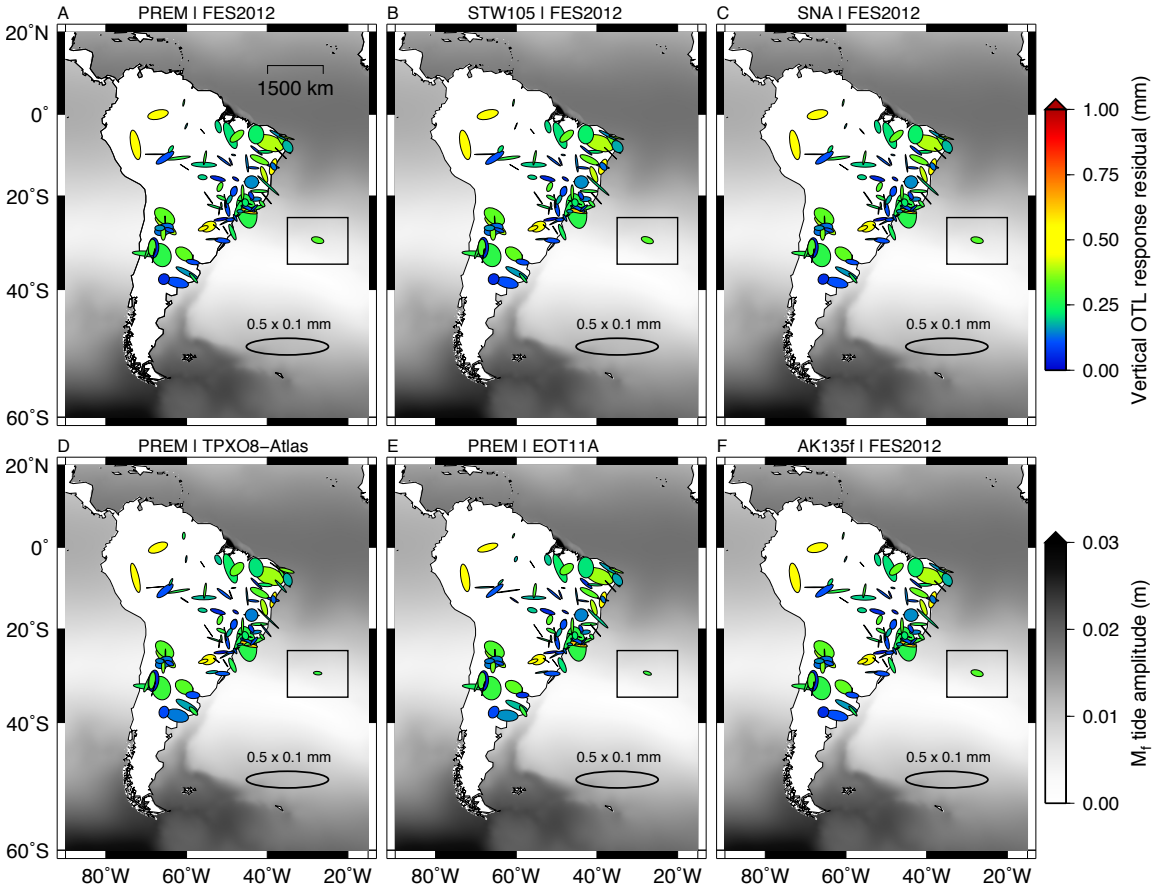

Figure 7.16: Same as Fig. 7.14, but for the M_f tidal harmonic. Note, however, that the scales for the ellipses and ocean-tide amplitude differ from Fig. 7.14. The GOT4.10 model does not include M_f; therefore, panel F shows the residuals between the observed and predicted OTL-induced surface displacements computed using AK135f and FES2012.

7.5 Discussion

We have derived observations and predictions of OTL-induced surface displacements across South America for the M_2, O_1 and M_f tidal harmonics. For each harmonic, the observed OTL responses exhibit spatiotemporal coherency and match the predicted responses at most stations to within about 0.3 mm (Figs. 7.12–7.16). Both modeling and observational uncertainties contribute to the sub-mm residuals, and an improved understanding of each contribution may potentially be used to refine ocean tide models and to constrain solid Earth structure. In particular, we find large uniform-displacement components in the differences between predicted OTL-induced site displacements for various ocean tide models. Removal of the "common-mode" component (network-mean OTL-induced displacement) significantly reduces the discrepancies between predictions of OTL response made using different ocean tide models (Figs. 7.4 and 7.5). Moreover, the residuals between the observed and predicted OTL-induced surface displacements are also substantially reduced by removing the common-mode component, particularly for the O_1 harmonic (Fig. 7.15).

Although a detailed investigation into the origin(s) of the common-mode component is beyond the scope of this paper, we suggest that large ocean tide model uncertainties in the polar regions, such as under the Antarctic ice shelves, could contribute to the offset in OTL-induced displacement. Direct differences between three pairs of ocean tide models reveal large discrepancies in the polar regions around both the Arctic and the Antarctic (Fig. 7.2). In Fig. 7.22, we partition the direct differences for the M_2 harmonic into latitude bands and compute the predicted displacement response in South America due to the discrepancies between ocean tide models. Notice the strong north-south trend in the PMEs in response to the southern-most band from 90°S to 60°S (Fig. 7.22, panel F; cf., Fig. 7.3). Significant contributions, however, also come from mid-latitude bands.

We suggest that a second contributor to the common-mode component could involve reference-frame inconsistencies. Reference-frame inconsistencies can manifest at several points in an analysis of OTL response. First, if the load Green's functions used to predict the OTL-induced surface displacements are computed in a reference frame that differs from that

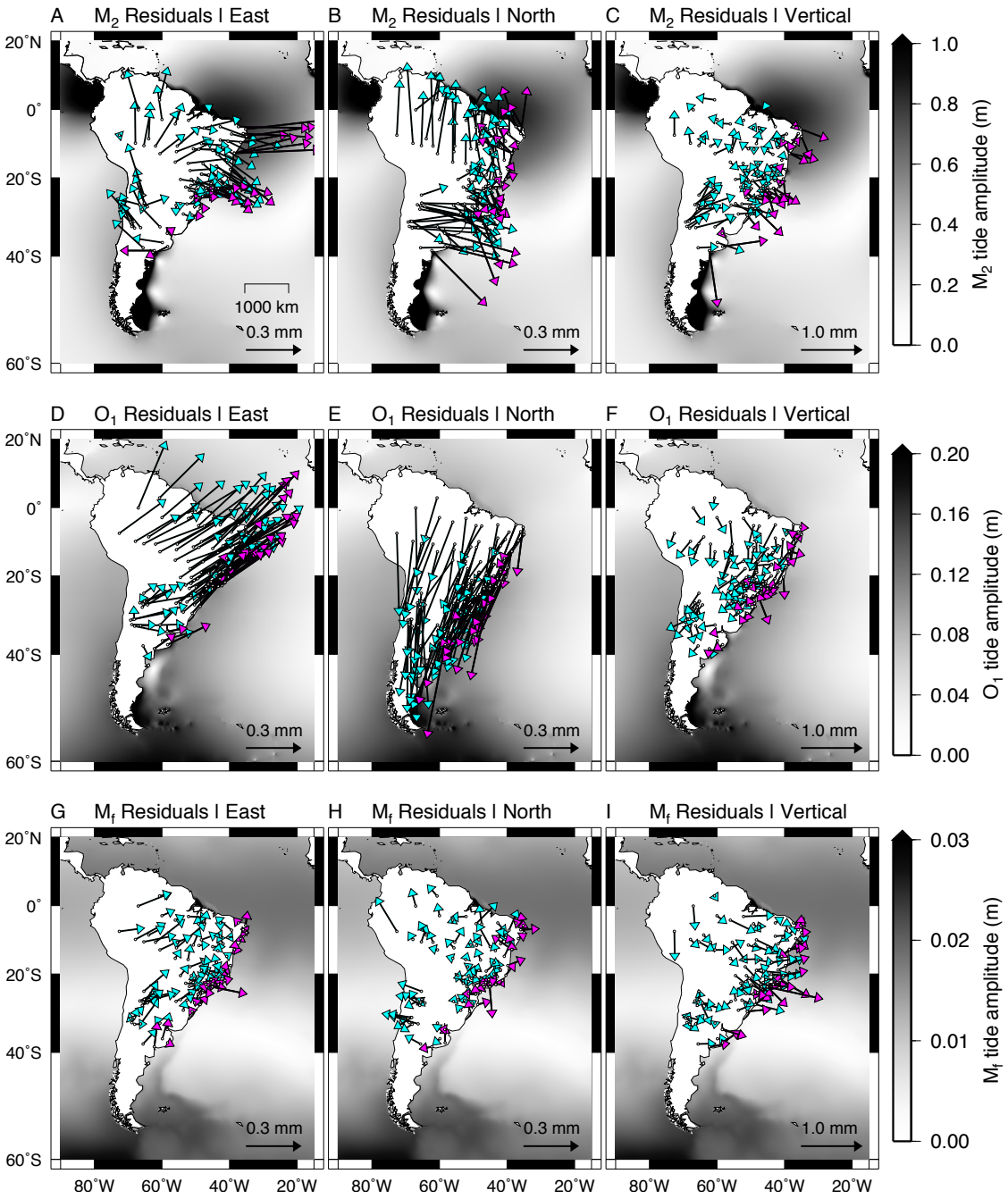

Figure 7.17: Residual OTL-induced displacements for the M_2 (top), O_1 (center) and M_f (bottom) tidal harmonics shown as vectors for each spatial component. The pink vectors highlight stations that are located within 150 km of the coastline. The residuals represent the vector differences between the observations and predictions computed using PREM and the FES2012 ocean tide model (Carrère et al., 2012; Lyard et al., 2006). The angle of each residual vector, defined counter-clockwise relative to the positive real axis (east direction on the map projection), represents the phase residual for each spatial component. We define phase lags positive and relative to the equilibrium tide at Greenwich. The magnitude of each vector represents the residual OTL-induced displacement amplitude. The color bars on the right provide the scaling for the background ocean tide models.

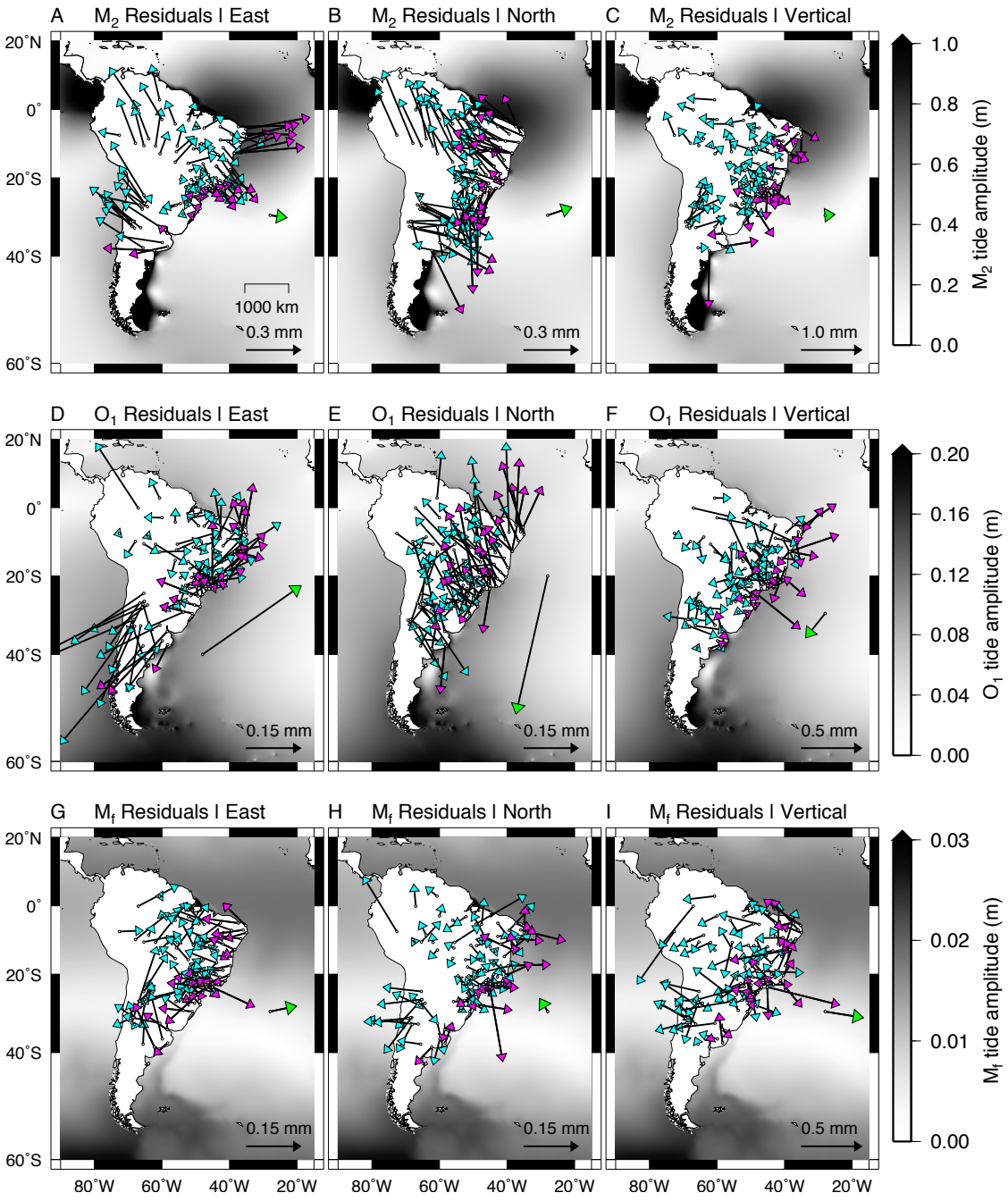

Figure 7.18: Same as Fig. 7.17, but with the common-mode component (network-mean OTL-induced displacement) removed. Subtracting the common-mode component reduces some of the spatial coherency for O_1 and M_f, but the residuals remain largely non-random for M_2. Note the change in vector scale for O_1 and M_f. The green arrows, arbitrarily placed outside the South American continent, denote the common-mode component removed from all stations.

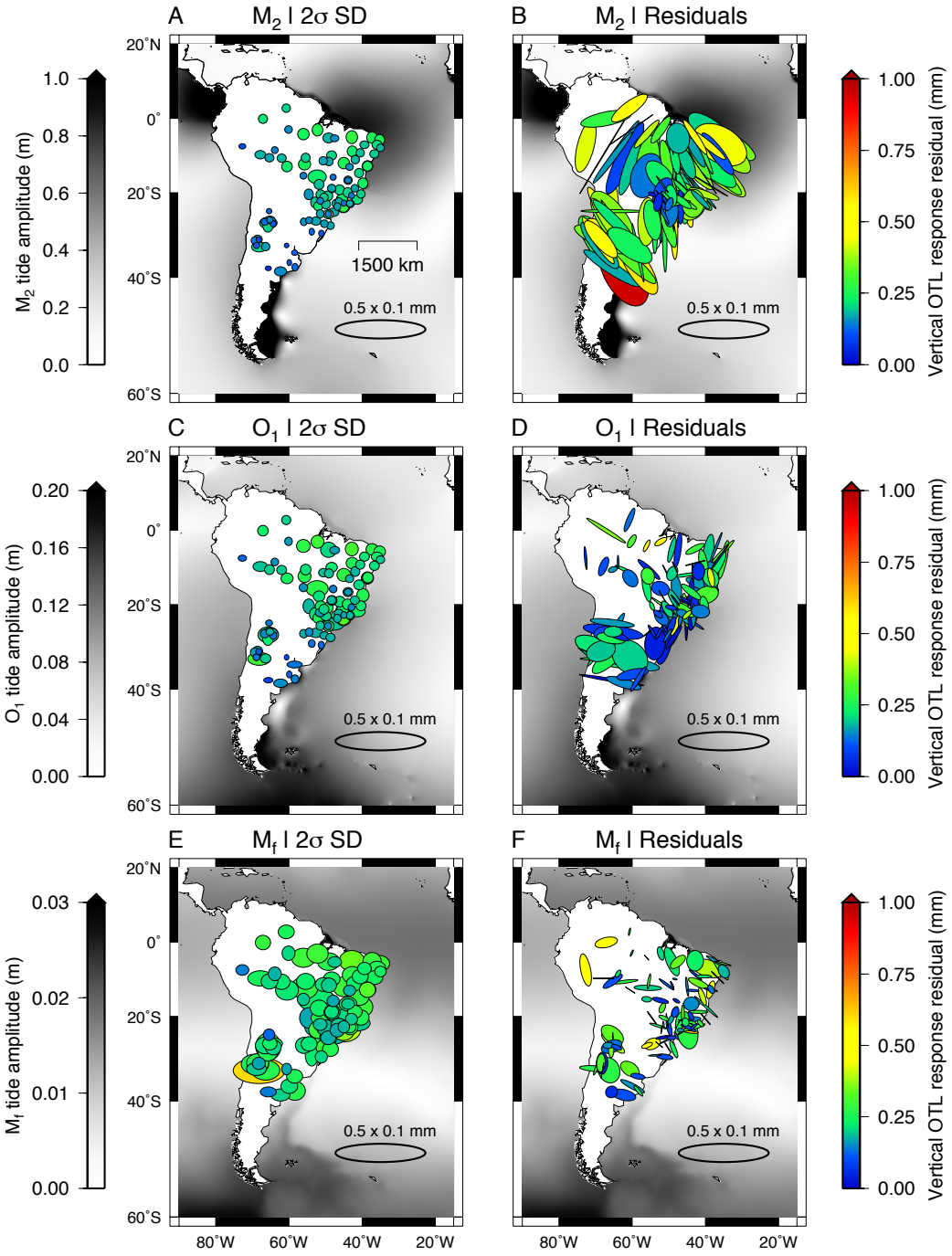

Figure 7.19: Observational uncertainties computed from a windowed power spectrum and bootstrap analysis (see text for details). The left panels show two-sigma (2σ) standard-deviation error ellipses for the observed OTL-induced surface displacements. Specifically, the size of each ellipse denotes the horizontal-amplitude uncertainty in both the east and north components; the color of each ellipse denotes the vertical-amplitude uncertainty. Phase-uncertainty information is not displayed. For comparison, the right panels show the residual surface displacements derived from PREM and FES2012, reproduced from Figs. 7.14–7.16 (panel A in each case). All ellipses and vertical-displacement color bars (right) are shown on the same scale to facilitate comparison (note that the horizontal scale for the M_2 residuals shown in panel B differs from the scale in Fig. 7.14A by a factor of two). The left color bars show tidal amplitude in the oceans.

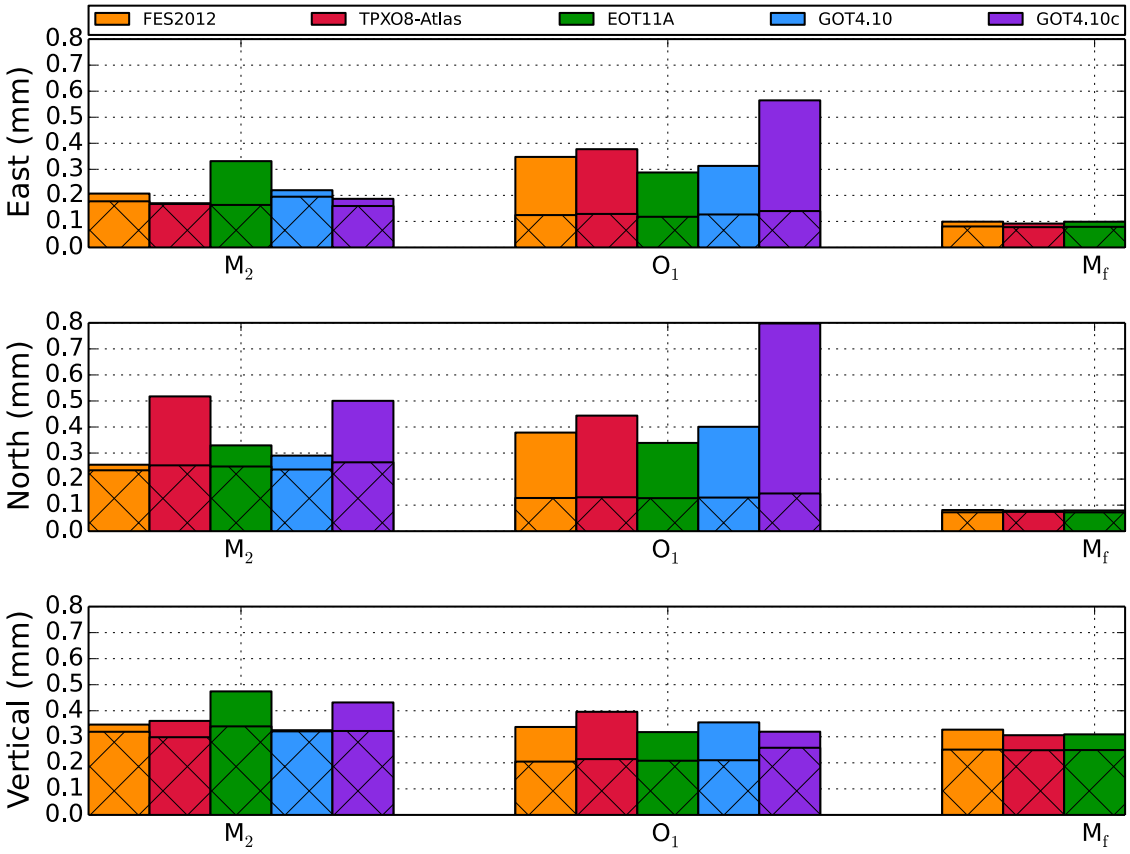

Figure 7.20: RMS misfits between observed and predicted OTL-induced surface displacements made using selected ocean tide models. In each case, we adopted the SNREI Earth structure of PREM. As with all other RMS computations, we excluded stations immediately adjacent to the Amazon river delta and the Patagonian shelf (Fig. 7.4) as well as stations that recorded fewer than 1000 days of data (Table 7.4). The hatching on the bars shows the RMS misfits after the removal of the common-mode component.

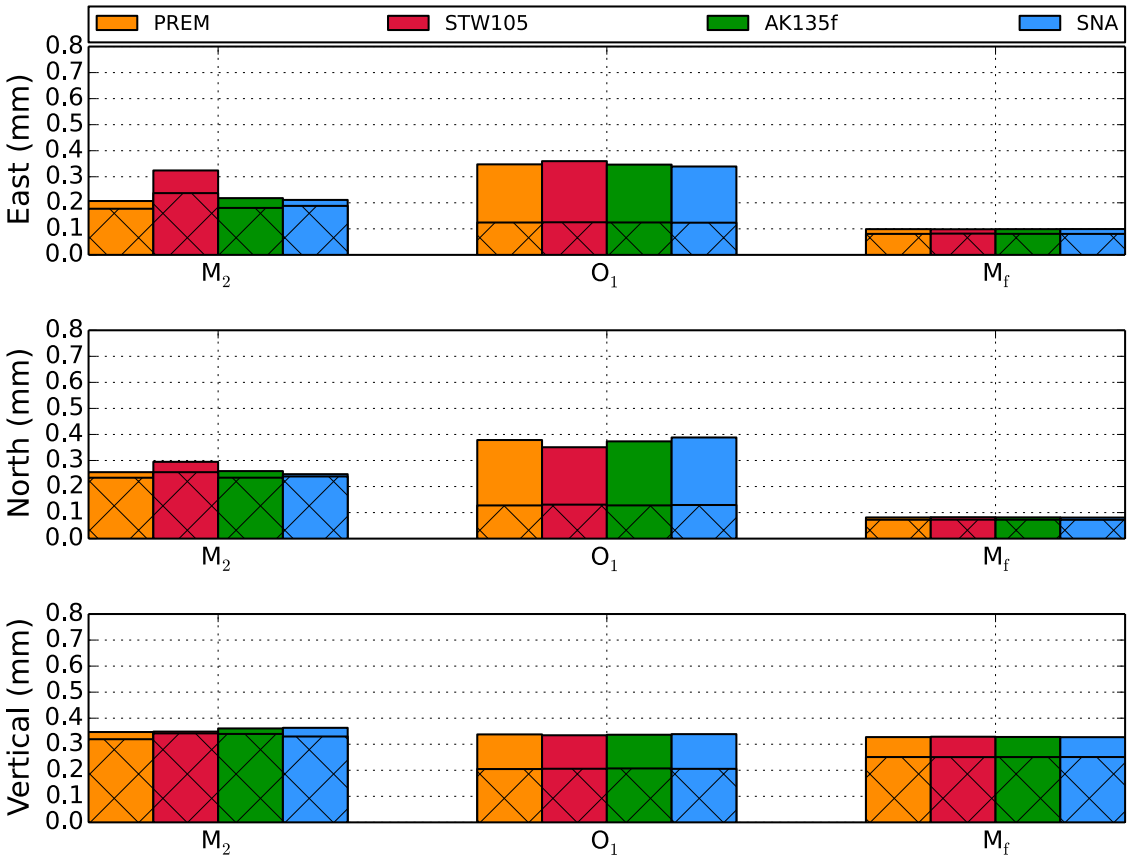

Figure 7.21: Same as Fig. 7.20, but showing the RMS misfits between observed and predicted OTL-induced surface displacements made using selected SNREI Earth models. In each case, we adopted the FES2012 ocean tide model. The orange bars (PREM) therefore match exactly the orange bars (FES2012) in Fig. 7.20.

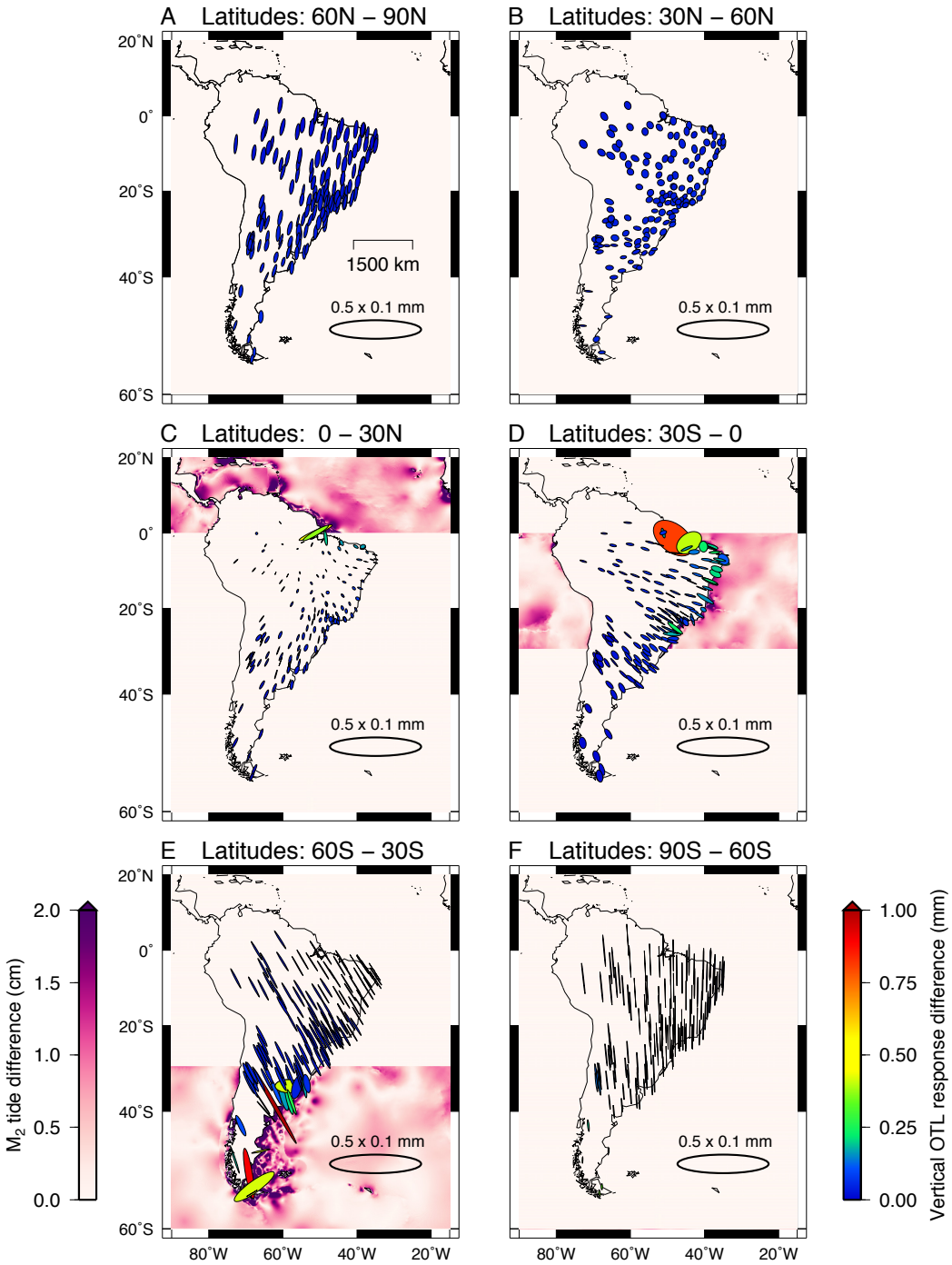

Figure 7.22: Predicted M_2 OTL-induced surface displacements across South America due to the direct differences between the ocean tide models FES2012 and TPXO8-Atlas, partitioned into six latitudinal bands: (A) 60°–90°N, (B) 30°–60°N, (C) 0°–30°N, (D) 30°–0°S, (E) 60°–30°S, and (F) 90°–60°S. Note that the PMEs in panel F, derived from ocean tide model discrepancies around the Antarctic continent, are oriented strongly in the north-south direction and exhibit non-diminishing amplitudes as a function of distance from the coast (cf., Fig. 7.3). The colorbar to the left of panel E represents the magnitude of the vector differences between ocean tide models and the colorbar to the right of panel F represents the predicted OTL-induced vertical displacement due to the ocean model differences.

of the observations, then errors of order 1–2 mm may arise in the residual displacements (e.g., Fu et al., 2012). The JPL orbit and clock products used in our analysis (version "repro2.0") were referenced to CM; therefore, we transformed the load Green's functions to the CM frame prior to the convolution with a load model (Eq. 7.1). Second, since most ocean tide models are constrained by satellite altimetry, with orbits typically referenced to CM (Desai et al., 2014), the altimetric observations of sea-surface height must be adjusted for load-induced variations in the geocenter (Desai & Ray, 2014). Fig. 7.23 shows the vector differences between predicted OTL-induced surface displacements computed using GOT4.10c and GOT4.10. The two ocean tide models differ only in one aspect: the altimetric measurements used to constrain GOT4.10c were adjusted for tidal geocenter variations, whereas the measurements used to constrain GOT4.10 were not. Desai & Ray (2014) demonstrated that, by accounting for the effects of tidal geocenter variations on altimetry-based observations of sea-surface height, the residual variance between ocean tide models and bottom-pressure observations could be improved by up to 30–40%, with the O_1 and K_1 tidal harmonics exhibiting the largest variance reduction. For South America, the average vector differences between predicted OTL-induced surface displacements computed using GOT4.10c and GOT4.10 for the M_2 harmonic are 0.13, 0.29, and 0.24 mm in the east, north, and vertical components, respectively (denoted by the mean ellipse in panel B of Fig. 7.23). The average vector differences for the O_1 harmonic are 0.26, 0.40, and 0.12 mm in the east, north, and vertical components, respectively (panel D of Fig. 7.23). Since the geocenter-motion correction is primarily a degree-1 adjustment, the substantial diminishment of the inter-model response differences after the removal of the common-mode component is not surprising. Thus, removing the common-mode factor can effectively eliminate OTL-response discrepancies due to inconsistent reference frames. Third, the development of CM-referenced orbit and clock products for the GPS processing requires an input ocean tide model to account for load-induced displacements. We used JPL orbit and clock products version "repro2.0" for our GPS processing, which adopted FES2004 (Lyard et al., 2006) as the input ocean tide model. The altimetric measurements used to constrain FES2004 were not corrected for the effects of tidal geocenter variations (Desai & Ray, 2014). To our knowledge, none of the ocean tide models compared in Sec.

7.3.1 were adjusted to account for geocenter motion, and should therefore be internally consistent with the "repro2.0" orbit and clock products. Interestingly, prior to removal of the common-mode component, the residuals between observed and predicted OTL-induced surface displacements are smaller for predictions made using GOT4.10 than for predictions made using GOT4.10c (Fig. 7.20). Consistent with the results of Desai & Ray (2014), the discrepancies are largest for the O_1 tidal harmonic. Furthermore, the discrepancies effectively vanish after removal of the common-mode component, as expected for a reference-frame inconsistency (cf., Fig. 7.23). Future investigations should explore these matters further and consistently use geocenter-corrected ocean tide models for both the development of the GPS orbit and clock products (now available in version "repro2.1" of the JPL orbit and clock products) as well as for the computation of the predicted OTL-induced surface displacements.

Regardless of the origin of the common-model component, however, the removal of the network-mean OTL-induced displacement can significantly reduce the magnitude of the residuals (Figs. 7.14–7.16). With the size of the residuals reduced, the remaining response appears markedly non-random for the M_2 harmonic (Fig. 7.14), suggesting that random GPS measurement errors probably do not account for a majority of the discrepancy between observations and predictions. In contrast, the smaller amplitude harmonics, O_1 and M_f, show less obvious signs of regional spatial coherency and are closer to the level of observational uncertainty due to random errors. The consistency between forward models, observed most prominently after the removal of the common-mode component, indicates that the sensitivity to errors in the ocean tide models may no longer be a limiting factor in predicting OTL-induced surface displacements (Fig. 7.14).

With the common-mode component removed, the sensitivity to choice of ocean model is reduced to a level comparable with the sensitivity to choice of SNREI Earth model. In both cases, the response differences between forward models are predominantly less than 0.1 mm. Thus, to discern the appropriateness of one model over another, the observed OTL-induced surface displacements would need to be accurate to at least within 0.1 mm and often much better. For comparisons of SNREI Earth models, the discrepancies between predicted

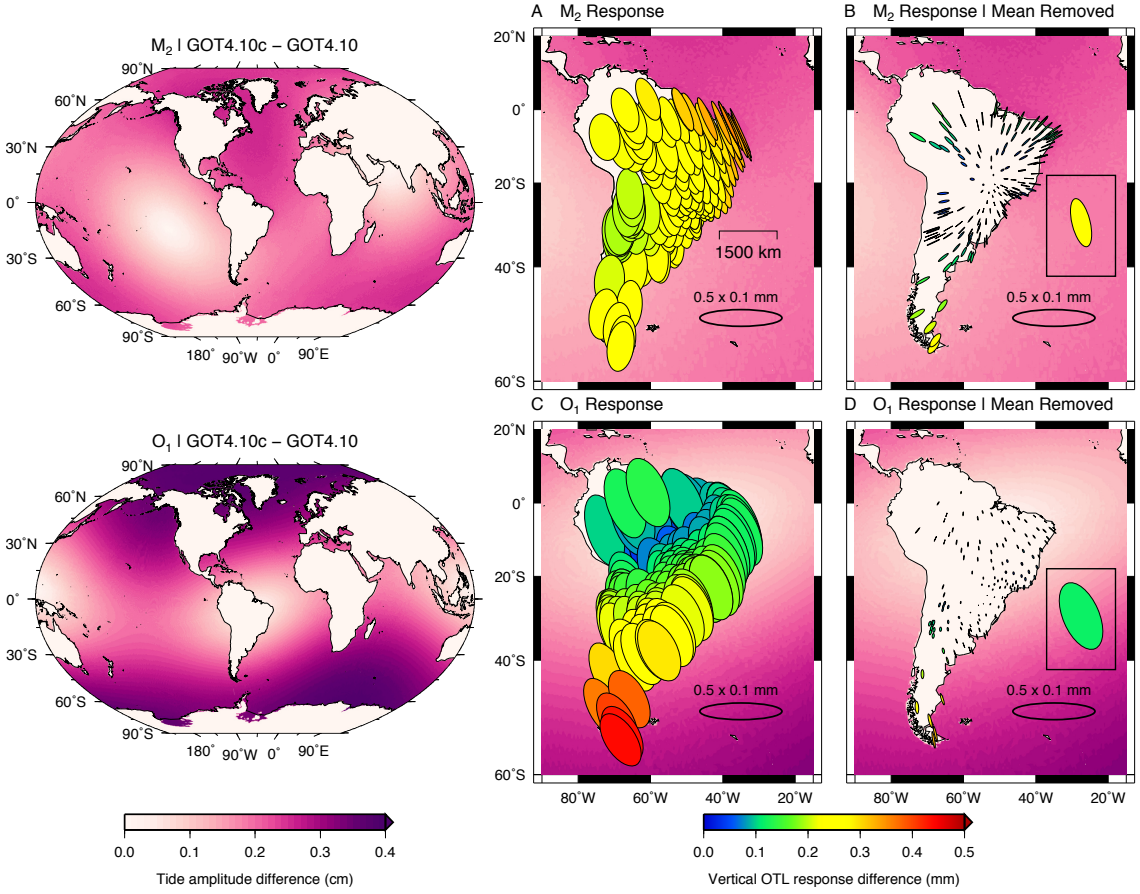

Figure 7.23: Vector differences between predicted OTL-induced surface displacements computed using the GOT4.10c and GOT4.10 ocean tide models. The direct differences between the ocean tide models, shown in the global maps to the left for the M_2 (top) and O_1 (bottom) tidal harmonics, reflect the influence of tidal geocenter variations on the satellite altimetry measurements of sea-surface height that are used to constrain the ocean tide models. The elastic surface displacements generated by loading due to the direct differences between GOT4.10c and GOT4.10 are shown in panel A for the M_2 harmonic and in panel C for the O_1 harmonic. Panels B and D show the remaining elastic surface displacements after a common-mode component (mean ellipse outlined by the black box) is removed.

OTL-induced displacements for our station network are generally less than 0.1 mm for the M_2 tidal harmonic, less than 0.02 mm for the O_1 tidal harmonic, and less than 0.001 mm (1 micron!) for the M_f tidal harmonic. At this level of sensitivity, supporting or rejecting SNREI Earth models based on measurements of OTL response remains tenuous, given the observational uncertainties. The large-amplitude M_2 and, perhaps, O_1 OTL responses provide the most promising outlooks at present.

The final set of residuals between observations and predictions for our station network exhibits RMS misfits of order 0.1–0.3 mm for each spatial component and tidal harmonic (Figs. 7.20 and 7.21). Differences between the ocean tide models or SNREI Earth models probably cannot account for all of the misfit. Indeed, swapping out the various forward models has little effect on the size of the RMS misfits after the common-mode component has been removed. Even the Earth model designed to represent stable continental shield structure, SNA, does not generate significantly better predictions of the OTL-induced surface displacements for South America than the globally averaged models. Other contributors to the misfit include observational uncertainties (e.g., GPS data acquisition, GPS data processing, harmonic analysis) and deficiencies in the forward model (e.g., coastline refinement within the convolution, spatial variations in seawater density, deviations from SNREI structure).

We estimated the observational error using two different techniques, which yielded similar results (Table 7.4). Processing multiple years of data in a single inversion clearly has the potential to improve the accuracy of observed OTL-induced surface displacements, as evidenced by the reduction of error for analyses of several years of data compared to analyses of one year of data. In particular, for thirteen stations with long data records (> 10 years), we estimate that the horizontal-displacement errors for the M_2 and O_1 tidal harmonics are, remarkably, less than 0.1 mm at two standard deviations, which rivals the sensitivity to choice of ocean tide model and SNREI Earth structure for many of the stations in the South America network.

In general, the residuals derived for the M_2 tidal harmonic in South America significantly outweigh the two-sigma observational uncertainties (Fig. 7.19), leaving open the possibil-

ity to invert for structural deficiencies at that frequency. Furthermore, the spatiotemporal characteristics of the M_2 residuals remain regionally coherent as well as consistent between forward models (Fig. 7.14), indicating that all of the RMS misfit cannot apparently be explained by errors in the observations and adopted forward models. Rather, we suggest that a significant part of the RMS misfit may be due to deviations from our assumed SNREI Earth structure, such as laterally heterogeneous and anelastic material properties (e.g., Latychev et al., 2009; Yuan et al., 2013; Bos et al., 2015).

Deficiencies in the solid Earth body tide (SEBT) model, removed at the GPS processing stage, could also contribute to the residual displacements; however, solid Earth body tides operate at very long (global) wavelengths and would thus produce residuals coherent across similarly large scales. Such long-wavelength coherency in the residuals could consequently contribute to the common-mode component for a regional GPS network. The removal of a uniform-displacement component from residual OTL-induced surface displacements at each station could therefore eliminate information about the long-wavelength deficiencies in the SEBT model. Notwithstanding, a significant contribution to the common-mode component appears to be derived from inaccuracies in the ocean tide models and inconsistencies in reference frames.

For the O_1 tidal harmonic, the residuals are more comparable to the noise levels, but nevertheless appear to exceed slightly the level of uncertainty at many of the South America stations and particularly in the horizontal components (Fig. 7.19, Tables 7.4 and 7.3). Fig. 7.15 shows consistency between forward models and some evidence for regional spatial coherency. In particular, many of the ellipses are oriented such that the semi-major axis points toward the maximum load amplitude. For the M_f tidal harmonic, the residuals are close to or below the level of observational uncertainty at most stations and therefore less conclusive (Fig. 7.19). The observed OTL-induced surface displacements, however, exhibit spatial coherency as well as a coherent northward offset in the vertical component of the displacements relative to the predictions (Fig. 7.12, panels E and F).

7.6 Summary & Conclusions

We derived OTL-induced surface displacements from sub-daily GPS time series using kinematic precise point positioning and harmonic analysis for a network of stations in Brazil, Argentina, and Uruguay. After a common-mode component representing the network-mean OTL response is removed from each station, the misfits between the observed and predicted OTL-induced displacements are approximately 0.1–0.3 mm for the dominant tidal harmonics in three distinct frequency bands: M_2, O_1 and M_f. An assessment of the observational error suggests that, at least for the M_2 harmonic and sufficiently long time series, the OTL-response residuals exceed random noise from the data processing. Therefore, OTL-response residuals may potentially be used to refine ocean tide models and to constrain solid-Earth structure.

Comparisons of forward-modeled predictions for South America suggest that the sensitivity to choice of ocean tide model still generally exceeds the sensitivity to choice of SNREI reference Earth model, albeit not substantially. Removal of the common-mode component across the network substantially reduces the discrepancies between ocean tide models. We suggest that possible sources for the common-mode component might include deficiencies in the ocean tide models at high latitude as well as reference-frame inconsistencies. Based on comparisons of selected ocean tide models and SNREI Earth models, RMS difference between predictions of OTL-induced displacements are at the sub-mm level for each harmonic considered, and often much less than 0.1 mm.

We find evidence for regional spatial coherency in the residuals between observed and predicted OTL-induced displacements that remains consistent for a variety of ocean-tide and SNREI-Earth model combinations. We postulate that part of the spatial coherency could be attributed to deficiencies in the a priori Earth model, which would undoubtedly include deviations from an assumed SNREI structure (e.g., anelasticity, anisotropy, and lateral heterogeneities). As ocean tide models, OTL-response modeling, and data processing methods continue to improve, the ability to probe Earth structure through observations of OTL-induced surface displacements becomes increasingly tractable.

7.7 Acknowledgments

We are indebted to Duncan Agnew, Richard Ray, Matt King, and an anonymous reviewer for insightful ideas and valuable critiques that greatly improved our manuscript. We also sincerely thank Shailen Desai for helpful discussions on OTL analysis and tidal geocenter variations as well as Angelyn Moore and Willy Bertiger for providing ongoing GIPSY support. Dan Bower graciously supplied scripts to extract and plot the seismic tomography data shown in Fig. S5. The GPS data used in our study was made available by the governments of Brazil (Instituto Brasileiro de Geografia e Estatística), Argentina (Instituto Geográfico Nacional), and Uruguay (Servicio Geográphico Militar). We used geographic information from the Scientific Committee on Antarctic Research (SCAR) Antarctic Digital Database (ADD) to develop a land-sea mask around Antarctica. We gratefully acknowledge support from the National Science Foundation Geophysics Program funding under Grant No. EAR-1417245. This manuscript is based upon work supported by the NASA Earth and Space Science Fellowship to HRM under Grant No. NNX14AO04H. Some figures were generated using Generic Mapping Tools (Wessel et al., 2013).

7.8 Appendix A: Process Noise Settings for GPS Analysis

We performed basic synthetic tests to inform our selection of appropriate coordinate and tropospheric process noise settings for the GPS data processing. We generated the synthetic signals within GIPSY by differencing pre-fit residuals computed using two different OTL-response models: (1) the OTL-response model for a coastal station in Brazil with a large offshore tide ("master site") and (2) the OTL-response model at a separate station in the network ("test site"). We selected six test sites for our analysis, each exhibiting small OTL-response amplitudes relative to the master site. The displacement-response signal at the master site has a vertical amplitude of 3.69 cm for the M_2 harmonic, whereas the M_2 displacement-response amplitudes at the test sites do not exceed 1 cm.

We then added the differenced pre-fit-residuals to the raw GPS data of each test site as modifications to the pseudorange and phase observables for each transmitter-reciever pair

in the GIPSY quick-measurement files. The raw GPS data contain information about the actual OTL response at each test site; thus, when the differenced pre-fit residuals (i.e., master-site residuals − test-site residuals) are added to the original data, the revised data should contain only the OTL-response signal for the master site, along with any pre-existing noise and non-tidal signals. Note that we deliberately selected test sites with small OTL-response amplitudes, since errors in our prediction of the tidal response signals at the test sites can bias our attempts to recover the synthetic tidal signal (i.e., the predicted OTL response at the master site). All synthetic tests used up to one year of data from 2010 at each of the six test stations in South America.

To guide our exploration of coordinate process noise values to test, we first computed a range of theoretically suitable values. We estimated the instantaneous velocity, v_{inst}, experienced by any given station as:

$$v_{\mathrm{inst}} = \frac{d}{dt}(A\ \cos\omega t) = -A\,\omega\ \sin\omega t, \tag{7.4}$$

where A is the signal amplitude, ω is the frequency of the signal, and t is time. The absolute value of the instantaneous velocity given by Eq. 7.4 is maximized when the quantity $\sin\omega t = \pm 1$, which occurs at the maximum slope of the harmonic wave. For the M_2 tidal harmonic, $\omega = 0.5059$ rad hr^{-1} and the response amplitudes in South America reach as high as ∼4 cm. Thus, the maximum instantaneous velocity, v_{max}, expected for our network is ∼20 mm hr^{-1}.

To parameterize the coordinate process noise within GIPSY, one must specify the variance per unit time of the allowed site displacement (or, more specifically, the square root of the variance per unit time). Constraints that are too strict will bias the solutions, whereas constraints that are too loose will retain large data outliers. Following Elosegui et al. (1996), the variance per unit time, σ^2_{RW}, may be related to the maximum site velocity, v_{max}, and the time between solution epochs, Δt, by a constant of proportionality, ξ_{RW}, known as the

dynamic resolution parameter:

$$\xi_{\mathrm{RW}} = \frac{\sigma_{\mathrm{RW}}}{v_{\max}\sqrt{\Delta t}}. \tag{7.5}$$

For $\xi_{\mathrm{RW}} \gg 1$, solutions will be weakly constrained; for $\xi_{\mathrm{RW}} \ll 1$, solutions will be tightly constrained. Elosegui et al. (1996) opted for a "standard," yet somewhat arbitrary, value of $\xi_{\mathrm{RW}} = 10$. For $v_{\max} = 20$ mm hr^{-1} and $\Delta t = 300$ s between solution epochs, a plausible range of random-walk standard deviations to test should include $1.9 \times 10^{-7} < \sigma_{\mathrm{RW}} < 1.9 \times 10^{-6}$ km s$^{-\frac{1}{2}}$, corresponding to dynamic resolution parameters in the range of $2 < \xi_{\mathrm{RW}} < 20$.

The root-mean-square (RMS) misfits between the recovered and synthetic signals, averaged across all six test stations, are shown in Fig. 7.24. We examined six settings for the coordinate process noise: 1.0×10^{-8}, 1.0×10^{-7}, 3.0×10^{-7}, 5.0×10^{-7}, 7.0×10^{-7} and 1.0×10^{-3} km s$^{-\frac{1}{2}}$. In each case, we held the process noise setting for the tropospheric zenith delay fixed at 5.0×10^{-8} km s$^{-\frac{1}{2}}$, which is the `GIPSY`-recommended value for slow-moving platforms. We find that the tightest random-walk constraint we considered, 1.0×10^{-8} km s$^{-\frac{1}{2}}$, severely dampens the amplitudes of the station-position estimates and of the recovered tidal signals. The constraint of 1.0×10^{-7} km s$^{-\frac{1}{2}}$ also somewhat overdamped the recovered tidal response, particularly for the vertical component of the M_2 harmonic. The exceptionally loose random-walk constraint of 1.0×10^{-3} km s$^{-\frac{1}{2}}$ produced good amplitude recovery of the synthetic tidal response, but also limited the constraint on the noise. Tests of intermediary values revealed that a coordinate process noise value of 5.0×10^{-7} km s$^{-\frac{1}{2}}$ recovers both the amplitude and the phase of the synthetic tidal response to relatively high precision. Loosening the parameter does not significantly affect the ability to resolve the synthetic signals, even compared with very loose parameterizations such as 1.0×10^{-3} km s$^{-\frac{1}{2}}$, yet any stricter constraints begin to bias the recovered signal towards zero. Furthermore, the preferred parameterization of 5.0×10^{-7} km s$^{-\frac{1}{2}}$ is suitable for even the largest OTL-induced surface displacements observed in South America, yet strict enough to limit noise substantially.

For a random-walk coordinate setting of $\sigma_{\mathrm{RW}} = 5.0 \times 10^{-7}$ km s$^{-\frac{1}{2}}$ and for $\Delta t = 300$ s between solution epochs, we derive a dynamic resolution parameter of:

$$\xi_{\mathrm{RW}} = \frac{\sigma_{\mathrm{RW}}}{v_{\max}\sqrt{\Delta t}} = \frac{5.0 \times 10^{-7}}{\frac{20 \times 10^{-6}}{3600}\sqrt{300}} \approx 5. \tag{7.6}$$

Our result of $\xi_{\mathrm{RW}} = 5$ from the synthetic tests is very near to the value adopted by Elosegui et al. (1996), albeit with a slightly tighter constraint on the solution to limit noise contamination, thus lending support to the validity of our preferred random-walk parameterization. The selection of a relatively tight random-walk constraint also mitigates the effects of multipath (e.g., Larson et al., 2010).

In comparison, Penna et al. (2015) derived an optimal (minimum) coordinate process noise setting of 3.2×10^{-6} km s$^{-\frac{1}{2}}$, which is somewhat looser than 5.0×10^{-7} km s$^{-\frac{1}{2}}$. We have, however, constructed the synthetic tests to explore the ability of the GPS processing to retain the full OTL-response signals, as opposed to the residuals after OTL is removed, and we find that 5.0×10^{-7} km s$^{-\frac{1}{2}}$ is sufficiently loose to recover even the largest amplitude OTL responses predicted for our station network.

In addition to the coordinate process noise setting, recovering the OTL-response signal also depends largely on the ability to account for propagation delays in the transmitted carrier wave signals through the troposphere (e.g., Bar-Sever et al., 1998; Dach & Dietrich, 2000; Dragert et al., 2000; Vey et al., 2002; Khan & Scherneck, 2003; Larson et al., 2010; Penna et al., 2015). The tropospheric wet delay (non-hydrostatic) arises from the interaction between the electromagnetic (EM) carrier wave signal and the static dipole moment of water molecules in the atmosphere (e.g., Blewitt, 2015). The tropospheric dry delay (hydrostatic) refers to the dynamic dipole moment induced on all atmospheric molecules, including water, by the propagating EM wave. In our analysis, we account for both types of delays.

We find that the tropospheric zenith delays are best estimated stochastically along with the station coordinates in a single kinematic run. We therefore explored the effects of varying the tropospheric process noise on the ability to recover the synthetic tidal response. In each test, we supplied the kinematic runs with initial tropospheric zenith delay estimates

from ECMWF. With the coordinate process noise held fixed at 5.0×10^{-7} km s$^{-\frac{1}{2}}$, we examined five settings for the tropospheric process noise: 1.0×10^{-8}, 2.5×10^{-8}, 5.0×10^{-8}, 1.0×10^{-7}, and 2.0×10^{-7} km s$^{-\frac{1}{2}}$. The RMS misfits between the recovered and synthetic OTL-response signals for each process noise setting are depicted in Fig. 7.25.

The vertical-displacement component clearly exhibits greater sensitivity to tropospheric process noise than the horizontal-displacement components. For the M_2 harmonic, the RMS misfits in the vertical-displacement component are minimized for a tropospheric process noise setting of 2.5×10^{-8} km s$^{-\frac{1}{2}}$, followed closely by a setting of 5.0×10^{-8} km s$^{-\frac{1}{2}}$. For the O_1 tidal harmonic, looser constraints of 1.0×10^{-7} and 2.0×10^{-7} km s$^{-\frac{1}{2}}$ seem more suitable, although a setting of 5.0×10^{-8} km s$^{-\frac{1}{2}}$ yields similar results. The RMS misfits for the M_f harmonic do not vary substantially with changes to the tropospheric process noise.

Consistent with the results of Penna et al. (2015), we do not find significant leakage of the synthetic signal between the spatial components. The synthetic signal applied to the M_2 harmonic band, for example, had an amplitude of 36.9 mm, 4.4 mm, and 7.6 mm in the vertical, east, and north components, respectively. Given that the vector differences between the recovered and synthetic signals are sub-mm in each component, we infer that nearly all of the input signal for a particular coordinate maps directly into the recovered signal for the same coordinate.

Based on the six test sites that we considered, the optimal setting for the tropospheric process noise is not sharply defined, but a setting of 5.0×10^{-8} km s$^{-\frac{1}{2}}$ performs well overall and corresponds to the value recommended by `GIPSY` for slow-moving objects. We therefore adopt a tropospheric process noise setting of 5.0×10^{-8} km s$^{-\frac{1}{2}}$ for our analysis, recognizing that the truly optimal value will likely differ between individual tidal harmonics and various geographic locations. The optimal tropospheric process noise value found by Penna et al. (2015), 1.0×10^{-7} km s$^{-\frac{1}{2}}$, differs from 5.0×10^{-8} km s$^{-\frac{1}{2}}$ by only a factor of two, which might be due in part to different climatic settings between western Europe and South America. The two parameterizations do not, however, yield appreciably different RMS misfits in our analysis for South America (Fig. 7.25).

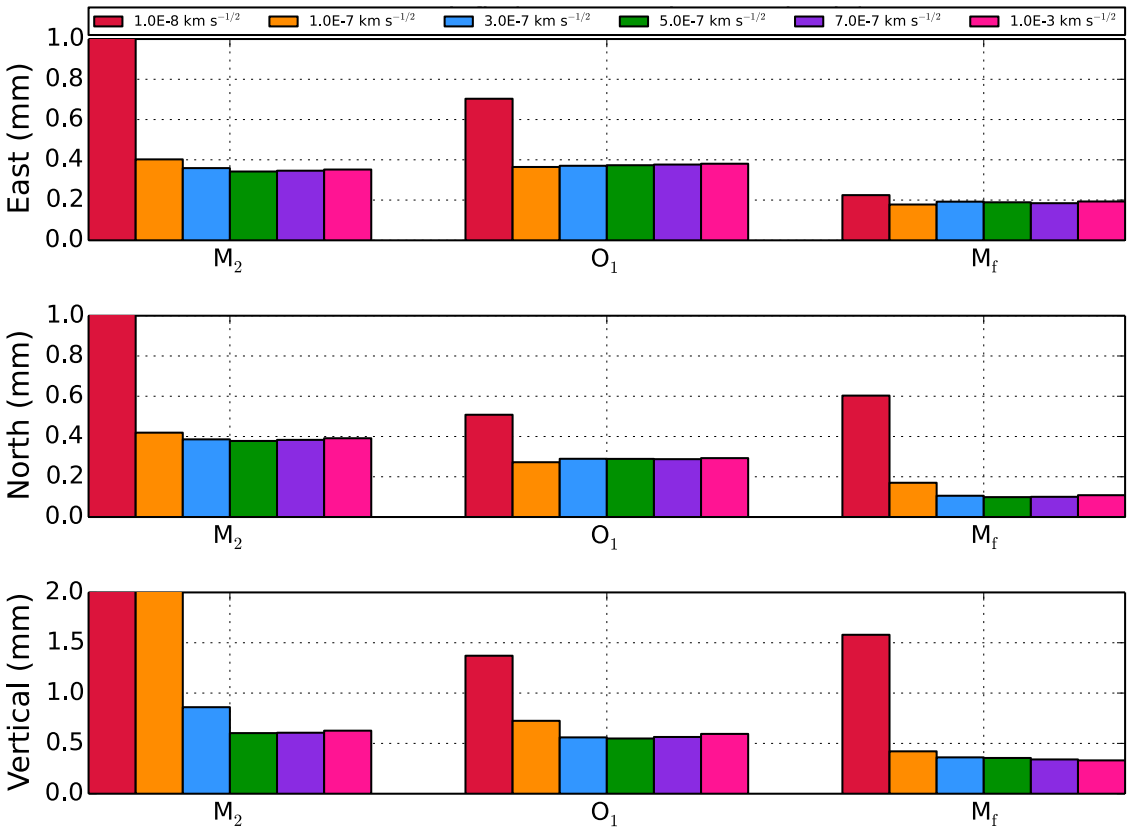

Figure 7.24: Root-mean-square (RMS) misfits between recovered and synthetic OTL-induced surface displacements. Here, we compare coordinate process noise settings used to estimate receiver positions during the kinematic PPP GPS data processing.

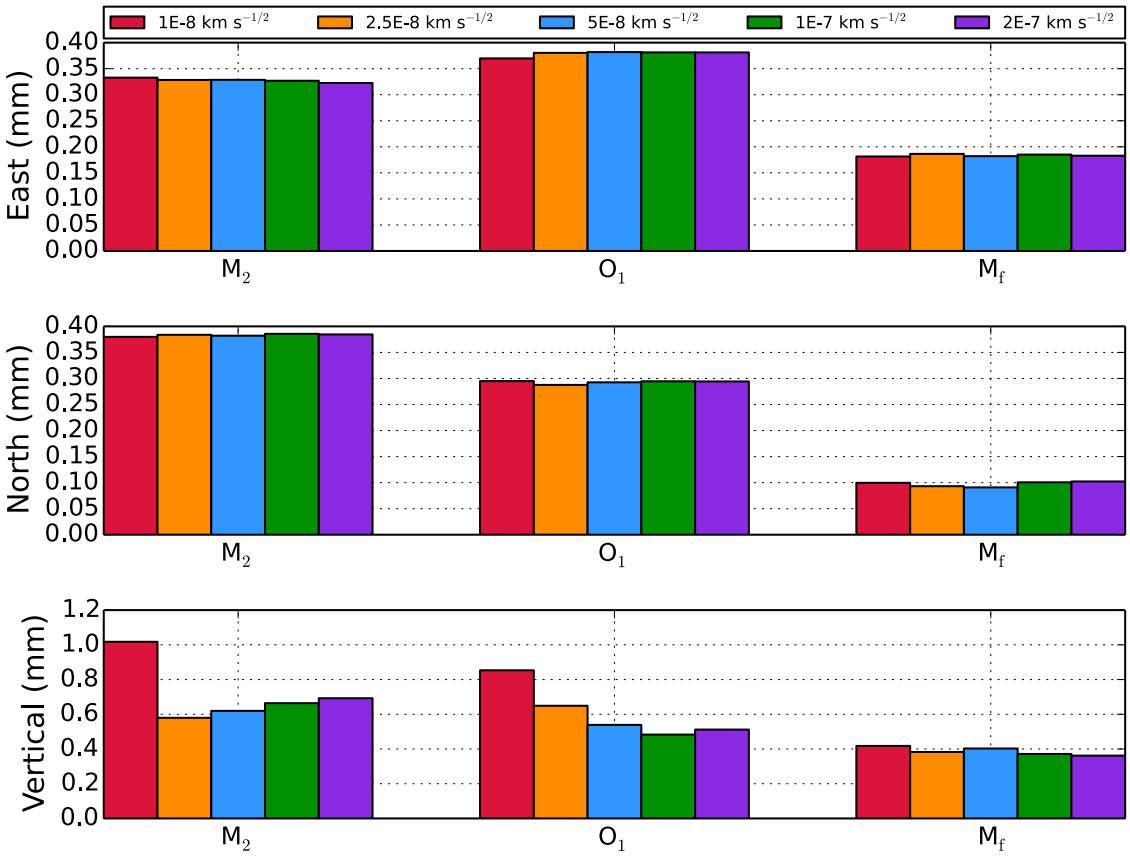

Figure 7.25: RMS misfits between recovered and synthetic OTL-induced surface displacements. Here, we compare a selection of tropospheric process noise settings.

The smallest RMS misfits from Figs. 7.24 and 7.25 are generally consistent with our 2σ uncertainty estimates from Table 7.4 for one year of data or less. It should be recalled, however, that our synthetic tests were developed by adding modeled OTL-response signals to real data in the dominant tidal bands, and therefore should not be used to make strict assertions about uncertainties in tidal-response estimation from GPS data. Notably, any errors in the predicted OTL response at a particular test site will be contained within our RMS estimates of signal recovery, and therefore compound the uncertainties derived from noise in the time series. Although injecting the synthetic signal into a non-dominant tidal band could reduce the prediction errors considerably and thereby allow for better estimation of the uncertainties in GPS estimates of OTL response using synthetic tests (Penna et al., 2015), the errors should remain consistent between each synthetic test and thus should not significantly bias our selection of suitable process noise parameters.

7.9 Appendix B: Harmonic Analysis Procedure

The equation representing the model fit, $Z(t)$, to the GPS-inferred displacement time series is given by:

$$Z(t) = m_0 + m_1 t + \sum_{\eta=1}^{N} A_\eta \; f_\eta(t) \; \cos(V_\eta(t) + u_\eta(t) - \phi_\eta), \tag{7.7}$$

where m_0 is a constant-offset term, m_1 is a linear-trend term, f_η represents the harmonic-modulation correction factor for the amplitude, u_η represents the harmonic-modulation correction factor for the phase, η represents a particular tidal harmonic, N represents the total number of tidal harmonics used in the model, and t is time.

We seek the set of model terms [m_0, m_1, A_η, ϕ_η] by minimizing the misfit between data and model using an iterative re-weighted least-squares (IRLS) approach. To perform the inversion, we first separate the harmonic portion of Eq. 7.7 into in-phase and quadrature components:

$$A_\eta \; f_\eta(t) \; \cos(V_\eta(t) + u_\eta(t) - \phi_\eta) \quad = \quad A_\eta \; \cos(\phi_\eta) \; f_\eta(t) \; \cos(V_\eta(t) + u_\eta(t))$$

$$+ \quad A_\eta \ \sin(\phi_\eta) \ f_\eta(t) \ \sin(V_\eta(t) + u_\eta(t)). \quad (7.8)$$

Defining $c_\eta \equiv A_\eta \ \cos(\phi_\eta)$ and $s_\eta \equiv A_\eta \ \sin(\phi_\eta)$, Eq. 7.8 becomes:

$$\begin{aligned} A_\eta \ f_\eta(t) \ \cos(V_\eta(t) + u_\eta(t) - \phi_\eta) &= c_\eta \ f_\eta(t) \ \cos(V_\eta(t) + u_\eta(t)) \\ &+ s_\eta \ f_\eta(t) \ \sin(V_\eta(t) + u_\eta(t)). \end{aligned} \quad (7.9)$$

The amplitude and phase modulation factors, $f_\eta(t)$ and $u_\eta(t)$, as well as the astronomical argument, $V_\eta(t)$, are known functions derived from the astronomical ephemeris (e.g., Foreman, 1977). We incorporate harmonic-modulation correction factors directly into our inversion framework (Foreman et al., 2009), rather than apply constant and thus approximate correction terms at the post-processing stage, thereby allowing multiple years of data to be processed in a single analysis.

Substituting Eq. 7.9 back into the full formula for a tidal signal, Eq. 7.7, we have:

$$\begin{aligned} Z(t) &= m_0 + m_1 t + \sum_{\eta=1}^{N} [c_\eta \ f_\eta(t) \ \cos(V_\eta(t) + u_\eta(t)) \\ &+ s_\eta \ f_\eta(t) \ \sin(V_\eta(t) + u_\eta(t))]. \end{aligned} \quad (7.10)$$

Eq. 7.10 may now be used to invert real tidal data for the unknown model parameters (i.e., m_0, m_1, c_η and s_η). Note that if Z_0 (mean sea level) is included as a tidal constituent, then m_0 must be removed from the model parameters to avoid ill-conditioning in the matrix inversion.

We develop a system of linear equations of the form:

$$G\,m = d, \quad (7.11)$$

where d is the observed tidal data, m is a vector of model parameters, and G is a matrix of known quantities that interact with the model parameters. We aim to match the model, $G\,m$, with the observed data, d, by initially minimizing the norm of the squared residuals,

and then iterating on the solution residuals. The data and model vectors are given by:

$$d = [\ d(t_0)\ \ d(t_1)\ \ d(t_2)\ \ d(t_3)\ \ d(t_4)\ \ d(t_5)\ \ d(t_6)\ \ d(t_7)\ \ \cdots\ ]^T \tag{7.12}$$

and

$$m = [\ m_0\ \ m_1\ \ c_1\ \ s_1\ \ c_2\ \ s_2\ \ c_3\ \ s_3\ \ c_4\ \ s_4\ \ \cdots\ \ c_N\ \ s_N]^T, \tag{7.13}$$

respectively. The subscripts for c and s represent individual tidal harmonics (e.g., M_2).

The G^T matrix (transpose of G) is given by:

$$G^T = \begin{bmatrix} 1 & 1 & 1 & \cdots \\ t_0 & t_1 & t_2 & \cdots \\ f_1(t_0)\cos[V_1(t_0)+u_1(t_0)] & f_1(t_1)\cos[V_1(t_1)+u_1(t_1)] & \cdots & \cdots \\ f_1(t_0)\sin[V_1(t_0)+u_1(t_0)] & f_1(t_1)\sin[V_1(t_1)+u_1(t_1)] & \cdots & \cdots \\ f_2(t_0)\cos[V_2(t_0)+u_2(t_0)] & f_2(t_1)\cos[V_2(t_1)+u_2(t_1)] & \cdots & \cdots \\ f_2(t_0)\sin[V_2(t_0)+u_2(t_0)] & f_2(t_1)\sin[V_2(t_1)+u_2(t_1)] & \cdots & \cdots \\ f_3(t_0)\cos[V_3(t_0)+u_3(t_0)] & f_3(t_1)\cos[V_3(t_1)+u_3(t_1)] & \cdots & \cdots \\ f_3(t_0)\sin[V_3(t_0)+u_3(t_0)] & f_3(t_1)\sin[V_3(t_1)+u_3(t_1)] & \cdots & \cdots \\ f_4(t_0)\cos[V_4(t_0)+u_4(t_0)] & f_4(t_1)\cos[V_4(t_1)+u_4(t_1)] & \cdots & \cdots \\ f_4(t_0)\sin[V_4(t_0)+u_4(t_0)] & f_4(t_1)\sin[V_4(t_1)+u_4(t_1)] & \cdots & \cdots \\ \vdots & \vdots & \vdots & \vdots \\ f_N(t_0)\cos[V_N(t_0)+u_N(t_0)] & f_N(t_1)\cos[V_N(t_1)+u_N(t_1)] & \cdots & \cdots \\ f_N(t_0)\sin[V_N(t_0)+u_N(t_0)] & f_N(t_1)\sin[V_N(t_1)+u_N(t_1)] & \cdots & \cdots \end{bmatrix}.$$

To solve for the model vector, we perform an iterative re-weighted least squares (IRLS) inversion, which evaluates a series of weighted least-squares problems that converge to an L1-norm solution (Aster et al., 2013). The L1-norm minimizes the absolute value of the residuals and is therefore highly effective at down-weighting outliers. For the initial model vector, we compute an L2-norm solution, from which a weighting matrix may be constructed based on the residuals between the observations and the forward model. Since the weighting matrix is a nonlinear function of the model vector, the normal equations must

be solved iteratively. Thus, updated model vectors are derived from subsequent L1-norm solutions to the normal equations and tested against a tolerance value. The process repeats until a suitable level of convergence is achieved.

The resulting in-phase and quadrature coefficients for each isolable tidal harmonic may be re-combined to obtain amplitude and phase values:

$$A_\eta = \sqrt{c_\eta^2 + s_\eta^2} \tag{7.14}$$

$$\phi_\eta = \mathrm{atan2}\left(s_\eta, c_\eta\right). \tag{7.15}$$

8

Some Remarks on Surface Mass Loading from Non-OTL Sources

8.1 Introduction

The procedure for predicting Earth's deformation response to surface mass loading (SML) outlined in Ch. 4 extends beyond the ocean tides to include any type of surface mass load. Surface mass loads come from many different sources with very different frequencies. The redistribution of mass in Earth's atmosphere, for example, loads the surface of the Earth and thus causes load-induced deformation (e.g., Stolz & Larden, 1979; van Dam et al., 1994; Tregoning & van Dam, 2005). Atmospheric loading (ATML) occurs at tidal periods due to solar heating and gravitational forcing as well as at non-tidal periods due to weather and climate systems. In addition to the atmosphere, changes in ocean mass at non-tidal periods apply pressure to Earth's surface (e.g., Williams & Penna, 2011; van Dam et al., 2012). Spatiotemporal variations in non-tidal ocean loading (NTOL) arise from internal instabilities, which are driven primarily by wind stress, atmospheric loading, and internal density gradients. The density gradients develop due to spatial variations in ocean temperature and salinity. Furthermore, variations in terrestrial water storage due to precipitation and mass-exchange between hydrological systems, known as hydrological loading (HYDL), contribute to the dynamic load-generated deformation response of the solid Earth (e.g., Fu et al., 2015). Rivers, lakes, glaciers, snow fields, reservoirs, and tsunami waves constitute additional examples of surface mass loads (e.g., Bevis et al., 2005; Tsai et al., 2013).

Geodetic time series are typically corrected for OTL response, but accounting for the effects of other mass loads is not yet standard practice. In the future, routine corrections for ATML, NTOL, and HYDL, in particular, could help to improve the precision of a geodetic time se-

ries and to facilitate the detection of subtle geophysical signals, such as aseismic tectonic transients and postglacial rebound (e.g., van Dam et al., 2010). An improved understanding of atmosphere-ocean interactions, including mass loading, also enhances the ability to measure sea-surface height using satellite altimetry, estimate ocean-bottom pressure, and model global sea-level rise (e.g., van Dam et al., 1997; Ponte & Ray, 2002; Ponte, 2006; Vinogradova et al., 2007; Ray & Byrne, 2010; Ray et al., 2013; Ray, 2013).

Here, I briefly discuss three of the primary sources of non-OTL surface mass loading: ATML, NTOL, and HYDL. For ATML and NTOL, I compute predicted surface displacements generated by the mass loading at three locations globally. The predicted load-induced surface displacements are derived from convolutions of the load model (e.g., atmospheric pressure) with load Green's functions for Earth structure (Eq. 4.1). I compare the magnitudes of the ATML- and NTOL-induced surface displacements to OTL-induced surface displacements at the same locations. The purpose of this chapter is to provide a brief introduction to surface mass loading derived from sources other than the ocean tides. Moreover, I compare predicted surface displacements induced by ATML and NTOL to recent work by Williams & Penna (2011) as a preliminary validation of the methods.

8.2 Atmospheric Loading

Variations in atmospheric pressure manifest due to direct solar heating, temperature gradients at Earth's surface, Earth rotation, land-sea interactions, and individual weather systems (e.g., van den Dool et al., 1997). Anomalies in atmospheric surface pressure are typically on the order of 0.1–5 kPa (e.g., Wunsch & Stammer, 1997), as depicted in Fig. 8.1. Estimates of the atmospheric surface pressure on global grids are routinely computed by reanalysis centers such as the European Centre for Medium-Range Weather Forecasts (ECMWF) and the National Centers for Environmental Prediction/National Center for Atmospheric Research (NCEP/NCAR).

Fig. 8.1 shows atmospheric pressure anomalies from the ECMWF. The ECMWF models are distributed with six-hour temporal resolution on global grids of $0.75^\circ \times 0.75^\circ$ spatial resolution. ECMWF uses data assimilation techniques to incorporate a range of space- and

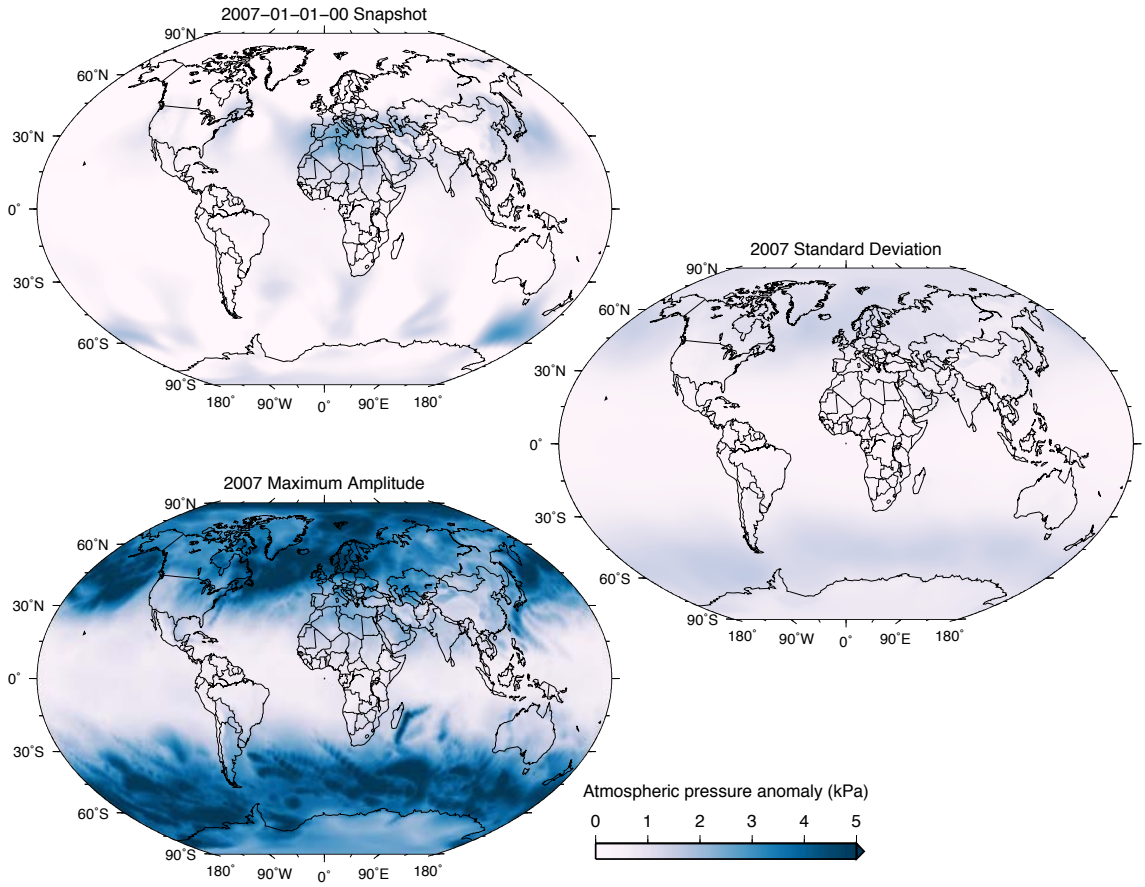

Figure 8.1: Global grids of atmospheric surface pressure from ECMWF. The top-left panel shows a snapshot of the atmospheric pressure anomaly from a single epoch on 1 January 2007. The center-right panel shows the standard deviation in the atmospheric pressure anomaly during 2007. The bottom-left panel shows the maximum anomaly in surface pressure at each grid node during 2007. I removed a spatial mean of the pressure anomaly from every temporal epoch as well as a temporal mean for 2007 from every grid node.

land-based empirical weather measurements into general circulation models. Variations in atmospheric pressure tend to be largest at high latitude due to geostrophic force balance (e.g., Wunsch & Stammer, 1997), where vertical surface displacements induced by atmospheric loading can sometimes exceed one centimeter (e.g., van Dam et al., 1994; Petrov & Boy, 2004). Petrov & Boy (2004) were the first to detect atmosphere-induced surface displacements in the horizontal component, which were on the order of a few millimeters. For comparison, Fig. 8.2 depicts the pressure exerted by ocean tides at the M_2, O_1, and M_f harmonics. In general, typical variations in atmospheric pressure are similar in magnitude to ocean loading by the O_1 harmonic.

As a first-order approximation, the oceans respond to atmospheric pressure forcing as **inverted barometers**, whereby an increase in atmospheric pressure generates a drop in sea level (e.g., Doodson, 1924b; Wunsch & Stammer, 1997; Ponte & Gaspar, 1999). The inverted barometer effect does not happen instantaneously; rather, the equilibration between atmosphere and oceans generally occurs over time scales of hours to days (e.g., Ponte & Gaspar, 1999). To first-order, however, the oceans compensate for variations in atmospheric pressure such that the total pressure at the sea floor remains roughly unchanged. Due to pressure-compensation by advection of ocean mass, Earth's displacement response to ATML tends to be largest at inland sites (e.g., van Dam et al., 2010).

ATML-induced deformation signals are ubiquitous in geodetic time series, and should therefore be accounted for in routine analysis. van Dam et al. (1994), for example, found that accounting for Earth's deformation response to atmospheric pressure loading could reduce the variance in GPS coordinate time series by upwards of 25%. Atmospheric loading has also been shown to have a measurable effect on VLBI baselines (van Dam & Herring, 1994). Estimates of predicted ATML-induced surface displacements at several hundred geodetic monitoring stations worldwide may be obtained from a NASA-maintained atmospheric pressure loading service.[3]

Here, I estimate ATML-induced surface displacements using Eq. 4.1 at the locations of three GPS stations: TERS (5.219°E, 53.363°N) in the Netherlands, AC34 (-153.279°E, 57.220°N) in Alaska, and RIO2 (-67.751°E, -53.785°N) in Argentina. I generate the predictions using the ECMWF model for atmospheric surface pressure (with the oceans masked out) and LGFs from PREM in the CM reference frame. Figs. 8.3, 8.4 and 8.5 show time series of ATML-induced surface displacements for TERS, AC34, and RIO2, respectively, during 2007. Horizontal-displacement amplitudes are generally on the order of a few millimeters, whereas maximum vertical displacements reach about 1 centimeter. The three sites considered are located in coastal areas; inland sites could exhibit larger displacements. As an aside, it is perhaps worth noting that the coarseness of atmospheric pressure models can lead to inaccuracies in predicted ATML-induced surface displacements, particularly in

[3] `http://gemini.gsfc.nasa.gov/aplo/`

regions with complicated surface topography (van Dam et al., 2010). More information about ATML may be found in the literature (e.g., Ray & Ponte, 2003; Guo et al., 2004; Tregoning & van Dam, 2005; Bingham & Hughes, 2008; Tregoning & Watson, 2009, 2011).

In Fig. 8.6, I compare ATML-induced surface displacements computed using `LoadDef` with modeled and observed displacements from Williams & Penna (2011) for station TERS. The `LoadDef` predictions, which were computed based on the ECMWF model for surface pressure variations and CE LGFs from PREM, are superimposed on the Williams & Penna (2011) predictions, which were computed based on the NCEP/NCAR model for surface pressure variations and CE LGFs from PREM. Despite the difference in pressure models, however, the correspondence between the two sets of predicted displacements is strong. The two sets of predictions match best when I apply the atmospheric load only over land (i.e., I assume that variations in atmospheric pressure over the oceans are effectively neutralized due to the inverted barometer effect). The Williams & Penna (2011) datasets used to generate Fig. 8.6 were provided by Simon Williams through personal communication (27–28 April 2016).[4] Fig. 8.7 is identical to Fig. 8.6, except that I have now included personally derived estimates for the GPS station positions (in the CM frame), rather than the position estimates derived by Williams & Penna (2011), as well as CM-referenced predicted displacements from `LoadDef`.

8.3 Non-Tidal Ocean Loading

NASA's *Estimating the Circulation and Climate of the Oceans* (ECCO) consortium provides time series of non-tidal ocean loading (NTOL) on global grids (e.g., Stammer et al., 2002). The most recent installment of the consortium, the ECCO2 model,[5] includes daily estimates of ocean bottom-pressure potential anomalies on a global grid of resolution $0.25^\circ \times 0.25^\circ$ for the years 1992–2015. The ECCO2 estimates of bottom-pressure anomalies are diagnostic quantities derived from anomalous water-column height (e.g., van Dam et al.,

[4] As a preliminary observation, I noticed that removing an annual signal from the `LoadDef`-modeled CM-referenced displacements improved the fit to the CE-referenced (modeled) displacements provided by S. Williams. The interpretation here is that reference-frame inconsistencies could manifest much like the harmonic signals in a displacement time series.

[5] `http://ecco2.jpl.nasa.gov/products/`

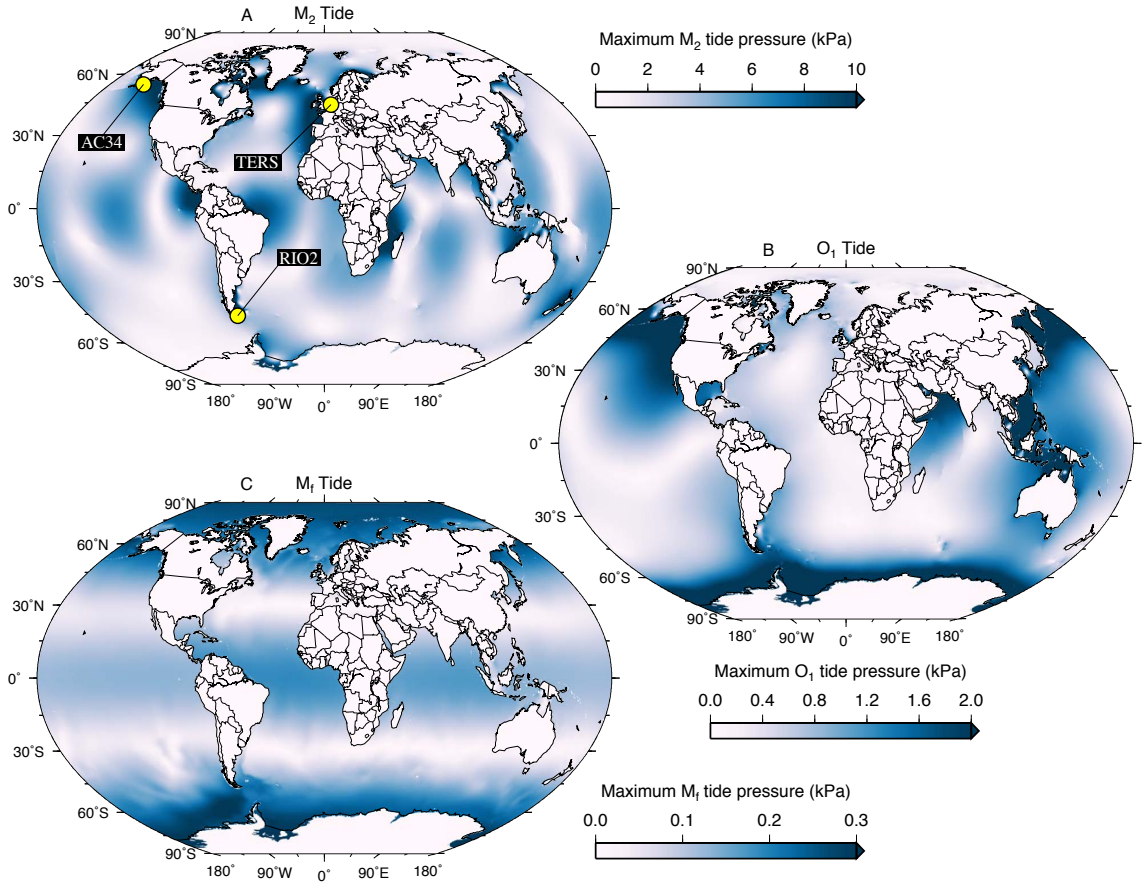

Figure 8.2: Global grids of ocean tide pressure from FES2012 for the M_2 (A, top left), O_1 (B, center right), and M_f (C, lower left) tidal harmonics. Note the change in scale with respect to Fig. 8.1. The yellow circles in panel A denote the locations of three GNSS stations referred to throughout the chapter. The three stations are TERS (5.219°E, 53.363°N) in the Netherlands, AC34 (-153.279°E, 57.220°N) in Alaska, and RIO2 (-67.751°E, -53.785°N) in Argentina. The amplitudes of the vertical-displacement response for the M_2 harmonic are 7.6 mm, 29.8 mm, and 23.8 mm for TERS, AC34, and RIO2, respectively. For the O_1 harmonic, the vertical-displacement response amplitudes are 0.9 mm, 14.1 mm, and 12.4 mm for TERS, AC34, and RIO2, respectively. For the M_f harmonic, the vertical-displacement response amplitudes are 0.4 mm, 1.2 mm, and 1.8 mm for TERS, AC34, and RIO2, respectively.

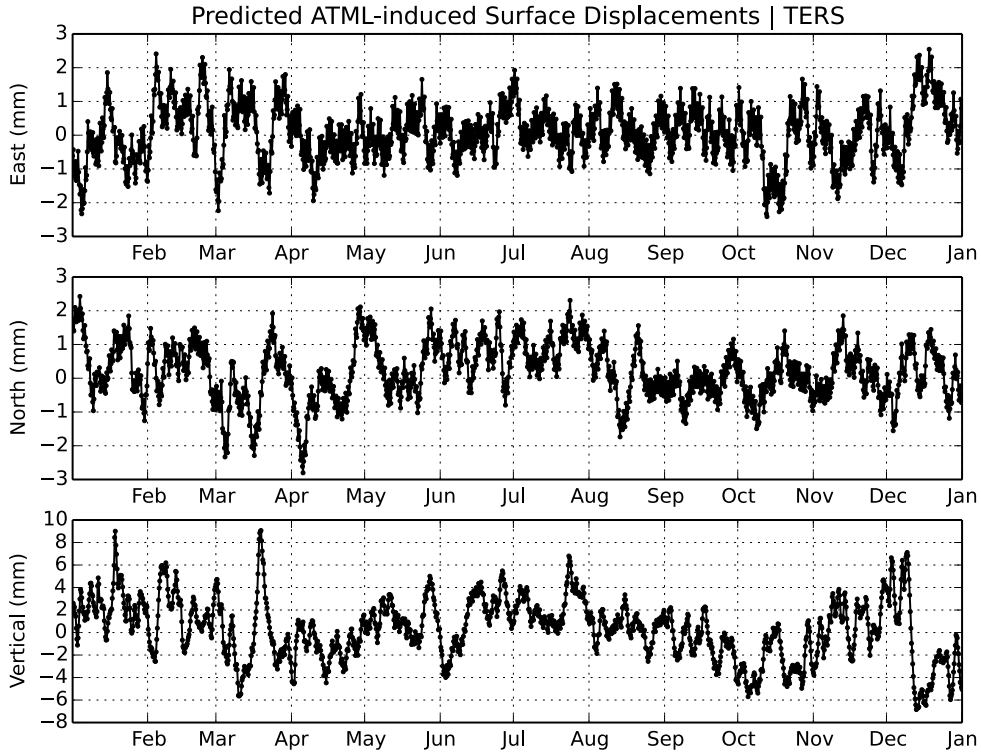

Figure 8.3: East (top), north (center), and vertical (bottom) displacements (in the CM reference frame) induced by variations in atmospheric pressure from ECMWF at the location of GNSS station TERS (denoted by a yellow circle in Fig. 8.2) during 2007. Constant-offset, linear-trend, and annual signals have been removed. Assuming first-order compensation due to the inverted barometer effect, I did not include the ocean regions in the convolution of the atmospheric pressure model with the load Green's functions (derived from PREM structure). The vertical displacements may be compared with the modeled displacements due to atmospheric loading shown in fig. 2 (upper-right panel, solid black lines) of Williams & Penna (2011). Note that Williams & Penna (2011) did not use the atmospheric pressure model of ECMWF, which has a spatial resolution of $0.75^\circ \times 0.75^\circ$; they instead used the atmospheric pressure model of NCEP/NCAR with a spatial resolution of $2.5^\circ \times 2.5^\circ$.

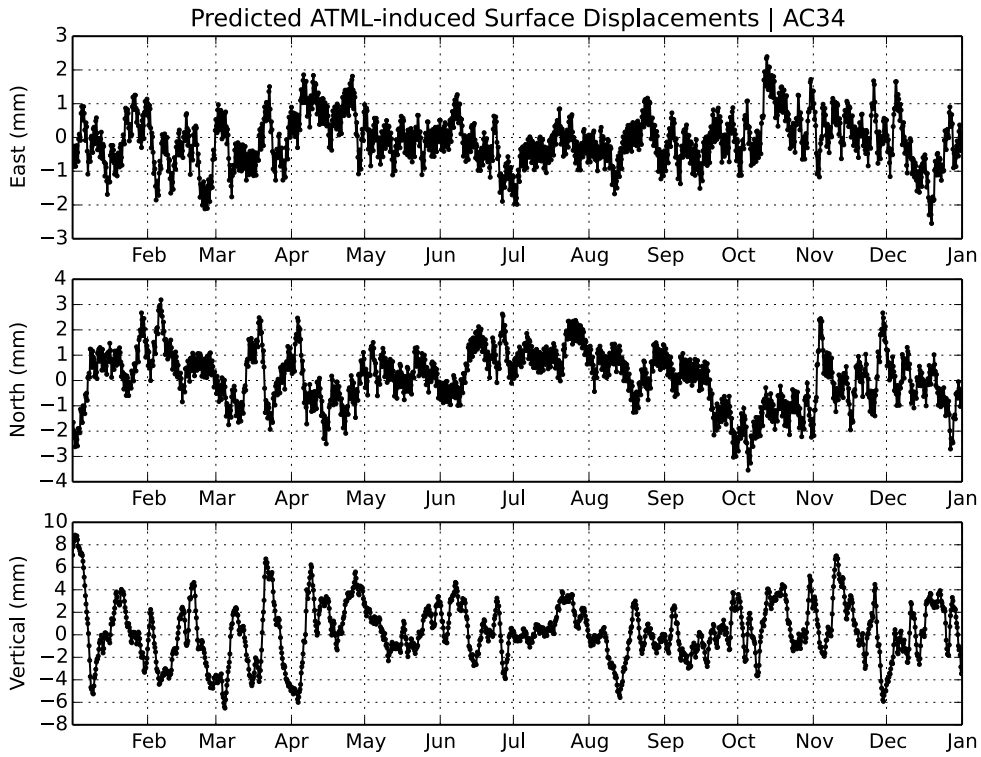

Figure 8.4: East (top), north (center), and vertical (bottom) displacements (in the CM reference frame) induced by variations in atmospheric pressure at the location of GNSS station AC34 (denoted by a yellow circle in Fig. 8.2) during 2007. Constant-offset, linear-trend, and annual signals have been removed. Assuming first-order compensation due to the inverted barometer effect, I did not include the ocean regions in the convolution of the atmospheric pressure model (ECMWF) with the load Green's functions (derived from PREM structure).

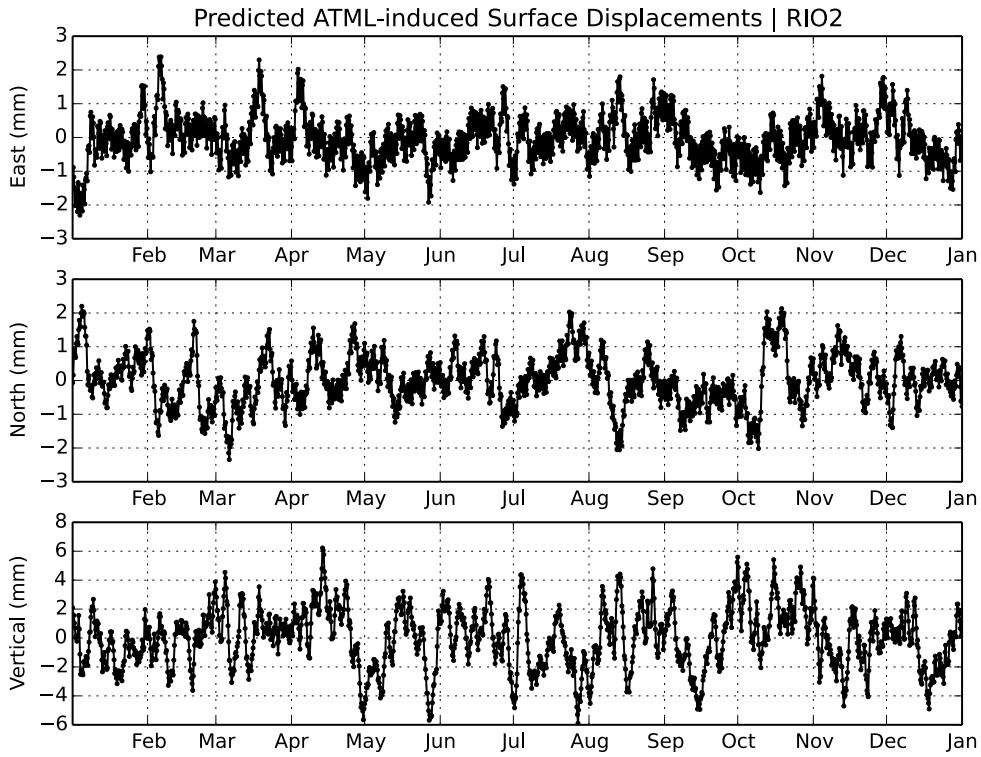

Figure 8.5: East (top), north (center), and vertical (bottom) displacements (in the CM reference frame) induced by variations in atmospheric pressure at the location of GNSS station RIO2 (denoted by a yellow circle in Fig. 8.2) during 2007. Constant-offset, linear-trend, and annual signals have been removed. Assuming first-order compensation due to the inverted barometer effect, I did not include the ocean regions in the convolution of the atmospheric pressure model (ECMWF) with the load Green's functions (derived from PREM structure).

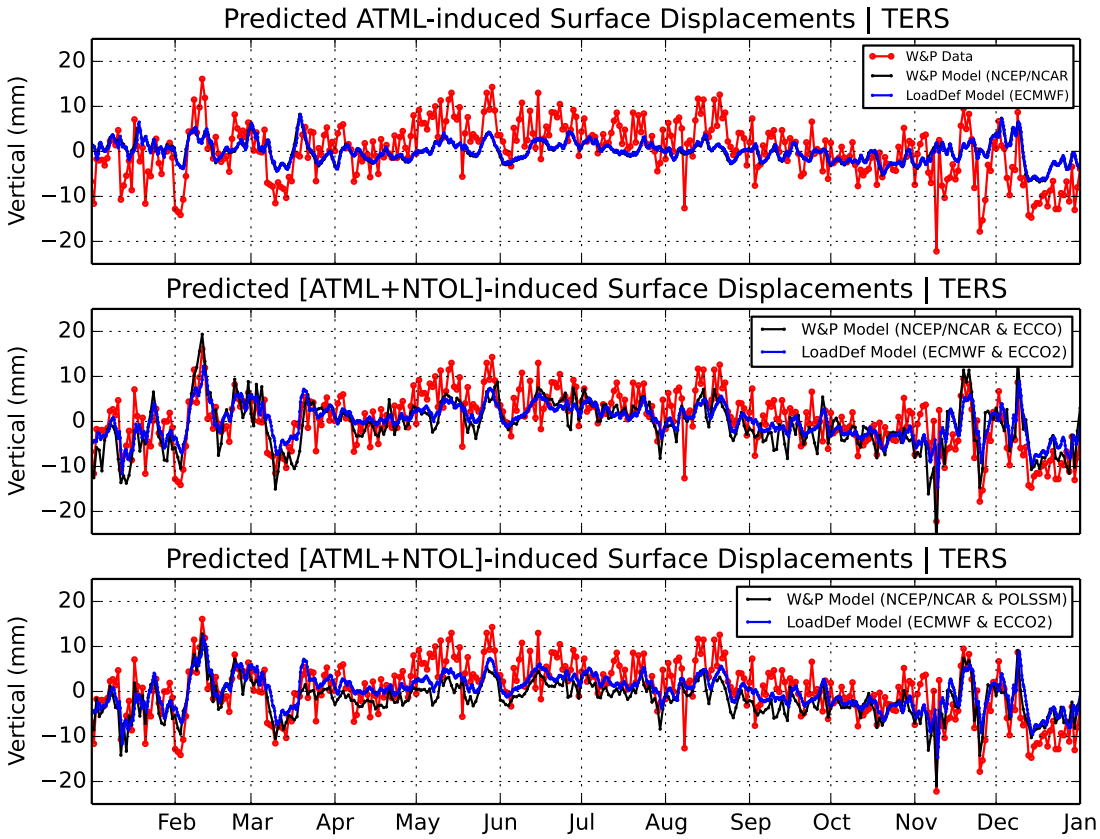

Figure 8.6: Predicted surface displacements in the vertical component induced by variations in atmospheric pressure (top) and by variations in the combined atmospheric and non-tidal oceanic pressure (middle and bottom) at the location of GNSS station TERS (Fig. 8.2) during 2007. The figure has been adapted from fig. 2 of Williams & Penna (2011) (WP2011). GNSS-inferred displacements estimated by WP2011 are shown in red. Modeled displacements derived by WP2011 are depicted in black. Both the measured (red) and predicted (black) displacements were furnished by Simon Williams (personal communication, 28 April 2016) to facilitate reproduction of the figure. The `LoadDef`-modeled displacements (blue) were computed in the CE reference frame to remain consistent with the methods of WP2011. The `LoadDef`-modeled response to ATML was computed only over land, and not over the oceans, using the ECMWF atmospheric pressure model; compensation due to the inverted barometer effect was assumed. A constant offset was removed from the `LoadDef` results, but not linear or annual signals. The `LoadDef` predictions in the middle and bottom panels are identical and represent the combined response due to atmospheric and non-tidal oceanic pressure variations from the ECMWF and ECCO2 models, respectively. The WP2011 predictions in the middle panel represent the combined response due to atmospheric and non-tidal oceanic pressure variations from the NCEP/NCAR and ECCO models, respectively. The WP2011 predictions in the bottom panel represent the combined response due to atmospheric and non-tidal oceanic pressure variations from the NCEP/NCAR and POLSSM models, respectively. Note that the predicted displacements due to variations in atmospheric pressure match remarkably well (top panel); it is difficult to discern the black line beneath the blue line. See also Figs. 8.3 and 8.9.

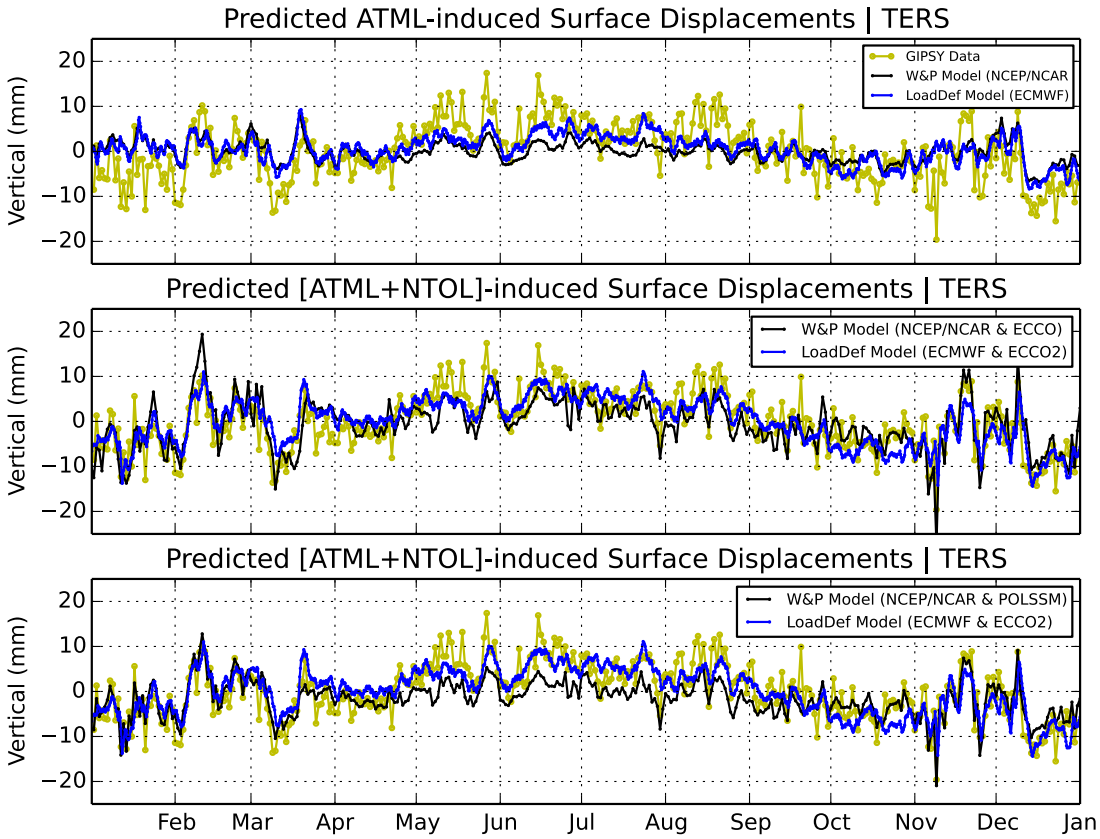

Figure 8.7: Same as Fig. 8.6, but with GPS-inferred vertical displacements computed locally using GIPSY-OASIS II (yellow) and with `LoadDef`-modeled displacements referenced to the CM frame (blue). I estimated the daily (static) GPS site positions using methods similar to those discussed in Ch. 3, albeit without random-walk position estimation. In particular, I adopted a tropospheric process noise parameter of 5.0×10^{-8} km $\mathrm{s}^{-\frac{1}{2}}$, provided nominal tropospheric zenith delay estimates (at the data rate of 30 s) as input, used VMF1 mapping functions, applied an elevation angle cut-off of 10°, modeled and removed the solid Earth body tides and ocean tidal loading (`http://holt.oso.chalmers.se/loading/`), included antenna calibration and ambiguity resolution, and used the JPL orbit and clock products in final and fiducial form ('flinnR' format, version 'repro2.0'). A constant offset was removed from the data. The RINEX data were retrieved from `gnss1.tudelft.nl/dpga/rinex/`. The GPS-inferred estimates of site positions (yellow) are referenced to the CM frame. The modeled displacements from WP2011 (black) are referenced to the CE frame (as in Fig. 8.6).

1997). Fig. 8.8 shows global distributions of non-tidal ocean pressure anomalies from 2007. It is recommended that global and temporal averages be removed from the ECCO2 bottom-pressure anomalies to account for drifts in the global balance of evaporation and precipitation (D. Menemenlis and H. Zhang, personal communication). Moreover, the ECCO2 simulations of ocean-bottom pressure anomalies do not include the effects of atmospheric or tidal forcing (D. Menemenlis, personal communication). Recall, however, that the ocean-bottom pressure does not change (to first-order) with variations in atmospheric pressure due to the inverted barometer effect, but could have issues on timescales less than a few days.

NTOL can generate vertical surface displacements on the order of 5–10 mm or more at coastal stations (e.g., van Dam et al., 1997; Zerbini et al., 2004; van Dam et al., 2012; Nordman et al., 2015), as depicted in Fig. 8.9 for station TERS. Predicted surface displacements caused by non-tidal ocean loads at stations AC34 and RIO2 are shown in Figs. 8.10 and 8.11, respectively. For the coastal stations considered here, the surface displacements induced by NTOL are roughly equivalent to the surface displacements induced by ATML (both on the order of 1–10 mm) (e.g., Williams & Penna, 2011). Contributions to the displacement time series from OTL tend to be larger, but not substantially so (Fig. 8.2). In particular, the M_2 OTL-induced displacements at stations AC34 and RIO2 exceed 2 cm. The M_f OTL-induced displacements, in contrast, hardly exceed 1 mm. The combined effects of atmospheric and non-tidal oceanic pressure forcing are shown in Fig. 8.12 for station TERS, which may be compared with Fig. 8.6 (cf., fig. 2 in Williams & Penna (2011)). In combination, the NTOL and ATML effects can account for up to about 50% of the residual variance in a GNSS coordinate time series (Williams & Penna, 2011).

8.4 Hydrological Loading

Variations in continental water storage occur largely on seasonal cycles, generating typical vertical displacements on the order of millimeters, but ranging up to a centimeter or more (e.g., van Dam et al., 2001; Ray et al., 2013). Localized surface displacements can be even higher. Bevis et al. (2005), for example, detected vertical displacement amplitudes of about 2–4 cm in the immediate vicinity of the Amazon river basin due to seasonal hydrological

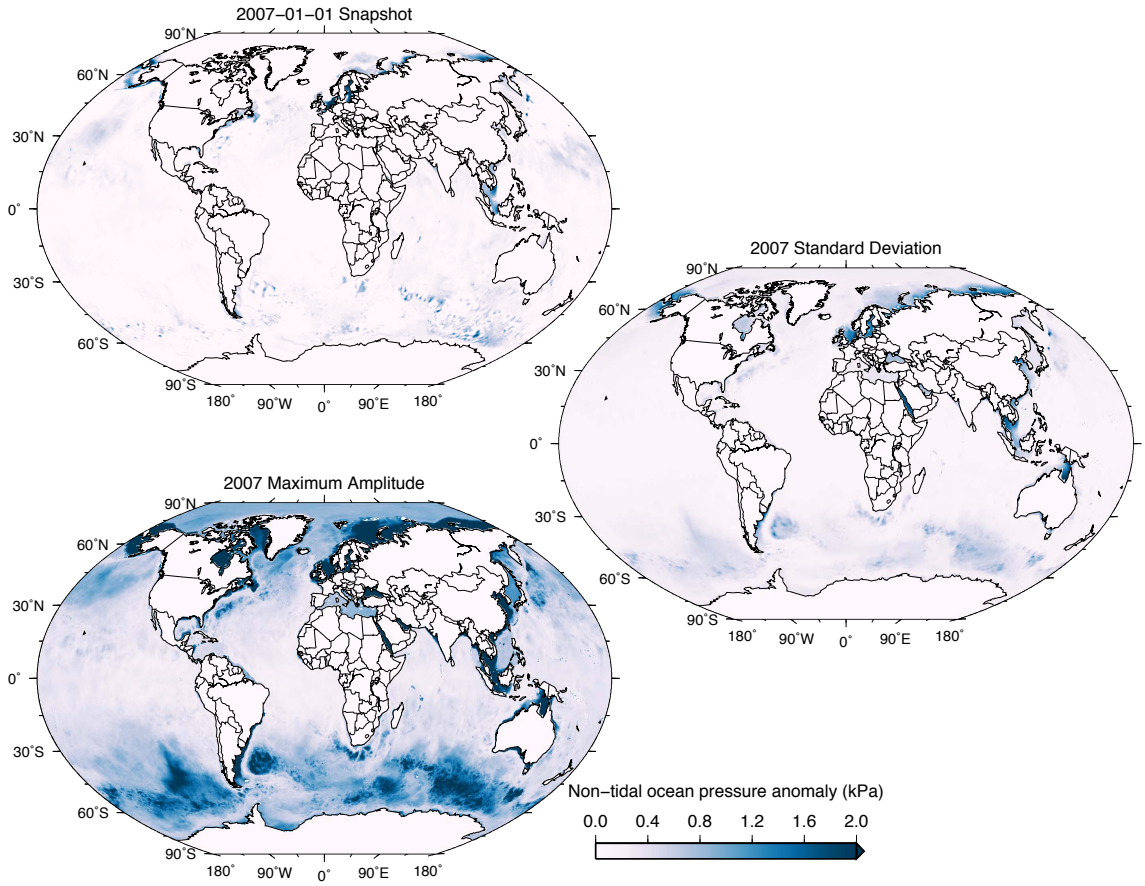

Figure 8.8: Global grids of anomalous non-tidal ocean pressure from ECCO2. The top-left panel shows a snapshot of the non-tidal ocean pressure from 1 January 2007. The center-right panel shows the standard deviation in the non-tidal ocean pressure anomaly during 2007. The bottom-left panel shows the maximum anomaly in non-tidal ocean pressure at each grid node during 2007. I removed a spatial mean of the pressure anomaly from every temporal epoch as well as a temporal mean for 2007 from every grid node. Note the change in scale with respect to Figs. 8.1 and 8.2.

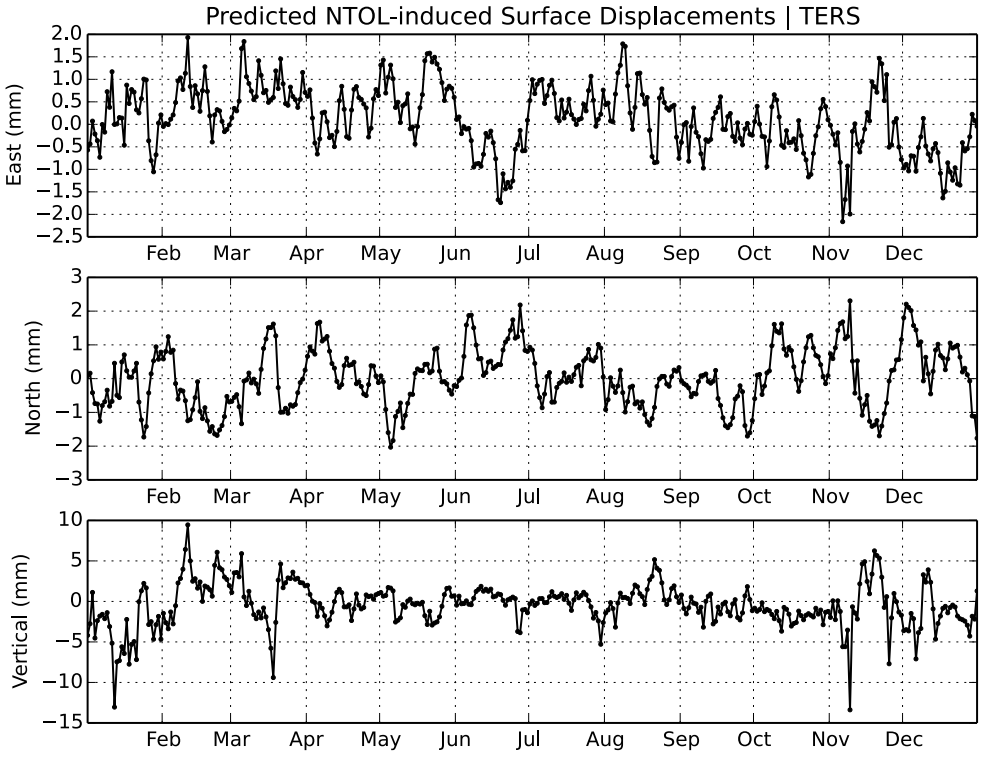

Figure 8.9: East (top), north (center), and vertical (bottom) displacements (in the CM reference frame) induced by variations in non-tidal ocean loading from ECCO2 at the location of GNSS station TERS in the Netherlands (cf., Fig. 8.2) during 2007. Constant-offset, linear-trend, and annual signals have been removed. The load Green's functions used in the convolution were derived from PREM structure.

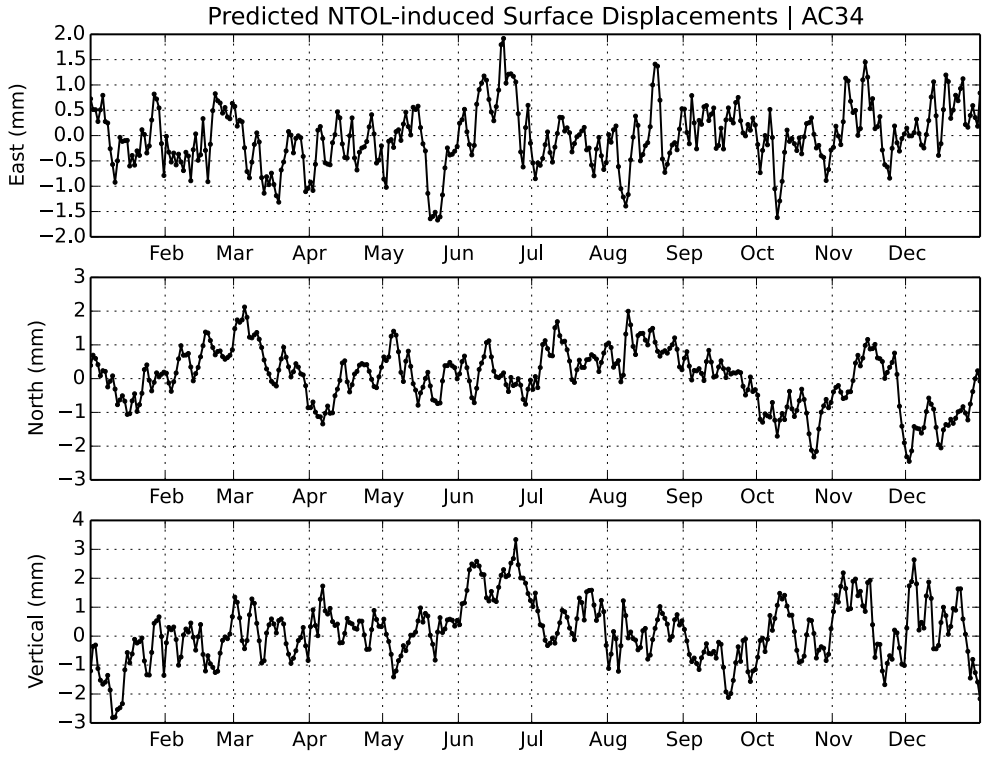

Figure 8.10: East (top), north (center), and vertical (bottom) displacements (in the CM reference frame) induced by variations in non-tidal ocean loading from ECCO2 at the location of GNSS station AC34 in Alaska (cf., Fig. 8.2) during 2007. Constant-offset, linear-trend, and annual signals have been removed. The load Green's functions used in the convolution were derived from PREM structure.

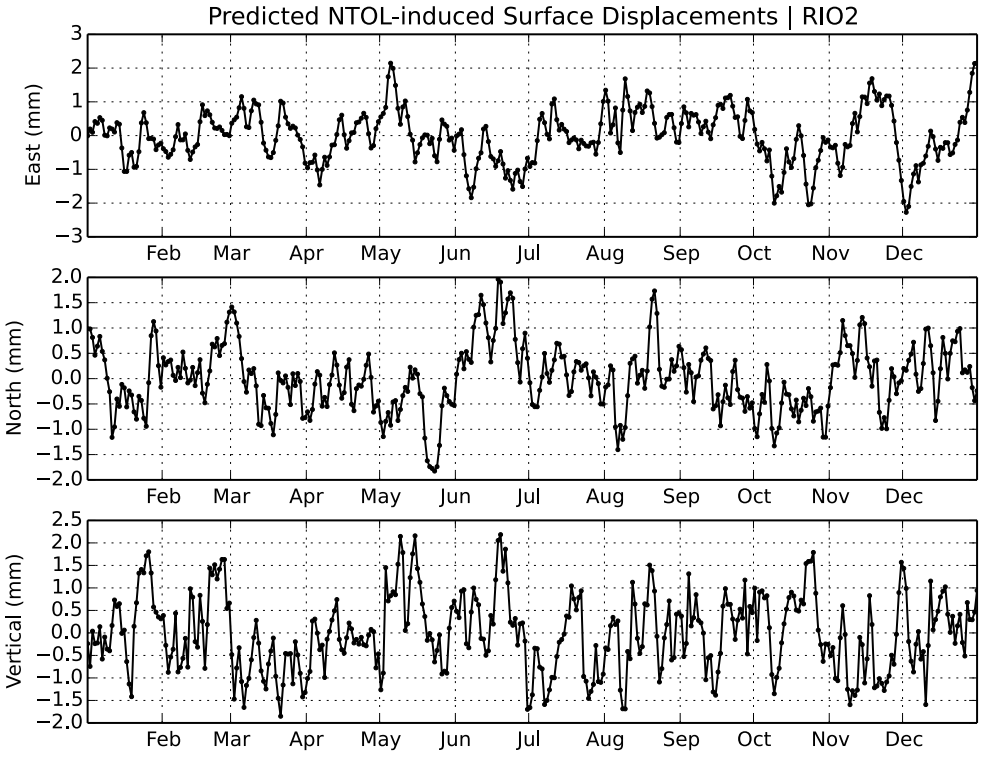

Figure 8.11: East (top), north (center), and vertical (bottom) displacements (in the CM reference frame) induced by variations in non-tidal ocean loading from ECCO2 at the location of GNSS station RIO2 in Argentina (cf., Fig. 8.2) during 2007. Constant-offset, linear-trend, and annual signals have been removed. The load Green's functions used in the convolution were derived from PREM structure.

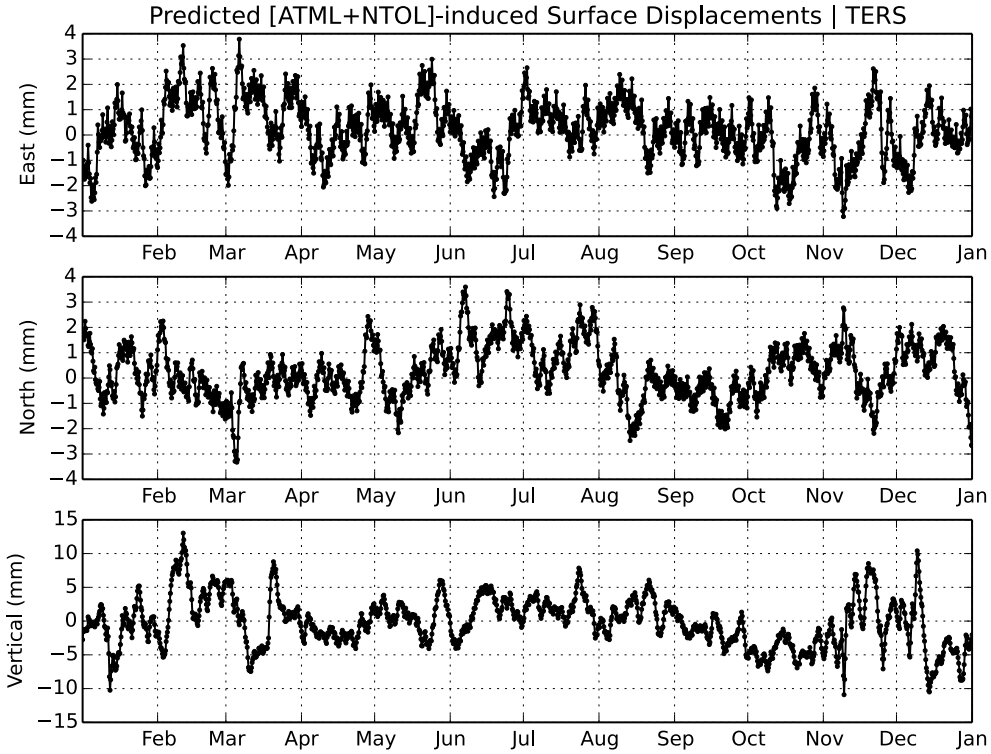

Figure 8.12: East (top), north (center), and vertical (bottom) displacements (in the CM reference frame) induced by variations in atmospheric (ECMWF) and non-tidal oceanic (ECCO2) pressure at the location of GNSS station TERS in the Netherlands during 2007. Constant-offset, linear-trend, and annual signals have been removed. Assuming first-order compensation due to the inverted barometer effect, I did not include the ocean regions in the convolution of the atmospheric pressure model with the load Green's functions (derived from PREM structure). The vertical displacements may be compared with the modeled displacements due to atmospheric loading shown in fig. 2 (center-right panel, solid black lines) of Williams & Penna (2011). Slight discrepancies are present, probably due in part to the use of different versions of the ECCO model for non-tidal ocean loading (I used ECCO2; Williams & Penna (2011) used ECCO), different atmospheric pressure models (I used ECMWF; Williams & Penna (2011) used NCEP/NCAR), and possibly different reference frames for the convolution (I used CM; Williams & Penna (2011) appear to have used CE). See also Figs. 8.3 and 8.6.

loading. The hemispherical exchange of hydrological mass with the seasons, due to changes in snow cover, soil moisture, and the atmosphere, produces a degree-one displacement response of the Earth at the level of a few millimeters (Blewitt et al., 2001). Mangiarotti et al. (2001) also examined vertical displacements caused by annual variations in atmospheric pressure, oceanic pressure, soil moisture, and snow cover. Contributions from soil moisture and snow cover to Earth's vertical-displacement response at annual time scales were found to range from about 1–10 mm in amplitude. In the Himalaya region specifically, seasonal hydrological loading generates maximum surface pressures on the order of 1–5 kPa (Chanard et al., 2014), as seen in data collected by the Gravity Recovery and Climate Experiment (GRACE) satellite mission. Chanard et al. (2014) show that the monsoon-driven hydrological loading causes vertical displacements of up to several millimeters or more on annual time scales.

Particularly in regions that experience substantial variations in river flow, lake levels, precipitation, and snow pack, the HYDL signal may contribute significantly to the noise of a geodetic time series. Moreover, the HYDL signal is large enough to be interpreted at some locations. As with other types of surface mass loading, surface displacements induced by HYDL are sensitive to the material properties of Earth's interior. Chanard et al. (2014), for example, inverted observations of HYDL-induced surface displacements in the Himalaya region for a new local model of one-dimensional elastic structure. Chanard et al. (2014), however, made no mention of reference frames used in the analysis; the described methodology suggests that CE load Green's functions may have been compared with CM observations, which would have introduced long-wavelength artifacts in the residual displacements and thus biased the inferred Earth model. Dill et al. (2015) explored the effects of local variations in crustal structure on Earth's response to HYDL. Alternatively, observed HYDL-induced surface displacements may be used to constrain the spatial extent and volume of the load. Recently, Fu et al. (2015) demonstrated that GNSS-inferred measurements of surface displacements on the west coast of the United States provide an effective means for constraining spatiotemporal variations in terrestrial water storage in that area.

9

Summary and Future Directions

In this thesis, I have described both a theoretical framework and an experimental methodology that may be used to explore the response of a spherically symmetric, non-rotating, elastic, and isotropic (SNREI) Earth (e.g., Dahlen & Tromp, 1998, Sec. 8.2) to surface mass loading (SML). Even with SNREI structure assumed, observed and predicted OTL-induced surface displacements generally coincide at the sub-millimeter level (Ch. 7), implying that models for the ocean tides and solid-Earth structure as well as methods for processing the geodetic data are already quite good. The apparent regional spatial coherency in the residual displacements, however, suggests that random observational errors are unlikely to account for all of the discrepancy, particularly for the M_2 harmonic. Thus, the residual displacements potentially contain useful information about deficiencies in the forward model, which probably arise due to errors in both the ocean-tide and SNREI-Earth models.

Variations in SNREI-Earth structure seem to have very little effect on predicted OTL-induced surface displacements (generally much less than 0.1 mm), and spatiotemporal characteristics of the residuals do not change much with different SNREI-Earth models employed in the convolution (Ch. 7). The residual displacements also remain consistent for different ocean-tide models. The consistency of the spatially coherent residuals between forward models implies that additional deficiencies, not yet considered here, likely persist in the forward models. In particular, the residuals might indicate sensitivity to non-sphericity, lateral heterogeneities, Earth rotation, anelasticity, and anisotropy in the crust and mantle. A natural extension of the work presented here would be to investigate the effects of non-SNREI structure on the induced deformation (cf., Bos et al., 2015).

For now, research into Earth's deformation response to surface mass loading relies primarily on Love-number and Green's-function theory. The theory, however, applies specifically to Earth structure that is spherically symmetric. To generalize the analysis to include non-

sphericity and lateral heterogeneities, perturbation techniques (e.g., Wang, 1997) or fully numerical procedures may be adopted (e.g., Agnew, 2015, Sec. 3.06.3.3). Fully numerical approaches probably represent the future of investigations into SML-induced deformation, but they also require a substantial re-working of the current SML-modeling framework. Latychev et al. (2009) explored the effects of lateral heterogeneities on the solid Earth body tides and found that the displacement response could be perturbed by up to about 1 mm.

Earth rotation perturbs the spheroidal shape of the Earth and couples the deformation response to additional spherical harmonic degrees and modes of deformation (e.g., Agnew, 2015, Sec. 3.06.3.2). Toroidal modes of deformation, for example, become coupled to the spheroidal modes (e.g., Wang, 1997; Dahlen & Tromp, 1998; Smylie, 2013). Moreover, to first-order, the Love numbers acquire a small dependence on latitude (Wang, 1997; Agnew, 2015). In addition, the interaction between the outer core and the mantle generates a resonance effect known as the nearly diurnal free wobble (NDFW) (e.g., Zürn, 1997; Agnew, 2015). The frequency of the NDFW coincides with the diurnal tidal band.

Anelastic dispersion, particularly within the mantle, can also have a significant effect on the SML-induced deformation (e.g., Bos et al., 2015). Anelastic dispersion causes the elastic moduli and the Love numbers to become both frequency-dependent and complex-valued (e.g., Agnew, 2015, Sec. 3.06.3.2.3). At present, scaling relationships exist to extrapolate the elastic moduli to frequencies outside the seismic band (e.g., Dahlen & Tromp, 1998, Sec. 9.7). Not much is known, however, about Earth's anelastic response at non-seismic periods, including tidal periods. Thus, detecting and modeling the effects of anelastic dispersion at tidal periods can provide important constraints on the Q structure of the solid Earth at lower frequencies (e.g., Agnew, 2015). Based on observations of OTL in western Europe, Bos et al. (2015) determined that the phase changes associated with imaginary components of the M_2-period deformation were very small ($\approx 0.2^\circ$). Extrapolating the shear modulus to tidal periods, however, improved the model fit to the observations (Bos et al., 2015).

The procedure outlined in Ch. 4 to compute Earth deformation caused by SML may be extended without too much additional effort to account for some forms of anisotropy within the solid Earth. In effect, the equations of motion must be expanded to include additional

elastic parameters (e.g., Takeuchi & Saito, 1972). To model the spheroidal deformation of a transversely isotropic Earth, for example, radial variations in five elastic moduli as well as density are required (e.g., Dahlen & Tromp, 1998, Sec. 8.9).

Relaxing the assumptions of SNREI Earth structure constitutes one avenue of future exploration in geodetic tomography using observations of load-generated deformation. Additional future projects could exploit observations of load-generated deformation to constrain the spatial extent and volume of dynamic loads, such as seasonal fluctuations in continental water storage (e.g., Fu et al., 2015). Dense local arrays of GNSS receivers could also be used to develop local ocean-tide models where coastal morphology is complicated, such as Puget Sound. Moreover, GNSS receivers deployed near rivers or lakes could track the volume of seasonal runoff. The possibilities of using SML to perform geodetic tomography and to constrain surface mass loads are immense and varied.

Still, most studies consider SML an inconvenient source of noise. The effects of OTL are routinely removed from GNSS time series; the effects of additional forms of SML, however, are not. Models for atmospheric, non-tidal oceanic, and hydrological loading are typically less accurate and spatially coarser than the models for OTL. Ocean tides, which are forced directly by the astronomical ephemeris, are more predictable. Furthermore, OTL signals are generally larger in magnitude than the ATML, NTOL, and HYDL signals. Nevertheless, geodetic measurements are now sufficiently precise to detect load-induced deformation of the solid Earth from a variety of sources. Therefore, accounting for the combined effects of Earth's deformation response to OTL, ATML, NTOL, and HYDL can lead to improvements, for example, in the ability to investigate subtle tectonic signals, detect aseismic transients, assess glacial isostatic adjustment, and monitor sea-level rise.

Moreover, models of OTL are sometimes imprecise, particularly near coastlines and shallow seas (e.g., Fig. 7.4). At sites with large ocean-tide model uncertainties, empirical estimates of OTL-induced surface displacements may be more accurate than modeled predictions. Accurate empirical estimates can improve the ability to infer accurate station positions from GPS time series and to constrain ocean-tide models.

A

Earth Models

Here, I provide information on six radially symmetric Earth models that were used as examples within the thesis: 1066A (Gilbert & Dziewonski, 1975), PREM (Dziewonski & Anderson, 1981), STW105 (Kustowski et al., 2008), AK135f (Kennett et al., 1995; Montagner & Kennett, 1996), SNA (Grand & Helmberger, 1984), and CR (Chu et al., 2012). Fig. A.1 shows profiles of the elastic parameters for each model down to 1000 km depth.

The model 1066A, which I acquired directly from Table 5 of Gilbert & Dziewonski (1975), was derived using normal mode data constrained by Earth mass and moment of inertia. I generated the model PREM using the polynomial functions from Table 1 of Dziewonski & Anderson (1981), evaluated every 100 km within the core regions and every 100 m within the mantle and crust. I also assumed effective isotropic velocities between 24.4 and 220 km depth (using the formulae from Table 1 of Dziewonski & Anderson (1981)) and replaced the water layer at the surface by the properties of the upper-most crust: V_P = 5.8 km/s, V_S = 3.2 km/s, and ρ = 2.6 g/cc. The water layer could alternatively be removed altogether, but then the radius of the Earth would be slightly smaller than average to satisfy the assumption of spherical symmetry (Ch. 4). The PREM model was derived from normal-mode and body-wave data, as well as moment of inertia and mass constraints.

Models STW105 and AK135f were acquired directly from the Incorporated Research Institutions for Seismology (IRIS) Data Management Center (DMC) (Trabant et al., 2012). STW105 was derived from observed body- and surface-wave data as well as long-period waveforms (Kustowski et al., 2008). AK135f was derived from seismic body waves (Kennett et al., 1995), with density and Q structure contributed by Montagner & Kennett (1996). For both models, I have replaced the water layers at the surface by the elastic properties of the upper-most crust: V_P = 5.8 km/s, V_S = 3.2 km/s, and ρ = 2.6 g/cc.

Whereas 1066A, PREM, STW105, and AK135f represent globally averaged structure, the

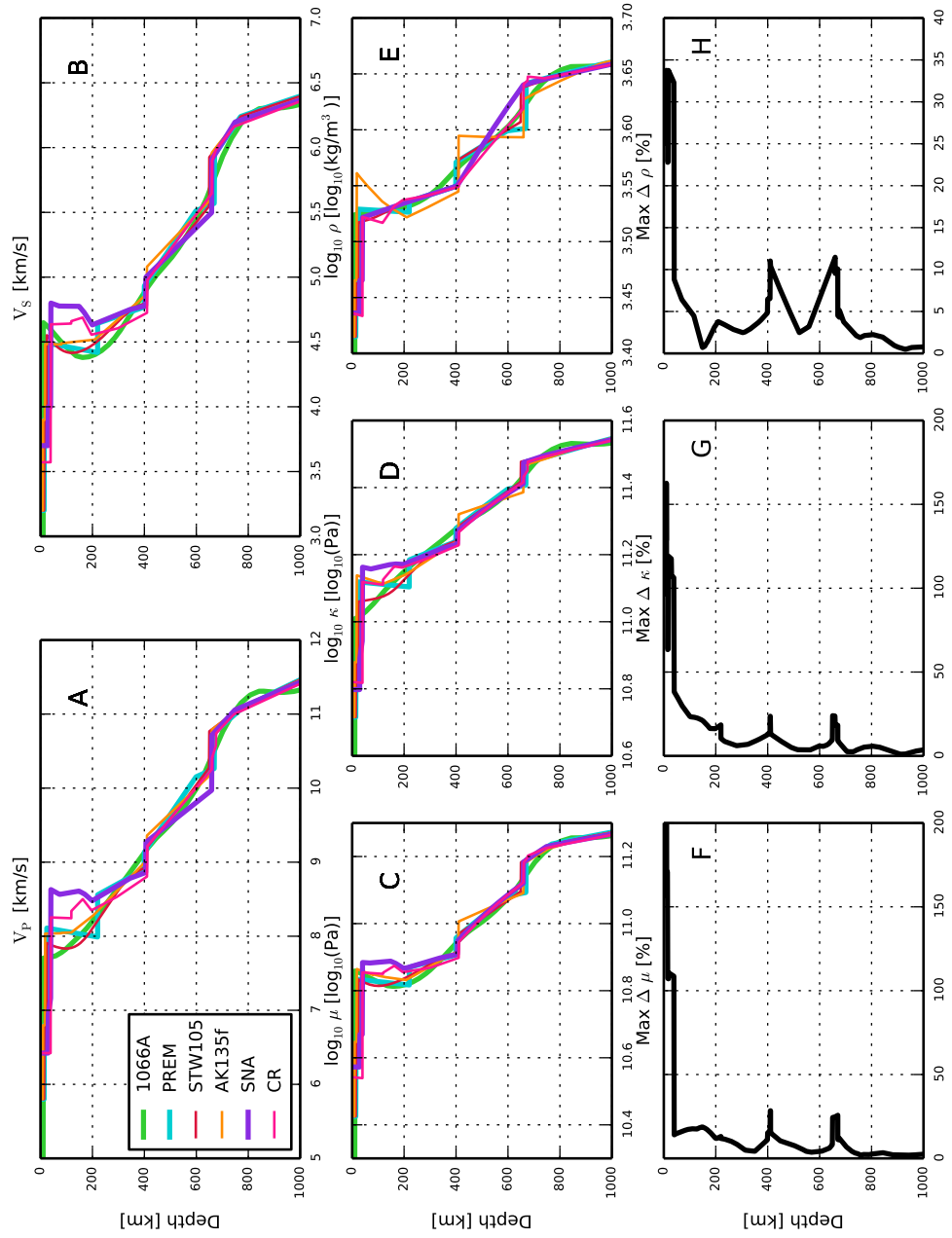

Figure A.1: Profiles of elastic material parameters down to 1000 km depth for the Earth models 1066A, PREM, STW105, AK135f, SNA, and CR. Panels A and B show profiles of seismic P- and S-wave velocities, respectively. Panels C, D, and E show profiles of the shear modulus (μ), the bulk modulus (κ) and density (ρ), respectively, in log-space. Panels F, G, and H show the maximum percentage differences (in linear-space) between μ, κ, and ρ at each depth level.

Earth Model SNA			
Radius (km)	V_P (km/s)	V_S (km/s)	ρ (g/cc)
6371.0	6.422	3.700	2.730
6341.0	6.422	3.700	2.730
6341.0	6.933	4.000	2.920
6331.0	7.192	4.000	2.920
6331.0	8.630	4.800	3.323
6296.0	8.562	4.775	3.344
6221.0	8.611	4.775	3.390
6196.0	8.558	4.710	3.407
6171.0	8.477	4.630	3.423
6021.0	8.793	4.755	3.514
5965.0	8.862	4.780	3.548
5965.0	9.269	5.000	3.548
5711.0	9.974	5.500	4.370
5711.0	10.717	5.910	4.370
5621.0	11.062	6.200	4.424
5346.0	11.470	6.385	4.571

Table A.1: Tabulated values were provided by Risheng Chu (personal communication). Details on the model derivation may be found in Grand & Helmberger (1984). Below 1000 km depth, the model assumes the elastic properties of AK135f (Kennett et al., 1995; Montagner & Kennett, 1996; Trabant et al., 2012).

models CR and SNA represent regional cratonic and stable North American structure, respectively. SNA was derived from an average of upper mantle shear-wave velocity structure in North America (Grand & Helmberger, 1984). CR was derived from an average of upper mantle P-wave velocity structure beneath stable North America (Chu et al., 2012); the values for V_S and ρ were obtained from ratios of AK135 (R. Chu, personal communication). The elastic properties for models SNA and CR are provided in Tables A.1 and A.2. Below 1000 km depth, the SNA and CR models assume the structural properties of AK135f.

Earth Model CR			
Radius (km)	V_P (km/s)	V_S (km/s)	ρ (g/cc)
6371.000	6.422	3.572	2.730
6331.125	6.422	3.572	2.713
6331.125	8.254	4.636	3.327
6252.123	8.243	4.642	3.286
6252.123	8.341	4.661	3.286
6208.118	8.502	4.689	3.406
6174.107	8.347	4.554	3.447
6068.421	8.547	4.608	3.481
5959.866	8.808	4.726	3.542
5959.866	9.216	4.973	3.561
5710.773	10.256	5.649	4.162
5710.773	10.404	5.898	4.375
5694.662	10.583	5.989	4.407
5694.662	10.740	5.989	4.442
5623.601	11.004	6.165	4.425
5369.145	11.412	6.358	4.554

Table A.2: Tabulated values were provided by Risheng Chu (personal communication). Details on the model derivation may be found in Chu et al. (2012). Below 1000 km depth, the model assumes the elastic properties of AK135f (Kennett et al., 1995; Montagner & Kennett, 1996; Trabant et al., 2012).

B

Ocean Tide Models

One of the most prominent forms of SML comes from the periodic rise and fall in sea-level due to the ocean tides. Cartwright (1999) provides a detailed account of the historical development of ocean tide models through the end of the 20th century. Pugh (1987) also discusses important aspects of pre-satellite-era tidal predictions. Modern ocean tide models fall predominantly into two classes: empirical models and data-assimilation models (e.g., Zahel, 1997; Lyard et al., 2006). Generally, the first class of models are constrained mostly by satellite altimetry measurements of sea-surface height as well as tide-gauge observations. For the second class of models, the satellite-altimetry and tide-gauge data are assimilated into global hydrodynamic solutions. The hydrodynamic models are formed by numerically solving the Laplace tidal equations (LTEs), including terms for eddy dissipation and bottom friction as well as loading and self-attraction (LSA, or sometimes SAL (Ray, 1998)), at each tidal frequency of interest (Hendershott, 1972; Schwiderski, 1980; Melchior, 1983; Cartwright, 1999; Zahel, 1997).

Modern ocean tide models are typically distributed on regularly spaced latitude-longitude grids, with amplitude and phase values computed for up to 30 tidal harmonics or more. In contrast to the solid Earth body tides, which respond essentially coincident with the equilibrium tide, the ocean tides exhibit a complicated spatial structure due to interactions with continental boundaries, bathymetry, and the Coriolis force (Melchior, 1983; Pugh, 1987; Zahel, 1997; Cartwright, 1999). The ocean basins and earth rotational effects produce tidal circulation systems, centered on points of zero tidal amplitude called **amphidromes**. Lines of equal phase radiating away from the amphidromic points are called **cotidal lines**.

B.1 Global Ocean Tide Models

FES2012[6] is a recent installment in a series of tidal atlases produced by the "French Tidal Group" under the generic name of Finite Element Solution (FES) (Le Provost et al., 1994; Lyard et al., 2006; Carrère et al., 2012). The FES2012 atlas, generated by assimilating satellite altimetry observations into a global hydrodynamic model, provides the complex-valued amplitudes of 32 tidal harmonics on a $0.0625^\circ \times 0.0625^\circ$ grid. FES2012 represents an improvement upon previous atlases, such as FES2004 (Lyard et al., 2006), in grid and bathymetry resolution, data assimilation techniques, enhanced coastlines around Antarctica, and longer-term altimetry data acquired from multiple missions (Carrère et al., 2012). Fig. B.1 shows the amplitude of the M_2 ocean tide from the FES2012 model.

TPXO8-Atlas[7], developed at Oregon State University, integrates a global tidal solution (TPXO8) with a multitude of high-resolution local solutions produced for shelf and coastal regions at several locations around the world (Egbert et al., 1994; Egbert & Erofeeva, 2002; Egbert et al., 2010). Tidal amplitudes and phases are provided on a global grid of $\frac{1}{30}^\circ$ resolution for the harmonics M_2, S_2, N_2, K_2, K_1, O_1, P_1, Q_1, and M_4. Additional long-period and compound tidal harmonics (M_f, M_m, MS_4, and MN_4) are provided on a $\frac{1}{6}^\circ$-resolution grid. Satellite altimetry data from the TOPEX/Poseidon and Jason missions are assimilated into global solutions of the LTEs to generate TPXO8. Tide gauges are primarily used for validation, particularly in the shelf and coastal regions.

EOT11A[8], a purely empirical ocean tide model generated from a harmonic analysis of multi-mission satellite altimetry data, provides amplitudes and phases for thirteen tidal harmonics (Savcenko & Bosch, 2012). The harmonic analysis was performed on the combined altimetry residuals, using FES2004 (Lyard et al., 2006) as a reference model.

HAMTIDE11A[9] (i.e., the Hamburg direct data Assimilation Methods for TIDEs) provides amplitude and phase information for nine tidal harmonics on a regular grid of 0.125° resolution. A direct minimization of model and observational residuals using least-squares

[6] www.aviso.altimetry.fr/en/data/products/auxiliary-products/global-tide-fes.html
[7] volkov.oce.orst.edu/tides/
[8] ftp://ftp.dgfi.badw.de/pub/EOT11a
[9] ftp://ftp.icdc.zmaw.de/hamtide

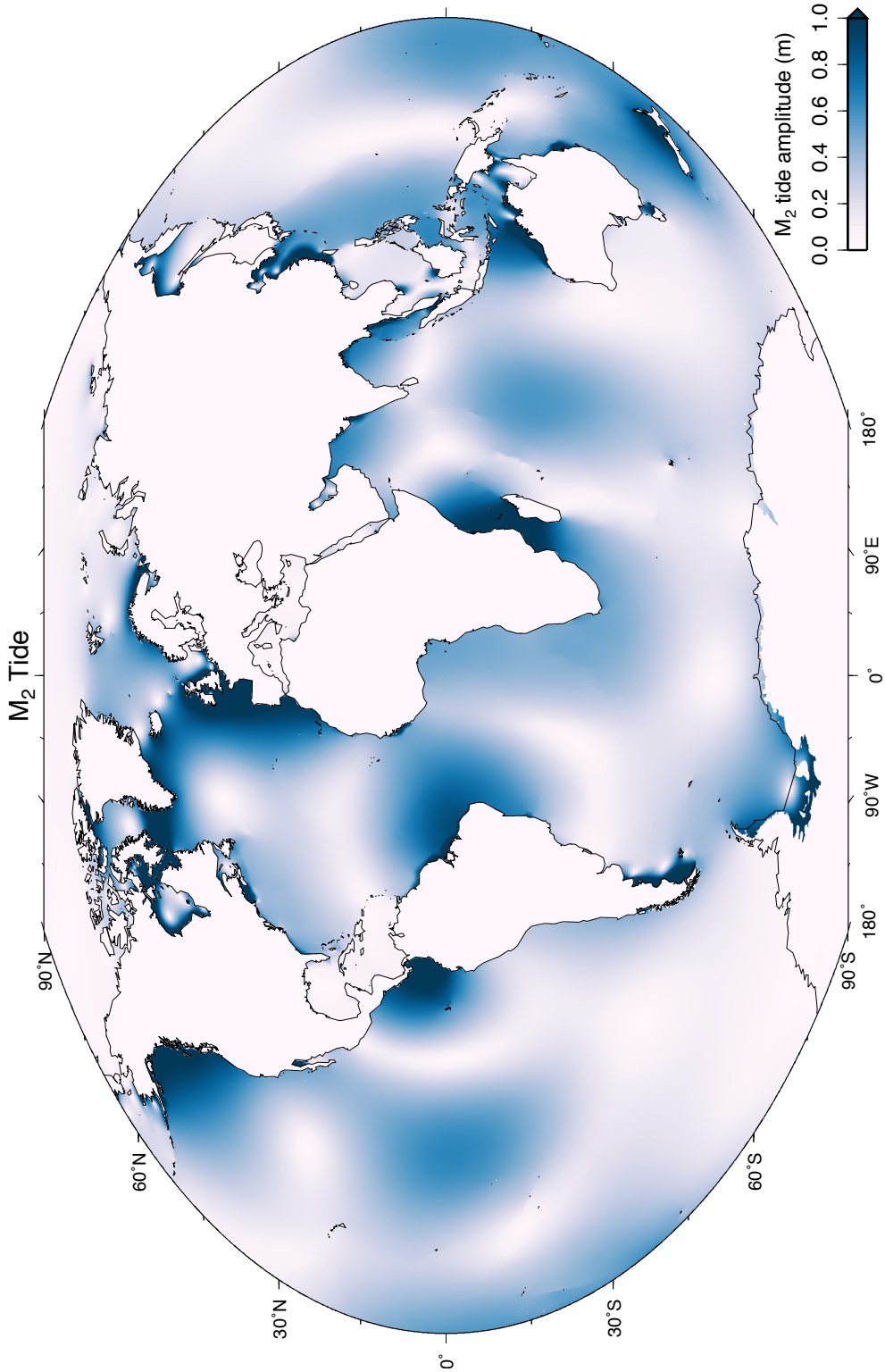

Figure B.1: Map depicting the amplitude of the M_2 ocean tide from the FES2012 model (Lyard et al., 2006; Carrère et al., 2012). Note that the tides remain active beneath the ice shelves in Antarctica.

inversion generates the HAMTIDE11A atlas.

GOT4.10c[10], generated by performing a harmonic analysis of satellite altimetry residuals with respect to an *a priori* hydrodynamic model, is the latest release in a series of global ocean tide models developed by Richard Ray at the Goddard Space Flight Center (Ray, 1999; Ray & Egbert, 2004; Ray, 2013). The satellite altimetry observations of sea-surface height were corrected for tidal geocenter variations induced by the loading (Desai & Ray, 2014).

OSU12[11], developed and distributed by The Ohio State University, is an empirical global ocean tide model based on multi-mission satellite altimetry data (Fok et al., 2013). Ten tidal harmonics are provided at a spatial resolution of $0.25^\circ \times 0.25^\circ$. Gaps in the polar regions are patched with the GOT4.7 ocean tide model.

B.2 Local Ocean Tide Models

Tidal predictions near coastlines and in shallow seas are less reliable than in the open ocean due to nonlinearities in the tidal equations and limited empirical constraints (e.g., Ray et al., 2011). High-resolution, local ocean tide models may be obtained from Oregon State University[12] (Egbert & Erofeeva, 2002; Egbert et al., 1994, 2010). Additional providers of local tidal models are listed in Agnew (2012), and the references therein. Local models for Canadian waters have also been developed by Lambert et al. (1998).

B.3 Quality Assessment

Modern ocean tide models are typically accurate to about 1 cm in pelagic zones of the ocean and to about 5 cm in shelf and coastal regions (Stammer et al., 2014). Errors can arise from a misrepresentation of the coastline, discretization of the model grid, inaccurate bathymetry, hydrodynamic modeling uncertainties, incomplete depictions of non-linear tidal interactions, insufficient or sparse empirical observations, satellite altimetry and tide gauge data

[10] Richard Ray, personal communication.

[11] `http://geodeticscience.org/oceantides/OSU12v1.0/`

[12] `volkov.oce.orst.edu/tides/region.html`

uncertainties, and inaccurate LSA estimates, among other issues (e.g., Bosch et al., 2009; Ray et al., 2011). Ocean tide models have traditionally been considered the largest source of error in forward-modeled predictions of OTL response (e.g., Bos & Baker, 2005; Penna et al., 2008); however, ocean tide models are continually being improved (Stammer et al., 2014) and evidence now suggests that ocean tide models may no longer be the limiting factor in analyses of OTL-induced surface displacements (e.g., Yuan et al., 2013; Penna et al., 2015; Bos et al., 2015).

C

Love Number and Green's Function Tables

Here, I present Love numbers of four different types (potential, load, shear, and stress) and displacement load Green's functions for the six radially symmetric Earth models described in Appendix A, as well as a homogeneous sphere model with the elastic properties V_P = 10 km/s, V_S = 5 km/s, and ρ = 5 g/cc. Details on the boundary conditions used to derive the four types of Love numbers may be found in Table 6.1. Figs. C.1, C.2, C.3, and C.4 show profiles of the potential, load, shear, and stress Love numbers, respectively, as a function of spherical harmonic degree n. Fig. C.5 shows the displacement load Green's functions derived from the load Love numbers in the CE and CM reference frames (Blewitt, 2003).

The Love numbers may be compared with, e.g., Table 2 from Longman (1963), Table 2 from Okubo & Endo (1986), Table 1 from Saito (1978), Table 1 from Merriam (1985), Table 2 from Merriam (1986), Table 1 from Guo et al. (2004), Table 2.1 from Jentzsch (1997), Table 1 from Varga (1992), and Table 1 from Varga (1983)[13]. The displacement LGFs may be compared with, e.g., Table 2 from Guo et al. (2004), Table A5 from Farrell (1972a), and Table A.1 from Jentzsch (1997). Caution must be exercised when making detailed comparisons, however, since even slight variations in the input Earth structural model (e.g., different versions of PREM for different crustal types) can yield significant differences in the Love numbers and, by extension, the LGFs.

To aid in comparisons, Tables C.1–C.4 provide lists of Love numbers for a subset of models: 1066A, PREM, AK135f, and the homogeneous sphere. Similarly, Tables C.5 through C.11 provide lists of displacement LGFs in both the CE and CM reference frames for all seven Earth models. The only difference between the CE and CM reference frames for the

[13]Note, however, that the double-prime notation in (Varga, 1983) represents potential-free normal stress boundary conditions rather than shear traction.

displacement LGFs involves a shift of the degree-1 load Love numbers (Blewitt, 2003). For more details on the conversion between the two types of displacement LGFs, please refer to Sec. 4.3.5. Note that the Love numbers associated with the homogeneous sphere may be computed either analytically (Sec. 4.2.9 and Takeuchi & Saito (1972)) or numerically via an integration of the equations of motion through a radially homogeneous Earth (Ch. 4).

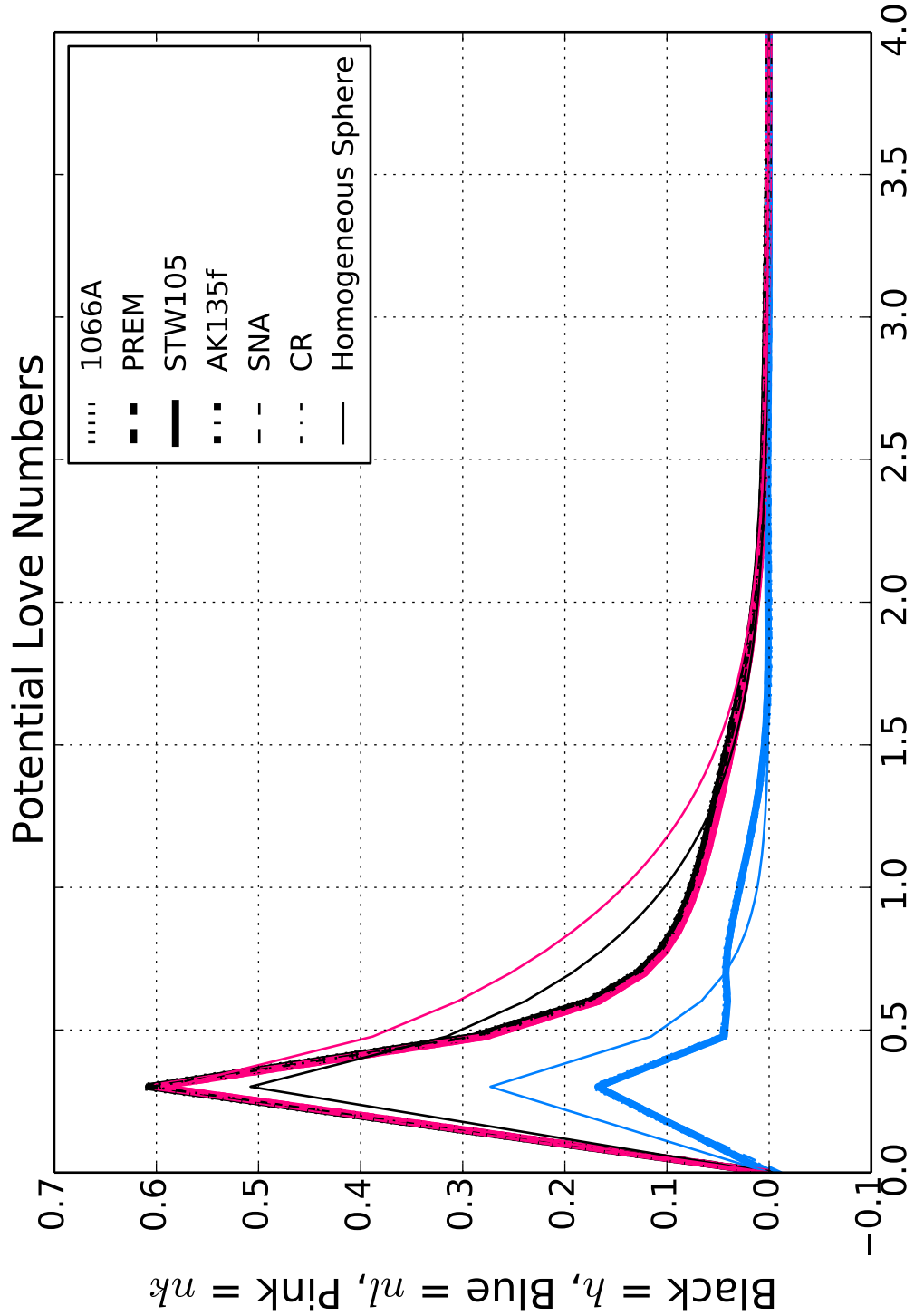

Figure C.1: Potential, or tide, Love numbers for seven radially symmetric Earth models: 1066A, PREM, STW105, AK135f, SNA, CR, and a homogeneous sphere with properties V_P = 10 km/s, V_S = 5 km/s, and ρ = 5 g/cc.

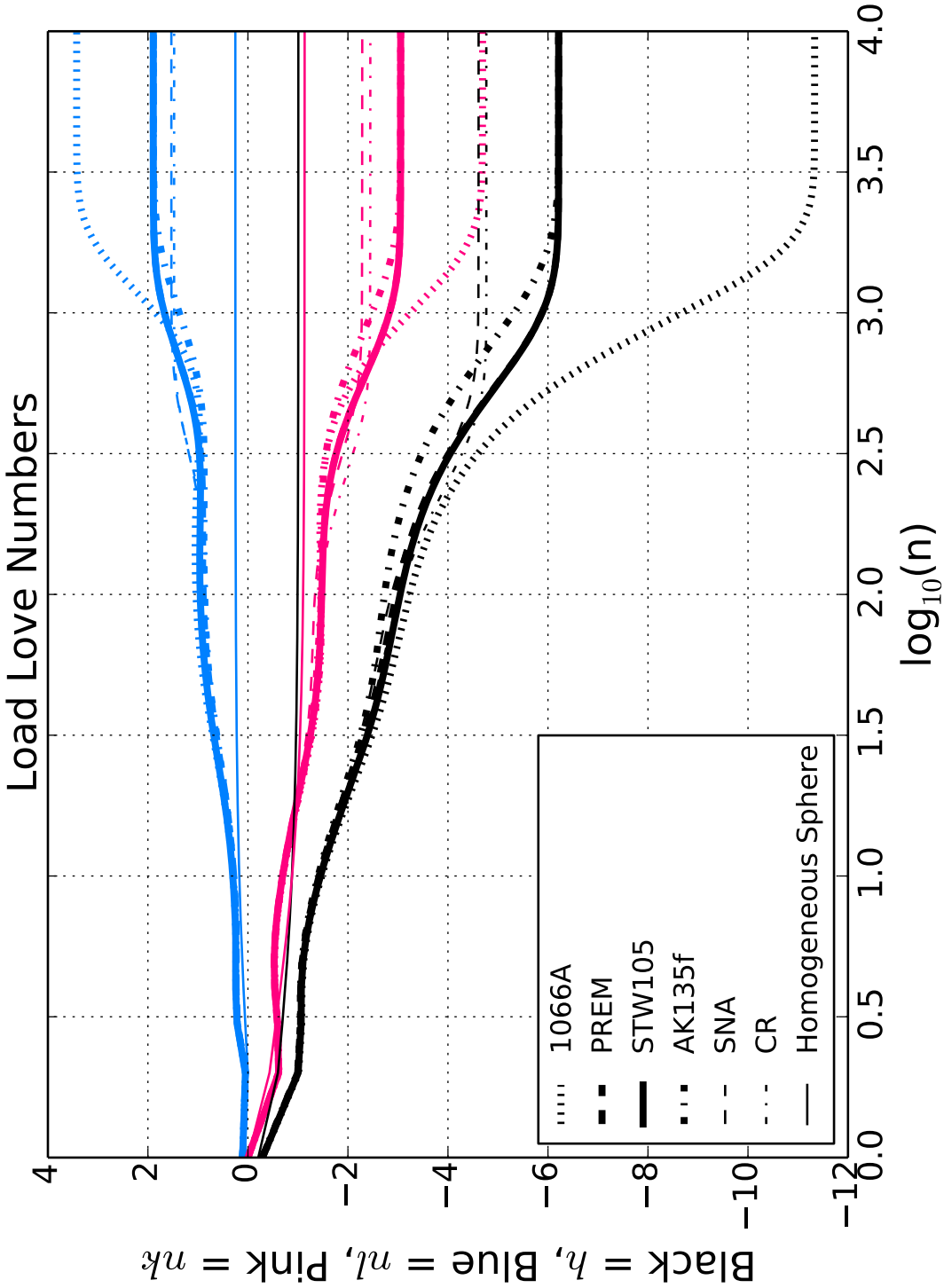

Figure C.2: Same as Fig. C.1, but for the load Love numbers.

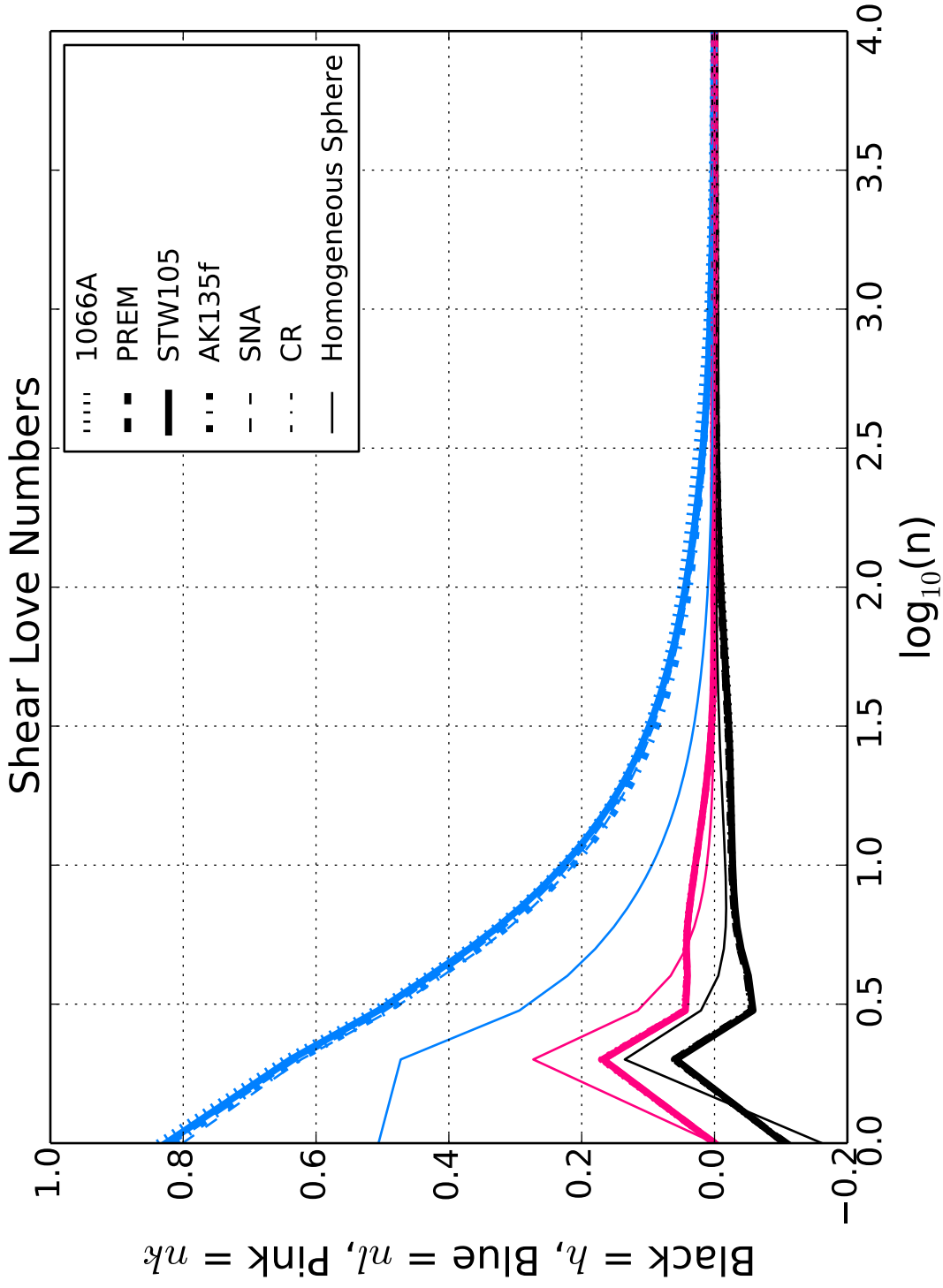

Figure C.3: Same as Fig. C.1, but for the shear Love numbers.

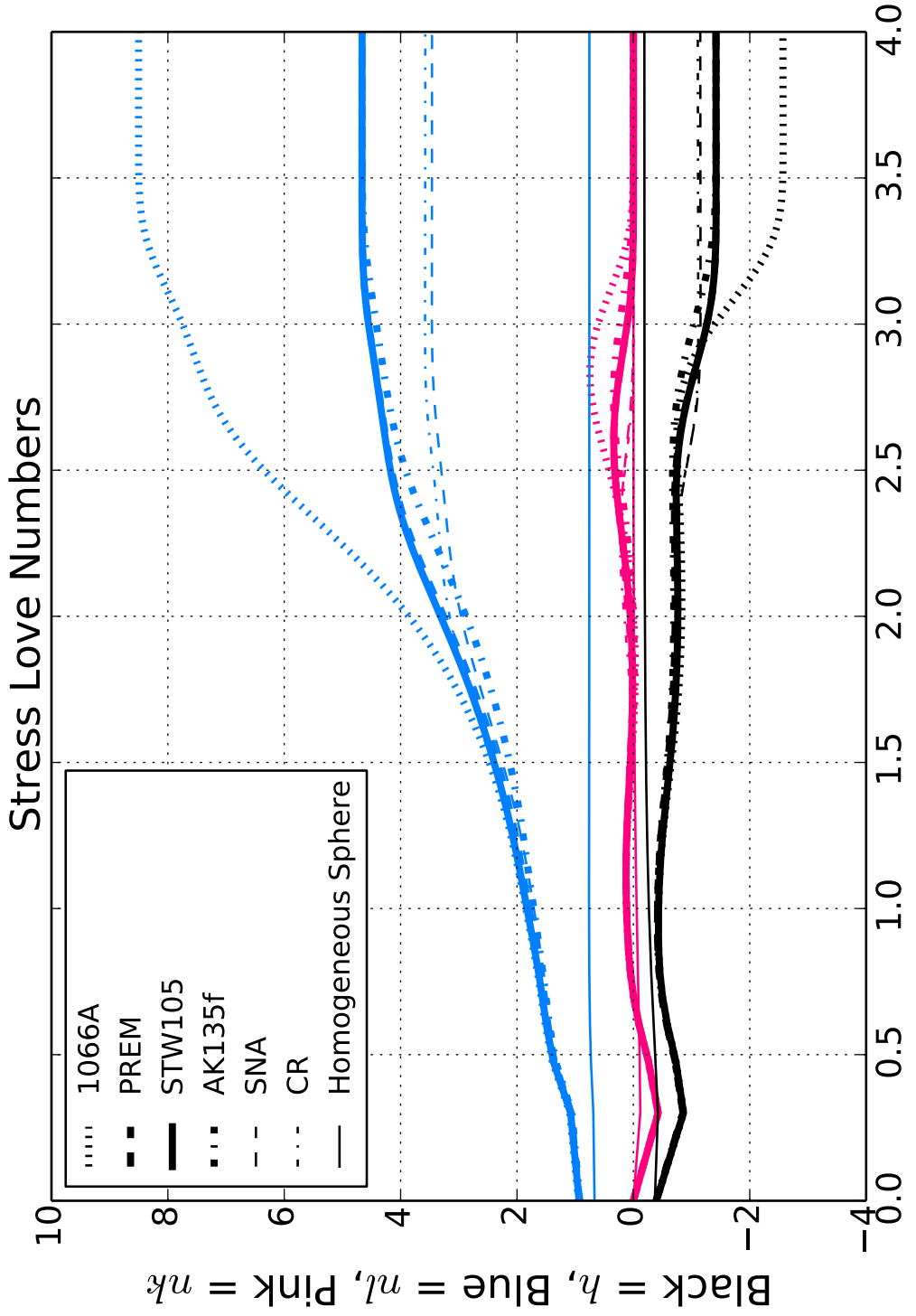

Figure C.4: Same as Fig. C.1, but for the stress Love numbers.

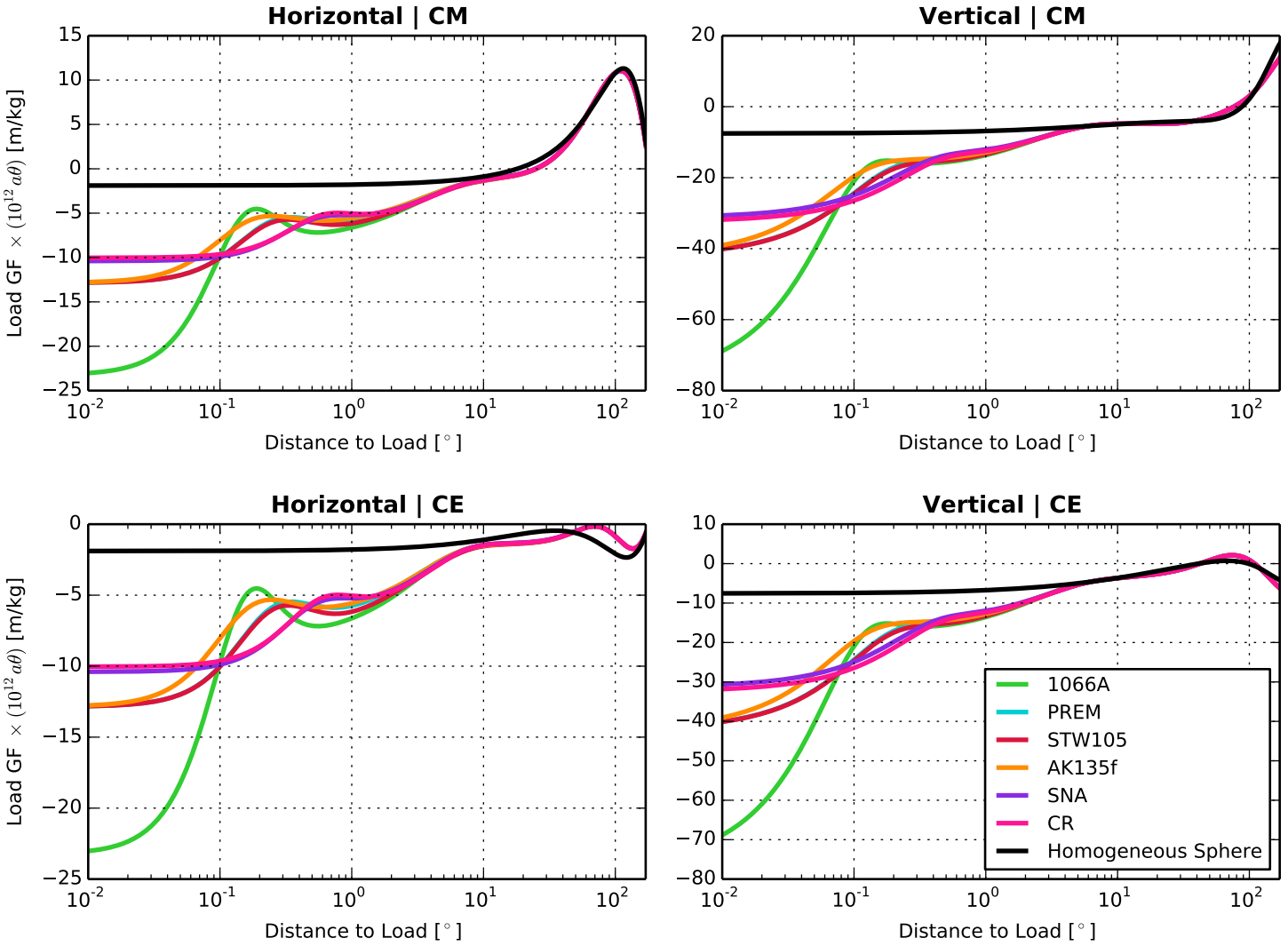

Figure C.5: Normalized displacement load Green's functions for seven radially symmetric Earth models: 1066A, PREM, STW105, AK135f, SNA, CR, and a homogeneous sphere with properties V_P = 10 km/s, V_S = 5 km/s, and ρ = 5 g/cc. The upper panels show the horizontal (left) and vertical (right) load Green's functions in the CM reference frame. The bottom panels show the horizontal (left) and vertical (right) load Green's functions in the CE reference frame. The load Green's functions are normalized by a factor of $10^{12} a\theta$, where a is Earth's radius in meters and θ is angular distance from the load in radians.

Love Numbers for Earth Model 1066A												
	Potential			Load			Shear			Stress		
n	h	nl	nk	h'	nl'	nk'	h''	nl''	nk''	h'''	nl'''	nk'''
0	0.0000	0.0000	0.0000	-0.1347	0.0000	0.0000	0.0000	0.0000	0.0000	-0.4042	0.0000	0.0000
1	0.0000	0.0000	0.0000	-0.2933	0.1052	0.0000	-0.1059	0.8385	0.0000	-0.3985	0.9438	0.0000
2	0.6130	0.1703	0.6049	-1.0137	0.0486	-0.6210	0.0609	0.6480	0.1703	-0.8665	1.0933	-0.4290
3	0.2924	0.0451	0.2800	-1.0760	0.2158	-0.5971	-0.0569	0.5136	0.0451	-0.7327	1.3939	-0.2600
4	0.1777	0.0417	0.1682	-1.0809	0.2420	-0.5425	-0.0501	0.4342	0.0417	-0.5864	1.5140	-0.0979
5	0.1309	0.0432	0.1237	-1.1167	0.2387	-0.5309	-0.0391	0.3744	0.0432	-0.5002	1.5848	-0.0016
10	0.0774	0.02931	0.0718	-1.4752	0.2973	-0.7023	-0.0268	0.2303	0.0293	-0.4323	1.8480	0.1197
100	0.0147	0.0002	0.0123	-3.2353	1.0387	-1.4551	-0.0104	0.0510	0.0002	-0.8313	3.8577	-0.0058
1000	0.0033	0.0008	0.0020	-8.6837	1.8450	-3.2503	-0.0018	0.0103	0.0008	-1.3968	7.7489	0.6083
10000	0.0005	0.0000	0.0003	-11.3331	3.4245	-4.6929	-0.0003	0.0011	0.0000	-2.5702	8.5022	-0.0008

Table C.1: Potential, load, shear and stress Love numbers for model 1066A (Gilbert & Dziewonski, 1975). For the boundary conditions used to compute each set of Love numbers, refer to Table 6.1.

Love Numbers for Earth Model PREM												
	Potential			Load			Shear			Stress		
n	h	nl	nk	h'	nl'	nk'	h''	nl''	nk''	h'''	nl'''	nk'''
0	0.0000	0.0000	0.0000	-0.1322	0.0000	0.0000	0.0000	0.0000	0.0000	-0.3967	0.0000	0.0000
1	0.0000	0.0000	0.0000	-0.2863	0.1040	0.0000	-0.1070	0.8213	0.0000	-0.3903	0.9266	0.0000
2	0.6067	0.1683	0.5993	-0.9953	0.0470	-0.6141	0.0606	0.6346	0.1683	-0.8520	1.0695	-0.4251
3	0.2888	0.0443	0.2768	-1.0525	0.2110	-0.5894	-0.0556	0.5019	0.0443	-0.7177	1.3621	-0.2574
4	0.1753	0.0409	0.1661	-1.0543	0.2360	-0.5353	-0.0488	0.4236	0.0409	-0.5725	1.4771	-0.0976
5	0.1292	0.0423	0.1219	-1.0870	0.2320	-0.5240	-0.0379	0.3648	0.0423	-0.4869	1.5442	-0.0030
10	0.0762	0.0286	0.0705	-1.4237	0.2843	-0.6916	-0.0256	0.2236	0.0286	-0.4151	1.7931	0.1162
100	0.0148	0.0010	0.0124	-2.9659	0.8963	-1.4684	-0.0090	0.0431	0.0010	-0.7193	3.2594	0.0529
1000	0.0028	0.0001	0.0020	-5.8816	1.6714	-2.8295	-0.0017	0.0061	0.0001	-1.2629	4.5516	0.1057
10000	0.0003	0.0000	0.0002	-6.2132	1.8916	-3.0547	-0.0002	0.0006	0.0000	-1.4197	4.6610	-0.0003

Table C.2: Potential, load, shear and stress Love numbers for model PREM (Dziewonski & Anderson, 1981). For the boundary conditions used to compute each set of Love numbers, refer to Table 6.1.

Love Numbers for Earth Model AK135f												
	Potential			Load			Shear			Stress		
n	h	nl	nk	h'	nl'	nk'	h''	nl''	nk''	h'''	nl'''	nk'''
0	0.0000	0.0000	0.0000	-0.1319	0.0000	0.0000	0.0000	0.0000	0.0000	-0.3957	0.0000	0.0000
1	0.0000	0.0000	0.0000	-0.2845	0.1052	0.0000	-0.1061	0.8155	0.0000	-0.3896	0.9213	0.0000
2	0.6074	0.1694	0.5999	-0.9928	0.0477	-0.6150	0.0608	0.6267	0.1694	-0.8507	1.0550	-0.4240
3	0.2893	0.0453	0.2774	-1.0484	0.2116	-0.5906	-0.0554	0.4923	0.0453	-0.7158	1.3373	-0.2556
4	0.1760	0.0415	0.1668	-1.0487	0.2371	-0.5373	-0.0489	0.4135	0.0415	-0.5713	1.4434	-0.0964
5	0.1299	0.0427	0.1228	-1.0795	0.2340	-0.5266	-0.0383	0.3545	0.0427	-0.4864	1.5024	-0.0024
10	0.0768	0.0288	0.0715	-1.4044	0.2866	-0.6969	-0.0258	0.2131	0.0288	-0.4142	1.7114	0.1163
100	0.0148	0.0003	0.0132	-2.7304	0.8663	-1.4684	-0.0087	0.0380	0.0003	-0.6937	2.8767	-0.0006
1000	0.0025	0.0003	0.0018	-5.3241	1.3725	-2.4802	-0.0014	0.0059	0.0003	-1.0376	4.4198	0.2374
10000	0.0003	0.0000	0.0002	-6.2140	1.8918	-3.0549	-0.0002	0.0006	0.0000	-1.4199	4.6616	-0.0003

Table C.3: Potential, load, shear and stress Love numbers for model AK135f (Kennett et al., 1995; Montagner & Kennett, 1996). For the boundary conditions used to compute each set of Love numbers, refer to Table 6.1.

Love Numbers for a Homogeneous Earth of Elastic Properties V_P = 10 km/s, V_S = 5 km/s, and ρ = 5 g/cc.												
	Potential			Load			Shear			Stress		
n	h	nl	nk	h'	nl'	nk'	h''	nl''	nk''	h'''	nl'''	nk'''
0	0.0000	0.0000	0.0000	-0.1251	0.0000	0.0000	0.0000	0.0000	0.0000	-0.3752	0.0000	0.0000
1	0.0000	0.0000	0.0000	-0.2069	0.1617	0.0000	-0.1617	0.0506	0.0000	-0.3686	0.6677	0.0000
2	0.5079	0.2729	0.5845	-0.6000	0.0026	-0.4313	0.1352	0.4725	0.2729	-0.4215	0.6884	-0.1183
3	0.3159	0.1157	0.3881	-0.6886	0.0542	-0.5597	0.0205	0.2938	0.1157	-0.3778	0.7291	-0.1088
4	0.2383	0.0661	0.3043	-0.7452	0.0888	-0.6488	-0.0057	0.2215	0.0661	-0.3468	0.7458	-0.0974
5	0.1935	0.0432	0.2537	-0.7846	0.1133	-0.7141	-0.0140	0.1796	0.0432	-0.3241	0.7537	-0.0872
10	0.1025	0.0116	0.1427	-0.8799	0.1730	-0.8827	-0.0161	0.0941	0.0116	-0.2672	0.7623	-0.0555
100	0.0112	0.0001	0.0167	-0.9934	0.2430	-1.1037	-0.0024	0.0100	0.0001	-0.1981	0.7577	-0.0071
1000	0.0011	0.0000	0.0017	-1.0068	0.2512	-1.1312	-0.0003	0.0010	0.0000	-0.1900	0.7564	-0.0007
10000	0.0001	0.0000	0.0002	-1.0082	0.2520	-1.1341	0.0000	0.0001	0.0000	-0.1892	0.7563	-0.0001

Table C.4: Potential, load, shear and stress Love numbers for a homogeneous Earth model of elastic properties V_P = 10 km/s, V_S = 5 km/s, and ρ = 5 g/cc. For the boundary conditions used to compute each set of Love numbers, refer to Table 6.1.

Table C.5: Displacement load Green's functions for Earth model 1066A in the CM and CE reference frames. The angular distance from the load is given by θ in degrees. The vertical and horizontal displacement responses are given by u and v, respectively. The variables a and θ in the normalization factor ($10^{12}a\theta$) represent Earth's radius in meters and the angular distance from the load point in radians, respectively.

Displacement Load Green's Functions for Earth Model 1066A ($\times 10^{12}a\theta$) **[m/kg]**				
θ (°)	u_{CM}	v_{CM}	u_{CE}	v_{CE}
0.0001000000	-7.688756e+01	-2.324888e+01	-7.688755e+01	-2.324888e+01
0.0001354588	-7.685841e+01	-2.324901e+01	-7.685840e+01	-2.324901e+01
0.0001834909	-7.681896e+01	-2.324912e+01	-7.681893e+01	-2.324912e+01
0.0002485545	-7.676555e+01	-2.324925e+01	-7.676552e+01	-2.324925e+01
0.0003366890	-7.669326e+01	-2.324937e+01	-7.669322e+01	-2.324937e+01
0.0004560749	-7.659541e+01	-2.324929e+01	-7.659536e+01	-2.324929e+01
0.0006177936	-7.646297e+01	-2.324910e+01	-7.646289e+01	-2.324910e+01
0.0008368557	-7.628371e+01	-2.324863e+01	-7.628361e+01	-2.324863e+01
0.0011335948	-7.604108e+01	-2.324764e+01	-7.604094e+01	-2.324764e+01
0.0015355539	-7.571270e+01	-2.324562e+01	-7.571252e+01	-2.324562e+01
0.0020800429	-7.526830e+01	-2.324168e+01	-7.526806e+01	-2.324168e+01
0.0028176012	-7.466699e+01	-2.323412e+01	-7.466666e+01	-2.323412e+01
0.0038166888	-7.385358e+01	-2.321978e+01	-7.385313e+01	-2.321978e+01
0.0051700409	-7.275384e+01	-2.319289e+01	-7.275323e+01	-2.319289e+01
0.0070032754	-7.126839e+01	-2.314282e+01	-7.126756e+01	-2.314282e+01
0.0094865529	-6.926552e+01	-2.305017e+01	-6.926439e+01	-2.305017e+01
0.0128503709	-6.657389e+01	-2.287985e+01	-6.657237e+01	-2.287985e+01
0.0174069584	-6.297908e+01	-2.256938e+01	-6.297702e+01	-2.256939e+01
0.0235792572	-5.823393e+01	-2.201066e+01	-5.823113e+01	-2.201066e+01
0.0319401793	-5.210592e+01	-2.102672e+01	-5.210214e+01	-2.102672e+01
0.0432657841	-4.449903e+01	-1.935875e+01	-4.449390e+01	-1.935875e+01
0.0586073126	-3.569368e+01	-1.671493e+01	-3.568674e+01	-1.671493e+01
0.0793887632	-2.672419e+01	-1.299320e+01	-2.671478e+01	-1.299321e+01
0.1075390672	-1.947195e+01	-8.748884e+00	-1.945921e+01	-8.748908e+00
0.1456711316	-1.572768e+01	-5.465633e+00	-1.571041e+01	-5.465677e+00
0.1973243691	-1.528689e+01	-4.542910e+00	-1.526351e+01	-4.542991e+00

0.2672932255	-1.589656e+01	-5.509410e+00	-1.586488e+01	-5.509558e+00
0.3620721999	-1.601560e+01	-6.642114e+00	-1.597268e+01	-6.642385e+00
0.4904586627	-1.566417e+01	-7.144690e+00	-1.560604e+01	-7.145188e+00
0.6643694266	-1.500941e+01	-7.117618e+00	-1.493067e+01	-7.118531e+00
0.8999468630	-1.406740e+01	-6.785275e+00	-1.396075e+01	-6.786951e+00
1.2190572352	-1.283999e+01	-6.284972e+00	-1.269554e+01	-6.288046e+00
1.6513203209	-1.134816e+01	-5.643566e+00	-1.115252e+01	-5.649206e+00
2.2368587164	-9.682043e+00	-4.853655e+00	-9.417119e+00	-4.864003e+00
3.0300220094	-8.019086e+00	-3.948233e+00	-7.660451e+00	-3.967217e+00
4.1044315004	-6.584909e+00	-3.026243e+00	-6.099674e+00	-3.061063e+00
5.5598137207	-5.563136e+00	-2.222489e+00	-4.907252e+00	-2.286335e+00
7.5312570341	-5.007031e+00	-1.636923e+00	-4.122080e+00	-1.753920e+00
10.2017505195	-4.824342e+00	-1.269606e+00	-3.634283e+00	-1.483768e+00
13.8191689902	-4.839278e+00	-1.002523e+00	-3.248754e+00	-1.393757e+00
18.7192806974	-4.882451e+00	-6.406382e-01	-2.781089e+00	-1.352698e+00
25.3569132902	-4.790463e+00	2.723662e-02	-2.074555e+00	-1.259869e+00
32.0000000000	-4.486702e+00	9.041241e-01	-1.270190e+00	-1.105776e+00
38.0000000000	-4.053226e+00	1.852527e+00	-5.040262e-01	-9.204123e-01
44.0000000000	-3.512083e+00	2.912780e+00	2.393877e-01	-7.099729e-01
50.0000000000	-2.905174e+00	4.038245e+00	9.041884e-01	-5.015759e-01
56.0000000000	-2.264412e+00	5.179052e+00	1.447216e+00	-3.236629e-01
62.0000000000	-1.608333e+00	6.289639e+00	1.841641e+00	-1.988166e-01
68.0000000000	-9.436271e-01	7.331495e+00	2.075623e+00	-1.414107e-01
74.0000000000	-2.683737e-01	8.274943e+00	2.149227e+00	-1.562324e-01
80.0000000000	4.233922e-01	9.098534e+00	2.069942e+00	-2.395160e-01
86.0000000000	1.140706e+00	9.787195e+00	1.851752e+00	-3.812368e-01
92.0000000000	1.891581e+00	1.033039e+01	1.511022e+00	-5.673848e-01
98.0000000000	2.682695e+00	1.072125e+01	1.066119e+00	-7.812833e-01
104.0000000000	3.518543e+00	1.095529e+01	5.364362e-01	-1.005289e+00
110.0000000000	4.399545e+00	1.102961e+01	-5.967754e-02	-1.222004e+00
116.0000000000	5.322669e+00	1.094154e+01	-7.045182e-01	-1.416023e+00
122.0000000000	6.281573e+00	1.069004e+01	-1.381171e+00	-1.572913e+00

128.0000000000	7.266001e+00	1.027409e+01	-2.074425e+00	-1.681114e+00
134.0000000000	8.264737e+00	9.693803e+00	-2.768193e+00	-1.731129e+00
140.0000000000	9.262455e+00	8.948596e+00	-3.449044e+00	-1.717618e+00
146.0000000000	1.024225e+01	8.039950e+00	-4.104113e+00	-1.636794e+00
152.0000000000	1.118667e+01	6.970683e+00	-4.720513e+00	-1.487316e+00
158.0000000000	1.207890e+01	5.744304e+00	-5.284613e+00	-1.271012e+00
164.0000000000	1.290106e+01	4.365319e+00	-5.784249e+00	-9.926061e-01
170.0000000000	1.363568e+01	2.840381e+00	-6.207672e+00	-6.585386e-01
176.0000000000	1.426542e+01	1.178142e+00	-6.544390e+00	-2.770222e-01
177.0000000000	1.436008e+01	8.900904e-01	-6.590320e+00	-2.078738e-01
178.0000000000	1.444888e+01	5.976930e-01	-6.635947e+00	-1.386055e-01
179.0000000000	1.453013e+01	3.012988e-01	-6.682847e+00	-6.897513e-02
180.0000000000	1.458125e+01	-5.648395e-08	-6.753484e+00	-6.062143e-08

Table C.6: Displacement load Green's functions for Earth model PREM in the CM and CE reference frames. The angular distance from the load is given by θ in degrees. The vertical and horizontal displacement responses are given by u and v, respectively. The variables a and θ in the normalization factor ($10^{12}a\theta$) represent Earth's radius in meters and the angular distance from the load point in radians, respectively.

Displacement Load Green's Functions for Earth Model PREM ($\times 10^{12}a\theta$) **[m/kg]**				
θ (°)	u_{CM}	v_{CM}	u_{CE}	v_{CE}
0.0001000000	-4.218585e+01	-1.284773e+01	-4.218584e+01	-1.284773e+01
0.0001354588	-4.217820e+01	-1.284780e+01	-4.217818e+01	-1.284780e+01
0.0001834909	-4.216784e+01	-1.284784e+01	-4.216782e+01	-1.284784e+01
0.0002485545	-4.215383e+01	-1.284791e+01	-4.215380e+01	-1.284791e+01
0.0003366890	-4.213488e+01	-1.284798e+01	-4.213484e+01	-1.284798e+01
0.0004560749	-4.210923e+01	-1.284796e+01	-4.210918e+01	-1.284796e+01
0.0006177936	-4.207453e+01	-1.284793e+01	-4.207446e+01	-1.284793e+01
0.0008368557	-4.202759e+01	-1.284786e+01	-4.202749e+01	-1.284786e+01
0.0011335948	-4.196407e+01	-1.284770e+01	-4.196394e+01	-1.284770e+01
0.0015355539	-4.187814e+01	-1.284738e+01	-4.187796e+01	-1.284738e+01
0.0020800429	-4.176189e+01	-1.284676e+01	-4.176165e+01	-1.284676e+01
0.0028176012	-4.160464e+01	-1.284556e+01	-4.160430e+01	-1.284556e+01
0.0038166888	-4.139193e+01	-1.284328e+01	-4.139148e+01	-1.284328e+01
0.0051700409	-4.110430e+01	-1.283901e+01	-4.110369e+01	-1.283901e+01
0.0070032754	-4.071551e+01	-1.283105e+01	-4.071468e+01	-1.283105e+01
0.0094865529	-4.019040e+01	-1.281630e+01	-4.018928e+01	-1.281630e+01
0.0128503709	-3.948219e+01	-1.278908e+01	-3.948066e+01	-1.278908e+01
0.0174069584	-3.852953e+01	-1.273912e+01	-3.852747e+01	-1.273912e+01
0.0235792572	-3.725424e+01	-1.264803e+01	-3.725144e+01	-1.264803e+01
0.0319401793	-3.556201e+01	-1.248371e+01	-3.555822e+01	-1.248372e+01
0.0432657841	-3.335219e+01	-1.219251e+01	-3.334706e+01	-1.219252e+01
0.0586073126	-3.054848e+01	-1.169223e+01	-3.054153e+01	-1.169224e+01
0.0793887632	-2.716863e+01	-1.087829e+01	-2.715922e+01	-1.087830e+01
0.1075390672	-2.343884e+01	-9.673026e+00	-2.342609e+01	-9.673050e+00
0.1456711316	-1.988314e+01	-8.149030e+00	-1.986587e+01	-8.149074e+00
0.1973243691	-1.718174e+01	-6.656794e+00	-1.715835e+01	-6.656875e+00

0.2672932255	-1.568668e+01	-5.695364e+00	-1.565499e+01	-5.695511e+00
0.3620721999	-1.507745e+01	-5.463118e+00	-1.503452e+01	-5.463389e+00
0.4904586627	-1.471141e+01	-5.665808e+00	-1.465327e+01	-5.666306e+00
0.6643694266	-1.417007e+01	-5.864808e+00	-1.409131e+01	-5.865722e+00
0.8999468630	-1.334248e+01	-5.822978e+00	-1.323580e+01	-5.824654e+00
1.2190572352	-1.223907e+01	-5.521001e+00	-1.209458e+01	-5.524076e+00
1.6513203209	-1.090051e+01	-5.017747e+00	-1.070482e+01	-5.023388e+00
2.2368587164	-9.410675e+00	-4.366012e+00	-9.145698e+00	-4.376362e+00
3.0300220094	-7.913853e+00	-3.618278e+00	-7.555147e+00	-3.637265e+00
4.1044315004	-6.588431e+00	-2.850626e+00	-6.103100e+00	-2.885453e+00
5.5598137207	-5.593566e+00	-2.152679e+00	-4.937553e+00	-2.216538e+00
7.5312570341	-5.014084e+00	-1.607771e+00	-4.128957e+00	-1.724791e+00
10.2017505195	-4.804800e+00	-1.245216e+00	-3.614507e+00	-1.459421e+00
13.8191689902	-4.808587e+00	-9.758500e-01	-3.217749e+00	-1.367162e+00
18.7192806974	-4.852672e+00	-6.140062e-01	-2.750896e+00	-1.326207e+00
25.3569132902	-4.769587e+00	5.115946e-02	-2.053143e+00	-1.236200e+00
32.0000000000	-4.477697e+00	9.241335e-01	-1.260551e+00	-1.086163e+00
38.0000000000	-4.055452e+00	1.868088e+00	-5.055521e-01	-9.053975e-01
44.0000000000	-3.524391e+00	2.923510e+00	2.278194e-01	-6.999573e-01
50.0000000000	-2.925861e+00	4.044308e+00	8.842526e-01	-4.964083e-01
56.0000000000	-2.290952e+00	5.181385e+00	1.421408e+00	-3.224148e-01
62.0000000000	-1.638117e+00	6.289182e+00	1.812537e+00	-2.005537e-01
68.0000000000	-9.742118e-01	7.329543e+00	2.045634e+00	-1.448363e-01
74.0000000000	-2.980199e-01	8.272899e+00	2.120057e+00	-1.599387e-01
80.0000000000	3.966275e-01	9.097383e+00	2.043502e+00	-2.425087e-01
86.0000000000	1.118093e+00	9.787892e+00	1.829280e+00	-3.825447e-01
92.0000000000	1.874481e+00	1.033344e+01	1.493847e+00	-5.664832e-01
98.0000000000	2.672367e+00	1.072742e+01	1.055472e+00	-7.773827e-01
104.0000000000	3.514946e+00	1.096457e+01	5.322504e-01	-9.983653e-01
110.0000000000	4.402892e+00	1.104187e+01	-5.720993e-02	-1.212156e+00
116.0000000000	5.332872e+00	1.095681e+01	-6.955037e-01	-1.403188e+00
122.0000000000	6.298574e+00	1.070749e+01	-1.365680e+00	-1.557883e+00

128.0000000000	7.289795e+00	1.029308e+01	-2.052473e+00	-1.664481e+00
134.0000000000	8.294881e+00	9.712964e+00	-2.740223e+00	-1.714221e+00
140.0000000000	9.298373e+00	8.967889e+00	-3.415632e+00	-1.700428e+00
146.0000000000	1.028470e+01	8.058243e+00	-4.064488e+00	-1.620409e+00
152.0000000000	1.123528e+01	6.987418e+00	-4.675043e+00	-1.472249e+00
158.0000000000	1.213308e+01	5.758580e+00	-5.233860e+00	-1.258119e+00
164.0000000000	1.295890e+01	4.376660e+00	-5.730092e+00	-9.823223e-01
170.0000000000	1.369669e+01	2.848864e+00	-6.150577e+00	-6.507448e-01
176.0000000000	1.432746e+01	1.182523e+00	-6.486460e+00	-2.729284e-01
177.0000000000	1.442066e+01	8.921684e-01	-6.533876e+00	-2.060123e-01
178.0000000000	1.451034e+01	5.981970e-01	-6.578648e+00	-1.382467e-01
179.0000000000	1.459776e+01	3.022136e-01	-6.619403e+00	-6.813331e-02
180.0000000000	1.468281e+01	-1.155252e-07	-6.656134e+00	-1.196635e-07

Table C.7: Displacement load Green's functions for Earth model STW105 in the CM and CE reference frames. The angular distance from the load is given by θ in degrees. The vertical and horizontal displacement responses are given by u and v, respectively. The variables a and θ in the normalization factor ($10^{12}a\theta$) represent Earth's radius in meters and the angular distance from the load point in radians, respectively.

Displacement Load Green's Functions for Earth Model STW105 ($\times 10^{12}a\theta$) **[m/kg]**				
θ (°)	u_{CM}	v_{CM}	u_{CE}	v_{CE}
0.0001000000	-4.219078e+01	-1.284916e+01	-4.219077e+01	-1.284916e+01
0.0001354588	-4.218322e+01	-1.284922e+01	-4.218320e+01	-1.284922e+01
0.0001834909	-4.217298e+01	-1.284927e+01	-4.217296e+01	-1.284927e+01
0.0002485545	-4.215913e+01	-1.284934e+01	-4.215910e+01	-1.284934e+01
0.0003366890	-4.214039e+01	-1.284941e+01	-4.214035e+01	-1.284941e+01
0.0004560749	-4.211504e+01	-1.284939e+01	-4.211499e+01	-1.284939e+01
0.0006177936	-4.208075e+01	-1.284936e+01	-4.208067e+01	-1.284936e+01
0.0008368557	-4.203435e+01	-1.284929e+01	-4.203425e+01	-1.284929e+01
0.0011335948	-4.197157e+01	-1.284913e+01	-4.197144e+01	-1.284913e+01
0.0015355539	-4.188664e+01	-1.284882e+01	-4.188646e+01	-1.284882e+01
0.0020800429	-4.177174e+01	-1.284820e+01	-4.177150e+01	-1.284820e+01
0.0028176012	-4.161632e+01	-1.284701e+01	-4.161599e+01	-1.284701e+01
0.0038166888	-4.140610e+01	-1.284476e+01	-4.140565e+01	-1.284476e+01
0.0051700409	-4.112183e+01	-1.284054e+01	-4.112122e+01	-1.284054e+01
0.0070032754	-4.073760e+01	-1.283267e+01	-4.073677e+01	-1.283267e+01
0.0094865529	-4.021865e+01	-1.281807e+01	-4.021753e+01	-1.281807e+01
0.0128503709	-3.951878e+01	-1.279115e+01	-3.951726e+01	-1.279115e+01
0.0174069584	-3.857741e+01	-1.274172e+01	-3.857535e+01	-1.274172e+01
0.0235792572	-3.731736e+01	-1.265161e+01	-3.731457e+01	-1.265161e+01
0.0319401793	-3.564567e+01	-1.248908e+01	-3.564188e+01	-1.248908e+01
0.0432657841	-3.346339e+01	-1.220113e+01	-3.345827e+01	-1.220113e+01
0.0586073126	-3.069632e+01	-1.170673e+01	-3.068937e+01	-1.170673e+01
0.0793887632	-2.736446e+01	-1.090330e+01	-2.735505e+01	-1.090331e+01
0.1075390672	-2.369582e+01	-9.716439e+00	-2.368307e+01	-9.716463e+00
0.1456711316	-2.021422e+01	-8.223474e+00	-2.019695e+01	-8.223518e+00
0.1973243691	-1.759489e+01	-6.780318e+00	-1.757150e+01	-6.780398e+00

0.2672932255	-1.617695e+01	-5.888833e+00	-1.614526e+01	-5.888980e+00
0.3620721999	-1.561954e+01	-5.741704e+00	-1.557662e+01	-5.741975e+00
0.4904586627	-1.526041e+01	-6.026836e+00	-1.520228e+01	-6.027333e+00
0.6643694266	-1.467359e+01	-6.281332e+00	-1.459484e+01	-6.282245e+00
0.8999468630	-1.375804e+01	-6.250399e+00	-1.365137e+01	-6.252074e+00
1.2190572352	-1.255008e+01	-5.915938e+00	-1.240561e+01	-5.919013e+00
1.6513203209	-1.112068e+01	-5.359609e+00	-1.092502e+01	-5.365250e+00
2.2368587164	-9.566336e+00	-4.660809e+00	-9.301389e+00	-4.671158e+00
3.0300220094	-8.018488e+00	-3.874579e+00	-7.659822e+00	-3.893564e+00
4.1044315004	-6.644532e+00	-3.059097e+00	-6.159255e+00	-3.093920e+00
5.5598137207	-5.615069e+00	-2.303295e+00	-4.959128e+00	-2.367146e+00
7.5312570341	-5.024535e+00	-1.710612e+00	-4.139508e+00	-1.827620e+00
10.2017505195	-4.818548e+00	-1.320428e+00	-3.628386e+00	-1.534610e+00
13.8191689902	-4.825386e+00	-1.036446e+00	-3.234724e+00	-1.427714e+00
18.7192806974	-4.867090e+00	-6.624486e-01	-2.765547e+00	-1.374570e+00
25.3569132902	-4.779020e+00	1.448268e-02	-2.062878e+00	-1.272734e+00
32.0000000000	-4.481793e+00	8.952195e-01	-1.265004e+00	-1.114854e+00
38.0000000000	-4.054584e+00	1.844677e+00	-5.050780e-01	-9.285010e-01
44.0000000000	-3.519313e+00	2.904842e+00	2.324808e-01	-7.182232e-01
50.0000000000	-2.917118e+00	4.030142e+00	8.925725e-01	-5.100704e-01
56.0000000000	-2.279801e+00	5.170872e+00	1.432147e+00	-3.323170e-01
62.0000000000	-1.625658e+00	6.281828e+00	1.824613e+00	-2.071875e-01
68.0000000000	-9.615428e-01	7.324353e+00	2.057968e+00	-1.491982e-01
74.0000000000	-2.860534e-01	8.269290e+00	2.131756e+00	-1.626121e-01
80.0000000000	4.072639e-01	9.094471e+00	2.053956e+00	-2.443848e-01
86.0000000000	1.126554e+00	9.785121e+00	1.837662e+00	-3.841884e-01
92.0000000000	1.880753e+00	1.033028e+01	1.500161e+00	-5.684391e-01
98.0000000000	2.675840e+00	1.072350e+01	1.059124e+00	-7.800303e-01
104.0000000000	3.516030e+00	1.095981e+01	5.336654e-01	-1.001801e+00
110.0000000000	4.401025e+00	1.103617e+01	-5.858221e-02	-1.216498e+00
116.0000000000	5.328418e+00	1.095027e+01	-6.992895e-01	-1.408364e+00
122.0000000000	6.291514e+00	1.070019e+01	-1.371891e+00	-1.563816e+00

128.0000000000	7.280671e+00	1.028553e+01	-2.060561e+00	-1.670702e+00
134.0000000000	8.283166e+00	9.705057e+00	-2.750715e+00	-1.720861e+00
140.0000000000	9.284597e+00	8.960300e+00	-3.427998e+00	-1.706834e+00
146.0000000000	1.026903e+01	8.050736e+00	-4.078569e+00	-1.626843e+00
152.0000000000	1.121806e+01	6.980924e+00	-4.690498e+00	-1.477804e+00
158.0000000000	1.211436e+01	5.752606e+00	-5.250651e+00	-1.263315e+00
164.0000000000	1.293873e+01	4.372575e+00	-5.748190e+00	-9.858132e-01
170.0000000000	1.367504e+01	2.845823e+00	-6.170027e+00	-6.533978e-01
176.0000000000	1.430496e+01	1.181457e+00	-6.506652e+00	-2.738328e-01
177.0000000000	1.439964e+01	8.907968e-01	-6.552576e+00	-2.072621e-01
178.0000000000	1.448880e+01	5.961972e-01	-6.597854e+00	-1.401648e-01
179.0000000000	1.457557e+01	3.028999e-01	-6.639235e+00	-6.740590e-02
180.0000000000	1.466630e+01	7.901050e-09	-6.670281e+00	3.763218e-09

Table C.8: Displacement load Green's functions for Earth model AK135f in the CM and CE reference frames. The angular distance from the load is given by θ in degrees. The vertical and horizontal displacement responses are given by u and v, respectively. The variables a and θ in the normalization factor ($10^{12}a\theta$) represent Earth's radius in meters and the angular distance from the load point in radians, respectively.

Displacement Load Green's Functions for Earth Model AK135f ($\times 10^{12}a\theta$) **[m/kg]**				
θ (°)	u_{CM}	v_{CM}	u_{CE}	v_{CE}
0.0001000000	-4.217821e+01	-1.284856e+01	-4.217820e+01	-1.284856e+01
0.0001354588	-4.216688e+01	-1.284861e+01	-4.216687e+01	-1.284861e+01
0.0001834909	-4.215155e+01	-1.284865e+01	-4.215153e+01	-1.284865e+01
0.0002485545	-4.213081e+01	-1.284871e+01	-4.213078e+01	-1.284871e+01
0.0003366890	-4.210272e+01	-1.284875e+01	-4.210268e+01	-1.284875e+01
0.0004560749	-4.206471e+01	-1.284869e+01	-4.206466e+01	-1.284869e+01
0.0006177936	-4.201327e+01	-1.284858e+01	-4.201319e+01	-1.284858e+01
0.0008368557	-4.194364e+01	-1.284836e+01	-4.194354e+01	-1.284836e+01
0.0011335948	-4.184940e+01	-1.284794e+01	-4.184927e+01	-1.284794e+01
0.0015355539	-4.172187e+01	-1.284712e+01	-4.172169e+01	-1.284712e+01
0.0020800429	-4.154928e+01	-1.284559e+01	-4.154903e+01	-1.284559e+01
0.0028176012	-4.131577e+01	-1.284273e+01	-4.131543e+01	-1.284273e+01
0.0038166888	-4.099990e+01	-1.283740e+01	-4.099945e+01	-1.283740e+01
0.0051700409	-4.057287e+01	-1.282755e+01	-4.057226e+01	-1.282755e+01
0.0070032754	-3.999611e+01	-1.280938e+01	-3.999528e+01	-1.280938e+01
0.0094865529	-3.921848e+01	-1.277600e+01	-3.921736e+01	-1.277600e+01
0.0128503709	-3.817341e+01	-1.271498e+01	-3.817189e+01	-1.271498e+01
0.0174069584	-3.677717e+01	-1.260423e+01	-3.677510e+01	-1.260423e+01
0.0235792572	-3.493168e+01	-1.240564e+01	-3.492888e+01	-1.240564e+01
0.0319401793	-3.253940e+01	-1.205701e+01	-3.253561e+01	-1.205702e+01
0.0432657841	-2.954442e+01	-1.146744e+01	-2.953929e+01	-1.146745e+01
0.0586073126	-2.601709e+01	-1.053351e+01	-2.601014e+01	-1.053352e+01
0.0793887632	-2.227145e+01	-9.210229e+00	-2.226204e+01	-9.210242e+00
0.1075390672	-1.890286e+01	-7.647968e+00	-1.889011e+01	-7.647992e+00
0.1456711316	-1.653309e+01	-6.259481e+00	-1.651582e+01	-6.259525e+00
0.1973243691	-1.533088e+01	-5.469103e+00	-1.530749e+01	-5.469183e+00

0.2672932255	-1.490904e+01	-5.330191e+00	-1.487735e+01	-5.330338e+00
0.3620721999	-1.473661e+01	-5.552469e+00	-1.469369e+01	-5.552740e+00
0.4904586627	-1.445984e+01	-5.788531e+00	-1.440170e+01	-5.789028e+00
0.6643694266	-1.395144e+01	-5.832148e+00	-1.387269e+01	-5.833061e+00
0.8999468630	-1.319634e+01	-5.664126e+00	-1.308967e+01	-5.665802e+00
1.2190572352	-1.219157e+01	-5.341816e+00	-1.204709e+01	-5.344891e+00
1.6513203209	-1.094094e+01	-4.896534e+00	-1.074527e+01	-4.902175e+00
2.2368587164	-9.493570e+00	-4.320951e+00	-9.228610e+00	-4.331301e+00
3.0300220094	-7.983588e+00	-3.617926e+00	-7.624905e+00	-3.636912e+00
4.1044315004	-6.622533e+00	-2.851933e+00	-6.137233e+00	-2.886758e+00
5.5598137207	-5.615785e+00	-2.147869e+00	-4.959814e+00	-2.211723e+00
7.5312570341	-5.046926e+00	-1.618745e+00	-4.161857e+00	-1.735758e+00
10.2017505195	-4.838408e+00	-1.274228e+00	-3.648191e+00	-1.488420e+00
13.8191689902	-4.829514e+00	-1.002679e+00	-3.238778e+00	-1.393966e+00
18.7192806974	-4.862385e+00	-6.284633e-01	-2.760744e+00	-1.340618e+00
25.3569132902	-4.773392e+00	4.602523e-02	-2.057123e+00	-1.241252e+00
32.0000000000	-4.479072e+00	9.224234e-01	-1.262132e+00	-1.087744e+00
38.0000000000	-4.055805e+00	1.866724e+00	-5.061335e-01	-9.065835e-01
44.0000000000	-3.524513e+00	2.920977e+00	2.274564e-01	-7.022576e-01
50.0000000000	-2.926068e+00	4.039855e+00	8.838003e-01	-5.005693e-01
56.0000000000	-2.291234e+00	5.174540e+00	1.420888e+00	-3.289063e-01
62.0000000000	-1.638489e+00	6.280221e+00	1.811943e+00	-2.090976e-01
68.0000000000	-9.746483e-01	7.318922e+00	2.045003e+00	-1.549768e-01
74.0000000000	-2.984873e-01	8.261020e+00	2.119435e+00	-1.712760e-01
80.0000000000	3.962118e-01	9.084935e+00	2.042981e+00	-2.543561e-01
86.0000000000	1.117835e+00	9.775159e+00	1.828976e+00	-3.946245e-01
92.0000000000	1.873923e+00	1.032120e+01	1.493314e+00	-5.780246e-01
98.0000000000	2.671529e+00	1.071563e+01	1.054738e+00	-7.884341e-01
104.0000000000	3.513533e+00	1.095380e+01	5.310298e-01	-1.008372e+00
110.0000000000	4.400883e+00	1.103190e+01	-5.893232e-02	-1.221337e+00
116.0000000000	5.330180e+00	1.094767e+01	-6.978086e-01	-1.411539e+00
122.0000000000	6.294612e+00	1.069950e+01	-1.369150e+00	-1.565085e+00

128.0000000000	7.284877e+00	1.028605e+01	-2.056791e+00	-1.670740e+00
134.0000000000	8.288367e+00	9.707013e+00	-2.746029e+00	-1.719438e+00
140.0000000000	9.290696e+00	8.962584e+00	-3.422492e+00	-1.705048e+00
146.0000000000	1.027525e+01	8.054192e+00	-4.073015e+00	-1.623839e+00
152.0000000000	1.122487e+01	6.983796e+00	-4.684423e+00	-1.475327e+00
158.0000000000	1.212079e+01	5.755632e+00	-5.245035e+00	-1.260617e+00
164.0000000000	1.294605e+01	4.374621e+00	-5.741737e+00	-9.840165e-01
170.0000000000	1.368160e+01	2.847026e+00	-6.164391e+00	-6.523583e-01
176.0000000000	1.431335e+01	1.182143e+00	-6.499228e+00	-2.732144e-01
177.0000000000	1.440744e+01	8.923812e-01	-6.545745e+00	-2.057290e-01
178.0000000000	1.449543e+01	5.977719e-01	-6.592205e+00	-1.386245e-01
179.0000000000	1.458503e+01	3.009079e-01	-6.630769e+00	-6.941518e-02
180.0000000000	1.465755e+01	-2.395484e-08	-6.680016e+00	-2.809286e-08

Table C.9: Displacement load Green's functions for Earth model SNA in the CM and CE reference frames. The angular distance from the load is given by θ in degrees. The vertical and horizontal displacement responses are given by u and v, respectively. The variables a and θ in the normalization factor ($10^{12}a\theta$) represent Earth's radius in meters and the angular distance from the load point in radians, respectively.

Displacement Load Green's Functions for Earth Model SNA ($\times 10^{12}a\theta$) [m/kg]				
θ (°)	u_{CM}	v_{CM}	u_{CE}	v_{CE}
0.0001000000	-3.131425e+01	-1.039663e+01	-3.131424e+01	-1.039663e+01
0.0001354588	-3.131182e+01	-1.039668e+01	-3.131181e+01	-1.039668e+01
0.0001834909	-3.130854e+01	-1.039672e+01	-3.130852e+01	-1.039672e+01
0.0002485545	-3.130410e+01	-1.039678e+01	-3.130407e+01	-1.039678e+01
0.0003366890	-3.129810e+01	-1.039684e+01	-3.129806e+01	-1.039684e+01
0.0004560749	-3.128998e+01	-1.039683e+01	-3.128993e+01	-1.039683e+01
0.0006177936	-3.127901e+01	-1.039684e+01	-3.127893e+01	-1.039684e+01
0.0008368557	-3.126417e+01	-1.039684e+01	-3.126407e+01	-1.039684e+01
0.0011335948	-3.124410e+01	-1.039683e+01	-3.124396e+01	-1.039683e+01
0.0015355539	-3.121697e+01	-1.039680e+01	-3.121678e+01	-1.039680e+01
0.0020800429	-3.118028e+01	-1.039673e+01	-3.118003e+01	-1.039673e+01
0.0028176012	-3.113067e+01	-1.039659e+01	-3.113033e+01	-1.039659e+01
0.0038166888	-3.106359e+01	-1.039630e+01	-3.106314e+01	-1.039630e+01
0.0051700409	-3.097290e+01	-1.039574e+01	-3.097229e+01	-1.039574e+01
0.0070032754	-3.085030e+01	-1.039466e+01	-3.084947e+01	-1.039466e+01
0.0094865529	-3.068458e+01	-1.039261e+01	-3.068346e+01	-1.039261e+01
0.0128503709	-3.046066e+01	-1.038876e+01	-3.045913e+01	-1.038876e+01
0.0174069584	-3.015824e+01	-1.038161e+01	-3.015617e+01	-1.038161e+01
0.0235792572	-2.975023e+01	-1.036834e+01	-2.974743e+01	-1.036834e+01
0.0319401793	-2.920080e+01	-1.034389e+01	-2.919702e+01	-1.034389e+01
0.0432657841	-2.846349e+01	-1.029910e+01	-2.845836e+01	-1.029911e+01
0.0586073126	-2.748021e+01	-1.021773e+01	-2.747327e+01	-1.021773e+01
0.0793887632	-2.618388e+01	-1.007184e+01	-2.617448e+01	-1.007185e+01
0.1075390672	-2.450991e+01	-9.816168e+00	-2.449717e+01	-9.816192e+00
0.1456711316	-2.242702e+01	-9.385560e+00	-2.240976e+01	-9.385604e+00
0.1973243691	-1.999842e+01	-8.708666e+00	-1.997504e+01	-8.708747e+00

0.2672932255	-1.746183e+01	-7.762425e+00	-1.743015e+01	-7.762573e+00
0.3620721999	-1.524025e+01	-6.671915e+00	-1.519735e+01	-6.672187e+00
0.4904586627	-1.372830e+01	-5.750186e+00	-1.367018e+01	-5.750683e+00
0.6643694266	-1.291445e+01	-5.285970e+00	-1.283573e+01	-5.286883e+00
0.8999468630	-1.234552e+01	-5.211242e+00	-1.223889e+01	-5.212917e+00
1.2190572352	-1.160788e+01	-5.176945e+00	-1.146346e+01	-5.180018e+00
1.6513203209	-1.059677e+01	-4.946460e+00	-1.040118e+01	-4.952099e+00
2.2368587164	-9.352851e+00	-4.479938e+00	-9.087993e+00	-4.490283e+00
3.0300220094	-7.979534e+00	-3.810861e+00	-7.620989e+00	-3.829840e+00
4.1044315004	-6.664088e+00	-3.017489e+00	-6.178974e+00	-3.052300e+00
5.5598137207	-5.632718e+00	-2.237311e+00	-4.976998e+00	-2.301140e+00
7.5312570341	-5.029588e+00	-1.623556e+00	-4.144858e+00	-1.740524e+00
10.2017505195	-4.816520e+00	-1.234366e+00	-3.626759e+00	-1.448476e+00
13.8191689902	-4.817267e+00	-9.607311e-01	-3.227141e+00	-1.351868e+00
18.7192806974	-4.854318e+00	-5.952856e-01	-2.753482e+00	-1.307167e+00
25.3569132902	-4.766571e+00	7.300001e-02	-2.051343e+00	-1.213784e+00
32.0000000000	-4.474112e+00	9.450270e-01	-1.258405e+00	-1.064370e+00
38.0000000000	-4.052932e+00	1.885553e+00	-5.046206e-01	-8.866916e-01
44.0000000000	-3.523813e+00	2.935926e+00	2.267185e-01	-6.859196e-01
50.0000000000	-2.927294e+00	4.050887e+00	8.811144e-01	-4.877979e-01
56.0000000000	-2.294112e+00	5.181975e+00	1.416587e+00	-3.193618e-01
62.0000000000	-1.642477e+00	6.284312e+00	1.806633e+00	-2.025193e-01
68.0000000000	-9.792783e-01	7.320163e+00	2.039216e+00	-1.508728e-01
74.0000000000	-3.033421e-01	8.260087e+00	2.113653e+00	-1.689777e-01
80.0000000000	3.914989e-01	9.082354e+00	2.037637e+00	-2.533589e-01
86.0000000000	1.113456e+00	9.771528e+00	1.824324e+00	-3.943589e-01
92.0000000000	1.870409e+00	1.031696e+01	1.489945e+00	-5.780925e-01
98.0000000000	2.668712e+00	1.071127e+01	1.052540e+00	-7.883830e-01
104.0000000000	3.511811e+00	1.094944e+01	5.304506e-01	-1.008147e+00
110.0000000000	4.399959e+00	1.102798e+01	-5.814745e-02	-1.220568e+00
116.0000000000	5.329947e+00	1.094438e+01	-6.957314e-01	-1.410094e+00
122.0000000000	6.295168e+00	1.069681e+01	-1.365657e+00	-1.563071e+00

128.0000000000	7.286170e+00	1.028396e+01	-2.051918e+00	-1.668243e+00
134.0000000000	8.290294e+00	9.705380e+00	-2.739874e+00	-1.716693e+00
140.0000000000	9.293000e+00	8.961374e+00	-3.415317e+00	-1.702170e+00
146.0000000000	1.027799e+01	8.053321e+00	-4.064779e+00	-1.621000e+00
152.0000000000	1.122773e+01	6.983532e+00	-4.675468e+00	-1.472349e+00
158.0000000000	1.212439e+01	5.755560e+00	-5.234784e+00	-1.258000e+00
164.0000000000	1.294951e+01	4.374579e+00	-5.731124e+00	-9.820058e-01
170.0000000000	1.368589e+01	2.847254e+00	-6.152497e+00	-6.507895e-01
176.0000000000	1.431676e+01	1.182051e+00	-6.487848e+00	-2.727483e-01
177.0000000000	1.441025e+01	8.917301e-01	-6.534908e+00	-2.059593e-01
178.0000000000	1.450087e+01	5.978491e-01	-6.578681e+00	-1.382651e-01
179.0000000000	1.458739e+01	3.006820e-01	-6.620277e+00	-6.949919e-02
180.0000000000	1.467189e+01	3.765835e-08	-6.657506e+00	3.352191e-08

Table C.10: Displacement load Green's functions for Earth model CR in the CM and CE reference frames. The angular distance from the load is given by θ in degrees. The vertical and horizontal displacement responses are given by u and v, respectively. The variables a and θ in the normalization factor ($10^{12}a\theta$) represent Earth's radius in meters and the angular distance from the load point in radians, respectively.

Displacement Load Green's Functions for Earth Model CR ($\times 10^{12}a\theta$) [m/kg]				
θ (°)	u_{CM}	v_{CM}	u_{CE}	v_{CE}
0.0001000000	-3.243024e+01	-1.003482e+01	-3.243023e+01	-1.003482e+01
0.0001354588	-3.242801e+01	-1.003487e+01	-3.242799e+01	-1.003487e+01
0.0001834909	-3.242500e+01	-1.003490e+01	-3.242497e+01	-1.003490e+01
0.0002485545	-3.242092e+01	-1.003496e+01	-3.242090e+01	-1.003496e+01
0.0003366890	-3.241542e+01	-1.003501e+01	-3.241538e+01	-1.003501e+01
0.0004560749	-3.240799e+01	-1.003501e+01	-3.240794e+01	-1.003501e+01
0.0006177936	-3.239795e+01	-1.003501e+01	-3.239788e+01	-1.003501e+01
0.0008368557	-3.238439e+01	-1.003501e+01	-3.238429e+01	-1.003501e+01
0.0011335948	-3.236607e+01	-1.003501e+01	-3.236593e+01	-1.003501e+01
0.0015355539	-3.234131e+01	-1.003500e+01	-3.234113e+01	-1.003500e+01
0.0020800429	-3.230786e+01	-1.003497e+01	-3.230762e+01	-1.003497e+01
0.0028176012	-3.226266e+01	-1.003491e+01	-3.226233e+01	-1.003491e+01
0.0038166888	-3.220157e+01	-1.003480e+01	-3.220111e+01	-1.003480e+01
0.0051700409	-3.211895e+01	-1.003457e+01	-3.211833e+01	-1.003457e+01
0.0070032754	-3.200714e+01	-1.003412e+01	-3.200631e+01	-1.003412e+01
0.0094865529	-3.185564e+01	-1.003320e+01	-3.185452e+01	-1.003320e+01
0.0128503709	-3.165004e+01	-1.003126e+01	-3.164851e+01	-1.003126e+01
0.0174069584	-3.137059e+01	-1.002708e+01	-3.136852e+01	-1.002708e+01
0.0235792572	-3.099106e+01	-1.001804e+01	-3.098826e+01	-1.001804e+01
0.0319401793	-3.047856e+01	-9.999466e+00	-3.047477e+01	-9.999468e+00
0.0432657841	-2.979132e+01	-9.964854e+00	-2.978618e+01	-9.964858e+00
0.0586073126	-2.886762e+01	-9.902141e+00	-2.886066e+01	-9.902148e+00
0.0793887632	-2.764019e+01	-9.785023e+00	-2.763076e+01	-9.785036e+00
0.1075390672	-2.603383e+01	-9.576513e+00	-2.602106e+01	-9.576537e+00
0.1456711316	-2.399475e+01	-9.214874e+00	-2.397745e+01	-9.214918e+00
0.1973243691	-2.153698e+01	-8.623152e+00	-2.151355e+01	-8.623232e+00

0.2672932255	-1.883214e+01	-7.744061e+00	-1.880040e+01	-7.744209e+00
0.3620721999	-1.628179e+01	-6.641414e+00	-1.623879e+01	-6.641685e+00
0.4904586627	-1.439444e+01	-5.607596e+00	-1.433620e+01	-5.608095e+00
0.6643694266	-1.334777e+01	-5.040644e+00	-1.326887e+01	-5.041559e+00
0.8999468630	-1.271359e+01	-5.004429e+00	-1.260673e+01	-5.006108e+00
1.2190572352	-1.193759e+01	-5.102658e+00	-1.179285e+01	-5.105738e+00
1.6513203209	-1.085364e+01	-4.978256e+00	-1.065761e+01	-4.983907e+00
2.2368587164	-9.528339e+00	-4.560086e+00	-9.262899e+00	-4.570454e+00
3.0300220094	-8.078426e+00	-3.897131e+00	-7.719092e+00	-3.916152e+00
4.1044315004	-6.696454e+00	-3.079494e+00	-6.210274e+00	-3.114382e+00
5.5598137207	-5.624306e+00	-2.261694e+00	-4.967145e+00	-2.325664e+00
7.5312570341	-5.014870e+00	-1.625812e+00	-4.128196e+00	-1.743037e+00
10.2017505195	-4.813259e+00	-1.240188e+00	-3.620884e+00	-1.454768e+00
13.8191689902	-4.822484e+00	-9.785198e-01	-3.228864e+00	-1.370516e+00
18.7192806974	-4.862332e+00	-6.184127e-01	-2.756881e+00	-1.331858e+00
25.3569132902	-4.775433e+00	5.150879e-02	-2.054239e+00	-1.238102e+00
32.0000000000	-4.482596e+00	9.282443e-01	-1.259824e+00	-1.085567e+00
38.0000000000	-4.060461e+00	1.874503e+00	-5.043535e-01	-9.038322e-01
44.0000000000	-3.530049e+00	2.931586e+00	2.287224e-01	-6.982173e-01
50.0000000000	-2.932124e+00	4.053647e+00	8.846519e-01	-4.950087e-01
56.0000000000	-2.297664e+00	5.191753e+00	1.421187e+00	-3.216712e-01
62.0000000000	-1.644810e+00	6.300600e+00	1.811877e+00	-2.004838e-01
68.0000000000	-9.805296e-01	7.342117e+00	2.044596e+00	-1.453330e-01
74.0000000000	-3.035135e-01	8.286708e+00	2.118792e+00	-1.608754e-01
80.0000000000	3.924237e-01	9.112588e+00	2.042178e+00	-2.436349e-01
86.0000000000	1.115570e+00	9.804390e+00	1.828000e+00	-3.838318e-01
92.0000000000	1.874053e+00	1.035144e+01	1.492754e+00	-5.675484e-01
98.0000000000	2.673963e+00	1.074655e+01	1.054241e+00	-7.783711e-01
104.0000000000	3.519055e+00	1.098488e+01	5.311438e-01	-9.989791e-01
110.0000000000	4.409485e+00	1.106296e+01	-5.841577e-02	-1.212499e+00
116.0000000000	5.342112e+00	1.097827e+01	-6.968049e-01	-1.403341e+00
122.0000000000	6.310216e+00	1.072911e+01	-1.367440e+00	-1.557709e+00

128.0000000000	7.304101e+00	1.031445e+01	-2.054503e+00	-1.664016e+00
134.0000000000	8.311521e+00	9.733648e+00	-2.742879e+00	-1.713519e+00
140.0000000000	9.317486e+00	8.987060e+00	-3.418751e+00	-1.699912e+00
146.0000000000	1.030570e+01	8.076014e+00	-4.068582e+00	-1.619563e+00
152.0000000000	1.125869e+01	7.002945e+00	-4.679448e+00	-1.471514e+00
158.0000000000	1.215834e+01	5.771445e+00	-5.238973e+00	-1.257525e+00
164.0000000000	1.298631e+01	4.386510e+00	-5.735363e+00	-9.818424e-01
170.0000000000	1.372487e+01	2.855172e+00	-6.157102e+00	-6.505569e-01
176.0000000000	1.435772e+01	1.185482e+00	-6.492593e+00	-2.725138e-01
177.0000000000	1.445168e+01	8.943100e-01	-6.539499e+00	-2.057910e-01
178.0000000000	1.454249e+01	5.995070e-01	-6.583370e+00	-1.382244e-01
179.0000000000	1.462901e+01	3.011713e-01	-6.625248e+00	-6.982324e-02
180.0000000000	1.471259e+01	1.755699e-08	-6.663669e+00	1.341147e-08

Table C.11: Displacement load Green's functions for a homogeneous Earth with elastic properties V_P = 10 km/s, V_S = 5 km/s, and ρ = 5 g/cc in the CM and CE reference frames. The angular distance from the load is given by θ in degrees. The vertical and horizontal displacement responses are given by u and v, respectively. The variables a and θ in the normalization factor ($10^{12}a\theta$) represent Earth's radius in meters and the angular distance from the load point in radians, respectively.

Displacement Load Green's Functions for a Homogeneous Earth ($\times 10^{12}a\theta$) **[m/kg] of Elastic Properties V_P = 10 km/s, V_S = 5 km/s, and ρ = 5 g/cc.**				
θ (°)	u_{CM}	v_{CM}	u_{CE}	v_{CE}
0.0001000000	-7.556604e+00	-1.889169e+00	-7.556590e+00	-1.889169e+00
0.0001354588	-7.556522e+00	-1.889174e+00	-7.556505e+00	-1.889174e+00
0.0001834909	-7.556415e+00	-1.889175e+00	-7.556391e+00	-1.889175e+00
0.0002485545	-7.556274e+00	-1.889178e+00	-7.556242e+00	-1.889178e+00
0.0003366890	-7.556089e+00	-1.889179e+00	-7.556045e+00	-1.889179e+00
0.0004560749	-7.555845e+00	-1.889166e+00	-7.555785e+00	-1.889166e+00
0.0006177936	-7.555524e+00	-1.889149e+00	-7.555443e+00	-1.889149e+00
0.0008368557	-7.555102e+00	-1.889126e+00	-7.554993e+00	-1.889126e+00
0.0011335948	-7.554549e+00	-1.889096e+00	-7.554401e+00	-1.889096e+00
0.0015355539	-7.553824e+00	-1.889054e+00	-7.553623e+00	-1.889054e+00
0.0020800429	-7.552875e+00	-1.888998e+00	-7.552603e+00	-1.888998e+00
0.0028176012	-7.551635e+00	-1.888921e+00	-7.551266e+00	-1.888921e+00
0.0038166888	-7.550015e+00	-1.888817e+00	-7.549516e+00	-1.888817e+00
0.0051700409	-7.547903e+00	-1.888676e+00	-7.547227e+00	-1.888676e+00
0.0070032754	-7.545153e+00	-1.888486e+00	-7.544237e+00	-1.888486e+00
0.0094865529	-7.541578e+00	-1.888228e+00	-7.540338e+00	-1.888228e+00
0.0128503709	-7.536940e+00	-1.887878e+00	-7.535259e+00	-1.887879e+00
0.0174069584	-7.530933e+00	-1.887405e+00	-7.528656e+00	-1.887406e+00
0.0235792572	-7.523170e+00	-1.886764e+00	-7.520086e+00	-1.886765e+00
0.0319401793	-7.513160e+00	-1.885897e+00	-7.508982e+00	-1.885899e+00
0.0432657841	-7.500287e+00	-1.884722e+00	-7.494627e+00	-1.884726e+00
0.0586073126	-7.483776e+00	-1.883132e+00	-7.476110e+00	-1.883140e+00
0.0793887632	-7.462667e+00	-1.880981e+00	-7.452283e+00	-1.880995e+00
0.1075390672	-7.435772e+00	-1.878070e+00	-7.421706e+00	-1.878097e+00

0.1456711316	-7.401639e+00	-1.874134e+00	-7.382586e+00	-1.874182e+00
0.1973243691	-7.358512e+00	-1.868811e+00	-7.332702e+00	-1.868900e+00
0.2672932255	-7.304291e+00	-1.861618e+00	-7.269329e+00	-1.861781e+00
0.3620721999	-7.236512e+00	-1.851902e+00	-7.189153e+00	-1.852201e+00
0.4904586627	-7.152342e+00	-1.838783e+00	-7.088191e+00	-1.839332e+00
0.6643694266	-7.048615e+00	-1.821081e+00	-6.961720e+00	-1.822089e+00
0.8999468630	-6.921929e+00	-1.797207e+00	-6.804230e+00	-1.799056e+00
1.2190572352	-6.768841e+00	-1.765022e+00	-6.609423e+00	-1.768414e+00
1.6513203209	-6.586190e+00	-1.721639e+00	-6.370285e+00	-1.727863e+00
2.2368587164	-6.371618e+00	-1.663146e+00	-6.079258e+00	-1.674566e+00
3.0300220094	-6.124330e+00	-1.584196e+00	-5.728554e+00	-1.605146e+00
4.1044315004	-5.846145e+00	-1.477383e+00	-5.310658e+00	-1.515809e+00
5.5598137207	-5.542854e+00	-1.332261e+00	-4.819046e+00	-1.402718e+00
7.5312570341	-5.225763e+00	-1.133707e+00	-4.249164e+00	-1.262821e+00
10.2017505195	-4.913028e+00	-8.591439e-01	-3.599725e+00	-1.095486e+00
13.8191689902	-4.629708e+00	-4.737342e-01	-2.874468e+00	-9.054854e-01
18.7192806974	-4.403839e+00	7.776147e-02	-2.084858e+00	-7.080402e-01
25.3569132902	-4.252236e+00	8.838003e-01	-1.255065e+00	-5.365997e-01
32.0000000000	-4.169625e+00	1.758016e+00	-6.200073e-01	-4.600312e-01
38.0000000000	-4.091593e+00	2.599851e+00	-1.748338e-01	-4.602563e-01
44.0000000000	-3.970715e+00	3.481925e+00	1.692616e-01	-5.160043e-01
50.0000000000	-3.779030e+00	4.392161e+00	4.248335e-01	-6.178086e-01
56.0000000000	-3.495633e+00	5.316077e+00	6.003758e-01	-7.565052e-01
62.0000000000	-3.105185e+00	6.237260e+00	7.020714e-01	-9.231475e-01
68.0000000000	-2.597088e+00	7.137828e+00	7.348389e-01	-1.108981e+00
74.0000000000	-1.964979e+00	7.998862e+00	7.029913e-01	-1.305455e+00
80.0000000000	-1.206401e+00	8.800841e+00	6.106676e-01	-1.504268e+00
86.0000000000	-3.225653e-01	9.524067e+00	4.621174e-01	-1.697419e+00
92.0000000000	6.818592e-01	1.014908e+01	2.618893e-01	-1.877287e+00
98.0000000000	1.798940e+00	1.065705e+01	1.494989e-02	-2.036703e+00
104.0000000000	3.017689e+00	1.103019e+01	-2.732484e-01	-2.169038e+00
110.0000000000	4.324285e+00	1.125212e+01	-5.967389e-01	-2.268285e+00

116.0000000000	5.702325e+00	1.130819e+01	-9.490445e-01	-2.329142e+00
122.0000000000	7.133099e+00	1.118583e+01	-1.323207e+00	-2.347090e+00
128.0000000000	8.595895e+00	1.087483e+01	-1.711837e+00	-2.318467e+00
134.0000000000	1.006833e+01	1.036758e+01	-2.107185e+00	-2.240528e+00
140.0000000000	1.152669e+01	9.659316e+00	-2.501226e+00	-2.111503e+00
146.0000000000	1.294633e+01	8.748245e+00	-2.885755e+00	-1.930634e+00
152.0000000000	1.430205e+01	7.635707e+00	-3.252494e+00	-1.698212e+00
158.0000000000	1.556849e+01	6.326244e+00	-3.593209e+00	-1.415587e+00
164.0000000000	1.672055e+01	4.827626e+00	-3.899832e+00	-1.085173e+00
170.0000000000	1.773377e+01	3.150836e+00	-4.164582e+00	-7.104348e-01
176.0000000000	1.858480e+01	1.310005e+00	-4.380102e+00	-2.958577e-01
177.0000000000	1.870931e+01	9.884122e-01	-4.410748e+00	-2.232585e-01
178.0000000000	1.882859e+01	6.628214e-01	-4.439805e+00	-1.497290e-01
179.0000000000	1.894257e+01	3.333204e-01	-4.467245e+00	-7.529946e-02
180.0000000000	1.905114e+01	3.285706e-08	-4.493047e+00	2.829110e-08

D

Partial Derivatives of Love Numbers

Here, I include additional figures of partial derivatives of potential, load, shear, and stress Love numbers for multiple spherical harmonic degrees.

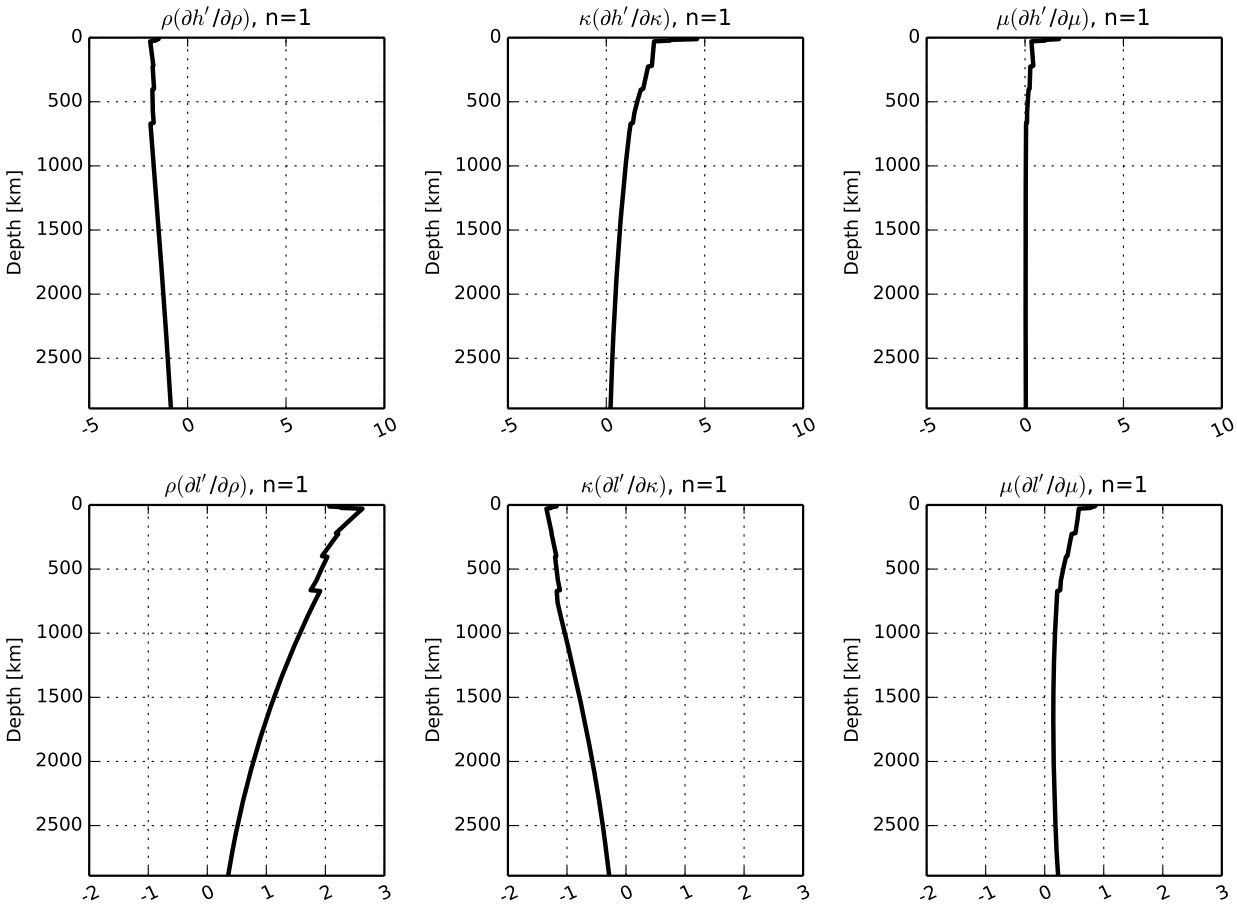

Figure D.1: Partial derivatives of degree-1 load Love numbers with respect to μ, κ, and ρ, derived from PREM. The horizontal axes are in units of 10^{-4}/km (cf., Okubo & Endo (1986), Fig. 3). The partial derivatives for l do not match those of Okubo & Endo (1986); however, I verified my results against the numerically derived partial derivatives (from finite differences) to confirm the shape of the partial derivatives plotted here.

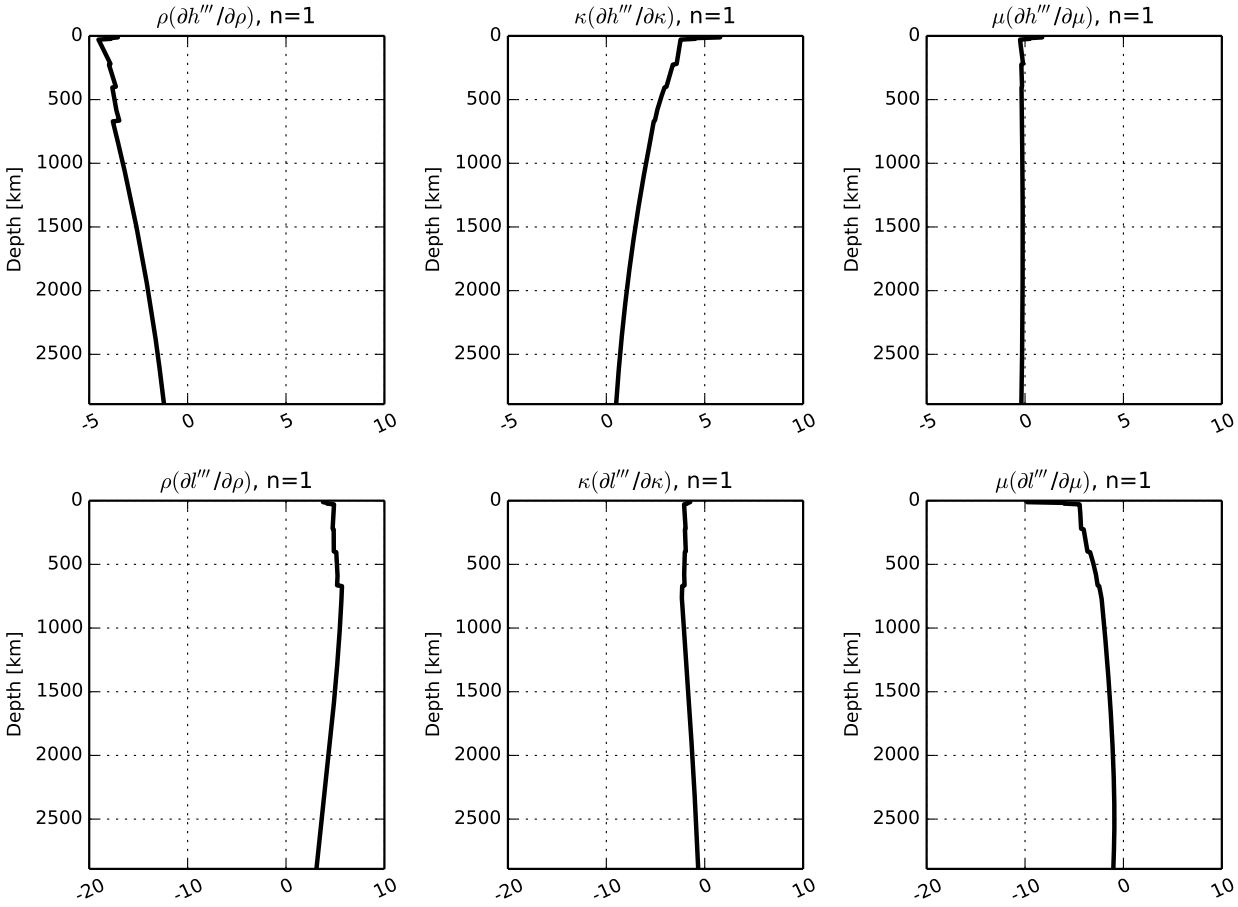

Figure D.2: Same as Fig. D.1, but for degree-1 stress Love numbers.

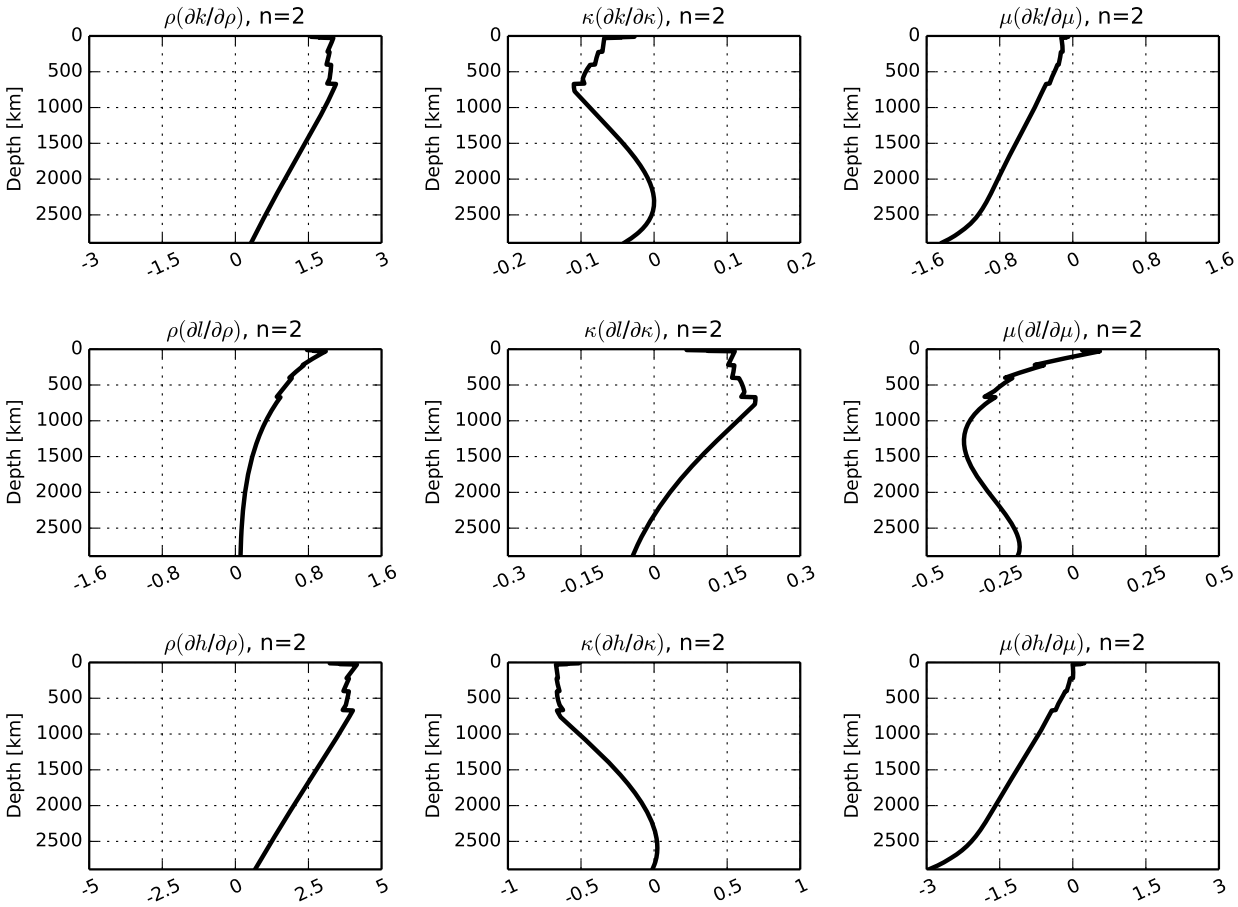

Figure D.3: Partial derivatives of degree-2 potential Love numbers with respect to the shear modulus, μ, the bulk modulus, κ, and density, ρ, derived from PREM. The partials have been multiplied by the depth profile of each elastic parameter to remove scaling dependencies. The horizontal axes are in units of 10^{-4}/km (cf., Okubo & Saito (1983), Fig. 1).

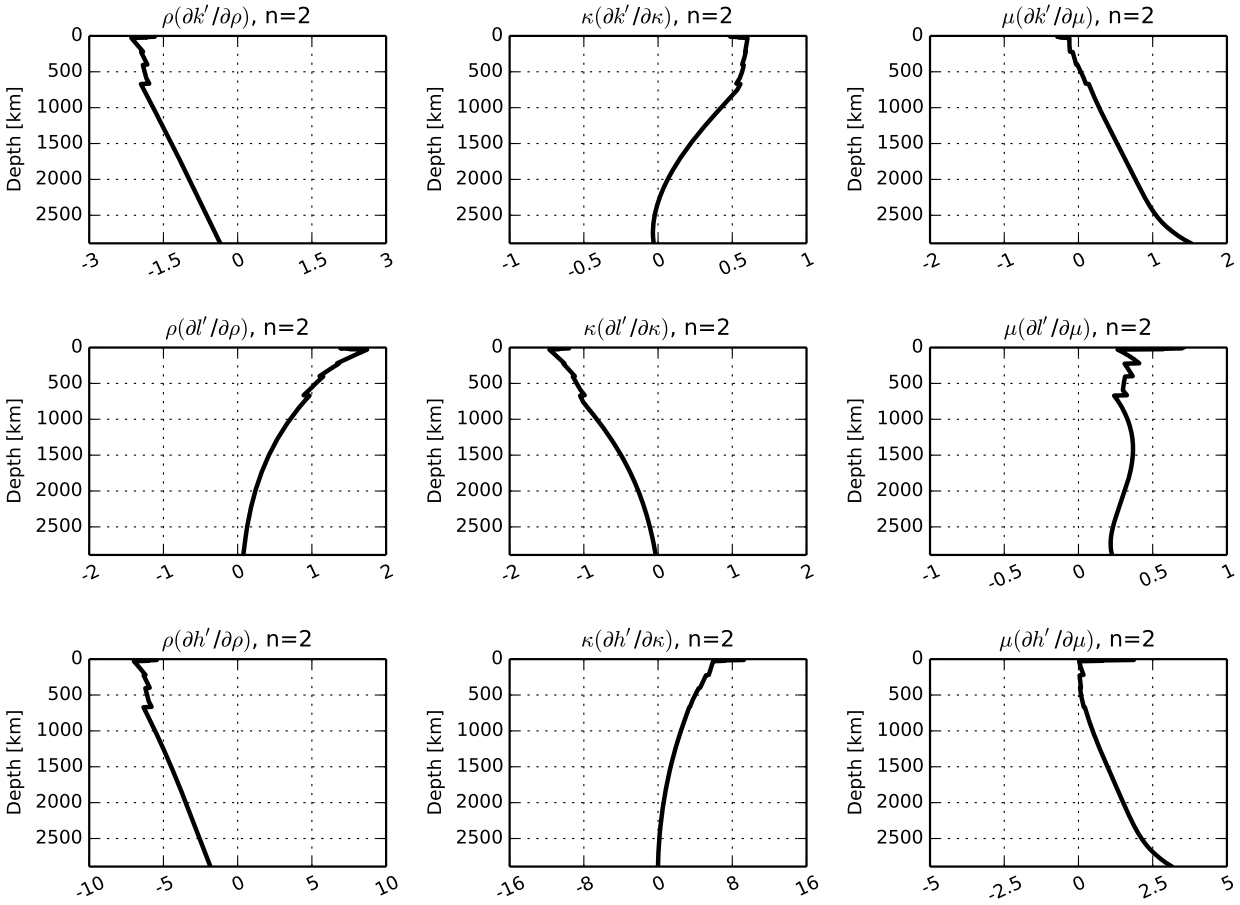

Figure D.4: Same as Fig. D.3, but for degree-2 load Love numbers.

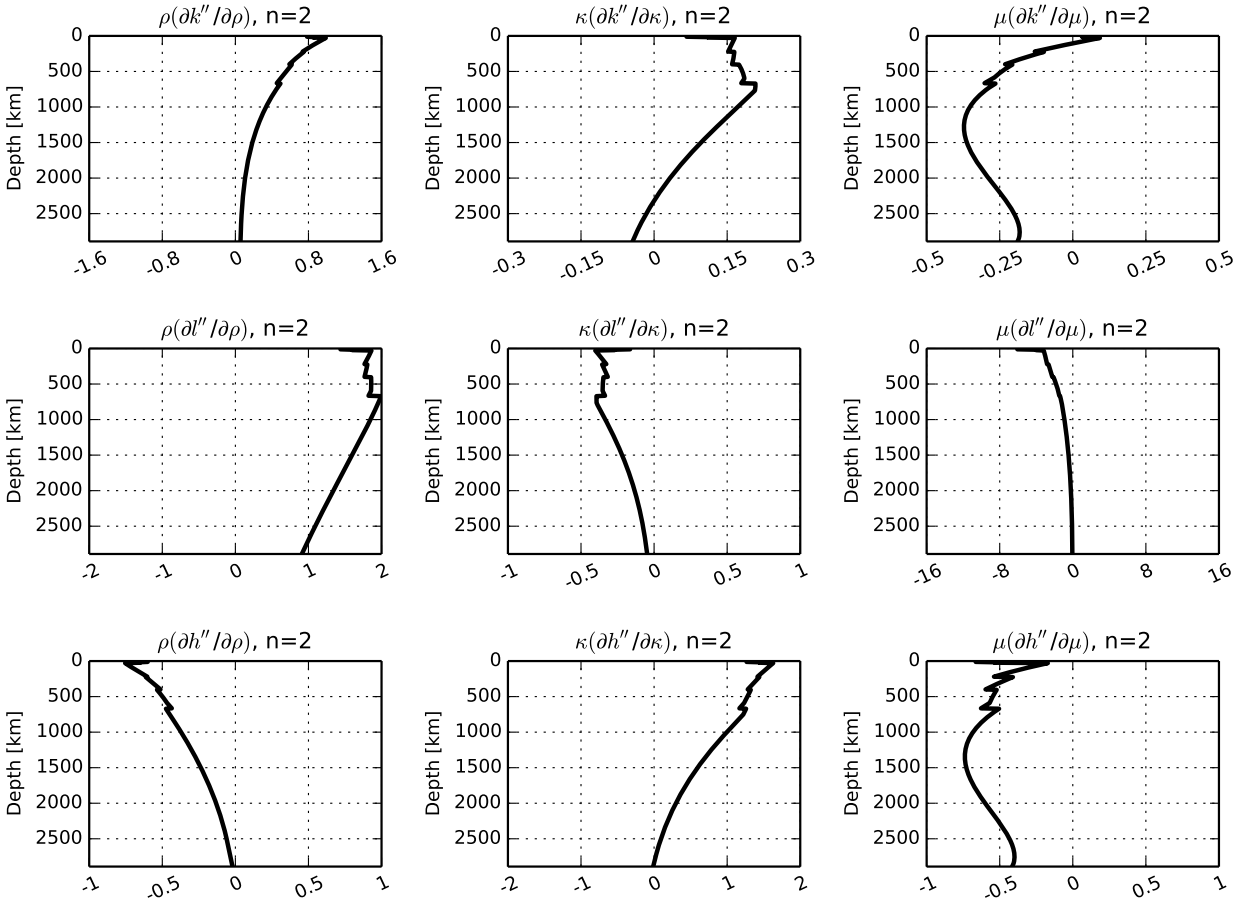

Figure D.5: Same as Fig. D.3, but for degree-2 shear Love numbers.

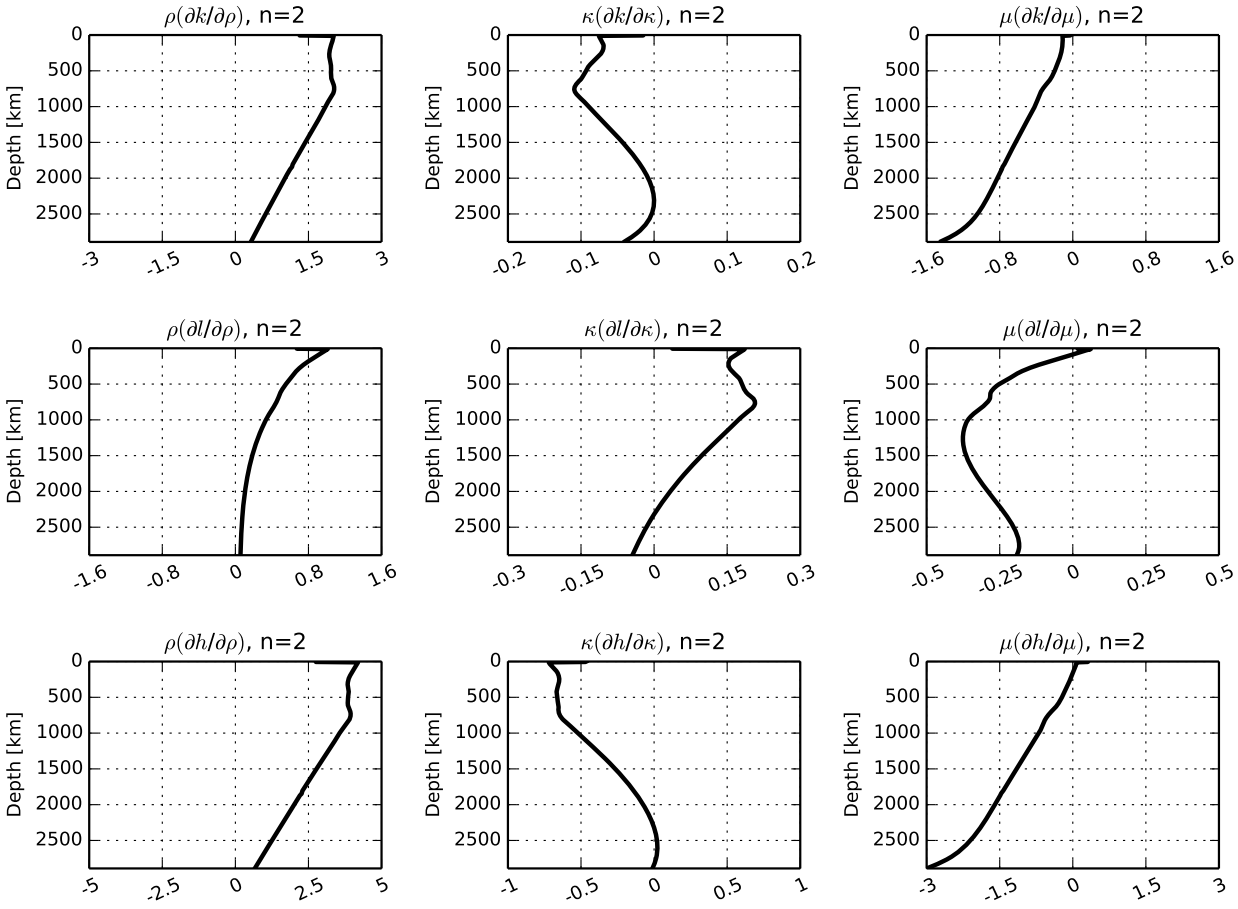

Figure D.6: Same as Fig. D.3, but derived from the Earth model 1066A rather than PREM. The figure may be compared directly with fig. 1a in Okubo & Saito (1983) for Earth's crust and mantle.

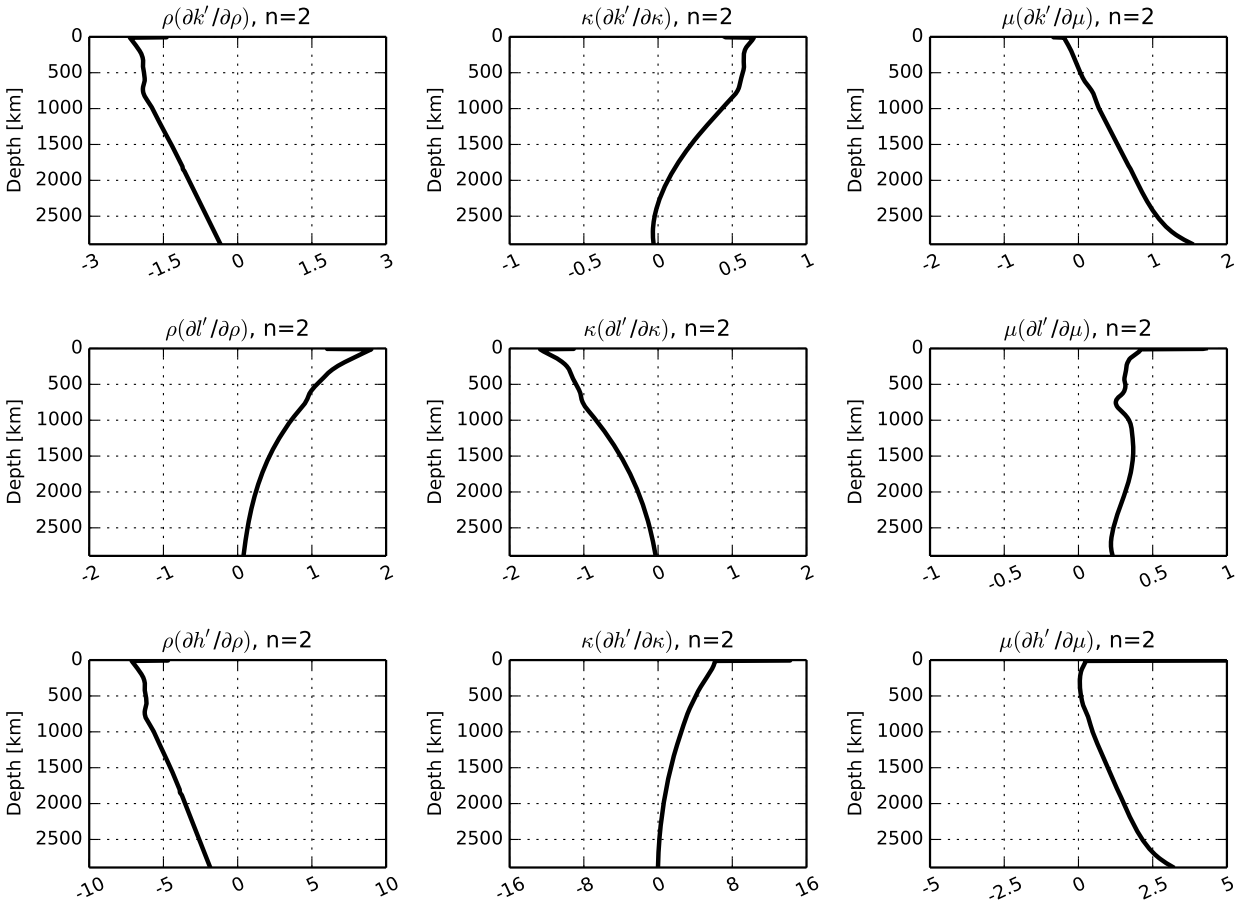

Figure D.7: Same as Fig. D.6, but for load, rather than potential, Love numbers (cf., Okubo & Saito (1983), fig. 1b).

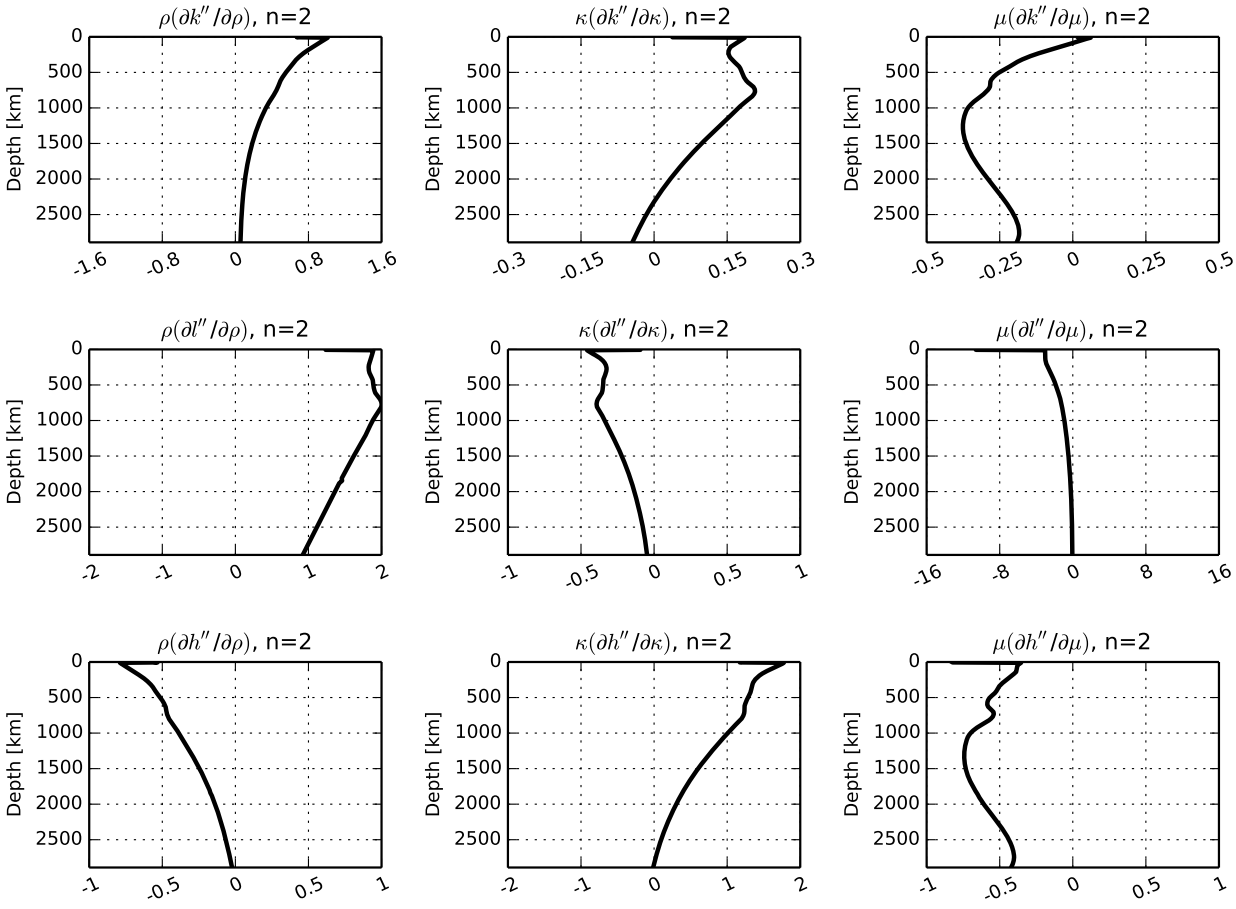

Figure D.8: Same as Fig. D.6, but for shear, rather than potential, Love numbers (cf., Okubo & Saito (1983), fig. 1c).

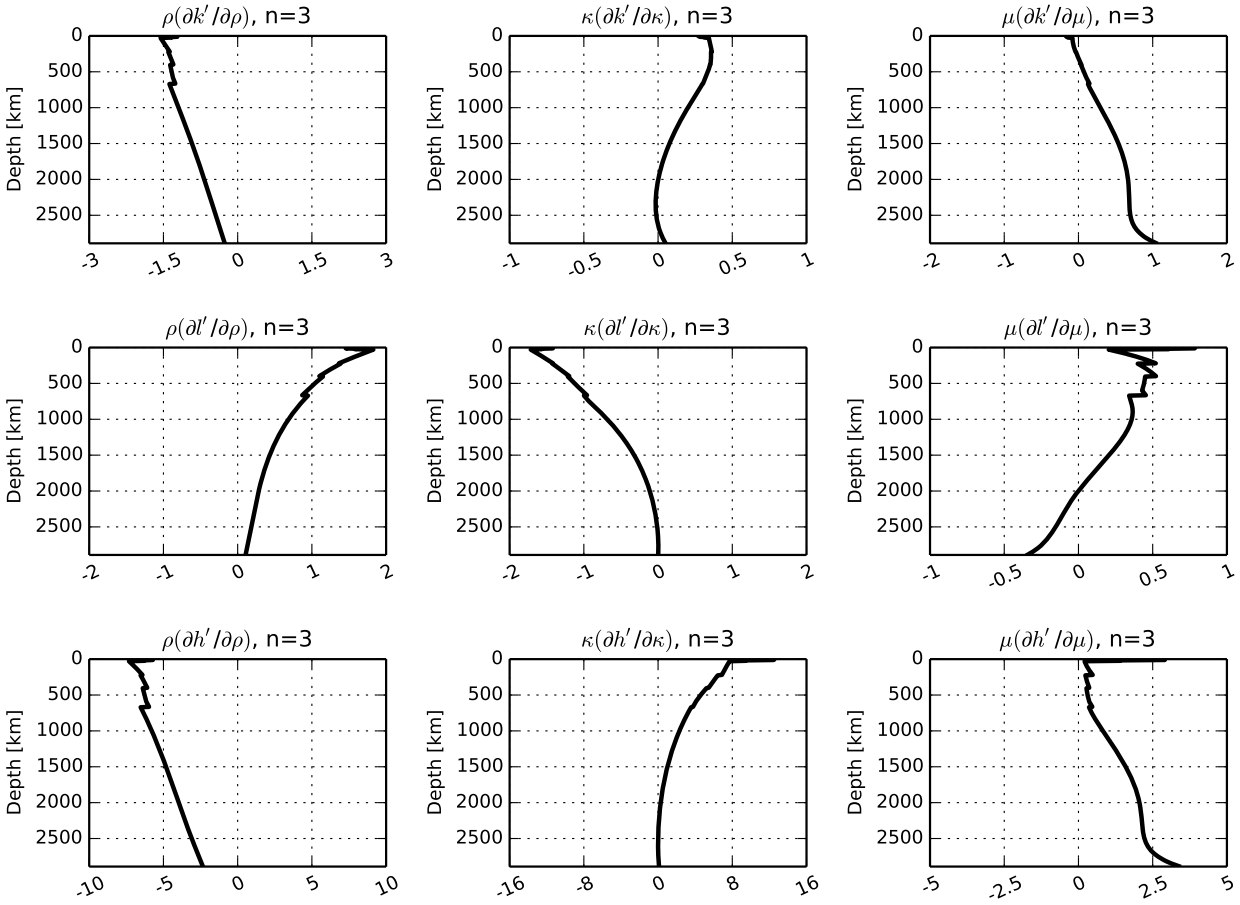

Figure D.9: Same as Fig. D.4, but for spherical harmonic degree $n = 3$.

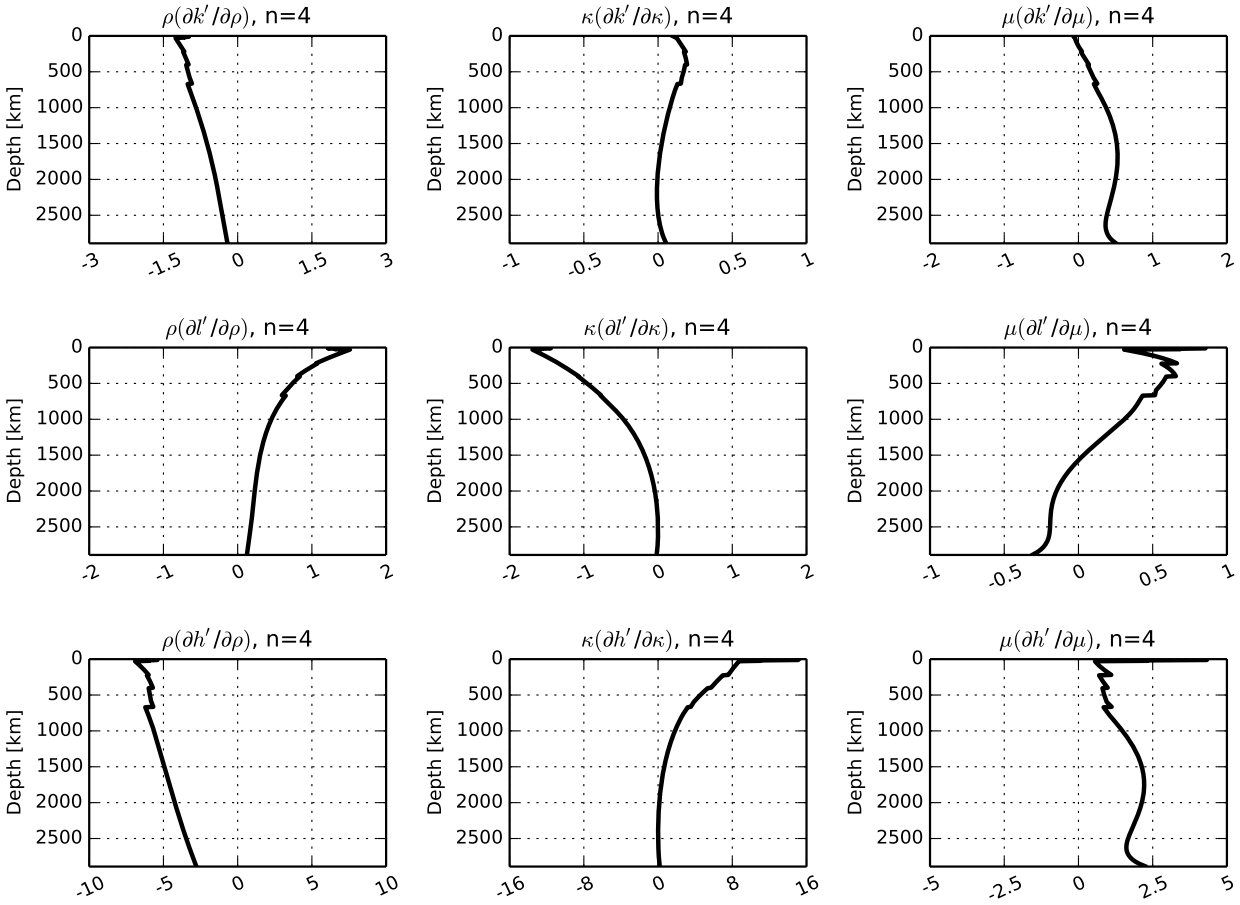

Figure D.10: Same as Fig. D.4, but for spherical harmonic degree $n = 4$.

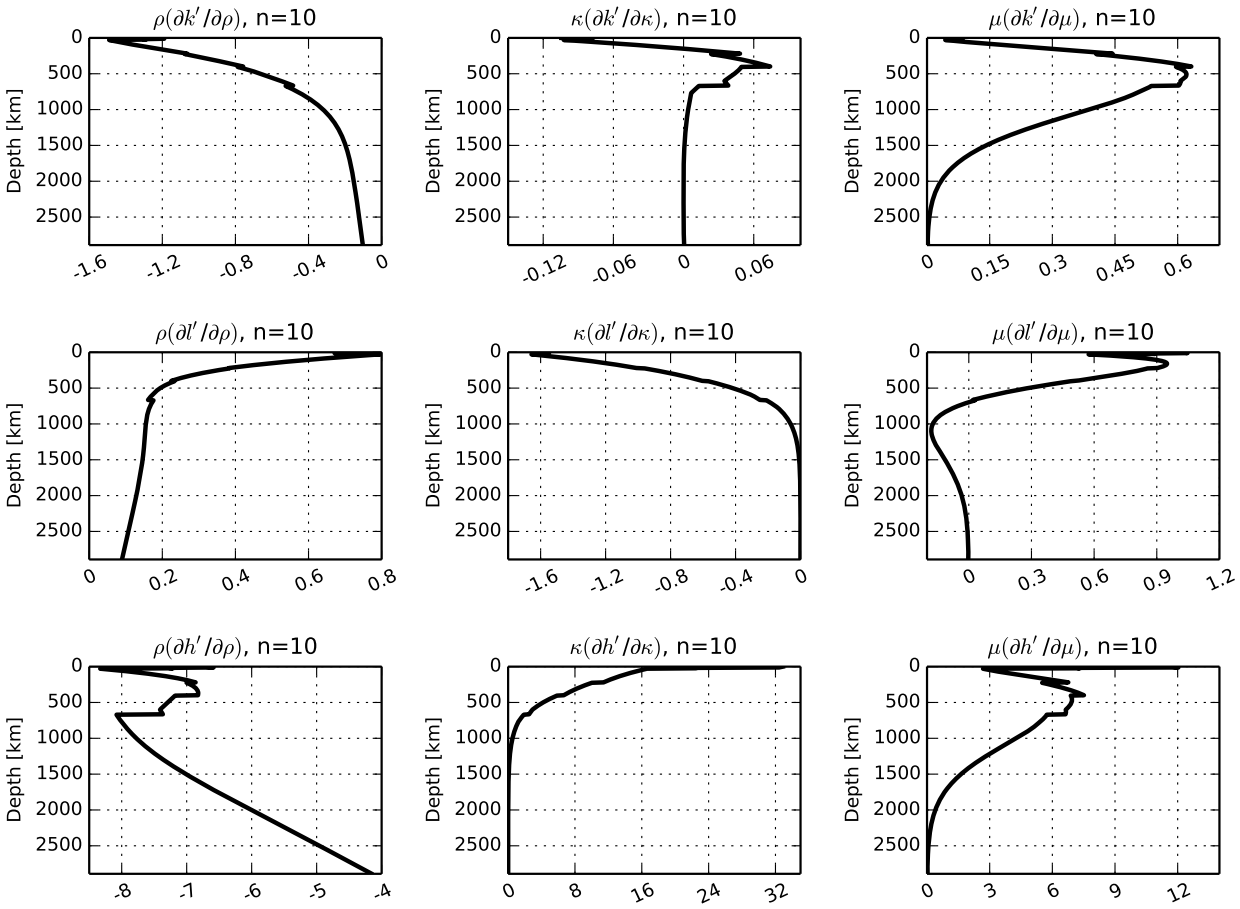

Figure D.11: Same as Fig. D.4, but for spherical harmonic degree $n = 10$.

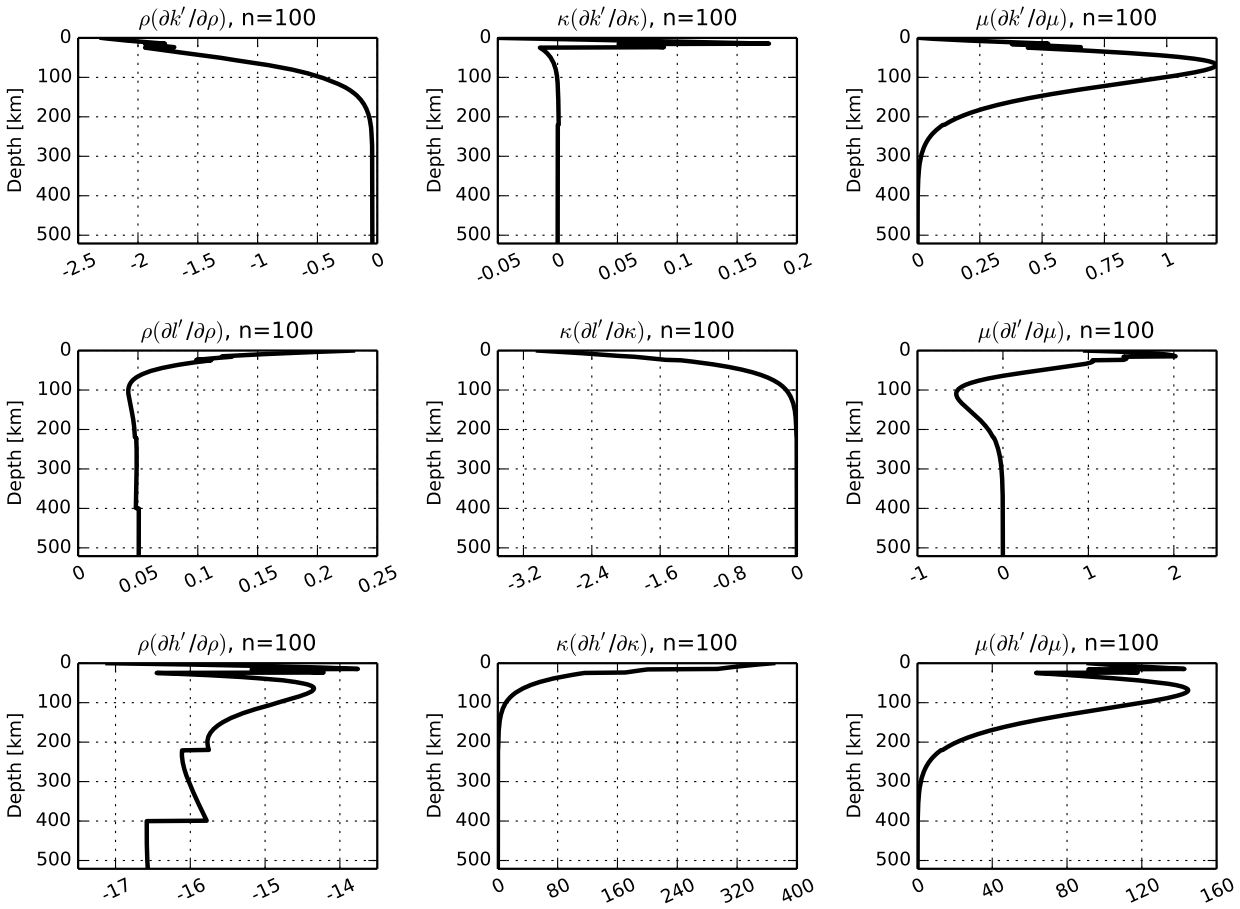

Figure D.12: Same as Fig. D.4, but for spherical harmonic degree $n = 100$.

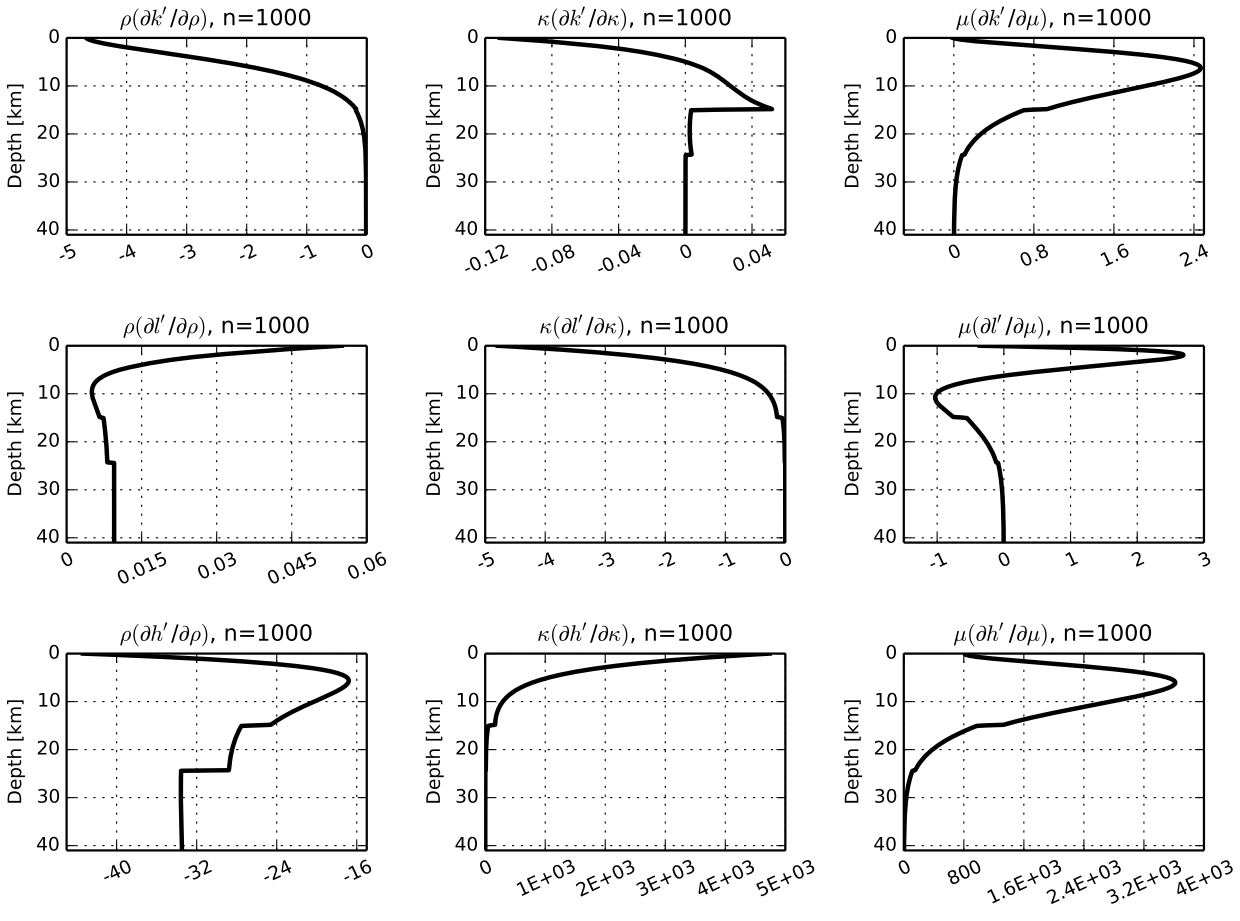

Figure D.13: Same as Fig. D.4, but for spherical harmonic degree $n = 1000$.

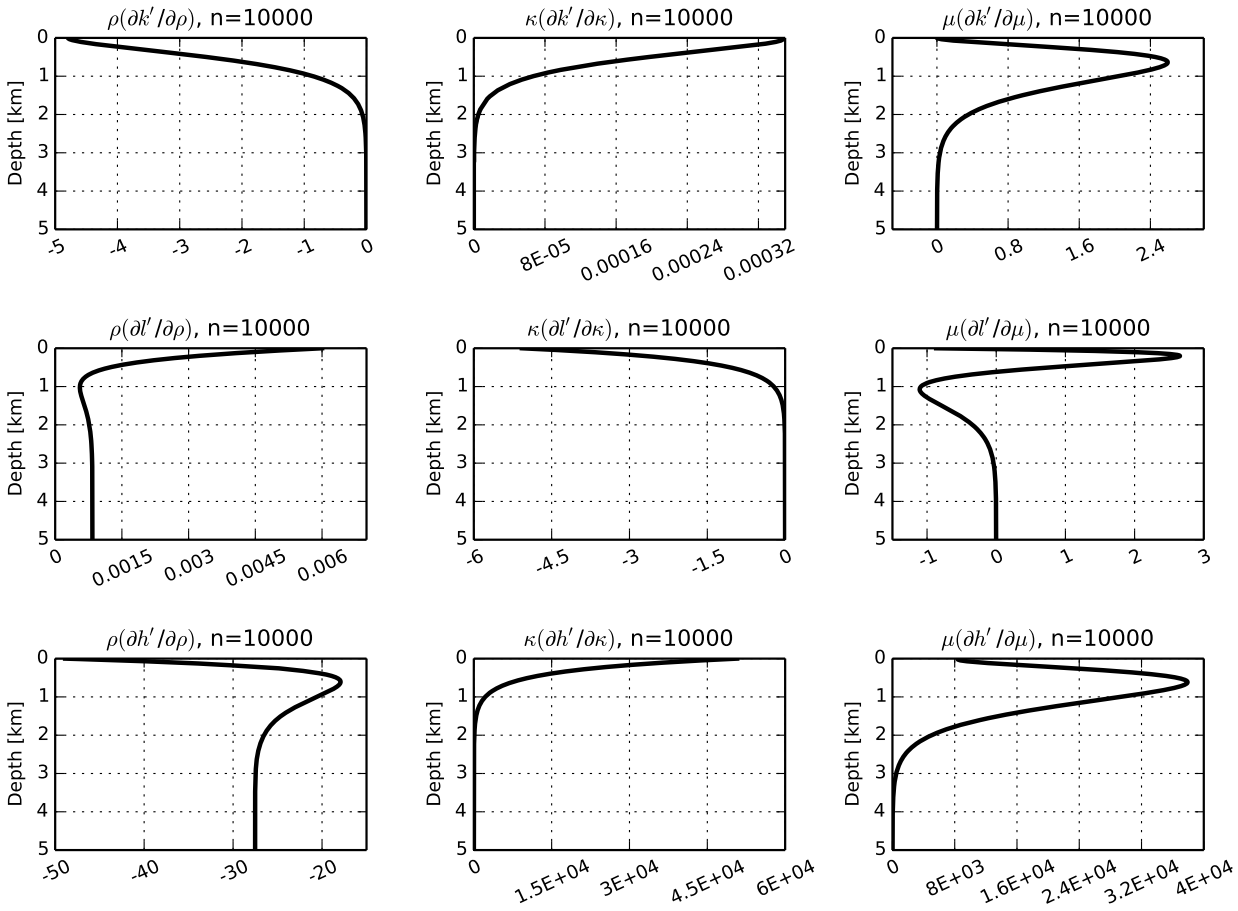

Figure D.14: Same as Fig. D.4, but for spherical harmonic degree $n = 10000$.

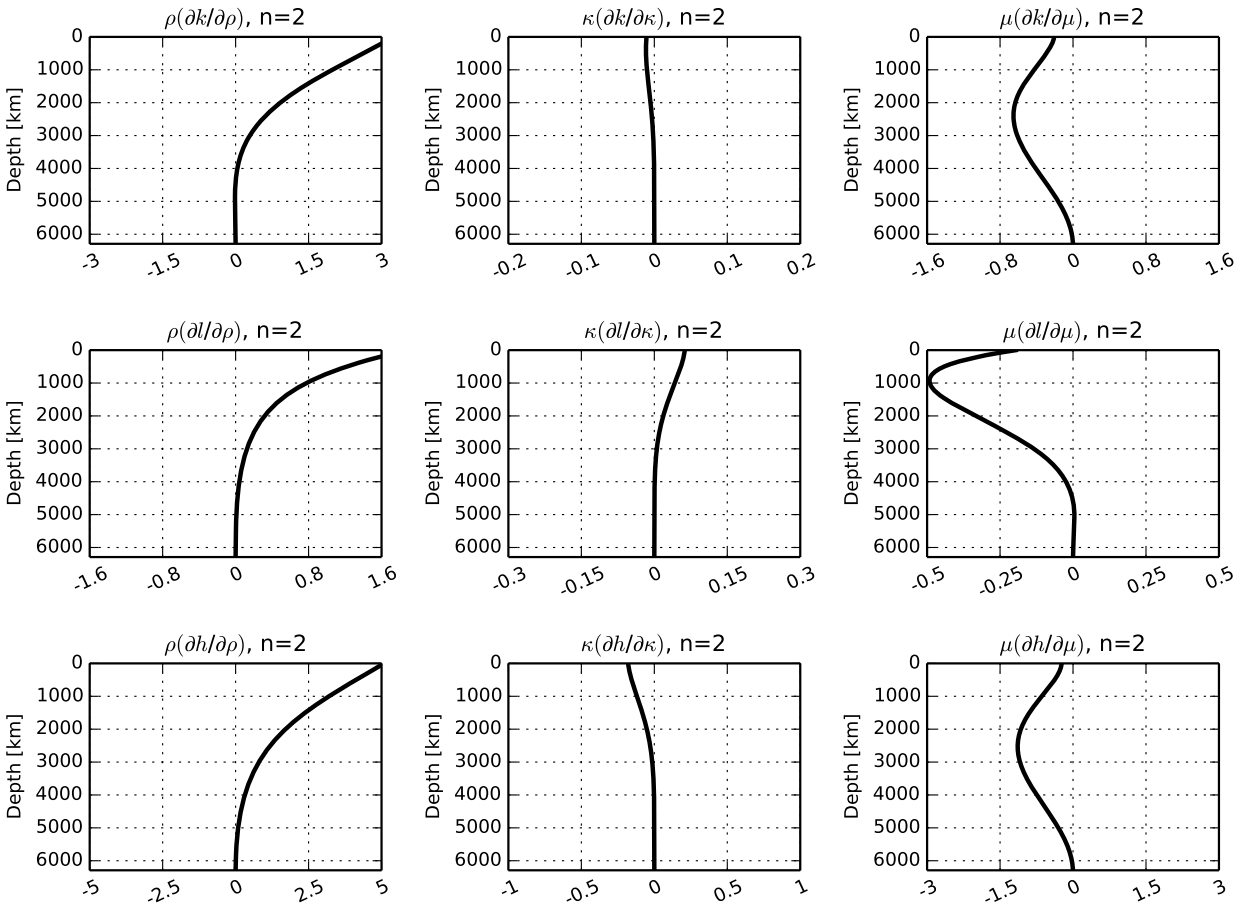

Figure D.15: Partial derivatives of degree-2 potential Love numbers with respect to the shear modulus, μ, the bulk modulus, κ, and density, ρ, derived from a homogeneous sphere with properties: V_P = 10000 m s^{-1}, V_S = 5000 m s^{-1}, and ρ = 5000 kg m^{-3}. The partials have been multiplied by the depth profile of each elastic parameter to remove scaling dependencies. The horizontal axes are in units of 10^{-4}/km.

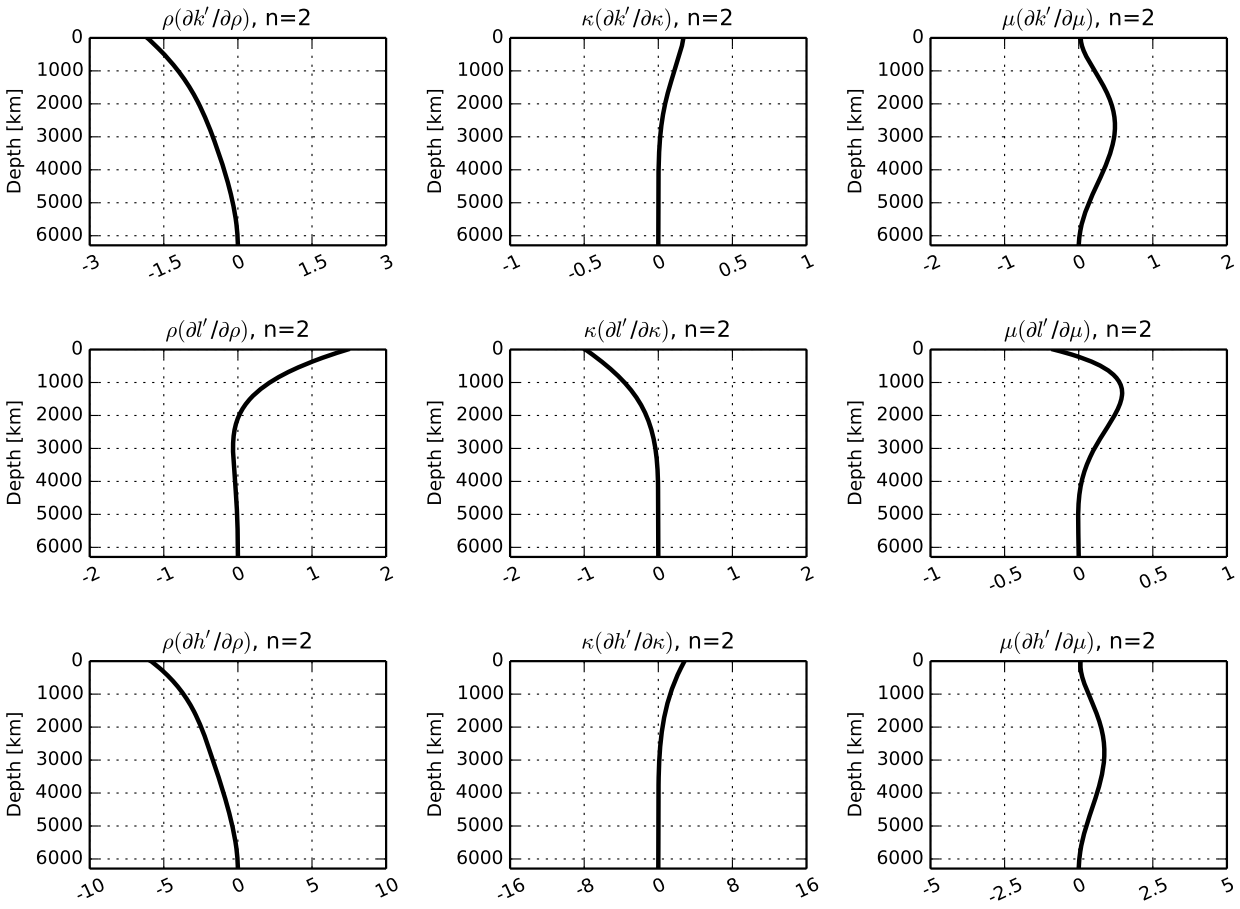

Figure D.16: Same as Fig. D.15, but for degree-2 load Love numbers.

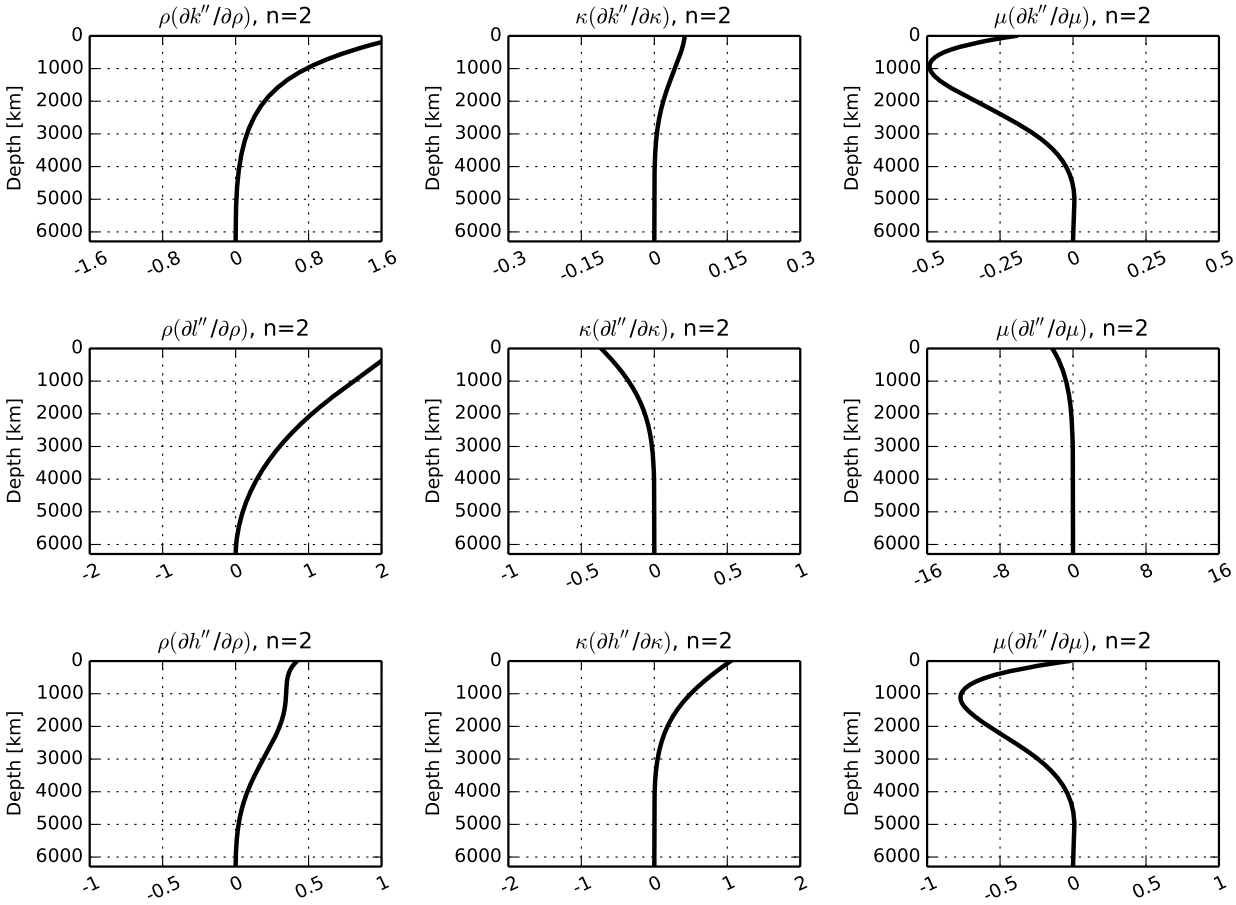

Figure D.17: Same as Fig. D.15, but for degree-2 shear Love numbers.

E

GPS Station Network

Table E.1: Names and locations for each GPS station used in the case study from Ch. 7. The locations are given as latitude (positive North), longitude (positive East), and country. The country codes A, B, and U represent Argentina, Brazil, and Uruguay, respectively.

GPS Station Network							
Country	Name	Latitude (°)	Longitude (°)	Country	Name	Latitude (°)	Longitude (°)
A	ABRA	-22.72203	-65.69731	B	PAAT	-3.20098	-52.18131
B	ALAR	-9.74922	-36.65342	B	PAIT	-4.28766	-56.03636
A	ALUM	-27.32343	-66.59663	B	PARA	-25.44837	-49.23095
B	AMCO	-4.87199	-65.33398	B	PAST	-2.50473	-54.72197
B	AMHU	-7.50325	-63.02852	B	PBCG	-7.21368	-35.90714
B	AMTE	-3.34569	-64.70665	B	PBJP	-7.13628	-34.87342
B	APSA	-0.06026	-51.16747	A	PDE2	-47.75663	-65.89938
A	AUTF	-54.83953	-68.30357	B	PEAF	-7.76411	-37.63196
A	AZUL	-36.76702	-59.88128	A	PEJO	-35.80632	-61.89464
B	BABR	-12.15004	-44.99490	B	PEPE	-9.38442	-40.50612
B	BAIL	-14.79660	-39.17239	B	PISR	-9.03069	-42.70276
B	BAIR	-11.30565	-41.85852	B	PITN	-5.10248	-42.793030
B	BATF	-17.55487	-39.74334	B	POAL	-30.07404	-51.11976
B	BAVC	-14.88831	-40.80270	B	POLI	-23.55565	-46.73031
A	BCAR	-37.76123	-58.30110	B	POVE	-8.70934	-63.89632
B	BELE	-1.40879	-48.46255	B	PPTE	-22.11990	-51.40853
B	BOAV	2.84518	-60.70112	B	PRCV	-24.96275	-53.46633
B	BOMJ	-13.25556	-43.42174	B	PRGU	-25.38400	-51.48758
A	BORC	-60.73978	-44.74062	B	PRMA	-23.40969	-51.93842
B	BRAZ	-15.94747	-47.87787	A	PRNA	-31.78144	-60.46944
B	BRFT	-3.87745	-38.42554	B	RECF	-8.05096	-34.95152
A	CATA	-28.47098	-65.77412	A	RIO2	-53.78547	-67.75112
B	CEEU	-3.87755	-38.42554	A	RIO4	-33.12525	-64.34939
B	CEFE	-20.31079	-40.31946	B	RIOB	-9.96546	-67.80281
B	CEFT	-3.71081	-38.47292	B	RIOD	-22.81784	-43.30628
B	CESB	-3.68127	-40.33749	B	RJCG	-21.76486	-41.32616
A	CFAG	-31.60217	-68.23265	B	RNMO	-5.20423	-37.32546

A	CHLT	-49.34046	-72.88556	B	RNNA	-5.83614	-35.20771
B	CHPI	-22.68715	-44.98516	B	ROCD	-13.12228	-60.54391
B	CRAT	-7.23802	-39.41561	B	ROGM	-10.78424	-65.33061
B	CRUZ	-7.61116	-72.67211	B	ROJI	-10.86390	-61.95972
A	CSJ1	-31.98053	-68.42724	B	ROSA	-22.52330	-52.95209
A	CSLO	-31.78489	-69.30221	B	RSAL	-29.78944	-55.76884
B	CUIB	-15.55526	-56.06987	B	SAGA	-0.14385	-67.05778
A	EBYP	-27.36894	-55.89217	B	SALU	-2.59346	-44.21248
B	EESC	-22.00495	-47.89918	B	SALV	-13.00867	-38.51236
A	ESQU	-42.91711	-71.32340	B	SAVO	-12.93925	-38.43225
B	FORT	-3.87745	-38.42561	A	SBAL	-30.30878	-61.22656
B	GOGY	-16.66473	-49.25467	B	SCAQ	-26.39376	-48.73744
B	GOJA	-17.88328	-51.72611	B	SCCH	-27.13756	-52.59951
B	GVAL	-18.85561	-41.95762	B	SCFL	-27.59938	-48.51953
A	IGM0	-34.57220	-58.43937	B	SCLA	-27.79283	-50.30426
A	IGM1	-34.57224	-58.43932	B	SEAJ	-10.92963	-37.10428
B	ILHA	-20.42778	-51.34338	B	SJRP	-20.78552	-49.35995
B	IMBT	-28.23484	-48.65572	B	SJSP	-23.20713	-45.86174
B	IMPZ	-5.49177	-47.49723	A	SL01	-33.15636	-66.31401
A	JBAL	-27.58441	-65.62275	B	SMAR	-29.71892	-53.71659
A	LHCL	-38.00266	-65.59525	B	SPAR	-21.18467	-50.43979
B	MABA	-5.36238	-49.12230	B	SPBO	-22.85247	-48.43230
B	MABB	-4.24096	-44.81572	B	SPCA	-22.81629	-47.06269
B	MABS	-7.53381	-46.03972	B	SPJA	-21.24107	-48.28670
B	MAPA	0.04669	-51.09734	B	SSA1	-12.97516	-38.51648
B	MCLA	-16.72039	-43.88132	A	SVIC	-26.99371	-54.48752
A	MECO	-29.18489	-58.07585	A	TERO	-27.78914	-64.25678
B	MGBH	-19.94190	-43.92490	B	TOGU	-11.74671	-49.04910
B	MGIN	-22.31856	-46.32802	B	TOPL	-10.17105	-48.33068
B	MGMC	-16.71639	-43.85832	A	TUC1	-26.83265	-65.19567
B	MGRP	-19.20986	-46.13255	A	TUCU	-26.84326	-65.23035
B	MGUB	-18.91916	-48.25605	B	UBA1	-23.50018	-45.11890
B	MGVA	-21.54262	-45.43499	B	UBAT	-23.50018	-45.11890
A	MPL2	-38.00577	-57.57130	B	UBER	-18.88957	-48.31706
B	MSCG	-20.44090	-54.54070	A	UCOR	-31.43496	-64.19350
B	MSCO	-19.00352	-57.63698	B	UEPP	-22.11990	-51.40853
B	MSDR	-22.19410	-54.93040	B	UFPR	-25.44837	-49.23095
B	MTBA	-15.88997	-52.26473	A	UNPA	-51.64799	-69.20865
B	MTCN	-13.55583	-52.27136	A	UNRO	-32.95935	-60.62843
B	MTCO	-10.80386	-55.45626	A	UNSA	-24.72746	-65.40764

B	MTJU	-11.42733	-58.76932	A	UNSJ	-31.54126	-68.57706
B	MTSF	-11.61928	-50.66351	U	UYDU	-33.31588	-55.60243
B	MTSR	-12.54523	-55.72741	U	UYLP	-34.65570	-54.14210
B	MTVB	-15.00643	-59.95156	U	UYMO	-34.88832	-56.25988
A	MZAC	-32.89515	-68.87557	U	UYPA	-32.29125	-58.06719
A	MZAE	-33.25484	-68.15006	U	UYRI	-30.89576	-55.55911
A	MZAU	-33.73596	-69.11842	U	UYRO	-34.00100	-53.55483
A	MZSR	-34.61547	-68.33431	U	UYSO	-33.26126	-58.01362
B	NAUS	-3.02292	-60.05502	U	UYTA	-31.68307	-55.93753
B	NEIA	-25.02024	-47.92497	B	VARG	-21.54268	-45.43488
A	NESA	-40.10539	-64.45401	A	VBCA	-38.70077	-62.26923
A	NGAQ	-26.68591	-60.72935	B	VICO	-20.76150	-42.86999
B	ONRJ	-22.89570	-43.22433				
B	OURI	-22.94917	-49.89504				

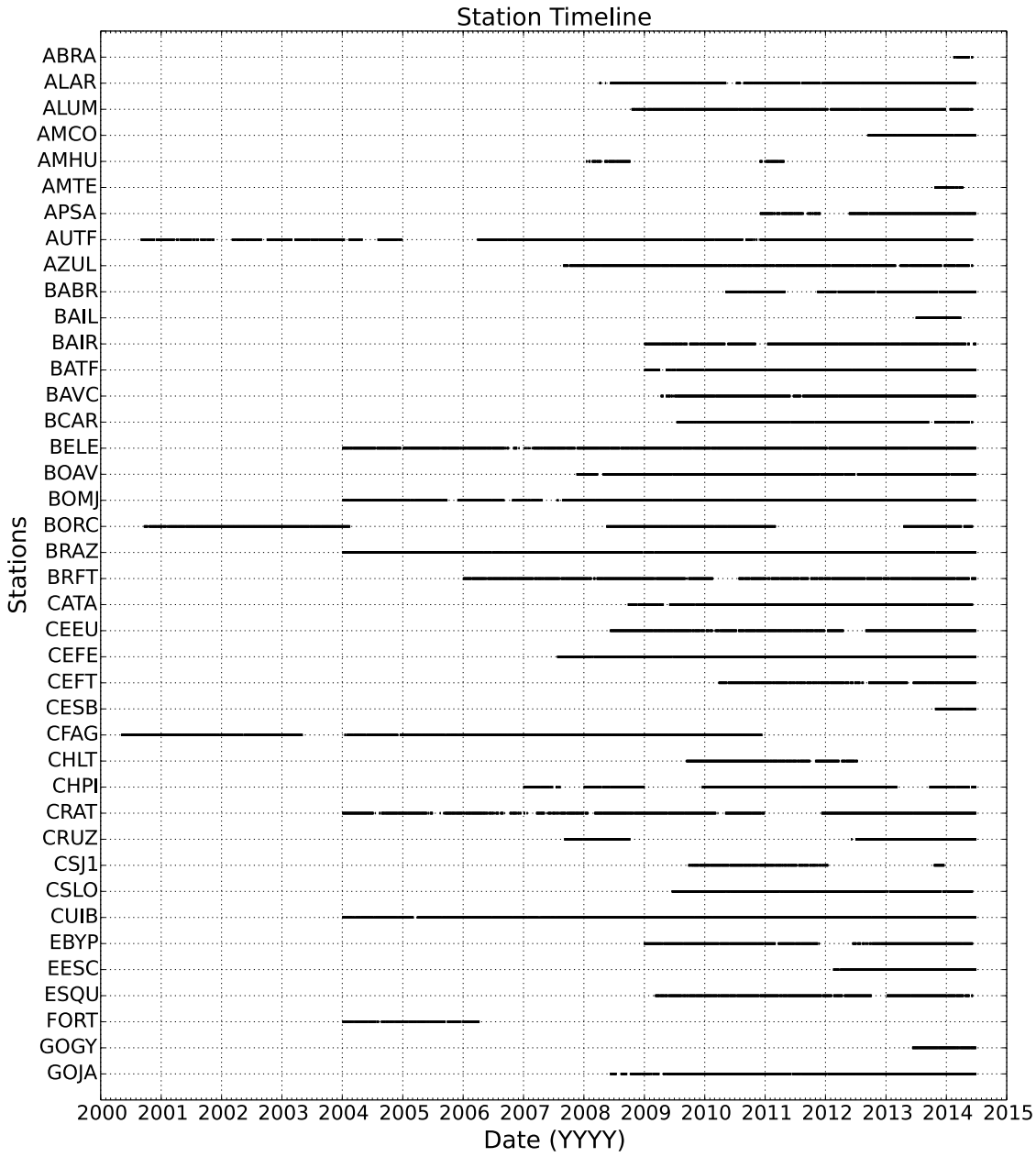

Figure E.1: Timeline of station activity for the first 40 receivers in the GPS network across Brazil, Argentina, and Uruguay, ordered alphabetically by station name.

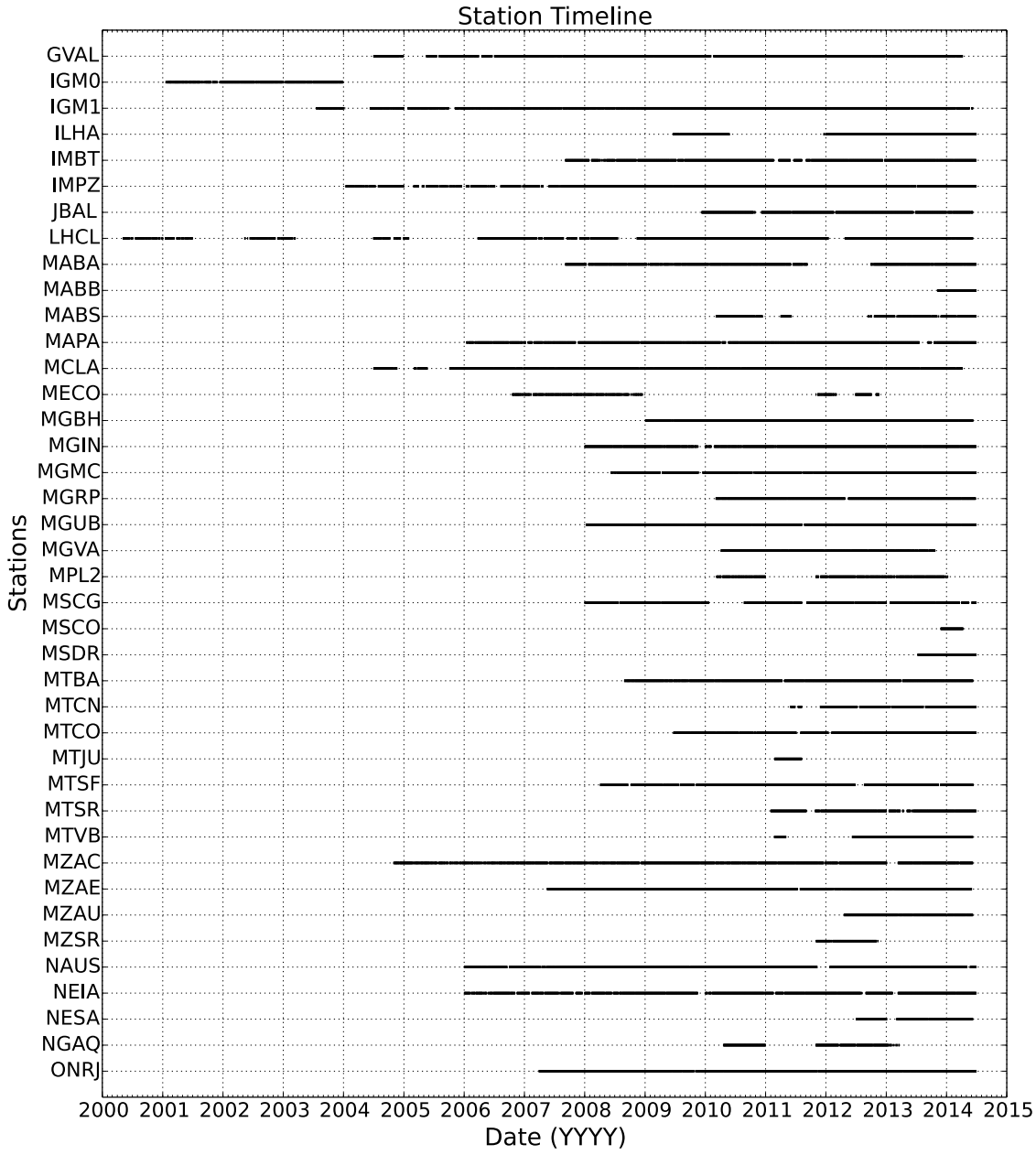

Figure E.2: Continued timeline of station activity for the next 40 receivers.

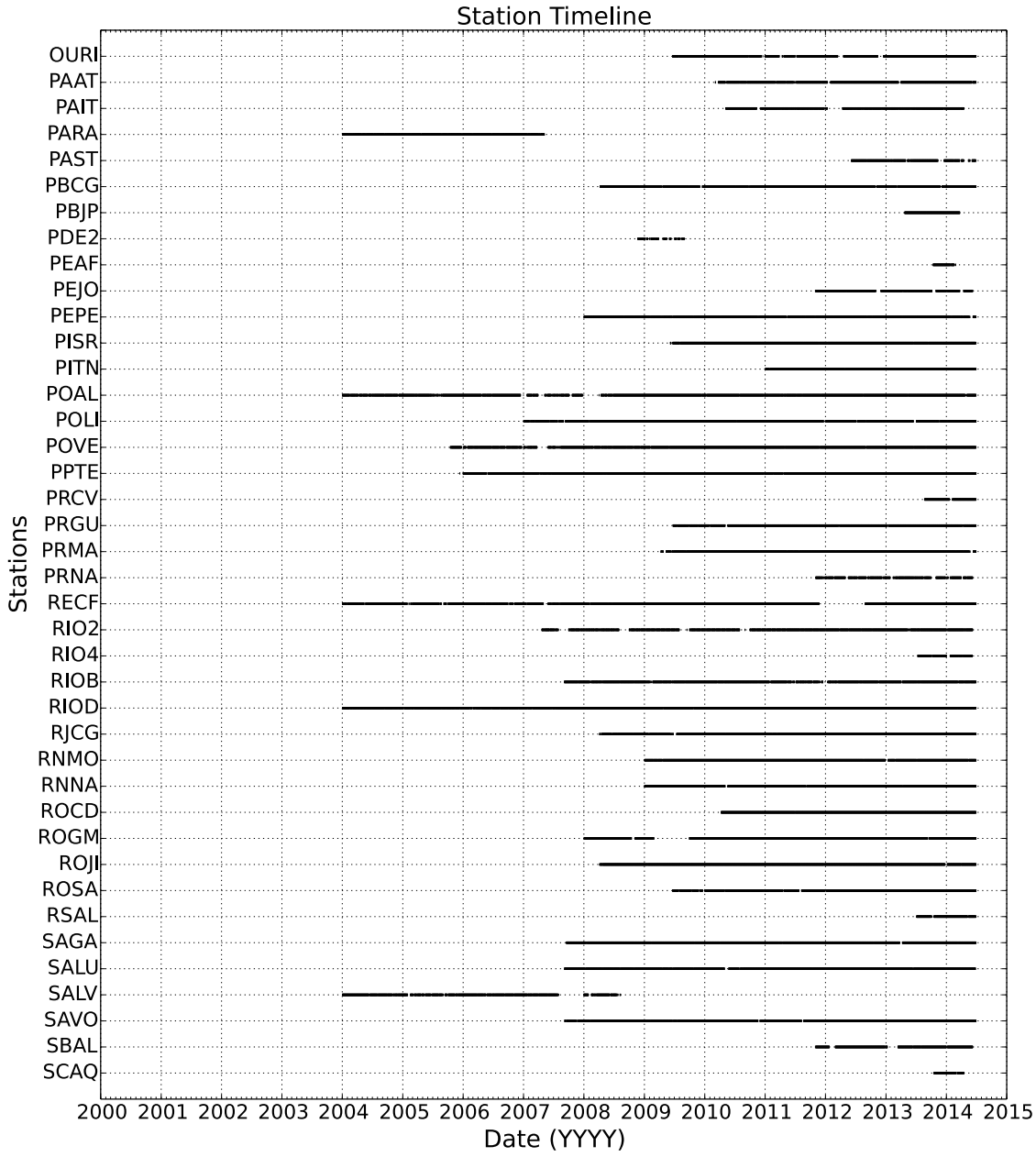

Figure E.3: Continued timeline of station activity for the next 40 receivers.

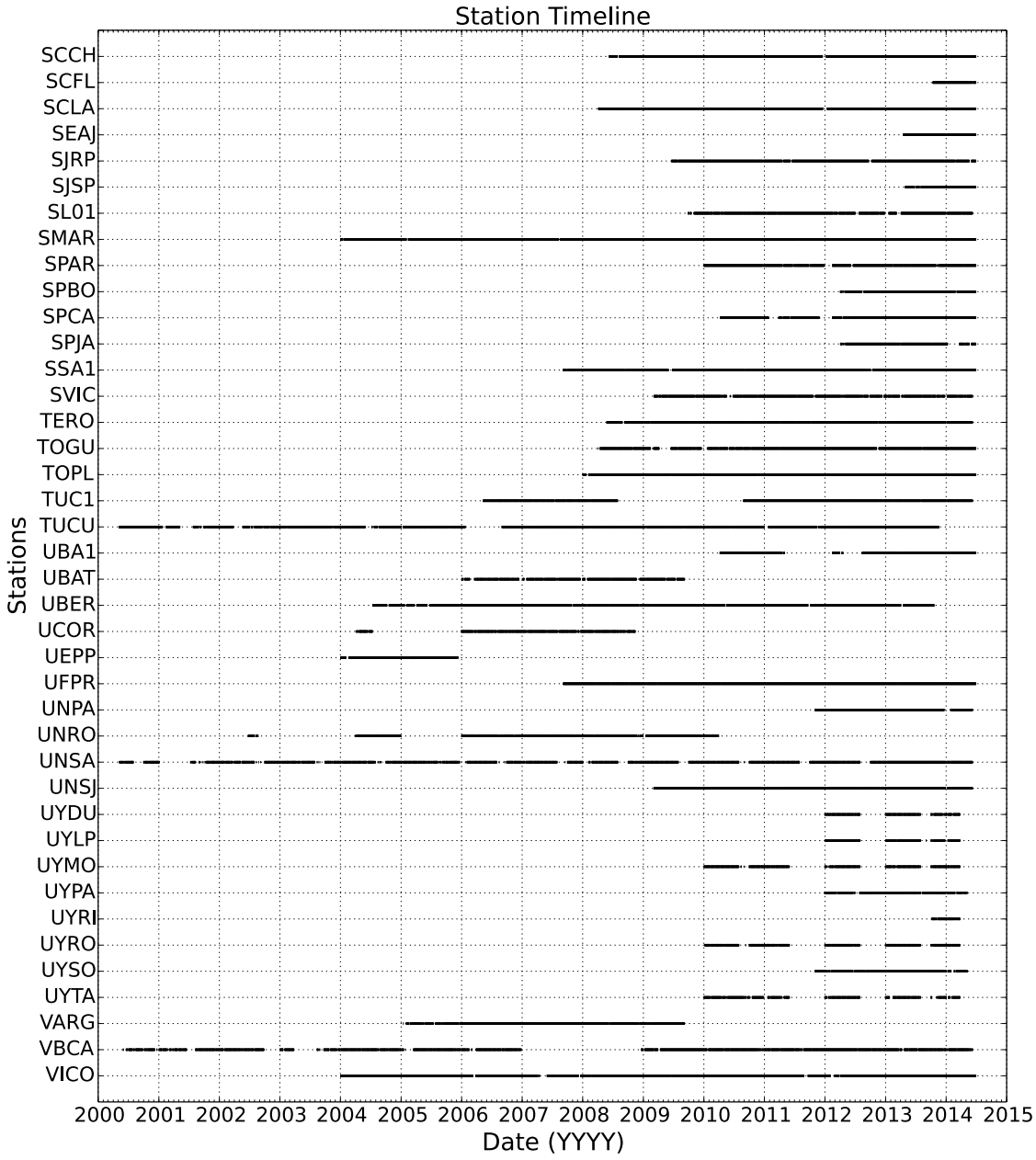

Figure E.4: Continued timeline of station activity for the next 40 receivers.

F

Supplemental GPS Theory

F.1 Carrier Wave Signals and Satellite Orbits

Electromagnetic (EM) signals are transmitted from satellite to receiver at two distinct frequencies: 1575.42 MHz (L1) and 1227.60 MHz (L2) (e.g., Blewitt, 2015, Sec. 3.11.2.2). The two signals are generated from a sinusoidal base wave that has a frequency of 10.23 MHz (e.g., Blewitt, 2015, Sec. 3.11.2.4). The frequency of the base signal is modulated by factors of 154 and 120 to create the L1 and L2 carrier wave channels, respectively. Each carrier wave signal is encoded into binary via phase modulation and contains three distinct codes: the Course Acquisition (C/A) Code, the Precise (P) Code, and the Navigation Message (e.g., Blewitt, 1997, Sec. 2.3.1). The C/A Code is a pseudo-random number sequence, encoded only onto the L1 signal, that contains the time of signal transmission by the satellite. The P Code carries the same information as the C/A Code, but it has ten times the resolution and is transmitted on both the L1 and L2 channels. The P Code is also encrypted with Anti-Spoofing (A/S) technology by the US Department of Defense (e.g., Blewitt, 1997, Sec. 2.3.2).[14] C/A Code is generally used by the receiver to initialize communication with a GPS satellite, whereas the P Code is generally used for precise positioning.

The Navigation Message, transmitted at a slow data rate, delivers information about satellite orbital parameters and clock biases to the receiver (e.g., Blewitt, 1997, Sec. 2.3.1). The receiver can then use the orbital information to derive cartesian coordinates of satellite position in a geocentric coordinate system (e.g., WGS84). If high-precision positioning is required (e.g., mm-level precision), then the Navigation Message on its own is insufficient for providing ephemeris data (satellite location and clock bias) to the receiver. To improve the satellite ephemeris, the International GNSS Service (IGS) computes orbital and clock

[14] An additional "denial of accuracy" technique called Selective Availability was phased out in May 2000.

parameters for each satellite using a global array of reference receivers.[15] Although ultra-rapid orbital products are available from IGS within a 3-9 hour latency period, product accuracy improves with greater latency. Final orbit and clock products are typically available after a two-week latency period. Methods for circumventing inaccurate satellite ephemeris include relative positioning (e.g., double-differencing) or solving for satellite clock bias (in addition to the receiver clock bias) at every epoch (e.g., Blewitt, 2015, Sec. 3.11.2.3).

NASA's JPL also provides continually updated orbit and clock products to the community.[16] JPL releases three orbital and clock products that differ by latency period: *Ultra-Rapid*, with a latency period of less than 2 hours; *Rapid*, with a latency period of approximately 24 hours; and *Final*, with a latency period of up to two weeks. The Ultra-Rapid products are released almost in real-time, but suffer slightly in accuracy, with a characteristic 3D RMS accuracy of 5 cm. The accuracy of the Rapid products is improved to 3.5 cm and the accuracy of the Final products is enhanced further to 2.5 cm, on average. High-rate (i.e., 30-second) clock products are only available for the Rapid and Final products and only since May 2000 (following the discontinuation of Selective Availability).

The receiver-perceived geometry of the satellite constellation has significant implications for precise position estimates. The degradation of receiver position due to unfavorable satellite geometries is referred to as *Dilution of Precision* (DOP) (e.g., Blewitt, 1997, Sec. 4.2.4). DOP is divided into five separate categories: vertical (VDOP), horizontal (HDOP), time (TDOP), position (PDOP), and geometric (GDOP). All are derived from elements of a covariance matrix, which itself is derived from the least-squares solution for the receiver position. For satellites that are not well distributed and appear in approximately the same position in the sky, the covariance matrix approaches singularity (e.g., Blewitt, 1997, Sec. 4.2.4).

Signal delay during transmission through the ionosphere, which is dispersive at L-band frequencies, may be self-calibrated by computing both pseudorange and carrier phase observables for signals transmitted at two different L-band wavelengths: 19.0 cm (L1) and 24.4 cm (L2) (e.g., Blewitt, 2015, Sec. 3.11.2.4).

[15] http://igscb.jpl.nasa.gov/components/prods.html
[16] ftp://sideshow.jpl.nasa.gov/pub/JPL_GPS_Products/Final/

F.2 Pseudorange and Carrier Phase Observables

Distances, or ranges, between GPS satellites and a receiver cannot be measured directly, but are instead derived from the time it takes for an EM signal to travel from the satellite to a receiver multiplied by the speed of light (e.g., Blewitt, 2015, Sec. 3.11.2.4). The result has units of distance and is known as a **pseudorange** because it differs from the true range by biases in clock error, actual speed of signal transmission, and so on. The equation for pseudorange, p, is given by (e.g., Blewitt, 2015, Sec. 3.11.2.1):

$$p = (t_R - t_S)\, c, \tag{F.1}$$

where t_S is the time the EM signal leaves the satellite according to an atomic clock on board the satellite, t_R is the time the signal is received according to the receiver's local clock, and c is the speed of light in a vacuum. The receiver computes the time difference, $t_R - t_S$, by cross-correlating a replica signal generated in situ with the incoming satellite signal. One important thing to note here is that any bias in the receiver clock will be the same for all observed satellites at any moment in time; thus, receiver clock bias may be solved for as an additional parameter in the location computation. Obtaining an estimate for receiver clock bias along with receiver position requires a minimum of four pseudorange observations (e.g., Blewitt, 1997, Sec. 2.1.3). Timing uncertainties in the atomic clocks aboard the satellites are much less significant than receiver clock bias, but are nonetheless relayed to the receiver along with other timing and navigation information (e.g., Blewitt, 1997, Sec. 2.3.1). Monitoring and predicting satellite clock errors is performed by the US Department of Defense and uploaded to the satellites, which can then transmit the information to the receiver. GPS positioning using this method yields location information at an accuracy of meters and furthermore provides a feedback system, by which receiver clocks may periodically synchronize with the more accurate satellite clocks (e.g., Blewitt, 2015, Sec. 3.11.2.3).

The carrier phase observable is another means by which the precision of receiver positioning may be enhanced. In contrast to the pseudorange, the carrier phase observable represents

the difference in *phase* (i.e., the beat phase) between the incoming signal (or carrier wave) and the receiver-generated replica signal (e.g., Blewitt, 2015, Sec. 3.11.2.3). Multiplying the phase difference by the wavelength of the signal (≈20 cm) yields an estimate for the distance between the satellite and the receiver that is approximately 100 times more precise than a pseudorange observable (e.g., Blewitt, 2015, Sec. 3.11.2.3). The drawback to this technique, however, is that an ambiguity of an integer number of wavelengths is introduced as an additional bias (e.g, Bertiger et al., 2010; Blewitt, 2015). Accounting for the phase-ambiguity bias, the carrier phase observable, ϕ_C, may be written as (e.g., Blewitt, 2015, Sec. 3.11.2.3):

$$\phi_C = (\phi_R - \phi_S + i)\ \lambda_C, \tag{F.2}$$

where ϕ_R is the phase of the reference signal generated by the receiver clock, ϕ_S is the phase of the carrier wave transmitted by the satellite, i represents the integer-wavelength ambiguity, and λ_C is the wavelength of the transmitted carrier signal. Since precise GPS positioning relies primarily on the beat phase of the carrier wave itself with the replica receiver signal, as opposed to the pseudorange of the P Code, the Anti-Spoofing encryption of the P Code is generally not significant. Acquiring pseudorange observables from both the L1 and L2 channels also reduces the impact of the Anti-Spoofing encryption (e.g., Blewitt, 1997, Sec. 2.3.2).

F.3 Ambiguity Resolution, Cycle Slips, and Multipath

Ambiguity resolution is the process by which an unknown integer number of signal wavelengths between the satellite and receiver (i.e., variable i in Eq. F.2) may be estimated (e.g., Blewitt, 2015). For single station precise point positioning, ambiguity resolution may be accomplished using wide-lane and phase bias estimates from a network of reference receivers (e.g., Bertiger et al., 2010). Otherwise, double- or triple-differencing the satellite-to-receiver pseudorange and phase observables may be used.

Occasionally a GPS receiver may lose contact with a communicating GPS satellite. This could occur, for example, if a GPS receiver temporarily loses power or if an object temporar-

ily obstructs the line-of-sight path between the satellite and the receiver. In such situations, large outliers or sudden steps in the integer ambiguity may occur in the data stream. When the so-called cycle slips occur, combinations of the pseudorange and phase observables may be used to correct for the bias introduced by the short-term communication gaps (e.g., Blewitt, 2015, Sec. 3.11.2.3). The ability to detect and correct for cycle slips is now standard in most modern GPS processing packages.

Since the ground tracks of GPS satellites repeat at the period of one sidereal day, any errors associated with the geometry of the satellite constellation repeat with the same periodicity (e.g., Blewitt, 2015, Sec. 3.11.2.2). Multipath signals, for example, occur when satellite-transmitted EM waves arrive at the receiver indirectly (i.e., the waves are refracted through or reflected from neighboring objects, such as vegetation or buildings). As a rule of thumb, an elevation mask up to 15° above the horizon may be set in order to limit multipath errors, cycle slips, and tropospheric delays (Blewitt, 1997). Filtering the repeating multipath signals remains an active area of research (e.g., Larson et al., 2010; Ragheb et al., 2007; Blewitt, 2015, Sec. 3.11.1.7, and references therein).

F.4 Reference Frame Considerations

Spatial and temporal changes in mass loading at Earth's surface generate a deformation response of the solid Earth. One such response is due to a change in the "load moment" or, in other words, a shift in the center of mass of the global system of surface loads relative to the center of mass of the solid Earth (Blewitt et al., 2001). Such a shift is characterized by degree-one deformation. In tidal analysis, it is imperative that data and models be determined using consistent reference frames (e.g., Blewitt et al., 2001; Blewitt, 2003; Fu et al., 2012). Since GPS observations are often made relative to the entire Earth system (CM), it is best to predict deformations using load Love numbers computed in the CM reference frame (Blewitt, 2003; Fu et al., 2012). In GPS processing, orbit and clock products that are defined in, or tied to, a particular reference frame are referred to as **fiducial**. For orbit and clock products distributed by the Jet Propulsion Laboratory (JPL), information about the

adopted reference frame is provided in the `.frame` file.[17]

The International Terrestrial Reference Frame (ITRF), for example, is a realization of the International Terrestrial Reference System (ITRS) (Boucher, 2000; Altamimi et al., 2002; Ray et al., 2004; Altamimi et al., 2011). The reference frame is derived using a variety of space geodetic techniques: Very Long Baseline Interferometry (VLBI), Lunar Laser Ranging (LLR), Satellite Laser Ranging (SLR), Doppler and Radiopositioning Integrated by Satellite (DORIS), and GNSS. The ITRS, from which the ITRF is based, is geocentric, with the center of mass defined as that of the whole Earth system (including the solid Earth, oceans, and atmosphere) (Boucher, 2000). Such a reference frame is abbreviated CM, which stands for "center of mass of the Earth system" (Blewitt, 2003). CM is a natural reference frame for space geodetic techniques, such as the GPS, which observe the whole Earth system. Blewitt (2003) documents the CM frame, along with other isomorphic frames, and the relationships between them. For isomorphic reference frames, which are compatible with Love number theory, load Love numbers from one frame may be transformed into a different frame by a simple constant of proportionality, α (Blewitt, 2003).

[17] ftp://sideshow.jpl.nasa.gov/pub/JPL_GPS_Products/Final/

References

Abramowitz, M. & Stegun, I. A., 1964. *Handbook of mathematical functions: With formulas, graphs, and mathematical tables*, Courier Corporation, Dover Publications, New York.

Agnew, D. C., 1983. Conservation of mass in tidal loading computations, *Geophys. J. Int.*, **72**(2), 321–325.

Agnew, D. C., 1997. NLOADF: A program for computing ocean-tide loading, *J. Geophys. Res.*, **102**(B3), 5109–5110.

Agnew, D. C., 2012. SPOTL: Some programs for ocean-tide loading, *Scripps Institute of Oceanography Technical Report*.

Agnew, D. C., 2015. Earth Tides, *Treatise on Geophysics, 2nd Ed.*, **3**(06), 151–178.

Aki, K. & Richards, P. G., 1980. *Quantitative Seismology, Theory and Methods: Volume II*, W. H. Freeman and Company.

Allinson, C., Clarke, P., Edwards, S., King, M., Baker, T., & Cruddace, P., 2004. Stability of direct GPS estimates of ocean tide loading, *Geophys. Res. Lett.*, **31**(15), L15603.

Altamimi, Z., Sillard, P., & Boucher, C., 2002. ITRF2000: A new release of the International Terrestrial Reference Frame for earth science applications, *J. Geophys. Res.*, **107**(B10), 2214.

Altamimi, Z., Collilieux, X., & Métivier, L., 2011. ITRF2008: An improved solution of the International Terrestrial Reference Frame, *J. Geod.*, **85**(8), 457–473.

Alterman, Z., Jarosch, H., & Pekeris, C., 1959. Oscillations of the Earth, *Proc. R. Soc. London, Ser. A*, **252**(1268), 80–95.

Amante, C. & Eakins, B. W., 2009. *ETOPO1 1 arc-minute global relief model: Procedures, data sources and analysis*, US Department of Commerce.

Aster, R. C., Borchers, B., & Thurber, C. H., 2013. *Parameter estimation and inverse problems*, Academic Press.

Baker, T., 1980a. Tidal gravity in Britain: Tidal loading and the spatial distribution of the marine tide, *Geophys. J. Int.*, **62**(2), 249–267.

Baker, T., 1980b. Tidal tilt at Llanrwst, North Wales: Tidal loading and Earth structure, *Geophys. J. Int.*, **62**(2), 269–290.

Baker, T., 1984. Tidal deformations of the Earth, *Sci. Prog. Oxford*, **69**, 197–233.

Baker, T., Curtis, D., & Dodson, A., 1996. A new test of Earth tide models in central Europe, *Geophys. Res. Lett.*, **23**(24), 3559–3562.

Baker, T. F. & Bos, M. S., 2003. Validating Earth and ocean tide models using tidal gravity measurements, *Geophys. J. Int.*, **152**(2), 468–485.

Baker, T. F., Edge, R., & Jeffries, G., 1991. Tidal gravity and ocean tide loading in Europe, *Geophys. J. Int.*, **107**(1), 1–11.

Bar-Sever, Y. E., Kroger, P. M., & Borjesson, J. A., 1998. Estimating horizontal gradients of tropospheric path delay with a single GPS receiver, *J. Geophys. Res. Solid Earth*, **103**(B3), 5019–5035.

Bertiger, W., Desai, S. D., Haines, B., Harvey, N., Moore, A. W., Owen, S., & Weiss, J. P., 2010. Single receiver phase ambiguity resolution with GPS data, *J. Geod.*, **84**(5), 327–337.

Bevis, M., Alsdorf, D., Kendrick, E., Fortes, L. P., Forsberg, B., Smalley, R., & Becker, J., 2005. Seasonal fluctuations in the mass of the Amazon River system and Earth's elastic response, *Geophys. Res. Lett.*, **32**(16).

Bingham, R. J. & Hughes, C. W., 2008. The relationship between sea-level and bottom pressure variability in an eddy permitting ocean model, *Geophys. Res. Lett.*, **35**(3).

Blewitt, G., 1997. Basics of the GPS technique: Observation equations, *Geodetic Applications of GPS*, pp. 10–54.

Blewitt, G., 2003. Self-consistency in reference frames, geocenter definition, and surface loading of the solid Earth, *J. Geophys. Res.*, **108**(B2), 2103.

Blewitt, G., 2015. GPS and space-based geodetic methods, *Treatise on Geophysics, 2nd Ed.*, **3**, 307–338.

Blewitt, G., Lavallée, D., Clarke, P., & Nurutdinov, K., 2001. A new global mode of Earth deformation: Seasonal cycle detected, *Science*, **294**(5550), 2342–2345.

Boas, M. L., 1983. *Mathematical Methods in the Physical Sciences, 2nd Edition*, John Wiley & Sons., Inc.

Boehm, J., Werl, B., & Schuh, H., 2006. Troposphere mapping functions for GPS and very long baseline interferometry from European Centre for Medium-Range Weather Forecasts operational analysis data, *J. Geophys. Res. Solid Earth*, **111**(B2).

Boon, J., 2004. *Secrets of the tide: Tide and tidal current analysis and applications, storm surges and sea level trends*, Horwood Publishing.

Bos, M., 2010. Comment on "Anomalous ocean load tide signal observed in lake-level variations in Tierra del Fuego" by A. Richter et al., *Geophys. Res. Lett.*, **37**(4).

Bos, M. & Baker, T., 2005. An estimate of the errors in gravity ocean tide loading computations, *J. Geod.*, **79**(1), 50–63.

Bos, M. & Scherneck, H.-G., 2013. Computation of Green's Functions for Ocean Tide Loading, in *Sciences of Geodesy II*, ed. Xu, G., Springer-Verlag, Berlin.

Bos, M., Baker, T., Lyard, F., Zürn, W., & Rydelek, P., 2000. Long-period lunar earth tides at the geographic south pole and recent models of ocean tides, *Geophys. J. Int.*, **143**(2), 490–494.

Bos, M. S., Penna, N. T., Baker, T. F., & Clarke, P. J., 2015. Ocean tide loading displacements in western Europe. Part 2: GPS-observed anelastic dispersion in the asthenosphere, *J. Geophys. Res. Solid Earth*, **120**(9), 6540–6557.

Bosch, W., Savcenko, R., Flechtner, F., Dahle, C., Mayer-Gürr, T., Stammer, D., Taguchi, E., & Ilk, K.-H., 2009. Residual ocean tide signals from satellite altimetry, GRACE gravity fields, and hydrodynamic modelling, *Geophys. J. Int.*, **178**(3), 1185–1192.

Boucher, C., 2000. Terrestrial coordinate systems and frames, *Encyclopedia of Astronomy and Astrophysics*, **1**, 1906.

Carrère, L., Lyard, F., Cancet, M., Guillot, A., & Roblou, L., 2012. FES2012: A new global tidal model taking advantage of nearly 20 years of altimetry, in *Proceedings of meeting "20 Years of Altimetry"*, Venice.

Cartwright, D. & Edden, A., 1973. Corrected tables of tidal harmonics, *Geophys. J. R. Astron. Soc.*, **33**, 253–264.

Cartwright, D. & Taylor, R., 1971. New computations of the tide-generating potential, *Geophys. J. R. Astron. Soc.*, **23**, 45–74.

Cartwright, D. E., 1999. *Tides: A scientific history*, vol. 7, Cambridge University Press.

Cathles, L. M., 1975. *The viscosity of the Earth's mantle*, vol. 386, Princeton University Press: Princeton, NJ.

Chanard, K., Avouac, J., Ramillien, G., & Genrich, J., 2014. Modeling deformation induced by seasonal variations of continental water in the Himalaya region: Sensitivity to Earth elastic structure, *J. Geophys. Res. Solid Earth*, **119**(6), 5097–5113.

Chu, R., Schmandt, B., & Helmberger, D. V., 2012. Upper mantle P velocity structure beneath the Midwestern United States derived from triplicated waveforms, *Geochem., Geophys., Geosyst.*, **13**(2).

Crossley, D., 1975. The free-oscillation equations at the centre of the Earth, *Geophys. J. Int.*, **41**(2), 153–163.

Dach, R. & Dietrich, R., 2000. Influence of the ocean loading effect on GPS derived precipitable water vapor, *Geophys. Res. Lett.*, **27**(18), 2953–2956.

Dahlen, F. & Tromp, J., 1998. *Theoretical global seismology*, Princeton University Press: Princeton, NJ.

Darwin, G. H., 1898. *The tides and kindred phenomena in the Solar System: The substance of lectures delivered in 1897 at the Lowell Institute, Boston, Massachusetts*, Houghton, Mifflin, & Company: Boston and New York.

Desai, S. D. & Ray, R. D., 2014. Consideration of tidal variations in the geocenter on satellite altimeter observations of ocean tides, *Geophys. Res. Lett.*, **41**(7), 2454–2459.

Desai, S. D., Bertiger, W., & Haines, B. J., 2014. Self-consistent treatment of tidal variations in the geocenter for precise orbit determination, *J. Geod.*, **88**(8), 735–747.

Dill, R., Klemann, V., Martinec, Z., & Tesauro, M., 2015. Applying local Green's functions to study the influence of the crustal structure on hydrological loading displacements, *J. Geodyn.*, **88**, 14–22.

Doodson, A. T., 1921. The harmonic development of the tide-generating potential, *Proc. R. Soc. London, Ser. A*, **100**, 305–329.

Doodson, A. T., 1924a. Perturbations of harmonic tidal constants, *Proc. R. Soc. London, Ser. A*, **106**(739), 513–526.

Doodson, A. T., 1924b. Meteorological perturbations of sea-level and tides, *Geophys. J. Int.*, **1**(S4), 124–147.

Doodson, A. T., 1928. The analysis of tidal observations, *Philos. Trans. R. Soc. London, Ser. A*, **227**, 223–279.

Doodson, A. T., 1957. The analysis and prediction of tides in shallow water, *Int. Hydrogr. Rev.*, **41**, 85–126.

Doodson, A. T. & Warburg, H., 1941. *Admiralty Manual of Tides*, HMSO, London.

Dragert, H., James, T., & Lambert, A., 2000. Ocean loading corrections for continuous GPS: A case study at the Canadian coastal site Holberg, *Geophys. Res. Lett.*, **27**(14), 2045–2048.

Dziewonski, A. M. & Anderson, D. L., 1981. Preliminary reference Earth model, *Phys. Earth Planet. Inter.*, **25**(4), 297–356.

Egbert, G. D. & Erofeeva, S. Y., 2002. Efficient inverse modeling of barotropic ocean tides, *J. Atmos. Oceanic Technol.*, **19**(2), 183–204.

Egbert, G. D., Bennett, A. F., & Foreman, M. G., 1994. TOPEX/POSEIDON tides estimated using a global inverse model, *J. Geophys. Res. Oceans*, **99**(C12), 24821–24852.

Egbert, G. D., Erofeeva, S. Y., & Ray, R. D., 2010. Assimilation of altimetry data for nonlinear shallow-water tides: Quarter-diurnal tides of the Northwest European Shelf, *Cont. Shelf Res.*, **30**(6), 668–679.

Elosegui, P., Davis, J., Johansson, J., & Shapiro, I., 1996. Detection of transient motions with the Global Positioning System, *J. Geophys. Res. Solid Earth*, **101**(B5), 11249–11261.

Farrell, W., 1972a. Deformation of the Earth by surface loads, *Rev. Geophys.*, **10**(3), 761–797.

Farrell, W., 1972b. Global calculations of tidal loading, *Nature*, **238**(81), 43–44.

Farrell, W., 1973. Earth tides, ocean tides and tidal loading, *Philos. Trans. R. Soc. London, Ser. A*, **274**(1239), 253–259.

Fodor, I. K. & Stark, P. B., 2000. Multitaper spectrum estimation for time series with gaps, *IEEE T. Signal Proces.*, **48**(12), 3472–3483.

Fok, H. S., Shum, C., Yi, Y., Braun, A., & Iz, H. B., 2013. Evidences of seasonal variation in altimetry derived ocean tides in the Subarctic Ocean, *Terr. Atmos. Ocean. Sci.*, **24**(4), 605–613.

Foreman, M., 1977. Manual for tidal heights analysis and prediction, *Pacific Marine Science Report*, **77-10**, 1–58.

Foreman, M., Cherniawsky, J., & Ballantyne, V., 2009. Versatile harmonic tidal analysis: Improvements and applications, *J. Atmos. Oceanic Technol.*, **26**(4), 806–817.

Francis, O. & Dehant, V., 1987. Recomputation of the Green's functions for tidal loading estimations, *Bull. Inf. Mar. Terr.*, **no. 100**, 6962–6986.

Francis, O. & Mazzega, P., 1990. Global charts of ocean tide loading effects, *J. Geophys. Res. Oceans*, **95**(C7), 11411–11424.

Fu, Y., Freymueller, J. T., & van Dam, T., 2012. The effect of using inconsistent ocean tidal loading models on GPS coordinate solutions, *J. Geod.*, **86**(6), 409–421.

Fu, Y., Argus, D. F., & Landerer, F. W., 2015. GPS as an independent measurement to estimate terrestrial water storage variations in Washington and Oregon, *J. Geophys. Res. Solid Earth*, **120**(1), 552–566.

Gilbert, F. & Backus, G. E., 1966. Propagator matrices in elastic wave and vibration problems, *Geophysics*, **31**(2), 326–332.

Gilbert, F. & Dziewonski, A., 1975. An application of normal mode theory to the retrieval of structural parameters and source mechanisms from seismic spectra, *Philos. Trans. R. Soc. London, Ser. A*, **278**(1280), 187–269.

Goad, C. C., 1980. Gravimetric tidal loading computed from integrated Green's functions, *J. Geophys. Res. Solid Earth*, **85**(B5), 2679–2683.

Godin, G., 1972. *The Analysis of Tides*, University of Toronto Press.

Grand, S. P., 2002. Mantle shear–wave tomography and the fate of subducted slabs, *Philos. Trans. R. Soc. London, Ser. A*, **360**(1800), 2475–2491.

Grand, S. P. & Helmberger, D. V., 1984. Upper mantle shear structure of North America, *Geophys. J. Int.*, **76**(2), 399–438.

Gregorius, T., 1996. GIPSY-OASIS II: How it works, *Department of Geomatics, University of Newcastle upon Tyne*.

Guo, J., Li, Y., Huang, Y., Deng, H., Xu, S., & Ning, J., 2004. Green's function of the deformation of the Earth as a result of atmospheric loading, *Geophys. J. Int.*, **159**(1), 53–68.

Harrison, J., 1985. *Earth Tides (Benchmark Papers in Geology)*, Van Nostrand Reinhold Company Inc.

Hartmann, T. & Wenzel, H.-G., 1995. The HW95 tidal potential catalogue, *Geophys. Res. Lett.*, **22**(24), 3553–3556.

Hendershott, M., 1972. The effects of solid earth deformation on global ocean tides, *Geophys. J. Int.*, **29**(4), 389–402.

Hofmann-Wellenhof, B. & Moritz, H., 2005. *Physical Geodesy, Second Edition*, Springer.

Ishii, M. & Tromp, J., 1999. Normal-mode and free-air gravity constraints on lateral variations in velocity and density of Earth's mantle, *Science*, **285**(5431), 1231–1236.

Ito, T. & Simons, M., 2011. Probing asthenospheric density, temperature, and elastic moduli below the western United States, *Science*, **332**(6032), 947–951.

Jeffreys, H., 1961. Small corrections in the theory of surface waves, *Geophys. J. Int.*, **6**(1), 115–117.

Jentzsch, G., 1997. Earth tides and ocean tidal loading, in *Tidal Phenomena*, pp. 145–171, Springer.

Jordan, T. H., 1978. Composition and development of the continental tectosphere, *Nature*, **274**(5671), 544–548.

Karney, C. F., 2013. Algorithms for geodesics, *J. Geod.*, **87**(1), 43–55.

Kennett, B., Engdahl, E., & Buland, R., 1995. Constraints on seismic velocities in the Earth from traveltimes, *Geophys. J. Int.*, **122**(1), 108–124.

Khan, S. A. & Scherneck, H.-G., 2003. The M2 ocean tide loading wave in Alaska: Vertical and horizontal displacements, modelled and observed, *J. Geod.*, **77**(3-4), 117–127.

Khan, S. A. & Tscherning, C. C., 2001. Determination of semi-diurnal ocean tide loading constituents using GPS in Alaska, *Geophys. Res. Lett.*, **28**(11), 2249–2252.

King, M., 2006. Kinematic and static GPS techniques for estimating tidal displacements with application to Antarctica, *J. Geodyn.*, **41**(1), 77–86.

King, M. & Aoki, S., 2003. Tidal observations on floating ice using a single GPS receiver, *Geophys. Res. Lett.*, **30**(3).

King, M. A., Penna, N. T., Clarke, P. J., & King, E. C., 2005. Validation of ocean tide models around Antarctica using onshore GPS and gravity data, *J. Geophys. Res. Solid Earth*, **110**(B8).

King, M. A., Watson, C. S., Penna, N. T., & Clarke, P. J., 2008. Subdaily signals in GPS observations and their effect at semiannual and annual periods, *Geophys. Res. Lett.*, **35**(3).

Kustowski, B., Ekström, G., & Dziewoński, A., 2008. Anisotropic shear-wave velocity structure of the Earth's mantle: A global model, *J. Geophys. Res. Solid Earth*, **113**(B06306).

Lambeck, K., 1988. *Geophysical Geodesy: The slow deformations of the Earth*, Clarendon Press, Oxford.

Lambeck, K., 2005. *The Earth's variable rotation: Geophysical causes and consequences*, Cambridge University Press.

Lambert, A., Pagiatakis, S., Billyard, A., & Dragert, H., 1998. Improved ocean tide loading corrections for gravity and displacement: Canada and northern United States, *J. Geophys. Res. Solid Earth*, **103**(B12), 30231–30244.

Lanzano, P., 1982. *Deformations of an elastic earth (International Geophysics Series; v. 31)*, Academic Press, New York.

Lapwood, E. R. & Usami, T., 1981. *Free Oscillations of the Earth.*, Cambridge University Press.

Larson, K. M., Cervelli, P., Lisowski, M., Miklius, A., Segall, P., & Owen, S., 2001. Volcano monitoring using the Global Positioning System: Filtering strategies, *J. Geophys. Res.*, **106**(B9), 19453–19464.

Larson, K. M., Poland, M., & Miklius, A., 2010. Volcano monitoring using GPS: Developing data analysis strategies based on the June 2007 Kīlauea Volcano intrusion and eruption, *J. Geophys. Res. Solid Earth*, **115**(B7).

Latychev, K., Mitrovica, J. X., Ishii, M., Chan, N.-H., & Davis, J. L., 2009. Body tides on a 3-D elastic earth: Toward a tidal tomography, *Earth Planet. Sci. Lett.*, **277**(1–2), 86–90.

Le Provost, C., Genco, M., Lyard, F., Vincent, P., & Canceil, P., 1994. Spectroscopy of the world ocean tides from a finite element hydrodynamic model, *J. Geophys. Res. Oceans*, **99**(C12), 24777–24797.

Lin, F.-C., Schmandt, B., & Tsai, V. C., 2012. Joint inversion of Rayleigh wave phase velocity and ellipticity using USArray: Constraining velocity and density structure in the upper crust, *Geophys. Res. Lett.*, **39**(12), L12303.

Longman, I., 1962. A Green's function for determining the deformation of the Earth under surface mass loads: 1. Theory, *J. Geophys. Res.*, **67**(2), 845–850.

Longman, I., 1963. A Green's function for determining the deformation of the Earth under surface mass loads: 2. Computations and numerical results, *J. Geophys. Res.*, **68**(2), 485–496.

Love, A., 1909. The yielding of the Earth to disturbing forces, *Proc. R. Soc. London, Ser. A*, **82**(551), 73–88.

Love, A. E. H., 1911. *Some Problems of Geodynamics: Being an essay to which the Adams Prize in the University of Cambridge was Adjudged in 1911*, Cambridge University Press.

Lyard, F., Lefevre, F., Letellier, T., & Francis, O., 2006. Modelling the global ocean tides: Modern insights from FES2004, *Ocean Dyn.*, **56**(5-6), 394–415.

Mangiarotti, S., Cazenave, A., Soudarin, L., & Crétaux, J., 2001. Annual vertical crustal motions predicted from surface mass redistribution and observed by space geodesy, *J. Geophys. Res. Solid Earth*, **106**(B3), 4277–4291.

Martens, H. R., Simons, M., Owen, S., & Rivera, L., 2016. Observations of ocean tidal load response in South America from sub-daily GPS positions, *Geophys. J. Int.*, **205**, 1637–1664.

Meeus, J. H., 1998. *Astronomical Algorithms, 2nd Edition*, Willmann-BeIl, Inc.: Richmond, VA.

Melchior, P., 1983. *The tides of the planet Earth, 2nd Ed.*, Pergamon Press: Oxford, UK.

Merriam, J., 1985. Toroidal love numbers and transverse stress at the earth's surface, *J. Geophys. Res. Solid Earth*, **90**(B9), 7795–7802.

Merriam, J., 1986. Transverse stress: Green's functions, *J. Geophys. Res. Solid Earth*, **91**(B14), 13903–13913.

Molodenskiy, S., 1977. Relation between Love numbers and load factors, *Izvestiya, Earth Physics*, **13**(3), 147–149.

Montagner, J.-P. & Kennett, B., 1996. How to reconcile body-wave and normal-mode reference Earth models, *Geophys. J. Int.*, **125**(1), 229–248.

Munk, W. & Cartwright, D., 1966. Tidal Spectroscopy and Prediction, *Philos. Trans. R. Soc. London, Ser. A*, **259**(1105), 533–581.

Munk, W. & MacDonald, G., 1960. *The Rotation of the Earth*, Cambridge University Press: New York.

Na, S.-H. & Baek, J., 2011. Computation of the load Love number and the load Green's function for an elastic and spherically symmetric earth, *J. Korean Phys. Soc.*, **58**(5), 1195–1205.

Na, S.-H. & Moon, W., 2010. Analysis of Earth tide as whole-Earth forced oscillation and its computation, *J. Korean Phys. Soc.*, **56**, 1866.

Nordman, M., Virtanen, H., Nyberg, S., & Mäkinen, J., 2015. Non-tidal loading by the Baltic Sea: Comparison of modelled deformation with GNSS time series, *GeoResJ*, **7**, 14–21.

Okubo, S., 1988a. Asymptotic solutions to the static deformation of the Earth - I. Spheroidal mode, *Geophys. J. Int.*, **92**(1), 39–51.

Okubo, S., 1988b. Green's function to a point load - its dependence on Earth model, *Bulletin d'Information, Bureau Gravimétrique International*, **62**, 68–74.

Okubo, S., 1993. Reciprocity theorem to compute the static deformation due to a point dislocation buried in a spherically symmetric earth, *Geophys. J. Int.*, **115**(3), 921–928.

Okubo, S. & Endo, T., 1986. Static spheroidal deformation of degree 1 - Consistency relation, stress solution and partials, *Geophys. J. Int.*, **86**(1), 91–102.

Okubo, S. & Saito, M., 1983. Partial derivative of Love numbers, *Bulletin Géodésique*, **57**(1), 167–179.

Okubo, S., Saito, M., Endo, T., & Okubo, S., 1984. A correction to "Partial derivative of Love numbers", *J. Geod.*, **58**(1), 73–74.

Pagiatakis, S. D., 1990. The response of a realistic earth to ocean tide loading, *Geophys. J. Int.*, **103**(2), 541–560.

Parker, B. B., 2007. *Tidal analysis and prediction*, vol. NOAA Special Publication: NOS CO-OPS 3, US Department of Commerce, National Oceanic and Atmospheric Administration, National Ocean Service, Center for Operational Oceanographic Products and Services.

Pawlowicz, R., Beardsley, B., & Lentz, S., 2002. Classical tidal harmonic analysis including error estimates in MATLAB using T_TIDE, *Computers & Geosciences*, **28**(8), 929–937.

Penna, N. T., Bos, M. S., Baker, T. F., & Scherneck, H.-G., 2008. Assessing the accuracy of predicted ocean tide loading displacement values, *J. Geod.*, **82**(12), 893–907.

Penna, N. T., Clarke, P. J., Bos, M. S., & Baker, T. F., 2015. Ocean tide loading displacements in western Europe. Part 1: Validation of kinematic GPS estimates, *J. Geophys. Res. Solid Earth*, **120**(9), 6523–6539.

Petit, G. & Luzum, B., 2010. IERS Technical Note No. 36, IERS Conventions (2010), *International Earth Rotation and Reference Systems Service: Frankfurt, Germany*.

Petrov, L. & Boy, J.-P., 2004. Study of the atmospheric pressure loading signal in very long baseline interferometry observations, *J. Geophys. Res.*, **109**(B3).

Petrov, L. & Ma, C., 2003. Study of harmonic site position variations determined by very long baseline interferometry, *J. Geophys. Res. Solid Earth*, **108**(B4).

Ponte, R. M., 2006. Low-frequency sea level variability and the inverted barometer effect, *J. Atmos. Oceanic Technol.*, **23**(4), 619–629.

Ponte, R. M. & Gaspar, P., 1999. Regional analysis of the inverted barometer effect over the global ocean using TOPEX/POSEIDON data and model results, *J. Geophys. Res. Oceans*, **104**(C7), 15587–15601.

Ponte, R. M. & Ray, R. D., 2002. Atmospheric pressure corrections in geodesy and oceanography: A strategy for handling air tides, *Geophys. Res. Lett.*, **29**(24).

Press, W. H., Teukolsky, S. A., Vetterling, W. T., & Flannery, B. P., 2007. *Numerical recipes, 3rd Edition: The art of scientific computing*, Cambridge University Press.

Pugh, D., 1987. *Tides, Surges and Mean Sea-Level*, John Wiley & Sons Ltd.

Pugh, D., 2004. *Changing sea levels: Effects of tides, weather and climate*, Cambridge University Press.

Pugh, D. & Woodworth, P., 2014. *Sea-level Science: Understanding Tides, Surges, Tsunamis and Mean Sea-level Changes*, Cambridge University Press.

Pugh, D. T., Woodworth, P. L., & Bos, M. S., 2011. Lunar tides in Loch Ness, Scotland, *J. Geophys. Res. Oceans*, **116**(C11).

Ragheb, A., Clarke, P., & Edwards, S., 2007. Gps sidereal filtering: coordinate-and carrier-phase-level strategies, *J. Geod.*, **81**(5), 325–335.

Ray, J., Dong, D., & Altamimi, Z., 2004. IGS reference frames: Status and future improvements, *GPS Solut.*, **8**(4), 251–266.

Ray, R., 1998. Ocean self-attraction and loading in numerical tidal models, *Mar. Geod.*, **21**(3), 181–192.

Ray, R., 2013. Precise comparisons of bottom-pressure and altimetric ocean tides, *J. Geophys. Res. Oceans*, **118**(9), 4570–4584.

Ray, R. & Ponte, R., 2003. Barometric tides from ECMWF operational analyses, *Annales Geophysicae, European Geophysical Union*, **21**(8), 1897–1910.

Ray, R., Egbert, G., & Erofeeva, S., 2011. Tide predictions in shelf and coastal waters: Status and prospects, in *Coastal Altimetry*, pp. 191–216, Springer.

Ray, R., Luthcke, S., & van Dam, T., 2013. Monthly crustal loading corrections for satellite altimetry, *J. Atmos. Oceanic Technol.*, **30**, 999–1005.

Ray, R. D., 1999. A global ocean tide model from TOPEX/POSEIDON altimetry: GOT99. 2., *NASA Technical Memorandum 209478*.

Ray, R. D. & Byrne, D. A., 2010. Bottom pressure tides along a line in the southeast Atlantic Ocean and comparisons with satellite altimetry, *Ocean Dyn.*, **60**(5), 1167–1176.

Ray, R. D. & Egbert, G. D., 2004. The global S1 tide, *J. Phys. Oceanogr.*, **34**(8), 1922–1935.

Rebischung, P., Griffiths, J., Ray, J., Schmid, R., Collilieux, X., & Garayt, B., 2012. IGS08: The IGS realization of ITRF2008, *GPS Solut.*, **16**(4), 483–494.

Richter, A., Hormaechea, J., Dietrich, R., Perdomo, R., Fritsche, M., Del Cogliano, D., Liebsch, G., & Mendoza, L., 2009. Anomalous ocean load tide signal observed in lake-level variations in Tierra del Fuego, *Geophys. Res. Lett.*, **36**(5).

Richter, A., Hormaechea, J., Dietrich, R., Perdomo, R., Fritsche, M., Del Cogliano, D., Liebsch, G., & Mendoza, L., 2010. Reply to comment by MS Bos on "Anomalous ocean load tide signal observed in lake-level variations in Tierra del Fuego", *Geophys. Res. Lett.*, **37**(4).

Roosbeek, F., 1996. RATGP95: a harmonic development of the tide-generating potential using an analytical method, *Geophys. J. Int.*, **126**, 197–204.

Sabadini, R. & Vermeersen, B., 2004. *Global dynamics of the Earth: Applications of normal mode relaxation theory to solid-earth geophysics*, Kluwer Academic Publishers.

Saito, M., 1974. Some problems of static deformation of the Earth., *J. Phys. Earth*, **22**(1), 123–140.

Saito, M., 1978. Relationship between tidal and load Love numbers, *J. Phys. Earth*, **26**(1), 13–16.

Savcenko, R. & Bosch, W., 2012. EOT11a–empirical ocean tide model from multi-mission satellite altimetry, *DGFI Report*, **89**.

Schenewerk, M. S., Marshall, J., & Dillinger, W., 2001. Vertical ocean-loading deformations derived from a global GPS network., *J. Geod. Soc. Japan*, **47**(1), 237–242.

Scherneck, H.-G., 1991. A parametrized solid earth tide model and ocean tide loading effects for global geodetic baseline measurements, *Geophys. J. Int.*, **106**(3), 677–694.

Scherneck, H.-G. & Bos, M. S., 2002. Ocean tide and atmospheric loading, in *IVS 2002 General Meeting Proceedings*, pp. 205–214.

Schureman, P., 1971. *Manual of Harmonic Analysis and Prediction of Tides*, U.S. Department of Commerce, Coast and Geodetic Survey.

Schwiderski, E. W., 1980. On charting global ocean tides, *Rev. Geophys.*, **18**(1), 243–268.

Smylie, D., 2013. *Earth Dynamics: Deformations and Oscillations of the Rotating Earth*, Cambridge University Press.

Souchay, J., Mathis, S., & Tokieda, T., 2012. *Tides in astronomy and astrophysics*, vol. 861, Springer.

Stacey, F. D. & Davis, P. M., 2009. *Physics of the Earth: Fourth Edition*, Cambridge University Press.

Stammer, D., Wunsch, C., Fukumori, I., & Marshall, J., 2002. State estimation improves prospects for ocean research, *Eos Transactions*, **83**(27), 289–295.

Stammer, D., Ray, R., Andersen, O., Arbic, B., Bosch, W., Carrère, L., Cheng, Y., Chinn, D., Dushaw, B., Egbert, G., et al., 2014. Accuracy assessment of global barotropic ocean tide models, *Rev. Geophys.*, **52**(3), 243–282.

Stolz, A. & Larden, D., 1979. Seasonal displacement and deformation of the earth by the atmosphere, *Journal of Geophysical Research: Solid Earth*, **84**(B11), 6185–6194.

Sun, W. & Okubo, S., 1993. Surface potential and gravity changes due to internal dislocations in a spherical earth – i. theory for a point dislocation, *Geophys. J. Int.*, **114**(3), 569–592.

Takeuchi, H., 1950. On the Earth tide of the compressible Earth of variable density and elasticity, *Eos Transactions*, **31**(5), 651–689.

Takeuchi, H., 1966. *Theory of the Earth's Interior*, Blaisdell Publishing Company.

Takeuchi, H. & Saito, M., 1972. Seismic surface waves, in *Methods in Computational Physics, Volume 11/Seismology: Surface Waves and Earth Oscillations*, pp. 217–295, Academic Press.

Tarantola, A., 2005. *Inverse problem theory: And methods for model parameter estimation*, Society for Industrial and Applied Mathematics.

Thomas, I. D., King, M. A., & Clarke, P. J., 2007. A comparison of GPS, VLBI and model estimates of ocean tide loading displacements, *J. Geod.*, **81**(5), 359–368.

Thornton, S. & Marion, J., 2004. *Classical Dynamics of Particles and Systems 5th Ed.*, Brooks/Cole: Belmont, CA.

Trabant, C., Hutko, A. R., Bahavar, M., Karstens, R., Ahern, T., & Aster, R., 2012. Data products at the IRIS DMC: Stepping stones for research and other applications, *Seismol. Res. Lett.*, **83**(5), 846–854.

Tregoning, P. & van Dam, T., 2005. Atmospheric pressure loading corrections applied to GPS data at the observation level, *Geophys. Res. Lett.*, **32**(22).

Tregoning, P. & Watson, C., 2009. Atmospheric effects and spurious signals in GPS analyses, *J. Geophys. Res.*, **114**(B9).

Tregoning, P. & Watson, C., 2011. Correction to "Atmospheric effects and spurious signals in GPS analyses", *J. Geophys. Res.*, **116**(B2).

Tsai, V. C., Ampuero, J.-P., Kanamori, H., & Stevenson, D. J., 2013. Estimating the effect of earth elasticity and variable water density on tsunami speeds, *Geophysical Research Letters*, **40**(3), 492–496.

van Dam, T. & Herring, T., 1994. Detection of atmospheric pressure loading using very long baseline interferometry measurements, *J. Geophys. Res. Solid Earth*, **99**(B3), 4505–4517.

van Dam, T., Wahr, J., Chao, Y., & Leuliette, E., 1997. Predictions of crustal deformation and of geoid and sea-level variability caused by oceanic and atmospheric loading, *Geophys. J. Int.*, **129**(3), 507–517.

van Dam, T., Wahr, J., Milly, P., Shmakin, A., Blewitt, G., Lavallée, D., & Larson, K., 2001. Crustal displacements due to continental water loading, *Geophys. Res. Lett.*, **28**(4), 651–654.

van Dam, T., Altamimi, Z., Collilieux, X., & Ray, J., 2010. Topographically induced height errors in predicted atmospheric loading effects, *J. Geophys. Res. Solid Earth*, **115**(B7).

van Dam, T., Collilieux, X., Wuite, J., Altamimi, Z., & Ray, J., 2012. Nontidal ocean loading: Amplitudes and potential effects in GPS height time series, *J. Geod.*, **86**(11), 1043–1057.

van Dam, T. M., Blewitt, G., & Heflin, M. B., 1994. Atmospheric pressure loading effects on Global Positioning System coordinate determinations, *J. Geophys. Res.*, **99**(B12), 23939–23950.

van den Dool, H., Saha, S., Schemm, J., & Huang, J., 1997. A temporal interpolation method to obtain hourly atmospheric surface pressure tides in reanalysis 1979–1995, *J. Geophys. Res. Atmos.*, **102**(D18), 22013–22024.

Varga, P., 1983. Potential free love numbers, *Manuscripta Geodetica*, **8**, 85–92.

Varga, P., 1992. Complete description of forced tangential elastic deformations, *Phys. Earth Planet. Inter.*, **73**(3), 199–205.

Vey, S., Calais, E., Llubes, M., Florsch, N., Woppelmann, G., Hinderer, J., Amalvict, M., Lalancette, M., Simon, B., Duquenne, F., et al., 2002. GPS measurements of ocean loading and its impact on zenith tropospheric delay estimates: A case study in Brittany, France, *J. Geod.*, **76**(8), 419–427.

Vinogradova, N. T., Ponte, R. M., & Stammer, D., 2007. Relation between sea level and bottom pressure and the vertical dependence of oceanic variability, *Geophys. Res. Lett.*, **34**(3).

Wang, H., Xiang, L., Jia, L., Jiang, L., Wang, Z., Hu, B., & Gao, P., 2012. Load Love numbers and Green's functions for elastic Earth models PREM, iasp91, ak135, and modified models with refined crustal structure from Crust 2.0, *Computers & Geosciences*, **49**, 190–199.

Wang, R., 1997. Tidal response of the solid Earth, in *Tidal Phenomena*, pp. 27–57, eds Wilhelm, H., Zürn, W., & Wenzel, H.-G., Springer.

Wenzel, H.-G., 1997. Tide-generating potential for the Earth, in *Tidal Phenomena*, pp. 9–26, Springer.

Wessel, P. & Smith, W. H., 1996. A global, self-consistent, hierarchical, high-resolution shoreline database, *J. Geophys. Res. Solid Earth*, **101**(B4), 8741–8743.

Wessel, P., Smith, W. H., Scharroo, R., Luis, J., & Wobbe, F., 2013. Generic mapping tools: Improved version released, *Eos Transactions*, **94**(45), 409–410.

Widmer, R., Masters, G., & Gilbert, F., 1991. Spherically symmetric attenuation within the Earth from normal mode data, *Geophys. J. Int.*, **104**(3), 541–553.

Wiggins, R. A., 1968. Terrestrial variational tables for the periods and attenuation of the free oscillations, *Phys. Earth Planet. Inter.*, **1**(4), 201–266.

Williams, S. & Penna, N., 2011. Non-tidal ocean loading effects on geodetic GPS heights, *Geophys. Res. Lett.*, **38**(9).

Woodhouse, J., 1988. The calculation of eigenfrequencies and eigenfunctions of the free oscillations of the Earth and the Sun, in *Seismological Algorithms: Computational Methods and Computer Programs*, pp. 321–370, Academic Press.

Wright, J., Colling, A., & Park, D., 1999. *Waves, tides, and shallow-water processes*, Butterworth-Heinemann, in association with The Open University.

Wu, P. & Peltier, W., 1982. Viscous gravitational relaxation, *Geophys. J. Int.*, **70**(2), 435–485.

Wu, X., Collilieux, X., Altamimi, Z., Vermeersen, B., Gross, R., & Fukumori, I., 2011. Accuracy of the International Terrestrial Reference Frame origin and earth expansion, *Geophys. Res. Lett.*, **38**(13).

Wu, X., Ray, J., & van Dam, T., 2012. Geocenter motion and its geodetic and geophysical implications, *J. Geodyn.*, **58**, 44–61.

Wunsch, C. & Stammer, D., 1997. Atmospheric loading and the oceanic "inverted barometer" effect, *Rev. Geophys.*, **35**(1), 79–107.

Yeh, T.-K., Huang, C., & Xu, G., 2008. GPS height and gravity variations due to ocean tidal loading around Taiwan, *Surv. Geophy.*, **29**(1), 37–50.

Yuan, L. & Chao, B. F., 2012. Analysis of tidal signals in surface displacement measured by a dense continuous GPS array, *Earth Planet. Sci. Lett.*, **355**, 255–261.

Yuan, L., Chao, B. F., Ding, X., & Zhong, P., 2013. The tidal displacement field at Earth's surface determined using global GPS observations, *J. Geophys. Res. Solid Earth*, **118**, 2618–2632.

Zahel, W., 1997. Ocean Tides, in *Tidal Phenomena*, pp. 113–143, Springer.

Zerbini, S., Matonti, F., Raicich, F., Richter, B., & van Dam, T., 2004. Observing and assessing nontidal ocean loading using ocean, continuous GPS and gravity data in the Adriatic area, *Geophys. Res. Lett.*, **31**(23).

Zumberge, J., Heflin, M., Jefferson, D., Watkins, M., & Webb, F., 1997. Precise point positioning for the efficient and robust analysis of GPS data from large networks, *J. Geophys. Res.*, **102**(B3), 5005–5017.

Zürn, W., 1997. The nearly-diurnal free wobble-resonance, in *Tidal Phenomena*, pp. 95–109, eds Wilhelm, H., Zürn, W., & Wenzel, H.-G., Springer.